Author:
Pennington, Derek Steven

Title:
The anisotropic small strain stiffness of Cambridge Gault Clay.

The anisotropic small strain stiffness of Cambridge Gault clay

by

Derek Steven Pennington

BSc MSc (CapeTown) MPhil (Cantab) CEng MICE

A thesis submitted to

The University of Bristol

in accordance with the requirements of the

degree of Doctor of Philosophy in the

Faculty of Engineering,

Department of Civil Engineering

March 1999

61000 Words

Abstract

New bender element devices have been developed to enable the small strain anisotropic stiffness of the Cambridge Gault clay to be investigated in a laboratory study based on triaxial testing incorporating orthogonal shear wave velocity and local strain measurement. These have enabled complete exploration of the influences at small strain on the cross-anisotropy of a clay. It has been shown that the Gault clay is significantly anisotropic, and that evaluations of shear moduli based on assumed isotropy are misleading.

A triaxial soils testing system capable of resolving vertical and horizontal strains on 100 mm diameter samples down to 0.001% strain was commissioned. While the system included bender elements for the measurement of vertical shear wave velocity $V_{s(vh)}$, it was shown that end effects can lead to errors of up to 30% in this measurement. Two sets of devices were developed to measure horizontal shear wave velocities, $V_{s(hv)}$ and $V_{s(hh)}$, though the mid-height of a triaxial sample. These were a bender belt with orthogonal mini bender elements mounted in the pads of a horizontal strain measuring belt, and bender probes, also incorporating orthogonal mini bender elements, but with geometric and installation similarities to mid-height pore pressure transducers.

The shear modulus, $G_{0(ij)}$, and the anisotropy of shear modulus given by $G_{0(hh)}/G_{0(hv)}$, were investigated by measuring $V_{s(ij)}$ during stress path tests carried out on both reconstituted and natural samples of Gault clay. The tests on reconstituted samples focused on exploration of the parameters involving voids ratio and stress state. They showed that $G_{0(ij)}$ is inherently anisotropic, and that anisotropy is proportional to voids ratio for a material that has experienced one dimensional consolidation. This anisotropy is defined as the ratio $G_{0(hh)}/G_{0(hv)}$ and was found to increase by 0.58 for every log cycle decrease in voids ratio. Further, it was confirmed both implicitly and explicitly that $G_{0(ij)}$, and the ratio $G_{0(hh)}/G_{0(hv)}$, are highly dependent on stress state in the plane *ij*, whereas they are insensitive to the stress normal to the plane *ij*. The equation given by Hardin and Blandford (1989) was found to be inadequate for describing the influences on anisotropy, and an alternative incorporating directional functions of voids ratio was proposed.

High quality triaxial testing with local small strain measurements of ε_v and ε_h were carried out on undisturbed samples of natural Gault clay. The samples were reconsolidated to the *in situ* stress state from where multiple mini stress path excursions were carried out, and orthogonal shear wave velocities measured to enable deduction of cross-anisotropic elastic parameters.

The three parameter formulations, (G' K' J', G^* K^* J and E^* ν^* α), used to describe the cross-anisotropic behaviour of soils, were investigated. It was shown that all of them are functions of the four independent parameters E'_v E'_h ν'_{vh} and ν'_{hh}. An alternative three parameter formulation comprising E'_v ν'_{vh} and F'_h ($= E'_h/(1+\nu'_{hh})$) was presented and shown to provide as complete a description of soil behaviour as any of the other three parameter formulations, yet probably with more reliable values.

The test results enabled assessment of all five independent cross-anisotropic parameters $E_{0(h)}$ $E_{0(v)}$ $\nu_{0(vh)}$ $\nu_{0(hh)}$ and $G_{0(hv)}$ at very small strain, and found them to be consistent with the theory of elasticity. That the independent shear modulus G'_{hv} cannot be measured in a conventional triaxial test was emphasised by indicating the wide discrepancies that exist between correctly measured values of $G_{0(hv)}$ and derivations based incorrectly on assumptions of either isotropy or a three parameter model. The anisotropy of natural Gault clay at *in situ* stress states was shown to be highly anisotropic with anisotropy ratios $E_{0(h)}/E_{0(v)} = 4.0$ and $G_{0(hh)}/G_{0(hv)} = 2.3$.

Acknowledgements and dedication

I am grateful to the EPSRC for sponsoring the research project on which this thesis is based, and the Building Research Establishment for providing the clay samples. The successful design, fabrication and assembly of the laboratory equipment and bender devices would not have been possible without the willingness to share ideas by Jim Bennell, University of Wales at Bangor, Vojkan Jovičić, now of Arup Geotechnics, and colleagues at City University, London, and Steve Ackerley, Imperial College, London. Mike Pope has been invaluable in the manufacture and development of the devices, and provided endless wise words on what is possible with the aged tools in the department workshops. Tim Hetherington assisted in the laboratory testing, and Andrew Ridley, Imperial College, gave selflessly of his time to take suction measurements and advise on testing methods. David Hight arranged for the scanning electron microscope and fabric photographs and provided encouraging distractions involving use of the new bender devices on site at Bothkennar, Scotland. Martin Lings and David Nash suffered tirelessly my enthusiasms, scrutinised many harebrained ideas and provided help and guidance. I am extremely grateful to them for their distinctive support and comradeship.

This project was carried out during one period of leave of absence from Arup Geotechnics, and finally completed during another. I am extremely grateful to Arup Geotechnics for this flexibility, and visionary support, and in particular to colleagues who wrestled with concepts and challenged me to keep the real world of Geotechnics in mind.

Pam Sharpe suffered late night interruptions due to "a vital stage of testing", had the sensitivity to allow me distractions, proof-read the script, and supported me in every way towards final completion of this document. For these and everything, my lifelong thanks are due.

I would like to dedicate this work to Ron, who schooled me in mathematics and the stratagems of a "Mr Fixit". Both the science and art enabled the efforts recounted in the pages that follow. Thank you Dad!

Declaration

I declare that the work in this dissertation was carried out in accordance with the *Regulations of the University of Bristol*. The work is original except were indicated by special reference in the text and no part of this dissertation has been submitted for any other degree.

Parts of the work have and are in the process of being published under joint authorship, and therefore represent collaborative efforts. I acknowledge the detailed and significant contributions of David Nash and Martin Lings in the preparation of the following papers:

Pennington, D. S., Nash, D. F. T. & Lings, M. L. (1997). Anisotropy of G_0 shear stiffness in Gault Clay. *Géotechnique* **47**, No. 3, 391-398.

Nash, D. F. T., Pennington, D. S. & Lings, M. L. (1999). Stiffness anisotropy and voids ratio functions for Gault Clay. *Proceedings 2nd International Symposium on Pre-Failure Deformation Characteristics of Geomaterials (IS Torino 99)*

Lings, M. L., Pennington, D. S. & Nash, D. F. T. Anisotropic elastic parameters and their measurement in stiff natural clay. *Géotechnique* , Submitted Jan 1999

Any views expressed in the dissertation are personal and in no way represent those of the University of Bristol. The dissertation has not been presented to any other University for examination either in the United Kingdom or overseas.

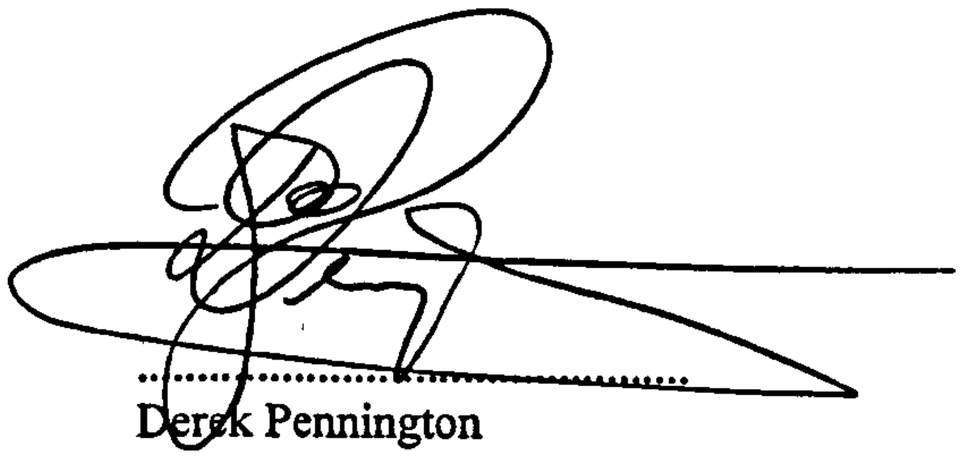

.....

Derek Pennington

Contents

List of symbols and abbreviations

1 D	refers to one dimensional consolidation / swelling
A	cross-sectional area of triaxial sample
A/D	Analogue to Digital converter
A_0	initial cross-sectional area of triaxial sample
a_{ab}	coefficients in generalised 3D stiffness matrix
C_e	electrical capacitance
C_m	mechanical impedance of piezo ceramic
c_v	coefficient of consolidation
D	displacement of bender tip
D_0	initial sample diameter
DSO	Digital Storage Oscilloscope
ΔT_L	transducer drift as gradient of line in transducer units per day
e	voids ratio
E'_h E'_v	horizontal / vertical Young's modulus
E^*	a Young's modulus parameter (Graham & Houlsby, 1983)
E_G E_T	transducer error representing gross / typical scatter band
E_u	undrained Young's modulus
f	bender driver pulse frequency
F	deviatoric force on triaxial sample measured by load cell
$F(e)$	voids ratio function as defined by Hardin and Blandford (1989)
F'_h	horizontal modulus ($=E'_h/(1-\nu'_{hh})$)
f_R	resonant frequency
G'	a shear modulus (Atkinson *et al.*, 1990)
G'_{hh} G'_{hv}	horizontal / vertical shear modulus ($G'_{hv} \equiv G'_{vh}$)
G^*	a shear modulus (Graham & Houlsby, 1983)
G_{max}	terminology for $G_{0(vh)}$ frequently used in the literature
$G_{0(ij)}$	very small strain shear moduli in the *ij* plane
G_s	specific gravity of soil particles
J'	a coupling modulus (Atkinson *et al.*, 1990)
J'_{pq}, J'_{qp}	coupling moduli (Hird & Pierpoint, 1994)
J^*	a coupling modulus (Graham & Houlsby, 1983)
k	an exponent applied to *OCR* that depends on the plasticity index of the soil
K'	a bulk modulus (Atkinson *et al.*, 1990)
K^*	a bulk modulus (Graham & Houlsby, 1983)
K_0	coefficient of earth pressure at rest
l, w, t	length, width and thickness of bender element
L_t	transmission length between bender tips in *i* direction
LVDT	Linearly Variable Differential Transducer

LDT	Local Deformation Transducer - based on bending strain in elastic metal strip
M	effective mass of piezo ceramic
M_s	mass of solids in a soil
m_v	coefficient of volume change
M_w	mass of water
N	electro-mechanical transducer ratio for a piezo-ceramic
nij	stress exponents
OCR	Over Consolidation Ratio
p′	effective triaxial confining pressure = $(\sigma'_v + 2\,\sigma'_h)/3$
p_0'	normalising mean effective stress
p_a	atmospheric pressure
p_r	a reference stress taken to have a value of 1 kPa in this thesis
PC	Personal Computer
q	deviator stress = $\sigma'_v - \sigma'_h$
R_d	frequency ratio term for shearwave interpretation
S_{ij}	a dimensionless elastic stiffness coefficient
SPC	Stress Path Cell
S_R	degree of saturation
T_{ij}	transmission time of shear wave propagated in *i* direction with *j* polarisation
UPS	Uninterruptible Power Supply
v_0	initial sample volume
VCM	Volume Change Meter
v_s	volume of solids
$V_{s(ij)}$	shear wave velocity for wave propagated in *i* direction with *j* polarisation
w	moisture content
x	index applied to voids ratio defined by Lo Presti (1989)
x y z	horizontal / horizontal / vertical axes in Cartesian system
$G_{(0)iso}$	very small strain pseudo-isotropic shear modulus
α	anisotropy parameter (Graham & Houlsby, 1983)
β	stress ratio function
γ_{xy} γ_{yz}, γ_{zx}	shear strain in horizontal / vertical / vertical plane
ε_h ε_v	horizontal direct strain / vertical direct strain
ε_p ε_q	triaxial volumetric strain / distortional strain
ε_{xx}, ε_{yy} ε_{zz}	horizontal / horizontal / vertical direct strain in Cartesian co-ordinates
η	stress ratio = *q/p′*
θ	change in stress path angle in *q vs. p′* space
κ	slope of unload-reload line in *v vs.* ln *p′* space
λ	slope of normal compression line in *v vs.* ln *p′* space
λ_{ij}	wavelength of shear wave propagated in *i* direction with *j* polarisation

ν'_{hh} ν'_{hv} ν'_{vh}	Poisson's ratios horizontal to horizontal / horizontal to vertical / vertical to horizontal
ν^*	a Poisson's ratio parameter (Graham & Houlsby, 1983)
ρ	bulk density
σ'_h σ'_v	effective horizontal / vertical stress
σ'_i σ'_j	principal effective stress in the *i* direction / in the *j* direction
σ'_{xx}, σ'_{yy} σ'_{zz}	effective horizontal / horizontal / vertical stress in Cartesian co-ordinates
τ_{xy} τ_{yz}, τ_{zx}	shear stress in horizontal / vertical / vertical plane
ϕ'	effective angle of friction

prefix δ	indicates small increment
subscript "$_0$"	indicates value at very small strain
subscript $_{ij}$	indicates plane in which parameter is measured, and usually involves combinations of *h* and *v*, horizontal and vertical
superscript $'$	indicates effective stress parameter

List of tables

List of figures

1. INTRODUCTION

1.1 Background to the project

Safe and efficient design of geotechnical structures requires good prediction of the interaction between ground and structure. This interaction will be governed by both soil and structure stress/strain parameters, *in situ* stress states, and construction techniques. These parameters feed into detailed back analysis of the behaviour of structures offering the opportunity to refine methods of predicting this interaction, and thereby improving our design capability. This thesis is about developing techniques to measure, and measuring stiffness properties of the Cambridge Gault clay, with the goal of providing better soil parameters for geotechnical back analysis.

Lings *et al.* (1991) had the opportunity to monitor the behaviour of a deep excavation in the Cambridge Gault clay and compare it with that predicted during design. The 65 m × 45 m Lion Yard site in the centre of Cambridge was developed as a three level underground car park with a hotel complex above ground. The structure was founded on large diameter bored piles and the 10 m deep excavation was retained by a diaphragm wall constructed using the top down method. Back analysis of this excavation, Ng *et al.* (1995b), showed that high values of soil stiffness had to be inferred to account for the small ground movements and significant reduction in lateral stress in the ground. This stiffness was of the order suggested by Powell & Butcher (1991) on the basis of *in situ* geophysical measurements carried out at the High Cross[‡] test site, which is considered representative of the Lion Yard site despite lying some 3 km to the east. However, no complete determination of stiffness properties was available, and a research contract[§] was initiated to investigate stiffness of the Cambridge Gault clay. This thesis has resulted from the subsequent research project.

The role of significant non-linearity in the explanation of ground movements has long been realised, e.g. Simpson *et al.* (1979). However at this time parameters derived from laboratory data were still found to result in significant over predictions of movements, and it was not until the development of local strain measuring devices (Jardine *et al.* 1984) that significant advances could be made towards measuring the stiffness of soils at small strain, and laboratory measurements began to approach those measured *in situ* with geophysical techniques. At about the same time Dyvik & Madshus (1985) reported the use of shear wave techniques in the laboratory following installation of bender elements in triaxial, direct simple shear, oedometer and resonant column devices to measure what they termed G_{max}, or what shall be referred to in this thesis as G_0 - the initial shear stiffness in the vertical plane.

In both field and laboratory techniques where shear wave velocity is determined, the shear modulus is derived from the shear wave velocity, V_s, using the relationship given by Equation 1.1:

---

‡ This test site is misleadingly referred to as the Madingley Test site by Powell and Butcher, (1991)
§ EPSRC contract GR/JR46302, Directors Nash, DFT, Lings, ML and Davison, LR. *Small strain stiffness of Cambridge Gault clay*

$$G_0 = \rho V_s^2 \quad \text{..... Equation 1.1}$$

where ρ is the bulk density.

The initial shear modulus G_0, is now widely considered to be a fundamental soil stiffness property. It is not only material to the prediction of soil structure interaction but also to practical geotechnical problems in earthquake engineering, particularly with the advent of sophisticated finite element analysis techniques for the prediction of the engineering behaviour of foundations, excavations and tunnels. Usual engineering interest however extends to larger strain, where the typical strain levels are higher by some orders of magnitude, and plastic deformation is therefore of more significance. G_0 on its own is therefore not usually sufficient for making predictions of the geotechnical performance of structures.

Although G_0 is often not directly relevant to strains of engineering interest, the reliable determination of G_0 offers the possibility of inferring complete stress-strain curves from an assumed functional relationship between shear modulus degradation and strain.

More recently there has been growing awareness that the anisotropy of clay soils may also be significant in the prediction of soil / structure interaction. For example, numerical analyses by Lee & Rowe (1989) and Simpson *et al.* (1996) have highlighted the importance of considering anisotropy when predicting deformations due to tunnelling. Anisotropy of G_0 - denoted in this thesis by $G_{0(ij)}$, the initial shear modulus in the plane *ij* - provides an indication of the initial structure of the soil resulting from its geological history. This will in turn influence the anisotropy of the plastic stress-strain response at larger strains, and the anisotropy of permeability of the soil.

Sedimentary soils might be expected to behave as cross-anisotropic materials, with the same (or similar) stiffness in all horizontal directions, but with different vertical stiffness. Strong indications of naturally occurring cross-anisotropy have been widely observed in geophysical field tests, e.g. White *et al.* (1983); Butcher & Powell (1995); Sully & Campanella (1995).

Cross-anisotropy of an elastic material is described by reducing the fully anisotropic elastic description given by 21 independent material properties, to cross-anisotropy which is represented by five independent elastic constants E_v E_h ν_{vh} ν_{hh} and G_{hv} (Love, 1927). Shear deformations in the horizontal plane are governed by the dependent shear modulus G_{hh} as given in Equation 1.2 where:

$$G_{hh} = \frac{E_h}{2(1+\nu_{hh})} \quad \text{..... Equation 1.2}$$

However it is difficult to obtain both non-linear and anisotropic stress strain data necessary for use in state-of-the-art constitutive models. Most small strain and bender G_0 measurements have been carried out in triaxial cells, yet the shear modulus G_{hv} cannot be measured in a triaxial cell. Further, it has been possible to measure only the initial shear modulus, $G_{0(vh)}$, in the vertical plane using bender techniques

developed to date. There was therefore a need to develop techniques and equipment to measure small strain anisotropic parameters in the laboratory.

This thesis describes the development of devices and techniques which were used to carry out a laboratory based exploration of the anisotropy of the Cambridge Gault clay over the small and very small strain range.

1.2 Objectives

The primary goal of the project was to investigate the small strain anisotropic stiffness of the Cambridge Gault clay. This required not only the development of new bender equipment, but also the establishment of a high quality triaxial test facility at Bristol University to bring it into line with current small strain testing capabilities. The objectives set for the project were:

- to establish a laboratory triaxial testing facility capable of measuring small strain stiffness using local strain measuring devices,
- to develop bender element devices to measure anisotropic shear moduli $G_{0(ij)}$,
- to explore the factors which influence $G_{0(ij)}$ in the Cambridge Gault clay,
- to compare laboratory measurements of $G_{0(ij)}$ on samples reconstituted to the *in situ* stress state with field measurements of $G_{0(ij)}$,
- to measure the anisotropic stiffness of natural Cambridge Gault clay in the small strain range using both the shear wave and local small strain testing devices developed for the triaxial stress path cell.

1.3 Thesis structure

Following this introduction, Chapter 2 describes the state of the art in relation to significant testing developments incorporating small strain and bender element devices. Developments in the understanding of the factors influencing the anisotropy of soils are discussed, and finally significant previous investigations of anisotropy in the triaxial cell are discussed.

Chapter 3 starts with a description of the establishment of high quality triaxial stress path testing facilities, involving three Bishop Wesley stress path cells at Bristol University, before discussing in detail the design, fabrication and commissioning of new bender devices to measure $G_{0(ij)}$. The success of these devices provided the main focus for the advances in equipment for soils testing developed in the project.

Chapter 4 introduces the methodology used to sample, prepare and test the Cambridge Gault clay. It begins by setting the regional geological context of the deposit before describing in detail methods used to obtain 250 mm diameter undisturbed samples, the techniques used to prepare and set samples in the

triaxial cells, and the testing programme carried out. The later sections of the chapter consider the validation of both the small strain and bender element data.

Chapter 5 presents the results of the shear wave explorations of the anisotropy of $G_{0(ij)}$. The first half of the chapter considers tests carried out on reconstituted samples to investigate the influence of soil state (as defined by voids ratio and stress state) on $G_{0(ij)}$. The results of these investigations are used to provide context to measurements of $G_{0(ij)}$ obtained from both laboratory tests on undisturbed samples and *in situ* shear wave measurements of Gault clay at its natural state.

Chapter 6 considers the deduction of cross anisotropic parameters from the results of small strain triaxial measurements and bender element tests carried out during stress path tests on undisturbed samples. These show convincingly that the Cambridge Gault clay is highly anisotropic, and that innovative approaches using multiple mini stress path excursions in the triaxial cell can lead to the successful derivation of cross-anisotropic parameters in the small strain range.

Chapter 7 draws together conclusions from the investigations, and in the context of acknowledging the limitations of the project, suggests further work.

The figures referred to in the text are grouped by chapter following the references.

2. THE STATE OF THE ART

2.1 Introduction

Muir Wood (1995) in introducing a session on the *Evaluation of material properties* in a conference devoted to pre-failure deformation of geo-materials, noted that all testing is conducted against a background of an assumed material model. Measurement of properties implies that we know what form these properties take and ***we*** therefore have to have a clear model of material behaviour in mind. As engineers who use material properties, we have to choose the appropriate model to view the material and then hone in on the property to be measured. If that model is too narrow we will fail to observe some features of the behaviour which we have implicitly chosen to ignore.

This project is about measurement of soil properties and is specifically centred on the measurement of the shear modulus, most frequently referred to as an isotropic modulus, G, but in the context of this study which includes anisotropy, G_{ij} where ij refers to the plane within which the modulus is measured. The model used to visualise shear modulus must therefore broaden to encompass anisotropy.

Lee & Rowe (1989) have identified that because of arching support mechanisms induced by tunnelling, high shear strains may be expected to develop around tunnel openings. In order to model the pre-failure deformation associated with these shear strains, it was important to adopt realistic values of G_{vh} and E_v in the analyses. Arching support mechanisms may also be expected to be significant in deep basement structures. In such structures it is likely that both G_{vh} and G_{hh} along with E_v and E_h may be expected to influence deformation. However, as Lee and Rowe point out, measurements of these anisotropic stiffness parameters are difficult to obtain, and design frequently proceeds on the basis of assumed properties.

This chapter will describe:

- techniques for measuring the small strain stiffness of soils,
- the implications of anisotropy on the measurement of shear modulus in the triaxial cell,
- previous studies of the small strain anisotropy of soils using triaxial equipment.

2.2 The measurement of small strain stiffness

2.2.1 Static local strain measurement of small strain stiffness

The introduction of local strain measuring devices to soils testing by Jardine *et al.* (1984), and the improvement of the reliability of data capture at small strains, has led to improvements in the use of such data when modelling soil / structure interaction. This broadening of our vision to appreciate soil non-linearity has arguably been the most significant contribution to advances in design practice over the past decade. It has also focused our attention on methods to measure stiffness to ever lower strain levels. Atkinson & Sällfors (1991) idealised divisions of strain into very small, small and large as indicated in

Figure 2.1, and these relate to a typical "backbone" shaped curve of stiffness plotted against log strain. Below a critical strain level, ε_c, the backbone shows essentially constant stiffness, interpreted to represent the elastic small strain stiffness. In the same paper, Atkinson & Sällfors (1991) estimated the limit of reliable measurement of local strain to be approximately 0.005% strain. This was modified two years later with a revised limit for local strain of 0.0015% as shown in Figure 2.2 where strain ranges appropriate to other techniques are also indicated. By 1995, Cuccovillo & Coop (1997) had further improved their application using locally mounted LVDT's to reliable resolutions of approximately 0.0002% strain.

The challenge to develop devices to measure strains locally has continued to be taken up at laboratories around the world. A comprehensive review of the development of devices and their relative capabilities (current at the time this project was started) is given by Scholey *et al.* (1995). Subsequent developments e.g. Heymann *et al.* (1997) have focused on improved calibration techniques which enable use of current transducers at significantly higher resolutions than specified by manufacturers.

Strain measurements to levels of 10^{-3} to 10^{-4} % strain extend the line representing local strain measurement shown in Figure 2.2 well into the range covered by dynamic methods of testing, including resonant column and bender element techniques. These techniques will be discussed before attempting to resolve any issues of compatibility between static and dynamic techniques.

2.2.2 Dynamic methods for measuring very small strain stiffness

Dynamic methods of determining stiffness moduli in elastic media are based on body wave velocity measurements.

The theory of propagation of elastic waves in fluid saturated elastic porous media was initially given by Biot (1956). In this theory propagation of elastic waves is dependent on a large number of parameters, ranging from density and compressibility of pore fluid and solid grains, to the elastic properties of the solid skeleton, and to the magnitude of viscous and inertial coupling. Gajo & Mongiovì (1994) have shown that for low viscous coupling, as may be expected for a clay, (and this definitely includes the Gault clay), the velocity of the compression wave in an isotropic soil, (also known as the primary wave because it travels faster and therefore is seen to arrive before the shear, or secondary wave) is given by:

$$V_p = \sqrt{\frac{M + \alpha^2 Q}{(1-n)\rho_s + n\rho_f}} \quad \text{..... Equation 2.1}$$

where M is the constrained modulus of the soil skeleton given by:

$$M = \frac{E(1-\nu)}{(1-2\nu)(1+\nu)} \quad \text{..... Equation 2.2}$$

$$\frac{1}{Q} = \frac{n}{K_f} + \frac{\alpha - n}{K_s} \quad \text{..... Equation 2.3}$$

$$\alpha = 1 - \frac{K}{K_s} \quad \text{..... Equation 2.4}$$

and n is porosity, ρ_s and ρ_f are the solid grain and pore fluid densities, K_f and K_s are the bulk moduli of the solid grains and pore fluid, E is the Young's modulus of the solid skeleton in the direction of wave propagation, ν is the Poisson's ratio of the solid skeleton relating strain transverse to the propagation direction and K is the bulk modulus. The shear wave velocity in an isotropic soil is given by:

$$V_s = \sqrt{\frac{G_0}{(1-n)\rho_s + n\rho_f}} \quad \text{..... Equation 2.5}$$

where G_0 is the shear modulus of the soil and $(1\text{-}n)\rho_s + \rho_f = \rho$ is the bulk density of the soil.

It can be seen from Equations 2.1 and 2.5 that whereas the compression wave velocity is proportional to both the Young's modulus E of the soil and the relative bulk moduli of the soil particles and pore fluid, the shear wave velocity relates directly to the shear modulus of the soil. On the basis of their analyses, Gajo & Mongiovì (1994) conclude that G can be measured with both certainty and accuracy of the order of 1-2%, whereas K and M are highly sensitive to the stiffness of the solid skeleton. Even for stiff clays where the effects of coupling have been evaluated correctly, the error in K may be up to 60%. For this reason the decision was taken in this project not to pursue the measurement of compression wave velocity, and to focus on improvements in the accurate measurement of V_s and ρ.

Shear wave velocity is deduced from either pulse excitation or continuous vibration torsional resonance techniques. Torsional resonance measurements are usually carried out in a resonant column (RC) test (Richart *et al.* 1970) while pulse excitation methods include:

- shear plates (based on quartz crystal or piezo-ceramic transducers),
- bender elements (based on bimorph piezo-ceramic transducers).

Details of the more traditional implementation of these techniques are reviewed by Bennell & Taylor-Smith (1991) and apart from bender element techniques will not be considered in any detail in this thesis.

Resonant column devices can only measure the shear wave velocity in one direction in each test, namely that which propagates between the top and base of the sample. Similarly, where bender elements have been incorporated in oedometers and triaxial cells, they are generally used to measure shear-wave velocity propagated in only one direction with one polarity.

Explorations of the equivalence of G_0 measured using either bender elements or resonant column methods include Dyvik & Madshus (1985) and Thomann & Hryciw (1990). Results of the comparisons from these

two sources, based on measurements carried out on the same samples at the same time, are reproduced in Figure 2.3. Clearly there are indications of broad agreement between the two techniques. However differences between individual determinations of the ratio $G_{max\ bender} / G_{max\ RC}$ vary from 1.30 through zero to 0.92, a range of some 38% in the case of Dyvik & Madshus (1985), and 1.10 to 0.95, a range of 15% in the case of Thomann & Hryciw (1990). This in itself implies discrepancy in excess of normal testing accuracy, and suggests that further scrutiny of conventional bender element techniques is warranted.

While Dyvik & Madshus (1985) were not the first to introduce bender elements to soils testing, they can arguably be credited with developing the first bender elements suitable for use in saturated soils. Their design, illustrated in Figure 2.4, incorporated an epoxy coating which successfully insulated the high impedance piezo-ceramic from the conductive environment of the soil. No further review of bender element design aspects will be given here, but will be considered in detail in Chapter 3, along with the design of the new bender element devices developed in this project.

2.2.3 The rationalisation of static and dynamic methods

The problem of matching strain dependent moduli from more than one apparatus has perplexed engineers for decades. However more recently Woods (1994) argued that "we should no longer distinguish between 'dynamic' and 'static' properties as they are indeed a continuum, and we should rather distinguish properties on the basis of strain level. A rational analysis of small strain behaviour requires a soil testing system that is capable of accurately defining the behaviour of soils at strain levels comparable with those encountered in dynamic tests is required and now exists." Similarly Jardine (1995) notes that research into linear elastic properties has intensified simply because static and dynamic behaviour can be unified.

While much of this research effort has concentrated on testing sands, Georgiannou *et al.* (1991), Powell & Butcher (1991), Stokoe *et al.* (1995), Pierpoint (1996) and Coop *et al.* (1997) have, amongst others, all extended their comparisons to clays. The research tools employed include resonant column devices, torsional shear devices and the triaxial cell. Comparisons are drawn between accurate small strain measurements and shear moduli determined from shear-wave velocity measurements. The success of the comparisons vary, and it may be argued that it is the failure to consider anisotropy in the model used to view the soil that is responsible for the discrepancies, rather than any fundamental incompatibility.

2.3 Anisotropy

2.3.1 Anisotropy in geophysics

Over the past three decades a number of developments in the understanding of anisotropic media have been published mainly in the geophysical literature, and while these refer specifically to seismological problems, they nevertheless have relevance to a study into the anisotropy of a clay soil.

Anisotropy is a rather common phenomenon, (Crampin, 1981), and may be caused by a variety of mechanisms including crystal alignments, lithological alignments, stress induced effects (both direct and

indirect), regular sequences of fine layers, commonly aligned cracks and other two-phase configurations. These mechanisms, may cause effective anisotropy in geo-materials, and also in many man-made structures.

The geophysical implications of anisotropy are most keenly applied to hydrocarbon production. For example, Crampin & Lovell (1991) consider it in fractured reservoir characterisation, with financial implications which dwarf those of geotechnical structures. Nevertheless, this body of literature does offer relevant insights to the information that may be obtained from wave propagation data, and in this case, particularly with reference to shear waves. Crampin (1985) holds that shear waves are usually complicated and rich in information whereas compression waves are simple and poor in information. This is well illustrated in the behaviour of shear waves crossing an anisotropic region is illustrated schematically in Figure 2.5. A shear -wave travelling along a propagation path generally splits into two components with different arrival times and different, but often nearly orthogonal, polarisations. In geophysical measurements it has been found that the polarisation of the fastest component is usually parallel or sub-parallel to the direction of maximum horizontal stress. This splitting appears to be caused by stress aligned fluid-filled cracks, micro-cracks and preferentially oriented pore spacings, which pervade most rocks in the uppermost 10 to 20 km of the crust. While this obviously has implications for geophysical exploration, its implication at a much smaller scale in soils testing applications is also clear. For example, despite possible variations between the axes of the test sample, and orientations of the anisotropy, shear waves passing though the sample will tend to adopt the polarisation of the anisotropy. By measuring the difference in propagation time between waves polarised in the principal planes of anisotropy, different shear moduli representing the anisotropy of the sample can be obtained.

2.3.2 Anisotropic elasticity

Investigation of anisotropy is most simply carried out within a framework of elasticity. Hooke's law of elasticity, *Ut tensio sic vis*, (Hooke, 1675), can be generalised for use in three dimensions with axes x, y horizontal and z vertical. This is given in Equation 2.6:

$$\begin{bmatrix} \varepsilon_{xx} \\ \varepsilon_{yy} \\ \varepsilon_{zz} \\ \gamma_{yz} \\ \gamma_{zx} \\ \gamma_{xy} \end{bmatrix} = \begin{bmatrix} a_{11} & a_{12} & a_{13} & a_{14} & a_{15} & a_{16} \\ a_{21} & a_{22} & a_{23} & a_{24} & a_{25} & a_{26} \\ a_{31} & a_{32} & a_{33} & a_{34} & a_{35} & a_{36} \\ a_{41} & a_{42} & a_{43} & a_{44} & a_{45} & a_{46} \\ a_{51} & a_{52} & a_{53} & a_{54} & a_{55} & a_{56} \\ a_{61} & a_{62} & a_{63} & a_{64} & a_{65} & a_{66} \end{bmatrix} \cdot \begin{bmatrix} \sigma_{xx} \\ \sigma_{yy} \\ \sigma_{zz} \\ \tau_{yz} \\ \tau_{zx} \\ \tau_{xy} \end{bmatrix} \quad \text{..... Equation 2.6}$$

where strains are related to stresses through a matrix of 36 coefficients of the form a_{ab}. Elastic strain energy considerations, and the laws of thermodynamics require the symmetry of this matrix, (Love, 1927), and therefore:

$$a_{ab} = a_{ba} \quad \text{..... Equation 2.7}$$

This reduces the number of coefficients from 36 to 21. While it is theoretically possible to determine this matrix without making any further assumptions on symmetry, most natural materials show some behavioural symmetry, which results in cross-coupling between the normal and shear components of stress and strain, (Lekhnitskii, 1963), and the number of coefficients can be reduced further. Crampin (1981) has summarised the elastic tensors of the six most symmetric anisotropic symmetry systems and these are reproduced in Figure 2.6. These matrices represent increasing degrees of anisotropy starting from the case of isotropy (where there is complete behavioural symmetry and only two coefficients are needed), and develop towards monoclinic anisotropy, which is described by 13 independent parameters.

Soils, while not strictly inherently anisotropic, have almost invariably had anisotropy imposed on them through the processes by which they were formed. Gravity has influenced all earthly formation of soils, and the vertical direction consequently retains significance with the variation of properties usually reflecting this vertical significance. This is the form of anisotropy usually known in the physics and geophysics literature as *hexagonal anisotropy*, (Crampin 1981), but as *transverse anisotropy* or *cross-anisotropy* in the soil mechanics literature (Graham and Houlsby 1983).

2.3.3 The implications of anisotropy to the measurement of shear stiffness in the small strain range

Elastic cross-anisotropy is described by five independent parameters. The form of the compliance matrix given by Crampin (1981) for a cross anisotropic material can be used to relate strain increments to stress increments as shown in Equation 2.8.

$$\begin{bmatrix} \delta\varepsilon_{xx} \\ \delta\varepsilon_{yy} \\ \delta\varepsilon_{zz} \\ \delta\gamma_{yz} \\ \delta\gamma_{zx} \\ \delta\gamma_{xy} \end{bmatrix} = \begin{bmatrix} a & b & c & . & . & . \\ b & a & c & . & . & . \\ c & c & d & . & . & . \\ . & . & . & e & . & . \\ . & . & . & . & e & . \\ . & . & . & . & . & x \end{bmatrix} \begin{bmatrix} \delta\sigma'_{xx} \\ \delta\sigma'_{yy} \\ \delta\sigma'_{zz} \\ \delta\tau_{yz} \\ \delta\tau_{zx} \\ \delta\tau_{xy} \end{bmatrix} \quad \text{..... Equation 2.8}$$

In this equation, stress and strain increments are referred to rectangular Cartesian axes with the z-axis vertical. By identifying that the material properties are the same in both the horizontal directions, the five independent coefficients (a to e in Equation 2.8) can be written in terms of elastic parameters referred to only two directions, vertical, "v", and horizontal, "h". This resulting compliance matrix is illustrated in Equation 2.9:

$$\begin{bmatrix} \delta\varepsilon_{xx} \\ \delta\varepsilon_{yy} \\ \delta\varepsilon_{zz} \\ \delta\gamma_{yz} \\ \delta\gamma_{zx} \\ \delta\gamma_{xy} \end{bmatrix} = \begin{bmatrix} \boxed{\begin{matrix} \frac{1}{E_h} & \frac{-\nu_{hh}}{E_h} & \frac{-\nu_{vh}}{E_v} \\ \frac{-\nu_{hh}}{E_h} & \frac{1}{E_h} & \frac{-\nu_{vh}}{E_v} \\ \frac{-\nu_{vh}}{E_h} & \frac{-\nu_{vh}}{E_h} & \frac{1}{E_v} \end{matrix}} & \begin{matrix} . & . & . \\ . & . & . \\ . & . & . \end{matrix} \\ \begin{matrix} . & . & . \\ . & . & . \\ . & . & . \end{matrix} & \begin{matrix} \frac{1}{G_{vh}} & . & . \\ . & \frac{1}{G_{vh}} & . \\ . & . & \frac{2(1+\nu_{hh})}{E_h} \end{matrix} \end{bmatrix} \begin{bmatrix} \delta\sigma'_{xx} \\ \delta\sigma'_{yy} \\ \delta\sigma'_{zz} \\ \delta\tau_{yz} \\ \delta\tau_{zx} \\ \delta\tau_{xy} \end{bmatrix} \quad \text{..... Equation 2.9}$$

where the five independent elastic parameters are defined as follows:

E_v = Young's modulus in the vertical direction

E_h = Young's modulus in the horizontal direction

ν_{vh} = Poisson's ratio for horizontal strain due to vertical strain

ν_{hh} = Poisson's ratio for horizontal strain due to horizontal strain at right angles

G_{vh} = Shear modulus in the vertical plane (also written as G_{hv})

and the shear modulus term given by $x = 2(a\text{-}b)$ in Equation 2.8 has a similar relationship in Equation 2.9 with $1/G_{hh} = 2(1+\nu_{hh})/E_h$.

In triaxial tests only the components of the stiffness matrices enclosed within dashed boxes in Equations 2.8 and 2.9 can be investigated. So, while for an isotropic material $G_{hh} = G_{hv} = 2(a\text{-}b)$, and the shear modulus can be determined using either triaxial or shear wave velocity measurements, for a cross-anisotropic material, only partial investigation of the shear modulus G_{hh} is possible[§]. Therefore G_{vh} as determined from measurements of shear wave velocity using bender elements mounted in the platens of a triaxial cell or resonant column, cannot be compared with any moduli derived from static measurements for a cross-anisotropic material using these instruments.

In many cases in the literature no explicit reference is made to the assumptions on which the measurement of a shear modulus is made, and this can lead to confusion. Two examples will be considered: Atkinson *et al.* (1993), and Coop *et al.* (1997).

- Atkinson *et al.* (1993) present results of shear stiffness for London Clay determined from triaxial shear tests carried out at constant mean effective stress, $p' = (\sigma'_v + 2\sigma'_h)/3$. The shear modulus G' was defined as $3G' = dq / d\varepsilon_s$ where $dq = (\sigma'_v - \sigma'_h)$ and $\varepsilon_s = 2(\varepsilon_v - \varepsilon_h)/3$. It is implied that the evaluation of G' using this approach enables comparison at small strain with measurements of $G_{\alpha(vh)}$ obtained using bender elements propagating shear waves in the vertical direction. Isotropy has therefore been implicitly assumed despite previous experience of anisotropic behaviour of London clay, (Atkinson,

[§] Details of the possible ways of evaluating shear moduli using triaxial tests will be explored in Chapter 6.

1973), albeit at higher strain levels.

- Coop *et al.* (1997) compared soils stiffness in laboratory tests using dynamic and static loading. The dynamic measurements were obtained using bender elements mounted in the platens of triaxial cells, and the continuous loading measurements were obtained from undrained triaxial compression tests carried out on the same samples. In this case zero volume strain ($d\varepsilon_p$) is assumed and the shear modulus is defined as $G^* = (dq / d\varepsilon_v)/3$ **. Comparisons for tests carried out on kaolin and Boom clay are reproduced in Figure 2.7 where the triaxial modulus G^* is normalised by the bender modulus G_0. For kaolin Figure 2.7a shows comparable values of normalisedG_0^* and $G_{0(vh)}$ at 0.0001% vertical strain for one of the four tests, with the remaining three tests showing $G_0^* \approx 0.88\ G_{0(vh)}$. The comparison for Boom clay in Figure 2.7b indicates that on average $G_0^* \approx 0.6\ G_{0(vh)}$. Whereas Coop *et al.* (1997) attributed the significant differences in the Boom clay comparison to possible rate effects, it will be argued in this thesis on the basis of the Gault clay (which has similarities to the Boom clay), that anisotropy is more likely to be responsible for this difference.

These two examples probably reflect the inadequacy of triaxial tests more than any intentional disregard for anisotropy in a real soil. Comparisons of dynamic and static measurements can be more accurately carried out using alternative techniques. For example, in order to explore the continuum of strain Lo Presti *et al.* (1995) used a combination of resonant column, bender elements, triaxial tests and torsional hollow cylinder testing. Rampello & Silvestri (1993) used cyclic and dynamic torsional shear tests to study the continuity of G_{vh} on samples of two over-consolidated clays. These studies show reasonable agreement. However there are still clearly differences between measurements carried out using different instruments, and these differences are probably more an indication of influences of the test methods themselves on the measurements. There is therefore still a caution that when exploring small strain stiffness close consideration should still be given to precisely understanding the constraints implied by the test method itself.

2.4 Previous studies of the anisotropic stiffness of clays

2.4.1 Laboratory exploration of the influence of stress-volume soil state on $G_{0(ij)}$

In Section 2.2.2 Equation 2.5 was used to describe the relationship between G_0 and V_s for an isotropic soil on the basis of Biot's theory. It can however be extended for anisotropic soils simply by defining both the modulus, G_0, and the shear wave velocity, V_s, in terms of the co-incidental plane *ij* within which they exist. This expansion is shown in Equation 2.10:

** Note that the term G^* has been introduced here to refer to tests carried out at zero volumetric strain, whereas G' was used previously to refer to tests carried out at constant p'. A more detailed discussion of the implication of these differences is included in Chapter 6.

$$V_{s(ij)} = \sqrt{\frac{G_{0(ij)}}{\rho}} \quad \text{.....Equation 2.10}$$

From this equation the anisotropy of shear moduli at very small strain, $G_{0(ij)}$ can be explored. As generators and receivers of shear waves, bender elements should offer opportunities to investigate these cross anisotropic shear moduli. Yet most previous research has only used vertical platen mounted bender elements in triaxial cells, e.g. Viggiani (1992a); Rampello *et al.* (1994a); Jovičić *et al.* (1996), and this configuration severely limits the investigation possibilities. The main limitations are:

- end effects lead to non-uniform stress fields through which the shear waves travel,
- only a single shear wave path can be investigated at any one time so that comparisons between orthogonal shear moduli cannot be performed within a single test set-up.

Experimental data for sands have confirmed that small strain anisotropy incorporates two basic components: inherent anisotropy and stress-induced anisotropy, Roesler (1979); Stokoe *et al.* (1985); Bellotti *et al.* (1995). By comparison, there have been few investigations into the anisotropy of natural and reconstituted clays. The notable exception is Jamiolkowski *et al.* (1995). Their interpretation of data is based on relationships and terminology which incorporate the discovery by Roesler (1979) that the elastic stiffness of sand is independent of the stress normal to the plane of shear. Tests were carried out on fine round grained sand in a cubical sample 30 cm squared. The main test results are reproduced in Figure 2.8 where the symbols σ'_a σ'_p and σ'_s denote the three principal effective stresses with σ'_a acting in the direction of propagation, and σ'_p acting in the direction of polarisation, and σ'_s normal to the plane defined by σ'_a and σ'_p. The important discovery is that shear wave velocity increases when either σ'_a or σ'_p increases, but is independent of σ'_s. Curves fitted to the data points in Figure 2.8 are defined by $V_s = (G_{0(ap)} / \rho)^{1/2}$ where $G_{0(ap)} = K(\sigma'_a \sigma'_p)^{n/2}$, K is a constant and $n = 0.5$. This discovery was incorporated in the expression used to introduce the concept of a reference fabric (Hardin & Black 1969; Hardin, 1978 and Hardin & Blandford, 1989) given by Equation 2.11:

$$G_{ij} = \frac{OCR^k}{F(e)} \frac{S_{ij}}{2(1+\nu)} p_a^{1-n} \left(\sigma'_i \sigma'_j\right)^{n/2} \quad \text{.....Equation 2.11}$$

where G_{ij} is the elastic shear modulus in the plane containing the principal stresses σ_i' and σ_j', and p_a is the atmospheric pressure. The combination of these stresses defines stress-related components of anisotropy. The components influencing fabric anisotropy include OCR, the power ^{k} which depends on the plasticity index of the soil, the elastic isotropic Poisson's ratio ν, a dimensionless elastic stiffness coefficient S_{ij}, and the voids ratio function given by:

$$F(e) = 0.3 + 0.7e^2 \quad \text{.....Equation 2.12}$$

Jamiolkowski *et al.* (1995) use this equation as the basis for their study of six Italian clays using instrumented oedometers. The oedometers had vertical bender elements to measure $V_{s(vh)}$, horizontal

benders to measure $V_{s(hh)}$ and pressure transducers to measure horizontal stress under K_0 conditions. The layout of bender elements in the oedometer is illustrated schematically in Figure 2.9a. In order to interpret their data, a modified version of Equation 2.11 was proposed as given in Equation 2.13. In this equation the stress dependency is based on the effective stresses in the plane of the propagating shear wave:

$$G_{0(ij)} = S_{ij} F(e)(OCR)^k \, p_a^{(1-ni-nj)} (\sigma'_i)^{ni} (\sigma'_j)^{nj} \quad \text{.....Equation 2.13}$$

In these expressions S_{ij} refers to similarly non-dimensional material constants reflecting the soil's fabric, p_a is again atmospheric pressure, and the stress exponent ^{n} has been separated into exponents ^{ni} and ^{nj} which are applied to σ_i' and σ_j' respectively, noting however that $^{2n} = {}^{ni} \approx {}^{nj}$. The voids ratio function $F(e)$ is that adopted on the basis of Lo Presti (1989) and Jamiolkowski *et al.* (1991) given by Equation 2.14:

$$F(e) = e^{-x} \quad \text{.....Equation 2.14}$$

where "e" is the voids ratio. The value of ^{x} is proposed to be 1.3 by Lo Presti (1995) [††]. Consistent with this, Jamiolkowski *et al.* (1995) show that if the state of a soil is expressed as a combination of e and p', then further effects of over-consolidation, other than determining the current value of e, are not expected. Hence the effect of OCR in Equation 2.11 is negligible, the index $^k \approx 0$.

Jamiolkowski *et al.* (1995) used Equation 2.13 to describe the very small strain shear modulus both in the plane perpendicular to the bedding plane, and within the bedding plane, but were only able to carry out their investigations on samples tested under one dimensional compression / extension states.

Results from tests carried out on Pisa and Panigaglia clays are summarised in Figure 2.9b to e. These show the normalised values of $G_{0(hh)}$ and $G_{0(vh)}$ and of their ratio during the tests. The data show reasonably clear trends. Best fit curves to the data appear to give a reasonable comparison with the form of Equation 2.13, apparently confirming for clays the Roesler (1979) findings for sands that $G_{0(ij)}$ depends only on the stresses in the plane of propagation and polarisation. However, the authors note that difficulties arise when attempting to measure σ'_h during recompression stages, so that only data obtained in virgin compression and unload phases of tests can be utilised. This makes impossible any rigorous exploration of the influence of voids ratio functions, OCR or material constants S_{ij} as given in Equations 2.13 and 2.14, and reiterates the need for development of bender devices that can measure horizontal shear wave velocities in triaxial tests where stresses and stress ratios can be controlled.

In an alternative approach, Jovičić & Coop (1998) used a conventional bender arrangement in a triaxial cell, (i.e. a single pair of platen mounted bender elements), to measure the anisotropy within reconstituted kaolin and both reconstituted and natural London clay samples. Rather than having multiple shear wave paths aligned within and perpendicular to the plane of deposition on a single sample of clay, multiple sub-

---

[††] It is presumed that this is based on assessments of G_{vh} using a combination of bender element and resonant column tests, although this is not explicitly stated.

sampling was carried out along orthogonal directions as shown in Figure 2.10a, and these sampling directions aligned with the bender elements in the triaxial cell. While this approach does not have the limitation of not being able to control stress paths as in the oedoemeter described by Jamiolkowski *et al.* (1995), the range of investigation is nevertheless very limited. Strain induced anisotropy can be investigated by only one measurement of $G_{0(ij)}$ on each sample under isotropic stress states. Stress effects cannot be investigated because the stress perpendicular to the plane of propagation and polarisation of a vertically propagated shear wave cannot be varied independently in a triaxial cell. Nevertheless, two sets of results from these investigations are considered. Figure 2.10b shows the relationship between $G_{0(hh)}$ $G_{0(hv)}$ and $G_{0(vh)}$ *vs.* confining isotropic stress for tests carried out on samples on natural London clay. This shows that London clay is essentially strongly cross anisotropic since $G_{0(hv)} \approx G_{0(vh)}$ and $G_{0(hh)} / G_{0(hv)} \approx 1.5$. Figure 2.10c shows the influence on anisotropy, defined both by $G_{0(hh)} / G_{0(hv)}$ and strain ratio $\Delta\varepsilon_h / \Delta\varepsilon_v$, as samples of reconstituted London clay are isotropically consolidated to high stress. Up to the preconsolidation pressure of 1000 kPa both ratios remain essentially constant, but afterwards, whereas the strain increment ratio immediately becomes isotropic, the convergence of the $G_{0(hh)} / G_{0(hv)}$ data is only gradual, indicating that the effects of strain induced anisotropy on $G_{0(ij)}$ persist long after they are removed from the engineering strain behaviour of the sample.

In a significantly earlier investigation using resonant column techniques, Saada *et al.* (1978) created isotropic and anisotropic samples of kaolin which were then also sampled either horizontally or vertically to assess the anisotropy of E' and G'. The data showed the importance of considering anisotropy, and as with the bender tests described by Jovičić & Coop (1998), they were able to illustrate that an anisotropic clay does not easily turn into an isotropic one, even after severe cyclic strains. Interestingly, in their introduction they stated "....it is now generally recognised that the fabric of a clay has a substantial effect on its response under static loading. Indeed relatively recent studies have shown that cross-anisotropic clays do not follow many of the concepts whose validity has been taken for granted for many years Yet relatively little effort has been made to study the influence of anisotropy on the dynamic behaviour." That sentiment is still valid some 20 years later. The evidence for significant anisotropy in clay soils is well acknowledged, but how to measure very small strain anisotropy using dynamic methods in the practice of geotechnics remains an issue which this thesis addresses.

2.4.2 Laboratory derived parameters for constitutive models

While the measurement of anisotropic dynamic properties is a goal in itself, as described in the previous section, knowledge of dynamic anisotropic material properties alone is inadequate when it comes to requiring parameters for constitutive models which incorporate the non-linearity of stiffness over a range of strain. This section will consider possible formulations which enable recovery of non-linear anisotropic parameters from triaxial tests, and present a recent example.

The difficulty with measuring anisotropic properties does not apply to soil mechanics alone. Techniques have been considered with respect to more general materials testing spheres for some time. Van

Cauwelaert (1977) provided a solution to the problem of measuring cross anisotropic parameters by proposing a formulation which reduced the five coefficients of cross-anisotropic elasticity to three. The five anisotropic parameters can be written in terms of the three parameters, E, v and n, where n is the assumed degree of anisotropy given by $n = E_v / E_h$, as shown in Equations 2.15:

$$E_v = E$$

$$E_h = \frac{E}{n}$$

$$v_{vh} = v$$

$$v_{hh} = \frac{v}{n}$$

$$G_{vh} = \frac{E}{1+n+2v} \quad \text{..... Equations 2.15}$$

Some time later, and quite without reference to Van Cauwelaert (1977), Graham and Houlsby (1983) independently considered the limitations of the triaxial cell to measurement of cross anisotropy in soils and developed a very similar formulation involving the three parameters E^*, v^* and α. Again the five independent parameters (and one dependent parameter) can be established in terms of these three parameters using the relationships shown in Equations 2.16:‡‡

$$E_v = E^*$$

$$E_h = \alpha^2 E^*$$

$$v_{vh} = \frac{v^*}{\alpha}$$

$$v_{hh} = v^*$$

$$G_{vh} = \frac{\alpha E^*}{2(1+v^*)}$$

$$G_{hh} = \alpha G_{vh} = \frac{\alpha^2 E^*}{2(1+v^*)} \quad \text{..... Equations 2.16}$$

Both of these formulations imply restrictions on the form of anisotropy in the model, with the factors n and α controlling the ratio of Young's modulus, Poisson's ratio and shear modulus terms.

Graham and Houlsby (1983) illustrated the significance of their formulation with the results of triaxial tests carried out on Winnipeg clay. Clay samples were reconsolidated to the K_0 *in situ* stress, and then loaded along controlled straight lines paths in q *vs.* p' space in order to define the yield locus. Sample results from their testing programme are reproduced in Figure 2.11. Two plots in Figure 2.11a illustrate

---

‡‡ A more complete derivation of the Graham and Houlsby (1983) model will is given in Chapter 6 along with consideration of alternative formulations.

the slope change points used to determine the yield surface in a particular test. Only data from within this yield surface were used in the subsequent analysis on the basis that they represented approximately elastic behaviour. As can be seen, the data correspond to strains of the order of 2%, and would not be referred to as "elastic" in more current terminology. However, linear elasticity appears reasonable at the plotting scale shown, and the slopes of the pre-yield lines were interpreted to give measured values of the equivalent bulk and shear moduli K_{eq} and G_{eq}. For all tests, these determinations are plotted against the direction of the stress path in q *vs.* p' space in Figure 2.11b. This illustrates clearly that K_{eq} and G_{eq} are not constants, which indicates anisotropy. The data sets were further interpreted in both the three parameter cross-anisotropic formulation involving E^*, ν^* and α, and the isotropic two parameter formulation involving only E and ν. Average results of this interpretation for the data set are given in Table 2.1, using the relationships given in Equations 2.16. This shows that:

- the three parameter formulation is able to identify clear anisotropy (indicated by $\alpha = 1.37$)
- Whereas differences between the evaluations of the three common parameters are of the order of ±20%, an assumption of isotropy results in differences of between -42 and +66% for the remaining parameters.

Parameter	*Anisotropic evaluation*	*Isotropic evaluation*	*Difference*
$E_v / \sigma'_{vc} = E^*$	15.4	17.5	13%
E_h / σ'_{vc}	28.8	17.5	-39%
ν_{vh}	0.16	0.27	66%
$\nu_{hh} = \nu^*$	0.22	0.27	21%
G_{vh} / σ'_{vc}	8.6	6.9	-20%
G_{hh} / σ'_{vc}	11.8	6.9	-42%
α	1.37	1	-27%

σ'_{vc} = preconsolidation pressure:
Shaded cells = parameters common to both anisotropic and isotropic formulations

Table 2.1 Normalised parameters obtained using anisotropic and isotropic formulations on Winnipeg clay (interpreted from Set B, Table 3, Graham and Houlsby, 1983)

Hird & Pierpoint (1997) used the Graham and Houlsby (1983) cross-anisotropic formulation to model deformations of an excavation in Oxford clay, and their measurement of stiffness parameters of the Oxford clay will be considered here. High quality samples of Oxford clay were tested in a triaxial cell incorporating proximity transducers to measure both vertical and horizontal small strain deformations. They used a sequence of stress paths, shown schematically in Figure 2.12a, to investigate the stiffness of samples by multiple excursions at either constant p' or constant q in the region of the *in situ* stress state. Used in combination, these stress paths permitted the determination of all four of the stiffness terms in the constitutive equation represented in Equation 2.17 (Atkinson & Richardson, 1985):

$$\begin{bmatrix}\delta\varepsilon_p\\ \delta\varepsilon_q\end{bmatrix}=\begin{bmatrix}\frac{1}{K'} & \frac{1}{J'_{qp}}\\ \frac{1}{J'_{pq}} & \frac{1}{3G'}\end{bmatrix}\cdot\begin{bmatrix}\delta p'\\ \delta q'\end{bmatrix} \quad \text{.....Equation 2.17}$$

where K' is a bulk modulus, G' is a shear modulus , J'_{pq} and J'_{qp} are the coupling moduli linking changes in deviator stress / strain to changes in volumetric strain / stress, and ε_p and ε_q are the volumetric and distortional strain parameters corresponding to p' and q respectively. A strain energy formulation was used to provide a generalised basis for expressing the non-linearity of the soil stiffness for the different stress paths followed. A sample set of data is reproduced in Figure 2.12b, and the summarised stiffness relationships used in model development in Figure 2.12c. These show finite measurements of J'_{pq} and J'_{qp} indicating cross coupling and hence anisotropy in the samples. It is also clear that experimental data were only considered reliable to a lower limit of strain energy ≈ 0.0001 kJ/m^3, whereas the model relationships are extrapolated to 0.00001 kJ/m^3. These strain energies correspond to deviatoric strains of approximately 0.005% and 0.001%. At the upper limit, a strain energy of 0.1 kJ/m^3 corresponds to approximately 1% deviatoric strain. Using equations given by Pierpoint (1996)[§§], values of G', K' and J' can be converted to the Graham and Houlsby (1985) parameters involving E^*, ν^* and α, and hence to cross-anisotropic parameters using Equations 2.16. The curves for K', G' ($\Delta q>0$) and J'_{qv} ($\Delta q>0$) provide values at both small and large strain energies (corresponding to very small strain and large strain) and conversion leads to the parameters summarised in Table 2.2. Measurements from bender tests indicated $G_{o(vh)} \approx 75$ - 85 MPa. At a strain energy of 0.1 kJ/m^3 the results are comparable with those for Winnipeg clay discussed previously. Significant implications of these results are that:

- at 0.01 kJ/m^3 the Oxford clay is significantly anisotropic, indicated by $\alpha = 2.42$,
- Poisson's ratios for the Oxford clay are very small at both small and large strain,
- the three parameter model evaluation of G_{vh} underpredicts the value measured with bender elements.

Strain energy ⇒ Parameter ⇓	***0.00001 kJ/m^3***	***0.1 kJ/m^3***
E_v (MPa) $= E^*$	80	15
E_h (MPa)	157	89
ν_{vh}	0.05	0.00
ν_{hh} $= \nu^*$	0.07	0.01
G_{vh} (MPa)	52	18
G_{hh} (MPa)	73	44
α	1.40	2.42

Table 2.2 Parameters obtained using anisotropic formulations for Oxford clay (interpreted from Figure 17, Hird and Pierpoint, 1997)

[§§] These equations are presented and discussed in detail in Chapter 6.

Pierpoint (1996) concludes that these triaxial tests may have failed to measure the initial elastic behaviour and that tests with finer resolution of the triaxial strain measurements should be used to confirm these results and check this comparison with $G_{0(vh)}$. Clearly, additional measurements of G_0 transversely across triaxial samples would also enable anisotropy of the small strain stiffness to be evaluated more fully. However, the Pierpoint (1996) study represents an advanced investigation of the stiffness at small strain of a stiff overconsolidated clay, and therefore challenged the current project to explore anisotropic stiffness at smaller strain levels.

2.5 Summary

This chapter has considered recent developments in the use of triaxial tests to measure both the non-linearity and anisotropy of clay soils. Non-linearity is arguably currently best measured in the triaxial cell using local strain transducers. By contrast, the triaxial cell has severe limitations to exploration of anisotropy which requires the development of additional instrumentation to measure horizontal shear wave velocities. Development of such devices would also enable more complete exploration of the factors influencing the development of anisotropy where current bender applications in both triaxial cells and oedometers fail.

The next chapter will discuss the commissioning of a high quality triaxial facility and the development of bender devices to measure cross-anisotropic shear moduli.

3. EQUIPMENT: LABORATORY, LOCAL STRAIN AND BENDER

3.1 Introduction

Choosing the platform for conducting the research outlined previously inevitably resulted in a compromise between an ideal instrument (full flexibility on three dimensional stress/strain control), and pragmatic assessment of the resources available in a small soil mechanics laboratory such as that at Bristol University. To enable full flexibility the ideal instrument would allow three degrees of freedom and rotation of principal stresses on the element of soil. It would be able to change these stresses at frequencies from static up to truly dynamic, and incorporate devices for the measurement of shear wave velocities. Visions of a large hydraulically-driven hollow-cylinder apparatus with local strain and local bender devices perched on the walls come to mind. However, at the outset of the project the idea of even hanging local bender element devices off the side of simple triaxial samples meant breaking new ground. Some years later, the hollow-cylinder vision now seems an achievable goal, and such an instrument has recently been commissioned at Bristol. But that is another story. This chapter will concentrate on describing triaxial equipment suitable for high quality testing in the small strain range, and the development of new bender devices for shear wave measurement.

Local strain instrumentation has not only found acceptance in research communities over the past decade, but its importance in obtaining useful strain dependent stiffness moduli has led to frequent use in commercial laboratories. As a result there are many sources of local strain instruments based on a wide range of transducer types as summarised by Scholey *et al.*, (1995). Therefore the discussion about local strain instrumentation for this project considers the choice, not development, of such equipment.

Bender elements have been used in many applications in soils testing as discussed in the previous chapter. These range from the more esoteric such as crosshole uses, Nishio and Katsura, (1994); centrifuge applications, Gohl and Finn, (1991); through resonant columns, Dyvik and Madshus, (1985); to more conventional soils laboratory instruments such as the oedometer, and triaxial cell. Yet unlike local strain instrumentation, bender elements have not been developed to the stage of being "off the shelf" items available in high quality reliable forms which can simply be incorporated in standard testing equipment. A success in this project has been the development and fabrication of new bender element devices that are simple, yet of the quality which leads to clear interpretation.

This first part of this chapter discusses the establishment of the high quality triaxial stress path testing facility which formed the platform for the more innovative bender element testing. The second part of the chapter describes the development of the bender element devices that enabled the reliable simultaneous exploration of $G_{o(hv)}$, $G_{o(vh)}$ and $G_{o(hh)}$ in triaxial stress space.

3.2 Triaxial testing facility with local strain capability

3.2.1 Introduction

One of the objectives of the research project was to establish a facility incorporating local strain instrumentation to track the small strain response of the clay samples during triaxial stress path tests. The existing triaxial facilities in the Bristol Geotechnics Laboratory were generally configured to conduct tests at levels of accuracy more applicable to commercial requirements than a research environment. They consisted of two 38 mm Bishop Wesley cells of Imperial College design and manufacture. The systems were controlled by BBC computers running an in-house BBC Basic control programme. Data acquisition was via 12 bit SIL analogue to digital converters. Test configurations of either 38 or 75 mm sample diameter could be achieved. These had previously been used to investigate strength and stiffness parameters of the Cambridge Gault clay in the EPSRC/JT Design Build Grant: Performance and Back Analysis of a Deep Excavation in Gault Clay, (Ng 1992).

For this research project the triaxial cells were refurbished and the workstations upgraded. This included upgrading the control and data acquisition systems, and the acquisition of local strain devices.

3.2.2 Triaxial stress path testing apparatus' and instrumentation

The heavily fissured nature of Gault clay led to the early decision that tests on natural material would have to be conducted on samples of at least 100 mm diameter, despite the penalty paid in time taken to consolidate samples of this size. Therefore, in addition to the two 38 mm stress path cells, a 100 mm stress path cell, also of Imperial College design and manufacture, was obtained on long term loan from the Department of Civil Engineering at Bath University. This cell is illustrated in Figure 3.1. Note the use of internal vertical tie bars and a large diameter outer cell wall. This arrangement is particularly advantageous where local instrumentation is to be utilised because the top cap and load cell can be connected to the sample early on in the set-up, avoiding the potential for sample disturbance due to misalignment if connection is carried out at elevated cell pressures, (Baldi *et al.*, 1988). Further, early connection to the base and top of the sample offers greater rigidity during the assembly of local instrumentation than is possible for a free standing sample, again leading to reduced disturbance.

The two 38 mm stress path cells were of the external tie bar design, and connection with the top of the sample to provide tension capabilities was achieved through the use of a suction cap. These two cells were used for tests on reconstituted samples. All three cells were dismantled for cleaning, refurbishment of the axial bearings and re-greasing. This ensured smooth control of vertical stresses during testing. In addition, the vertical load-cells in each cell were re-strain-gauged to remove drift believed to be caused by the deterioration of the bonding of the strain gauges. New hydraulic pipe-work boards were designed and assembled for each of the three triaxial experimental work-stations. The boards were designed to the same common layout, and all fittings standardised. This not only ensured full interchangeability of components, but also made operator errors less likely when running tests on more than one cell at the same time. Colour-coded polyurethane tubing was used for each of the cell, ram, and back pressure

circuits. For ease of use, 5 mm push fittings were used as standard on these lines. All sample drainage lines were upgraded to $^1/_{16}$ inch annealed stainless steel tubing with Swagelok compression connectors and taps. This ensured essentially leak-proof operation of these lines.

During the early stages of this project, a decision was made to include permeability testing under anisotropic stress states in the investigations on the Gault Clay. The technique chosen to do this was the Constant Rate of Flow permeability test (CRoF) because of its simplicity of interpretation and accuracy. The CRoF test is performed by pumping a known rate of pore-fluid into one end of a triaxial sample, awaiting confirmation of the steady state by recording the rate it flows from the other end of the sample, and measuring the head difference across the sample. The success of the method for fine grained materials is highly dependent on the ability to measure the flow from the sample to the required accuracy.

In 1994 the Newcastle Volume Change Meter or VCM, was developed by Araruna *et al.*, (1996). This instrument operates over full scale ranges of either 5 ml or 100 ml, and offers substantially greater accuracy than the more standard rolling seal volume change meters seen in most UK soils laboratories. Bristol University acquired two of these instruments (manufactured by the department of Civil Engineering in Newcastle University in 1995). While the results of early CRoF tests will not be presented here, the combination of the VCMs with the stainless steel pore-fluid pipe-work provided a leak free high accuracy volume measurement system for the long term drained tests that were carried out.

3.2.3 Laboratory infrastructure

The previous section considered the establishment of high quality triaxial work-stations. To support these work-stations, the establishment of reliable laboratory infrastructure was considered essential for the success of long term tests. The four "utilities" listed below were given careful attention during re-commissioning of the laboratory:

- compressed air
- un-interruptible power supply
- air-conditioning
- de-aired water

The quality of the provision of these services can enhance the testing environment significantly, and improvements made to certain aspects will be discussed here.

Compressed air

Failure of the compressed air supply can lead to significant setbacks to test programmes, particularly when considering that some tests conducted in this research lasted up to 2.5 months. Indeed it is not only having air pressure, but also maintaining the quality of the supply that is crucial. In the context of using pressure-controllers, air quality includes both stability of the supply air pressure and air condition (how wet and oily it is). It was found that the precision and stability of these controllers was downgraded by

fluctuating input pressures or "dirty" air, leading to hunting by the stepper-motors in their attempts to maintain control.

The air supply system was upgraded to address these issues. A new continuous run Hydrovane 902 compressor was installed to provide compressed air at 1000 kPa, although the supply to the laboratory was regulated to about 900 kPa. Back-up to this compressor was a Hydrovane intermittent delivery compressor which was configured such that it cut in if the pressure dropped below 900 kPa. Both of these compressors were connected to a reservoir tank with sufficient capacity to cover power cuts of up to ten minutes when six controllers were maintaining an average pressure of about 500 kPa. After leaving the reservoir tank the air was passed through first stage oil and water traps to reduce the oil content and remove the bulk of the water. Before delivery to the laboratory it was further dried in an Edward's refrigeration cycle drying unit. As mentioned above, the supply was regulated from the 1000 kPa supply to 900 kPa by manostats controlling the supply to each bench in the laboratory. Regulation at this stage was found to have the advantage of both smoothing fluctuations in the compressor supply, and minimising the effects of other users in the laboratory drawing air.

The backup arrangement proved its worth a number of times during the 2.5 years of testing, during which it not only covered breakdowns, but also enabled regular servicing of the primary compressor to be carried out without interruption to the air supply.

Electricity Supply

An un-interruptable power supply (UPS) was interfaced into the laboratory electricity supply such that all the computers running stress path tests, the A/D units and the pressure controllers were powered from the UPS. This ensured that even in the event of unplanned power interruptions the tests could be continued. The UPS was able to provide these electrical needs for up to half an hour. In combination with the compressed air ballast tank, this offered secure protection against short power interruptions such as those sometimes experienced in Bristol, particularly due to lightning strikes. Again, this system proved the value of power backup on a number of occasions during the testing period.

Temperature Control

The influence of temperature variations on triaxial tests can be significant. Not only can apparent or actual pore water volume changes be induced by changes in temperature, but the secondary influences on transducers with dual sensitivity leads to further errors, (Dally *et al.*, 1993). Efforts were made to improve the control of temperature in the laboratory by redesigning the delivery ducting from the air-conditioner to ensure that the triaxial apparatus' and related equipment were not directly in the flow of cooled or heated air. The temperature of the cell water was recorded automatically during triaxial tests both as a check on the efficacy of the air conditioner, and to augment the interpretation of test data. The influence of temperature on laboratory data will be discussed in Section 3.2.6.

De-aired water

In order to reduce the errors in the measurement of sample volume changes and pore pressure changes caused by the presence of gas in the triaxial system, de-aired water was used not only to flush all pore pressure lines, but as the cell fluid in all tests. This helps to slow air migration from the cell into the specimen, (Pollard *et al.*, 1977), particularly in the long duration tests. The method of production of reliably de-aired water in the laboratory elevated vacuum tank was therefore addressed.

As it is usually inconvenient to test each volume of de-aired water produced, it was considered more pragmatic to introduce a form of agitation to the de-aired water production chamber that would not only lead to accelerated de-airing under vacuum, but would also provide a visual indication of the progress of the de-airing procedure, Channa, (1995). A submersible pump was placed in the bottom of the tank, and run at high speed to agitate the water. Agitated water under vacuum undergoes a relatively sharp transition from a cloudy state to a clear state when de-airing is sufficiently advanced, and observation of this transition point was used to ensure uniformly deaired water during the laboratory testing programme.

3.2.4 Improvements to stress control and data logging

The control and logging systems in use at the start of the project needed upgrading. The control requirements for conducting slow (consolidated) tests on clays are not arduous in terms of computing power, or complexity of operation. Operator convenience is probably the most important requirement. A useful control system should enable test status to be assessed at a glance and facilitate simple, reliable user interaction for aspects such as calibration, test initiation, test control and data acquisition.

After a review of the options, which included rewriting the in-house programme and implementing an updated analogue to digital converter, a decision was made to purchase the control programme TRIAX, developed and marketed by Durham University, (Toll, 1993). TRIAX has the advantage of being widely used and validated, and having a relatively simple user friendly graphical interface.

The program interfaces with the triaxial cell measurement transducers through an A/D unit connected to a PC serial port, and sends pulsed digital control signals to controller devices through simple low cost Type 8255 digital output cards. The A/D units comprised 16 channel self-ranging DATASCAN 7220 units boxed with stabilised power supplies following an Imperial College design, (Ackerley, 1994). These A/D units were configured to acquire data at 16 bit resolution, giving the units minimum resolutions of 0.62 μv. Further implications of this data resolution will be discussed in Section 3.2.6

Data were automatically logged to the hard disk of the PC at intervals specified by the user. These data were written as a series of voltages for each logged data channel. Engineering values are obtained by listing the data files in conjunction with the calibration file applicable to the transducers in use.

Cell pressure, back pressure and vertical stress were controlled though stepper motor driven pneumatic manostats. The existing pressure controllers had a minimum resolution of approximately 0.4 kPa / step, which was considered too coarse for stress controlled small strain excursions. They were upgraded to

controllers with a single bit resolution of approximately 0.07 kPa. These controllers provided air pressure control between 14 and 900 kPa. The air pressure was converted to water pressure though air / water interfaces incorporating flexible bellophragm rolling seals.

Vertical stress control for the 100 mm cell had a resolution greater than the 0.07 kPa due to the 3:1 area ratio of the drive cylinder to the platen. This resulted in minimum deviator stress control steps of about 0.2 kPa in this cell. An additional water / hydraulic oil interface was used in conjunction with this axial cylinder so that the oil acted both as a pressure transmission medium but also as a lubricant to the submersed axial bearing.

The choice of back-pressure level has implications on the working stress ranges possible. For all tests a back pressure of 300 kPa was used. The combination of this with the air supply pressure described above resulted in possible stress ranges limited to a maximum isotropic effective stress of about 600 kPa with possible effective confining pressures, p', increasing as deviator stresses increased, or decreasing as deviator stress decreased as shown in Figure 3.2. This test range was increased by switching in devices with higher pressure ratings to both the ram and the cell pressure circuit. A constant rate of strain pump (CRSP) could be switched into the ram supply lines of any of the three triaxial cells used. With this arrangement the maximum controllable working pressure was extended to 2 MPa, but in practice limited to about 1.8 MPa - a value determined by the safe working pressure limit of the ram systems.

To achieve boosted cell pressure, a pressure intensifier of Imperial College design was used. The unit has a moving piston with different diameters at each end to which bellophragm rolling seals are attached. Controlled air pressures are introduced to the large diameter end, and used to pressurise the de-aired water connected to the cell at the smaller end, giving a pressure multiplication of about 1:2.2. This gave a theoretical maximum cell pressure of about 2 MPa. However, due to the uncertainty in the factors of safety on the perspex cell walls due to ageing, it was considered necessary to limit the maximum cell pressure to 1250 kPa.

The extended stress ranges these additions made possible are also illustrated in Figure 3.2, along with the theoretical stress state limits for natural Gault clay approximated by lines corresponding to a soil effective angle of friction $\phi' = 27°$. This extended possible stress space was used in tests where reconstituted Gault clay was re-consolidated to voids ratios significantly closer to those of the natural material than would have been possible with the standard range.

3.2.5 Local strain instrumentation

Local strain measuring devices had not been used at Bristol prior to this project. There was therefore no experience in either their use or design. As the principal objective of the project was development of innovative instruments for the measurement of anisotropic $G_{0(ij)}$ by shear wave velocity measurement, the decision to buy in existing technology to measure local strains was made at an early stage.

This section discusses the selection of devices to measure local strains.

Drained *vs.* undrained testing

Techniques for measuring local strains both horizontally and vertically have been reviewed by Scholey *et al.*, (1995). It has been argued that LVDTs and LDTs offer the greatest resolution (0.0001% distortional strain) for the measurement of vertical local strains in triaxial tests, e.g. Cuccovillo & Coop (1997), Heymann *et al.* (1997). However in the measurement of local distortional stiffness it is the combination of both vertical and horizontal strains that is required to establish distortional strains ($\varepsilon_q = 2/3(\varepsilon_v - \varepsilon_h)$). Cuccovillo & Coop (1997) achieved strain measurement as low as 0.0001% by carrying out their tests undrained so that zero volume change was assumed and horizontal strains were determined merely from the vertical strain readings using the right cylinder assumption ($\varepsilon_h = \varepsilon_v/2$). However the investigation of anisotropy is severely limited if only undrained paths can be followed, and so drained testing was considered essential.

Further, in tests where $G_{\alpha(ij)}$ is determined using shear wave velocities, the influence of components of stress in the planes of propagation and polarisation make it necessary to be able to follow prescribed stress paths in order to isolate or include stress effects. In this research, all tests were therefore performed drained and it was considered essential to have methods of establishing both horizontal and vertical local strains during drained stress path excursions.

Hall effect gauges

The use of Hall effect gauges to measure vertical strains in soils testing was developed at the University of Surrey, Clayton and Khatrush, (1986), and Clayton *et al.*, (1989). The Hall effect is observed when a metallic or semiconductor plate, though which a current is flowing, is placed in a magnetic field where flux lines are directed perpendicular to both the plate and the current flow. This causes deflection of the charge carriers, and a voltage is produced across the plate in a direction normal to the current flow. The magnitude of the voltage is a function of the flux density and varies depending on the relative position of the semiconductor sensor within the magnetic field. For their use as vertical strain measuring devices, the sensor is attached to one of the gauge length end positions on the sample, and a system of permanent magnets is configured at the end of an arm attached to the other end of the gauge length, as shown in Figure 3.3. A relationship between output voltage and the relative displacement between the gauge ends can then be established by calibration. Particular advantages of these devices are:

- an energisation voltage of only 5 Vdc results in an output of between 1 and 4 volts and no signal conditioning is required,
- semiconductor devices are small and light,
- semiconductor devices which are compensated against temperature and voltage changes are readily available.

Horizontal strain measurements

Horizontal strain in the triaxial cell is most frequently measured indirectly on the basis of volume change and the assumption of right cylinder deformation. Considering the restricting effect of end constraint on this shape near the top and bottom of a triaxial sample, the accuracy of the method is uncertain. Even if the assumptions are taken as valid, then volume strains based on conventional rolling seal volume change devices are limited to best resolutions as indicated in Table 3.1. These are significantly greater than the order required for small strain testing. However, if working with 100 mm diameter samples and using the 0.005 ml accuracy possible with the Newcastle VCM discussed previously, horizontal strain resolution approaches 0.003%, which is of the order of magnitude for strains assumed to show elastic behaviour, and therefore appropriate as a means for measuring very small volume strain changes.

Sample Diameter (mm)	*Volume change device*	*Volume change resolution (ml)*	*Horizontal Strain Resolution (%)*
38	Conventional rolling seal unit	0.05	0.220%
100	Conventional rolling seal unit	0.05	0.032%
38	Newcastle VCM	0.005	0.022%
100	Newcastle VCM	0.005	0.003%

Table 3.1 Comparison of horizontal strain resolutions for different volume change devices

Horizontal strain measurements using horizontal belt devices also make assumptions which imply uncertainty. The assumptions include:

- that there is no membrane compression,
- that test samples retain perfectly circular cross-sections with horizontal strain being determined on the basis of changes across only one diameter.

Even if these assumptions are entirely valid, equipment for measuring horizontal strains to resolutions of 0.0001% are currently unavailable. However the GDS horizontal belt for 100 mm systems does offer resolution to theoretical limit of about 0.001% horizontal strain. The instrument is light, easy to use and robust, and one was acquired to compliment the two vertical devices also purchased from GDS.

Considering the uncertainties in both methods (diameter measurement or volume measurement linked to the right cylinder assumption) of determining triaxial horizontal strains, and the importance of horizontal strain measurements to the research goals, it was decided that both a GDS horizontal belt and the Newcastle VCM would be used to determine small horizontal strains in key tests.

Stability of Hall effect devices

Electrical stability of the local strain devices is essential for measuring strains at or near the resolution of the measuring devices. Lo Presti *et al.* (1994) found their Hall effect devices to be both temperature sensitive, and unstable. However, in the controlled temperature environment of the Bristol laboratory they

were found to be stable and their performance was considered highly successful. An illustration of this electrical stability will be discussed in conjunction with accuracy considerations in Section 3.2.6.

Displacement range

The Hall effect chips used in the GDS vertical and horizontal devices have a full range of about 12 mm, but are severely non-linear and non-monotonic outside the middle third of this range. Where used as vertical gauges on 100 mm diameter samples over a vertical gauge length of 75 mm this equates to a strain range of just over 5%. Due to the ratio effects in the design of the horizontal belt, the same 4 mm displacement range corresponds to a horizontal strain range of only about 2.5%. Despite this, the transducers were calibrated over the full 12 mm range. Then when being used in a test, consolidation strains were estimated and used to set the gauges at an initial point on their calibration curve such that after consolidation they would be operating within the optimum central 4 mm. Details of the calibration procedures and accuracy of the Hall effect gauges are discussed in the next section, along with illustrations of the non-linearity over the full displacement range.

3.2.6 Transducers and accuracy of measurement

The management of accuracy

A knowledge of the accuracy and reliability of the instruments and systems, measuring, transmitting and converting data from tests, is essential to enable a level of confidence to be attached to results. Up to 35 transducers of various types were used in the testing programme covered in this research project. With calibrations on working testing equipment being carried out approximately every 3 months during the two year testing programme, it was necessary to develop systems to manage the calibration of these transducers. The systems developed were based in Microsoft Excel workbooks, in which an inventory worksheet was used to manage the use of transducers in the laboratory. An extract from this worksheet listing all the transducers actually used in this project is given in Figure 3.4. This gives a description of the transducer which includes manufacturer, model, serial number, the quantity it measures, its rated limit, and excitation levels and output. When a set of transducers was assigned to a triaxial workstation for a series of tests, the inventory sheet was linked to individual calibration sheets through lookup tables.

Fundamental measurement parameters

Transducers were used to measure four fundamental parameters. The actual application of the transducers within each of these parameter divisions is given in Table 3.2. Also given are the transducer type and the type of reference equipment against which the transducers were calibrated.

Parameter	*Transducer application*	*Transducer type*	*Calibration Reference*
Load	Vertical load	Submersible pressure balanced loadcell	Reference masses – Load applied to loadcells by transfer through rotating hydraulic piston cylinders (Budenberg S/N 21096/380)
Pressure	Cell, back, ram and mid-height pore pressure	Externally mounted gauge pressure diaphragm transducers. For the 38mm cells, submersible minature gauge pressure transducers were used	Reference masses converted to pressure though rotating piston cylinder (Budenberg S/N 21096/380)
	Volume change	Differential pressure transducers for measuring height of water column in the Newcastle VCMs	Mass of water allowed to drain from unit, and weight on balance (0.01g balance S/N 12778)
	Atmospheric pressure	Absolute pressure transducers mounted adjacent to cell	Water Manometer
Displacement	External sample strains	LVDT	10 μm Micrometer mounted in gauge block
	Displacement of syringe plunger on the constant rate of flow pump used for CRoF tests	LVDT	
	Local vertical strain and horizontal strain	Submersible Hall effect gauges	1 μm Micrometer
Temperature	Cell water temperature variations	Thermistor temperature transducer	Boiling water, Ice/water mix

Table 3.2 Division of transducer application by fundamental parameter

Calibration

Great care was taken over calibration. The A/D unit was turned on at least one day before the procedure began in order to allow a stable operating temperature to be reached in the box housing the unit. To ensure minimum variation of the 5 V dc power supply used to energise the transducers, no transducer changes were made once calibration of the transducer set had been started. This helped ensure a constant load on the power supply. If changes were required, calibration of all transducers attached to the unit was repeated.

Two examples of calibrations will be illustrated. Since local small strain measurement was a specific objective of the project, these examples include calibrations of a vertical local strain gauge and the horizontal belt as shown in Figure 3.5 and Figure 3.6 respectively. The calibrations include assessment of the accuracy of individual calibration points, both in absolute terms and as a percentage of the calibrated range. In these calibration worksheets polynomial curve fitting was performed automatically to the order selected. Statistical quantities such as standard error and the quality of the "fit" are also listed. The monotonic operating range of about 10 mm can be seen from the plot included in Figure 3.5. Within

this range the gauge performance is non-linear. For stress path excursions where small strain measurements were of particular interest, calibrations applying to approximately the middle 4 mm of this monotonic range were used, and it is these best fit equations that are derived and illustrated in Figure 3.5 and Figure 3.6. An indication of the quality of the overall fit is given by the " R^2 " term. Maximum deviations between calibration points and the curve fit are also given to enable individual calibration points to be checked. For the local vertical gauge (Figure 3.5) the maximum deviation of a single reading is 0.0027 mm and for the horizontal belt (Figure 3.6) 0.0046 mm. Since the calibration micrometer used was accurate to 0.001 mm, the differences could be due to

- the inability of the polynomial to describe the actual gauge characteristic,
- operator error,
- transducer error / drift,
- data acquisition errors.

Efforts were made to evaluate the last of these two sources of error by calculating the theoretical errors based on both manufacturer's specifications, and combination with the performance specifications for the A/D unit. The results of this approach are summarised in Figure 3.7. This shows a summary table of data applying to a set of transducers connected to the 16 channels of the A/D unit attached to the 100 mm stress path cell at location "Right" in the laboratory. (This table is generated automatically in the Excel calibration workbook, and similar tables were therefore produced for each triaxial workstation each time a set of calibrations was carried out.) The rows of data applying to the two transducers already discussed are shaded. Columns two to four list the variable, its abbreviation for the purposes of the TRIAX control program, and the units measured. Manufacturer-supplied details are listed in the next five column blocks, giving some indication of the manufacturer's guaranteed accuracy in the final column of the block. Calibration information (linked through from a complete set of calibration worksheet pages such as those for the horizontal belt discussed earlier) is listed in the next four columns, and is used as input for the final four column block. In this block the transducer performance is evaluated in terms of the A/D unit performance specification. Column (c) indicates the lowest resolution in engineering units possible for each transducer. Column (e) represents the largest absolute error in the A/D conversion process. When undertaking small strain measurements, the initial or small strain section of the stress path being followed occurs within a period of only a few minutes (possibly 10 to 30 minutes). In this short time it is reasonable to presume that the errors are more likely to be represented by columns (c) or (d), rather than (e). This presumption is tested later in this section.

Column (f) provides an indication of the quality of fit to the calibration data. It is based only on a linear fit to the calibrated range, and hence for the local vertical gauge and horizontal belt the standard errors of 0.0035 and 0.0044 are significantly greater than the standard errors of 0.0019 and 0.0033 for the 4th order polynomial fits given in Figure 3.5 and Figure 3.6

To interpret the implications of these evaluations of accuracy to triaxial tests, the results listed in Figure 3.7 are summarised in terms of their triaxial test equivalents in Table 3.3. The first three rows of Table 3.3 refer to a controlled triaxial stress, where the minimum control resolution was 0.07 kPa. It can be seen that both the lowest resolution and the maximum excitation variation effect are less than 0.07 kPa in all cases. This gives the assurance that the controllers are unlikely to "hunt" due to insufficient transducer resolution or typical variations in supply voltage.

Interpreted parameter	*Units*	*Lowest resolution (units)*	*Max. excitation variation effect (+/-units)*	*Max. error in A/D conv's'n (+/-units)*	*'Std. error' in regression fit (+/-units)*
Deviatoric Stress	kPa	0.031	0.031	0.37	0.739
Confining stress	kPa	0.013	0.063	0.316	0.632
Back pressure	kPa	0.004	0.027	0.111	0.615
Mid ht. Pore Pressure	kPa	0.009	0.026	0.159	0.591
External vertical strain	%	0.0009%	0.0018%	0.0124%	0.0071%
Volume strain	%	0.0005%	0.0010%	0.0068%	0.0029%
Horizontal strain	%	0.0007%	0.0007%	0.0035%	0.0063%
Local vertical strain 1	%	0.0020%	0.0020%	0.0099%	0.0079%
Local vertical strain 2	%	0.0020%	0.0020%	0.0100%	0.0100%

Table 3.3 Typical accuracy achieved for key triaxial variables

For stress path excursions where small strain readings are taken over relatively short periods of time, the accuracy of the readings is considered to be best indicated by the *lowest resolution* and *maximum excitation variation effect* columns in Table 3.3. These indicate accuracies of $\approx \pm 0.001\%$ for horizontal strain, and $\pm 0.002\%$ for each of the vertical strain transducers. As the vertical local strains are measured by two transducers, the effective accuracy is somewhat better than with a single gauge, and probably closer to the value of 0.001% estimated for the horizontal belt. Discussion on the accuracy of the interpreted stiffness from strain data will be developed in Chapter 4.

Drift

The calibrations discussed above were typically carried out over a relatively short period of time during which it may reasonably be presumed that equipment and laboratory conditions were relatively unchanging. However, the drained tests on Cambridge Gault clay planned for the research were to take significantly longer (1-3 months), and transducer stability over longer periods was therefore also assessed. The same procedure and terminology as described by Smith, (1992) was used. This involved carrying out monitoring of all the transducers attached to a work station over a period of about a week. The triaxial cell was filled with water to ensure similar thermal inertia as when a sample is present. The results of a seven day test of system performance (transducer and A/D conversion) for most of the 16 channels are illustrated in Figure 3.8. In this figure data from each transducer are scaled to fill the range of the plot space allowed to each channel. Channel 1, for example, monitors the transducer energisation voltage, and shows deviations of $\pm$ 1 bit or 0.7 mV over the period of the week, with no noticeable drift. To the right of the plot is a table where the terms E_T (typical scatter band), E_G (gross scatter band) and ΔT_L (transducer

drift) are evaluated. The latter is quoted in terms of the gradient of the line in transducer units per day. The meaning of these three terms is illustrated on the data from Channel 3 in Figure 3.8.

Before considering the transducers used to measure triaxial variables it is worth noting the changes in cell water temperature over the one week period shown for Channel 6 in Figure 3.8. After an initial cooling of 1.3°C over the first 12 hours, daily fluctuations of approximately 0.4°C can be seen. The only channel with apparent temperature dependence is (not surprisingly) the volume gauge (Channel 9). By comparing with the theoretical errors listed in Figure 3.7, it is apparent that the drift test typical errors (E_T) exceed the lowest resolution predicted for volume change, but are in most cases of similar order to the maximum excitation variation effect values given in Figure 3.7 and somewhat less than the "standard errors" based on the calibration regressions.

These errors are given in terms of triaxial variables in Table 3.4. Apart from volumetric and horizontal strain where the measured typical, or short term, errors (E_T) are slightly larger than the lowest resolutions, these errors (or the accuracy of the readings) appear to be of the order required for small strain measurements i.e. $E_T \approx 0.002\%$ and in the longer term, $E_G < 0.005\%$.

	Errors		
Strain	E_T *(Typical)*	E_G *(Gross)*	ΔT_L *(Long term drift % / day)*
External vertical	0.0010%	0.0010%	below measurable levels
Volume	0.0025%	0.0036%	0.00015%
Horizontal	0.0060%	0.0100%	0.00001%
Local vertical 1	0.0022%	0.0065%	-0.00008%
Local vertical 2	0.0021%	0.0043%	-0.00008%

Table 3.4 Strain transducer errors assessed from drift test

The implications of the drift test for the long term accuracy of triaxial variables can be assessed from the long term drift values listed in Figure 3.8 and Table 3.4. The most important finding is that there is no drift in channel 1, the transducer energisation source. Considering total test times of the order of one or two months, the drift results confirm that likely changes due to supply voltage drift will have negligible impact on the data.

The picture of assured accuracy that has been presented in this section does not represent the outcome of the assessment when it was carried out early in the project. For example, the first attempt at a drift test revealed more significant errors in all channels which were traced to supply voltage fluctuation caused by the malfunction of the atmospheric pressure transducer used at the time. In conclusion, the procedures developed to routinely assess accuracy of the data acquisition systems formed a useful check on the performance of the transducers and ensured reliable data.

3.3 Bender element equipment

3.3.1 Introduction

The incorporation of shear wave velocity measurement in the controlled environment of laboratory tests marries techniques usually considered the separate domains of geophysicists and soil mechanicians respectively. To the practising geotechnical engineer, geophysics data often appear incomprehensible, and one does not have to look far in the literature e.g.: Thomann & Hryciw (1990); Gohl & Finn (1991); de Alba and Baldwin, (1991), Viggiani (1992); Pierpoint (1996) to see examples of bender element traces where the interpretation of arrival times is highly subjective. Discussions on the identification of first arrival have led to the use of signal processing techniques such as presented by Viggiani, (1995). However, by definition these methods modify the received signals to facilitate apparently reliable identification procedures which may be repeatable for a particular soil and experimental set-up, but are inherently inaccurate, (Arulnathan *et al.*, 1998)

In a controllable environment (such as a laboratory) it is an achievable goal to develop systems which generate, propagate and receive shear waves with a degree of clarity that leaves no doubt (even to a sceptical Geotechnical engineer!) as to how long it takes for a wave to pass through a soil. In this section each component of the system is discussed.

During this project bender devices, which enabled shear wave velocity measurements to be made easily and reliably, were successfully developed. Bender elements are made from high impedance piezo-ceramic material, and therefore need perfect insulation in the conductive watery environment of soils and the triaxial cell. Signals from bender elements which pass into, through and out of soil, are attenuated and distorted. The magnitudes of the sent and received signals are usually significantly different (maybe 10^4 to 10^6 times different) and the instrumentation used to send and detect signals therefore needs to be matched to the signal levels. Development of the technique therefore requires that both the bender elements and the systems within which they are used, are optimised.

The use of bender elements in UK soils laboratories in 1994 was limited to the Universities of Bangor, City, Imperial College and Sheffield. The bender elements in use in these laboratories were either produced by the University of North Wales, Bangor, the Norwegian Geotechnical Institute, or City University. In all cases the design developed by Dyvik and Madshus (1985) as illustrated in Figure 2.4 was being followed. It was clear from visits to the UK labs listed above that there was significant variation in both the quality of element encapsulation, and the acquisition of signals. Whereas the establishment of triaxial workstations with small strain capability for this project was made by choosing from existing technology in the UK, available bender systems were not of sufficient proven quality to do

the same. Significant effort was therefore put into designing and developing fabrication facilities at Bristol, and improving the associated driver and receiver signal systems[§].

Major points in favour of this approach were:

- the control of supply (lead times for purchase of the elements from third parties were variable)
- quality control (observation of elements in use at other UK centres showed wide variations in quality)
- freedom to innovate and experiment with design.

Piezo-ceramic material forms the basis of many transducers manufactured commercially. However the commercial applications to date do not produce forms suitable for mounting in soils testing environments. While there is nothing particularly difficult in the assembly of bender elements, this operation has been done badly or avoided by many in the soils testing fraternity. This section will expand on the design of transducers using piezo-ceramic theory, will detail the methods of fabrication developed at Bristol, discuss the instrumentation systems used to obtain and process data, and discuss issues relevant to their use in both the triaxial cell and on unconfined specimens on the bench-top.

3.3.2 Design of new bender devices

In order to measure cross-anisotropy, two orthogonal shear wave velocity measurements are required. The usual form of anisotropy is evidenced by differences between properties in the horizontal plane (perpendicular to the direction of sedimentation and consolidation) and properties in any vertical plane. However, since real intact specimens of Gault clay (known to have been subject to additional asymmetry in their history due to tectonic movements) were to be tested, a decision was taken to build in more shear wave testing paths. The system was designed with four sets of bender elements incorporated to propagate and receive shear waves in orthogonal pairs both vertically and horizontally across the sample as shown in Figure 3.9. The terminology for the four measurements of shear wave velocity made possible with this configuration is:

$V_{s(vh)b}$ wave propagating vertically with horizontal polarisation at the same azimuth (horizontal direction relative to north) as waves propagating from the horizontal "bender belt".

$V_{s(vh)}$ wave propagating vertically with horizontal polarisation at the azimuth perpendicular to the waves propagating from the horizontal "bender belt".

$V_{s(hv)}$ wave propagating horizontally with vertical polarisation.

$V_{s(hh)}$ wave propagating horizontally with horizontal polarisation. (This wave coincides with the plane of isotropy in a cross-anisotropic material.)

---

§ Acknowledgement is given to Bennell, (1994) and Coop *et al.*, (1994) who provided some starting points from which the Bristol systems and techniques were developed.

Since in a truly cross-anisotropic material $V_{s(vh)} = V_{s(vh)b} = V_{s(hv)}$, the taking of three such measurements introduces the ability to cross check that the shear wave velocity measurement system is actually self-consistent. It is well documented that in triaxial tests end effects introduce non-uniform stress conditions in the soil adjacent to the rigid platens, (Lacasse & Berre, 1988; Ueng *et al.*, 1988). While impossible to assess with vertical platen mounted bender elements, investigation of the influence this has on the shear wave velocity measured using bender elements mounted in the rigid end platens of a triaxial cell is possible with the four shear wave paths proposed, and will be discussed in Chapter 4.

The design of bender elements for installation in the top and bottom platens of the triaxial cells (both 38 mm and 100 mm) was modelled on the design illustrated by Dyvik & Madshus (1985). These elements were 1 mm thick, 12 mm wide, and protrude approximately 10 mm from the platen. While contact with the soil samples only required a penetration of about 3 mm, the length that the bender protruded from the platen was kept significantly longer to account for the thickness of porous stones. The design of elements to receive and transmit shear waves horizontally across a triaxial sample at the mid height where there was no fixed rigid platen, and a thin flexible impermeable membrane rather than a porous stone clearly required a completely different design concept. Two systems for achieving this were developed. The first was based on incorporation of bender elements into the pads of the GDS horizontal belt, and the second was the development of bender probes with dimensions and installation procedures similar to those for mid-height pore pressure measurement such as illustrated by Baldi *et al.* (1988). Clearly there are significantly different mounting and spatial restrictions for this application than for the Dyvik & Madshus (1985) design, and the process of development required reconsideration of the nature of piezo-ceramic materials.

In this section the implications to the design of bender elements is explored by:

- considering the nature of the piezo-ceramic PZT-5B for use as a shear wave driver and receiver,
- considering the effect of design on the effectiveness of shear wave transmission through a triaxial sample,
- discussing the physics of the piezo-ceramic materials with respect to their application as bender elements,
- describing the other materials used in the fabrication of bender elements.

Piezo-ceramic material

The piezo-ceramic material used was the Bimorph PZT-5B as supplied by Morgan Matroc (Pty) Ltd in strips 10 mm wide by 79 mm. The material consists of two layers of piezo-ceramic sandwiched together with a metallic conductor forming the filling. Piezo-ceramic presented in this format can be made to act in a similar fashion to a bi-metallic strip. A bi-metallic strip deflects or bends when the metals it is composed of expand or contract differing amounts in response to a change in temperature. A piezo-

ceramic bimorph can bend or deflect in response to the application of an electrical charge, when the piezo-ceramic each side of the sandwiched conductor expands or contracts.

However, unlike a bi-metallic strip, the application of a mechanical load to the end of a bimorph will result in the development of an electrical charge, which can be monitored. This feature enables the same type of elements to be used for both transmission and reception of shear waves. The terms "driver" and "receiver" are used to indicate the mode in which the element is operated.

Whether the piezo-ceramic expands or contracts depends on the direction of polarisation of the crystal. If each piezo-ceramic layer is polarised in opposite directions, then the material deflects in response to opposite charges being applied to its surfaces. This is known as a series polarised bender. If each side is polarised in the same direction, then a deflection is only produced if the same sign charge is applied to each side of the element, and the opposite charge is applied to the sandwiched conductor. This is known as a parallel element, and it has an electrical impedance of a quarter of the impedance of an equivalent series element.

There is inevitably attenuation of the signal as it proceeds from the driver to the receiver. Different combinations of series and parallel poled elements can be used to reduce the magnitude of the differences between input and received signals. The use of a parallel poled bender as driver results in approximately double the deflection (and hence transmitted signal strength) that could be expected from a series poled bender subject to the same charge. Conversely, the use of a series poled bender as a receiver results in double the charge that a parallel bender would generate in response to the same deflection amplitude. Diagrammatic illustrations of the differences between parallel and series poled elements are given in Figure 3.10. The arrangement of a parallel driver with a series receiver gives essentially a built in 2 × magnification over using the same type of bender element as driver and receiver, and a 4 × magnification over a series driver - parallel receiver combination.

Shear wave transmission

The transmission of shear waves from a driver source, though a soil and into a receiver involves attenuation or partial loss of the signal. The loss depends on the quality of the series of interfaces or connections between the driver input signal and the received signal. Quantification of the losses depends on the actual soils being tested and the quality of the bender elements being used, and is therefore difficult (if not impossible) to assess in advance of developing the design. However, based on experience gained during the project, Table 3.5 has been compiled retrospectively to summarise the factors influencing the transmission across the interfaces and through materials between "driver" and "received" signal. Also included is an estimation of the signal strength at each stage of the propagation in terms of a voltage amplitude.

Transmission interface / material	*Factors influencing*	*Factors leading to improvement*	*Estimated loss in signal*	*Signal amplitude (V)*
Driver signal to PZT-5B	impedance of connections	Quality of soldering of connectors to PZT 5B	<1%	≈20
PZT-5B Piezo-ceramic	variations in purity of PZT-5B	manufacturing variations unavoidable	2 - 5%	19.8
PZT-5B to resin	quality of bond between ceramic and resin	fully de-grease and clean PZT-5B before potting	10 - 20%	19
resin	elastic modulus of resin, quality of casting process	use fresh resin, fully de-air before injection into mould, fully cure	10 - 20%	16
resin - soil	fit between transducer and soil, soil type and state	accuracy and control in the manner of insertion of the bender element, amount of consolidation following insertion	70 - 90%	12
soil	soil type and state	dry sands best, wet normally consolidated clays worst	30 - 70%	1.4
soil - resin	fit between transducer and soil, soil type and state	accuracy and control in the manner of insertion of the bender element, amount of consolidation following insertion	70 - 90%	0.5
resin	elastic modulus of resin, quality of casting process	use fresh resin, fully de-air before injection into mould, fully cure	10 - 20%	0.06
resin to PZT-5B	quality of bond between ceramic and resin	fully de-grease and clean PZT-5B before potting	10 - 20%	0.05
PZT-5B Piezo-ceramic	variations in purity of PZT-5B	manufacturing variations unavoidable	2 - 5%	0.04
PZT-5B to received signal	impedance of connections	Quality of soldering of connectors to PZT 5B	<1%	0.04

Table 3.5 Estimated signal loss at each interface and in each material

This table highlights the observation that the largest source of attenuation is across the interfaces between bender element and soil and that the magnitude of the received signal is usually many orders of magnitude smaller than that imparted to the driver element. As will be discussed in more detail in the next section, typical theoretical deflections of the bender elements fabricated for this project were of the order of 0.1 to 1 μm. The quality of the fit between the bender element and the soil is thus vital to good transmission or reception, and has the implication that the higher the quality of the fabrication of bender elements, i.e. the more regular and parallel the surfaces of the potted ceramic, the better will be the fit when the element is inserted into the soil.

Frequency and deflection response

The theoretical response of a series poled bimorph piezo-ceramic under ideal cantilever beam mounted conditions can be estimated from the Equations 3.1 to 3.6 for material PZT-5B, (Vernitron, 1992):

$$\text{Resonant frequency } f_R = \frac{1}{2\pi\sqrt{MC_m}} \text{ (Hz)} \quad \text{.....Equation 3.1}$$

Displacement $D = N \times Q = N \times C_e \times V$ (m) .....Equation 3.2

Effective mass $M = 0.033 \times l \times w \times t$ (kg).....Equation 3.3

Mechanical compliance $C_m = 2.8 \times 10^{-9} \times \frac{l^3}{w \times t^3}$ (m/N) .....Equation 3.4

Electrical capacitance $C_e = 500 \times \frac{l \times w}{t}$ (pico-Farads) .....Equation 3.5

Electro-mechanical transducer ratio $N = 0.6 \times \frac{l}{w \times t}$ (m/Coulomb).....Equation 3.6

These equations apply only at low drive levels and l, w, t are the beam cantilever length, width and thickness as illustrated in Figure 3.11. The drive levels of 2 to 20V used in this research were considered "low" voltages.

Since an objective in this research project was to develop a system capable of measuring shear wave velocities horizontally through the flexible membrane enclosing a sample, a design which is significantly different from that described in Dyvik & Madshus (1985) had to be developed. Bender elements for horizontal mounting therefore had to be significantly smaller. A length of 3.5 to 4 mm was considered desirable, as this results in a similar projection of the bender element into the soil sample (having passed though a membrane) as the platen mounted bender elements. This difference in projection length of about 4 mm reflects the difference in thickness between the porous stones and membranes used.

Equations 3.1 to 3.6 can be used to assess the implications of these changes, remembering that the equations apply to PZT-5B in air and not when encapsulated in resin. From Equation 3.2 it can be seen that the deflection of a bender element is proportional to the square of its length, and hence a change in cantilever length from 8 to 4 mm theoretically results in deflections a quarter of that for the Dyvik & Madshus (1985) design. This implies lower energy driver signals. However, since the path length horizontally across a sample is approximately half that vertically, and geometric damping is proportional to the square of the distance, the amplitude of the received signal should remain approximately equivalent to that in the vertical direction.

Equation 3.1 indicates that the resonant frequency is inversely proportional to l^2, and hence that a 4 mm element length has a theoretical resonant frequency four times higher than that for the standard design. The elements were encapsulated within a resin casing to enable use in the conductive environment of the soil, and it was considered impractical to scale down the encapsulation procedure that had been developed. The effect of not scaling this detail was thus evaluated by comparing actual measured resonant frequencies with theoretical predictions. Spectral analysis on the performance of prototypes subject to sweeps of pulses of varying frequency were therefore carried out. Typical response curves for a long (standard) and short (mini) bender element are illustrated in Figure 3.12. The results of five tests carried out on resin encapsulated bender elements of varying size are summarised in Table 3.6.

Bender Serial number	*Length (mm)*	*Width (mm)*	f_R *measured (kHz)*	f_R *calculated (kHz)*	$f_{R\ measured}$ / $f_{R\ calculated}$	*Calculated deflection (μm)*
100mm T b	7.0	10.0	4.1	4.3	0.95	1.18
BP04	3.6	8.0	17.5	16.2	1.08	0.31
BP07	3.3	5.0	19.0	19.3	0.98	0.26
BP09	3.2	10.0	23.5	20.5	1.14	0.25
RB b	3.0	5.0	23.9	23.4	1.02	0.22

Note: Dimensions are for the piezo-ceramic element only. Additional size due to resin potting has been ignored. Thickness of piezo-ceramic plate =0.5mm.

Table 3.6 Bender measured and calculated resonant frequencies, and calculated deflections

The calculated frequency is based only on the dimensions of the piezo-ceramic that actually projects as a cantilever from the mounting. The range of 0.95 to 1.14 for the ratio of measured to calculated frequencies clearly shows that the resonant frequency of bender elements in air was not significantly affected by the encapsulation in resin, and the optimum performance range of the "mini" bender elements was therefore likely to be four times higher than that of the standard design. This was reinforced by experience during the testing phase of the project, where test frequencies of between 10 and 25 kHz were found to be optimum for use with the mini elements, whereas 1.5 to 4 kHz was found optimum with the standard elements.

Also listed in Table 3.6 are the calculated deflections for the bender elements subject to a 20V driving signal. Since, as has just been discussed, the resin appeared to have little demonstrable effect on the resonant frequencies of the elements, it seems justifiable to presume that the calculated deflections are also reasonably good indications of the actual deflections**. These deflections can be used to estimate the amplitude of the shear waves during typical tests, and subsequently to estimate shear strains. If the estimated losses given in Table 3.5 are assumed to apply to the amplitude of the shear wave, and the wave length of the shear wave is given by the product of typical velocities and driver periods, then shear strains of the order of 0.0001% are calculated. This value is comparable with triaxial vertical strain levels at which material response is assumed, and observed, to be elastic.

The theoretical frequencies and deflections discussed in this section predicted significantly different performance characteristics for the "mini" bender elements from those of the "standard" bender design. On this basis it may not have seemed prudent to have continued with fabrication and use of the "mini" elements. However, prototype trials, and iterative improvement of the fabrication of these elements were successful and showed that high quality signals could be obtained at the smaller scale.

These smaller elements were integrated into devices to be used primarily in the triaxial cell. The design of these devices is discussed in the following sections.

** This was not checked by direct measurement in this research project.

Design of "Bender Belt" for flexible membrane mounting

The first horizontal bender device developed was a bender belt based on the GDS horizontal strain belt used to measure sample diameter. Modifications to the belt design included redesign of the pads used to attach the belt to the sample so that they could incorporate a set of orthogonally mounted "mini" bender elements in each pad. The re-design of these pads is illustrated in Figure 3.13a. This shows a pad with slots cut to incorporate the bender elements. During assembly, the elements are located and then additional resin is cast into the "dam" in the pad to provide rigid fixing. Figure 3.13b shows the general arrangement of the pads in the bender belt and their position relative to the Hall effect gauge, used to measure diameter. Note the addition of a slot in the belt to allow access for the bender cables. The pads are mounted in the belt using pin joints. The pins are essential to the operation of the benders as without them shear-waves would be transmitted around the belt, and the shear-wave velocity of the aluminium belt would mask any signal transmitted though the sample.

The bender belt design is considered suitable for application on relatively large diameter triaxial samples. While the device proved very successful, it did require considerable dexterity and time to mount on samples. Therefore, it was decided to design bender probes which were not only easier to mount, but could also be used on samples of any diameter.

Design of bender probes

The bender probe design was developed by combining the mounting concept of a mid-height pore pressure measurement probe, e.g. Baldi *et al.* (1988), with the bender belt concept. Two "mini" bender elements were mounted orthogonally in a 12.7 mm outside diameter brass "cup". The bender elements protruded approximately 4 mm from the face of the cup. The outside surface of the brass cup was polished to ensure leak-proof operation when sealed into the membrane with a rubber grommet. The design is illustrated in Figures 3.14 to 3.16. Figure 3.14 and Figure 3.15 show the details of the devices as designed for use as driver (parallel poled) and receiver (series poled) probes respectively. During use the probes were mounted diametrically opposite each other across a triaxial sample and were held in place by a rubber grommet until there was sufficient cell pressure to keep the probes flush with the sample. The initial distance between probes tips was determined by measuring the distance between the backs of the exposed cups and subtracting the full length of each probe from this.

3.3.3 Fabrication of bender elements and devices

Having introduced design concepts in the previous section, this section details the fabrication techniques developed to produce the bender elements and the devices in which they are mounted.

Preparation of piezo-ceramic platelets

The first stage of fabrication involved preparing platelets of piezo-ceramic which formed the basis of the fabricated bender element. Strips of PZT-5B 69 mm long by 10 mm wide were purchased, and then cut into platelets of either 10 mm x 12 mm for the "standard" sized elements, or 5 mm x 8 mm for the "mini" elements. This cutting was initially carried out using a ceramic rotating cutting disk as suggested by the

manufacturers. However due to difficulties in obtaining the use of a such a cutter, an alternative method involving breaking along a scored line was developed. The piezo-ceramic was rigidly clamped at one end to ensure accurate breaking. This method was found to be both reliable and quick. Whatever the initial sizing method used, final sizing and shaping to remove sharp corners was done using a fine grade diamond file. The diamond file was also used to remove partially one side of the piezo-ceramic on parallel poled elements to expose a corner of the sandwiched conductor for attachment of cable as shown in Figure 3.14.

Once sized, cables were attached using a low melting point silver solder and a relatively hot (No. 6) pointed soldering tip. During soldering, care was taken to ensure that the piezo-ceramic platelets were not overheated. As PZT 5B piezo-ceramic has a Curie point above 300°C, heating to anywhere near this temperature can lead to debonding of the composite.

Two types of cable were used: a 2.8 mm diameter circular section co-axial cable and a 1.8 mm oval section twin core cable with screen. The 2.8 mm cable was a relatively stiff cable, but one which was well suited to applications where benders were mounted in the rigid top and base platens of the triaxial cells. The 1.8 mm cable was significantly more flexible, and despite having a relatively thin outer shield, remained sufficiently impervious to moisture to never need replacing during the test programme.

Once cables had been soldered onto the platelets, the operation of each platelet was checked by connecting a signal source and listening for clear uninterrupted sound. The platelets and cable were then thoroughly cleaned using a degreasing agent in preparation for potting.

Potting the bender elements

Potting involved encapsulating the piezo-ceramic platelets and their cable connections in insulating resin, (Ciba Araldite, MY 753 with hardener HY 951). This high impedance clear resin proved to be durable for the length of the project, with the very first of the fabricated bender elements still working at the end of the project having endured some 196 days under a back pressure of 300 kPa over a period of approximately two years.

The bender elements were potted in two part perspex moulds. The moulds were lightly sprayed with a mould release agent before assembly. Once assembled, the PZT-5B platelets were lowered into position and clamped centrally with locating pins. The resin was mixed by volume in accordance with the manufacturers instructions and heated to approximately 50°C using an air gun to lower the viscosity[††], and then placed under vacuum for approximately ten minutes in order to remove air. Back at atmospheric pressure, the resin was again heated and drawn into a syringe taking care to avoid introducing any air. A 0.8 mm diameter hypodermic needle was used to inject the resin to the lowest point of the mould. Once the mould was full, the needle was withdrawn slowly, taking care not to introduce air bubbles.

[††] This led to quicker and more effective de-airing and also made injection into the potting moulds significantly easier.

The resin was allowed to set for approximately 24 hours before the moulds were opened, and the bender elements removed. Function of the bender elements was again checked by connecting a signal source and listening for clear continuous sound. Finally, all traces of mould release agent were removed in preparation for mounting.

Mounting of bender elements

The next stage of fabrication involved mounting the bender elements in either the end platens or the bender belt pads and bender probe cups.

Attention was paid to the arrangement of the cables to ensure shielding of all electrical conductors. Cable screening was continued as close to the element as possible, to minimise the risk of signal deterioration through interference. It was also established by experience that the most stable signals were received if the ground or screen of the cable to the receiver bender elements was connected to the soil sample. In the case of the bender belt pads grounding was achieved by connecting the earth line to one of the stainless steel pins used to pin the bender belt pad through the membrane and into the sample[‡‡].

The completed bender belt can be seen in the photograph in Figure 3.17, where it is pictured in conjunction with a 100 mm top cap incorporating orthogonally mounted "standard" sized bender elements.

In the case of the bender probes, only the receiver probes incorporated the connection from the cable screen to ground through to the sample. For a receiver probe, the brass cup therefore acted as a Faraday shield where the cable core was "exposed" before connection to the piezo-ceramic platelet. The cable screen was attached to the brass cup linking it to the ground of the instrumentation system, (see Figure 3.15). During tests the cup was earthed to the receiver through contact with the soil pore fluid. For the driver probes, all earthing routes were avoided, in order to prevent earth induction loops though the sample to the receiver probe.

Three bender probes are illustrated in the photograph in Figure 3.18. This shows two orthogonally mounted dual element "mini" probes, and a 9 mm wide single element probe. The latter probe was found to be useful in certain bench top (as opposed to triaxial cell) situations where the additional energy provided by the bigger probe helped improve received signal quality. This use of bender probes in bench top situations will be discussed in Chapter 4.

3.3.4 Shear wave velocity measurement instrumentation system

The instrumentation used to drive and receive signals from the bender devices is described in this section. As has been discussed, an objective of this research was to transmit and receive shear waves both horizontally and vertically and with orthogonal polarisation during triaxial tests on samples of Gault clay.

---

‡‡ Subsequent experience at Bristol University has shown that the use of screened twisted pair cables results in even cleaner signals.

The process of acquiring data at different stages during a test has to be reliable and efficient. The instrumentation system used was similar to that illustrated by Dyvik & Madshus (1985), but was augmented to improve both the quality of the received signal and the means of interpretation. The different elements in the system are illustrated diagramatically in Figure 3.19, and will be described in the order they were used from signal generation to storage on a PC.

Signal generator

Square waves signals were traditionally used to drive bender elements. While these waves are simple to generate, the conversion of these "digital" signals into shear waves by the "analogue" bender elements requires a change in the wave shape. Even if the bender elements could reproduce a square wave reliably, the transmission of these waves through soil is similarly not achieved as an "digital" wave, and hence the received signal from square waves will not be a square wave but effectively a Fourier decomposition of the square wave with the number of frequencies transmitted dependent on the damping properties of the soil. The use of sinusoidal waves of various forms has been reported by Jovičić *et al.* (1996), and their approach formed the basis for exploration of suitable waves for use in this project. To generate the more complex waves a programmable function generator, TG 1010 (a digital direct sampling function generator), was used. This instrument provided the possibility of complete flexibility in defining wave shapes.

The wave found consistently most reliable was termed a "sine pulse" and consists of a single sinusoidal pulse with a phase delay of 90°. This wave ramps sinusoidally from zero, and therefore never imposes a step signal on the bender element, leading to minimal "ringing" or overshoot. The waves mostly used in this project are illustrated in Figure 3.20. All four waves illustrated are based on a single sine pulse but with variations in their starting phase angle, and symmetry.

Charge amplifier

Bender elements are piezo-ceramic based transducers, and therefore essentially charge rather than current driven devices. They therefore perform best when matched with appropriate signal receiver equipment. While oscilloscopes have traditionally been used to view the received signals from bender elements, it was found that interfacing a charge amplifier (in this case a Kistler 5011) between the bender elements and the oscilloscope provided a significantly lower load on the receiver bender element. With this configuration received signals were of greater amplitude than if connected directly to the oscilloscope, even with amplification on the charge amplifier set to unity. Making use of this interface resulted in there never being a need to consider ways of increasing the voltage to the driver elements in order to increase the amplitude of the received signal.

Digital storage oscilloscope

Both the driver and receiver traces were fed into a 20 MHz Gould 1425 Digital storage oscilloscope (DSO) with the driver signal being used to trigger the capture of the received signal. The time difference between the driver pulse and the arrival of the received signals was measured to enable shear wave velocities to be determined. In most cases the quality of the received signal was improved by using the

stacking function on the oscilloscope. With this function successive arrivals of the wave were digitally summed, and averaged. This resulted in clearer signals due to the minimisation of spurious noise, such as mechanical vibrations or human disturbance in the laboratory. The DSO stored the signals in 12 bit arrays, typically at time base resolutions of 1 μsec.

During testing, first estimates of wave transmission times were made by using the cursor function on the oscilloscope to pick off transmission times. In addition all signals were downloaded to a PC, and at the end of a test a Microsoft Excel spreadsheet macro was used to load and plot each captured wave in charts with the same time-base, and with amplitudes stretched such that each plotted trace had the same peak to peak amplitude. As there is always some subjectivity in the interpretation of arrival times, particularly if taken over a period of months during a single test, this method was found to facilitate a more consistent interpretation, and led to significantly higher measurement accuracy as will be discussed in the following section.

3.3.5 Bender device measurement accuracy

The bender element method is used to calculate $G_{0(ij)}$ using the equation:

$$G_{0(ij)} = \rho V_{s(ij)}^2 = \rho \frac{L_i^2}{T_{ij}^2} \quad \text{.....Equation 3.7}$$

where "i" is the direction of propagation, "j" the direction of polarisation, ρ is the density, L_i is the distance between the tips of the benders oriented in the "i" direction, and T_{ij} is the transmission time of the shear wave propagated in the "i" direction, but polarised in the "j" direction. The accuracy with which $G_{0(ij)}$ is measured depends on the accuracy of the measurement of sample bulk density, the path length between the tips of the bender probes and the accuracy of the time of travel.

Bulk density

The accuracy in measuring changes in density is proportional to the accuracy of volume change measurement, and therefore of the order of 0.003% for relatively short test periods of less than a day, as discussed in Section 3.2.6 For tests carried out over a period of about two months absolute accuracy of bulk density was estimated to decrease to ± 0.1%.

Shear wave path length

The resolution of distance measurement in tests conducted with the bender belt was ±0.002 mm, or ±0.002%, with an estimated gross accuracy of ±0.01% on 100 mm diameter samples (see Table 3.4). However, with the bender probes used on 38 mm diameter samples there was significantly more uncertainty. The estimated uncertainty in initial separation between the driver and receiver bender elements was ±0.2 mm. During a test, changes in diameter were established using the assumption that the sample deformed as a right cylinder, leading to an uncertainty of approximately ±0.1 mm. The absolute overall accuracy of this measurement was therefore approximately 0.8% for the 38 mm tests.

Travel time

The resolution of time on bender element traces was generally 1 μsec for horizontal measurements on samples 100 mm diameter and vertical measurements on 38 mm samples. For vertical 100 mm diameter samples (path lengths of 180 - 190 mm) this was generally 2 μsec, while horizontally on 38 mm samples 0.5 μsec. In order to check for delays between a signal being sent to a bender element and a received signal due to the performance characteristics of the bender element system, two sets of experiments were carried out.

In the first, the responses of a self-monitoring element were observed. A self-monitoring element is a parallel poled element where the driver signal is applied to the sandwiched conductor and one of the other sides of the element, causing the element to deflect. The charge generated as a result of the deflection is observed by monitoring the signal between the other side of the element and the central conductor. The instrumentation set up was as illustrated in Figure 3.19, and includes a charge amplifier as an interface between the bender element and the oscilloscope. The results of monitored signals with frequencies of between 2 and 16 kHz are given in Figure 3.21a. This shows absolute delays of 5.5 ±1 μs for all frequencies.

In order to check that the result of this self-monitoring test was not being affected by the charge amplifier or electrical "cross talk" between driver and receiver pulses, the second experiment involved bringing two bender elements into tip to tip contact, and monitoring the output from one in response to an input signal to the other. This time the receiver element cables were connected directly to the oscilloscope, excluding the charge amplifier. The results of are given in Figure 3.21b. A very similar delay of 5 ±2 μs was measured. On the basis of these tests, a constant offset of 5 μs was applied to all bender traces, and an uncertainty of ±3 μs was assumed.

These uncertainties lead to estimates of accuracy of better than 1% in vertical shear wave velocity measurements on 100 mm samples, 1.5% on horizontal propagation through 100 mm samples and up to approximately 2.5% in the horizontal measurements on 38 mm samples. Comparing these accuracies with those for either the bulk density or distance measurement highlights that it is the measurement of travel times that dominates accuracy in determinations of $G_{\alpha(ij)}$ in this project. The rider is that there is most to be gained by improving the quality of the bender element system.

Combined accuracy

Indicative accuracies based purely on the inaccuracy in the measurement of bulk density, and shear wave velocity are summarised in Table 3.7. As will be discussed in Chapter 4, these are not the only factors affecting the measurement of shear modulus. In particular, the presence of non uniform stress states along the shear wave path, such as those caused by end restraint effects, leads to uncertainty in determinations made vertically through samples. This effect is largely avoided by use of the horizontal bender element devices described in this chapter, where the transmission path is likely to be through that plane of the sample where stresses are most uniform.

	Measurement accuracy	
Triaxial sample size	$V_{s(ij)}$	$G_{0(ij)}$
100mm	± 0.8 - 1.2%	±2 - 3%
38mm	±1.5 - 2.5%	±3 - 6%

Table 3.7 Estimated shear wave velocity $V_{s(ij)}$ and shear modulus, $G_{0(ij)}$ measurement accuracies

The discussion in this section has referred to the use of bender elements in triaxial cells, either as horizontal devices or platen mounted benders. It is worth noting however, that the bender probes developed here have also been successfully used in the measurement of shear wave velocities on undisturbed core samples in "bench top" situations either in the laboratory or "on site" immediately after sampling where it is the suction in the sample which replaces the effective confining pressure in a triaxial cell. In these situations it has been estimated that the accuracy in the measurement of $V_{s(ij)}$ is of the order of ±2% on samples where the bender path dimension is in the range 80 - 100 mm.

3.4 Summary

This chapter has outlined the development and commissioning of a specialised triaxial testing facility and associated bender element devices to enable measurement of cross anisotropic shear moduli.

The development of the triaxial system considered the need for stability, reliability and precision in the triaxial testing stations. In order to achieve stability and reliability attention was paid to the detail of laboratory infrastructure and environment. Precision in the control of stress states was achieved by the use of controlling devices able to resolve to better than 0.1 kPa, and the high resolution measurement of strains was acheived with local strain devices incorporating Hall effect gauges. This enables strains to be measured with accuracy down to approximately 0.002%, but as will be discussed in Chapter 4, this can be extended by approximately one order of magnitude on the basis of careful individual interpretation of small strain excursions.

The second part of the chapter described the development of new bender element devices capable of high quality transmission and reception of horizontally propagated shear waves polarised in orthogonal planes across the mid-height of a triaxial sample. The development process made reference to physical properties of piezo-ceramics in order to optimise their performance. Effective fabrication procedures were developed and have been described. The instrumentation systems used to drive and receive signals were outlined and quantified estimations of the magnitude of the shear strains developed by the bender elements and the accuracy with which shear wave velocities can be determined were discussed.

The next chapter describes the methods used to undertake the research, and comments on their validity, particularly with respect to the bender element methods.

4. MATERIALS AND METHODOLOGY: SAMPLING, PREPARING AND TESTING CAMBRIDGE GAULT CLAY

4.1 Introduction

This research project aims to establish the deformation properties of a stiff overconsolidated clay appropriate to basement retaining walls. The stiff clay is the Cambridge Gault clay and the Lion Yard car park in Cambridge has the deep basement retaining walls from which the research project developed.

Monitoring and initial back analyses have identified that deformations at small and very small strain levels are most relevant to the actual deformations observed at Lion Yard, Lings *et al.* (1991); Ng *et al.* (1992 and 1995b). Since the Lion Yard site in now effectively inaccessible for sampling, the testing proposed for this project has been carried out on samples obtained from the High Cross Test Site some 3 km west of the Lion Yard site. In their overview of material properties at the High Cross site, Butcher & Lord (1993) did not identify the anisotropic stiffness properties of the material. Butcher & Powell (1995) reported significant anisotropy at very small strain as evidenced by *in situ* shear wave measurements at the site. More recently Ng *et al.*, (1995a) attempted to establish the small strain stiffness of the Cambridge Gault clay, but did not measure anisotropic stiffness.

As has been highlighted in Chapter 2, investigations into the shear wave anisotropy of clays in general have not yet provided satisfactory understanding of the factors affecting this anisotropy. Investigation of these factors must therefore necessarily form part of the research project. Once established, very small strain dynamic shear wave velocity measurements and quasi-static triaxial deformation measurements can be used to develop a broader deformation model including aspects of the anisotropy.

This chapter forms the interface between the descriptions of the laboratory equipment given in Chapter 3, and Chapter 5, where the factors influencing the anisotropic shear moduli at very small strain, $G_{\alpha(ij)}$, are investigated. The progression to the development of a meaningful deformation model follows in Chapter 6 where shear wave and triaxial engineering strain data are combined in a cross-anisotropic framework to derive a consistent set of deformation properties for the Gault clay.

This chapter begins with an introduction to the Gault clay highlighting the origin and history of the material. The methods used to obtain and prepare samples for triaxial stress path and bench-top testing are then described. An account of the laboratory tests actually carried out in the investigation follows. The later sections of the chapter are used to assess the validity of the methods used.

4.2 The Cambridge Gault clay

4.2.1 General

In his report on agricultural improvements for the fenlands, Vancouver (1794) described "a buttery clay or gault". Use of the term predated the first time in 1815 the Gault was shown as a discrete formation on the

geological map of England and Wales where it was referred to as the "Golt Brick Earth", (Gallois and Morter, 1982). Based mainly on experiences in the Weald to the South of London, and along the Cliffs of the Isle of Wight, the Gault aquired the ignominious title of "Blue Slipper". In their investigations into landslips at Folkestone Warren, both Toms, (1945) and Muir Wood, (1955) noted particular difficulties in obtaining samples of Gault clay for strength tests because of the highly fissured nature of the deposit. While these early impressions of the formation belie its revelation as a "soft rock" in the Lion Yard back-analysis, the earliest known reference in 1575 to the term "in grounde that is harde to dygge as in galte clay and stonye grounde" seems to show some resonance![*]

The Gault was deposited in a deepening muddy sea. In their BGS memoir, Worssam & Taylor (1975) describe the Cambridge Gault clay as a "tough grey clay or marl. Nodules of phosphatised, commonly fossiliferous marl are scattered in the clay or concentrated in seams...." The upper part of the Gault, with which this project is concerned, is highly calcareous, containing up to 30% calcium carbonate. The calcareous matter consists of "foraminifera, ostraceous, fragments of Inoceramus and a large measure of coccoliths....." which foreshadowed the deposition of the chalk as seas cleared.

The Gault is part of the Cretaceous, along with the underlying Lower Greensand, and overlying irregular Cambridge Greensand at the base of the Chalk. The underlying geological formation in the Cambridge region is the Jurassic and consists mainly of the Kimmeridge and Corallian clays. The Gault outcrops (or is near to the surface) in a band about 5-6 km wide which runs SE from the Wash in Eastern England as shown in Figure 4.1a. This outcrop constitutes the NW rim of the bigger European outcrop of Albian sediments (which include the Gault) which has its other major outcrop in a band running NE / SW across central France as shown in Figure 4.1b.

4.2.2 Basic engineering properties

Butcher & Lord (1993) have provided a geotechnically relevant summary of the engineering properties of the Gault at the High Cross site near Cambridge. Forster *et al.* (1994) conducted a wider based review of the Gault. These sources have been used to compile the summary of properties is listed in Table 4.1.

Property	*Value*
Bulk density	1900 - 2000 kg/m^3
Plastic limit	26 - 32%
Liquid limit	75 - 80%
Moisture content	29 - 31%
Carbonate content	30%
OCR	40 ± 10
In situ K_0 at 6 - 8 m depth	1.9 - 2.1
Coefficient of Consolidation, c_v	1.3 - 2.7 m^2 / yr
Coeficient of volume change, m_v	0.02 - 0.11 m^2 / MN
Reload shear modulus SBPM	30 - 40 MPa

Table 4.1 Summary of properties of the upper Gault clay (4 - 8 m depth at High Cross)

[*] Oxford English Dictionary

4.2.3 Post depositional history

The Gault has been subject to severe over-consolidation due to deglaciation and erosion. Estimates of depths of burial in the Cambridge region range from 150 m (Marsland and Powell, 1990) to 400 m (Ng and Nash, 1995c). This stress release perpendicular to the exposure surface of the Gault is also often an influencing factor in producing planar fissures parallel to the surface, and was inferred from the fissure patterns observed in the Gault by Fookes and Denness, (1969).

In addition to vertical stress relief, and along with the overlying Chalk, the Gault was subject to an episode of folding, presumed to have taken place in the mid-Tertiary, (Worssam & Taylor, 1975). This resulted in a number of anticlines and synclines in the Cambridge area with axes running NNE - SSW. A more minor fold also runs approximately E 10°S from North Cambridge as shown in Figure 4.2. These folding processes will have subjected the Gault to sustained non-uniform stress conditions in the horizontal plane. Possible consequences of this action on the Gault were investigated using bender element tests, and will be discussed in Chapter 5.

4.2.4 Mineralogy, microstructure and fabric

In their broad study of the Gault clay, Forster *et al.* (1994) bring together the body of published work on the Gault in England and provide useful context from an engineering geological perspective, and in particular discuss the mineralogy of the deposit.

The Gault contains both clay and non-clay minerals. The upper Gault in East Anglia is smectite rich, Samuels, (1975) and XRD measurements for equivalent horizons at Klondyke Farm 20 km NW of the High Cross site indicate 35-49% smectite, 10-15% illite and 41-56% kaolinite, (Prior *et al.*, 1993). Quartz and calcite are the major non-clay minerals. The calcite (or carbonate content) consists in macrofossil form of shell fragments and in micro fossil form of coccoliths. Other non clay minerals generally include feldspar, mica, pyrite and gypsum.

At the start of this project it was believed that the carbonate content ($CaC0_3$) of the Cambridge Gault might also include re-crystallised calcite which acts as a cementing agent, and that this could in part be responsible for the very high initial stiffness of the material. In order to look specifically at the occurrence of the carbonate, and the micro-structure of the actual horizon of the Gault being studied in this project, samples obtained from the High Cross site were prepared for thin section and SEM imaging. Two colour thin section images at different magnifications are presented in Figure 4.3 and in these the carbonate is seen to express itself in a number of forms:

- as selenite crystals within the clay,
- as granular carbonate in the clay matrix,
- as small particles of calcite,
- as carbonate shell fragments,

- as microfossils.

None of these forms appears compatible with the concept of an interlocking matrix cemented by re-crystallised carbonate. However, in Figure 4.3b strong orientation of the shell fragments approximately 0.1 mm in length indicate, even at this scale, a feature that may contribute to anisotropic behaviour.

The fabric of the natural clay is most clearly seen in Figure 4.4 where SEM images at two magnifications are shown. The clay particles are generally aggregated in "domains", (that is groups of parallel particles, Sides and Barden 1970), which probably originated as flocs during deposition. Like the observations made for Pappadai clay by Cotecchia and Chandler, (1997), this appears to indicate that the deposition of Gault clay originally resulted in a "book house" fabric which was subsequently compressed, leading to a largely preferentially oriented clay.

These features appear to provide a visual explanation for anisotropic mechanical deformation behaviour where a major plane of anisotropy would be oriented perpendicular to the predominating orientation of clay particles.

4.3 Sampling to stress path testing

4.3.1 The site

The Lion Yard development is in central Cambridge, and as could be expected at this location, the main geological unit of the Gault is overlain by 4 - 5 m of both river terrace deposits of sand and gravel, and made ground. The relative locations of Lion Yard and High Cross test site, from where samples were obtained, are shown in Figure 4.5a. Profiles from cone penetrometer tests, (Marsland and Powell, 1988) show matching features which occur at a level 10 m higher at High Cross than at Lion Yard as the base of the Gault rises over the 3 km separating the sites. The same units that intersect the Lion Yard basement may therefore be intersected at shallower depths at the High Cross site.

The High Cross site is maintained as a research facility (overseen by the University of Cambridge), and has been characterised by amongst others, Kay & Parry (1982), Marsland & Powell (1990), Butcher & Lord (1993). Of particular interest to this study is a detailed *in situ* seismic shear wave study reported by Butcher & Powell, (1995), in which various shear wave measurement techniques were used to provide profiles of $V_{s(vh)}$, $V_{s(hv)}$ and $V_{s(hh)}$ *vs.* depth.

At the time samples were obtained for this project the site had become overgrown with hawthorn which had reached heights of up to 4 m. This had to be cleared in order to obtain access. There was concern that the root systems of this growth had penetrated the layers of interest, and therefore careful inspection of samples was carried out during borehole construction. This established that evidence of rootlets extended to about 4 m depth, and it was concluded that the depths of 6 to 8 m from which samples were actually tested were probably free from significant influence.

4.3.2 Sampling

Sampling was carried out by the Building Research Establishment at locations illustrated in Figure 4.5b. This involved use of the rotary rig driven, large diameter, stiff clay over-auger system illustrated in Figure 4.6. This system is capable of obtaining samples of 254 mm diameter and up to 800 mm in length. Essentially a steel tube is pushed into the ground behind a cutting shoe, while an independent over-auger removes soil from the outer edge of the cutting shoe. This forms a clear annulus around the outside of the sampling tube so that it is only friction on the inside of the cutting shoe and sample tubes that needs to be overcome by downward thrust. A bearing at the top of the sampler (see Figure 4.6) enables independent rotation of the auger in the direction needed to advance the hole, while the sampling tube remains at the same azimuthal orientation it entered the ground. If the direction of auger rotation is reversed, the auger and the tube are locked and rotate together.

The sample tubes were fabricated from seamless mild steel tubing with internal diameters of 254 mm and wall thickness of 6.4 mm. The tubes were cut to 0.9 m lengths, and required machining and locating holes at one end to fit to the one way bearing system, and locating holes at the other to attach the cutting shoe. The cutting shoe has an internal diameter of 254 mm, a leading edge cutting shoe angle of 30°, which reduces to 7° 10 mm back from the leading edge. There are cutting teeth at the leading edge of the auger. These remove clay from just behind the cutting shoe 110 mm back from the leading edge. Baligh *et al.* (1987) used the strain path method to evaluate centre line shear strains in terms of the area ratio given by the tube thickness to diameter ratio. This approach is not strictly applicable to this sampling arrangement due to the removal of soil from the outside diameter of the sampler. However, if this is ignored, the system has an area ratio of 40, putting it in the same league as the University of Laval sampler for which vertical centre line strains less than about 0.7% are predicted.

Key steps in the preparation and sampling techniques were:

- The inside walls of the steel sample tubes were shot blasted to remove rust and then greased to reduce shear stress.
- The borehole was advanced to approximately 0.2 m above the required starting depth using a 24" OD auger. During this process only minimal water was added to the borehole when necessary to facilitate spoil removal.
- The hole was cleaned to the correct starting depth using a 20" bottom cutter cleaning bucket.
- The sampler was lowered to the base of the borehole, the cutting shoe was allowed to penetrate the base under self weight, the orientation of the sampler relative to the orientation of the boreholes used for cross-hole seismic studies reported by Butcher & Powell (1995) was determined using a reed switch / magnet device.
- The sample was obtained by rotating the outer auger system while advancing the whole device into the ground. The balance between auger speed and push force was controlled by the operator.

- Once the full sample depth was reached, the rotation direction of the auger was reversed. This caused the auger to lock to the sampling tube, and shear the sample at the base of the cutting shoe, allowing the full sampler to be withdrawn.

- On retrieval of the sample to ground level, the orientation of the tube relative to the seismic crosshole boreholes was transferred from the drilling rods to the tube, the bearing unit was removed allowing access to the sample tube, and the ends of the samples were waxed using a non shrink wax.

The first attempt at sampling was carried out in Borehole LS1 (Large sample 1) on 21 November 1995 as listed in Table 4.2. The sampling quality on two of the four samples retrieved was good. However, they were rejected for testing purposes on account of observed root content. The deeper samples were subject to significant vibration from the drill rods, and sampling was abandoned after an attempted sample at 6 m. The borehole was advanced to 7 m depth using dry open hole drilling, and a pneumatic piezometer was installed at this depth, before grouting the borehole back to ground level with a cement / bentonite mix.

Borehole	*Sample No*	*Depth min (m)*	*Depth max (m)*	*Comments*
LS1	1	2.00	2.80	Many roots but smooth sampling
LS1	2	3.00	3.80	Many roots but smooth sampling
LS1	3	4.00	4.65	Very disturbed due to rod vibration
LS1	4	5.00	5.40	Very disturbed due to rod vibration
LS1	5	6.00		failed to collect

Table 4.2 Samples retrieved from Borehole LS1: 58912.7N 42148.1E constructed 21/11/95

The drilling system had clearly not performed as required and modifications to the drilling rod connections and the auger cutting teeth were carried out before a second attempt was made in March 1996. The modifications attempted to improve the rigidity of the connection between the drilling rods and the sampler. The samples retrieved during the second visit are listed in Table 4.3. Two samples from below the influence of the roots were obtained successfully. However the drilling system again deteriorated and excessive vibrations lead to unacceptable sample disturbance below 8 m. The borehole was abandoned after attempting sample LS2 / 4, and grouted back to the surface.

Borehole	*Sample No*	*Depth min(m)*	*Depth max (m)*	*Comments*
LS2	1	5.9	6.8	Good sample
LS2	2	7.05	7.8	Good sample
LS2	3	8.2	8.85	Disturbed due to rod vibration
LS2	4	9.05	9.45	Disturbed due to rod vibration

Table 4.3 Samples retrieved from borehole LS2: 58909.4N 42150.8E constructed 2/3/96 - 4/3/96

The samples were transported back to Bristol, resting on foam rubber packing material in a light utility vehicle, where they were stored in the cold storage room at a temperature of approximately 8°C.

4.3.3 Ground water

Ground level at the site is at approximately 18 mOD. A standpipe, installed by Fugro at location P1 (see Figure 4.5b) during a previous unrelated research investigation, was monitored at the time Borehole LS1 was constructed in November 1995 and indicated a ground water level of 13.8 mOD.

A pneumatic piezometer was installed at a depth of 7.0m in Borehole LS1 constructed in November 1995. This indicated a piezometric level of 13.7 mOD.

On the basis of these collaborating readings, it was assumed that the water table over the depth range of the samples obtained, was hydrostatic below 13.8 mOD, or 4.2 m depth.

4.3.4 Test sample preparation

Undisturbed samples for triaxial tests

The large size and mass (up to 130 kg) of the samples necessitated the use of a small crane to manoeuvre the full sample tubes in the laboratory. Samples were extruded vertically using a modified tube retention system attached to the conventional 100 mm thin walled tube extrusion device in the Bristol laboratory. Despite the greasing of the insides of the tubes prior to sampling, extrusion loads of up to 3.5 tonnes were required. Most of the preparation was carried out in a high humidity room. Samples were trimmed initially by hand using small cuts with a sharp knife so as to avoid damaging the samples along fissure lines. To prepare cylindrical samples of approximately 105 mm diameter and 200 mm height took up to three hours. Following suggestions by Winter & Horseman (1993), the final sizing was carried out using a band saw in the Department of Civil Engineering workshops. The sample was placed in a portable soil lathe specifically constructed for use on the table of a band saw. Small vertical shavings were cut from the outer diameter using a relatively fine saw blade while rotating the sample to create a right cylinder. This procedure took approximately 15 minutes, and the sample was then returned to the high humidity room.

The sample azimuth (relative to the field crosshole seismic tests conducted at the site) was transferred from the marking on the sample tubes to one end of the prepared sample and maintained through all the preparation procedures so that the bender belt could be attached along the same azimuth. See Figure 4.7 for illustrative photographs of the sample preparation process.

Sample suction measurements using a suction probe, (Ridley & Burland, 1996) were taken to establish the influence of the sample preparation procedures on the initial effective stresses within the clay samples. The first measurements were carried out on sample tubes LS2 / 1 and LS 2 /2 two weeks after sampling on 5/3/96. As a suction probe was only available when Dr Andrew Ridley of Imperial College was able to journey to Bristol, measurements at the following stages were only carried out for the first of the high quality tests on natural material:

- as soon after sampling as possible,

- during extrusion,

- after final preparation on the band-saw.

The results are presented in Figure 4.8 where suction is plotted against time for three stages of monitoring. Comparison of Figure 4.8a and Figure 4.8b shows an increase in the suction within the sample of only 7 kPa over the three month period the sample was in the tube. This confirms that the most usual problem in stiff clays of significant increases in effective stress due to sampling, (Vaughan *et al.*, 1993) did not appear with the sampling technique used at High Cross. Figure 4.8b shows variations of up to 15 kPa in the suction resulting from the extrusion process. It is interesting to note the comparison of this 15 kPa with the average resisting shear stress on the sample circumference in contact with the sample tube during extrusion which had a peak value of about 25 kPa.

The suction measured after preparation in the band saw is illustrated in Figure 4.8c, and indicates a final suction 28 kPa greater than that first measured on the sample over three months earlier. Anecdotally, a 100 mm × 100 mm sample cut from the same tube was found to develop a suction of approximately 600 kPa within two hours while standing unsealed on the bench in the air-conditioned (and hence desiccated) environment of the laboratory. This contrast was considered to illustrate that negligible additional disturbance was caused by the preparation technique.

Reconstituted samples

Reconstituted samples were prepared on the basis of techniques learned in discussions with Coop *et al.*, (1994). Similar techniques used to reconstitute kaolin resulted in reproducible anisotropic highly oriented fabric. This was confirmed using SEM imaging, (Martin and Ladd, 1978).

The procedure involved remoulding air-dried shavings at a moisture content of 1.8 times the liquid limit of 74%. The shavings were obtained from comparable depths during the field sampling exercise, and during the preparation of the natural samples as described above. These were air dried at room temperature in accordance with recommendations by Delage and Lefebvre, (1984). De-ionised water was added to raise the moisture content from the *in situ* level of approximately 30% to 130%. The resulting slurry was thoroughly mixed for approximately two hours, and then de-aired under vacuum to remove air entrained during mixing. The slurry was carefully poured down the inclined walls of both 38 and 98.5 mm internal diameter consolidometers, and an initial nominal vertical stresses of about 20 kPa applied. The consolidometers were of the floating cylinder type, to minimise the effects of wall friction. Despite this, wall friction was estimated to reduce the applied vertical pressure by about 10%. The top and bottom pistons of the consolidometers contained porous disks to facilitate two way vertical pore-water flow. Once consolidation under the initial stress was nearing completion, further increments in vertical stress were applied. The maximum value of 150 kPa was reached in about two days for the 38 mm consolidameters and about 14 days for the 100 mm diameter samples. Allowing for wall friction, this value resulted in an effective confining stress of about 100 kPa (on the basis of the value of $K_o = 0.6$ as determined for the Gault, Ng, 1992).

The suction in a typical 38 mm sample after extrusion from the consolidometer tube was measured to be 25 kPa. While this was somewhat lower than the effective consolidation confining pressure, it was considered a suitable effective stress to apply to all triaxial tests on reconstituted material during the saturation stage since minimal changes in sample volume were measured to reach this state.

Preparation of samples for bench-top testing

Bender element tests were also carried out on samples outside the triaxial cell. For these tests, the effective confining pressure was assumed to be equivalent to the sample suction. Clearly this does not necessarily result in a uniform stress state in natural samples of Gault clay, due to fissures and the possibility of partial saturation. However, it was considered that reasonable uniformity would be present in both reconstituted samples, and samples of natural material that had already been saturated in the triaxial cell.

The purpose of carrying out tests "on the bench-top" was to

- enable relatively quick assessment of the performance of the newly developed horizontal bender devices,
- enable measurement of $V_{s(vh)}$ without the possible constraining end effects of the porous discs used in the triaxial tests,
- remove the constraints on the number of bender probes it is feasible to mount on a triaxial sample, and enable assessment of the shear wave velocities $V_{s(hv)}$ and $V_{s(hh)}$ along multiple azimuthal bearings.

Photographs illustrating the preparation of a sample of natural Gault clay for bench-top testing, and then its subsequent testing using multiple bender probes is given in Figure 4.9. The sample was first trimmed to size using the techniques described in the previous section, then sealed in low melting point wax. Locations for the bender probes were scribed onto the sample, and a drilling jig used to bore tight fitting sockets for the bender probes. For testing, bender probes were pushed firmly into the sockets, and the tip to tip distances between corresponding bender pairs calculated by subtracting the total length of the probe pair from the distance measured across the backs of the probes.

4.3.5 Test set-up

This section considers the procedures developed to set up the triaxial samples with the bender, local strain, and mid height pore pressure measuring devices. Details were developed from methods given by Bishop & Henkel (1962) and advances in setting procedures given by Lacasse & Berre (1988), Germaine & Ladd (1988) and Baldi *et al.* (1988). Much was also learned from discussions with laboratory experts who freely gave of their time and advice; Coop *et al.* (1994); Harwood (1994); Pierpoint (1994), Ackerley *et al.*, (1994), Tatsuoka, (1995), Ridley, (1996).

The specific goals in the setting up of these samples of either heavily overconsolidated or normally consolidated reconstituted clay were:

- to cause minimum sample disturbance,
- to ensure the best possible connection between the bender elements and the sample.

Approaches taken to minimise these and related causes of disturbance during set up and restoration to *in situ* stress states are summarised in Table 4.4.

Potential cause of disturbance	***Action taken to minimise cause***
Evaporation between preparation in high humidity environment and sealing in membrane	Wrapping sample in "cling film" for as long as possible and minimising exposure time before the sample is enclosed within the membrane
Swelling of natural samples resulting from contact with water in the porous disk during set up	Use of fuse-wire to separate sample from stone until sufficient cell pressure is applied to cause local bearing failure onto the fuse wire, *Ridley (1996) with additional considerations from Ampadu & Tatsuoka (1993)*, (Reconstituted samples too soft for this technique, but significantly lower suctions meant swelling not a big problem.)
Permeable membranes	Presoaking membranes in deaired tap water, *Ackerley et al. (1994)*
Membrane leakage during testing	Polishing platen surfaces which contact membranes and use of hose clamps to increase sealing effect of "o" rings *Hossain (1995)*
Disturbance of the horizontal bender / sample connections	Care during assembly that the bender probes are not "over pushed", and then "rebound", leaving a gap between the tip and the soil.
Non uniform stress states caused by top cap misalignment	Reduced through use of a single resin pot / loadcell spigot. This accommodates minor misalignement. *Developed from ideas presented in Baldi et al. (1988)*
End friction effects	Used samples with heights of 1.85 to 2D length which ensures most of sample experiences triaxial states, *Lacasse & Berre (1988)*
Excessive strains due to reconsolidations stress path	The application of initial isotropic stress = suction measured in the sample during preparation $\approx \sigma_v'$. and then increasing σ_h' until *in situ* stress state is reached, *Garga and Khan, (1991)*

Table 4.4 Causes and remedies to disturbance caused during set-up

The achievement of these goals was aided by the use of method trees used to ensure efficient set up procedures. A form of the method used to set up the 100mm undisturbed Gault samples is listed in Figure 4.10. While this does not contain every detail, it forms a useful checklist for the setting up procedures followed, particularly for setting up 100 mm samples with mid height pore pressure, local vertical strain, and bender devices, where total preparation and set up times were of the order of 12 hours.

The implications of end effects on triaxial testing have been recognised for many years, and the advantages and disadvantages associated with either frictional or lubricated ends continue to accumulate, e.g. Germaine & Ladd (1988). Since the effects of stress magnitude in particular directions are fundamental to interpretation of shear wave propagation velocities, improvement of uniformity of stress state by using lubricated ends was considered. However, the need for efficient drainage of the Gault clay, and the difficulties that would be associated with vertical bender elements protruding though any

lubricated layer, rendered impractical attempts to reduce end friction. Rather it was decided to use samples of height twice the diameter, where the end effects may reasonably be considered not to influence the middle third of the sample. Further, the use of both local horizontal and vertical gauges to measure triaxial strains over this middle third, and the development of bender devices for mid-height measurements, effectively offer a practical means of being able to assess and avoid (if necessary) end effects.

4.4 The stress path testing programme

A programme of stress path tests was devised to investigate the small strain anisotropy of the Gault clay in the following two broad categories:

- Tests carried out on samples of reconstituted Gault clay where the fundamental influences of stress state, voids ratio, fabric and anisotropy on shear wave velocities could be investigated. Measurements included both single and multiple shear wave velocities, but no local strain measurement.

- Tests carried out on carefully obtained and prepared samples of natural Gault clay. Local strain and multiple shear wave measurements were included.

The initial specified goal of the project did not include development of equipment to measure multiple shear wave velocities. The first stage of development was therefore to establish bender equipment to measure vertical shear wave velocity, $V_{s(vh)}$ and to carry out tests to establish techniques and enable comparison with previous work in the field.

The subsequent discovery that Gault clay is highly anisotropic led to the development of anisotropic shear wave velocity measuring devices, and the realisation that such tests provide significantly more insight into influences on $G_{0(ij)}$ than do tests where only $G_{0(vh)}$ is measured. The emphasis of the project was therefore adapted to concentrate on tests where three or four sets of shear velocity measurement were made. Tests where only $V_{s(vh)}$ was measured will therefore not be discussed in detail. However, results will be included in a general summary for comparison.

4.4.1 Tests on reconstituted samples

Tests where only $V_{s(vh)}$ was measured:

The initial suite of tests was carried out on 38 mm reconstituted samples with the measurement of $V_{s(vh)}$ only. The purpose of these tests was:

- to establish that the implementation of bender techniques and related systems was successful,

- to enable comparison of the influences of voids ratio under isotropically cycled stress for correlation with previous work e.g. Viggiani (1992b),

- to ascertain the influence of consolidation stress ratio (σ_h'/σ_v') on $G_{0(vh)}$

The stress paths followed, and the corresponding voids ratio *vs.* log p' plots for tests L08, N11, L15 and N20[†] are shown in Figure 4.11. In these plots the shear wave velocity was measured at each of the stress states indicated by a plot symbol. The tests consisted of cycles of increasing and decreasing stress at constant ratios of $\sigma_v'/\sigma_h' = 1$ (isotropic), 0.75, and 0.6 (the assumed K_0 ratio for one dimensional consolidation after Ng, 1992)

Tests on samples where $V_{s(vh)}$ $V_{s(hv)}$ and $V_{s(hh)}$ were measured:

Once the bender devices for horizontal shear wave propagation had been developed, the main suite of testing on reconstituted samples was carried out on both 100 and 38 mm diameter samples. The stress paths and associated voids ratio *vs.* log p' plots are shown in Figure 4.12 and Figure 4.13 respectively.

Tests on 100mm reconstituted samples

Figure 4.12a shows the two stages carried out in Test R09. The first stage consisted of incremental isotropic loading and unloading to stress states b c d e. This stage ended with the return of the sample to an isotropic stress of 100 kPa (point b) and an *OCR* of about 6. A second stage of testing was then carried out at constant p′ and involved two cycles of anisotropic stress reversal between $\sigma_v'/\sigma_h' = 0.4$ and 2.3.

Test R16 (illustrated in Figure 4.12b) was carried out as a true K_0 consolidation and swelling test on a 100 mm diameter sample. Horizontal strain (measured using the horizontal belt) was controlled to be zero using the method described in Toll (1993). The purpose of this test was to confirm the value of $K_0 = 0.6$ while measuring $V_{s(ij)}$. While some deviation from the $\sigma_h'/\sigma_v' = 0.6$ line in Figure 4.12b can be seen, this was considered relatively minor, and for the sake of simplicity, K_0=0.6 continued to be used as the one dimensional ratio for 38 mm diameter tests on reconstituted Gault clay where horizontal strain measurements were not made directly.

Tests on 38mm reconstituted samples

Tests carried out on 38 mm diameter reconstituted samples with the measurement of $V_{s(vh)}$, $V_{s(hv)}$ and $V_{s(hh)}$ are illustrated in Figure 4.13.

- Test L24 was isotropically consolidated to 110 kPa, and then cycled between stress ratios of $\sigma_h'/\sigma_v' = 0.6$ to 2.0.

- Tests N19, L22 and N25 were initially saturated at an isotropic stress of approximately 25 kPa, which represented the initial sample effective stress determined using suction measurement. Vertical stress was then increased until the stress ratio $\sigma_h'/\sigma_v' = 0.6$ was reached. Cycles of incremental loading and unloading were then carried out.

  - Test N19 was consolidated to $\sigma_v' = 300$ kPa and then unloaded to $\sigma_v' = 65$ kPa while maintaining $\sigma_h' = 180$ kPa.

[†] The letter in the test reference refers to workstation North, Left (both 38 mm stress path cells) and Right (the 100 mm stress path cell). The number portion was incremented sequentially during the project. Missing numbers refer to tests that were either used to practise techniques, or failed before useful data could be obtained.

- Test L22 was cycled at $\sigma_h'/\sigma_v' = 0.6$ by loading to $\sigma_v' = 150$ and 300 kPa, with interim unloading to 50 kPa, before re-loading to 880 kPa. From this point it was unloaded at constant $\sigma_h' = 530$ kPa by decreasing σ_v' to 275 kPa and $\sigma_h'/\sigma_v' = 1.93$. It was then further unloaded at constant σ_v' until an isotropic stress state of 275 kPa was reached.

- Test N25 was cycled at $\sigma_h'/\sigma_v' = 0.6$ by loading to $\sigma_v' = 150$, 300, 600 and 1200 kPa, with interim unloading to $\sigma_v' = 150$ kPa. Each time unloading reached $\sigma_v' = 150$ kPa, a further unload / reload cycle was carried out at constant σ_h' to stress ratios $\sigma_h'/\sigma_v' = 1$, 1.68, 1 and back to 0.6. This testing sequence enabled voids ratio effects to be isolated from stress ratio effects, and these test results will be used extensively in the interpretation carried out in Chapter 5.

Summary of tests on reconstituted samples

A summary of data pertaining to tests carried out on reconstituted material is given in Table 4.5. This includes the diameter of tests samples, the date and duration of tests, the initial saturation of the sample and actual specific volumes before and after testing for comparison with specific volumes at the end of each test determined on the basis of volume change measurements made during the tests. These indicate generally high quality tests where it is reasonable to assume relatively high certainty on the subsequently derived stress / volume states. Also indicated in Table 4.5 is the use of mid height pore pressure probe and bender devices in each test.

Test No.	*Diam (mm)*	*Start Date*	*Duration (days)*	$S_{r(initial)}$ *(%)*	*Specific Volumes*				*Mid ht. pp probe*	*Bender data*			
					$v_{initial}$	v_{final}	$v_{f\,(vol)}$	$v_{f(belt)}$		G_{vh}	$G_{vh(b)}$	G_{hv}	G_{hh}
L08	38	15/02/96	13	97.9%	2.40	leak detected after 12 days		n/a	*	*			
R09	100	11/03/96	75	99.9%	2.27	leak detected after ≈70 days		1.93	*		*	*	*
L10	38	08/03/96	52	100.3%	2.37	1.89	1.83	n/a	*	*			
N11	38	14/05/96	51	99.2%	2.50	1.89	1.87	n/a	*	*			
L15	38	17/07/96	36	98.5%	2.47	2.26	2.22	n/a	*	*			
R16	100	01/10/96	76	96.4%	2.30	2.05	2.04	2.05	*	*	*	*	*
N19	38	01/11/96	19	94.7%	2.35	1.98	1.94	n/a			*	*	*
N20	38	22/11/96	32	98.2%	2.47	2.07	2.00	n/a	*	*			
L22	38	15/01/97	49	98.0%	2.35	1.88	1.83	n/a			*	*	*
L24	38	07/04/97	8	97.5%	2.37	leak		n/a			*	*	*
N25	38	09/04/97	48	97.2%	2.32	1.99	1.97	n/a			*	*	*

Table 4.5 Summary of tests on reconstituted samples

4.4.2 Tests on natural undisturbed samples

A series of three tests were carried out on high quality undisturbed samples of Cambridge Gault clay. The objective of the tests was to restore the samples to the *in situ* stress state, and from there to conduct Multiple Mini Stress Path Excursions (MMSPE) in order to derive anisotropic elastic parameters.

In order to reach the *in situ* stress state, an initial isotropic effective stress equivalent to the calculated *in situ* vertical effective stress, was first applied. The horizontal effective stress was then increased at a rate of 1 kPa / hour, while maintaining constant vertical effective stress, until the estimated *in situ* K_0 was reached. This procedure was adopted because it offers the quickest, minimal strain route to the *in situ* stress state, (Garga and Khan, 1991). Table 4.6 summarises the *in situ* vertical effective stress, the suctions measured on the samples, and at the vertical effective stress actually maintained during the re-consolidation procedure.

Test Number	Sample Tube	Depth (mbgl)	σ_v' in situ (kPa)	Measured Suction (kPa)			σ_v' maintained until in situ K_0 condition reached (kPa)
				20/3/96 2 weeks after sampling	17/6/96 before extrusion	17/6/96 after preparation	
R12	LS2-2	7.20	116	105	113	141	121
R14	LS2-2	7.60	122	105	113	not measured	126
R23	LS2-1	6.05	111	60	90	not measured	111

Table 4.6 Pre test conditions of undisturbed samples of Gault clay

This approach was considered successful on the basis of high measured saturation at the start of each test, and of virtually insignificant strains resulting from re-consolidating the samples both to the initial isotropic stress state and subsequently to the *in situ* stress state as listed in Table 4.7. Interestingly Lacasse & Berre (1988) consider volumetric strains < 1% in re-consolidation to *in situ* stresses to indicate a test quality of "very good to excellent".

Also shown are the specific volumes of the samples at the start and end of the tests based on measurements of soil mass and moisture content. Additional calculations of the final specific volumes determined from volume change measurements based on both the VCM measurements and the horizontal belt / right cylinder calculations are also shown.

Test No.	Diam. (mm)	Start Date	Duration (days)	$S_{r(i)}$ (%)	Measured strains reconsolidating to $p_0' = \sigma_{v'(insitu)}$		K_0 in situ		Specific Volumes			
					ε_q (%)	ε_p (%)	ε_q (%)	ε_p (%)	$v_{initial}$	v_{final}	$v_{f(vol)}$	$v_{f(belt)}$
R12	100	17/6/96	14	98.5	-0.06	1.04	-0.41	0.96	1.85	leak failure		1.81
R14	100	12/7/96	40	97.2	-0.22	0.11	-0.47	0.06	1.83	1.78	1.75	1.79
R23	100	25/2/97	55	97.1	0.00	0.30	-0.50	0.18	1.84	1.82	1.79	1.79

Table 4.7 Tests on samples of natural Gault clay - reconsolidation strains and specific volumes

The quality of these three tests was not equally high in all cases. Techniques for installing the bender belt in stiff clay samples were still being developed when tests R12 and R14 were set up. In these two tests it became apparent that small leaks developed in the membrane system, which lead to the tests being curtailed earlier than planned. However, Test R23 ran to its full planned conclusion with no evidence of any leak during its 55 day duration.

The stress paths actually followed by the three tests are summarised in Figure 4.14. It can be seen that Test R12 did not approach the estimated *in situ* stress state as planned. This was due to the membrane leak (mentioned above) leading to excess pore pressures at the mid height, and consequently lower effective confining pressures. The stress paths being followed were halted and strain rates allowed to decay to negligible amounts at each of the symbol markers shown on Figure 4.14 in order that bender element measurements could be carried out at known uniform stress states. Four sets of shear wave velocities ($V_{s(vh)}$ $V_{s(vh)b,}$ $V_{s(hv)}$ and $V_{s(hh)}$ as described in Chapter 3) were recorded at each point.

Test R14 consisted of a number of constant σ_v' sectors (0a, ab, bc) to the estimated *in situ* stress state at 'c', followed by a 180° reversal to 'd', a further 180° reversal back to 'c', and then a constant σ_h' sector to 'e', followed by a constant σ_v' sector following a p' - q stress path rotation of 48°. It had been planned that further constant σ_v' and σ_h' excursions would be carried out at an effective confining pressure twice that at which excursions bc, cd, dc and ce were carried out. However, a leak had developed and the test was curtailed when excess mid-height pore pressures exceeded approximately 10% of p_0'.

Test R23 provided a comprehensive range of stress paths excursions not only at constant σ_v' and σ_h', but also constant p' and q excursions. These were concentrated in the region of the estimated *in situ* stress state at a K_0 of approximately 2 (paths ab, bc, cb, bd, db, be).

A large multi-staged triaxial distortional sector was then carried out at constant cell pressure from the *in situ* state until the stress ratio was reversed to $\sigma_h'/\sigma_v' = 0.5$ (paths be, ef, fg and gh), before returning to an isotropic stress state again at constant σ_h' (path hf).

The results from these stress path tests will be presented and discussed in Chapter 5 with respect to the influences of stress, strain and structure on $G_{\alpha(ij)}$ and comparisons made with field measurements of $V_{s(ij)}$, and in Chapter 6 they will be used to evaluate anisotropic elastic parameters.

4.4.3 Calculation procedures

All triaxial variables were monitored and stored on the computer controlling the stress path test as described in Section 3.2. Sample state defined by stress state and specific volume was calculated as the tests proceeded on the basis of initial moisture content of sample trimmings. The calculation of effective stresses were based on the back pressure at the sample ends. Mid-height excess pore pressures were monitored, and testing rates kept low enough to ensure that these did not exceed approximately 5% of the effective confining pressure, p'. On completion of a test the data were downloaded to specifically devised spreadsheets more suited to data validation and analysis. At this state the final sample moisture content and total dry mass were measured. These were used in the spreadsheet to re-assess the quality of the initial measurements of moisture content, and to carry out cross checks with the volume changes measured directly with the VCM and indirectly by calculations based on measured local strains.

Initial sample moisture content, w, was calculated using:

$$w = \frac{M_w}{M_s} \quad \text{.....Equation 4.1}$$

where M_w is the mass of water and M_s the mass of solids. The voids ratio, e, can then be calculated using:

$$e = \frac{wG_s}{S_R} \quad \text{.....Equation 4.2}$$

where the specific gravity, G_s, of the soil particles was assumed to be 2.75 on the basis of reported values in Forster *et al.* (1994), and the degree of saturation, S_R, is assumed to be unity during the triaxial test. The total volume of the solids in the sample is given by:

$$v_s = \frac{M_s}{G_s} \quad \text{.....Equation 4.3}$$

and then any stage during the test, the voids ratio can be determined using:

$$e = \frac{v_0(1-\varepsilon_p) - v_s}{v_s} \quad \text{.....Equation 4.4}$$

where v_0 is the initial volume, and ε_p the volumetric strain. The bulk density of the soil, used in determining $G_{0(ij)}$ from $V_{s(ij)}$ using Equation 3.7, can then be obtained using:

$$\rho = \left(\frac{G_s + e}{1+e}\right)\rho_w \quad \text{.....Equation 4.5}$$

where the density of water, ρ_w, was assumed to be 1000 kg/m^3.

For tests carried out in the 38 mm stress path cells where horizontal strain was not measured directly, the calculation of strains was based on the assumption that the original shape of the sample was preserved during deformation. With this assumption, the cross-sectional area, A, of the sample at any stage during the test can be calculated from:

$$A = A_0 \frac{(1-\varepsilon_{p(V)})}{(1+\varepsilon_v)} \quad \text{.....Equation 4.6}$$

where A_0 is the initial cross-sectional area, ε_v is the vertical strain and $\varepsilon_{p(V)}$ is the volumetric strain based on volume change readings. The horizontal strain, ε_h, is then given by:

$$\varepsilon_h = -\frac{1}{D_0}\left(\sqrt{\frac{4A}{\pi}} - D_0\right) \quad \text{.....Equation 4.7}$$

where D_0 is the initial diameter.

For the tests carried out in the 100 mm triaxial cell where horizontal and vertical strains were measured locally during the test, additional options were available for determining triaxial variables. Vertical and horizontal strains could be calculated using:

$$\varepsilon_v = -\frac{1}{2}\left[\frac{\Delta L_1}{L_{o1}} + \frac{\Delta L_2}{L_{o2}}\right] \quad \text{.....Equation 4.8}$$

where L_1 and L_2 refer to local strain gauge 1 and local strain gauge 2, and

$$\varepsilon_h = -\frac{\Delta D}{D_o} \quad \text{.....Equation 4.9}$$

Then by using the right cylinder assumption described by Equation 4.6, the volumetric strain can be obtained from:

$$\varepsilon_{p(B)} = \frac{-(\pi/4\, L_0(1-\varepsilon_v)(D_0(1-\varepsilon_h))^2 - V_0)}{V_0} \quad \text{.....Equation 4.10}$$

and the current cross-sectional area from

$$A_B = \frac{\pi}{4}(D_0(1-\varepsilon_h))^2 \quad \text{.....Equation 4.11}$$

For both 38 and 100 mm stress path cells, the vertical stress on the sample was calculated

$$\sigma_v = \frac{F}{A} + \sigma_h \quad \text{.....Equation 4.12}$$

where F is the deviatoric force measured by the load cell and σ_h is the horizontal stress measured by the cell pressure transducer.

4.5 Obtaining small strain data

4.5.1 The procedures for validating and interpreting small strain triaxial data

Large quantities of data were inevitably obtained from tests of the complexity carried out in this project. Test duration was generally in the range 1 to 2.5 months; data were logged every ½ hour for 38 mm tests on reconstituted material, while for similar tests on 100 mm diameter samples readings were taken every hour. For tests on natural 100 mm samples, data were logged every 10 minutes at the start of every mini stress path excursion, but increased to hourly intervals during consolidation stages. This resulted in typical files with between 1500 and 2500 lines of data, with up to 16 records within each line. Excel workbooks were developed to process and carry out cross-checking to validate each set of data.

The triaxial small strain deformation measurements required data to be interpreted at resolutions close to both pressure and strain measurement transducer resolution limits. A clear appreciation of the influences

on such data sets was developed to enable reliable interpretation. The data were scrutinised particularly with respect to:

- the influences of temperature,
- the choice of whether to base volume strain determinations on volume change measurements or local strain measures and right cylinder deformation assumptions,
- the lowest meaningful resolution of the small strain data.

In the following sections these three aspects will be considered with reference to actual test data.

4.5.2 The influences of temperature

The problems of the obscuring influences of temperature on small strain results are well known. In many situations researchers accept the varying temperature trends for their laboratories and carry out the particularly sensitive stages of tests at times when the effects are likely to be minimal. In the case of undrained triaxial shearing, the small shear stages occur relatively rapidly, temperature changes are presumed to be minimal, and constant volume conditions are assumed. Jovičić (1997) reports covering the cell and related equipment with insulation, and turning off the air-conditioning in order to obtain readings which are only influenced by a slow rise in temperature, rather than the cyclic pattern associated with most air conditioning systems. In the case of drained tests such as carried out in this research, the duration of even a mini stress path excursion lasted of the order of a day. It was therefore necessary to understand the influences of temperature on both test measurements and soil samples in order to evaluate any impact on results.

Cell water temperature was monitored in all tests, and this enabled comparison between temperature and the difference in volume strain determinations based on measured and calculated volume changes with time. This comparison for two of the mini stress path excursions in Test R23 is shown in Figure 4.15. The calculated volume change is based on local vertical and horizontal belt measurements and the assumption of right cylinder deformation. Figure 4.15a shows clear cross correlation between volume and temperature fluctuations of about ±0.1°C for excursion R23ConQ3 over a period of about 3 days. Cell water temperature clearly follows a daily cycle which is mirrored in the volumetric strain difference. This daily cyclic fluctuation also confirms that it is not air temperature in the laboratory which influences the VCM and data acquisition equipment, as the air conditioning system follows in an approximately hourly cycle with an amplitude of about ±0.5°C. The VCM and data logging units have significantly lower thermal inertia than the full triaxial cell, and would certainly reflect these variations were they as sensitive to temperature as the sample. The total volume change during this stress path excursion was of the order of 1.1%, or some 9 ml.

Figure 4.15b shows a less clear correlation for excursion R23conH4 over a period of about 6 days, during which average cell water temperature is seen to decrease by only 0.2°C with daily fluctuations of ±0.03°C.

Yet the difference between volume determinations is seen to follow a increasing trend. The total volume change during this stress path excursion was 0.9%.

The correlations for these and the other eight mini stress path excursions carried out on test R23 are shown in Figure 4.16. Data from the constant p' and q excursion are shown in Figure 4.16a and indicate total differences in volume determinations of less than 0.03% in each excursion. Figure 4.16b shows similar results for the excursions carried out at constant vertical and horizontal stress. Total differences of up to 0.06% reflect the larger stress path excursions carried out for these results.

Also indicated in Figure 4.16 is the theoretical volume change of the pore water in the sample that would be expected for the temperature range shown. This would be measured in a perfect volume change measuring system if no temperature related volume changes occurred in the clay matrix. There is clearly very little correlation between this calculation and the measured volume changes. In fact there is a general inverse trend between cell water temperature and associated volume change. This may indicate more complex soil / pore fluid interactions. However investigations of these effects were considered beyond the scope of the project. Rather, the data presented point to potential complexities and inaccuracies when assumptions are made about volume change in triaxial testing.

4.5.3 Strain measurement: horizontal belt or VCM, local or external vertical strain?

The previous section has discussed the influence of temperature on volume change measurements. In this section data will be presented to illustrate the reasons for the decision to base small strain data interpretation on horizontal belt rather than volume change readings, and local vertical rather than external strain measurements. For continuity the same two mini stress path excursions, R23conQ3 and R23conH4 will be considered.

Figure 4.17 and Figure 4.18 show the volumetric horizontal strains determined from both the horizontal belt and VCM measurements for the small and intermediate strain ranges for excursions R23conQ3 and R23conH4 respectively. Both figures indicate significantly smoother trends for the strains based on the horizontal belt, but most importantly, negligible influence of temperature on the readings from the belt. Significantly there is very close agreement between the horizontal belt and VCM at the end of the constant deviator stress excursion R23conQ3 as indicated in Figure 4.17a. This close agreement in not in evidence with excursion R23conH4, where the volume strain determined from the VCM is approximately 10% higher than that determined using the horizontal belt. These assessments were made for all ten mini stress path excursions in Test R23. In four out of the ten there was negligible difference between the volume strain determination methods at the end of the excursion. In five of the excursions the VCM strain was approximately 20% higher, and in one it was 20% lower. No trends were found to exist between temperature or change in stress path angle from the previous path. It was concluded that these inconsistencies were due to both temperature effects and the constraining effect of end restraint between the sample and the platens. This restraint leads to zones adjacent to the platens where in particular, there

are large differences in shear-induced pore pressures or volumetric strains compared to the mid height of the sample, Germaine & Ladd (1988). The horizontal belt was therefore considered to provide the most reliable measurement of horizontal strain for the greater part of the sample, and readings from it were used to determine both horizontal and volumetric strain where possible.

Similar comparisons for the measured vertical strains determined using the two local vertical Hall effect gauges and the external vertical transducer were carried out. The results for stress paths R23conQ3 and R23conH4 again are presented in Figure 4.19 and Figure 4.20. In the first of these figures the external transducer clearly lags in its response to isotropic loading when compared with the local vertical gauges. This would result in a negative small strain response being incorrectly predicted if only the external transducer was available. However, in Figure 4.20 for stress path R23conH4 where loading was by an increase in vertical stress, the external and local vertical gauges are seen to measure a very similar response. In all tests and excursions, both external and local vertical gauges were compared, but ultimately an average of the two local vertical gauges was used as the final assessment of vertical strain.

4.5.4 From data to stiffness moduli

Having considered the determination of vertical, horizontal and volumetric strains, this short section describes the derivation of stiffness moduli from strain data. A typical set of data obtained from the average of the two local vertical Hall effect gauges during a constant p' excursion, R23conP1, is plotted in Figure 4.21 which shows change in deviatoric stress, q, plotted against deviatoric strain, $\delta\varepsilon_q$, for the range 0 - 0.006%.

In order to evaluate the tangent stiffness from the data sets obtained in this project, polynomial curves were fitted to the load / displacement data. Generally one curve was used to represent the 0 - 0.01% strain range, and a second curve fitted to the higher strain data. The gradient of the second curve was matched to that of the first at the transition point. Tangent moduli were then simply obtained by differentiation of the polynomial, and evaluation at any desired strain value. This procedure was performed in semi-automated Excel workbooks, where the data were plotted for a number of strain ranges, so that the quality of the fit could be assessed, and the order or strain range of the polynomial adjusted to result in the best fit for each excursion. The curve obtained in this manner for excursion R23conP1 is illustrated in Figure 4.21.

In Section 3.2.6 the minimum resolution of each local vertical strain gauge was established to equate to a strain of 0.0015%. Since $\delta\varepsilon_q = {}^2/_3\delta\varepsilon_v - {}^2/_3\delta\varepsilon_h$ and for this excursion the horizontal strain change was found to be less than the resolution of the horizontal belt, i.e. $\delta\varepsilon_h \approx 02$, then $\delta\varepsilon_q \approx {}^2/_3\delta\varepsilon_v$ and the minimum resolution per local vertical gauge is ≈ 0.001%. However there are two such gauges, so the effective resolution becomes ±0.0005%. This has been represented in error bars included in Figure 4.21, and as can be seen the best fit curve fits within the extremes of the error bars for all but one data point. Clearly this data-set indicates stability and resolution better than the 0.002% indicated in Section 3.2.6 on the basis of a drift test. For this reason, curve fits to the data obtained in the multiple mini stress path

excursions will (in Chapter 6) generally be indicated to strain levels as low as 0.001%, and sometimes lower. This is on the basis of individual assessment where, as in the case of R23conP1, there is sufficient evidence for moduli derived to such strain levels.

4.6 Obtaining shear wave velocities

The design, fabrication, instrumentation system and measurement accuracy of the bender element devices developed in this project were discussed in Chapter 3. In this section the use of these devices to obtain relevant shear wave data on samples will be considered.

Shear wave velocity measurements were made at specific stages during the stress path tests described in Section 4.4. In advance of setting up the sample in the cell, the polarity of each bender driver / receiver pair was established. This was done by holding the benders in tip to tip contact in the orientation they are used in during the test, and checking that the received signal shows the same direction of response as the driver. If not, the polarity switch on the oscilloscope was used to invert the incoming signal, and this setting carried though for the duration of the test.

During a stress path test, the triaxial control programme was used to hold the sample at a particular stress state, and bender measurements were generally carried out once excess pore pressures had been allowed to dissipate, and vertical strain rates had fallen below 0.02% / hour. At each stress state where velocity measurements were made, the date and time were recorded so that on post-test assessment of the data the bender element and triaxial data could be automatically correlated using look-up tables in a spreadsheet. Where tests included multiple shear wave paths, the measurements were carried out sequentially, switching from one set of bender elements to the next. Records of all pulses used in the interpretation of the shear wave velocities were stored electronically to enable subsequent checking.

As this is the first time that the arrangement of two adjacent orthogonal bender elements has been used in soils testing, this section will consider the validation procedures that were carried out on the devices.

4.6.1 Validation of signals to and from adjacent orthogonal elements

Shear wave splitting has been used to evaluate anisotropy in geological materials since the early 1980's, Crampin (1985). As described in Chapter 2, the "splitting" effect is seen when a shear wave travelling along a path which passes through an anisotropic medium generally splits into two components with different arrival times and orthogonal (or nearly orthogonal) polarisation. There are situations where this splitting does not occur, and these have also been observed in bench-top tests carried out during this project.

During these tests on samples of one dimensionally consolidated reconstituted Gault clay, shear wave velocity measurements were carried out using a single transmitter element which was arranged at approximately 45° to the direction of consolidation. An orthogonally-oriented receiver "bender probe" was inserted in the opposite side of the sample with the bender elements aligned parallel and

perpendicular to the direction of consolidation. In most cases, signals of approximately equal strength were received but with 15 to 25% difference in transmission time which indicates an anisotropic material. However, in some cases the lagging signal was completely obscured. No explanation for this was ascertained, but is seems to accord with the uncertainty in observations apparent in Crampin & Lovell (1991). Reassuringly it was found that when using matched orthogonally polarised drivers and receivers, the anisotropy could always be detected.

There was however, concern that the close proximity of the orthogonally mounted bender elements in both the bender belt and bender probe arrangement could lead to the generation of a significant compression pulse as soil lying between the two benders is compressed, and that this could mask any shear wave. In order to assess the impact of this phenomenon, further bench tests were carried out on reconstituted samples carefully sealed to prevent changes in moisture content. Two adjacent probe slots were cut into either side of the sample at different azimuthal directions using a technique similar to that indicated in Figure 4.9. The slots were advanced to the same depth so that bender probes could be inserted into each opposing pair and be used to send and receive signals over the same path length, and through essentially the same material.

A set of bender probes was pushed into an opposing set of slots with the "T" formed by the two bender elements on its side as shown in the inset at the base of Figure 4.22. A set of bender readings was taken on each of the aligned elements with element A measuring $V_{s(hv)}$ and element B measuring $V_{s(hh)}$. The probes were removed, rotated though 90° and inserted to the same depth in the second set of opposing slots. Again a set of bender readings was taken, but this time with element B measuring $V_{s(hv)}$ and element A measuring $V_{s(hh)}$.

The two pulses used to measure $V_{s(hv)}$ are shown in Figure 4.22a. Note that the pulse for element B has been inverted to facilitate comparisons. Similarly the two pulses measuring $V_{s(hh)}$ are shown in Figure 4.22b. The interpreted arrival times for each of the four traces are indicate arrival times of 0.576 and 0.564 ms for $T_{(hv)A}$ and $T_{(hv)B}$ respectively, and 0.455 for both $T_{(hh)A}$ and $T_{(hh)B}$. Significantly, the arrival times using each of the configurations are within the limits of accuracy discussed in Chapter 3, with just over 1% difference shown between the arrival times for the $V_{s(hv)}$ pulses, and no difference for the $V_{s(hh)}$ pulses. Further, there is very close qualitative comparison between the first three peaks on the corresponding pulses, with differences only becoming clearly apparent beyond this time, when different reflections would be expected to be received for the different configurations.

These results were taken as confirmation that interference between the two sets of benders does not influence the measurement of shear wave velocity.

4.6.2 Choice of driver frequency

As discussed in Chapter 3, it is the determination of the transmission time that most influences the accuracy of measuring $G_{0(ij)}$. Recent advances in the understanding of shear wave velocity measurements

as published by Jovičić *et al.* (1996) were adopted in the procedures used in this project. These are based on the clear identification of first arrival times of the shear wave, and not cross-correlation methods such as given by Viggiani and Atkinson, (1995). Specifically this entailed the use of driver signals which are variations on sine pulses, and the use of frequencies high enough to ensure that near field effects do not influence the received pulses.

The use of sufficiently high frequencies ensures that geometric damping separates the near field coupled compression and shear waves from the far field pure shear waves. Sanchez-Salerino *et al.* (1986) introduced a ratio term, R_d, which can be used to assess the degree of attenuation due to geometric damping. For the bender element system, this term is defined as the ratio of the length between the tips of the driver and receiver elements, L_i, to the wavelength of the shear wave, λ_{ij}, as given by:

$$R_d = \frac{L_i}{\lambda_{ij}} \quad \text{.....Equation 4.13}$$

This may be rewritten in terms of the frequency of the driver pulse, f, and the transmission velocity $V_{s(ij)}$ of the particular shear wave being monitored as:

$$R_d = f\frac{L_i}{V_{s(ij)}} \quad \text{.....Equation 4.14}$$

If this ratio is kept above a level of approximately 2, then the shape of the receiver pulse at the point of monitoring will not be obscured, Sanchez-Salerino *et al.*, (1986). It was found when carrying out the experiments using the horizontal bender devices that $2 < R_d < 10$ resulted in pulses that were most simple to interpret. A similar finding has more recently also been described by Arulnathan *et al.*, (1998). In addition they also use numerical analyses to predict that if $3 < R_d < 5$ then even cross correlation methods can be used to establish transmission times to an accuracy of approximately ±1%.

The ratio R_d was therefore calculated at the time of each measurement, and used to check that the choice of driver frequency did not compromise the received signal through possible near field effects.

4.6.3 Recognition and interpretation of first arrival time

The interpretation procedures used to establish the arrival of shear wave pulses invariably contain a certain element of subjectivity, and consistency of interpretation is therefore improved with experience. To ensure the same experience was applied to each interpretation, all relevant bender pulses obtained during the laboratory testing were stored digitally and re-interpreted at the end of the laboratory testing phase.

To illustrate some of the features of the shear waves pulses obtained, and to enable comparison of the quality of the data with that published in the literature, three sets of sample data have been presented in Figure 4.23 to Figure 4.25. In each figure, comparison between vertical and horizontally propagated and polarised driver and received pulses are shown plotted against time. Each pulse in annotated with the

driver frequency and the wavelength ratio, R_d. The soil state at the time each set of bender measurements was obtained is also indicated. For completeness, the appropriate bulk density and wave path length are also included.

Figure 4.23 shows a set of four Driver / Receiver bender pulse pairs obtained during the one dimensional swelling stage of Test R16, a test carried out on a 100 mm diameter reconstituted sample using the bender belt. Simple sine wave driver pulses were used in all cases, and result in received pulses with similar shape to the familiar "ground body waves". It has been a simple matter in all these cases to identify the pulse arrival time as the start of the first major signal to arrive. These four arrival times were used to determine $V_{s(vh)b}$, $V_{s(vh)}$, $V_{s(hv)}$ and $V_{s(hh)}$.

Figure 4.24 shows a set of bender pulses obtained on natural material at the estimated *in situ* stress state during Test R23. Again the sample is nominally 100mm in diameter, and the bender belt was used for the horizontally propagated shear waves. Each of $V_{s(vh)b}$, $V_{s(vh)}$, $V_{s(hv)}$ and $V_{s(hh)}$ were determined from these four pulse pairs. Sine waves were used for the two vertically propagated pulses. The arrival times for these two orthogonally polarised waves are seen to vary by almost 5%. This is believed to reflect both possible azimuthal variation in this natural sample, and variability in the stress state in the ends of the sample adjacent to the porous discs. Further evidence for the latter effect will be discussed in the next section. Sine pulses (sine waves with 90° phase shifts) were used for both horizontal driver pulses. The received pulses are seen to be preceded by an apparent "near field" effect, where the signal shows in each case the same gradual rise before the sharp arrival of the shear wave pulse. In the case of the horizontally polarised pulse, *hh*, the shear wave arrival coincides with the maximum of this preceding pulse, whereas the vertically polarised pulse, *hv*, arrives after most of the effect has passed. Despite this feature, the arrival times could still be clearly identified as the arrival of the first major pulse, and indicate that even when the frequency is chosen such that $R_d >> 2$, apparent near field effects are sometimes observed.

Figure 4.25 shows five driver / receiver pulse pairs obtained after swelling a sample of reconstituted material back to 110 kPa from a maximum effective consolidation pressure of about 900 kPa in the 38 mm stress path cell. A pair of bender probes were used to transmit and receive the horizontal shear waves. The first three pairs of pulses were used to measure $V_{s(vh)}$ and were carried out using the same (and only) set of platen mounted benders. However the following three different driver pulses (as discussed in Section 3.3.4.1) were used:

- a standard sine wave,
- a V Jovičić wave (a sine wave with modified phase angle and symmetry), and
- a sine pulse (a sine wave with a 90° phase shift).

In these measurements, the V Jovičić wave is seen to exhibit the least "near field" effect, and interpretation based on the first significant departure of the received pulse can clearly be used to assess the arrival time. For the horizontally propagated pulses, only received pulses resulting from sine pulse driver signals are shown. These were carried out at very similar R_d ratios to that vertical pulse labelled

N25aq66a.prn, yet the arrival times can be obtained with significantly greater clarity than the vertically propagated pulse. From these pulses, the three shear wave velocities $V_{s(vh)b}$, $V_{s(hv)}$ and $V_{s(hh)}$ were determined for the sample at this state.

The following points summarise features of the interpretation:

- The bender element devices that were developed enable clear signals to be received, and this leads to simple identification of transmission times on the basis of "first arrival" of the received shear wave pulse.

- For the vertically propagated waves, it was always easier to obtain clear signals at R_d ratios close to 2, whereas for the horizontally propagated waves, it was usually easy to obtain clear signals over a significantly greater range of 2 - 10. The differences are attributed to the difference in the bender mounting. The vertical benders are mounted in the relatively massive rigid reflecting platens between which the sample is mounted, whereas the horizontal benders are mounted in relatively light suspended pads / probes.

- It was considered prudent to utilise the same pulse type and frequency for the duration of a stress path test in order to minimise possible frequency effects. In resonant column tests on cohesive soils Kim & Stokoe (1995) identified a 4% change in shear modulus per log cycle of frequency for loading frequencies in the 5×10^{-2} to 50 Hz range. Attempts were made to quantify the impact of frequency in the bender element tests. However, the range of frequency (for which it is possible to obtain clear signals) is limited by the R_d value at the low end, and bender overshoot‡ at the high end. Typical ranges are significantly less than one log cycle of frequency, and within this range, no conclusions as to frequency effects could be drawn.

- For tests on reconstituted samples where the stress path being followed resulted in large changes in voids ratios, shear wave velocities increased significantly over the duration of the test. In order to facilitate use of the same frequency for the duration of a test, initial shear wave velocity measurements were made using a R_d significantly higher than 2, so that as the sample consolidated and shear wave velocities increased, the same frequency still resulted in R_d values higher than two, despite the lowered voids ratio.

- The optimum driver pulse type did not necessarily remain the same for the vertical bender for the duration of a test, whereas significantly more consistent response was observed for the horizontal devices. This was again considered to reflect changing non uniform stress states of the soil adjacent to the platens as tests progressed, and is included in the discussion in the next section.

- The clarity of the signals from the horizontal bender devices was generally significantly superior to those from the traditional platen mounted bender elements.

---

‡ Overshoot occurs when the driver signal rise time is quicker than the response time of the piezo-ceramic element, and the element fails to replicate the driver signal accurately. It is usually evidenced by spurious overshoot oscillations in the bender response.

No attempts were made to identify or interpret waves arriving later than the shear wave in any of the tests. Clearly, some of the pulses discussed in this section include additional information, and exploration of these aspects of bender testing may lead to further advances in the use of the method.

4.6.4 Inaccuracy in vertical shear wave measurements due to end effects

Using data obtained during the testing programme, this section will discuss the inaccuracy of the traditional platen mounted bender elements due to end effects. As has been mentioned in the previous section, experience obtained during bender element testing indicated:

- inconsistent differences between the two vertical measurements of $V_{s(vh)}$ made on samples tested in the 100mm cell,
- more consistency in the shape of received signals measured using the horizontal bender devices than the vertical bender elements.

A natural sample of a soil may be anticipated to have a degree of layering and this may result in different $V_{s(vh)}$ and $V_{s(hv)}$ measurements, with $V_{s(hv)}$ being the shear wave velocity of a particular layer, while $V_{s(vh)}$ is an average of all the layers the wave passes through. However it is unlikely that layering would be present in the reconstituted samples of Gault clay. Yet differences between $V_{s(vh)}$ and $V_{s(hv)}$ measurements were measured in the triaxial stress path tests carried out on both natural and reconstituted samples. Conversely, in bench-top tests where the samples were unconfined, insignificant differences were observed between $V_{s(vh)}$ and $V_{s(hv)}$ in both reconstituted and natural samples.

The influence of end effects in materials testing in general, and soils triaxial testing in particular, are well documented with respect to triaxial stiffness and strength measurements e.g.: Baldi *et al.* (1988); Germaine & Ladd (1988); Lacasse & Berre (1988). However, their influence on bender element tests appears to have missed consideration. The measurements made using the bender belt and bender probes in this project offer the opportunity of identifying whether end effects influence vertical measurements of shear wave velocity, $V_{s(vh)}$ to a measurable degree.

The ratio of the shear moduli $G_{0(vh)} / G_{0(hv)}$ for three of the stress path tests carried out on both natural and reconstituted material has been plotted against a normalised effective confining pressure during the stress path test in Figure 4.26. The normalising pressure chosen is the suction in the sample shortly before setting up in the cell. These values of suction are based on the suction probe measurements discussed in Section 4.3.4. The data show a clear trend of decreasing difference between $G_{0(vh)}$ and $G_{0(hv)}$ with increasing p'/p_0', but with a significant scatter band width of approximately $0.1 \times G_{0(vh)} / G_{0(hv)}$. This appears to give clear evidence to indicate that as confining stress increases, the significance of the frictional end restraint on the stress distribution surrounding the vertical bender elements reduces.

Possibly even clearer evidence is plotted in Figure 4.27 where the same shear modulus ratio, $G_{0(vh)} / G_{0(hv)}$ is plotted against absolute confining pressure for measurements taken during the dismantling of Test R23.

This test was never taken to failure, as the stress path given in Figure 4.14 indicates. On completion of the test, shear wave velocity measurements continued to be taken as the cell pressure and back pressure were reduced prior to dismantling. During this reduction in triaxial cell pressure, the ratio $G_{\alpha(vh)} / G_{\alpha(hv)}$ changed from 0.75 to 0.79. The sample was then quickly and carefully removed from the end platens, wiped of free water to avoid swelling, and wrapped in clingfilm. A further set of bender element readings were taken using bender probes installed into the sample along the same azimuthal orientations as the bender belt and vertical bender elements were during the triaxial test. The ratio of the shear moduli at this bench-top atmospheric "confining" stress was found to be close to unity as indicated in Figure 4.27. The point is seen to lie on the extrapolation of the data points obtained during lowering of the cell pressure, and provides further evidence that it is the effect of the friction in the end platens which substantially influences the stress distribution in the region of the vertical bender elements, leading in the case of the natural Gault clay tests, to errors in the measurement of $G_{\alpha(vh)}$ of up to 30%.

This finding has led to lowered credibility of the $G_{\alpha(vh)}$ data obtained during the testing programme, and Chapters 5 and 6 will therefore concentrate on the $G_{\alpha(hv)}$ and $G_{\alpha(hh)}$ measurements.

4.7 Summary

This chapter began by describing the Gault clay in terms of its geological origin, basic engineering properties, stress history and microstructure. The methods by which high quality undisturbed samples were obtained, prepared and set in the triaxial cell were then detailed in the context of best current practice in triaxial testing methods. The testing programme that was developed to investigate the small and very small strain stiffness properties of the Gault clay, using both reconstituted tests and tests on natural samples, was then described. The reconstituted tests focused on using the innovative bender element devices capable of measuring $G_{\alpha(hv)}$ and $G_{\alpha(hh)}$ at the mid height of the sample. The tests on natural material focused on restoring the *in situ* stress state before carrying out stress path excursions during which both local small strain measurements and shear wave velocity measurements were taken. The latter half of the chapter considered the methods by which the local strain and bender element data were scrutinised to ensure that the measurements were valid and accurate. The chapter concluded with evidence that conventional bender element testing techniques using vertically propagating elements may include errors of up to 30% if no attempt is made to lubricate the interface between soil and platen.

In Chapter 5, results from the bender element measurements of $G_{\alpha(ij)}$ will be presented, and used to explore the factors influencing the anisotropy of very small strain shear modulus, $G_{\alpha(ij)}$.

5. RESULTS: SHEAR WAVE EXPLORATIONS OF THE ANISOTROPY OF $G_{0(IJ)}$

5.1 Introduction

The bender element devices developed in this research programme offer new opportunities to investigate cross-anisotropic shear moduli of fine grained soils at very small strain. They are distinctly suited to use in tests on samples in triaxial stress states where for the first time both $G_{0(hv)}$ and $G_{0(hh)}$ can be measured on the same sample of clay, and at any triaxial stress state. That is stress states where both the stresses in the vertical and horizontal directions can be independently controlled, enabling isolation of either of the σ_i' or σ_j' terms in Equation 5.1 (introduced previously in Chapter 2 as Equation 2.13)

$$G_{0(ij)} = S_{ij} F(e)(OCR)^k p_a^{(1-ni-nj)} (\sigma_i')^{ni} (\sigma_j')^{nj} \quad \text{.....Equation 5.1}$$

The testing programme carried out therefore explored the various components of Equation 5.1 in ways that have not been possible with triaxial or oedometer bender testing to date.

There is frequently confusion over the terms used to describe the factor influencing anisotropy. This is particularly so of Jamiolkowski *et al.* (1995), who, in using an oedometer, were unable to separate the components of stress-induced anisotropy from inherent anisotropy. It is only under isotropic stress conditions that this can be achieved, and the triaxial cell is therefore a more suitable tool. The following terminology, clarified by Jovičić & Coop (1998), will be adopted in this chapter:

- *Stress-induced anisotropy* results solely from the current stress condition and is independent of the stress and strain history of the soil. It must account for both isotropic and anisotropic stress states.

- *Inherent (or structural) anisotropy* is that which results from the current structure and fabric of the soil. For clays, much of the inherent anisotropy might be expected to be related to the plastic strain history the soil has undergone, but it also includes the development of structure. Inherent anisotropy will therefore be used to describe the anisotropy of natural clays at the *in situ* state.

- *Strain-induced anisotropy* will be used to describe the non stress-induced anisotropy found in reconstituted samples where the influence of diagenetic processes related to the passage of geological time is small. As reconstituted samples are recreated from a slurry and have not had sufficient time for any modified bonding to be created, the structure may be expected to be predominantly related to the one-dimensional strain history rather than the mode of deposition. This is contrary to sand where the inherent anisotropy may result predominantly from the fabric resulting from the depositional process.

In this chapter, studies carried out on both reconstituted and natural samples will be used to investigate separately the *inherent* or *strain-induced* components of anisotropy and the *stress-induced* effects. The first section presents data and establishes an interpretation framework on the basis of tests on reconstituted Gault clay. These are used to define the influences of both strain and stress-induced effects on the

anisotropy on $G_{0(ij)}$ In the second part of the chapter, data from the tests on natural undisturbed samples will be considered in the light of the relationships derived for reconstituted samples. The chapter will conclude with comparisons with *in situ* measurements of shear wave velocities.

5.2 Triaxial tests on reconstituted material

5.2.1 Introduction

Reconstituted samples have long been used to enable investigation of fundamental properties of soils. Sample formation by "reconstitution" is here differentiated from "remoulding". Traditional reconstitution by one dimensional (1 D) consolidation of a slurry to a desired voids ratio results in an inherently anisotropic soil, whereas remoulding is carried out at or near the desired voids ratio and attempts to recreate an isotropic material. The subsequent testing of the reconstituted samples invariably involves further consolidation, and the design of consolidation stress paths should consider the pre-existence of structure caused by the preferential orientation of soil particles in the samples. Saada *et al.* (1978) have demonstrated that this preferential orientation developed in reconstitution is not destroyed within the moderate stress range at which most laboratory testing on soils is carried out (0-1000 kPa). Despite this, subsequent studies of $G_{0(ij)}$ e.g. Viggiani (1992b); Rampello *et al.* (1994a) have based their tests on isotropic stress path cycles carried out on 1 D reconstituted samples.

The investigations of shear wave moduli in reconstituted samples in this project were focused on 1 D consolidation. This allows more logical comparison with tests on natural samples of Gault clay which are presented later in this chapter. However, comparisons will be drawn with data from an isotropically consolidated test.

5.2.2 Test results

"1 D" consolidation

Test N25[§] will be used as the basis for the investigation of anisotropy of reconstituted materials. The stress path followed in this test has already been discussed in Section 4.4.1 and compression characteristics were illustrated in Figure 4.13. The sample was consolidated with $\sigma_h' / \sigma_v' = 0.6$, the stress ratio established to lead to essentially "1 D" consolidation of reconstituted Gault clay. However, in order to enable assessment of strain-induced anisotropy, the sample was also unloaded, also at $\sigma_h' / \sigma_v' = 0.6$. This unload path resulted in relatively small deviations from true 1 D swelling, however these deviations were reversed on reloading back to $\sigma_h' / \sigma_v' = 0.6$, and the strain path for the whole test approximated to "1 D" consolidation. The term "1 D" is therefore used in quotations to indicate these deviations.

In summary, the stress path entailed loading to $\sigma_v' = 150$, 300, 600 and 1200 kPa, with interim unloading to $\sigma_v' = 150$ kPa. Each time unloading reached $\sigma_v' = 150$ kPa, a further unload / reload cycle was carried

---

§ Grateful acknowledgement is given to David Nash who essentially carried out this test.

out at constant σ_h' to the isotropic stress state $\sigma_h' / \sigma_v' = 1$. This constant σ_h' unload path was followed further to a negative deviator stress at $\sigma_h' / \sigma_v' = 1.68$ before returning back to 1, and subsequently the 1 D ratio of 0.6.

The variations of the three shear moduli, $G_{\alpha(vh)}$, $G_{\alpha(hv)}$ and $G_{\alpha(hh)}$ with effective confining pressure, and voids ratio are shown in Figure 5.1a and b respectively. Also included in Figure 5.1a is the stress ratio history illustrating the planned departure from the constant stress ratio of 0.6.

Trend lines fitted to the measurements carried out at normally consolidated stress states indicate that $G_{\alpha(hh)}$ is significantly higher than both $G_{\alpha(hv)}$ and $G_{\alpha(vh)}$. Smaller but still clearly discernible differences can be seen between the $G_{\alpha(hv)}$ and $G_{\alpha(vh)}$ trends at lower stresses, but these are eliminated as the confining stress approaches about 900 kPa.

Also clear in both Figure 5.1a and b is a marked difference between the trends of the measurements made at normal and over-consolidated states.

"Isotropic" consolidation

Test R09 will be used to illustrate the effect of isotropic consolidation on a 1 D reconstituted sample. The test consisted of two stages. The first stage involved incremental isotropic loading and unloading as was illustrated in Figure 4.12a. Despite being loaded isotropically, the inherent anisotropy of the sample led to anisotropic deformation where the ratio of vertical to volumetric strains varied between 0.4 to 0.5**. Since both strain and stress influences on $G_{\alpha(ij)}$ are being investigated, the use of the term "isotropic" will also include quotation marks when only one of these conditions is met.

The results of the measurement of $G_{\alpha(hh)}$ $G_{\alpha(hv)}$ and $G_{\alpha(vh)}$ are shown in Figure 5.2 where the corresponding $G_{\alpha(ij)}$ *vs.* p' and $G_{\alpha(ij)}$ *vs.* voids ratio measurements are plotted. Again, best fit lines have been added to the measurements carried out at normally consolidated states.

The results show different $G_{\alpha(hv)}$ *vs.* p' relationships for the normally consolidated loading paths and overconsolidated (unload-reload) paths, as found previously by Viggiani & Atkinson (1995). The $G_{\alpha(hh)}$ *vs.* p' results show a similar pattern, but are consistently higher than the $G_{\alpha(hv)}$ results. Contrary to the results for Test N25, the $G_{\alpha(vh)}$ results are virtually coincident and similar to the $G_{\alpha(hv)}$ results.

Comparison of "1 D" and "isotropic" consolidation results

In order to set the context for comparison of the "1 D" and "isotropic" consolidation tests, the strain paths followed by Tests N25 and R09 have been plotted in Figure 5.3a. This illustrates the deviation of these tests from true 1 D and isotropic consolidation paths, also shown in the figure. In Figure 5.3b data from five other tests are compared with Tests R09 and N25. These tests were also carried out at stress ratios of $\sigma_h' / \sigma_v' = 1$ or 0.6 and show trends consistent with those found for Test R09 and N25.

** In true isotropic compression the ratio $\Delta\varepsilon_v / \Delta\varepsilon_p = 0.33$.

In order to illustrate the interdependence of the bender data with soil state, the results from the measurements carried out at normally consolidated states for Tests R09 and N25 have been combined in Figure 5.4. This is a form of the diagram given by Rampello *et al.* (1997) and enables the data to be considered in terms of a linear e *vs.* log p' framework. In Figure 5.4a voids ratio is plotted against log p'. The data show close agreement with the two average compression lines established from all tests and previously plotted in Figures 4.12 and 4.13. These lines are characterised by the same compression index C_c (defined as the gradient of the e *vs.* log p' curve) but have different values of reference voids ratio, e_0, as indicated in the summary table on Figure 5.4. In Figure 5.4b the corresponding log $G_{0(hv)}$ and log $G_{0(hh)}$ measurements are plotted against log p'. While there is close comparison between $G_{0(ij)}$ for both "1 D" and "isotropic" consolidation at low values of p' which correspond to the start of the tests, it can be seen in the tabulated data that the trend lines have different indices with $G_{0(hv)}$ and $G_{0(hh)}$ from "1 D" consolidation being 5 and 10% higher respectively than those for "isotropic" consolidation.

Consistent with the observations from Figure 5.4a and 5.4b, the curves for $G_{0(ij)}$ plotted against voids ratio in Figure 5.4c indicate values of "isotropic" $G_{0(ij)}$ lying above those for "1 D" consolidation. Rampello *et al.* (1997) have used this approach to justify consistent relationships between $G_{0(vh)}$ and soil state as described in specific volume, and p' space. However, the data for both $G_{0(hv)}$ and $G_{0(hh)}$ obtained from the tests carried out in this project do not fit this approach as well as the they do a framework based on that proposed by Hardin & Blandford (1989). A form of this framework will be presented in the next section.

5.2.3 Interpretation of results

Framework

As discussed in Section 5.1, the term "strain-induced" anisotropy will be used here to identify for reconstituted Gault clay what is also frequently referred to as "structural", "inherent" or "fabric" induced anisotropy.

Fabric is a term used to describe the arrangement of particles in a volume of soil. To quantify fabric for a granular material which consists of contacting bulky particles and spaces, terms such as porosity, distribution of contact normals, and distribution of branch vectors have been used.

However for clays, (including Cambridge Gault clay as shown in Figure 4.4), the particles are platey, and physico-chemical interactions act in addition to mechanical ones. X-ray diffraction methods have been used to track the interaction of particles and observe the development of anisotropy with increasing compression, e.g. Martin & Ladd (1978), Delage & Lefebvre (1984), Adamcewicz *et al.* (1997). The disadvantage of these methods is that they are destructive and the evolution of anisotropy cannot be traced during consolidation or along a stress path on a single sample. Nevertheless Martin & Ladd (1978) did find that the initial rate of particle orientation was quite high with the rate slowing down as the consolidation stresses increase. They also found that even reversing the direction of consolidation and increasing stresses by a multiple of 32 was insufficient to completely reverse the direction of particle anisotropy that had developed during a 1 D consolidation stage under a stress of about 100 kPa.

Conversely Ting (1968), amongst others, has found that the stress strain behaviour of K_0 consolidated specimens becomes "isotropic" with respect to stress strain behaviour when they are consolidated to a pressure of about three times the K_0 pre-consolidation pressure. This observation is significantly more in line with conventional soil mechanics which describes soils as particulate materials, and where isotropic measures such as voids ratio, porosity and specific volume are very useful.

However, these are partial descriptions of soils state, independent of history and different from strains, which describe geometric relations between two states. Dean (1998) argues that specific volume can be further developed into a new set of "descriptions of state". He uses three specific lengths which map to orthogonal components of specific volume in three dimensional space.

In a similar vein, Pietruszczak & Krucinski (1989) introduce the concept of directional variation in porosity. Anandarajah & Kuganenthira (1995) and Anandarajah *et al.* (1996) have investigated this concept with the measurement of electrical conductivity in different directions. Since clay particles are essentially non-conducting, the path length through the conducting pore fluid provides an indication of the fabric anisotropy. This technique confirmed the variation of fabric anisotropy in both sands and clays during 1 D consolidation.

It seems a relatively obvious step to attempt to observe this evidence for anisotropic fabric with the new bender devices, and a broader framework than that encompassed in Equation 5.1 is required.

This proposed broader framework is given in Equation 5.2:

$$G_{\alpha(ij)} = S_{(d)ij} S_{(s)ij} e^{mij} \frac{(\sigma'_i \sigma'_j)^{nij/2}}{p_r^{(nij-1)}} = S_{ij} e^{mij} \frac{(\sigma'_i \sigma'_j)^{nij/2}}{p_r^{(nij-1)}} \quad \text{.....Equation 5.2}$$

where

- $G_{\alpha(ij)}$ refers to a shear wave propagating in the i direction with polarisation in the j direction and therefore includes $G_{\alpha(vh)}$ $G_{\alpha(hv)}$ and $G_{\alpha(hh)}$.

- e^{mij} is used to describe the strain-induced components of anisotropy and includes the possibility of planar variation dependent on the i-j plane within which $G_{\alpha(ij)}$ is being measured. The function allows directional variations with similarities to the concept of directional porosity which was discussed earlier in this section. This voids ratio function is expressed in the form of a power function where ^{mij} are the indices applied to voids ratio.

- $(\sigma_i' \sigma_j')^{nij/2}$ describes the stress dependent anisotropy of the soil, again in the form of an empirical power function where:
    - σ_i' and σ_j' are the effective principal stresses acting on the plane in which $G_{\alpha(ij)}$ is measured
    - $^{nij/2}$ are empirical anisotropic indices in the power function which relates small strain shear modulus to stress in the plane ij. They are different from either ^{nv} or ^{nh} as given in Equation

5.1, in that they refer to the stress function for shear waves that have components of propagation AND polarisation in the *ij* plane in which the principal stresses are σ_i' and σ_j'. This is considered more likely to reflect the nature of particle contacts in a platey material than individual indices applied separately to each stress component.

- S_{ij} are non dimensional material constants used to combine the diagenetic and elastic stiffness coefficients into non-dimensional material constants, i.e. $S_{ij} = S_{(d)ij} \times S_{(s)ij}$, where:

  - $S_{(s)ij}$ are elastic stiffness coefficients which account for anisotropy of the reference fabric in addition to depending on elastic particle properties,

  - $S_{(d)ij}$ are material constants which incorporate additional diagenetic influences such as ageing, cementing, the formation of inter-particulate bonds and the conversion of minerals from one type to another.

- p_r is a reference stress used to maintain dimensional consistency. It has been assumed to have a value of 1 kPa in this dissertation.

The term involving *OCR* has been omitted. This is not because *OCR* does not have an influence on $G_{0(ij)}$. Clearly there is a relationship between *OCR* and voids ratio in conventional soil mechanics, and use of either should lead to an equivalent approach in a perfect $e : p' : OCR$ framework, such as that proposed by Rampello *et al.* (1997). If however the behaviour of a soil is dependent on strains, which describe geometric relations between two states, then *OCR* cannot capture this behaviour, and is therefore inadequate as a substitute for directional voids ratio functions.

The material constants in Equation 5.2 can be evaluated from the results for Tests N25 and R09 presented in Section 5.2.2. This is achieved in the following sequential approach:

- Assume that diagenetic processes have not had time to develop to any significant extent within tests carried out on reconstituted Gault clay, i.e. $S_{(d)ij} = 1$

- Compare measurements of $G_{0(ij)}$ at a constant isotropic stress so that the stress components $(\sigma_i'\sigma_j)^{mij/2}$ can be eliminated from Equation 5.2 and a relationship between $G_{0(ij)}$ and voids ratio can used to evaluate the strain-induced anisotropy in terms of voids ratio power functions ^{mij}.

- Compare measurements of $G_{0(ij)}$ normalised by the voids ratio effects determined in step two in order to evaluate $S_{(s)ij}$ and ^{nij}

These steps will be evaluated in the following sections.

Evaluation of strain-induced anisotropy: voids ratio functions

The soil samples in Tests R09 and N25 were returned to isotropic stress states at the end of each cycle of increasing consolidation stress, and measurements of $G_{0(ij)}$ taken. Log $G_{0(hh)}$ and log $G_{0(hv)}$ at these

isotropic states are plotted against log e in Figure 5.5a. For the range of voids ratio plotted (≈ 1 - 1.3), there is clearly a good power fit to all four sets of data, and also clearly different trends between the "isotropically" consolidated and "1 D" consolidated sample. The significance of these trends can be established from the form of the small strain shear modulus for constant isotropic stress presented in Equation 5.3:

$$G_{0(ij)} = S_{(s)ij} e^{mij} \frac{\left(\sigma'_i \sigma'_j\right)^{nij/2}}{p_r^{(nij-1)}} = C e^{mij} \quad \text{.....Equation 5.3}$$

where C includes the constant terms due to the constant stress state. The evaluations of ^{mij} parameters are summarised in Table 5.1. The value of C has not been quoted as this has no meaning on its own.

Consolidation type	*Test Number*	*mhv*	*mhh*	*mhv§*
"1 D"	N25	-1.57	-2.13	-1.47
"isotropic"	R09	-1.83	-1.91	-1.86

§ Included for completeness although data used to obtain these values have not been plotted.

Table 5.1 Anisotropic strain-induced parameters for "1 D" and "isotropic" consolidation

The stress path followed by the "1 D" consolidated sample, Test N25, involved a constant σ_h' path from $\sigma_h' / \sigma_v' = 0.6$ to the isotropic stress state (for which the $G_{0(ij)}$ data were plotted against voids ratios in Figure 5.5), and then on to $\sigma_h' / \sigma_v' = 1.67$. If Equation 5.2 is valid, we should find that the same $G_{0(ij)}$ *vs.* voids ratio relationship exists for $G_{0(hh)}$ at all three stress state at which $\sigma_h' = 90$ kPa, despite p_0' varying from 110 kPa at $\sigma_h' / \sigma_v' = 0.6$ to 78 kPa at $\sigma_h' / \sigma_v' = 1.67$. Log $G_{0(hh)}$ and log $G_{0(hv)}$ for all three states have therefore been plotted against log e in Figure 5.5b. There is clearly close agreement between the $G_{0(hh)}$ *vs.* voids ratio trends, but a significantly different trend for each of the three $G_{0(hv)}$ sets of results. This confirms both that a unique relationship exists between the directional strain-induced anisotropy in the horizontal plane, and that $G_{0(hh)}$ is essentially independent of the out of plane stress, σ_v'.

The observations of different relationships between voids ratio and $G_{0(ij)}$ confirm that different voids ratio functions are required for each plane as implied in Equation 5.2.

To conclude the presentation of data used to assess strain-induced anisotropy, Figure 5.6 shows $G_{0(hh)}$ $G_{0(hv)}$ and $G_{0(vh)}$ data from all tests on reconstituted samples at an isotropic stress state of approximately 100 kPa. This includes tests where only $V_{s(vh)}$ was measured. The indices, ^{mij}, to the power functions relating $G_{0(ij)}$ to voids ratio are -2.11, -1.56 and -1.35 for the $G_{0(hh)}$ $G_{0(hv)}$ and $G_{0(vh)}$ data respectively. These are in close agreement with the indices -2.13 and -1.57 for $G_{0(hh)}$ and $G_{0(hv)}$ given in Table 5.1 which were derived from Test N25 alone. Interestingly the value of $^{mvh} = -1.35$ is close to the value of $^{x} = -1.3$ suggested by Lo Presti (1995). However the inaccuracy inherent in vertical shear wave velocity measurements, which are also believed to have influenced the data on which Lo Presti (1995) based the index value of -1.3, brings into question the significance of this value.

Evaluation of stress-induced anisotropy: stress functions

Two approaches were used to evaluate stress-induced anisotropy:

- An *implicit approach* where the relationship given in Equation 5.2 is assumed, and the fit of data to it is tested. $G_{\alpha(ij)}$ data from any stress path can be used in this approach.
- An *explicit approach* in which particular stress paths, where one of the principal stresses is held constant, are followed in a test, enabling the influence of the other to be evaluated.

Implicit evaluation

In this approach $G_{\alpha(ij)}$ measurements from the "1 D" and "isotropic" tests N25 and R09 are normalised by the strain-induced anisotropy functions e^{mij} and plotted against the product of the principal stresses in the plane of the appropriate shear wave on a log *vs.* log plot. The results for measurements taken on both normally and overconsolidated stress path excursions, and excursions at constant horizontal effective stress (between stress ratios of $\sigma_h'/\sigma_v' = 0.6$ and 1.64, during Test N25) are given in Figure 5.7. The data for both $G_{\alpha(hv)}$ and $G_{\alpha(hh)}$ indicate clear dependency of $G_{\alpha(ij)} / e^{mij}$ on the product $\sigma_v'\sigma_h'$. Least square fits to "1 D" consolidated data in Figure 5.7a indicate values of ^{nhv} and ^{nhh} of 0.51 and 0.49 respectively. The difference between these indices lies within the ±2% accuracy estimated for these measurements.

Normalised data from the "isotropically" consolidated Test R09 are compared with the "best fit" lines from the "1 D" consolidated sample in Figure 5.7b, and again the results plotted include the excursions at constant p' during which the stress ratio varied between 0.44 and 2.4. Very similar least squares fits to the "hv" data can be seen indicating values of ^{nhv} for this "isotropically" consolidated sample of 0.52. There is discrepancy between the "hh" data for both $S_{(s)hh}$ and ^{nhh}. For the "isotropically" consolidated sample $^{nhh} = 0.53$ whereas a value of 0.49 was obtained for the "1 D" consolidated sample.

The evaluations of the $S_{(s)ij}$ and ^{nij} parameters are summarised in Table 5.2.

Consolidation type	*Test Number*	$S_{(s)hv}$	^{nhv}	$S_{(s)hh}$	^{nhh}	$S_{(s)vh}$[§]	^{nvh}[§]
"1 D"	N25	4.81	0.51	9.21	0.49	3.32	0.56
"isotropic"	R09	4.77	0.52	6.51	0.53	4.40	0.52

[§] Included for completeness although data used to obtain these values have not been plotted

Table 5.2 Anisotropic stress-induced parameters for "1 D" and "isotropic" consolidation

The differences between the "stress anisotropy" indices ^{nij} indicated by these four sets of data are considered almost negligible within the context of the accuracy of the experiments, and seem to confirm the finding by Jamiolkowski *et al.* (1995) that $^{n} = ^{nhv} = ^{nhh}$. The value of $^{nij} = 0.5$ is precisely that found by Roesler (1979) for tests on sand. It will therefore be used as a basis for comparison with the explicit evaluation of stress anisotropy involving specific stress path excursions.

Explicit evaluation

As for the investigations of strain-induced anisotropy, Equation 5.3 can be rearranged to isolate one of the principal stresses which can then be controlled to a specific value, and hence enable the influence of the other principal stress to be evaluated. It would also be convenient to isolate the strain-induced anisotropy terms, but this would require tests to return periodically to predetermined voids ratios along specific stress paths. For a clay this would be virtually impossible to achieve. It is therefore necessary to incorporate the strain-induced terms derived in the previous section when investigating stress effects.

Three stress paths will be considered in this section: constant σ_h', constant σ_v', and constant p'.

Constant σ_h' excursions

If Equation 5.3 is normalised by the expressions for small strain shear moduli at isotropic stress conditions as shown in Equation 5.4:

$$\frac{G_{0(ij)}}{G_{0(ij)isotropic}} = \frac{S_{ij}e^{mij}}{S_{ij}e^{mij}}\left(\frac{(\sigma_i'\sigma_j')^{nij/2}}{(\sigma'_{(isotropic)})^{nij}}\right) \quad \text{.....Equation 5.4}$$

then if σ_h' = constant, this reduces to

$$\frac{G_{0(hv)}/S_{hv}e^{mhv}}{G_{0(hv)}/S_{hv}e^{mhv}{}_{isotropic}} = \left(\frac{\sigma_v'}{\sigma_h'}\right)^{nhv/2} = \left(\frac{\sigma_h'}{\sigma_v'}\right)^{-nhv/2} \quad \text{.....Equation 5.5}$$

and

$$\frac{G_{0(hh)}/S_{hh}e^{mhh}}{G_{0(hh)}/S_{hh}e^{mhh}{}_{isotropic}} = \left(\frac{\sigma_h'}{\sigma'_{(isotropic)}}\right)^{nhh} = 1 \quad \text{.....Equation 5.6}$$

Tests N25, L22 and L24 were all carried out on reconstituted material and included stress path excursions at constant horizontal stress. These excursions all incorporated measurements carried out at isotropic stress which have been used to normalise the measurements taken where the stress ratio $\sigma_h'/\sigma_v' \neq 1$. The ratio $(G_{0(ij)}/S_{ij}e^{mij})$ / $(G_{0(ij)}/S_{ij}e^{mij})_{isotropic}$ for these three tests is plotted against stress ratio in Figure 5.8. There are clear trends for both the "*hh*" and "*hv*" data, and power function trend lines have been fitted. The best fit trend line to the "*hv*" data indicates a value of ^{nhv} = 0.5, which is the same as the value obtained from the implicit assessment of the data from Test N25 described above. A small gradient of 0.03 through the "*hh*" data indicates slight discrepancy from a constant value of one if the slope had been zero. There is significantly more scatter in these data than in the plots used to explore strain-induced anisotropy. This is largely due to relatively small changes in shear moduli of ±15% for these constant σ_h' excursions, compared to the ±25% variation in $G_{0(ij)}$ with voids ratio at constant stress observed in the previous section.

Constant σ_v' excursions

For stress path excursions carried out with σ_v' held constant, Equation 5.5 still holds for the ratio $(G_{\alpha(ij)}/S_{ij}e^{mij})$ / $(G_{\alpha(ij)}/S_{ij}e^{mij})_{isotropic}$, whereas for the horizontally polarised shear modulus Equation 5.7 is applicable:

$$\frac{G_{\alpha(hh)}/S_{(e)hh}e^{mhh}}{G_{\alpha(hh)}/S_{(e)hh}e^{mhh}{}_{(isotropic)}} = \left(\frac{\sigma'_h\sigma'_h}{\sigma'^{2}_{(isotropic)}}\right)^{nhh/2} = \left(\frac{\sigma'_h}{\sigma'_{(isotropic)}}\right)^{-nhh/2} \quad \text{.....Equation 5.7}$$

Test L22 included a constant σ_v' stress path excursion to assess these relationships. The results are plotted in Figure 5.9. While the slope of best fit to the "*hh*" data is approximately double that of the "*hv*" data, showing consistency with equations 5.5 and 5.7, the values of $^{nhh} = 0.43$ and $^{nhv} = 0.42$ are slightly lower than the value of 0.5 which has been recurring so far. However, considering that the accuracy of the shear moduli is ± 2%, these discrepancies are not particularly significant.

The development of anisotropy

The evaluation of the strain and stress-induced indices in the previous sections imply that the degree of anisotropy is not a constant, and it is therefore appropriate to define a ratio which can be used to link anisotropy to soil state. Considering that only shear moduli are being measured at this stage (Young's moduli will also be derived in Chapter 6), the ratio $G_{\alpha(hh)}$ / $G_{\alpha(hv)}$ will be considered. Making use of Equation 5.2, this ratio can be described by Equation 5.8:

$$\frac{G_{\alpha(hh)}}{G_{\alpha(hv)}} = \frac{S_{(s)hh}e^{mhh}}{S_{(s)hv}e^{mhv}}\left(\frac{\sigma'^{\,nhh}_h}{(\sigma'_v\sigma'_h)^{nhv/2}}\right) = \frac{S_{(s)hh}}{S_{(s)hv}}e^{mhh-mhv}\left(\frac{\sigma'^{\,nhh}_h}{(\sigma'_v\sigma'_h)^{nhv/2}}\right) \quad \text{.....Equation 5.8}$$

The significance of the voids ratio functions can now be further illustrated in Figure 5.10 where, having removed the influence of stress state by normalising by $(\sigma'_i\sigma'_j)^{nij}$, the degree of anisotropy, $G_{\alpha(hh)}$ / $G_{\alpha(hv)}$ is plotted for four tests on reconstituted material. This shows that for "1 D" consolidation tests, N19 and N25, the anisotropy increases from approximately 1.6 to 2.15 as voids ratio decreases from 1.35 to 0.85, leading to the evaluation of $^{mhh\,-\,mhv} = -0.58$ (which is very similar to the difference $^{mhh\,-\,mhv} = -0.56$ using the values in Table 5.1) and $S_{(s)hh}$ / $S_{(s)hv}$ = 1.92. By contrast, the anisotropy of the "isotropically" consolidated sample only increases from about 1.57 to 1.67 as voids ratios decreases from 1.3 to 0.98 giving $^{mhh\,-\,mhv} = -0.24$ and $S_{(s)hh}$ / $S_{(s)hv}$ = 1.67. That the ratio for isotropic consolidation increases at all, and does not decrease, is significant. This implies memory, with the consolidation strains continuing to be influenced by the preceding strain path. This was also observed in the sample strain data plotted in Figure 5.3. Over the range of data shown, the "isotropically" consolidated sample strained a total of 2.9 % horizontally, and 4.2% vertically, indicating the continuation of anisotropic (albeit less than 1 D) consolidation. Conversely the "1 D" consolidated sample strained 22.5% vertically with horizontal strains totalling less than 0.7%. This closely represents a true 1 D consolidation strain path.

Data from Test R16 have also been included in Figure 5.10, despite this sample having been failed in compression part-way through the consolidation stage due to failure of computer control. This failure

resulted in significant distortional strain as the sample initially barrelled, and then, as control was restored, recovered an approximately 1 D consolidation strain path. Despite this large strain event, the initial anisotropy, as indicated in Figure 5.10, was not destroyed by the failure. Saada *et al.*, (1978) similarly found in cyclic tests on reconstituted kaolin that despite severe cyclic straining, their samples did not lose their anisotropy. However on restoration of the 1 D strain path to Test R16, further development of anisotropy was found to be limited.

The following implications can be drawn from the observations made on Figure 5.10:

- "Isotropic" consolidation of a 1 D reconstituted sample results in a sample which is neither isotropic, nor representative of "1 D" consolidation processes in terms of anisotropy.
- The evaluations of $^{mhh} - ^{mhv}$ obtained from Figure 5.10 are in agreement with the differences between the indices from the appropriate regressions given in Figure 5.5 and Table 5.1.
- Significant triaxial distortional strain appears not to destroy the anisotropy present at the time of distortion, but it does reduce subsequent development of anisotropy during 1 D consolidation.

Evaluation of elastic stiffness coefficients $S_{(s)ij}$

The elastic stiffness coefficients $S_{(s)ij}$ can be evaluated by normalising $G_{0(ij)}$ for both voids ratio and stress influences as given in Equation 5.9:

$$\frac{G_{0(ij)} p_r^{(nij-1)}}{e^{mij} (\sigma_i' \sigma_j')^{nij/2}} = S_{(d)ij} S_{(s)ij} \quad \text{.....Equation 5.9}$$

Assuming $S_{(d)ij} = 1$ for reconstituted material, $S_{(s)hv}$ and $S_{(s)hh}$ are plotted *vs.* voids ratio in Figure 5.11 for Tests R09, R16 and R25. These results confirm the experimental evidence noted by Hardin and Blandford (1989) that S_{ij} are constant i.e. independent of voids ratio and stress. Horizontal lines representing the numerical average of $S_{(s)ij}$ for each test are included in the figure and annotated with the test they represent and the associated value. These results are summarised in Table 5.3. While the values of $S_{(s)hv}$ are closely grouped about an average of 4.7 ±2.3%, the value of $S_{(s)hh}$ from the three tests is 7.81±18%. The variation in $S_{(s)hh}$ is clearly significant, while that for $S_{(s)hv}$ is within the measurement accuracy of $G_{0(ij)}$. Interestingly there is a correlation between the initial specific volumes of each of these samples and the ratio $S_{(s)hh} / S_{(s)hv}$ as listed in Table 5.3. This correlation may be indicative of variations within the reconstitution procedures such as length of time of hydration, degree of de-airing of slurry, or variations in source material. However, there is insufficient evidence to confirm the source of the variation, and it remains a point for further research.

Test number	$S_{(s)hv}$	$S_{(s)hh}$	$S_{(s)hh}/S_{(s)hv}$	*initial specific volume*
R09	4.61	6.57	1.42	2.27
R16	4.67	7.65	1.64	2.30
N25	4.81	9.22	1.92	2.32

Table 5.3 Elastic stiffness coefficients $S_{(s)ij}$ and initial specific volumes for Tests R09, R16 & R25

5.2.4 Additional influences on $G_{0(ij)}$

In the framework implied by Equation 5.1 strain-induced anisotropy is represented by both the *OCR* and *F(e)* terms. It is widely held in conventional soil mechanics that both these terms describe the current state of the soil and that either term can therefore be used to capture features of soil state, e.g. Jamiolkowski *et al.* (1995); Rampello *et al.* (1997). The evidence presented in the previous two sections shows clear and predominating influences on $G_{0(ij)}$ of directional functions of voids ratio and principal stresses in the plane of propagation and polarisation. However, closer scrutiny of the data reveals that this does not completely describe the data obtained, and the discrepancies bear some re-examination.

The data for test N25 presented in Figure 5.7 have been re-plotted in Figure 5.12 but normalised by stress and voids ratio influences so that effectively the elastic stiffness coefficients $S_{(s)hv}$ and $S_{(s)hh}$ are plotted. Data points relating to measurements made at normally and overconsolidated states are differentiated by filled and empty plot symbols. Superimposed on both these plots are the constant average values of $S_{(s)ij}$ obtained on the basis of the strain and stress parameters presented in Table 5.1 and Table 5.2. Error bars representing the estimated certainty of 2% in the value of measured $G_{0(ij)}$ are included in the over-consolidated data. These plots show that in general the data relating to over-consolidated states lie above those for normally consolidated states, even when the uncertainty indicated by the error bars is taken into account. Consideration has therefore been given to *OCR* having additional effects on $G_{0(ij)}$ which are not embodied in the directional voids ratio functions.

The ratio of measured $G_{0(ij)}$ to calculated $G_{0(ij)}$ using Equation 5.2 is plotted against *OCR* in Figure 5.13. In Figure 5.13a all results from Test N25 are included, and show a generally decreasing discrepancy between measured and calculated values with increasing *OCR*. There is, however, significant scatter in the data, and a reduced data set consisting only of over-consolidated states at the constant stress ratio $\sigma'_h / \sigma'_v = 0.6$ has been plotted in Figure 5.13b. While there is clearly still significant scatter in the data, a trend represented by a power function seems to fit the data in a tolerable fashion. In this form, the implication is that *OCR* has a non zero index ^{k} with value -0.03, as defined in Equation 5.1.

However, this derivation of an influence of *OCR* from the data is not rigorous, as inclusion of *OCR* at this stage conflicts with the relationships between $G_{0(ij)}$ and voids ratio derived previously, and a circular argument ensues.

In conclusion, it is considered that the relationships represented by Equation 5.2 , which was derived on the basis of the discoveries made in this study, represent the limit to which the current data can be used. While there are tentative indications of additional effects, these are of significantly lower magnitude than either strain or stress-induced anisotropy, and may bear investigation in the future.

5.2.5 Alternative interpretations

Alternative frameworks to that proposed in Section 5.2.3 have been used by others to interpret $G_{0(ij)}$ data. Jovičić & Coop (1998) consider two alternatives to the equation introduced by Hardin and Blandford

(1989) and given here as Equation 2.1. These alternatives attempt to use stress invariants to overcome the apparent implausibility of the out of plane stress having no influence on $G_{\alpha(ij)}$ in the expressions considered so far in this chapter. In the first of these the triaxial invariants p' and q are used in place of triaxial principal stresses σ_h' and σ_v', while in the second, they apply a thermodynamically rigorous expression for the elastic behaviour of granular materials as proposed by Lade & Nelson (1987) to their measurements of $G_{\alpha(ij)}$.

Whereas Jovičić & Coop (1998) only attempt to modify the stress components of the Hardin & Blandford (1989) type equations, Rampello *et al.* (1997) consider the influence of consolidation stress ratio in a fundamental $e : p' : G_{\alpha(ij)}$ framework, where the interrelationships are described by perfect Cam clay type parameters.

These alternatives will be considered by investigating their application to the data set obtained in this study.

Use of triaxial invariants p' and q

Equation 5.2 can be re-written in terms of triaxial invariant p' and the stress ratio η by rearranging the standard relationships $p' = (\sigma_v' + 2\sigma_h')/3$, $\eta = q/p'$ and $q = (\sigma_v' - \sigma_h')$ to the forms:

$$\sigma_h' = p'(1-\eta/3) \quad \text{.....Equation 5.10}$$

$$\sigma_v' = p'(1+2\eta/3) \quad \text{.....Equation 5.11}$$

These expressions for σ_h' and σ_v' can be substituted into Equation 5.2 to give:

$$G_{\alpha(ij)} = S_{ij} e^{mij} \frac{p'^{nij}}{p_r^{(nij-1)}} \beta_{ij}^{nij/2} \quad \text{.....Equation 5.12}$$

where $$\beta_{hv} = 1+\eta/3-2\eta^2/9 \quad \text{.....Equation 5.13}$$

and $$\beta_{hh} = (1-\eta/3)^2 \quad \text{.....Equation 5.14}$$

The equation implies a significant conceptual change from Equation 5.2 in that the out of plane stress is now included in the expression. It should also be noted that Jovičić & Coop (1998) only described the use of a single β term since they were unable to vary the out of plane stress when making measurements of $G_{\alpha(hh)}$.

Using Equation 5.12, all the $G_{\alpha(ij)}$ data from Tests N25 and R09 have been normalised and plotted against $p'\beta_{ij}^{1/2}$ in Figure 5.14 and Figure 5.15 respectively. This is a repeat of the data plotted in Figure 5.11 and Figure 5.7, however here the x-axis is in terms of triaxial stress invariants. As can be seen, precisely the same values for the constants $S_{(s)ij}$ and indices ^{nij} are derived directly using this approach.

Stress path excursions carried out at constant p' or non-zero stress ratio $\eta = q/p' \neq 0$, do not lend themselves to isolation of any of the stress anisotropy indices in Equation 5.2. However, normalisation of Equation 5.12 by the shear modulus ratio $G_{0(ij)} / S_{(s)ij}\, e^{mij}$ and elimination of the constant p' terms leads to:

$$\frac{G_{0(ij)} / S_{(s)ij} e^{mij}}{G_{0(ij)} / S_{(s)ij} e^{mij}{}_{isotropic}} = \beta_{ij}^{\,nij/2} \qquad \text{.....Equation 5.15}$$

By plotting the log of the left hand side against log $\beta_{ij}^{1/2}$, the power relationship between stress state and shear modulus can be tested using the results from the second stage of testing carried out in Test R09.

After returning to an isotropic stress of 100 kPa (an *OCR* of 6), a second stage of stress path cycling was undertaken in Test R09. While maintaining p' constant, the sample was subject to two cycles of anisotropic stress reversal between $\sigma_h' / \sigma_v' = 0.4$ and 2.3. The ratio of $(G_{0(ij)}/S_{ij}e^{mij}) / (G_{0(ij)}/S_{ij}e^{mij})_{isotropic}$ is plotted against the stress ratio σ_h' / σ_v' in Figure 5.16a and against the invariant stress ratio function $\beta_{ij}^{1/2}$ in Figure 5.16b. In Figure 5.16a theoretical curves obtained by substitution into Equation 5.4 (assuming $^{nij} = 0.5$) have been superimposed on the experimental data, and show clear correlations. The ratio of "hh" measurements change from -15 to +11%, while those of "hv" from +4% to -11% over the stress ratio range tested. Jovičić & Coop (1998) attempted to investigate this same influence of stress ratio on measurements of $G_{0(vh)}$ in constant p′ tests on kaolin where the stress ratio ranged from $\sigma_h' / \sigma_v' = 0.5$ to 2.0. They were not able to find any discernible effect, but as their investigation considered only $G_{0(vh)}$, and was concentrated on the $\sigma_h' / \sigma_v' = 0.5$ to 1 range (seen to demonstrate the least influence in this study), and involved platen mounted benders with uncertainties due to end effects, this is possibly not surprising.

The same data are re-plotted against the square root of the stress ratio functions β_{ij} (as defined in Equations 5.13 and 5.14) in Figure 5.16b. Also shown in this figure are the least squares trend fits to each of the "*hv*" and "*hh*" data sets, and the average for the combined "*hv*" and "*hh*" data. There are clear trends fitting both data sets, with indices ^{nhv} and ^{nhh} equal to 0.63 and 0.46 respectively. Considering the 4% accuracy of the $G_{0(ij)}$ results, it seems quite reasonable to apply a common regression to the combined "*hv*" "*hh*" data set, and in this case and index $^{nij} = 0.49$ is found.

The same analysis to that presented in Figure 5.16b was carried out without normalising by the voids ratio functions e^{mij}, and the resulting parameters are listed along with those from the normalised moduli in Table 5.4. This shows even larger discrepancies between the ^{nhv} and ^{nhh} values if voids ratio functions are not utilised. While in theoretical p' *vs.* voids ratio soil mechanics, tests conducted at constant p' should show no change in voids ratio, a weak trend of increasing voids ratio with increasing stress ratio, η, was observed in Test R09, and accounting for it increases convergence towards a common single stress index $^{n} = ^{nhv} = ^{nhh} = 0.5$, as illustrated in Table 5.4.

nij	$\frac{G_{0(ij)}/e^{mj}}{G_{0(ij)}/e^{mj}{}_{isotropic}}$	$\frac{G_{0(ij)}}{G_{0(ij)isotropic}}$
nhv	0.63	0.72
nhh	0.46	0.43
n(average) (for both hv & hh data)	0.49	0.48

Table 5.4 Comparison between stress indices with and without voids ratio influences: Test R09

These results from constant p' excursions seem to illustrate a use for the alternative $p : q : \eta$ framework, particularly when compared with Figure 5.16a. However, both this and the framework outlined above can be criticised for not being thermodynamically sound. Based on the assumption of no energy dissipation or energy generation for any closed loop stress path, Lade & Nelson (1987) proposed an analytical expression for the dependence of Young's modulus of an elastic isotropic material in terms of generalised invariants of stress. Jovičić & Coop (1998) have assumed that the shear modulus $G_{0(ij)}$ measured by a bender element system is equivalent to the parameter G for an isotropic soil given by:

$$G = \frac{E}{2(1+\nu)} \qquad \text{Equation 5.16}$$

This has been used to express the power function proposed by Lade & Nelson (1987) in the form:

$$G_{max} = \frac{M 3^{n}}{2(1+\nu)} p_r^{(1-n)} (p')^{n} \beta \qquad \text{Equation 5.17}$$

where
$$\beta = \left[1 + 6\frac{(1+\nu)}{(1-2\nu)}\frac{\eta^2}{27}\right]^{n/2} \qquad \text{Equation 5.18}$$

and M is a constant, ν is the drained Poisson's ratio, and n is again the same stress index as used previously. Since the form of Equation 5.17 is the same as Equation 5.12, the same approach as before can be used to assess the data from the constant p′ stress path excursions, but this time Equation 5.18 is used to define the stress ratio term β. The results of this approach are shown in Figure 5.17, along with the predicted trend line if the data were to match a curve with β raised to the power $n = 0.5$. Clearly neither the $G_{0(hv)}$ nor the $G_{0(hh)}$ data show any resonance with this function. The problem is in the assumption that the independent shear modulus, $G_{0(hv)}$, which is measured by the bender elements, is equivalent to the widely referred to "shear modulus" for an isotropic material which can be found from the relationship given in Equation 5.16. That this assumption can even be made, when measurement of significantly different $G_{0(hv)}$ and $G_{0(hh)}$ values have been measured, is surprising, and the errors are clearly reflected in Figure 5.17. A detailed discussion on the correct derivation of elastic parameters for anisotropic materials will be given in Chapter 6.

A idealised Cam clay type interpretation

Rampello *et al.* (1997), building on the work of Viggiani (1992b), and Rampello *et al.* (1994a), carried out a series of tests on reconstituted Vallericca clay in which cycles of loading and unloading were carried

out at stress ratios varying between $\eta = 0$ and 0.7. Unlike Test N25 described above, these tests did not involve returning to an isotropic stress state at the end of each cycle of increasing and decreasing stress. Also, unlike the tests carried out in this study, only $G_{0(vh)}$ was measured using platen mounted bender elements.

By plotting log $G_{0(vh)\ \text{normally consolidated}}$ *vs.* p' for each test, they found their data fitted expressions of the form

$$\frac{G_{0(vh)nc}}{p_r} = S_\eta^* \left(\frac{p'}{p_r}\right)^{n^*} \quad \text{.....Equation 5.19}$$

where S_η^* is the material constant appropriate for stress ratio η, and $^{n^*}$ is an index found to be constant for both isotropic and anisotropic stress states. To include overconsolidated states they used Equation 5.20

$$\frac{G_{0(vh)}}{p_r} = S_\eta^* \left(\frac{p'}{p_r}\right)^{n^*} \left(\frac{p'_{e\eta}}{p'}\right)^{c} = \frac{G_{0(vh)nc}}{p_r} \left(\frac{p'_{e\eta}}{p'}\right)^{c} \quad \text{.....Equation 5.20}$$

where the equivalent pressure p'_{e_η} is determined on the constant stress ratio (or η line) virgin compression line relevant to each sample using:

$$p'_{e\eta} = p_r \exp\left(\frac{N_\eta - v}{\lambda}\right) \quad \text{.....Equation 5.21}$$

where N_η is the specific volume at the reference stress for constant η virgin compression, v is the current specific volume and λ the compression index in natural log scale. The index "*c*" in Equation 5.20 can be evaluated by plotting $\log(G_0/G_{0(nc)})$ against $\log (p'_{e_\eta}/p')$. While only suggested in passing, and not included in their analysis, Rampello *et al.* (1997) note that stress states that deviate from the consolidation stress ratio can be accounted for though use of the same stress ratio term, β, as given in Equation 5.13. Since in this study $G_{0(hh)}$ data have also been measured, Equation 5.20 has been extended as follows:

$$\frac{G_{0(ij)}}{p_r} = S_{\eta(ij)}^* \left(\frac{p'}{p_r}\right)^{n^*} \beta_{ij}^{1/2} \left(\frac{p'_{e\eta}}{p'}\right)^{cij} = \frac{G_{0(ij)nc}}{p_r} \beta_{ij}^{1/2} \left(\frac{p'_{e\eta}}{p'}\right)^{cij} \quad \text{.....Equation 5.22}$$

This procedure has been applied to the data from both Test R09 and Test N25. To assess S_η^* and $^{n^*}$ on the basis of Equation 5.19, $G_{0(ij)\ nc}$ was plotted against p' in Figure 5.4. In order to evaluate the indices ^{cij}, $G_{0(ij)} / G_{0(ij)\ nc}$ is plotted *vs.* $(p'_{e_\eta}/p')\beta^{1/2}$ in Figure 5.18 and Figure 5.19 for Test R09 and Test N25 respectively. The results are summarised in Table 5.5.

η	Test Number	$S_{n\,(hv)}^*$	n^*hv	$S_{n\,(hh)}^*$	n^*hh	chv	chh
0.6	N25	0.66	0.84	0.69	0.91	0.32	0.40
0	R09	0.78	0.80	0.99	0.83	0.30	0.30

Table 5.5 Stiffness parameters for "1 D" and "isotropic" consolidation after Rampello *et al.* (1997)

While only the results involving shear waves in the plane "*hv*" can strictly be compared with results given by, Rampello *et al.* (1997), certain points of difference to note between the trends observed are:

- Whereas Rampello *et al.* (1997) found equal indices n^{*hv} for all consolidation stress ratios, they were found to increase with stress ratio in this study. This was also found for the values of $S_{\pi(hv)}$.

- There is significantly more scatter in the interpretation of the data in Figure 5.18 and Figure 5.19 when compared with the similar stage of interpretation using Equation 5.2 and plotting the data in Figure 5.7.

- While the use of the stress ratio term β in Equation 5.22 has been shown to be partially successful in accounting for stress states different from an isotropic consolidation path, it does not successfully predict the variation of $G_{0(hh)}$ for 1 D consolidation paths.

5.2.6 Summary

In summary, successful measurement of $G_{0(ij)}$ using the horizontal bender devices developed in this project have shown clear evidence for dependency on:

- directional voids ratio functions,

- the principal stresses in the plane of wave propagation.

A framework to relate $G_{0(ij)}$ to soil state in terms of voids ratio and stress has been developed and parameters evaluated for reconstituted Gault clay. Alternative frameworks published in the literature have been shown to be inadequate. These results will be used in the following section to inform the explorations of $G_{0(ij)}$ on natural Gault clay.

5.3 Tests on natural Gault clay

5.3.1 Introduction

Measurements of $G_{0(ij)}$ have also been made on natural samples of Cambridge Gault clay. The sampling, setting and reconsolidation procedures have been described in Chapter 4, and the results will be presented in this section. The objectives of these tests were:

- to explore differences between the strain-induced anisotropy evaluated for reconstituted samples, and the inherent anisotropy of natural Gault clay in order to make some assessment of the additional influences of ageing in natural material.

- to measure $V_{s(ij)}$ on natural samples under controlled conditions for comparison with *in situ* measurements of anisotropic shear wave velocities.

- to provide $G_{0(ij)}$ data on natural samples for consideration with the results of small strain triaxial stress *vs.* strain data in Chapter 6.

As indicated at the beginning of this chapter, the term "inherent anisotropy" will be used in relation to natural Gault clay where strain-induced anisotropy was used for reconstituted Gault clay. This enables inclusion of structure within the soil mass due to ageing or diagenetic processes.

5.3.2 Test Results

Measurements of $V_{s(vh)}$, $V_{s(vh)b}$, $V_{s(hv)}$ and $V_{s(hh)}$ were carried out during stress path tests on three samples of natural Gault clay. The results from these three tests, R12, R14 and R23, are summarised in Figure 5.20. Voids ratio is plotted against p' in Figure 5.20a where the estimated *in situ* effective confining stresses for Tests R14 and R23 are also indicated. No *in situ* stress is indicated for Test R12 because the test was curtailed prematurely due to a membrane leak prior to reaching the *in situ* value. Despite this curtailment, the results from the initial stages of this test contribute to the data-set and so are included where appropriate. All tests started from similar voids ratios of between 0.81 and 0.83 and, as expected, voids ratio changes during the tests were substantially smaller than for the tests on reconstituted material. For simplicity, $G_{0(ij)}$ measurements are plotted against p' in Figure 5.20b There is broad agreement between the measured shear moduli for the three tests which confirms substantial and similar anisotropy ($G_{0(hh)} / G_{0(hv)} > 2$) in all three undisturbed samples.

In this section this data will be considered with the following objectives:

- consideration of the relevance of the voids ratio functions established for reconstituted samples,
- evaluation of the stress indices for natural Gault clay samples,
- comparison of $G_{0(ij)}$ measurements on natural samples with all tests on reconstituted samples,
- consideration of whether a cross-anisotropic model is adequate for the natural samples, or if a higher order of anisotropy is appropriate,
- attempted evaluation of the structure term $S_{(d)ij}$ in Equation 5.2.

5.3.3 Inherent anisotropy

Strain-induced anisotropy for reconstituted material was found to require the use of directional voids ratio functions to account for the development of the anisotropy of $G_{0(ij)}$. The data used to establish these functions are reproduced in Figure 5.21 along with $G_{0(ij)}$ values for the natural material extrapolated[††] to the same isotropic stress state of $p' = 90$ kPa. Note that data for the vertically propagated shear wave $V_{s(vh)}$ have also been included.

The power functions fitted to the reconstituted data have been extrapolated to voids ratios of 0.8, similar to that of the natural material, to highlight the differences between the prediction made on the basis of the

---

[††] Extrapolations are required because the tests on natural material all started at an isotropic stress ≈ 110 kPa.

reconstituted data and the natural material results. This shows that the predictions under-estimate both the $G_{0(hh)}$ and $G_{0(hv)}$ measurements by about 18%. However, the measured anisotropy ratio of Sample R23 at the natural voids ratio of 0.813 (given by the ratio $G_{0(hh)}$ / $G_{0(hv)}$) is 2.01, and that predicted for the same voids ratio using the strain-induced anisotropy relationships is 1.98. That these ratios are remarkably similar needs to be tempered with the observation that the extrapolation is over a large voids ratio range, and therefore may or may not be an indication of additional inherent influences such as ageing and diagenetic effects.

The difference between the predicted and measured $G_{0(vh)}$ values is significantly less than those for either $G_{0(hv)}$ or $G_{0(hh)}$. However, with the uncertainty in the $G_{0(vh)}$ measurements due to end effects, the significance of this observation is limited.

5.3.4 Stress-induced anisotropy

To assess stress-induced anisotropy on the natural Gault clay, Equation 5.2 is again used and log $G_{0(ij)} / e^{mij}$ is plotted *vs.* log ($\sigma_i'\sigma_j'$). The results of this normalisation on the data from the tests carried out on natural material is presented in Figure 5.22. The normalisation has been carried out without attempting to incorporate any additional effects of possible structure identified in the previous section, but by simply using the values of ^{mij} established for the reconstituted material. For comparison the least squares fit to both the reconstituted "*hv*" and "*hh*" data from Test N25 is included. The data points for all three tests on natural material can be seen to fit tolerably within the scatter indicated for Test N25 when the corresponding $\sigma'_i\sigma'_j/p_r$ values are greater than *in situ* stress, i.e. $\sigma'_v\sigma'_h$ >2.2E+4 and σ'^2_h >4.5E+4. However the trend fitted to this data gives an index value $^{nij}{}_{average} = 0.30$. This is significantly lower than the value of $^{nij} = 0.5$ measured for the reconstituted material. Considering that the test data come from stress path tests where a number of path directions were followed in order to establish triaxial small strain stiffness parameters, it is worth isolating particular constant horizontal and vertical stress excursions in order to explore this difference in more detail.

For measurements made at constant σ_h' in Test R23, (See Figure 4.14 for details of the stress path excursion from K_0=2 to σ_h' / σ_v'=0.5, and back to σ_h' / σ_v'=1) the ratio $(G_{0(ij)}/S_{ij}e^{mij})$ / $(G_{0(ij)}/S_{ij}e^{mij})_{isotropic}$ is plotted against stress ratio in Figure 5.23. The trend though this data confirms the value of ^{nhv} = 0.3 obtained as the average for all tests on natural material, while an index of 0.01 on the "*hh*" data shows little dependence on stress ratio.

Three measurements obtained during the constant σ_v' stress path followed from the initial isotropic stress state to the estimated *in situ* state are plotted in Figure 5.24. As with the comparable data for test L22 plotted in Figure 5.9, there is consistency in the "*hv*" trend line having an index approximately half of the "*hh*" line, but the value implied is $^{nij} = 0.2$, again lower than the value of 0.3 determined for the natural data set as a whole, and significantly lower than the value of 0.5 obtained for the reconstituted data.

These results appear to indicate that different stress influences apply for natural Gault clay. However the data leading to this result cover a relatively small range of both voids ratio and stress states. Moreover, the stress paths used to return the samples to their *in situ* stress states were completely different from the consolidation and swelling tests used to establish these indices for reconstituted material. It is therefore possible that the trends being observed in the natural material are being unduly influenced by local effects, and an overview in the context of the total data set can provide a different impression. A summary plot of all the $G_{0(hh)}$ $G_{0(hv)}$ and $G_{0(vh)}$ data (normalised by the appropriate e^{mij} terms and plotted *vs.* $\sigma_i'\sigma_j'$) obtained from tests on both natural and reconstituted material during the project is presented in Figure 5.25. The trend lines fitted to the data from Tests N25 are included. These confirm that the data from the tests on natural material fit tolerably well within the scatter of the data set as a whole, and in the absence of test results on natural material which span significantly larger stress and voids ratio ranges, it is reasonable to presume that the influences of strain and stress on natural Gault clay can be approximated by those established in tests on reconstituted material.

5.3.5 Azimuthal anisotropy

The differences between the data from tests on natural material and the reconstituted material can be viewed in another context. Reconstituted samples are created in conditions that will lead to cross-anisotropy. Scatter in the measurements of $G_{0(ij)}$ from these tests may reflect variation in the precise details of their reconstitution, and imperfections in the triaxial test procedures. However, these variations may be anticipated to lead to axi-symmetric variation at worst, and measurement of $G_{0(ij)}$ at the sample mid height should find symmetry about the vertical axis. However, while the strains during sedimentation and consolidation of the natural material may have been primarily one dimensional, subsequent glaciation and tectonic action which caused the folding and faulting that the Cambridge Gault clay has experienced, are likely to have resulted in more complex stress and strain conditions. In an attempt to evaluate the possible variation in properties that this may lead to, a series of bench-top tests was carried out using the bender probes to measure $V_{s(hv)}$ and $V_{s(hh)}$ at multiple azimuths similar to those previously illustrated in Figure 4.9. In these tests the suction within the sample was assumed to lead to an isotropic stress state of value equivalent to the suction. It had been hoped to monitor this suction while bender element tests were being carried out, however suction probes were not available at this time, and velocity measurements alone were made.

These bench-top measurements were carried out on Sample R23 after removal from the triaxial cell. The sample was cut in half at the mid-height, and bender probes were installed in four azimuthal orientations to measure $G_{0(hv)}$ and $G_{0(hh)}$ across the diameter at what would have been 1/4 and 3/4 sample height. One set of probes was aligned with the orientation held by the bender belt during the triaxial test. The velocity measurements have been converted into anisotropy measurements using:

$$\frac{G_{0(hh)}}{G_{0(hv)}} = \frac{V_{s(hh)}^2}{V_{s(hv)}^2} \quad \text{.....Equation 5.23}$$

and have been plotted with respect to azimuth in Figure 5.26. Interpolation between the data points leads to similar elliptical loci which indicate variations in anisotropy between a maximum of 2.24 and a minimum of 1.84. At the same azimuth as the bender belt during the triaxial stress path test (at 0°) the two ellipses indicate anisotropy ratios of 1.91 and 2.08, either side of the ratio of 2.02 measured by the bender belt shortly before the sample was removed from the cell.

While these results are only available for one of the triaxial samples, and further testing would have been useful to confirm this set of measurements, they do nevertheless raise the possibility of reasonably significant (±10%) variations in anisotropy with azimuth. The magnitude of these variations would be sufficient to mask the differences observed between data for reconstituted and natural samples presented in Figure 5.25. However, the influence of structure must also be considered in tests carried out on samples of natural Gault clay.

5.3.6 The effects of structure on anisotropy

Post-depositional effects would generally be anticipated to result in differences between the anisotropic $G_{\alpha(ij)}$ measured on reconstituted and natural material. Mitchell (1976) includes in these effects:

- Authigenesis - the formation of new minerals in place after deposition and
- Diagenesis - phenomena such as
  - changes in particle surface texture,
  - chemical changes involving conversion of minerals from one type to another,
  - the formation of inter-particulate bonds,
  - fabric changes and cementation,
  - jointing and fissuring,
  - increased brittleness possibly due to syneresis - the mutual attraction of clay particles to form closely knit aggregates separated by fissures.

Leroueil & Vaughan (1990) proposed that these effects should be included along with the general concepts of initial voids ratio and stress history in describing soil behaviour. They proposed that the term "structured" be used to describe soils in which the descriptors of conventional soil state (voids ratio and stress state) are not able to account for differences between the properties of a soil in its natural state and one where the "structure" has been removed by straining or remoulding. While a detailed consideration of the effect of structure is beyond the scope of this investigation, Leroueil & Vaughan (1990) provided evidence that "structure" may be released on or within primary yield surfaces due to straining. The effect of significant strain paths on $G_{\alpha(ij)}$ measured during tests on natural samples of Gault clay can therefore be

used to obtain a preliminary indication of the likely magnitude of "destructuration" within the primary yield surface.

As has been described in Section 4.4.2 and Figure 4.14, Test R23 included an excursion at constant σ_h' from the estimated *in situ* stress state where $K_0 = 2$, to $\sigma_h' / \sigma_v' = 0.5$. Failure was anticipated to occur at a stress ratio of 0.38, equivalent to an effective angle of friction $\phi' = 27°$, Ng (1992). Axial strains changed by 3.4% during this excursion, and the test thus spanned a large proportion of the anticipated yield envelope to peak strength. Such magnitudes of strain may be considered to lead to significant loss of structure, Hight (1993). After reaching the highest compressive state at $\sigma_h' / \sigma_v' = 0.5$, the sample was returned to the initial isotropic consolidation stress of 100 kPa at a voids ratio similar to the starting voids ratio. The differences in the axial and radial strains between the start and end of the test were only 0.69% and 0.04% respectively, indicating relatively little permanent strain.

The variation of $G_{0(ij)}$ with deviatoric strain ε_q is plotted in Figure 5.27. In Figure 5.27a $G_{0(ij)}$ is normalised by $G_{0(ij)}$ at the start of the test, and an increase in all measurements of $G_{0(ij)}$ between the start and end of the test is shown. In Figure 5.27b the normalisation of $G_{0(ij)}$ includes the strain and stress functions $S_{(s)ij}\, e^{mij}\, (\sigma_i'\sigma_j')^{nij}$ in order to reduce the exaggeration seen in Figure 5.27a due to changes in voids ratio and stress state during the test. A decrease in the normalised $G_{0(hh)}$ measurement of approximately 2% can now be seen, but there are still increases of between 3 and 8% for $G_{0(hv)}$ $G_{0(vh)}$ and $G_{0(vh)b}$. Clearly there are no dramatic differences in $G_{0(ij)}$ between start and finish of the test. Any significance in the change in $G_{0(hh)}$ and $G_{0(hv)}$ is diminished by the observation that these changes are within the accuracy of measurement, while the larger increases in $G_{0(vh)n}$ and $G_{0(vh)}$ are more likely to reflect non homogeneous stress states due to end effects than any further development of "structure" within the time scale of the test.

This evidence, while not exhaustive, does hint that the differences in moduli measured between reconstituted and natural samples are not purely a function of the sort of structure which can be destroyed by strain processes, but a wider combination of the post-depositional effects outlined at the start of this section.

5.3.7 Comparisons between laboratory and *in-situ* measurements of $G_{0(ij)}$

Profiles of shear wave velocities $V_{s(vh)}$, $V_{s(hv)}$ and $V_{s(hh)}$ were obtained at the High Cross site by Butcher & Powell (1995). The *in situ* measurements pre-date the sampling carried out for this project by some years, but they were carried out within approximately 25 m of the large sample boreholes as shown in Figure 4.5.

$V_{s(vh)}$ was obtained using a seismic cone and a surface source to generate shear waves which were monitored by receivers on the seismic cone as it is pushed to known depths. The difference in travel time between successive measurements is combined with the depth between the measurements to calculate $V_{s(vh)}$ for that horizon of soil. The $V_{s(hv)}$ and $V_{s(hh)}$ measurements were obtained using the cross-hole technique involving three boreholes; one for the source and two for the receivers. The holes were in line with different distances from the source borehole to each of the two receiver holes. Shear waves for the

$V_{s(hv)}$ and $V_{s(hh)}$ crosshole measurements were generated using downhole axial and rotary hammers respectively. The accuracy of the field velocity measurements is of the order of ±1%, Butcher (1997), which is similar to that measured in the laboratory.

Profiles of the *in situ* data are reproduced in Figure 5.28 along with measurements taken in triaxial tests R14 and R23 at the estimated *in situ* stress state. The *in situ* $V_{s(hh)}$ data lie substantially above both the $V_{s(hv)}$ and $V_{s(vh)}$ measurements, and the $V_{s(hv)}$ results also lie distinctly above the $V_{s(vh)}$ measurements.

The laboratory data show a similar pattern, with $V_{s(hh)} >> V_{s(hv)} > V_{s(vh)}$, as already discussed in Section 5.3.2. However, the only laboratory measurements to agree with the field measurements were $V_{s(hv)}$ laboratory which lie some 4% below the field data. The $V_{s(hh)}$ laboratory results exceed the field data by approximately 20%, and even if the estimated *in situ* stress state of $K_0 = 2$ is ignored, the $V_{s(hh)}$ values at $\sigma_h' / \sigma_v' = 1$ are still some 6 to 10 % higher than the field values. The $V_{s(vh)}$ laboratory values exceed the $V_{s(vh)}$ field values by similar percentages.

The procedure of reconsolidation to *in situ* stress involved increasing σ_h' from an isotropic stress state $p' = \sigma_{v0}'$. Evidence for the influence of stress on $G_{0(ij)}$ presented in section 5.3.4 showed that $G_{0(hh)}$ increases at twice the rate that $G_{0(hv)}$ (or $G_{0(vh)}$) increases for this stress path. This influence of the consolidation procedure to *in situ* stress state is illustrated in Figure 5.29, along with the values of $G_{0(ij)}$ calculated from the *in situ* measurements of $V_{s(ij)}$ already presented in Figure 5.28. In the case of $G_{0(hv)}$, this shows clearly how the laboratory measured values for both Tests R14 and R23 approach the field measurements as the estimated *in situ* state is approached. In the case of $G_{0(hh)}$ the laboratory measurements greatly exceed the field measurements at all stress ratios.

To assist in deciphering the results presented in Figure 5.28 and Figure 5.29, the observation (discussed in Section 4.6.4) from bench-top measurements on half height 100 mm diameter triaxial samples that $V_{s(vh)} \approx V_{s(hv)}$ on both natural and reconstituted samples is recalled. The observation that the Gault clay from these depths is widely fissured, predominantly in the near horizontal plane, is also relevant. Close inspection of these fissures revealed dustings of silt or fine sand on the fissure surfaces. With these in mind, possible reasons for the observed differences between field and laboratory results include:

- Higher field $V_{s(hv)}$ than $V_{s(vh)}$ values are possibly due to natural layering resulting from changing depositional environments during the deposition process. Vertically propagated waves have to pass though each layer, whereas horizontally propagated waves will tend to travel along layers of highest stiffness, i.e. $V_{s(hv)}$ field > $V_{s(vh)}$ field. This effect is also reported by Hight *et al.* (1997) in their comparison of field and laboratory measurements of $V_{s(ij)}$ on London and Thanet clays.

- The $V_{s(vh)}$ field measurements were made by advancing the seismic cone in increments of 1m, and each measurement is therefore the average for a layer of 1m thickness. The laboratory bench top test results were obtained on samples approximately 0.1 m high cut from the large 10" diameter samples. These sub-samples avoided the "widely spaced" fissures in the material, whereas the field measurements

would have to transmit through these fissures. It is arguable that this would result in a reduction in $V_{s(vh)field}$. i.e. $V_{s(vh)field} < V_{s(vh)laboratory\ bench\text{-}top}$.

- The $V_{s(vh)laboratory}$ triaxial measurements were always found to be smaller than corresponding $V_{s(hv)}$ values. However the discrepancy was seen to reduce with increasing confining stress as illustrated in Figure 4.26. From bench-top measurements it was found that $V_{s(hv)} \approx V_{s(vh)}$. These differences were ascribed to end effects. Hence the bench top ratio of $V_{s(vh)} / V_{s(hv)}$ is considered more representative of any natural samples than the measurements in the triaxial cell.

- The significantly lower values of $V_{s(hh)}$ field may be caused by the coincidence of the horizontally polarised, horizontal shear waves with the near horizontal fissures observed in this material. The path length between the two measurement cross-hole boreholes was of the order of 5 m, and over this length it is virtually inconceivable that a shear wave would not have to cross at least one fissure. Because the plane of the wave would have nearly coincided with the plane of the fissure, the material on the fissure (which is likely to be at a significantly lower confining stress), will therefore have influenced this shear wave velocity more than it would a vertically polarised horizontally propagated wave, which would hardly "see" near horizontal fissures, i.e. $G_{0(hh)}$ laboratory > $G_{0(hh)}$ field.

- Included in the differences between $V_{s(hv)} / V_{s(vh)\ laboratory}$ and $V_{s(hv)} / V_{s(vh)\ field}$ could be azimuthal variations in both current stress state and strain history. The latter were discussed in Section 5.3.5. The stress effects which are included in the stress terms in Equation 5.2 suggest that $G_{0(vh)}$ measured *in-situ* would be influenced by variations of horizontal stress with azimuth, despite having the same vertical effective stress at any orientation. Since the field $V_{s(vh)}$ readings were taken with their plane of polarisation perpendicular to the direction of propagation of the crosshole $V_{s(hv)}$, (Butcher, 1997), it is plausible that a proportion of the observed differences is due to variation of *in situ* lateral stress with azimuth. Bearing in mind the complex stress history of the area, such azimuthal stress variations are not unexpected, and have previously been suspected in the Gault clay 7.4 km SW of the High Cross test site, (Dalton & Hawkins, 1982).

In their study on six Italian clays, Jamiolkowski *et al.* (1995) found that their laboratory measurements of $G_{0(vh)}$ were only slightly lower than field measurements. They postulate on the one hand that the reconsolidation procedures possibly reverse the detrimental effects of sampling at least as far as the measurement of shear wave velocities is concerned. On the other hand they also note that on average, the voids ratios of their laboratory samples were 10% lower than the *in situ* voids ratios, and that this may counteract any disturbance effects and lead to apparently good agreement between laboratory and field measurements. In the case of Test R23, the final voids ratio was only 3% lower than the best estimate of *in situ* voids ratio, and $G_{0(hv)laboratory}$ were 2-4% lower than $G_{0(hv)field}$. These differences are of similar order to the accuracy of measurement and therefore indicate that this effect was of lower significance than found by Jamiolkowski *et al.* (1995).

By contrast, measurements of $G_{0(hh)\ laboratory}$ were approximately 50% higher than $G_{0(hh)\ field}$. Since neither resonant column nor conventional triaxial platen mounted bender devices are capable of exploring $G_{0(hh)}$

under anisotropic stress states, no comparable data are available. Clearly, these discrepancies warrant further research, and the horizontal bender devices offer opportunities for further exploration.

5.4 Summary

This chapter has presented and analysed measurements of shear wave velocity obtained using the horizontal bender element devices developed during the project.

The chapter began with a detailed investigation of the influences of strain and stress-induced anisotropy on samples of reconstituted Cambridge Gault clay. These unique investigations of the development of anisotropy in reconstituted Gault clay led to the discovery that directional voids ratio functions are required to describe the development of anisotropy during consolidation. Further, they highlight that the use of isotropic consolidation cycles in the study of shear moduli $G_{\alpha(ij)}$ may result in misleading results because the strain paths do not follow the predominantly 1 D consolidation history of a natural clay. On the basis of the tests carried out on reconstituted samples, a new form of the equation used to relate shear moduli, $G_{\alpha(ij)}$ to soil state was proposed.

In the second half of the chapter, measurements of $G_{\alpha(ij)}$ on samples of natural Gault clay were considered in the light of the discoveries made on reconstituted material. These showed that the framework developed for reconstituted material is broadly applicable to natural material. However, comparison with *in situ* geophysical measurements of $G_{\alpha(ij)}$ showed significant discrepancies which illustrate that additional factors such as asymmetric stress states and fissuring need to be considered when trying to compare with laboratory measurements carried out under controlled axisymmetric conditions, and at a scale small enough not to be influenced by the fissure spacing present in the ground.

The final objective listed at the start of the chapter was also achieved. A comprehensive database of measurements of $G_{\alpha(ij)}$ was obtained for consideration with small strain triaxial stress / strain data. These will be considered in Chapter 6 within a cross-anisotropic elastic framework which seeks to clarify the stiffness relationships that can be obtained under triaxial conditions over a range of strain level.

6. ANISOTROPIC ELASTIC PARAMETERS: MERGING SMALL STRAIN AND BENDER DATA

6.1 Introduction

An objective of this research project, established in Chapter 1 and discussed in Chapter 2, was to investigate the continuum between very small strain data determined using dynamic methods, and the small strain response of a clay soil to changes in stresses. This has been complicated by the finding in the previous chapter that the Cambridge Gault clay is significantly anisotropic at very small strain. Any investigation of the continuum of stiffness with strain should therefore also explore more fully the anisotropic nature of the small strain or "elastic" stiffness of Gault clay.

The theory of elasticity still forms the basis for many investigations in Geotechnics. While flaws of this approach are manifest wherever stress conditions could lead to states even remotely in the region of the limiting strength of the soil, there is still the need for the calculation of deformations under working load conditions, which in many cases are significantly less than the stresses needed to pre-empt failure, (Muir Wood, 1990).

A significant body of data presented over the past decade has exhibited a flattening of the so called "backbone" shaped stiffness *vs.* strain curve at strains less than about 10^{-3} %. This is interpreted as indicating strain levels below which a single stiffness value is able to describe the relationship between stress and strain, in other words, a material which follows Hooke's law. In Chapter 3 the magnitude of the shear strains developed by the bender elements were estimated to be of the order of 10^{-4} to 10^{-5} %. That a unique relationship also exists between shear-wave velocity and soil state at this level of strain, (once account has been taken of factors such as stress regime, voids ratio, and fabric) has also long been established in soil mechanics, and was further demonstrated in the preceding chapter. It is therefore reasonable to use elasticity as a framework to investigate the bringing together of very small strain (shear wave) and small strain (local triaxial) data obtained in tests on samples of natural Gault clay.

The design of triaxial tests, used in this investigation and outlined in Chapter 4, was influenced by pointers from the work of Atkinson *et al.* (1990), Pierpoint (1996), Hird and Pierpoint, (1997) and the studies presented in the previous chapter. The exploration of the behaviour of a clay matrix with shear waves illuminates features of particle on particle contact. The shear waves pass quickest through the contacts exhibiting the highest stiffness. It is the first and therefore fastest travel time that is measured, and therefore the highest stiffness that is deduced by this technique. In tests where both shear wave and triaxial measurements are to be made to explore the potential continuity of stiffness with strain, it is logical that triaxial tests should also be designed to measure the highest small strain response of the material.

The evidence from Atkinson *et al.* (1990) is that the highest stiffness in triaxial space is observed after a 180° rotation in the recent stress path direction. The effect of changing stress path direction may be visualised as "bricks on string" (Simpson, 1992 & 1993), where a combination of strings of different

lengths leads to a greater stiffness being mobilised after changes in stress path direction, than would develop in a monotonically changing stress state. It has also been suggested that it is not necessarily only a stress path direction reversal that is required to mobilise a "maximum stiffness". A sufficiently long pause at a particular stress state may be just as likely to lead to a maximum stiffness being measured when the stress path is resumed, (Simpson, 1997). This geological "wait" allows a deeply settled state to be reached by the clay particles, long after all measurable creep has ended. Continuation of the stress path may measure just as high a stiffness as a 180° direction change simply because high inter-particulate contacts have resulted in the equivalent of micro welds which have to be overcome.

Current testing capabilities do not lend themselves to modelling geological time and therefore it is pragmatically more feasible to use 180° stress path direction changes to measure the highest stiffness. The multiple mini stress path excursion method has the particular advantage that it avoids the obvious problem of variations between samples and the expense of conducting multiple tests. The validation of the MMSPE procedure as a means of exploring stiffness under a range of changing stress conditions on a single sample has been demonstrated by Hird & Pierpoint (1994 & 1997).

Tests on reconstituted samples led the exploration of influences on $G_{\alpha(ij)}$ in Chapter 5. In this chapter it is triaxial tests on undisturbed natural samples of Cambridge Gault clay that are the focus. In the first part of the chapter, the elastic anisotropic formulations developed by various authors are explored, and the relationships between different anisotropic parameters are derived in the context of triaxial testing. In the second part of the chapter, results from the triaxial tests are reported, and enable a range of anisotropic parameters to be measured and compared. These results are combined with bender element test results leading to evaluation of all five independent cross-anisotropic elastic parameters. The chapter concludes with discussion on the implications of these results for the measurement of anisotropic elastic parameters and anisotropy ratios, the use of triaxial testing to explore anisotropy, and evaluation of the independent shear modulus, G'_{hv}. [§]

6.2 Anisotropic elasticity

Elastic cross-anisotropy is described by five independent parameters. There is a plane of symmetry associated with any single z-cut, or cut perpendicular to the x-y plane, and an infinite number of planes through the axis of symmetry, or the z-axis.

The form of the relationship (or compliance matrix) which relates stress increments and strain increments is described by Equation 6.1 :

[§] The paper *Lings ML., Pennington DS & Nash DFT Anisotropic elastic parameters and their measurement in stiff natural clay. Géotechnique , Submitted Jan 1999* forms a substantial part of this chapter. I therefore acknowledge the contribution of particularly Martin Lings to the interpretation of data presented in this chapter.

$$\begin{bmatrix} \delta\varepsilon_{xx} \\ \delta\varepsilon_{yy} \\ \delta\varepsilon_{zz} \\ \delta\gamma_{yz} \\ \delta\gamma_{zx} \\ \delta\gamma_{xy} \end{bmatrix} = \begin{bmatrix} \frac{1}{E'_h} & \frac{-\nu'_{hh}}{E'_h} & \frac{-\nu'_{vh}}{E'_v} & . & . & . \\ \frac{-\nu'_{hh}}{E'_h} & \frac{1}{E'_h} & \frac{-\nu'_{vh}}{E'_v} & . & . & . \\ \frac{-\nu'_{hv}}{E'_h} & \frac{-\nu'_{hv}}{E'_h} & \frac{1}{E'_v} & . & . & . \\ . & . & . & \frac{1}{G'_{hv}} & . & . \\ . & . & . & . & \frac{1}{G'_{hv}} & . \\ . & . & . & . & . & \frac{1}{G'_{hh}} \end{bmatrix} \cdot \begin{bmatrix} \delta\sigma'_{xx} \\ \delta\sigma'_{yy} \\ \delta\sigma'_{zz} \\ \delta\tau_{yz} \\ \delta\tau_{zx} \\ \delta\tau_{xy} \end{bmatrix} \quad \text{.....Equation 6.1}$$

where the stress increments and strain increments are referred to rectangular Cartesian axes, with the z-axis vertical. This enables two distinct horizontal directions to be identified, but shows the material properties to be the same in both horizontal directions. The seven elastic parameters shown in Equation 6.1 are defined as follows:

E'_v = Young's modulus in the vertical direction

E'_h = Young's modulus in the horizontal direction

ν'_{vh} = Poisson's ratio for horizontal strain due to vertical strain

ν'_{hv} = Poisson's ratio for vertical strain due to horizontal strain

ν'_{hh} = Poisson's ratio for horizontal strain due to horizontal strain at right angles

G'_{hv} = Shear modulus in the vertical plane (also written as G'_{vh})

G'_{hh} = Shear modulus in the horizontal plane

All parameters relate to effective stresses, and the use of subscripts follows that adopted by Pickering, (1970).

However, not all these seven parameters are independent. Because the horizontal plane is a plane of isotropy, the term G'_{hh} is a dependent parameter related to E'_h and ν'_{hh} as shown in Equation 6.2:

$$\frac{2(1+\nu'_{hh})}{E'_h} = \frac{1}{G'_{hh}} \quad \text{.....Equation 6.2}$$

For an elastic material, there is a thermodynamic requirement that the compliance matrix must be symmetric (Love, 1927). Therefore parameters in the third row and third column of Equation 6.1 can be equated, giving:

$$\frac{\nu'_{hv}}{E'_h} = \frac{\nu'_{vh}}{E'_v} \quad \text{.....Equation 6.3}$$

However G'_{hv} is truly independent, and along with the other independent parameters E'_h E'_v ν'_{hh} and ν'_{vh} constitute the five independent parameters required to describe cross-anisotropy as represented in Equation 6.4:

$$\begin{bmatrix} \delta\varepsilon_{xx} \\ \delta\varepsilon_{yy} \\ \delta\varepsilon_{zz} \\ \delta\gamma_{yz} \\ \delta\gamma_{zx} \\ \delta\gamma_{xy} \end{bmatrix} = \begin{bmatrix} \frac{1}{E'_h} & \frac{-\nu'_{hh}}{E'_h} & \frac{-\nu'_{vh}}{E'_v} & \cdot & \cdot & \cdot \\ \frac{-\nu'_{hh}}{E'_h} & \frac{1}{E'_h} & \frac{-\nu'_{vh}}{E'_v} & \cdot & \cdot & \cdot \\ \frac{-\nu'_{vh}}{E'_v} & \frac{-\nu'_{vh}}{E'_v} & \frac{1}{E'_v} & \cdot & \cdot & \cdot \\ \cdot & \cdot & \cdot & \frac{1}{G'_{hv}} & \cdot & \cdot \\ \cdot & \cdot & \cdot & \cdot & \frac{1}{G'_{hv}} & \cdot \\ \cdot & \cdot & \cdot & \cdot & \cdot & \frac{2(1+\nu'_{hh})}{E'_h} \end{bmatrix} \cdot \begin{bmatrix} \delta\sigma'_{xx} \\ \delta\sigma'_{yy} \\ \delta\sigma'_{zz} \\ \delta\tau_{yz} \\ \delta\tau_{zx} \\ \delta\tau_{xy} \end{bmatrix} \quad \text{.....Equation 6.4}$$

Note that shear strains have been expressed in terms of engineering shear strains γ_{ij} where $\gamma_{ij} = \varepsilon_{ij} / 2$, and the prime symbol " ′ " has been used to indicate drained moduli corresponding to changes in effective stresses $\delta\sigma'_{xx}$, $\delta\sigma'_{yy}$ and $\delta\sigma'_{zz}$.

Although all five parameters are independent, there are bounds to the values that they can have, because of the thermodynamic requirement that strain energy be positive in an elastic material. Pickering (1970) has shown that E'_v E'_h and G'_{hv} must all be positive, and that $-1 < \nu'_{hh} < 1$. He also showed that E'_v E'_h ν'_{vh} and ν'_{hh} must satisfy an inequality, which is equivalent to an expression given by Raymond (1970). Both may be expressed more conveniently as:

$$\frac{E'_v}{E'_h}\left(1-\nu'_{hh}\right)-2\nu'^{2}_{vh} \geq 0 \quad \text{.....Equation 6.5}$$

Raymond (1970) also showed that G'_{hv} is bounded by the expression:

$$G'_{hv} \leq \frac{E'_v}{2\nu'_{vh}\left(1+\nu'_{hh}\right)+2\sqrt{\left[\frac{E'_v}{E'_h}\left(1-\nu'^{2}_{hh}\right)\left(1-\frac{E'_h}{E'_v}\nu'^{2}_{hh}\right)\right]}} \quad \text{.....Equation 6.6}$$

6.2.1 Investigating anisotropy using triaxial testing

The Cartesian orthogonal notation used in Equation 6.1 is frequently transformed into triaxial notation where soil behaviour is described in terms of volumetric and distortional response, which relates directly to data obtained from triaxial tests. The stress invariants used are the mean effective stress p' and the distortional or deviator stress q, and are described in terms of the vertical and horizontal effective stresses by Equation 6.7, (Schofield & Wroth, 1968):

$$\begin{bmatrix} p' \\ q \end{bmatrix} = \begin{bmatrix} 1/3 & 2/3 \\ 1 & -1 \end{bmatrix} \cdot \begin{bmatrix} \sigma_v' \\ \sigma_h' \end{bmatrix} \quad \text{.....Equation 6.7}$$

The corresponding invariant strain parameters are volumetric strain and distortional strain. The relationships between increments in volumetric strain, $\delta\varepsilon_p$, and distortional strain, $\delta\varepsilon_q$, are described by Equation 6.8:

$$\begin{bmatrix} \delta\varepsilon_p \\ \delta\varepsilon_q \end{bmatrix} = \begin{bmatrix} 1 & 2 \\ 2/3 & -2/3 \end{bmatrix} \cdot \begin{bmatrix} \delta\varepsilon_v \\ \delta\varepsilon_h \end{bmatrix} \quad \text{.....Equation 6.8}$$

6.2.2 Three parameter G' K' J' and G* K* J formulations

The incremental constitutive equation for small increments of stress and strain can be defined in terms of volumetric and distortional components by Equation 6.9, (Atkinson *et al.*, 1990):

$$\begin{bmatrix} \delta\varepsilon_p \\ \delta\varepsilon_q \end{bmatrix} = \begin{bmatrix} \frac{1}{K'} & \frac{1}{J'_{qp}} \\ \frac{1}{J'_{pq}} & \frac{1}{3G'} \end{bmatrix} \cdot \begin{bmatrix} \delta p' \\ \delta q' \end{bmatrix} \quad \text{.....Equation 6.9}$$

where $K' =$ a bulk modulus

$G' =$ a shear modulus

$J'_{pq} =$ a coupling modulus linking changes in mean effective stress and changes in distortional strain

$J'_{qp} =$ a coupling modulus linking changes in deviator stress and changes in volumetric strain

As noted by Pierpoint (1996), the stiffness parameters J'_{pq} and J'_{qp} which couple volumetric and deviatoric responses are analogous to the parameters J'_1 and J'_2 defined by Atkinson & Sällfors (1991).

Each parameter in Equation 6.9 can be evaluated separately by conducting drained probing tests either at constant p' or at constant q. For an elastic material the compliance matrix must be symmetric, thus $J'_{qp} = J'_{pq} = J'$. For a material that is also isotropic, there is no coupling between volumetric and distortional behaviour, and the $1/J'$ terms are zero ($J' = \pm\infty$).

As an alternative to a compliance matrix, a constitutive equation can be written in terms of a stiffness matrix, (Graham & Houlsby, 1983):

$$\begin{bmatrix} \delta p' \\ \delta q \end{bmatrix} = \begin{bmatrix} K^* & J \\ J & 3G^* \end{bmatrix} \cdot \begin{bmatrix} \delta\varepsilon_p \\ \delta\varepsilon_q \end{bmatrix} \quad \text{.....Equation 6.10}$$

where $G^* =$ a shear modulus

$K^* =$ a bulk modulus

$J =$ a coupling modulus

For a material that is isotropic, here too there is no coupling between volumetric and distortional behaviour, and the J terms are zero. It should be emphasised that there is no equivalence between the G' K' and G^* K^* parameters *unless* the material behaviour is uncoupled (implying isotropy), when $G' = G^*$ and $K' = K^*$. The G^* parameter can be directly determined from undrained tests, for which $\delta\varepsilon_p = 0$.

Conversion between the two sets of parameters is readily undertaken by inverting the matrices. This leads to the Equations 6.11 and 6.12:

$$G^* = \frac{G'J'^2}{\left(J'^2 - 3K'G'\right)};\quad K^* = \frac{K'J'^2}{\left(J'^2 - 3K'G'\right)};\quad J = \frac{-3G'K'J'}{\left(J'^2 - 3K'G'\right)} \qquad \text{.....6.11}$$

and

$$G' = \frac{\left(3G^*K^* - J^2\right)}{3K^*};\quad K' = \frac{\left(3G^*K^* - J^2\right)}{3G^*};\quad J' = \frac{-\left(3G^*K^* - J^2\right)}{J} \qquad \text{.....6.12}$$

6.2.3 Three and four parameter descriptions of anisotropy

If a triaxial test is carried out on a cross-anisotropic soil, no shear stresses (τ_{yz}, τ_{zx}, τ_{xy}) can be applied and no shear strains (γ_{yz}, γ_{zx}, γ_{xy}) can be measured. Hence only the top left-hand corner of the compliance matrix in Equation 6.4 can be investigated. For the conditions in the triaxial cell, $\delta\varepsilon_{xx} = \delta\varepsilon_{yy} = \delta\varepsilon_h$ and $\delta\sigma'_{xx} = \delta\sigma'_{yy} = \delta\sigma'_h$, Equation 6.4 can be simplified and rewritten as:

$$\begin{bmatrix}\delta\varepsilon_v \\ \delta\varepsilon_h\end{bmatrix} = \begin{bmatrix}\frac{1}{E'_v} & \frac{-2\nu'_{vh}}{E'_v} \\ \frac{-\nu'_{vh}}{E'_v} & \frac{(1-\nu'_{hh})}{E'_h}\end{bmatrix}\cdot\begin{bmatrix}\delta\sigma'_v \\ \delta\sigma'_h\end{bmatrix} \qquad \text{.....Equation 6.13}$$

To enable differentiation between parameters derived at very small strain (using shear waves) and parameters derived at the low end of small strain (derived from local displacement transducers), notation is introduced. Moduli derived at very small strain will be immediately followed by the subscript "$_o$", and then any qualifying attributes e.g.: $G_{o(ij)}$. Moduli at greater strain will simply be followed by the qualifying attributes e.g. G_{ij}.

G' K' J' formulation

In constant p' stress path excursions, the terms involving $\delta p'$ in Equation 6.9 equal zero and G' and J'_{qp} can be evaluated using equations 6.14 and 6.15:

$$G' = \left(\frac{\delta q}{3\delta\varepsilon_q}\right)_{\delta p'=0} \qquad \text{.....Equation 6.14}$$

$$J'_{qp} = \left(\frac{\delta q}{\delta\varepsilon_p}\right)_{\delta p'=0} \qquad \text{.....Equation 6.15}$$

Since p' is held constant, $\delta\sigma'_v = -2\delta\sigma'_h$ and substitution into Equation 6.13 leads to:

$$\delta\varepsilon_v = \frac{1}{E'_v}\delta\sigma'_v + \frac{\nu'_{vh}}{E'_v}\delta\sigma'_v = \frac{(1+\nu'_{vh})}{E'_v}\delta\sigma'_v \quad \text{.....Equation 6.16}$$

and $$\delta\varepsilon_h = \frac{-\nu'_{vh}}{E'_v}\delta\sigma'_v - \frac{1-\nu'_{hh}}{2E'_h}\delta\sigma'_v = -\left[\frac{\nu'_{vh}}{E'_v} + \frac{(1-\nu'_{hh})}{2E'_h}\right]\delta\sigma'_v \quad \text{.....Equation 6.17}$$

By noting that $\delta\sigma'_v = -2\delta\sigma'_h$ and $\delta q = 3\delta\sigma'_v/2$, these can be combined into one equation by using the relationship for triaxial distortional strain $\delta\varepsilon_q$ as given in Equation 6.8. This leads to:

$$\delta\varepsilon_q = \frac{2}{3}(\delta\varepsilon_v - \delta\varepsilon_h) = \frac{2}{3}\cdot\left[\frac{1+2\nu'_{vh}}{E'_v} + \frac{(1-\nu'_{hh})}{2E'_h}\right]\cdot\frac{2}{3}\delta q \quad \text{.....Equation 6.18}$$

This can be rearranged to give an expression for G' shown in Equation 6.19:

$$G' = \frac{1}{3}\left(\frac{\delta q}{\delta\varepsilon_q}\right)_{\delta p'=0} = \frac{3}{4\cdot\left[\frac{1+2\nu'_{vh}}{E'_v} + \frac{(1-\nu'_{hh})}{2E'_h}\right]} \quad \text{.....Equation 6.19}$$

Similarly, using the relationship for volumetric strain $\delta\varepsilon_p$ given in Equation 6.8,

$$J'_{qp} = \left(\frac{\delta q}{\delta\varepsilon_p}\right)_{\delta p'=0} = \frac{3}{2\cdot\left[\frac{(1-\nu'_{vh})}{E'_v} - \frac{(1-\nu'_{hh})}{E'_h}\right]} \equiv J'_{pq} \quad \text{.....Equation 6.20}$$

In constant q stress path excursions, terms in Equation 6.9 involving δq equal zero, and K' and J'_{pq} can be evaluated using Equations 6.21 and 6.22:

$$K' = \left(\frac{\delta p'}{\delta\varepsilon_p}\right)_{\delta q'=0} \quad \text{.....Equation 6.21}$$

$$J'_{pq} = \left(\frac{\delta p'}{\delta\varepsilon_q}\right)_{\delta q'=0} \quad \text{.....Equation 6.22}$$

Since q is held constant, $\delta\sigma_v = \delta\sigma_h$, and substitution into Equation 6.13 gives:

$$\delta\varepsilon_v = \frac{1}{E'_v}\delta\sigma'_v - \frac{2\nu'_{vh}}{E'_v}\delta\sigma'_h \quad \text{.....Equation 6.23}$$

and $$\delta\varepsilon_h = \frac{-\nu'_{vh}}{E'_v}\delta\sigma'_v + \frac{1-\nu'_{hh}}{E'_h}\delta\sigma'_h \quad \text{.....Equation 6.24}$$

By noting that $\delta\sigma'_h = \delta\sigma'_v$ and $\delta p' = \delta\sigma'_v$ in a constant q test, Equations 6.23 and 6.24 can be combined into one using the relationship for volumetric strain, $\delta\varepsilon_p$, given in Equation 6.8. This leads to:

$$\delta\varepsilon_p = (\delta\varepsilon_v + 2\delta\varepsilon_h) = \left[\frac{1-4\nu'_{vh}}{E'_v} + \frac{2\cdot(1-\nu'_{hh})}{E'_h}\right]\cdot\delta p' \quad \text{.....Equation 6.25}$$

This can be rearranged to give an expression for K'

$$K' = \left(\frac{\delta p'}{\delta\varepsilon_p}\right)_{\delta q=0} = \frac{1}{\left[\frac{1-4\nu'_{hv}}{E'_v} + \frac{2\cdot(1-\nu'_{hh})}{E'_h}\right]} \quad \text{.....Equation 6.26}$$

Similarly, using the relationship for deviatoric strain, $\delta\varepsilon_q$, given in Equation 6.8:

$$J'_{pq} = \left(\frac{\delta p'}{\delta\varepsilon_q}\right)_{\delta\sigma_q=0} = \frac{3}{2\cdot\left[\frac{(1-\nu'_{hv})}{E'_v} - \frac{(1-\nu'_{hh})}{E'_h}\right]} \equiv J'_{qp} \quad \text{.....Equation 6.27}$$

which is precisely the same as that given for the cross-coupling term in Equation 6.20.

At the risk of labouring the point, it can be seen from Equations 6.19, 6.20, 6.26 and 6.27 that K' G' J' are each functions of all four independent elastic parameters E'_v E'_h ν'_{vh} and ν'_{hh} that appear in Equation 6.13.

G^* K^* J formulation

G^* K^* J can be evaluated from expressions for triaxial tests carried out at constant strain using Equations 6.28 to 6.30:

$$G^* = \frac{1}{3}\left(\frac{\delta q}{\delta\varepsilon_q}\right)_{\delta\varepsilon_p=0} \quad \text{.....Equation 6.28}$$

$$K^* = \left(\frac{\delta p}{\delta\varepsilon_p}\right)_{\delta\varepsilon_q=0} \quad \text{.....Equation 6.29}$$

$$J = \left(\frac{\delta q}{\delta\varepsilon_p}\right)_{\delta\varepsilon_q=0} = \left(\frac{\delta p}{\delta\varepsilon_q}\right)_{\delta\varepsilon_p=0} \quad \text{.....Equation 6.30}$$

For an undrained test $\delta\varepsilon_p = 0$ and therefore $\delta\varepsilon_v + 2\delta\varepsilon_h = 0$. Requiring this condition in Equation 6.13 leads to:

$$\frac{\delta\sigma'_h}{\delta\sigma'_v} = -\frac{1}{2}\left[\frac{\left(1-2\nu'_{vh}\right)E'_h}{\left(1-\nu'_{hh}\right)E'_v - \nu'_{vh}E'_h}\right] \quad \text{.....Equation 6.31}$$

which can be used to obtain δq by the rearrangement given in Equation 6.32:

$$\delta q = \delta\sigma'_v - \delta\sigma'_h = \delta\sigma'_v\left(1-\frac{\delta\sigma'_h}{\delta\sigma'_v}\right) = \frac{\delta\sigma'_v}{2}\left[\frac{2\left(1-\nu'_{hh}\right)E'_v + \left(1-4\nu'_{vh}\right)E'_h}{\left(1-\nu'_{hh}\right)E'_v - \nu'_{vh}E'_h}\right] \quad \text{.....Equation 6.32}$$

Substitution of Equation 6.31 into Equation 6.13 for $\delta\varepsilon_v$ gives:

$$\delta\varepsilon_v = \delta\sigma'_v\left[\frac{1}{E'_v}+\frac{\nu'_{vh}}{E'_v}\left[\frac{\left(1-2\nu'_{vh}\right)E'_h}{\left(1-\nu'_{hh}\right)E'_v-\nu'_{vh}E'_h}\right]\right] \quad \text{.....Equation 6.33}$$

Now since $\delta\varepsilon_v + 2\delta\varepsilon_h = 0$, it follows that $\delta\varepsilon_q = \delta\varepsilon_v$ and Equations 6.32 and 6.33 can be combined to give:

$$G^* = \frac{1}{3}\left(\frac{\delta q}{\delta\varepsilon_q}\right)_{\delta\varepsilon_p=0} = \frac{E'_v}{6}\left[\frac{2\left(1-\nu'_{hh}\right)E'_v+\left(1-4\nu'_{vh}\right)E'_h}{\left(1-\nu'_{hh}\right)E'_v-2\nu'^{2}_{vh}E'_h}\right] \quad \text{.....Equation 6.34}$$

While distinctly more difficult to carry out in the triaxial cell, but easily achieved by similar algebraic manipulation, assuming $\delta\varepsilon_q = 0$ leads to expressions for K^* and J given in Equations 6.35 and 6.36:

$$K^* = \frac{E'_v}{9}\left[\frac{\left(1-\nu'_{hh}\right)E'_v+2\left(1+2\nu'_{vh}\right)E'_h}{\left(1-\nu'_{hh}\right)E'_v-2\nu'^{2}_{vh}E'_h}\right] \quad \text{.....Equation 6.35}$$

$$J = \frac{E'_v}{3}\left[\frac{\left(1-\nu'_{hh}\right)E'_v-\left(1-\nu'_{vh}\right)E'_h}{\left(1-\nu'_{hh}\right)E'_v-2\nu'^{2}_{vh}E'_h}\right] \quad \text{.....Equation 6.36}$$

It is clear that like $G'\,K'\,J'$, $G^*\,K^*\,J$ are also each functions of all four independent elastic parameters E'_v E'_h ν'_{vh} and ν'_{hh}.

$E^*\,\nu^*\,\alpha$ formulation

Graham & Houlsby (1983) showed that it is not possible to recover more than three elastic constants from triaxial tests. Since two of these terms are needed to describe even isotropic elastic response, only one remains to incorporate anisotropy. They therefore proposed a form of cross-anisotropy involving only three parameters, which is represented by the stiffness matrix given in Equation 6.37:

$$\begin{bmatrix}\delta\sigma_{xx}\\ \delta\sigma_{yy}\\ \delta\sigma_{zz}\end{bmatrix} = \begin{bmatrix}A^* & \alpha B^* & \alpha B^*\\ \alpha B^* & \alpha^2 A^* & \alpha^2 B^*\\ \alpha B^* & \alpha^2 B^* & \alpha^2 A^*\end{bmatrix}\cdot\begin{bmatrix}\delta\varepsilon_{xx}\\ \delta\varepsilon_{yy}\\ \delta\varepsilon_{zz}\end{bmatrix} \quad \text{.....Equation 6.37}$$

where the anisotropy factor α has been introduced to enable the stiffness in the horizontal direction to be varied with respect to that in the vertical direction. When $\alpha = 1$, the material is isotropic, when $\alpha > 1$, the material is stiffer horizontally than vertically, and when $\alpha < 1$ the material is stiffer vertically than horizontally.

The form of the stiffness matrix given in Equation 6.37 is used to modify the fully cross-anisotropic matrix presented earlier in Equation 6.4 by introducing modified anisotropic parameters E^* and ν^* as shown in Equation 6.38.

$$\begin{bmatrix}\dot{\delta\sigma}_{xx}\\ \dot{\delta\sigma}_{yy}\\ \dot{\delta\sigma}_{zz}\\ \dot{\delta\tau}_{yz}\\ \dot{\delta\tau}_{zx}\\ \dot{\delta\tau}_{xy}\end{bmatrix}=\frac{E^*}{(1+\nu^*)(1-2\nu^*)}\begin{bmatrix}\alpha^2(1-\nu^*) & \alpha^2\nu^* & \alpha\nu^* & . & . & .\\ \alpha^2\nu^* & \alpha^2(1-\nu^*) & \alpha\nu^* & . & . & .\\ \alpha\nu^* & \alpha\nu^* & (1-\nu^*) & . & . & .\\ . & . & . & \frac{\alpha(1-\nu^*)}{2} & . & .\\ . & . & . & . & \frac{\alpha(1-\nu^*)}{2} & .\\ . & . & . & . & . & \frac{\alpha^2(1-\nu^*)}{2}\end{bmatrix}\begin{bmatrix}\dot{\delta\varepsilon}_{xx}\\ \dot{\delta\varepsilon}_{yy}\\ \dot{\delta\varepsilon}_{zz}\\ \dot{\delta\gamma}_{yz}\\ \dot{\delta\gamma}_{zx}\\ \dot{\delta\gamma}_{xy}\end{bmatrix}$$

.....Equation 6.38

The corresponding full 6 × 6 compliance is given in Equation 6.39:

$$\begin{bmatrix}\dot{\delta\varepsilon}_{xx}\\ \dot{\delta\varepsilon}_{yy}\\ \dot{\delta\varepsilon}_{zz}\\ \dot{\delta\gamma}_{yz}\\ \dot{\delta\gamma}_{zx}\\ \dot{\delta\gamma}_{xy}\end{bmatrix}=\frac{1}{E^*}\begin{bmatrix}\frac{1}{\alpha^2} & \frac{-\nu^*}{\alpha^2} & \frac{-\nu^*}{\alpha} & . & . & .\\ \frac{-\nu^*}{\alpha^2} & \frac{1}{\alpha^2} & \frac{-\nu^*}{\alpha} & . & . & .\\ \frac{-\nu^*}{\alpha} & \frac{-\nu^*}{\alpha} & 1 & . & . & .\\ . & . & . & \frac{2(1+\nu^*)}{\alpha} & . & .\\ . & . & . & . & \frac{2(1+\nu^*)}{\alpha} & .\\ . & . & . & . & . & \frac{2(1+\nu^*)}{\alpha^2}\end{bmatrix}\begin{bmatrix}\dot{\delta\sigma}_{xx}\\ \dot{\delta\sigma}_{yy}\\ \dot{\delta\sigma}_{zz}\\ \dot{\delta\tau}_{yz}\\ \dot{\delta\tau}_{zx}\\ \dot{\delta\tau}_{xy}\end{bmatrix}$$

.....Equation 6.39

By comparing Equation 6.39 with Equation 6.1, the model allows values of all the elastic parameters to be estimated as given in Equations 6.40:

$$E'_v=E^*;\quad E'_h=\alpha^2E^*;\quad \nu'_{vh}=\nu^*/\alpha;\quad \nu'_{hh}=\nu^*;$$

$$G'_{hv}=\alpha E^*/2(1+\nu^*);\quad G'_{hh}=\alpha^2E^*/2(1+\nu^*)$$

.....Equations 6.40

Due to the restrictions of the model, the anisotropy factor α controls the ratio of Young's modulus, Poisson's ratio and shear modulus terms, requiring them all to be the same:

$$\alpha=\sqrt{\frac{E'_h}{E'_v}};\quad \alpha=\frac{\nu'_{hh}}{\nu'_{vh}};\quad \alpha=\frac{G'_{hh}}{G'_{hv}}$$

.....Equations 6.41

Muir Wood (1990) has given explicit equations describing G^* K^* J in terms of E^* ν^* α as shown in Equations 6.42 to 6.44:

$$K^*=\frac{E^*(1-\nu^*+4\alpha\nu^*+\alpha^2)}{9(1+\nu^*)(1-2\nu^*)}$$

.....Equation 6.42

$$G^*=\frac{E^*(2-2\nu^*-4\alpha\nu^*+\alpha^2)}{6(1+\nu^*)(1-2\nu^*)}$$

.....Equation 6.43

$$J^* = \frac{E^*(1-\nu^*+\alpha\nu^*-\alpha^2)}{3(1+\nu^*)(1-2\nu^*)} \quad \text{.....Equation 6.44}$$

If these equations are combined with Equations 6.34 to 6.36, manipulation leads to:

$$E^* = E'_v \quad \text{.....Equation 6.45}$$

$$\nu^* = \frac{\nu'_{vh}E'_h\left[-\nu'_{vh}+\sqrt{\nu'^{\,2}_{vh}+4\frac{E'_v}{E'_h}\left(1-\nu'_{hh}\right)}\right]}{2E'_v\left(1-\nu'_{hh}\right)} \quad \text{.....Equation 6.46}$$

and $$\alpha = \frac{E'_h\left[-\nu'_{vh}+\sqrt{\nu'^{\,2}_{vh}+4\frac{E'_v}{E'_h}\left(1-\nu'_{hh}\right)}\right]}{2E'_v\left(1-\nu'_{hh}\right)} \quad \text{.....Equation 6.47}$$

From Equations 6.46 and 6.47 it is clear that $\nu^* = \nu'_{vh}\alpha$. Comparing this and Equation 6.45 with Equation 6.40 reveals that E'_v and ν'_{vh} are *always* correctly computed with the Graham & Houlsby (1983) model.

Hird & Pierpoint (1994) give relationships linking G' K' J' and E^* ν^* α as shown in Equations 6.48 to 6.50:

$$K' = \frac{\alpha^2 E^*}{\alpha^2-4\alpha\nu^*+2-2\nu^*} \quad \text{.....Equation 6.48}$$

$$G' = \frac{3\alpha^2 E^*}{4\alpha^2+8\alpha\nu^*+2-2\nu^*} \quad \text{.....Equation 6.49}$$

$$J' = \frac{3\alpha^2 E^*}{2\alpha^2-2\alpha\nu^*+2-2\nu^*} \quad \text{.....Equation 6.50}$$

In order to illustrate the importance of differentiating between the K^* G^* J and K' G' J' sets of parameters, Equations 6.42 to 6.44 and 6.48 to 6.50 have been used to plot the ratios K^*/K', G^*/G', and J/J'. These are illustrated in Figure 6.1 where their variation with the anisotropy ratio α is plotted for $\nu^* = 0$, 0.1 and 0.2. These plots confirm a similar influence of ν^* on each set of parameters, but demonstrate the significant differences between the two formulations for relatively minor deviations from isotropy.

An alternative 3 parameter formulation

Thus far, formulations involving the triaxial stress and strain variables p' q ε_p and ε_q have been used to obtain parameters describing anisotropy. However, if tests are performed at constant σ'_v and at constant σ'_h, Equation 6.13 gives explicit relationships between anisotropic parameters and the vertical and horizontal stresses and strains measured in triaxial tests. For tests carried out at constant σ'_h

$$E'_v = \left(\frac{\delta\sigma'_v}{\delta\varepsilon_v}\right)_{\delta\sigma'_h=0} \quad \text{.....Equation 6.51}$$

$$\frac{E'_v}{-\nu'_{vh}} = \left(\frac{\delta\sigma'_v}{\delta\varepsilon_h}\right)_{\delta\sigma_h'=0} \quad \text{.....Equation 6.52}$$

Combining Equations 6.51 and 6.52 leads to direct evaluation of ν'_{vh} as shown in Equation 6.53:

$$\nu'_{vh} = -\left(\frac{\delta\sigma'_v}{\delta\varepsilon_v}\right)\Big/\left(\frac{\delta\sigma'_v}{\delta\varepsilon_h}\right)_{\delta\sigma'_h=0} = -\left(\frac{\delta\varepsilon'_h}{\delta\varepsilon_v}\right)_{\delta\sigma_h'=0} \quad \text{.....Equation 6.53}$$

For tests carried out at constant σ_v' the relationships given in Equations 6.54 and 6.55 can be investigated:

$$\frac{E'_v}{-2\nu'_{vh}} = \left(\frac{\delta\sigma'_h}{\delta\varepsilon_v}\right)_{\delta\sigma_v'=0} \quad \text{.....Equation 6.54}$$

$$\frac{E'_h}{1-\nu'_{hh}} = \left(\frac{\delta\sigma'_h}{\delta\varepsilon_h}\right)_{\delta\sigma_v'=0} \quad \text{.....Equation 6.55}$$

Using these equations it is not possible to obtain explicit unique evaluations of the parameters E'_h and ν'_{hh} merely from triaxial measurements. However the symmetry of the stiffness matrix given by Equation 6.1 can be explored by manipulation of these equations. Dividing Equation 6.55 by Equation 6.54 leads to:

$$\left(\frac{\delta\varepsilon_v}{\delta\varepsilon_h}\right)_{\delta\sigma'_v=0} = \left(\frac{\delta\sigma'_h}{\delta\varepsilon_h}\right)\Big/\left(\frac{\delta\sigma'_h}{\delta\varepsilon_v}\right)_{\delta\sigma_v'=0} = \frac{E'_h}{1-\nu'_{hh}} \cdot \frac{-2\nu'_{vh}}{E'_v} \quad \text{.....Equation 6.56}$$

and substituting Equation 6.3 into this leads to the relationship

$$-\frac{2\nu'_{hv}}{1-\nu'_{hh}} = \left(\frac{\delta\varepsilon'_v}{\delta\varepsilon_h}\right)_{\delta\sigma'_v=0} \quad \text{.....Equation 6.57}$$

In obtaining Equation 6.57, E'_h and ν'_{hv} have been reintroduced into the top right hand term of the compliance matrix in Equation 6.13 so that the symmetry of the compliance matrix in Equation 6.1 can be investigated.

Inspection of Equations 6.19, 6.20 and 6.26 for G' K' J' in terms of E'_v E'_h ν'_{vh} and ν'_{hh} shows that the parameters E'_h and ν'_{hh} always appear together in the combination found in Equation 6.55. If we write

$$F'_h = \frac{E'_h}{\left(1-\nu'_{hh}\right)} \quad \text{.....Equation 6.58}$$

then the three parameters E'_v ν'_{vh} F'_h can provide as complete a description of behaviour in a triaxial test as the parameters G' K' J'. This is demonstrated by re-writing Equations 6.19, 6.20 and 6.26 as:

$$G' = \frac{3E'_v F'_h}{\left(4F'_h + 8\nu'_{vh}F'_h + 2E'_v\right)} \quad \text{.....Equation 6.59}$$

$$K' = \frac{E_v' F_h'}{\left(F_h' - 4\nu_{vh}' F_h' + 2E_v'\right)} \quad \text{.....Equation 6.60}$$

$$J' = \frac{3E_v' F_h'}{\left(2F_h' + 2\nu_{vh}' F_h' + 2E_v'\right)} \quad \text{.....Equation 6.61}$$

Manipulation of these equations leads to expressions for $E'_v\ \nu'_{vh}\ F'_h$ in terms of $G'\ K'\ J'$:

$$E_v' = \frac{9G'K'J'}{\left(6G'K' + G'J' + 3K'J'\right)} \quad \text{.....Equation 6.62}$$

$$\nu_{vh}' = -\frac{1}{2}\frac{\left(3G'K' + 2G'J' - 3K'J'\right)}{\left(6G'K' + G'J' + 3K'J'\right)} \quad \text{.....Equation 6.63}$$

$$F_h' = G'\left[\frac{\left(12G'K' - 4G'J' - 30K'J'\right) \pm 4\sqrt{G'^2(3K' - J')^2 + 12G'K'J'(3K' - J') + 36K'^2J'^2}}{\left(36G'K' - 12G'J' - 9K'J'\right)}\right]$$

.....Equation 6.64

Finally, given that K', G' and J' can all be evaluated directly from triaxial constant p' and q stress path excursions, Equations 6.48, 6.49 and 6.50 can be rearranged so that the modified stiffness parameters E^*, ν^* and α can be explicitly evaluated. The results of this re-arrangement are shown in Equations 6.65, 6.66 and 6.67:

$$E^* = 9 \cdot \frac{G'K'J'}{G'J' + 6G'K' + 3K'J'} \quad \text{.....Equation 6.65}$$

$$\nu^* = -\frac{1}{2} \cdot \frac{(2G'J' - 3K'J' + 3G'K') \cdot \alpha}{(G'J' + 6G'K' + 3K'J')} \quad \text{.....Equation 6.66}$$

$$\alpha = \frac{1}{2} \cdot \frac{-2G'J' + 3K'J' - 3G'K' \pm 3\sqrt{4J'^2G'^2 + 12G'J'^2K' + 12G'^2J'K' + 9K'^2J'^2 - 18J'G'K'^2 - 63G'^2K'^2}}{12G'K' - 3K'J' - 4G'J'}$$

.....Equation 6.67

In all cases, parameters of one formulation can be expressed as functions of all three parameters of another formulation, and this offers opportunities for the exploration of elastic parameters using a variety of stress paths involving constant $\sigma'_v\ \sigma'_h\ p'$ and q excursions.

Investigating five parameter anisotropy

The horizontal bender devices developed during the project enable, as has been discussed in detail in Chapter 5, the measurement of the three separate shear moduli, $G_{o(vh)}\ G_{o(hv)}$ and $G_{o(hh)}$. With high quality local strain measurements on 100 mm diameter samples, it has been possible to assess strains down to $2\text{x}10^{-4}\%$ for the small strain stress path excursion tests described in Chapter 4. This has made it possible to bring together both bender and small strain data from the same sample, assuming that there is continuity between dynamic and static measurements. The evidence from Atkinson *et al.* (1990) is that the highest

stiffness in the triaxial plane is observed after a 180° rotation of the stress path direction. In terms of kinematic soil modelling, this represents behaviour within a Linear Elastic Zone, as described for example by Jardine (1992). Provided such stress paths are followed, it is considered reasonable to combine the two types of data in this way.

At very small strains - where both bender and triaxial strains can be said to be illuminating elastic properties - bender element tests yield values of $G_{0(hv)}$ and $G_{0(hh)} = E_{0(h)}/2(1+\nu_{0(hh)})$, and very small strain data from triaxial tests can yield values of $E_{0(v)}$, $\nu_{0(vh)}$ and $F_{0(h)} = E_{0(h)}/(1-\nu_{0(hh)})$. The equations for $F_{0(h)}$ and $G_{0(hh)}$ can be combined to give $\nu_{0(hh)}$ and $E_{0(h)}$:

$$\nu_{0(hh)} = \frac{(F_{0(h)} - 2G_{0(hh)})}{(F_{0(h)} + 2G_{0(hh)})} \quad \text{.....Equation 6.68}$$

and

$$E_{0(h)} = \frac{4F_{0(h)}G_{0(hh)}}{(F_{0(h)} + 2G_{0(hh)})} \quad \text{.....Equation 6.69}$$

Hence all five of the elastic coefficients can be evaluated.

6.3 Results from stress path excursions

The details of the testing programme carried out on natural undisturbed samples of Gault clay were presented in Chapter 4. The objective of the tests was to restore the samples to the *in situ* stress state, and from there to conduct multiple mini stress path excursions in order to derive the elastic parameters discussed earlier in this chapter.

All results for both stress increments and moduli are presented as normalised values. This has been done because the two samples in Tests R14 and R23 were from different depths, and some stress excursions took the stresses some way from the assumed *in situ* values. Normalisation has been carried out by dividing by the value of p' at the start of the relevant stress probe, referred to as p_0'.

The absolute values of both the normalised stress increments and resulting strain increments are plotted to enable comparison between data regardless of stress path direction. Following the work of Atkinson *et al.* (1990), the recent stress history at the start of each probing test is indicated. Each set of data is annotated with the change in stress path direction, measured in degrees from the previous path direction. In the case of constant σ'_v and σ'_h excursions, this angle is in the the σ'_v *vs.* σ'_h plane, and in the case of constant p' and q excursions, in the p' *vs.* q plane.

6.3.1 Results from constant σ_h' and constant σ_v' excursions

The results of five constant σ_h' and five constant σ_v' excursions from tests R14 and R23 are presented in this section. The terminology used to refer to each relevant stress path excursion in Tests R14 and R23 is shown in Figure 6.2 and Figure 6.3 respectively.

Results from the excursions carried out at constant σ'_h are shown in Figure 6.4. In order to illustrate the trends observed over different strain ranges, the figure includes plots of data over the ranges $\varepsilon_v = 0$ - 0.01%, 0 - 0.1%, and 0 - 1.2%.

The data for the five excursions conducted at constant σ_h' show increasing gradients as the angle of stress path rotation increases, while the single set of data conducted at constant σ_v' shows the highest stiffness. These observations confirm the conclusions initiated by Atkinson *et al.* (1990), and will be used later in the manipulation of the data for drawing conclusions as to the maximum engineering stiffness observed.

The companion data to those presented in Figure 6.4 are shown in Figure 6.5 for excursions carried out at constant σ'_v where normalised horizontal stress changes are plotted against horizontal strains. The slope of the data for the constant σ_v' excursions is broadly higher than each of those conducted at constant σ_h' for all strains. However, more striking is the observation of very high initial stiffness for these excursions carried out at constant σ_v'. The significance of this observation is further emphasised in Figure 6.6 where vertical strains are plotted against horizontal strains for each of the relevant five excursions carried out on Test R23. A similar plot for selected stress path excursions for Test R14 is given in Figure 6.7. These plots represent the inverse of Poisson's ratio, $1/\nu'_{vh}$ in the case of the tests conducted at constant σ_h' (R23conH1 etc.) where $\nu'_{vh} = -\delta\varepsilon_h/\delta\varepsilon_v$ as derived in Equation 6.53. From the constant σ'_h excursions in both Figure 6.6 and Figure 6.7 there is clear evidence over a significant range of vertical strain that ν'_{vh} is very small. In the case of tests conducted at constant σ'_v, the gradients are infinite at small strain, but show deviations away from this after horizontal strains of between 0.005% to 0.015%.

The derivations for elastic moduli presented in Section 6.2.3, and curve fitting as described in Section 4.5.4, have been applied to the data presented in Figure 6.4 to Figure 6.7. The results of the conversions are plotted as moduli *vs.* log strain in Figure 6.8 to Figure 6.11. The strain ranges for which stiffness moduli are plotted reflect both the quality of the data (particularly at the very small strain end) and the magnitude of the stress path excursion.

The variation of E'/p_0' (as defined in Equation 6.51) for the five constant σ_h' tests is shown in Figure 6.8. This shows clear dependency of E'_v on both strain and change in stress path angle with a maximum E'/p_0' ratio after a 180° stress path change from excursion R23conH5 tending to 550, yet decaying to approximately 50 at 1% strain.

The variation of Poisson's ratio, ν'_{hv}, (as defined in Equation 6.53) for the same five constant σ_h' tests is shown in Figure 6.9. Clearly Poisson's ratio is seen to be essentially zero at strains below 0.01%, for three of the stress path excursions. The exception to this are paths R14conH1 and R23conH4 where ν'_{hv} departs from approximately zero at about $\delta\varepsilon_v \approx 0.001\%$. In the case of excursion R23conH4 the sample had already undergone a vertical strain of 2.2% in the same stress path direction at the start of this excursion. All curves show a rise in ν'_{hv} with increasing strain, which if extrapolated to ≈1% strain, indicates a value of approximately 0.2.

From the set of constant σ_v' excursions conducted in tests R14 and R23, an indication of the variation of ν'_{hv} with strain is apparent from Figure 6.10 where the ratio $\nu'_{hv} / (1-\nu'_{hh})$ is plotted against change in horizontal strain. This shows the value $\nu'_{hv} / (1-\nu'_{hh})$ tending to zero at very small strain levels in four out of the five excursions. This ratio is based on Equation 6.57 and the only way it can plausibly have a zero value is if $\nu'_{hv} \approx 0$. However significantly greater values are shown at horizontal strains greater than about 0.01%.

From the same set of constant σ'_v stress paths from Test R14 and Test R23, the variation of F'_h/p_0' as defined in Equation 6.55 is plotted in Figure 6.11. This shows clearly decreasing F'_h/p_0' with increasing horizontal strain and decreasing F'_h/p_0' with decreasing stress path rotation angle.

In order to illustrate the influence of stress path rotation angle more clearly, the data from Tests R14 and R23 are combined in Figure 6.12 to show the variation of the relationships E'_v/p_0' and F'_h/p_0' with change in stress path angle for strain levels of 0.0001, 0.001, 0.01 and 0.1%. The values at 0.0001% have been obtained by extrapolating back the essentially horizontal (interpreted as the elastic) section of the "backbone" shaped curves in Figure 6.8 and Figure 6.11. Despite data from two tests being represented in Figure 6.12, there is a clear trend showing some form of dependency of both E'_v/p_0' and F'_h/p_0' on angle of stress path rotation, confirming that the highest moduli are obtained after approximately 180° rotation.

In summary, the very small strain results from constant σ'_h and σ'_v stress path excursions lead to values of $E_{0(v)}/p_0' = 550$ from excursion R23conH5, and $F_{0(h)}/p_0' = 2100$ from excursion R14conV2. Values of $\nu_{0(vh)}$ and $\nu_{0(hv)}$ are zero.

6.3.2 Bender element tests

As has been discussed, the primary objective of carrying out stress path excursion tests was to establish all five elastic parameters for a cross-anisotropic representation of Gault clay.

Shear wave stiffness data are frequently referred to as the "G_{max}" stiffness. If continuity exists between shear wave and engineering strain derived moduli, then it is appropriate to use the maximum stiffness that can be obtained using triaxial engineering strain measurements when combining bender and triaxial strain data. The very small strain or "maximum" stiffness evaluations from triaxial data have thus been chosen to be the modulus value that is asymptotically approached at approximately 10^{-4} % strain after 180° change in stress path angle.

Shear wave velocity measurements were made at the start of each stress probe. Normalisation by p_0' has been carried out with these data too, despite the evidence that $G_{0(ij)}$ were shown to be dependent on components of stress in the plane of the shear wave in Chapter 5. The pragmatic reason for this apparent inconsistency is the need to combine bender element data with small strain data, for which there is a long history of normalisation by p_0'. Normalised $G_{0(hh)}$ and $G_{0(hv)}$ measurements for Tests R23 and R14 were plotted against p' in Figure 5.20. The normalised moduli clearly vary with confining pressure. The

averaged values at the *in situ* stress state for test R23 have been adopted, giving $G_{0(hv)}/p_0' = 507$ and $G_{0(hh)}/p_0' = 1140$.

6.3.3 The evaluation of five independent elastic moduli

As seen in the previous section, the triaxial small strain measurements lead to values of $E_{0(v)}$ and $\nu_{0(vh)}$. The $G_{0(hh)}$ shear modulus measured using the horizontally propagated shear waves is combined with the small strain relationships between E'_h and ν'_{hh} to give unique values for $E_{0(h)}$ and $\nu_{0(hh)}$. The independent parameter $G_{0(hv)}$ increases to five the elastic parameters that have been measured at very small strain. These results are summarised in Table 6.1 where columns two and three list the parameters derived directly, while column four lists the two parameters that are derived by combining small strain and bender element relationships using Equations 6.68 and 6.69.

Parameter	*Triaxial small strain*	*Bender*	*Combination*
$E_{0(v)} / p_0'$	550	×	
$E_{0(h)} / p_0'$	×	×	2186
$\nu_{0(vh)}$	0	×	
$\nu_{0(hh)}$	×	×	-0.041
$G_{0(hv)} / p_0'$	×	507	
$F_{0(h)} = E_{0(h)}/(1-\nu_{0(hh)})/p_0'$	2100	×	
$G_{0(hh)} / p_0' = E_{0(h)}/2(1+\nu_{hh})/p_0'$	×	1140	

Table 6.1 Measured normalised values of anisotropic elastic parameters for Gault clay.

The sensitivity of horizontal Young's modulus, $E_{0(h)}/p_0'$, and Poisson's ratio in the horizontal plane, $\nu_{0(hh)}$, to the small strain measured value $F_{0(h)}$ and bender element evaluated shear modulus $G_{0(hh)}$ is illustrated in Figure 6.13. Along the x axis $F_{0(h)}/p_0'$ varies by ±5% from the best estimate value of 2100. The calculated values of $E_{0(h)}/p_0'$ and $\nu_{0(hh)}$ are plotted against the left hand and right hand y axis respectively for a band of values of $G_{0(hh)}/p_0'$ which reflect the accuracy of this bender element determined modulus, namely ±2.5%. The variation in $E_{0(h)}/p_0'$ taking into consideration ±5% on $F_{0(h)}/p_0'$ and ±2.5% on $G_{0(hh)}$ is only ±4%, while $\nu_{0(hh)}$ varies by ±0.037 either side of the best estimate value of zero. Thus possible inaccuracy in the measurement of $G_{0(hh)}$ and $F_{0(h)}$ is not likely to cause significant inaccuracy in either $E_{0(h)}$ or $\nu_{0(hh)}$

The implications of these values of the five truly independent cross-anisotropic parameters will be explored in relation to the three parameter formulations discussed in Section 6.2.3.

6.3.4 Results from constant p' and constant q tests

To enable exploration of the elastic formulations based on triaxial variables, Test R23 included two stress path excursions at constant p' and two at constant q.

The results of normalised changes in stress are plotted *vs.* absolute triaxial distortional strain in Figure 6.14, and *vs.* volumetric strain in Figure 6.15. The data show noticeably more scatter in the small strain region than was shown for either the constant σ'_v or the constant σ'_h series of tests given in Figures 6.4 and 6.5. This is largely due to difficulties that were experienced in controlling the stress paths precisely. In excursion R23conQ1, as can be seen in Figure 6.14c, the deviator stress changed by 2.2 kPa during the excursion. Maximum deviations in excursions R23conQ2, R23conP1 and R23conP2 were 0.3, 0.6 and 0.7 kPa respectively. The effects of these deviations are believed to be small, but in the case of R23conQ1 they were nevertheless accounted for by using the coupling implied by Equation 6.9 and results from the constant p' tests. While further experience in the computer control of triaxial tests would lead to better control, there is arguably greater difficulty involved in conducting stress path excursions along constant p' or q paths where both vertical load and cell pressure have to be varied simultaneously. Nevertheless, the quality of the data was believed adequate to deduce the tangent moduli over an appropriate range of strain.

Figure 6.16 shows how K' and J'_{qp} vary with volumetric strain, while Figure 6.17 shows how G' and J'_{pq} vary with distortional strain, both on a logarithmic scale. The data all show typical "backbone" shaped curves as found with the tests conducted at constant σ_v' and constant σ_h'. The two plots for G' show good agreement, whereas those for K' do not. The reason for this becomes clear once the angle of stress path rotation is taken into account, with full stress path reversal clearly producing the largest values. The plots of J'_{pq} and J'_{qp} show quite a range of values at very small strain, with the largest value occurring with a stress path rotation of 87°. Interestingly, the coupling moduli J'_{pq} and J'_{qp} exhibit similar asymptotes at very small strain after 180° direction changes, despite being carried out along constant q and p' paths respectively.

In order to make comparisons over a range of strain, and not merely at strains considered to represent the very small or "zero" strain stiffness, a means of transforming the vertical, horizontal, distortional and volumetric strains (against which the data are plotted in Figure 6.8 to Figure 6.12 and Figure 6.16 and Figure 6.17) to a unified strain representation is required.

6.3.5 Unification through an incremental strain energy formulation.

Various definitions of a unifying strain formulations have been proposed and used to enable moduli determined with respect to different strains to be compared. Jardine *et al.* (1985) used the absolute value of the major principle strain. Simpson *et al.* (1979) used a definition based on strain axes defined by $(\varepsilon_x+\varepsilon_y, \varepsilon_x - \varepsilon_y, \gamma_{xy})$. Burland (1989) has suggested that there are particular advantages in the use of an "incremental" strain energy formulation as defined by Equation 6.70:

$$\Delta\varepsilon_{unified} \equiv U = \sum_0^{\varepsilon_1}(\sigma'_1 - \sigma'_{1_o})\delta\varepsilon_1 + \sum_0^{\varepsilon_2}(\sigma'_2 - \sigma'_{2_o})\delta\varepsilon_2 + \sum_0^{\varepsilon_3}(\sigma'_3 - \sigma'_{3_o})\delta\varepsilon_3 \quad \text{.....Equation 6.70}$$

where the initial stress state is defined by (σ'_{1o} ,σ'_{2o} ,σ'_{3o}), and the incremented state is defined by (σ'_1,σ'_2,σ'_3). This general formulation can be written more usefully in terms of stress and strain invariants, and triaxial stress and strain parameters respectively, in Equations 6.71 and 6.72:

$$\Delta\varepsilon_{unified} \equiv U = \sum_{0}^{\varepsilon_p}(p' - p'_0)\cdot\delta\varepsilon_p + \sum_{0}^{\varepsilon_q}(q - q_0)\cdot\delta\varepsilon_q \quad \text{.....Equation 6.71}$$

where the initial stress state is defined by (p_o',q), and the incremented state is defined by (p',q), and

$$\Delta\varepsilon_{unified} \equiv U = \sum_{0}^{\varepsilon_v}(\sigma'_v - \sigma'_{v0})\cdot\delta\varepsilon_v + 2\sum_{0}^{\varepsilon_h}(\sigma'_h - \sigma'_{h0})\cdot\delta\varepsilon_h \quad \text{.....Equation 6.72}$$

where the initial stress state is defined by (σ'_{v0},σ'_{h0}), and the incremented state is defined by (σ'_v,σ'_h). It is a simple procedure to show the equivalence of Equations 6.71 and 6.72. In all the tests analysed in this project, both triaxial and invariant parameters were calculated in the processing spreadsheets. A comparison of the incremental strain energy determined using each equation provided an internal check on the calculation routines.

In order to obtain the equivalent strain energy for each data point, the relevant strains used to determine the moduli presented in the previous sections were plotted *vs.* strain energy. It was found in all cases that relatively linear relationships resulted when these were plotted against strain energy (U) to the power 0.633. This is shown, for example, in Figure 6.18 where volumetric and distortional strains from constant p' and constant q excursions are plotted against incremental strain energy. The correlation of the linear fit to each set of data was better than 0.996 in all cases. The actual relationships used to unify the data involved 6th order polynomials fitted to these relatively linear plots. The quality of fit in the very small strain energy region is illustrated in Figure 6.19. Here it can be seen that there is some scatter about the 6th order polynomial fit in the very small strain region. The equivalent plots for the constant horizontal stress excursions are shown in Figure 6.20 where the scatter is seen to be significantly less in the very small strain region. This difference is attributed to the greater success achieved in controlling a constant horizontal stress excursion than either a constant p' or constant q excursion where the control process requires simultaneous changes to both vertical and horizontal stress.

These strain energy relationships were used in conjunction with the curve fitting carried out on the stress - strain data to re-plot all the data presented thus far in this chapter against the single variable of strain-energy and enable sound comparisons to be drawn between different stress path excursions.

The first comparison is the variation of moduli K', G' and J' (each normalised by p_o') with change in stress path angle for discrete values of strain energy. This has been plotted in Figure 6.21. Figure 6.21a shows significant variation of K'/p_o' with stress path angle, similar to that observed for E'_v in Figure 6.11. The variation of G'/p_o' is plotted in Figure 6.21b. However, there is insufficient variation in stress path angle to enable any trends to be identified. Interestingly the plot of J'/p_o' in Figure 6.21c appears to indicate J'/p_o' is weakly inversely proportional to stress path angle. As this trend seems to go against the intuitive

expectation based on the clear trends of E'_v/p_0' and K'/p_0', each of the four measurements of J'/p_0' will be considered in conjunction with the maximum values for E'_v/p_0', F'_h/p_0', G'/p_0' and K'/p_0' in future comparisons.

Measured values of normalised G' K' J' are plotted against strain energy on a logarithmic scale in Figure 6.22. Measured values of normalised E'_v ν'_{vh} F'_h are plotted against strain energy in Figure 6.23. In this case only excursions R23conH5 and R14conV2 are shown, as these are the ones with full 180° stress path reversal.

6.3.6 Comparison of three parameter cross-anisotropic formulations

It is now possible to compare measured values of E'_v ν'_{vh} F'_h and G' K' J' at the same strain energy by using Equations 6.59 to 6.64. The measured values of E'_v ν'_{vh} F'_h in Figure 6.23 have been used to calculate values of G' K' J', which are shown in Figure 6.22. These show flatter "back-bone" curves for the calculated values of all three parameters.

Similarly, the measured values of G' K' J' in Figure 6.22 have been used to calculate E'_v ν'_{vh} F'_h. However, when values of J' from R23conP1 and R23conQ2 were used, the calculated values of F'_h were negative at certain strain energies, and generally showed wide fluctuations. The calculated values of E'_v F'_h shown in Figure 6.23 are therefore only those calculated using J' values from tests R23conP2 and R23conQ1. Whereas reasonable comparison between the measured and calculated values of E'_v are seen, there is only approximate correlation between the F'_h curve calculated using J' from excursion R23conQ1 and the measured F'_h. Calculated values of ν'_{vh} show fluctuations between positive and negative values depending on the J' value used.

At very small strains, the values of $E_{0(v)}$ $\nu_{0(vh)}$ $F_{0(h)}$ and G'_0 K'_0 J'_0 can be compared. Table 6.2 shows both measured and calculated values, and the difference between them, at a common strain energy of 10^{-6} kJ/m^3. The largest value of J'_0, measured in test R23conQ1, has been used in this calculation. It is clear that, apart from $F_{0(h)}$, agreement is surprisingly good, with the difference in G'_0 evaluations of only 5%. The calculated $F_{0(h)}$ value is sensitive to the measured J'_0 value, and the difference there is 24%.

	$E_{0(v)}$	$\nu_{0(vh)}$	$F_{0(h)}$
Measured	550	0	2100
Calculated (from G_0' K_0' J_0')	540	-0.025	2607
Difference	2%	-	24%
	G_0'	K_0'	J_0'
Measured	385	356	990
Calculated (from $E_{0(v)}$ $\nu_{0(v)h}$ $F_{0(h)}$)	365	361	1118
Difference	5%	1%	11%

Table 6.2 Comparison of different normalised parameters

6.3.7 Comparison of five parameter cross-anisotropic formulations

At very small strains it is also possible to compare the measured values of the five independent elastic parameters $E_{0(v)}$ $E_{0(h)}$ $v_{0(vh)}$ $v_{0(hh)}$ and $G_{0(hv)}$ with those estimated from the Graham & Houlsby (1983) model. The measured values of $E_{0(v)}$ $v_{0(vh)}$ and $F_{0(h)}$ have been converted to E^* v^* and α using Equations 6.45 to 6.47. These have then been converted to estimated values of the five elastic parameters using Equation 6.40. The results are shown in Table 6.3, along with the differences between the two sets of parameters and values of $G_{0(hh)}$.

Parameter	*Measured (small strain / benders)*	*Calculated (Equations 6.45 to 6.47)*	*Calculated (Equation 6.40)*	*Difference*
$E_{0(v)}$	550		550	-
$E_{0(h)}$	2186		2100	4%
$v_{0(vh)}$	0		0	-
$v_{0(hh)}$	-0.041		0	4%**
$G_{0(hv)}$	507		537	6%
$G_{0(hh)}$	1140		1050	9%
E^*		550		
v^*		0		
α		1.95		

** based on $(1-v'_{hh})$

Table 6.3 Comparison of measured and Graham & Houlsby (1983) normalised parameters

From this table, it is clear the parameters $E_{0(v)}$ and $v_{0(vh)}$ are unchanged in passing through this transformation. This will always be the case, as comparison of Equations 6.40, 6.45, 6.46 and 6.47 shows. All the other parameters show some deviation from the measured values. However there is generally good agreement between the two approaches for Gault clay. Differences in $v_{0(hh)}$ are expressed in terms of $(1-v_{0(hh)})$, and because $E_{0(h)}$ is underestimated and $v_{0(hh)}$ is overestimated, $G_{0(hh)}$ is the parameter which shows the largest difference. The value of $G_{0(hv)}$ is overestimated. In the Graham & Houlsby (1983) model, the parameter α expresses a fixed ratio between $\sqrt{E_{0(h)} / E_{0(v)}}$ and $G_{0(hh)}/G_{0(hv)}$, and for the Gault α is 1.95. In contrast, the measured ratios are $\sqrt{E_{0(h)} / E_{0(v)}} = 1.99$ and $G_{0(hh)}/G_{0(hv)} = 2.25$.

6.4 DISCUSSION

6.4.1 Anisotropic elastic parameters

Values of all five independent anisotropic elastic parameters for natural Gault clay derived from a combination of triaxial small strain and bender data have been presented in Table 6.1. Two main strands of evidence have emerged to reinforce the presumption made at the beginning of this chapter that very small strain parameters are elastic:

- measurements have clearly shown that $v_{0(vh)} = v_{0(hv)} = 0$. From Equation 6.3, this implies that the compliance matrix is symmetric, which is a requirement for elastic behaviour.

- comparison of measured normalised values of $E_{0(v)}$ $\nu_{0(vh)}$ $F_{0(h)}$ and G'_0 K'_0 J'_0 in Table 6.2 shows good agreement. This implies that parameter values are relatively insensitive to stress path direction, which is also a requirement for elastic behaviour.

There is inevitably some uncertainty in the values of the five independent cross-anisotropic elastic parameters derived from combining small strain and bender element data, since the data from the local strain measuring devices was interpreted using curve fitting procedures. Nevertheless this work has reinforced and extended that of Atkinson *et al.* (1990) in showing the dependence of modulus on angle of stress path rotation. Their tests were on reconstituted soils, with measured strains generally in excess of 0.01%; while this research has included natural soil over a wider strain range (down to 0.001%) and shown the similar effects of recent stress history. The measured normalised value of $E_{0(v)}$ could perhaps be regarded as the least reliable, since the only relevant 180° stress path reversal occurred a relatively long way from the *in situ* stress state. However, errors in this parameter do not affect the determination of the remaining four. In contrast, the value of $F_{0(h)}$ is combined with $G_{0(hh)}$, and affects the value of both $E_{0(h)}$ and $\nu_{0(hh)}$. But in this case, the highest normalised value of $F_{0(h)}$ was measured following a 180° stress path reversal at the *in situ* stress state, and is therefore considered likely to be more reliable.

Certain combinations of anisotropic elastic parameters are inadmissible from considerations of strain energy. Considering the measured normalised values listed in Table 6.3 with respect to the two limiting conditions given in Section 6.2:

- inserting $E_{0(v)}$ $E_{0(h)}$ $\nu_{0(vh)}$ and $\nu_{0(hh)}$ into Equation 6.5 results in a value of 0.26 which is greater than 0,

- inserting the same four measured normalised values into Equation 6.6 results in an upper limit value for $G_{0(hv)}$ of 549. This exceeds the measured value of 507 by some 8%.

The measured normalised values are therefore given credibility by satisfying these two relationships.

6.4.2 Anisotropy ratios

Anisotropy ratios are often quoted when characterising a particular soil. Simpson *et al.* (1996) and Jovičić & Coop (1998) have presented evidence for significant cross-anisotropy defined by $G_{0(hh)}/G_{0(hv)} = 1.5$ for London clay. These moduli were determined from bender element tests using vertical platen mounted bender elements under isotropic stress states. The measured anisotropy ratios for Gault clay at very small strain reported in Chapter 5 are more comprehensive since the tests were carried out at *in situ* stress states ($K_0 \approx 2$) and combined with small strain triaxial data to enable *all* the independent parameters to be measured. It is clear that the ratios are different depending on how they are defined. The measured values of $\sqrt{E_{0(h)} / E_{0(v)}} = 1.99$ and $G_{0(hh)}/G_{0(hv)} = 2.25$ are respectively 2% and 15% bigger than the value of $\alpha = 1.95$ from the Graham & Houlsby (1983) model. Because of the independence of the parameters, there is no *a priori* reason why these ratios should be the same as each other, or even equal to α. Similarly, the anisotropy ratio based on the two shear moduli may be either

larger (as here) or smaller than that based on the square root of the ratio of the two Young's moduli. The ability of the Graham & Houlsby (1983) model to predict these anisotropy ratios fairly well in the case of the triaxial data presented here is strongly influenced by $\nu_{0(vh)}$ being zero.

There is no information on the G'_{hh}/G'_{hv} anisotropy ratio at larger strains, and, strictly speaking, there is none on the E'_h/E'_v ratio either. However, if it is assumed that the value of ν'_{hh} remains small, then an approximate value of the ratio can be obtained from F'_h/E'_v. The variation of this ratio is plotted on Figure 6.24, and it can be seen that it remains very close to 4 until a strain energy of about 10^{-4} kJ/m^3, after which it reduces steadily towards 2. Also plotted on Figure 6.24 are the two Graham and Houlsby (1983) anisotropy ratios calculated by substituting the values of G′ K′ J′ into Equation 6.67 based firstly on constant p' and q excursions and Equations 6.14, 6.21 and 6.22, and secondly on the constant σ'_h and σ'_v excursions and Equations 6.59 to 6.61. The ratio α based on the constant σ'_h and σ'_v excursions is seen to be equivalent to $\sqrt{E'_h / E'_v}$ and therefore shows an almost constant anisotropy of 2 up to strain energy of 10^{-4} kJ/m^3 before reducing to 1.5 at 10^{-2} kJ/m^3. The value of α measured using constant p' and q excursions is seen to fluctuate either side of this, although interestingly, the value at very small strain energy (10^{-6} kJ/m^3) is 2.25, the same as the ratio $G_{0(hh)} / G_{0(hv)}$ measured with the bender elements.

6.4.3 Triaxial testing

It has been shown that *all* four parameter formulations describing soil response in the triaxial apparatus ($G' K' J'$, $G^* K^* J$, $E^* \nu^* \alpha$ and $E'_v \nu'_{vh} F'_h$) can be expressed as unique functions of the four independent parameters $E'_v E'_h \nu'_{vh}$ and ν'_{hh}. Almost all of them depend on all four; the exceptions are $E'_v \nu'_{vh}$ and E^* ($\equiv E'_v$) which are single parameters, and F'_h which is a function of just two parameters (E'_h and ν'_{hh}).

If stress path triaxial testing is to be carried out to obtain soil parameters, which when used in subsequent modelling will probably be assumed to be stress path independent, there appear to be strong arguments for using a $E'_v \nu'_{vh} F'_h$ formulation. These are:

- The directness of measurement. Tests at constant σ'_h will produce two of the required parameters directly (E'_v and ν'_{vh}), and tests at constant σ'_v will obtain the third parameter (F'_h) as a function only of the remaining two. This contrasts with measurements at constant p' and constant q, when the resulting parameters are each functions of all four independent ones.

- The practicality of carrying out constant σ_h' and constant σ_v' tests over constant p' and q tests: Measurements of J' seem to show significant scatter, which will affect any subsequently derived parameters. Inspection of Figure 6.23b shows how four different tests at constant p' or q have been unable to produce the clarity of the direct measurement (at constant σ'_h) that $\nu'_{vh} = 0$, although this may also reflect some inherent stress path dependence in the parameters.

6.4.4 Independent shear modulus

The independent shear modulus G'_{hv} cannot be measured in any stress path triaxial test, since it does not appear in the top left hand corner of the full compliance matrix given in Equation 6.1. It therefore has no influence on soil behaviour measured in the triaxial cell. Yet it clearly affects the soil response in any plane strain application, as shown by Lee and Rowe, (1989), and Simpson *et al.* (1996). For such analyses, a full five parameter description of anisotropy is required, and no three parameter description can by itself be sufficient.

The "shear modulus" is widely referred to in the literature as a fundamental parameter, usually within an assumed isotropic framework. If an anisotropic soil was incorrectly assumed to be isotropic, then a pseudo-isotropic shear modulus may also incorrectly be determined from a relationship such as:

$$G_{iso} = \frac{E_v}{2(1+\nu_{vh})} \quad \text{.....Equation 6.73}$$

because such an equation would be correct for an isotropic soil.

Based on the measured normalised values of E'_v F'_h and ν'_{vh} for Gault clay, it is instructive to calculate a range of possible normalised values for the "shear modulus". These are plotted against strain energy in Figure 6.25 and the very small strain values are summarised along with measured $G_{0(hv)}$ in Table 6.4:

Shear term	*value / p_0'*	*Source*
G_0'	365	Equation 6.19
G_0	533	Equation 6.34
$G_{0(iso)}$	275	Equation 6.73
$G_{0(hv)}$	507	Measured value

Table 6.4 Range of possible values of shear modulus for Gault clay

These illustrate not only the independence of shear modulus, but also the importance of being very clear about which parameter is being referred to when describing the "shear modulus".

Earlier work has tried to show the continuity between dynamic and static measurements of stiffness, but has compared dynamic $G_{0(vh)}$ measurements with G^* measurements in an undrained triaxial test (for example Coop *et al.*, 1997). If the soil is anisotropic, there is no reason to expect agreement between these two parameters as they are independent. However, measurement of G^* in an undrained excursion might still be a good method of checking the credibility of E'_v ν'_{vh} F'_h values obtained in drained stress path excursions, through use of Equation 6.34.

6.5 Summary

This chapter has considered the deduction of cross-anisotropic elastic parameters for natural samples of Cambridge Gault clay from multiple mini stress path excursions and orthogonal determinations of bender

shear wave velocities. A framework on which to base the derivation of these non-linear elastic parameters has been developed. A test program involving high quality triaxial testing on samples of natural Gault clay was undertaken, and the data resulting from multistage stress path excursions have been presented.

Various three parameter formulations used to describe the cross-anisotropic behaviour of soils have been investigated. It has been shown that all of them are functions of the four independent parameters E'_v E'_h ν'_{vh} and ν'_{hh}. An alternative three parameter formulation comprising E'_v ν'_{vh} and F'_h (= $E'_h/(1+\nu'_{hh})$) has been presented and shown to provide as complete a description of soil behaviour as other three parameter formulations, yet probably with more reliable values. The Graham & Houlsby (1983) model has been investigated, and shown always to produce correct values of E'_v and ν'_{vh}. Conversion equations between the various formulations have been developed.

High quality triaxial testing on samples of natural Gault clay from the High Cross test site in Cambridge has been carried out, involving multiple drained stress path excursions and orthogonal determinations of horizontal shear wave velocity using bender elements. At very small strains, data from both engineering strain and shear wave velocity measurements have been combined to derive all five independent parameters needed to describe a cross-anisotropic elastic material. All moduli have been expressed as normalised values by dividing by p_0'. The measured value of $G_{0(hv)}$, the independent shear modulus, was found to be 8% less than the upper limit defined by Raymond (1970) as a function of E'_v E'_h ν'_{vh} and ν'_{hh}.

Atkinson *et al.* (1990) have shown the dependence of modulus on angle of stress path rotation for reconstituted soils for strains generally in excess of 0.01%. This has been extended here to a natural soil down to 0.001%, and the same effects of recent stress history have been observed. Moduli used for the assessment of elastic parameters have been measured after a full reversal in stress path direction.

When measured normalised values of the five independent cross-anisotropic elastic parameters were compared with those estimated using the Graham and Houlsby (1983) model, broad agreement was found to exist for natural Gault clay. Differences were confined to the parameters $E_{0(h)}$ $\nu_{0(hh)}$ $G_{0(hv)}$ and $G_{0(hh)}$, and the maximum error was found to be 12%. This agreement is probably strongly influenced by the clear experimental finding that $\nu_{0(vh)} = 0$.

The anisotropy of natural Gault clay has been investigated under anisotropic *in situ* stresses. Anisotropy ratios of $E_{0(h)}/E_{0(v)} = 4$ and $G_{0(hh)}/G_{0(hv)} = 2.25$ have been measured, showing the natural Gault clay to be highly anisotropic. The anisotropy ratio is also clearly seen to depend on the way it is defined.

Natural Gault clay can be convincingly described as a cross-anisotropic elastic material at very small strains. The evidence for elasticity at very small strains comes from finding that the compliance matrix is symmetric, with $\nu_{0(vh)} = \nu_{0(hv)} = 0$; also that very small strain parameters are almost independent of stress path direction.

7. SUMMARY AND CONCLUSIONS

New bender element devices have been developed to enable the small strain anisotropic stiffness of the Cambridge Gault clay to be investigated in a laboratory study based primarily on triaxial testing, but incorporating both shear wave velocity and local strain measurements. This has shown that the Gault clay is significantly anisotropic, and that conventional approaches based on triaxial tests and assumptions of isotropy to evaluate the shear modulus are misleading.

This chapter will summarise the development of the new devices, and the advantages these bring to understanding the anisotropy of a clay. It summarises results from the laboratory investigations including the factors influencing anisotropy, and the subsequent evaluation of all five cross-anisotropic parameters within an elastic framework. Limitations of the research are highlighted and used to propose further work.

7.1 Equipment and techniques for measuring the anisotropy of small strain stiffness

A triaxial soils testing system capable of resolving vertical and horizontal strains on 100 mm diameter samples down to 0.001% strain was commissioned. The system included bender elements for the measurement of vertical shear wave velocity, $V_{s(vh)}$. To enable anisotropic moduli $G_{0(hv)}$ and $G_{0(hh)}$ to be measured, two sets of devices were developed to measure horizontal shear wave velocities though the mid-height of a triaxial sample. These were:

- a bender belt with orthogonal mounted mini bender elements incorporated in the pads of a horizontal strain measuring belt suitable for use on 100 mm diameter samples,
- bender probes, also incorporating orthogonal mini bender elements, but suitable for use on samples down to 38 mm in diameter either in triaxial cells or on the bench-top.

These devices represent significant advances from the Norwegian Geotechnical Institute type bender elements which have been used in research and some commercial laboratories over the past fifteen years. The main advantages of the new devices over the standard devices are:

- The new devices enable measurement to be made through the mid-height of a triaxial sample where "end effects" associated with restraint by the platens are absent. The devices were used to show that end effects led to inaccuracy in the measurement of $G_{0(vh)}$ in natural Gault clay of up to 30%.
- Shear moduli $G_{0(hv)}$ and $G_{0(hh)}$ can be measured on a single sample at anisotropic stress states. This enables significantly more representative exploration of natural consolidation processes where one dimensional consolidation requires $\sigma'_v > \sigma'_h$, and also exploration of natural clays at *in situ* stress states.
- The new devices included signal shielding and earthing that resulted in high quality signals. This facilitated simple accurate interpretation procedures based on first arrival times to be followed, with assessed accuracy of the order of ±2% for $G_{0(hv)}$ and $G_{0(hh)}$.

7.2 Shear wave investigations of the anisotropy of small strain stiffness

The anisotropy of $G_{0(ij)}$ was investigated by measuring $V_{s(ij)}$ during stress path tests carried out on both reconstituted and natural samples of Gault clay. The investigations focused on explorations of the parameters involving voids ratio and stress state in equations of the form introduced by Hardin and Blandford (1989). Tests were carried out to enable strain induced anisotropy to be isolated from stress induced anisotropy on reconstituted samples. Comparisons were then made with measurements carried out on undisturbed samples of Gault clay reconsolidated to the *in situ* stress state, and *in situ* measurements obtained from cross-hole and seismic cone geophysical measurements. These investigations and comparisons showed that:

- $G_{0(ij)}$ is inherently anisotropic, with the degree of anisotropy dependent on voids ratio for a material that has experienced one dimensional consolidation. The measure of anisotropy given by $G_{0(hh)} / G_{0(hv)}$ was found to increase by 0.58 for every log cycle decrease in voids ratio.

- $G_{0(ij)}$, and thus the ratio $G_{0(hh)} / G_{0(hv)}$, is highly dependent on stress state in the plane ij, whereas it is insensitive to the stress normal to the plane ij. Hence $G_{0(ij)} \alpha (\sigma'_i\sigma'_j)^{nij/2}$ where σ'_i and σ'_j are the principal stresses in the direction of propagation and polarisation respectively. For the reconstituted soil ^{nij} was found to be equal to 0.5, whereas for the natural soil, $^{nij} = 0.3$.

Based on these two findings for Gault clay, the equation given by Hardin and Blandford (1989) was clearly inadequate for describing anisotropy, and the alternative proposed in Chapter 5 is restated here in Equation 7.1:

$$G_{0(ij)} = S_{(d)ij} S_{(s)ij} e^{mij} \frac{(\sigma'_i\sigma'_j)^{nij/2}}{p_r^{(nij-1)}} = S_{ij} e^{mij} \frac{(\sigma'_i\sigma'_j)^{nij/2}}{p_r^{(nij-1)}} \quad \text{.....Equation 7.1}$$

This makes use of directional voids ratio functions, given by e^{mij}, to describe increasing anisotropy with increasing one dimensional consolidation, and includes the finding that $^{nij/2} = {}^{nv} = {}^{nh}$ where ^{nv} and ^{nh} are the stress indices applied to σ'_v and σ'_h in the relationship given by Hardin and Blandford (1989). Within the framework implied by Equation 7.1, and through comparison of $G_{0(ij)}$ measurements on reconstituted and natural samples of Gault clay, the influence of structure was shown to have a relatively minor effect on $G_{0(ij)}$ after both voids ratio and stress effects had been accounted for.

Comparisons between laboratory measurements of $G_{0(ij)}$ on natural samples and field data showed close agreement only between $G_{0(hv)\text{field}}$ and $G_{0(hv)\text{laboratory}}$. $G_{0(hh)\text{laboratory}}$ were approximately 40% higher than $G_{0(hh)\text{field}}$ and this has been attributed to a combination of:

- azimuthal variation in anisotropy due to sustained non-uniform stress conditions in the horizontal plane due to the folding and faulting which led to horizontal variations in strain induced anisotropy,

- the influence of the predominantly horizontal fissure systems observed in the material.

7.3 Measurement of anisotropic elastic parameters

High quality triaxial testing with local small strain measurements of ε_v and ε_h was carried out on undisturbed samples of natural Gault clay. The samples were reconstituted to the *in situ* stress state from where multiple mini stress path excursions were carried out, and orthogonal shear wave velocities measured to enable deduction of cross-anisotropic elastic parameters.

Three *three parameter* formulations (G' K' J', G^* K^* J and E^* ν^* α) used to describe the cross-anisotropic behaviour of soils were investigated, and it was shown that all of them are functions of the four independent parameters E'_v E'_h ν'_{vh} and ν'_{hh}. An alternative *three parameter* formulation comprising E'_v ν'_{vh} and F'_h (= $E'_h/(1+\nu'_{hh})$) was presented and shown to provide as complete a description of soil behaviour as any of the other three parameter formulations, yet probably with more reliable values.

The test results enabled all five independent cross-anisotropic parameters $E_{0(h)}$ $E_{0(v)}$ $\nu_{0(vh)}$ $\nu_{0(hh)}$ and $G_{0(hv)}$ to be evaluated at very small strain. These measured values were found to be consistent with the theory of elasticity on the basis that:

- measurements clearly showed that $\nu_{0(vh)}=\nu_{0(hv)}=0$, which implies symmetry of the compliance matrix,

- the measured normalised values of $E_{0(v)}$ $\nu_{0(vh)}$ $F_{0(h)}$ and G'_0 K'_0 J'_0 when compared using the common framework based on the parameters E'_v E'_h ν'_{vh} and ν'_{hh} showed good agreement. Since these sets of parameters are measured by combinations of constant σ'_v σ'_h p' and q stress path excursions, this implies that the very small strain values are relatively insensitive to stress path direction,

- the values of the parameters were found to comply with considerations of inadmissible strain energy as given by Raymond (1970).

That the independent shear modulus G'_{hv} cannot be measured in a conventional triaxial test was emphasised by indicating the wide discrepancies that exist between correctly measured values of $G_{0(hv)}$ and derivations based incorrectly on assumptions of either isotropy or a *three parameter* model.

The natural Gault clay was shown to be highly anisotropic at *in situ* stress states with anisotropy ratios $E_{0(h)} / E_{0(v)} = 4.0$ and $G_{0(hh)} / G_{0(hv)} = 2.25$

7.4 Benefits of the research

Understanding the nature and variation of the anisotropic small strain stiffness is of relevance in advancing the knowledge of the behaviour of soils. As advances are made in the ability to design geotechnical structures though improved soil/structure interaction analysis, there is increasing industrial interest in the measurement of $G_{0(ij)}$ and the significance of anisotropy over a wider strain range.

This research contributes to the understanding of the nature of the anisotropy of soils and the factors that influence the degree of anisotropy. The evidence for anisotropic voids ratio functions presented in

Chapter 5 shows links with the anisotropy of structure, e.g. Bai and Smart, (1994), the anisotropy of permeability, e.g. Al-Tabbaa and Wood, (1987) and the anisotropy of electrical conductivity e.g. Anandarajah and Kuganenthira, (1995). In each case the effects that are observed are linked to the consolidation history of the soil, highlighting the need to consider the use of appropriate consolidation paths in any research project where reconstituted or normally consolidated materials are employed. Clearly, strain path history is important and isotropic stress consolidation paths will inevitably result in hybrid strain paths where neither 1 D nor isotropic consolidation dominate for considerable increments in stress over and above the initial 1 D pre-consolidation stress. Martin and Ladd, (1978) found a multiple of 32 on the 1 D pre-consolidation stress was not sufficient to remove the strain induced fabric.

Triaxial tests have the severe limitation that they cannot apply shear stresses to samples. Yet the test is very well suited to reproducing *in situ* stress states, and will continue to have a place in industry because of its simplicity, and cost effectiveness. This research has shown how its capabilities can relatively easily be extended beyond current conventional use not only by the addition of orthogonal bender element systems, but also in the effective use of stress path testing. Much research testing, has focused on the performance of soils under isotropic stress conditions, and constitutive model development has therefore been fundamentally skewed towards an isotropic framework. While the inaccuracies implied by this focus may be acceptable for coarse grained materials, this research contributes to the evidence that the anisotropy of fine grained materials is significant, and closely related to both the three dimensional strain history and current stress state in the elastic very small strain region.

This concentration on an isotropic framework has not only influenced model development, but also the framework within which most triaxial testing is conducted. This is implicit in the use of Equation 7.2 as a basis for soils testing:

$$\begin{bmatrix}\delta\varepsilon_p\\ \delta\varepsilon_q\end{bmatrix}=\begin{bmatrix}\frac{1}{K'} & \frac{1}{J'_{qp}}\\ \frac{1}{J'_{pq}} & \frac{1}{3G'}\end{bmatrix}\cdot\begin{bmatrix}\delta p'\\ \delta q'\end{bmatrix} \quad \text{.....Equation 7.2}$$

However, $K'G'J'$ have been shown to each be functions of all four of the elasticity parameters E'_v, E'_h ν'_{vh} and ν'_{hh}. Unless isotropy is assumed, this means that no single stress path can be used to evaluate any of $K'G'$ or J'. By contrast it has been shown that use the parameters E'_v ν'_{vh} F'_h in the framework implied by Equation 7.3

$$\begin{bmatrix}\delta\varepsilon_v\\ \delta\varepsilon_h\end{bmatrix}=\begin{bmatrix}\frac{1}{E'_v} & \frac{-2\nu'_{vh}}{E'_v}\\ \frac{-\nu'_{vh}}{E'_v} & \frac{1}{F'_h}\end{bmatrix}\cdot\begin{bmatrix}\delta\sigma'_v\\ \delta\sigma'_h\end{bmatrix} \quad \text{.....Equation 7.3}$$

enables two of the elastic parameters E'_v and ν'_{vh} to be determined directly from a single constant σ'_h stress path excursion, while the third, F'_h can be determined from a single constant σ'_v stress path. Not

only does this enable more direct access to anisotropic parameters, but it is also arguably easier to conduct stress path excursions at constant cell pressure or axial stress in a triaxial cell. Further, the confirmation that $G_{\alpha(ij)}$ measured by shear-wave techniques is clearly dependent on principal stresses in the plane of the shear-wave, means the stress indices ^{nij} in the Equation 7.1 can be evaluated explicitly from the same excursions at constant σ'_h and σ'_v. Thus using a horizontal bender device in combination with one stress path excursion at constant σ'_h and one at constant σ'_v enables all five elastic cross-anisotropic parameters to be determined at very small strain.

These elastic relationships only strictly apply to the elastic range. However, since an essential element of any stress strain model is a stiffness degradation relationship, it is logical to seek anchors for these relationships using values of stiffness that can be reliably determined. The techniques developed in this research to measure $E_{\alpha(v)}$ $E_{\alpha(h)}$ $\nu_{\alpha(vh)}$ $\nu_{\alpha(hh)}$ and $G_{\alpha(hv)}$ seem to offer both sophisticated and simple means of determining these anchors, and so feed naturally into the development of constitutive models for soils.

7.5 Limitations of the research and recommended further work

In retrospect there are perhaps inevitably both deficiencies in the experiments carried out, and additional questions which arise from the interpretation of results. This section concludes the thesis by specifically identifying deficiencies and proposing further work.

7.5.1 Voids ratio mismatch between tests on reconstituted and natural Gault clay

The investigations carried out on reconstituted samples of Gault clay have illuminated the development of the anisotropy of $G_{\alpha(ij)}$ with consolidation. However, due to limitations on the maximum cell pressure in the triaxial stress path cells, these investigations could not be continued to low enough voids ratios to enable direct comparison with the heavily overconsolidated natural Gault clay. The influence of structure could therefore not be quantified. For a more complete understanding of these effects, two approaches for further testing are proposed:

- Tests are carried out on 1 D reconstituted 38 mm samples prepared in a high pressure consolidometer to a range of vertical effective stresses of say 150, 300, 600, 1200, 2400 and 4800 kPa. After extrusion from the consolidometer, the sample suction is measured, the samples are set in a stress path cell and anisotropic consolidation stresses equivalent to the suction are applied, such that $\sigma'_h/\sigma'_v = 0.6$. $G_{\alpha(ij)}$ is measured and then the samples are swelled back to isotropic stress states of 90, 45 and 22.5 kPa, with $G_{\alpha(ij)}$ being measured at the end of each stage.

- Alternatively, using a high pressure triaxial cell, repeat the stress path and $G_{\alpha(ij)}$ measuring sequence carried out for Test N25 as described in Chapter 5, but continue by carrying out two additional cycles of stress increments to vertical effective stresses of 2400 and 4800 kPa. After the final unload stage, the sample is swelled back isotropically to 45 and 22.5 kPa, and $G_{\alpha(ij)}$ is measured at the end of each stage.

To complement these tests, a sample of natural Gault clay should be reconsolidated isotropically to its measured suction, and then be swelled back under reducing isotropic stress to 90, 45 and 22.5 kPa, with accurate measurements of $G_{0(ij)}$ at the end of each stage. The results of this combination of tests on reconstituted and natural Gault clay will enable investigation of both voids ratio functions and stress indices over similar ranges of voids ratio and stress state, and enable evaluation of the influence of structure.

7.5.2 Explanation of differences in $G_{0(hh)}$ between field and laboratory

Comparisons between *in situ* and laboratory measurements of $V_{s(ij)}$ showed $V_{s(hh)\text{field}} < V_{s(hh)\text{laboratory}}$, $V_{s(hv)\text{field}} \approx V_{s(hv)\text{laboratory}}$ and $V_{s(vh)\text{field}} < V_{s(vh)\text{laboratory}}$. These differences between field and laboratory measurements may be attributed to:

- significantly higher source signal frequencies in the laboratory than in the field,
- voids ratio differences between field and laboratory
- the effects of layers in naturally deposited soils,
- scale effects with respect to natural fissuring
- triaxial end effects (in the case of $V_{s(vh)}$)

However, because in this project all three velocities could be measured at the correct *in situ* stress state in the same sample, and there was good comparison in the case of $V_{s(hv)}$, the influence of frequency and voids ratio differences have to be excluded, as these effects would apply to all three velocities. It has been postulated in Section 5.3.7 that the preferentially horizontal fissures (observed during sampling) would have a greater influence on $G_{0(hh)}$ than $G_{0(hv)}$ measurements and result in field measurements, where shear waves intersect fissures, that are lower than laboratory measurements which were carried out on samples specifically prepared so as not to include fissures. These aspects were not explored in this project, but in order to bring a logical explanation to the significant differences it is proposed that:

- a review of the geophysics literature be carried out to explore possible explanations of the influences of fissures on shear wave velocities,
- a borehole be constructed at the High Cross site and continuous thin wall push samples be obtained to a depth of 12 m. These samples should be split vertically and logged with the specific intention of identifying details of the fabric and fissuring*, and this information used to:
- devise and carry out laboratory tests on samples from specific horizons which can be used to quantify the influences of layering and fissuring, and begin to resolve the differences measured.

---

* This would also contribute significantly to the value of the High Cross test site as a resource for research into heavily overconsolidated clays.

7.5.3 Investigations of the influence of azimuthal variations in anisotropy

Preliminary bench top tests reported in Section 5.3.5 indicated variations of ±10% with azimuth of the anisotropy ratio given by $G_{0(hh)}/G_{0(hv)}$. However, the tests at different azimuths were carried out without the measurement of suction to track any changes in stress state that may have occurred. This meant that only ratios of $G_{0(hh)}/G_{0(hv)}$ could be compared and no information was obtained on whether the changing ratio reflects variations in $G_{0(hv)}$, $G_{0(hh)}$ or both. While this magnitude of variation may not in itself be considered significant from the point of view of the design of foundations, knowledge of *in situ* variations may assist in the interpretation of monitored foundations, such as the diaphragm walls of the Lion Yard car park in Cambridge. To assess the possible impact of such variations, it is recommended that:

- controlled bench-top tests be carried out on high quality samples of Gault clay to confirm and quantify the source and magnitude of the variation in anisotropy with azimuth,
- numerical analyses be used to test the possible significance of variation in anisotropy of both $G_{0(hv)} / G_{0(hh)}$ and E'_h / E'_v with azimuth on a structure such as a deep basement,
- additional cross-hole geophysical investigations be carried out at High Cross using an array of boreholes to assess *in situ* azimuthal variations in anisotropy and that this is compared with known faulting and folding within the region.
- having identified planes of maximum and minimum azimuthal anisotropy, triaxial stress path tests are carried out on samples with two bender belts mounted close to the sample mid height, but with the orientation of the pads chosen to coincide with the planes of maximum and minimum anisotropy. Having reconsolidated to average *in situ* stress, carry out both constant σ'_v and σ'_h stress path excursions to investigate the variation not only of the shear wave moduli $G_{0(ij)}$ but also E'_v, ν'_{vh} and F'.

7.5.4 Understanding the influence of stress/strain history on triaxial parameters

Multiple mini stress path excursions were carried out during two tests on high quality samples of natural Cambridge Gault clay and the strains ε_v and ε_h measured down to approximately 0.001% strain. The stress paths followed represented compromises between paths designed to establish triaxial parameters (G' K' J' and E'_v ν'_{vh} F'_h) using a complete suite of excursions (constant σ'_h σ'_v p' and q stress paths at rotations spanning the range 0 to 180°) and tests which also enabled the influence of stress state on $G_{0(ij)}$ to be assessed. This was, for instance, the reason for the large constant σ'_h excursion away from the *in situ* state in Test R23 as shown in Figure 4.14. In attempting to investigate both aspects, the tests failed to:

- measure all of the triaxial parameters (G' K' J' and E'_v ν'_{vh} F'_h) at or near the *in situ* stress state on the same sample, since E'_v and ν'_{vh} were measured after a 180° rotation at an elevated stress,
- investigate the variation with change in stress path angle for each of these parameters (G' K' J' and E'_v ν'_{vh} F'_h) over the 0-180° rotation range and establish how to enable comparisons of stress path angle change where in this research the trends were established for either σ'_v *vs.* σ'_h or q *vs.* p' space.

While the trend for K', E'_v and F'_h confirmed maxima after a 180° turn, the results for G' and ν'_{vh} were inconclusive, and J' even appeared to indicate minima at 180°. Quantification of the influence of recent history on soil response was beyond the scope of this research project. However questions such as whether maxima should be anticipated for all parameters after 180° stress paths rotations, and what should be anticipated for intermediate rotations between 0 and 180° clearly influence the use of such data in soil modelling.

Further, the studies carried out at very small strain using bender elements have shown clear dependency on voids ratio for relatively large steps of strain history, where for example $OCR \geq 2$. In Section 5.2.4 there were indications that at $OCR \leq 2$ there are measurable deviations from the framework implied by Equation 7.1, and that these may have some correlation with OCR. Can stress and strain reversals be expected to result in changes in $G_{\alpha(ij)}$ that are only functions of voids ratio and stress?

These questions could not be answered using the data obtained in this project, and possible avenues for further research include:

- reviewing the literature for evidence of strain history influences over intermediate ranges of strain reversal - $0.01\ \% < \varepsilon_i < 1\%$

- carrying out triaxial tests on reconstituted samples which follow constant σ'_v, σ'_h p' and q paths after zero, partial and complete stress path direction changes. These tests should include measurement of local vertical and horizontal strains and horizontal shear wave velocity to enable the effects of strain changes on both triaxial parameters, and shear wave moduli to be assessed. These could be used to further clarify the advantages of the proposed three parameter framework involving E'_v ν'_{vh} and F'_h.

7.6 Closure

The ultimate objective of projects such as this must be to make some contribution to advancing our ability to create efficient and safe interactions between structure and soil. This must invariably involve use of many models to interface reality in the form of the ground to the realisation of a structure. While the obvious application of the data generated in this project is to inform the modelling of soil, and in particular the modelling of the soil surrounding the Lion Yard deep basement in Cambridge, the experience of the investigation reflects that the triaxial stress path cell is in itself an imperfect modeller of an ideal. But relative to the often indefinable interfaces of nature present in the deposition of soils, it represents bounded space with a finite number of interfaces which can be considered logically. This study has attempted to focus on some of the many interfaces that connect with it - the interface between the design and use of soil testing equipment, between geophysics, physics and geotechnics, and possibly most rewarding, the interface with other researchers and practitioners. Just as humanity has most to gain from successfully understanding and crossing interfaces, an interactive study of soil mechanics can lead to rewarding realisations of the repeating faces of physics in nature.

References

Ackerley, S., Standing, J. & Connolly, T. (1994). *Personal communication.* Discussions and advice ranging from small strain and mid height pore pressure set up techniques to data acquisition and equipment details.

Adamcewicz, A. S., Muhunthan, B. & Masa, E. (1997). Soil Fabric Changes During Consolidation. *Geotechnical Testing Journal* **20,** No. 3, 347-356.

Al-Tabbaa, A. & Wood, D. M. (1987). Some measurements of the permeability of Kaolin. *Géotechnique* **37,** 499-503.

Ampadu, S. K. & Tatsuoka, F. (1993). Effect of setting method on the behaviour of clays on triaxial compression from saturation to undrained shear. *Soils and Foundations* **33,** No 2, June, 14-34.

Anandarajah, A. & Kuganenthira, N. (1995). Some aspects of fabric anisotropy of soil. *Géotechnique* **45,** No. 1, 69-81.

Anandarajah, A., Kuganenthira, N. & Zhao, D. (1996). Variation of Fabric Anisotropy of Kaolinite in Triaxial Loading. *Jn. Geotech. Eng. Div. A.S.C.E.* **122,** No. 8, 633-640.

Araruna, J. T. J., Clarke, B. G. & Harwood, A. H. (1996). Quick, accurate, consistent measurements of permeability of clays. ICE *Advances in site investigation practice, Thomas Telford, London*, 840-849.

Arulnathan, R., Boulanger, R. W. & Riemer, M. F. (1998). Analysis of bender element tests. *Geotechnical Testing Journal* **21,** No. 2, June, 120-131.

Atkinson, J. H. (1973). *The deformation of undisturbed London Clay.* Ph.D. Dissertation, University of London.

Atkinson, J. H. & Richardson, D. (1985). Elasticity and normality in soil - experimental examinations. *Géotechnique* **35,** No. 4, 443-449.

Atkinson, J. H. & Sällfors, G. (1991). Experimental determination of stress-strain-time characteristics in laboratory and in-situ tests, General report. *Proc. 10th Eur. Conf. Soil Mech., Florence* **3,** 915-956.

Atkinson, J. H., Coop, M. R., Stallebrass, S. E. & Viggiani, G. (1993). Measurement of stiffness of soils and weak rocks in laboratory tests, *Proc. 26th Conf. Eng. Grp. Geological Society, Leeds, Cripps et al (eds), Balkema Rotterdam* The Engineering Geology Group, 21-27.

Atkinson, J. H., Richardson, D. & Stallebrass, S. E. (1990). Effect of recent stress history on the stiffness of overconsolidated soil. *Géotechnique* **40,** 4, 531-540.

Bai, X. & Smart, P. (1994). Study of microstructure on undrained clay. *Proc. Int. Sym on Pre Failure deformation of geomaterials, IS-Hokkaido, Saporo* **1,** Eds: Shibuya, S., Mitachi, T. & Muira, S., 371-374.

Baldi, G., Hight, D. W. & Gregory, E. T. (1988). *A re-evaluation of Conventional Triaxial Testing methods.* In: Advanced Triaxial Testing of Soil and Rock. (Eds: Donaghe, R. T., Chaney, R. C. & Silver, M. L.) (ASTM STP 977) American Society for the testing of Materials, Philadelphia, 219-263.

Baligh, M. M., Azzous, A. S. & Chin, C. T. (1987). Disturbance due to "ideal" tube sampling. *Jn. Geotech. Eng. Div. A.S.C.E.* **113,** No. 7, 739-757.

Bellotti, R., Jamiolkowski, M. & Lo Presti, D. C. F. (1995). Anisotropy of small strain stiffness in Ticino Sand. *Géotechnique* **46,** No. 1, 115-132.

Bennell, J. D. & Taylor-Smith, D. (1991). *A review of laboratory shear wave techniques and attenuation measurements with particular reference to the resonant column.* In: Shear Waves in Marine Sediments. (Eds: Hovem, J. M. et al.) Kluwer Academic Publishers, Netherlands, 83-93.

Bennell, J. D. (1994). *Personal communication.* Discussions on techniques for bender preparation/design.

Biot, M. A. (1956). Theory of propagation of elastic waves in a fluid saturated porous solid. *J. Acoust. Soc. Am.* **28,** No. 2, 168-178.

Bishop, A. W. & Henkel, D. J. (1962). *The measurement of Soil Properties in the Triaxial Test.* 2nd ed. Edward Arnold, London.

Burland, J. B. (1989). Ninth Laurits Bjerrum Memorial Lecture: "Small is beautiful" - the stiffness of soils at small strains. *Can. Geotech. J.* **26,** 499-516.

Butcher, A. P. & Lord, J. A. (1993). Engineering properties of Gault Clay in and around Cambridge. *Int. Sym. Hard Soils and Soft Rocks, Athens, Anagnostopolos* et al *(Eds), Balkema, Rotterdam,* 405-416.

Butcher, A. P. & Powell, J. M. M. (1995). The effects of geological history on the dynamic stiffness in soils. *Proceedings of the 11th European Conference on Soil Mechanics, Copenhagen* **1,** 1.27-1.36.

Butcher, A. P. (1997). *Personnal communication.* Discussions on the accuracy of field measurements carried out at High Cross.

Channa, B. (1995). *Personal communication* Techniques for the production of de-aired water in a soils laboratory.

Clayton, C. R. I. & Khatrush, S. A. (1986). A new device for measuring local axial strains on triaxial specimens. *Géotechnique* **36,** 4, 593-597.

Clayton, C. R. I., Khatrush, S. A., Bica, A. & Siddique, A. (1989). The Use of Hall Effect Semiconductors in Geotechnical Instrumentation. *Geotechnical Testing Journal* **12,** 1, March, 69-76.

Coop, M. R., Cuccuvillo, T. & Jovičić, V. (1994). *Personal communication.* Discussions on laboratory developments for small strain testing and bender element interpretation techniques.

Coop, M. R., Jovičić, V. & Atkinson, J. H. (1997). Comparisons between soil stiffnesses in laboratory tests using dynamic and continuous loading. *Proc. 14th Int. Conf. S.M.F.E.* **1,** 267-270.

Cotecchia, F. & Chandler, R. J. (1997). The influence of structure on the pre-failure behaviour of a natural clay. *Géotechnique* **47,** No. 3, 523-544.

Crampin, S. (1981). A review of wave motion in anisotropic and cracked elastic- media. *Wave Motion* **3,** 343-391.

Crampin, S. (1985). Evaluation of Anisotropy by shear wave splitting. *Geophysics* **50,** No. 1, 142-152.

Crampin, S. & Lovell, J. H. (1991). A decade of shear-wave splitting in the earth's crust: What does it mean? what use can we make of it? and what should we do next? *Geophys. J. Int.* **107,** 387-407.

Cuccovillo, T. & Coop, M. R. (1997). The measurement of local axial strains in triaxial tests using LVDTs. *Géotechnique* **47,** 167-172.

Dally, J. W., Riley, W. F. & McConnell, K. G. (1993). *Instrumentation for Engineering Measurements.* 2nd Edition ed. John Wiley and Sons, Singapore. p. 17.

Dalton, J. C. P. & Hawkins, P. G. (1982). Fields of stress - some measurements of the in-situ stress in a meadow in the Cambridgeshire country side. *Ground Engineering* **15,** No. 4, 15-23.

de Alba, P. & Baldwin, K. C. (1991). *Use of Bender elements in soil dynamics experiments.* In: Recent Advances in Instrumentation, Data Acquisition and Testing in Soil Dynamics. ASCE, New York, 86-101.

Dean, E. T. R. (1998). Specific length and some constitutive models. *Géotechnique* **48,** No. 1, 1-32.

Delage, P. & Lefebvre, G. (1984). Study of the structure of a sensitive Champlain Clay and of its evolution during consolidation. *Can. Geotech. J.* **21,** 21-35.

Dyvik, R. & Madshus, C. (1985). *Lab Measurements of Gmax using Bender Elements.* In: Advances in the Art of Testing Soils Under Cyclic Conditions. (Ed: Khosla, V.) (Proceedings of a session sponsored by the Geotechnical Engineering Division in Conjunction with the ASCE Convention in Detroit, Michigan.) ASCE, New York, 186-196.

Fookes, P. G. & Denness, B. (1969). Observational studies on fissure patterns in Cretaceous sediments of south-east England. *Géotechnique* **19,** No. 4, 453-477.

Forster, A., Hobbs, P. R. N., Cripps, A. C., Entwistle, D. C., Fenwick, S. M. M., Raines, M. R., Hallam, J. R., Jones, L. D., Self, S. J. & Meakin, J. L. (Eds.) (1994). *The Engineering Geology of British Rocks and Soils - The Gault Clay in England.* Technical Report WN/94/31 ed. British Geological Survey, Keyworth, Nottingham.

Gajo, A. & Mongiovì, L. (1994). The effects of measure accuracy in the interpretation of dynamic tests. *Proc. Int. Sym on Pre Failure deformation of geomaterials, IS-Hokkaido, Saporo* **1**, Eds: Shibuya, S., Mitachi, T. & Muira, S., 163-168.

Gallois, R. W. & Morter, A. A. (1982). The stratigraphy of the Gault of east Anglia. *Proc. Geol. Assoc.* **93**, 4, 351-368.

Garga, V. K. & Khan, M. A. (1991). Laboratory evaluation of K_0 for Overconsolidated Clays. *Can. Geotech. J.* **28**, 650-659.

Georgiannou, V. N., Rampello, S. & Silvestri, F. (1991). Static and dynamic measurements of undrained stiffness on natural overconsolidated clays. *Proc. 10th Eur. Conf. Soil Mech., Florence* **1**, 91-95.

Germaine, J. T. & Ladd, C. C. (1988). *Triaxial Testing of Saturated Cohesive Soils.* In: Advanced Triaxial Testing of Soil and Rock, ASTM STP 977. (Eds: Donaghe, R. T., Chaney, R. C. & Silver, M. L.) American Society for Testing and Materials, Philadelphia, 421-459.

Gohl, W. B. & Finn, W. D. L. (1991). *Use of Piezo ceramic bender elements in soil dynamics testing.* In: Recent Advances in Instrumentation, Data Acquisition and Testing in Soil Dynamics. ASCE, New York, 118-133.

Graham, J. & Houlsby, G. T. (1983). Anisotropic elasticity of a natural clay. *Géotechnique* **33**, 2, 165-180.

Hardin, B. O. & Black, W. L. (1969). Closure to "Vibration modulus of normally consolidated clay". *Journal of the Soil Mechanics and Foundations Division, ASCE* **95**, No. 6, 1531-1537.

Hardin, B. O. & Blandford, G. E. (1989). Elasticity of particulate materials. *Jn. Geotech. Eng. Div. A.S.C.E.* **115**, No. 6, 788-805.

Hardin, B. O. (1978). *The Nature of stress-strain behaviour for soils.* In: Proc. Conf. on Earthquake Engineering and Soil Dynamics. ASCE, Pasedena, 3-90.

Harwood, A. (1994). *Personal communication.* Discussion on triaxial testing set up methods, including details of CRoF testing.

Heymann, G., Clayton, C. R. I. & Reed, G. T. (1997). Laser interferometry to evaluate the performance of local displacement transducers. *Géotechnique* **47**, 399-406.

Hight, D. W. (1993). A review of the sampling effects in clays and sands. *Offshore site investigation and Foundation Behaviour* **28**, Society for Underwater technology, 115-146.

Hight, D. W., Bennell, J. D., Chana, B., Davis, P. D., Jardine, R. J. & Porovic, E. (1997). Wave Velocity and stiffness measurements of the Crag and Lower London Tertiaries at Sizewell. *Géotechnique* **47**, No. 3, 451-474.

Hird, C. C. & Pierpoint, N. D. (1994). A non-linear anisotropic elastic model for over consolidated clay based on strain energy. *E.C.O.N.M.I.G. 94* **1**, 67-74.

Hird, C. C. & Pierpoint, N. D. (1997). Stiffness determination and deformation analysis for a trial excavation in Oxford Clay. *Géotechnique* **47**, No. 3, 665-691.

Hooke, R. (1675). *A description of helioscopes, and some other instruments*, London.

Hossain, D. (1995). Leakage control in long duration testing of triaxial specimens. *Jn. Geotech. Eng. Div. A.S.C.E.* **121**, No. 11, November, 810-813.

Jamiolkowski, M., Leroueil, S. & Lo Presti, D. C. F. (1991). Design Parameters from theory to practice. *GEO-COAST '91* **1**, 877-917.

Jamiolkowski, M., Lancellotta, R. & Lo Presti, D. C. F. (1995). *Remarks of the stiffness' at small strains of six Italian Clays.* In: Developments in Deep Foundations and Ground Improvement Schemes. (Ed: Balasubramaniam et al) Balkema, Rotterdam, 197-216.

Jardine, R. J., Symes, M. J. & Burland, J. B. (1984). The measurement of soil stiffness in the triaxial apparatus. *Géotechnique* **34,** 3, 323-340.

Jardine, R. J., Brooks, N. J. & Smith, P. R. (1985a). The use of Electrolevel transducers for strain measurements in triaxial tests on Weak rocks. *Int. Jn. Rock Mech. Min. Sci. Geomech.* **22,** No. 5, 331-337.

Jardine, R. J., Fourie, A. B., Maswoswe, J. & Burland, J. B. (1985b). Field and laboratory measurements of soil stiffness. *Proc. 11th Int. Conf. Soil Mech. Fdn Engng., San Francisco* **Vol 2,** 511-514.

Jardine, R. J. (1992). Some observations of the kinematic nature of soil stiffness. *Soils and Foundations* **32,** No. 2, 111-124.

Jardine, R. J. (1995). One Perspective of the pre-failure deformation characteristics of some geomaterials. *Proc. Int. Sym on Pre Failure deformation of geomaterials, IS-Hokkaido, Saporo* **2,** Eds: Shibuya, S., Mitachi, T. & Muira, S., 855-885.

Jovičić, V., Coop, M. R. & Simic, M. (1996). Objective Criteria for Determining G_{max} from Bender Element Tests. *Géotechnique* **46,** No. 2, 357-362.

Jovičić, V. (1997). *The measurement and interpretation of small strain stiffness of soils.* Ph.D. Dissertation, City University.

Jovičić, V. & Coop, M. R. (1998). The Measurement of Stiffness Anisotropy in Clays with Bender Element Tests in the Traxial Apparatus. *Geotechnical Testing Journal* **21,** No. 1, March, 3-10.

Kay, J. N. & Parry, R. H. (1982). Screw plate tests in Gault Clay. *Ground Engineering* **15,** 9, September, 22-30.

Kim, D. S. & Stokoe, K. H. (1995). *Deformation characteristics of soils at small to medium strains.* In: Earthquake Geotechnical Engineering. (Ed: Ishihara) Balkema, Rotterdam, 89-94.

Lacasse, S. & Berre, T. (1988). *Triaxial Testing Methods for Soils.* In: Advanced Triaxial Testing of Soil and Rock, ASTM STP 977. (Eds: Donaghe, R. T., Chaney, R. C. & Silver, M. L.) American Society for Testing and Materials, Philadelphia, 264-289.

Lade, P. V. & Nelson, R. B. (1987). Modelling the elastic behaviour of granular materials. *International Journal of Numerical and Analytical Methods in Geomechanics* **11,** 521-542.

Lee, K. M. & Rowe, R. K. (1989). Deformations caused by surface loading and tunnelling: the role of elastic anisotropy. *Géotechnique* **39,** 125-140.

Lekhnitskii, S. G. (1963). *Theory of Elasticity of an Anisotropic Elastic Body.* Holden-Day, Inc., San Francisco.

Leroueil, S. & Vaughan, P. R. (1990). The General and Congruent effects of Structure in Natural Soils and Weak Rocks. *Géotechnique* **40,** 3, 467-488.

Lings, M. L., Nash, D. F. T., Ng, C. W. W. & Boyce, M. D. (1991). Observed behaviour of a deep excavation in Gault Clay: a preliminary appraisal. *Proc. 10th Eur. Conf. Soil Mech., Florence,* 467-470.

Lo Presti, D. C. F. (1989). Proprieta Dinamiche dei Terreni. XIV Conferenza Geotechnica di Torino, Department of Structural Engineering, Politecnico di Torino **1,** 1-62.

Lo Presti, D. C. F., Pallara, O., Costanzo, D. & Impavido, M. (1994). Small Strain Measurements during Triaxial Tests: Many Problems, some solutions. *Proc. Int. Sym on Pre Failure deformation of geomaterials, IS-Hokkaido, Saporo* **1,** Eds: Shibuya, S., Mitachi, T. & Muira, S., 11-16.

Lo Presti, D. C. F. (1995). General Report: Measurement of shear deformation of geomaterials in the laboratory. *Proc. Int. Sym on Pre Failure deformation of geomaterials, IS-Hokkaido, Saporo* **2,** Eds: Shibuya, S., Mitachi, T. & Muira, S., 1067-1088.

Lo Presti, D. C. F., Jamiolkowski, M. & Pallara, O. (1995). *Pisa Clay stiffness from static and dynamic laboratory tests.* In: Earthquake Geotechnical Engineering. (Ed: Ishihara) Balkema, Rotterdam, 113-118.

Love, A. E. H. (1927). *A treatise on the Mathematical theory of elasticity.* Fourth Edition (first Ed. in 1892) ed. University Press, Cambridge.

Marsland, A. & Powell, J. J. M. (1988). Investigation of cone penetration tests in British clays carried out by the Building Research Establishment 1960-86. *Penetration Testing in the UK,* Thomas Telford, London, 209-214.

Marsland, A. & Powell, J. J. M. (1990). Pressuremeter tests on stiff clays and soft rocks - factors affecting measurements and their interpretation. *Proc. 24th annual Conf. of engineering group of the Geology society* Field Testing in Engineering Geology, Special publication Issue 6, Eds: Bell, F. G., Cripps, J. C. & Culshaw, M. G., 91-110.

Martin, R. T. & Ladd, C. C. (1978). Fabric of Consolidated Koalinite. *Clays and Clay Minerals* **23,** 17-25.

Mitchell, J. K. (1976). *Fundamentals of Soil Behaviour.* John Wiley and Sons, Inc., New York. 422 pages. pp. 82-83.

Muir Wood, A. M. (1955). Folkstone Warren Landslips: Investigations 1948-1950. *Proc. I.C.E. Railway Eng. Div.* Paper no. 56,

Muir Wood, D. (1990). *Soil behaviour and critical state soil mechanics.* Cambridge University Press, Cambridge. p. 52.

Muir Wood, D. (1995). General Report: Evaluation of material properties. *Proc. Int. Sym on Pre Failure deformation of geomaterials, IS-Hokkaido, Saporo* **2,** Eds: Shibuya, Mitachi & Mura, 1179-1199.

Ng, C. W. W. (1992). An evaluation of soil structure interaction associated with a multi propped excavation. Ph.D. Thesis, University of Bristol, UK.

Ng, C. W. W., Lings, M. L. & Nash, D. F. T. (1992). Back-analysing the bending moment in a concrete diaphragm wall. *The Structural Engineer* **70,** 23&24, 421-426.

Ng, C. W. W., Bolton, M. D. & Desari, G. R. (1995a). The small strain stiffness of a carbonate stiff clay. *Soils and Foundations* **35,** No. 4, 109-114.

Ng, C. W. W., Lings, M. L., Simpson, B & Nash, D. F. T. (1995b). An approximate analysis of the three-dimensional effects of diaphragm wall installation. *Géotechnique* **45,** No. 3, 497-507.

Ng, C. W. W. & Nash, D. F. T. N. (1995c). *The compressibility of a carbonate clay.* In: Compression and Consolidation of Clayey Soils. (Eds: Yoshikuni & Kusakabe) Balkema, Rotterdam, 281-286.

Nishio, S. & Katsura, Y. (1994). Shear Wave Anisotropy in Edogawa Pleistocene Deposit. *Proc. Int. Sym on Pre Failure deformation of geomaterials, IS-Hokkaido, Saporo* **1,** Eds: Shibuya, S., Mitachi, T. & Muira, S., 169-174.

Pickering, D. J. (1970). Anisotropic elastic parameters for soil. *Géotechnique* **20,** 3, 271-276.

Pierpoint, N. (1994). *Personal communication.* Discussions on Laboratory testing methods, including the mulitple mini stress path excursion technique.

Pierpoint, N. D. (1996). *The prediction and back analysis of excavation behaviour in Oxford Clay.* Ph.D. Dissertation, University of Sheffield. 425 p.

Pietruszczak, S. & Krucinski, S. (1989). Description of clay anisotropy employing the concept of directional variation of porosity. *Proc. 3rd Conf. Numerical Models in Geomechanics* **1,** 61-70.

Pollard, W. S., Sangrey, D. A. & Poulos, S. J. (1977). Air diffusion through membranes in triaxial tests. *Jn. Geotech. Eng. Div. A.S.C.E.* **103,** GT10, 1169-1173.

Powell, J. J. M. & Butcher, A. P. (1991). Assessment of ground stiffness from field and laboratory tests. *Proc. 10th Eur. Conf. Soil Mech., Florence* **1,,** 153-156.

Price, R. J. (1977). The stratigraphical zonation of the Albian sediments of the north west Europe. *Proceedings of the Geologists association* **88,** 2, 65-91.

Prior, S. V., Kemp, S. J., Pearce, J. M. & Inglethorpe, S. D. J. (1993). *Mineralogy of the Gault clay from the Arlesey and Klondyke farm boreholes.* British Geological Survery Technical Report No. WG/93/17.

Rampello, S. & Silvestri, F. (1993). The stress strain behaviour of natural and reconstituted samples of two overconsolidated. *Int. Sym. Hard Soils and Soft Rocks, Athens, Anagnostopolos* et al *(Eds), Balkema, Rotterdam,* 769-778.

Rampello, S., Viggiani, G. & Silvestri, F. (1994a). The dependence of small strain stiffness on stress state and history for fine grained soils. *Proc. Int. Sym on Pre Failure deformation of geomaterials, IS-Hokkaido, Saporo* **1,** Eds: Shibuya, S., Mitachi, T. & Mura, S., 273-278.

Rampello, S., Viggiani, G. & Silvestri, F. (1994b). Panelist Discussion: The dependence of G_0 on Stress State and History in Cohesive Soils. *Proc. Int. Sym on Pre Failure deformation of geomaterials, IS-Hokkaido, Saporo* **2,** Eds: Shibuya, S., Mitachi, T. & Mura, S., 1155-1160.

Rampello, S., Viggiani, G. M. B. & Amorosi, A. (1997). Small-strain stiffness of reconstituted clay compressed along constant triaxial effective ratio paths. *Géotechnique* **47,** No. 3, 475-489.

Raymond, G. P. (1970). Discussion on Stress and Displacements in a Cross-anisotropic Soil (Barden,L (1963). Geotechnique 13, No.3, 198-210). *Géotechnique* **20,** No. 4, 456-458.

Richart, F. E., Hall, J. R. & Woods, R. D. (1970). *Vibrations of soils and foundations.* Prentice Hall Inc., New Jersey.

Ridley, A. M. (1996). *Personnal communication.* Particular advice on details of fuse wire method for reducing swelling in heavily overconsolidated samples during setup.

Ridley, A. M. & Burland, J. B. (1996). *A pore water pressure probe for the insitu measurement of a wide range of soil suctions.* In: Advances in site investigation practice. (Ed: Craig, C.) Thomas Telford, London, 510-520.

Roesler, S. K. (1979). Anisotropic shear modulus due to stress anisotropy. *Jn. Geotech. Eng. Div. A.S.C.E.* **105,** GT7, July, 871-880.

Saada, A. S., Bianchini, G. F. & Shook, L. P. (1978). The dynamic response of anisotropic clay. *Earthquake Engineering and Soil Dynamics* **2,** Proceedings of the ASCE Geotechnical Engineering Division, 777-799.

Samuels, S. G. (1975). Some properties of the Gault Clay from the Ely-Ouse Essex water tunnel. *Géotechnique* **25,** 2, 239-264.

Sanchez-Salerino, I., Roesset, J. M. & Stokoe, K. H. (1986). *Analytical Studies of Wave Propagation and Attenuation.* (Geotechnical Engineering Report No GR86-15) Civil Engineering Department, University of Texas, Austin.

Schofield, A. N. & Wroth, C. P. (1968). *Critical State Soil Mechanics.* McGraw-Hill, London.

Scholey, G. K., Frost, J. D., Lo Presti, D. C. F. & Jamiolkowski, M. (1995). A review of instrumentation for measuring small strains during triaxial testing of soil specimens. *Geotechnical Testing Journal* **18,** No. 2, 135-156.

Sides, G. & Barden, L. (1970). The microstructure of dispersed and flocculated samples of kaolinite, illite and montmorillonite. *Can. Geotech. J.* **8,** 391-400.

Simpson, B. (1992). Thirty-second Rankine Lecture: Retaining Structures: displacement and design. *Géotechnique* **42,** 4, 541-576.

Simpson, B. (1993). *Development and application of a new soil model for prediction of ground movements.* In: Predictive Soil Mechanics. (Eds: Houlsby, G. T. & Schofield, A. N.) (Proceedings of the Wroth Memorial Symposium held at St Catherine's College, Oxford.) Thomas Telford, London, 628-643.

Simpson, B. (1997): Verbal contribution at Géotechnique Symposium in Print, September.

Simpson, B., O'Riordan, N. J. & Croft, D. D. (1979). A computer model for the analysis of ground movements in London Clay. *Géotechnique* **29,** No. 2, 149-175.

Simpson, B., Atkinson, J. H. & Jovičić, V. (1996). The influence of anisotropy on calculations of ground settlements above tunnels. *Proc. Geotechnical Aspects of Underground Construction in Soft Ground, The City University,* 591-595.

Smith, P. R. (1992). *The behaviour of natural high compressibility clay with special reference to construction on soft ground.* Ph.D. Thesis, Imperial College, University of London.

Stallebrass, S. E. & Taylor, R. N. (1997). The development and evaluation of a constitutive model for the prediction of ground movements in overconsolidated clay. *Géotechnique* **47,** No. 2, 235-254.

Stokoe, K. H., Lee, S. H. H. & Knox, D. P. (1985). *Shear moduli measurements under true triaxial stresses.* In: Proceedings of a session sponsored by the Geotechnical Engineering Division in Conjunction with the ASCE Convention in Detroit, Michigan. ASCE, New York, 167-185.

Stokoe, K. H., Hwang, S. K., Lee, J. N.-K. & Andrus, R. D. (1995). Effects of various parameters on the stiffness and damping of soils at small to medium strains. *Proc. Int. Sym on Pre Failure deformation of geomaterials, IS-Hokkaido, Saporo* **1,** Eds: Shibuya, S., Mitachi, T. & Mura, S., 785-815.

Sully, J. P. & Campanella, R. G. (1995). Evaluation of in situ anisotropy from crosshole and down hole shear wave velocity measurements. *Géotechnique* **45,** No. 2, June, 267-282.

Tatsuoka, F. (1995). *Personal communication.* Encouragement and enthusiasm given during visit to Institute of Industrial Science Laboratories, University of Tokyo. Particular discussions concerned dry setting method, LLDT's and loadcell compliance, and the formation of shear bands, which may have influence on bender readings.

Thomann, T. G. & Hryciw, R. D. (1990). Laboratory measurements of small strain shear modulus under K_0 conditions. *Geotechnical Testing Journal* **13,** 2, June, 97-105.

Ting, W. H. (1968). *Some effects of history on the stress-strain behaviour of kaolin.* Ph.D. Dissertation, University of Cambridge.

Toll, D. G. (1993). *A Computer Control System for stress Path Triaxial Testing.* In: Developments in Civil Construction Engineering Computing. (Ed: Topping, B. V.) Civil-Comp press, Edinburgh, 107-117.

Toms, A. H. (1945). Folkstone Warren Landslips - Research carried out in 1939 by the Southern Railway Co. *Proc. I.C.E.* **IV,** 9-10.

Ueng, T. S., Tzou, Y. M. & Lee, C. J. (1988). *The effect of end restraint on volume change and particle breakage of sands in triaxial tests.* In: Advanced Triaxial Testing of Soil and Rock, ASTM STP 977. (Eds: Donaghe, R. T., Chaney, R. C. & Silver, M. L.) American Society for Testing and Materials, Philadelphia, 679-691.

Van Cauwelaert, F. (1977). Coefficients of deformation of an anisotropic body. *Jn. Geotech. Eng. Div. A.S.C.E.* **103,** No. 5, 823-835.

Vancouver, C. (1794). Eastern General View of the Agriculture in the County of Cambridge with Observations on the means of its improvements. *The review and abstract of the County Reports to the Board of Agriculture* **3,** Ed: Marshall, W., 229.

Vaughan, P. R., Chandler, R. J., Apted, J. P., Maguire, W. M. & Sandroni, S. S. (1993). *Sampling Disturbance - with particular reference to its effect on stiff clays.* In: Predictive Soil Mechanics. (Eds: Houlsby, G. T. & Schofield, A. N.) (Proceedings of the Wroth Memorial Symposium held at St Catherines College, Oxford.) Thomas Telford, London, 685-708.

Vernitron (1992). *Ceramic acoustic elements in bimorph and multimorph, for pick up cartridges, microphones paging systems and other low frequency uses.* Bulletin 66012/D.

Viggiani, G. (1992a). Dynamic measurement of small strain stiffness of fine grained soils in the triaxial apparatus. *Proc. Workshop Exp. Characterisation and modelling of soils and soft rock, Napoli,* 75-97.

Viggiani, G. (1992b). *Small strain stiffness of fine grained soils.* PhD Thesis, City University.

Viggiani, G. (1995). Panellist discussion: Recent Advances in the interpretation of bender element tests. *Proc. Int. Sym on Pre Failure deformation of geomaterials, IS-Hokkaido, Saporo* **2,** Eds: Shibuya, S., Mitachi, T. & Muira, S., 1099-1104.

Viggiani, G. & Atkinson, J. H. (1995). Stiffness of fine grained soil at very small strains. *Géotechnique* **45,** No. 2, June, 249-265.

White, J. E., Martineau-Nicoletis, L. & Monash, C (1983). Measured Anisotropy in Pierre Shale. *Geophysical Prospecting* **31,** No. 5, 709-726.

Winter, M. G. & Horseman, S. T. (1993). Specimen preparation technique for a very stiff clay. *Int. Sym. Hard Soils and Soft Rocks, Athens, Anagnostopolos* et al *(Eds), Balkema, Rotterdam* **1,** The Engineering geology of Weak Rock, 83-85.

Woods, R. D. (1994). *Laboratory measurements of Dynamic Soil Properties.* In: Dynamic Geotechnical Testing II, ASTM STP 1213. (Eds: Ebelhar, R. J., Drnevich, V. P. & Kutter, B. L.) ASTM, Philidelphia, 191-201.

Worssam, B. C. & Taylor, J. H. (1975). *Geology of the country around Cambridge. 2th edition.* Her Majesty's Stationary Office, London.

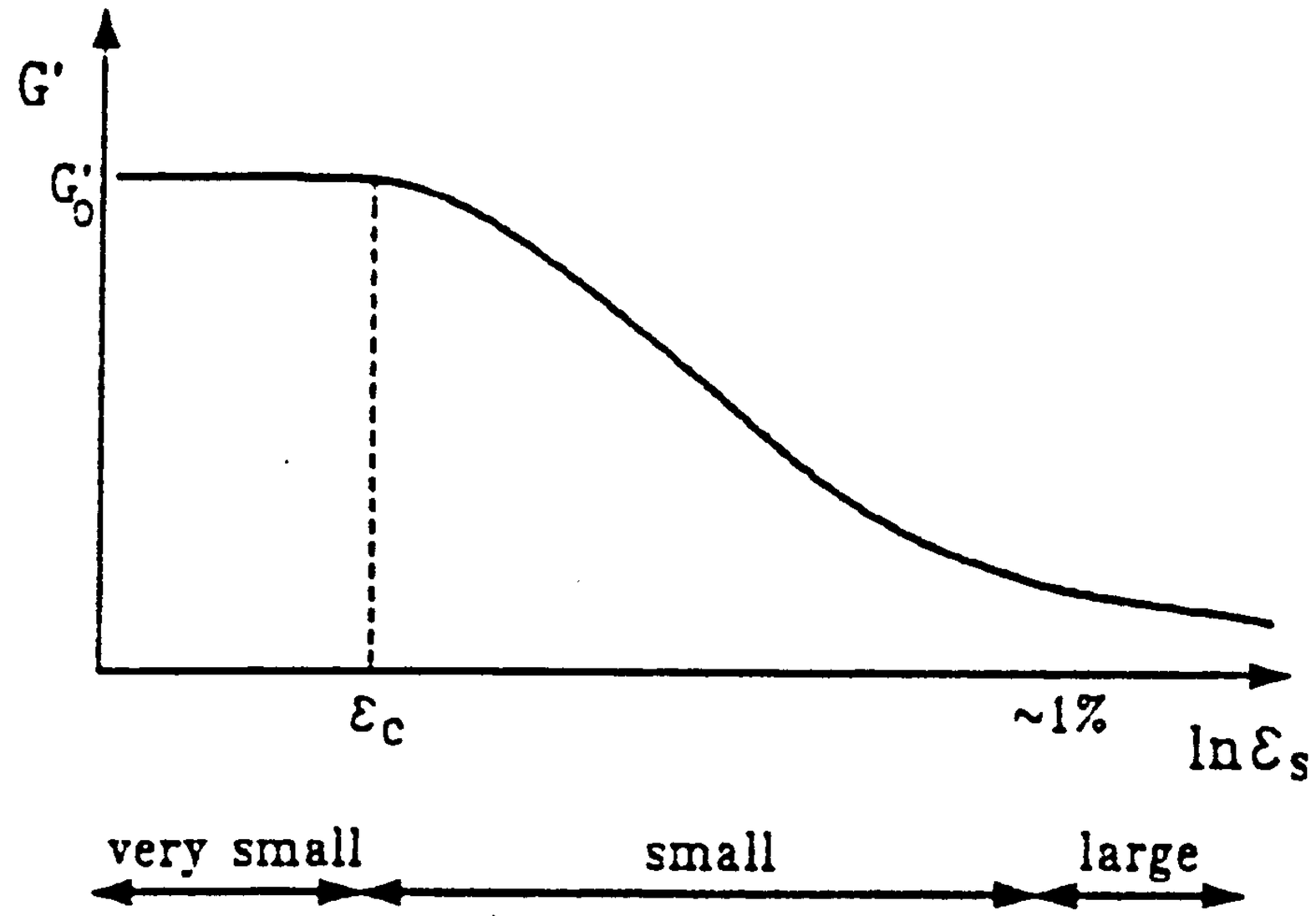

Figure 2.1 **An idealisation of the variation of stiffness with strain for soil (after Atkinson and Sällfors, 1991)**

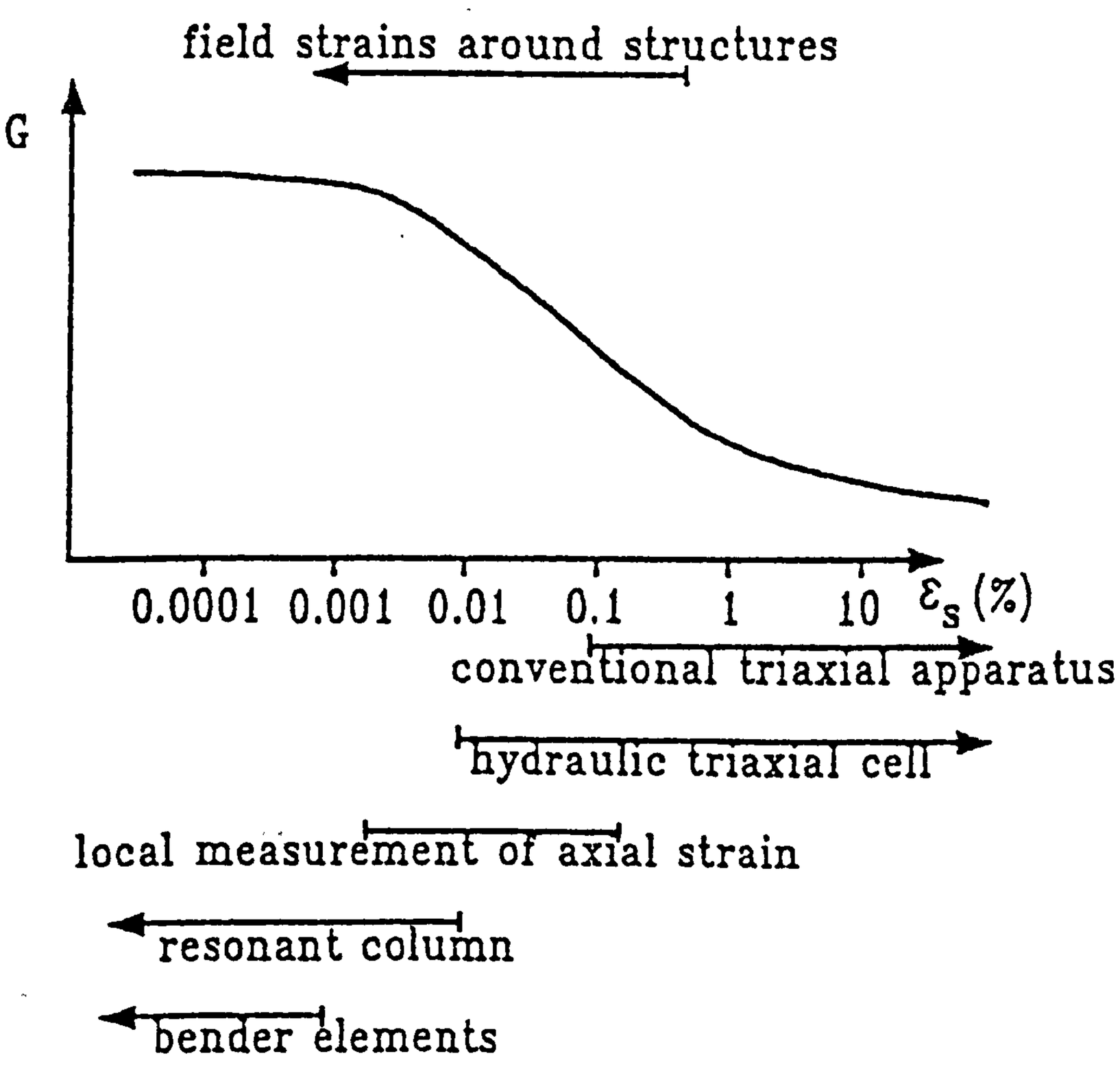

Figure 2.2 **Variation of stiffness with strain in the field and measured with different laboratory tests (after Atkinson *et al.*, 1993)**

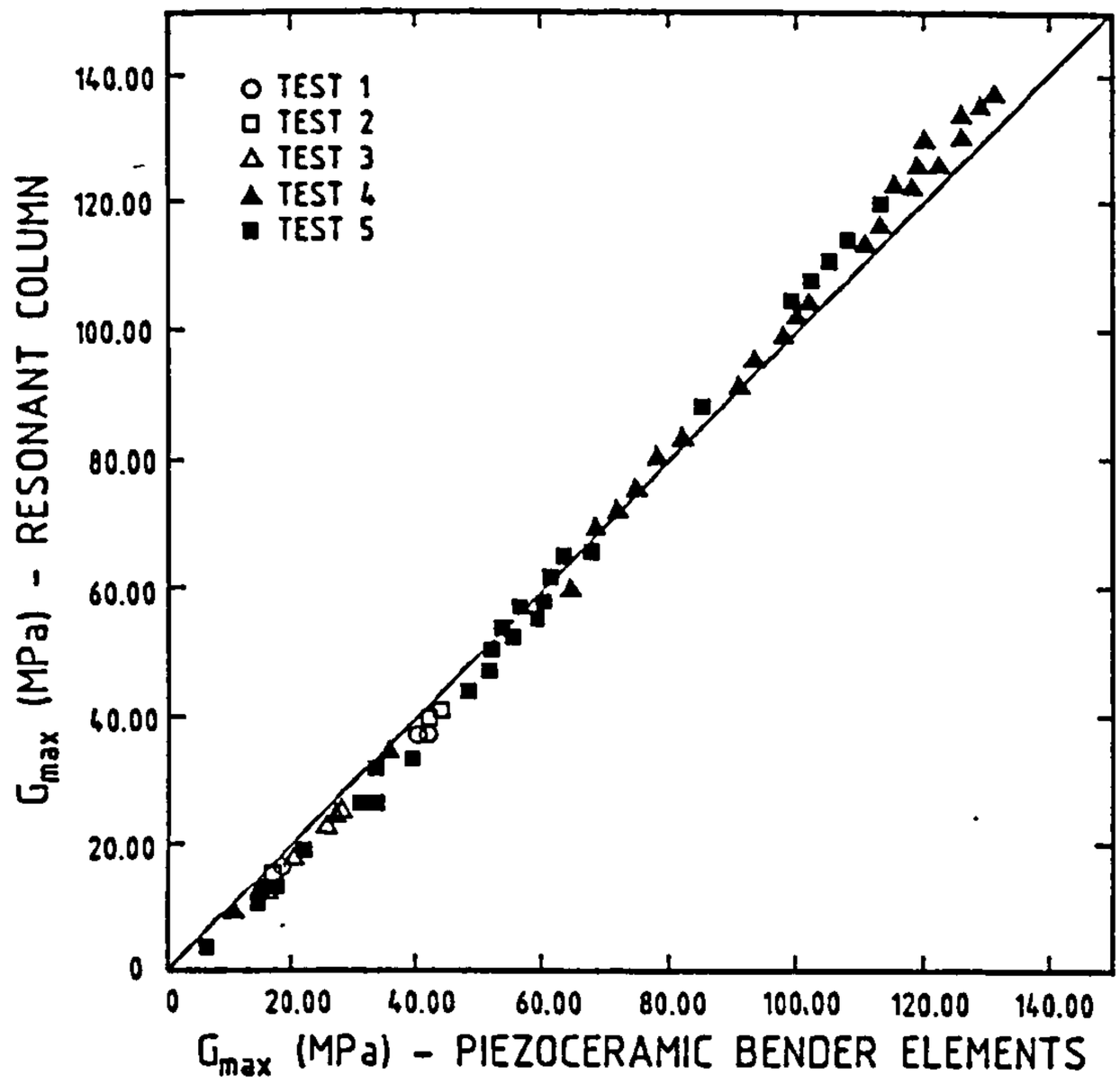

a) Based on tests on five clay soils (after Dyvik and Madshus, 1985)

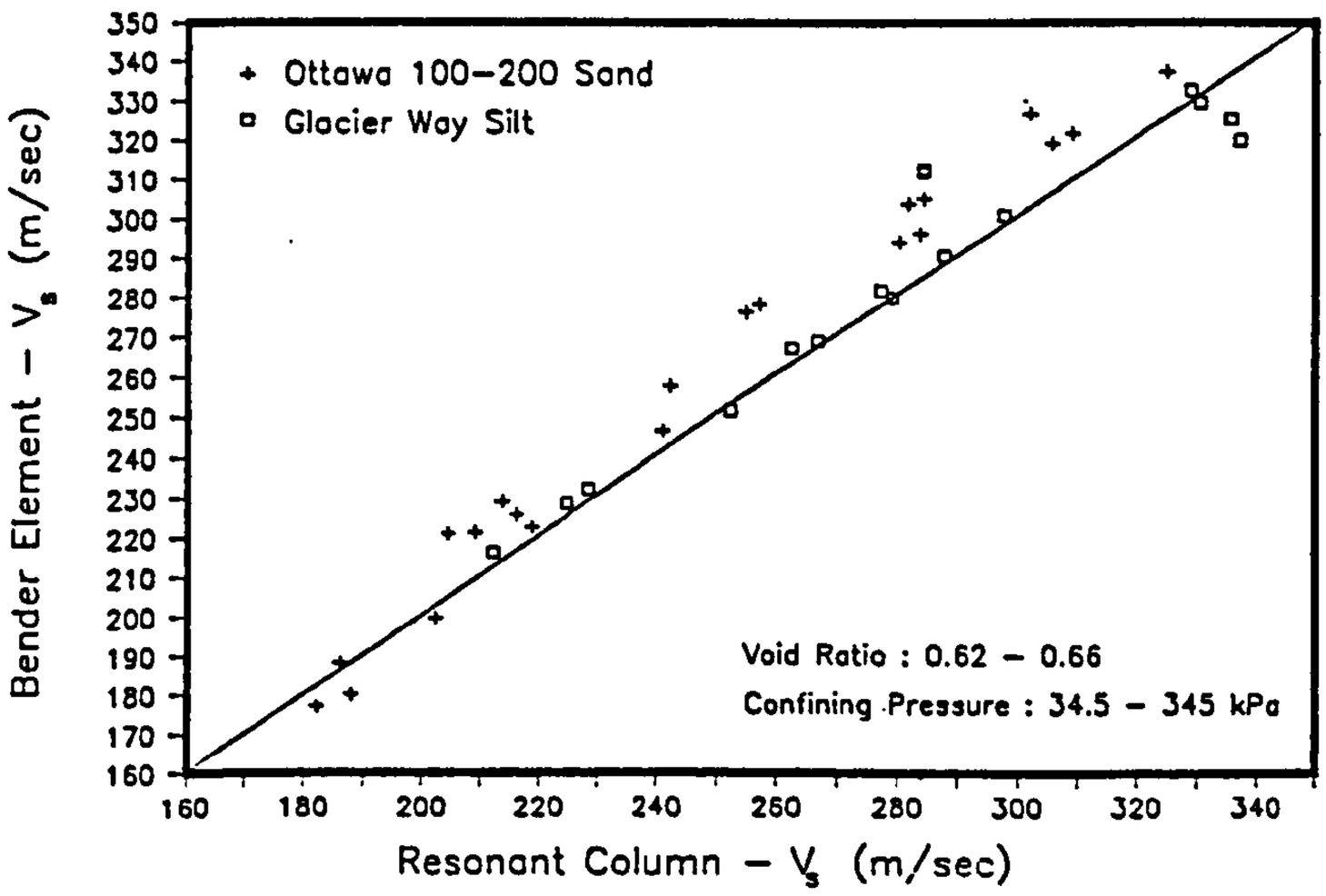

b) Based on tests on sand and silt (after Thomann and Hryciw, 1990)

Figure 2.3 Comparison of G_0 measurement by resonant column and bender element techniques

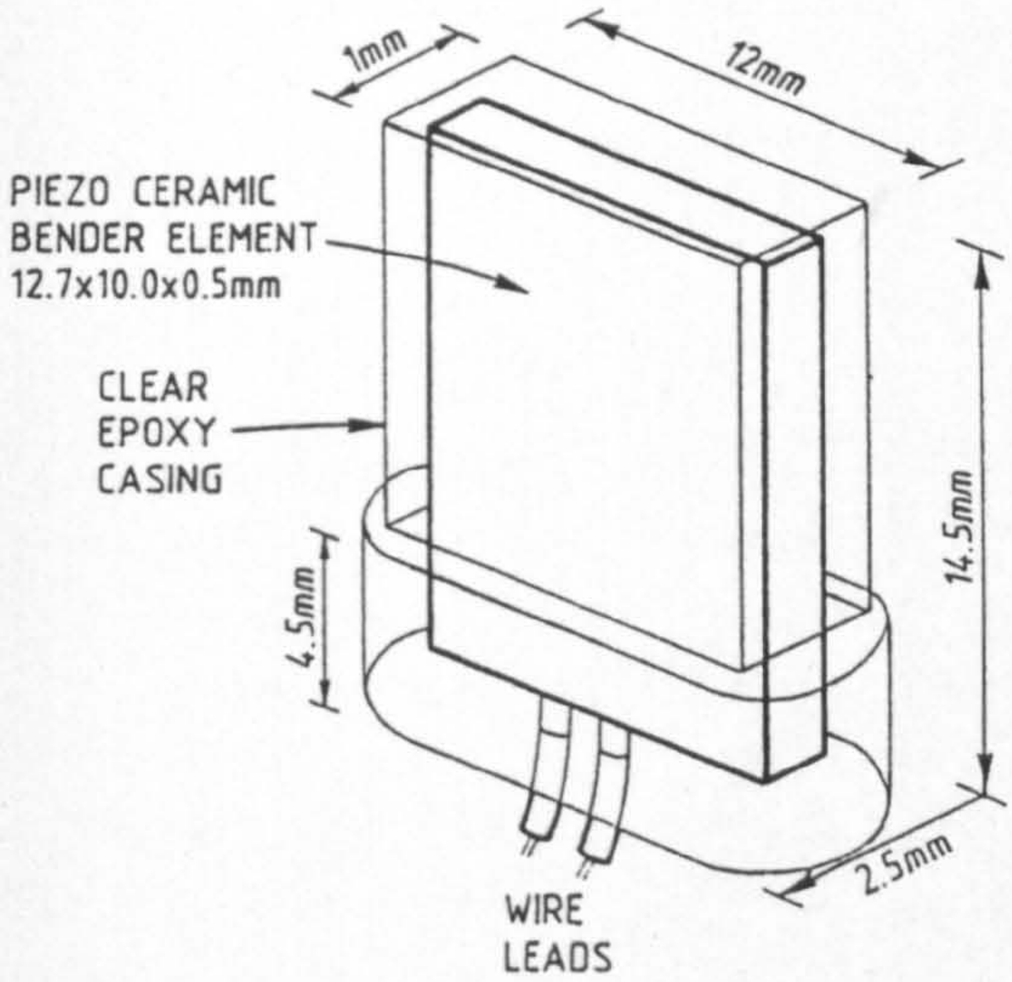

a) Bender element prepared for mounting in soil testing device

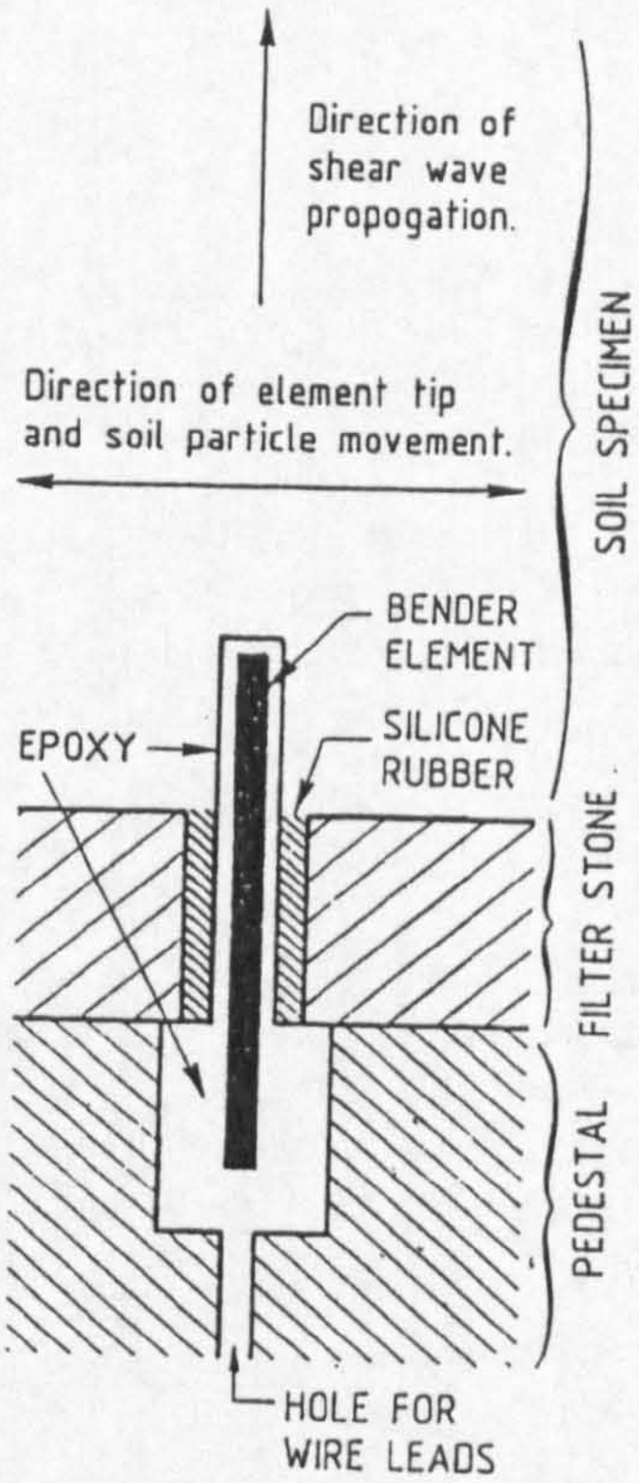

b) Bender element mounted in soil testing device

Figure 2.4 Bender elements in soil testing devices (after Dyvik and Madshus, 1985)

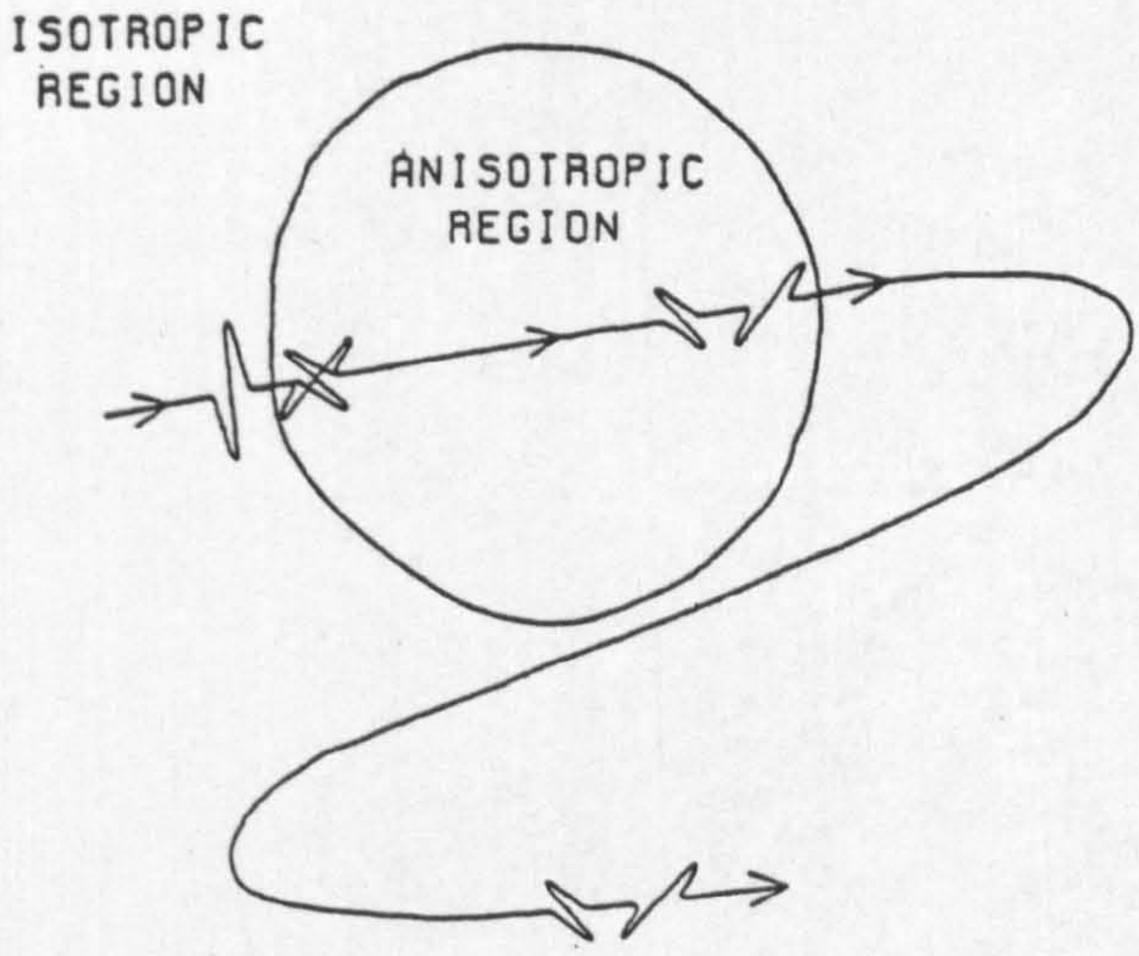

Figure 2.5 Schematic illustration of shear wave splitting (after Crampin, 1985)

Isotropic
(2 independent elastic constants)

$$\begin{bmatrix} a & b & b & . & . & . \\ b & a & b & . & . & . \\ b & b & a & . & . & . \\ . & . & . & x & . & . \\ . & . & . & . & x & . \\ . & . & . & . & . & x \end{bmatrix}$$

where x = (a-b)/2

Cubic
(3 independent elastic constants)

$$\begin{bmatrix} a & b & b & . & . & . \\ b & a & b & . & . & . \\ b & b & a & . & . & . \\ . & . & . & c & . & . \\ . & . & . & . & c & . \\ . & . & . & . & . & c \end{bmatrix}$$

Hexagonal
(5 independent elastic constants)

$$\begin{bmatrix} a & b & c & . & . & . \\ b & a & c & . & . & . \\ c & c & d & . & . & . \\ . & . & . & e & . & . \\ . & . & . & . & e & . \\ . & . & . & . & . & x \end{bmatrix}$$

where x = (a-b)/2

Trigonal (1)
(6 independent elastic constants)

$$\begin{bmatrix} a & b & c & d & . & . \\ b & a & c & -d & . & . \\ c & c & e & . & . & . \\ d & -d & . & f & . & . \\ . & . & . & . & f & y \\ . & . & . & . & y & x \end{bmatrix}$$

where x = (a-b)/2 and y = d

Trigonal (2)*
(6 independent elastic constants)

$$\begin{bmatrix} a & b & c & d & g & . \\ b & a & c & -d & -g & . \\ c & c & e & . & . & . \\ d & -d & . & f & . & z \\ g & -g & . & . & f & y \\ . & . & . & z & y & x \end{bmatrix}$$

where x = (a-b)/2 , y = d and z=-g

Tetragonal (1)
(6 independent elastic constants)

$$\begin{bmatrix} a & b & c & . & . & . \\ b & a & c & . & . & . \\ c & c & d & . & . & . \\ . & . & . & e & . & . \\ . & . & . & . & e & . \\ . & . & . & . & . & f \end{bmatrix}$$

Tetragonal (2)
(7 independent elastic constants)

$$\begin{bmatrix} a & b & c & . & . & d \\ b & a & c & . & . & -d \\ c & c & e & . & . & . \\ . & . & . & f & . & . \\ . & . & . & . & f & . \\ d & -d & . & . & . & g \end{bmatrix}$$

Orthorhombic
(9 independent elastic constants)

$$\begin{bmatrix} a & b & c & . & . & . \\ b & d & e & . & . & . \\ c & e & f & . & . & . \\ . & . & . & g & . & . \\ . & . & . & . & h & . \\ . & . & . & . & . & i \end{bmatrix}$$

Monoclinic
(13 independent elastic constants)

$$\begin{bmatrix} a & b & c & . & . & d \\ b & e & f & . & . & g \\ c & f & h & . & . & i \\ . & . & . & j & k & . \\ . & . & . & k & l & . \\ d & g & i & . & . & m \end{bmatrix}$$

Notes:

- The isotropic tensor is included for completeness. The matrices labelled '(2)*' are more complicated versions of the similarly named matrices labelled (1). These complicated versions do not commonly occur.
- Hexagonal anisotropy is the form referred to in this thesis as cross-anisotropy.

Figure 2.6 **The elastic stiffness matrices of the six most symmetric anisotropic symmetry systems referred to their principal axes (after Crampin, 1981)**

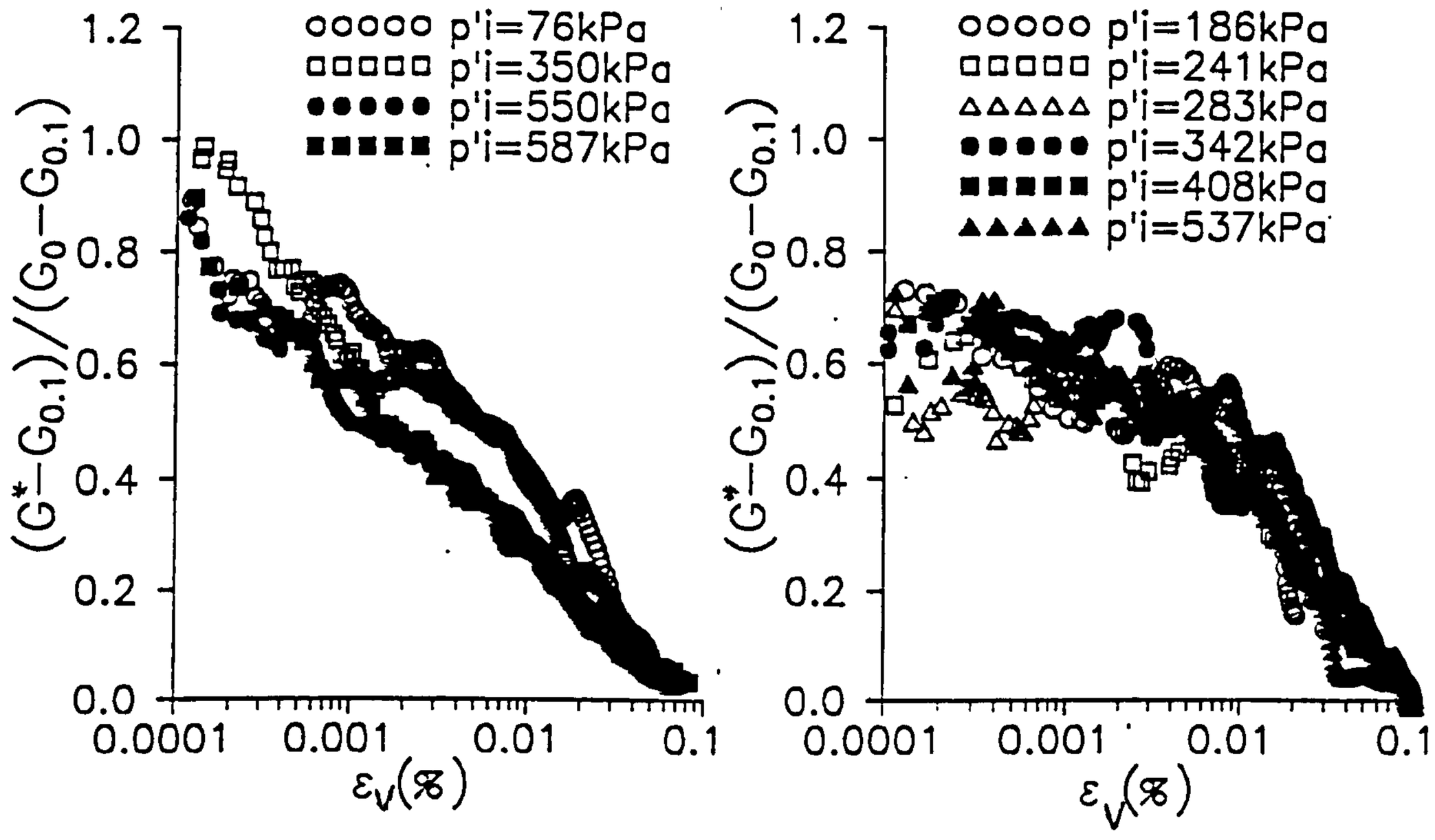

a) Normally consolidated kaolin

b) Normally consolidated Boom clay

Figure 2.7 Normalised stiffness : strain curves for three geo-materials illustrating comparison between bender and continuous loading data (After Coop *et al.*, 1997)

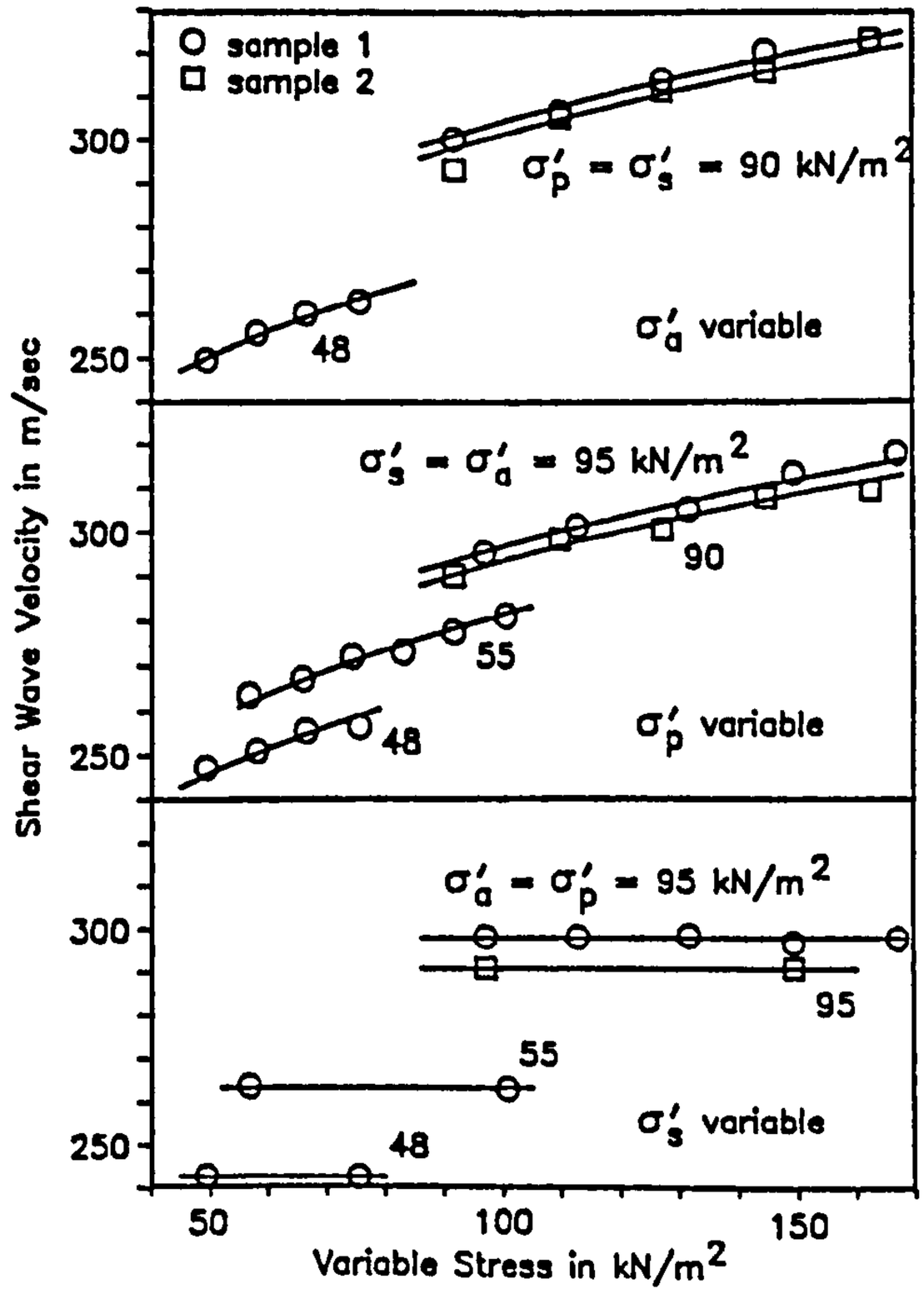

Figure 2.8 Variations in shear wave velocity due to independent variations of the principal stresses (after Roesler, 1979)

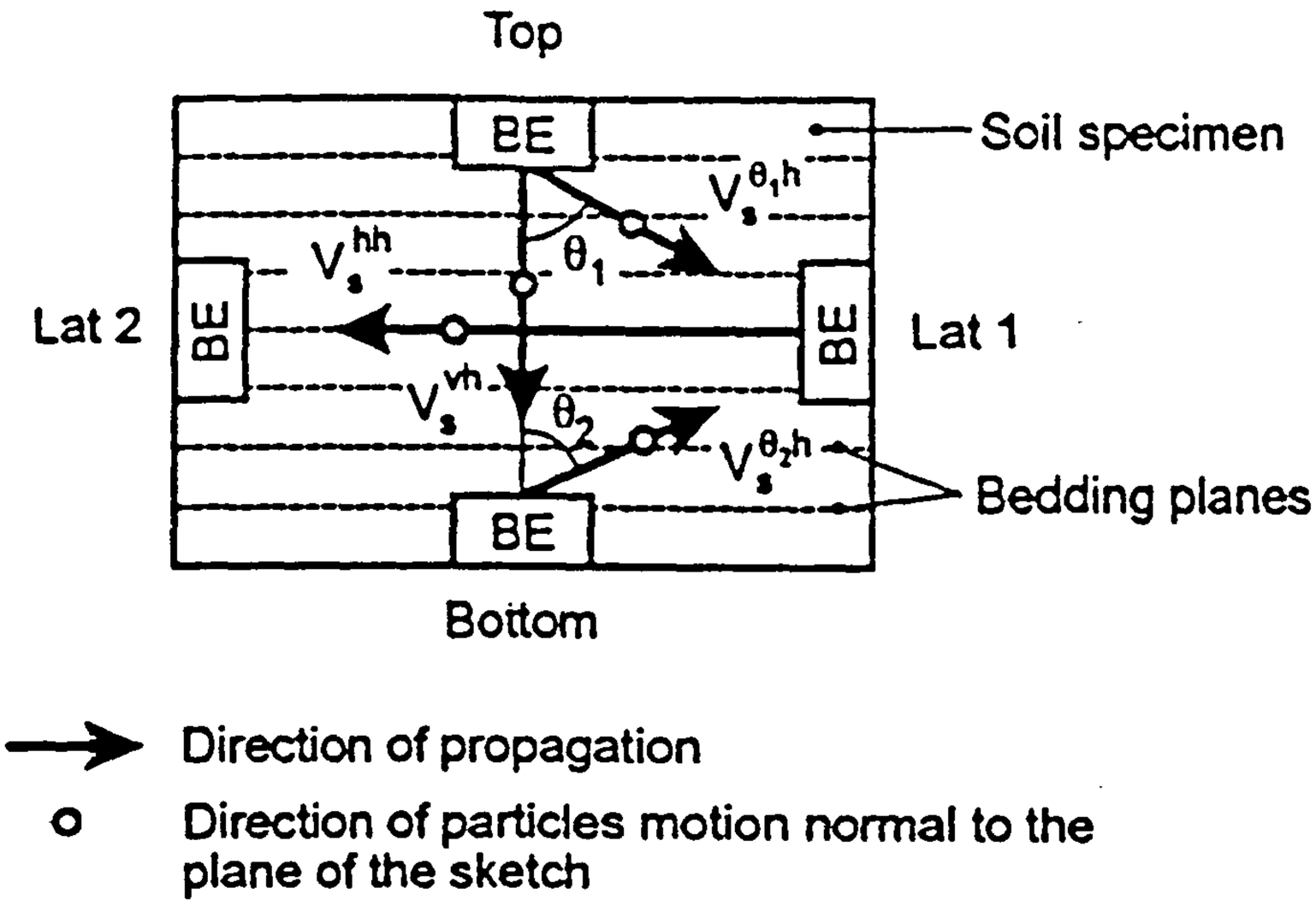

a) Layout of Type B oedometer with horizontal and vertical bender elements

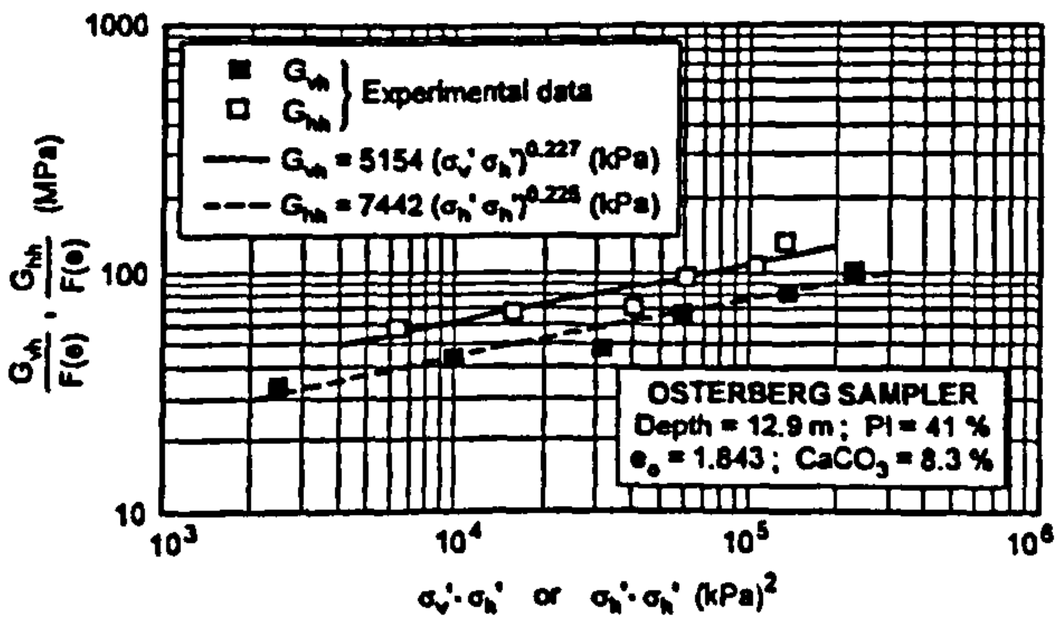

b) Pisa clay: normalised shear moduli *vs.* effective consolidation stresses

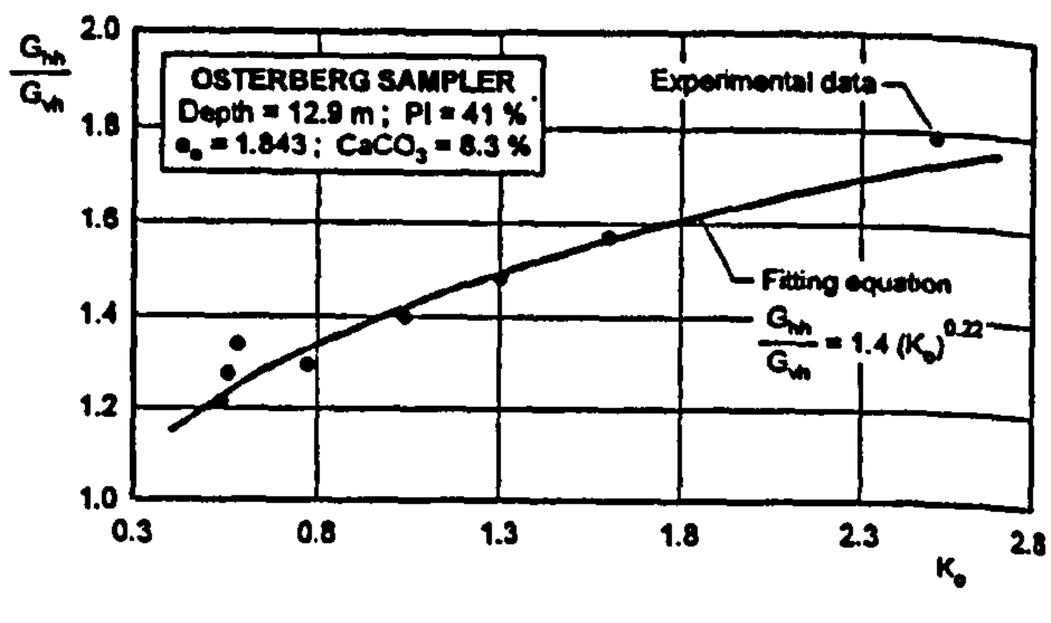

c) Pisa clay: anisotropy ratio G_{hh} / G_{vh} *vs.* stress ratio

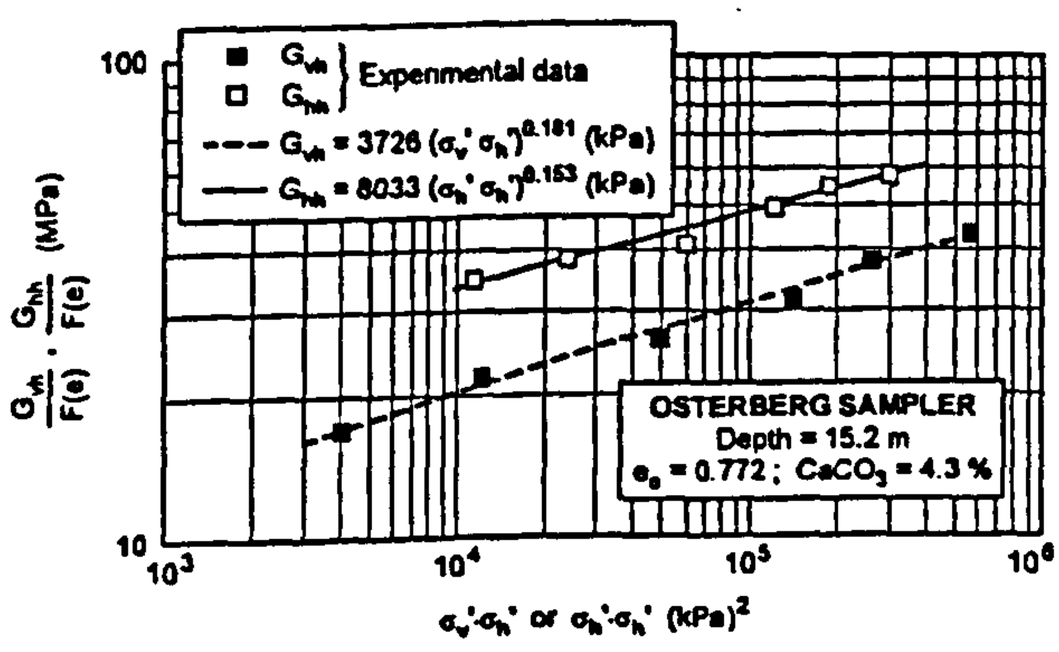

d) Panigaglia clay: normalised shear moduli *vs.* effective consolidation stresses

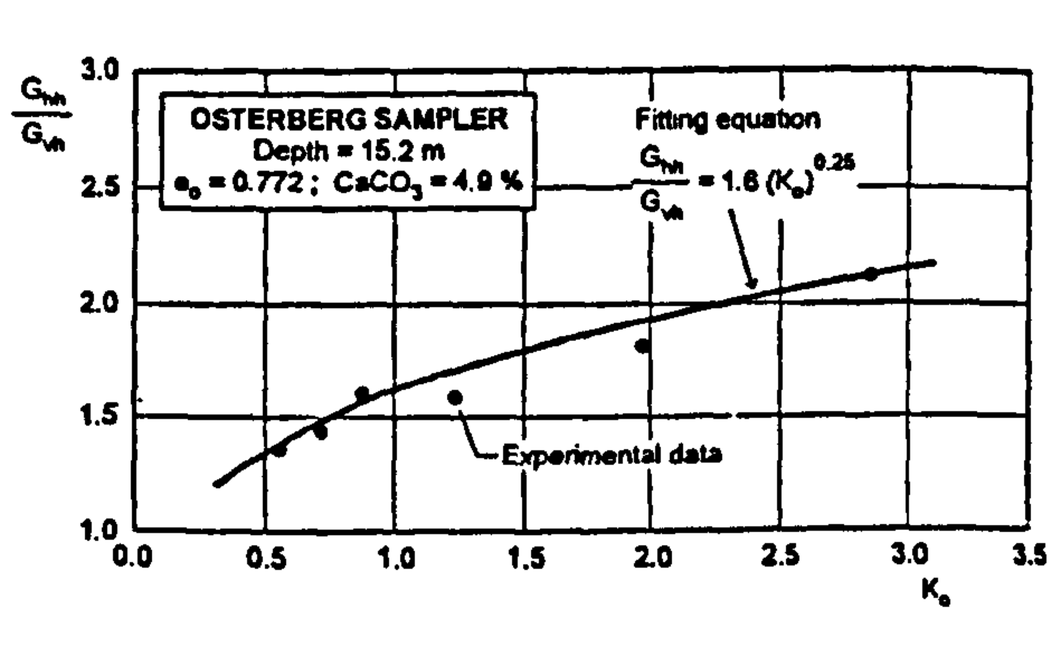

e) Panigaglia clay: anisotropy ratio G_{hh} / G_{vh} *vs.* stress ratio

Figure 2.9 Bender element tests on two Italian clays using an instrumented type B oedometer (After Jamiolkowski *et al.*, 1995)

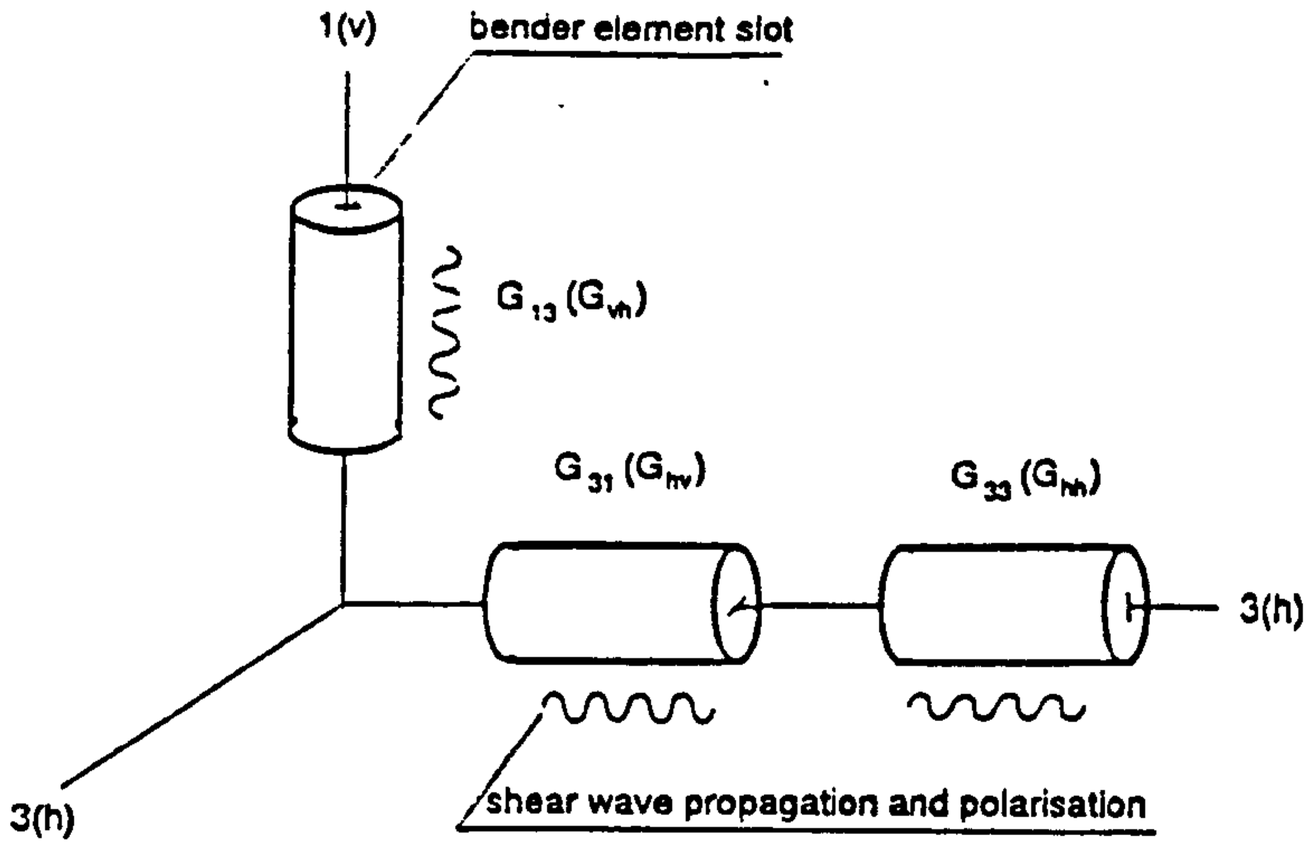

a) Orientations of clay samples prepared for measurement of anisotropic shear moduli

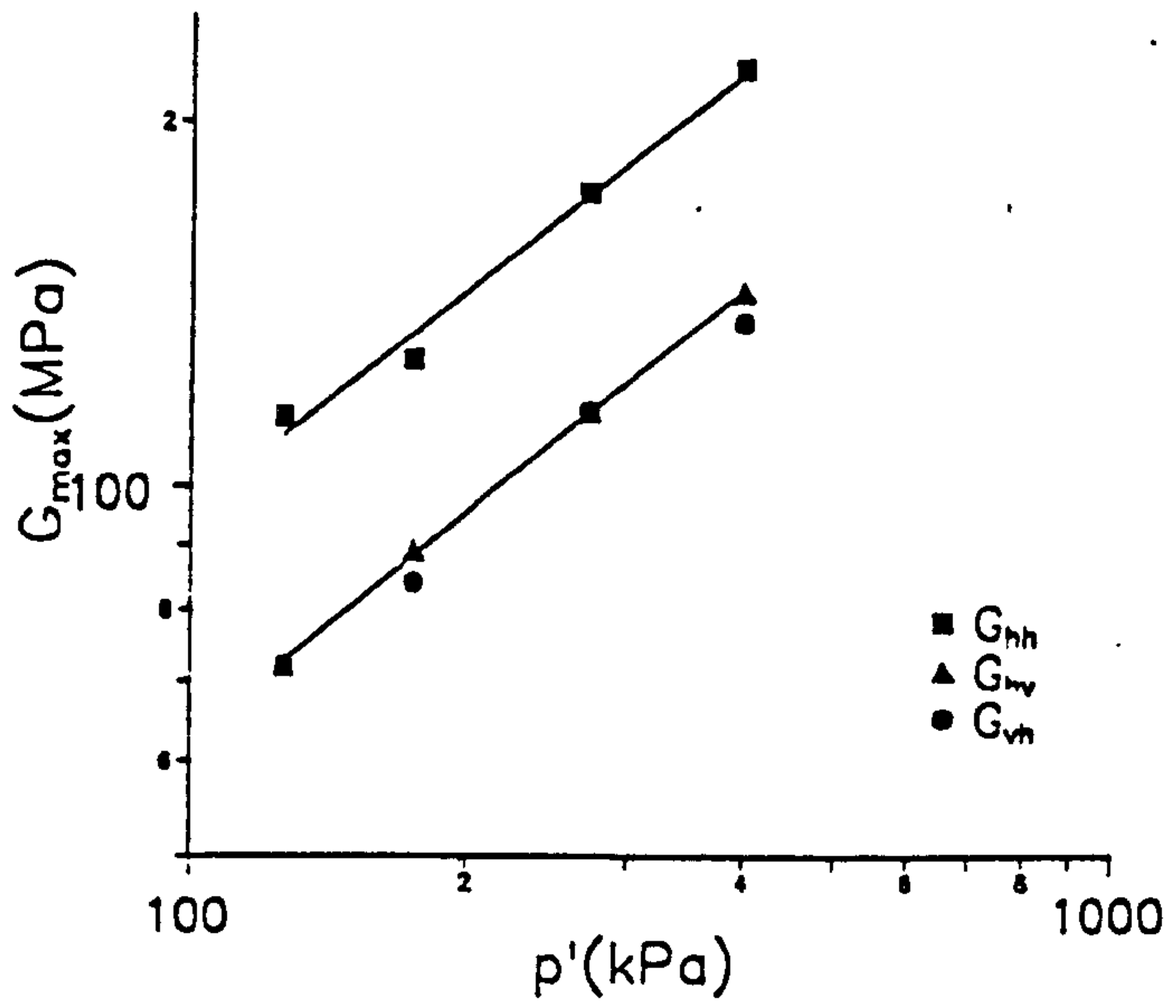

b)Shear moduli results from tests on undisturbed London clay

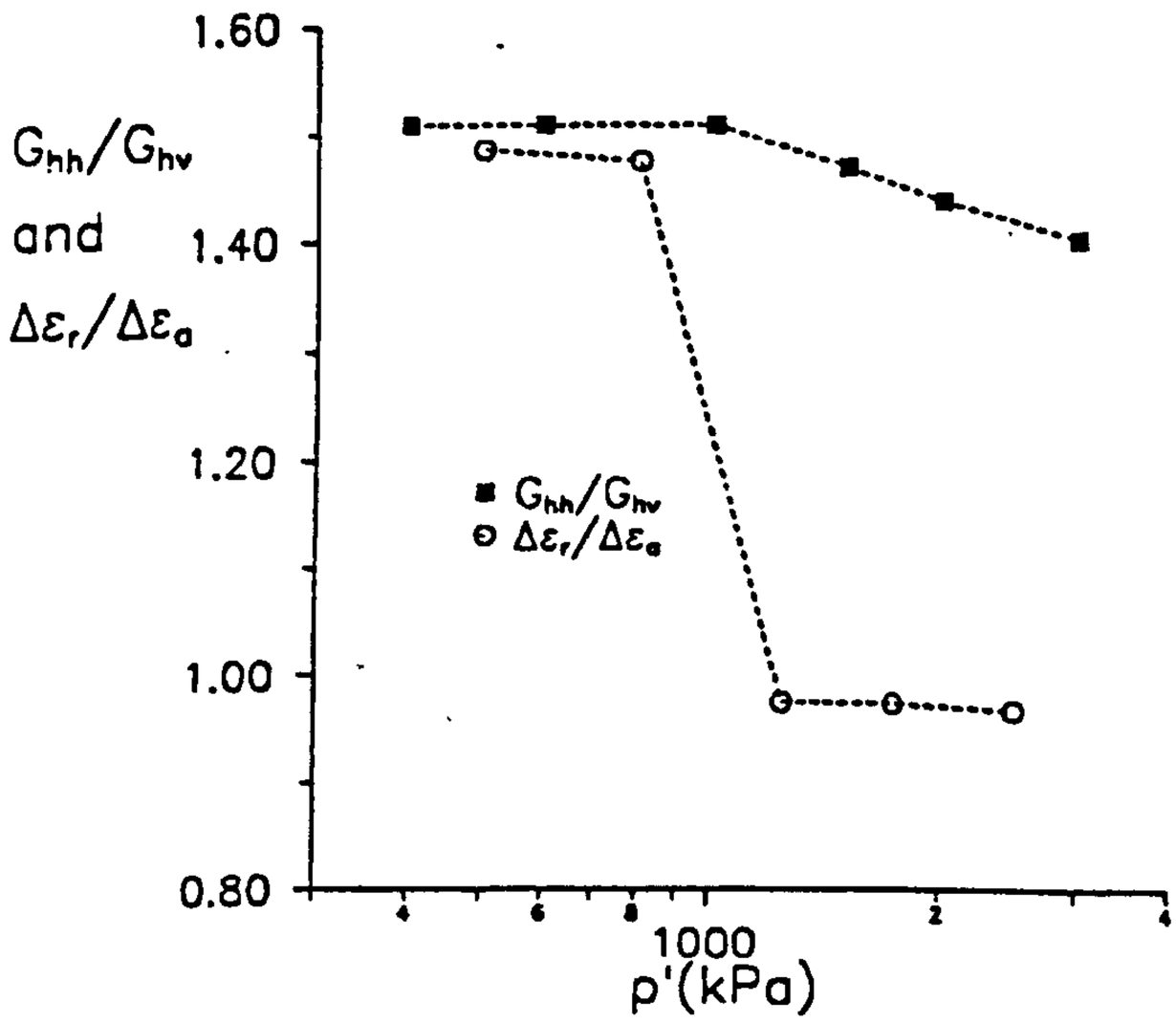

c) Anisotropy of reconstituted samples of London clay under isotropic consolidation

Figure 2.10 Measurement of anisotropic shear moduli on samples of natural and reconstituted London clay (After Jovicic and Coop, 1998)

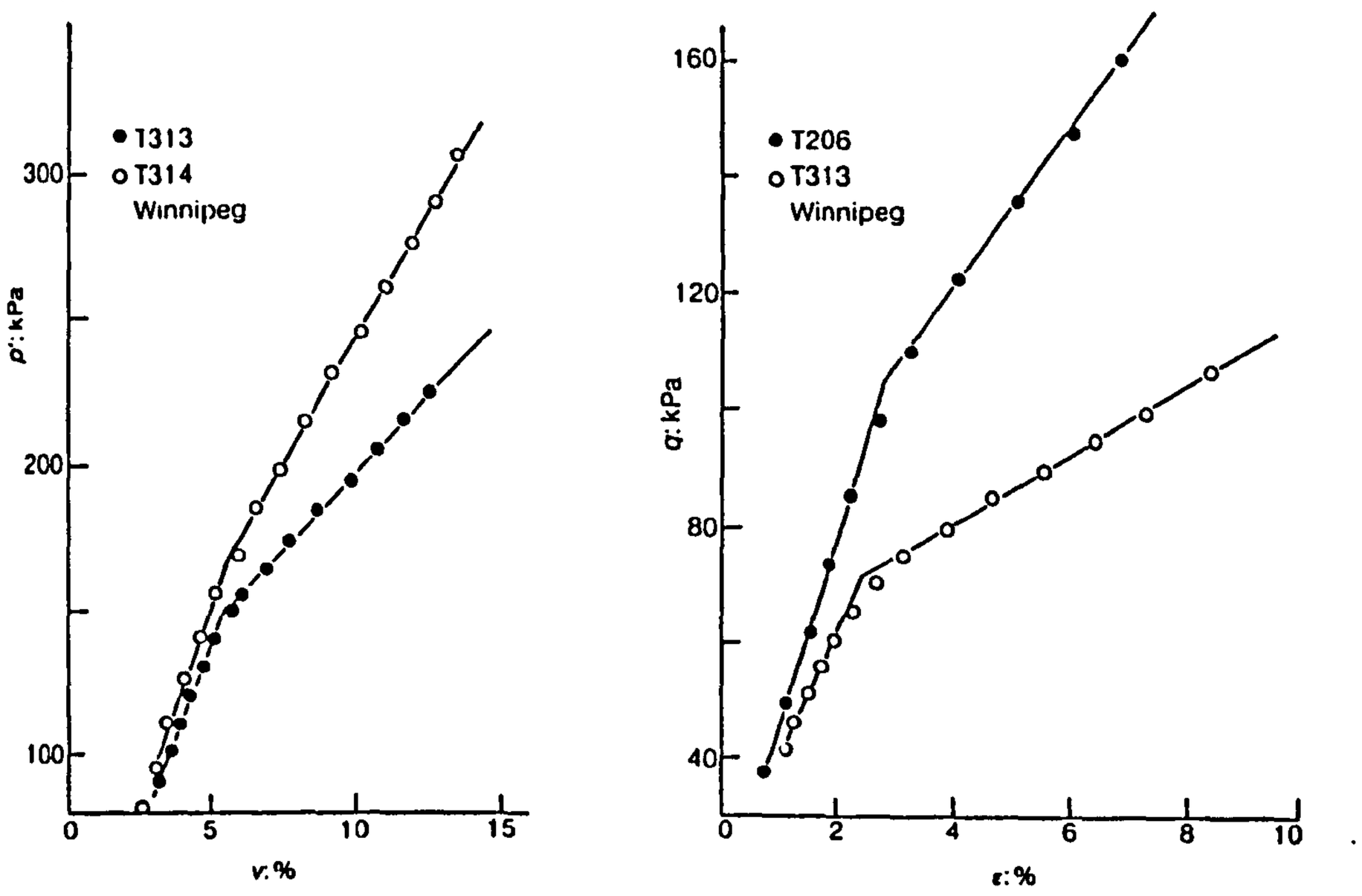

a) Stress-strain curve in p′ *vs.* ε_p space and q *vs.* ε_q space

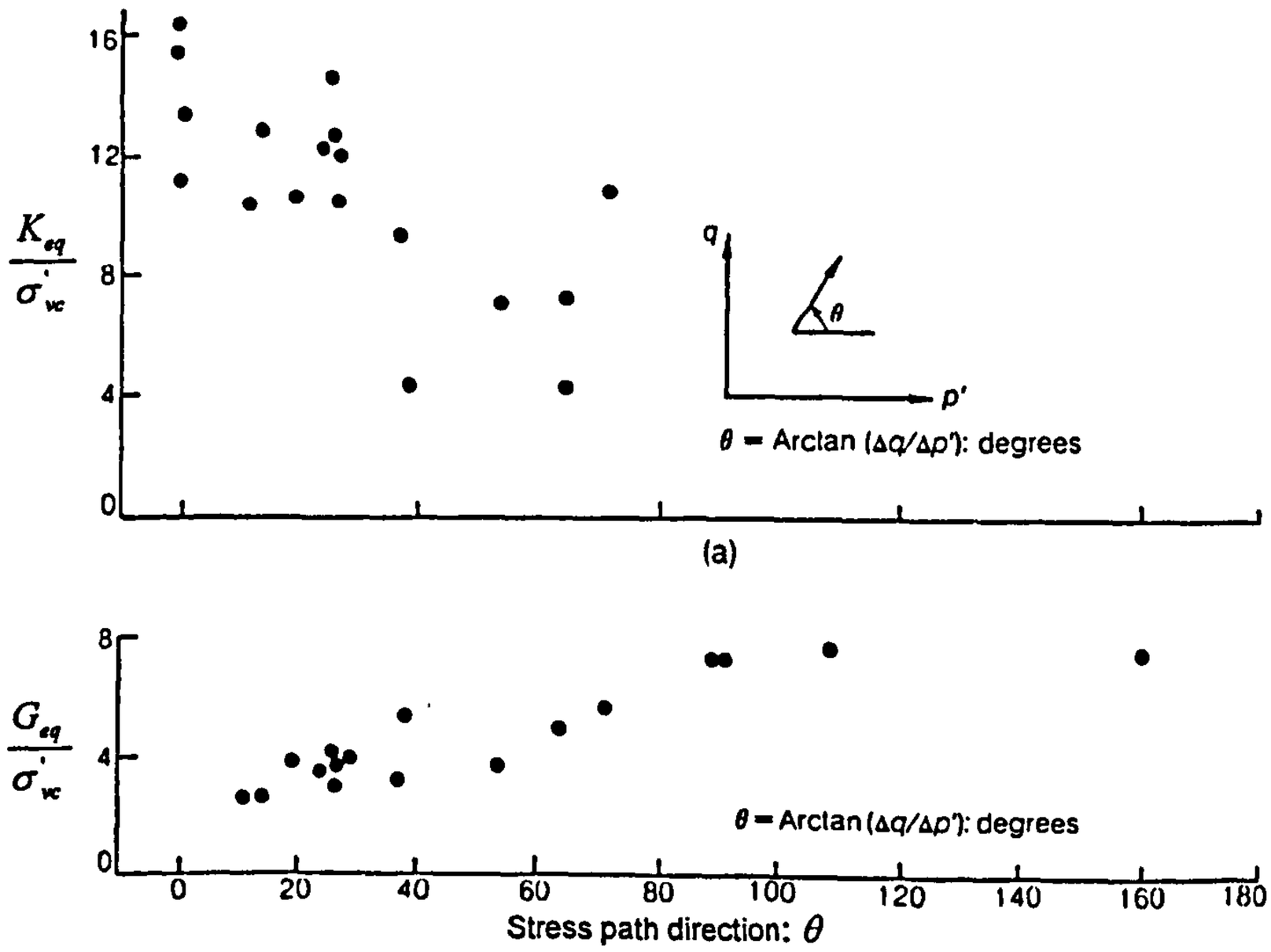

b) Variations of normalised equivalent bulk and shear moduli with stress path direction

Figure 2.11 **Results of triaxial tests on plastic Lake Agassiz clay from Winnipeg (After Graham and Houlsby (1983)**

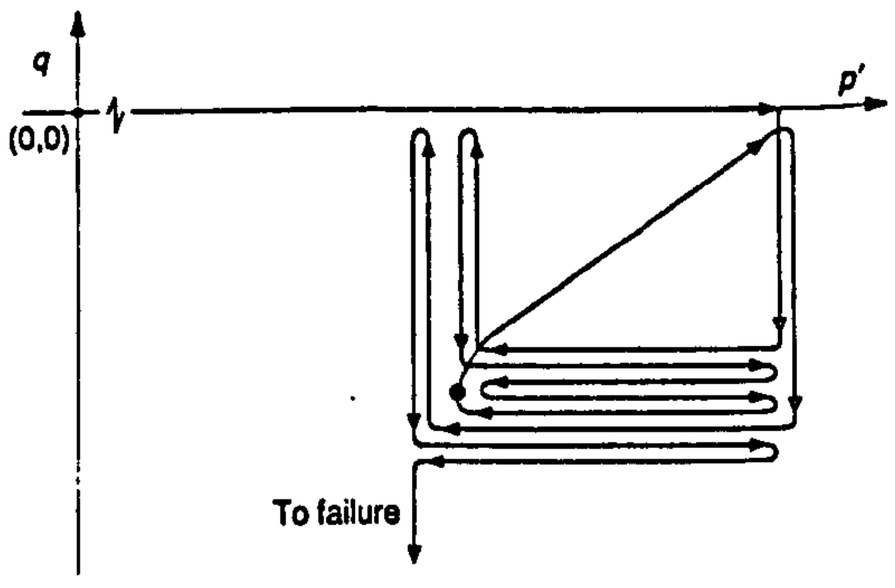

a) Typical schematic triaxial multiple mini stress paths excursions

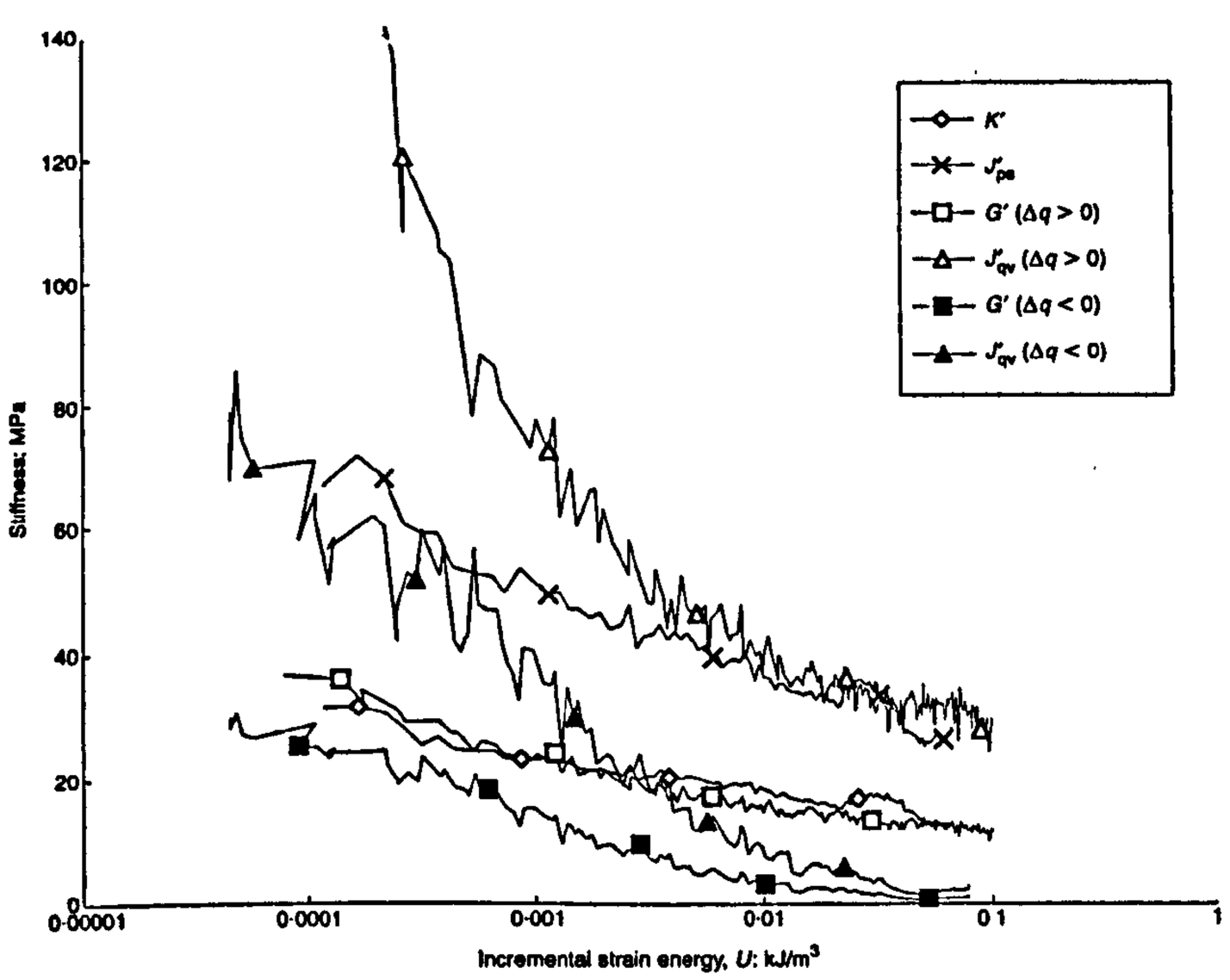

b) Variation of stiffness parameters with incremental strain energy for Test 6

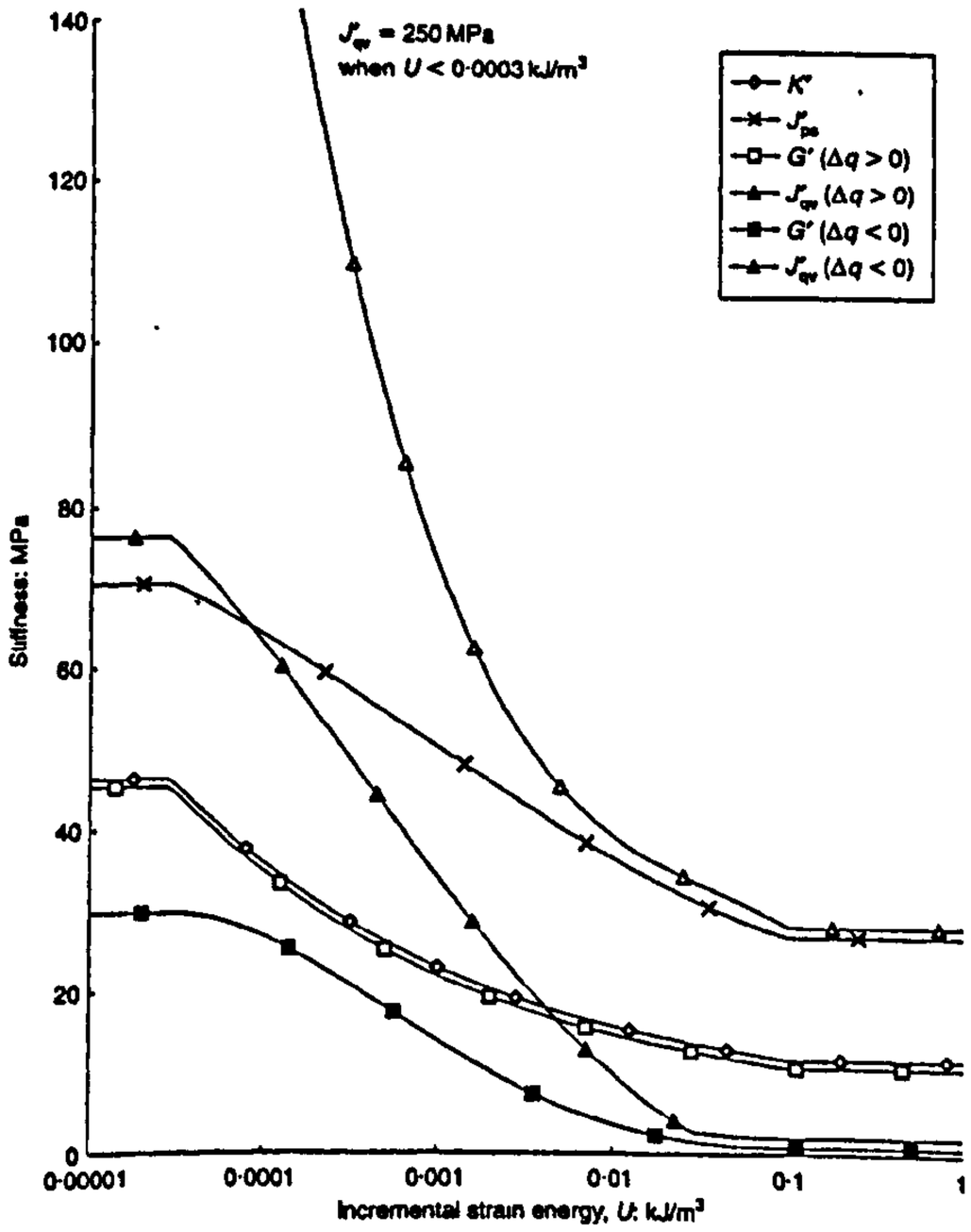

c) Summarised stiffness derived from multiple stress path excursions

Figure 2.12 Triaxial multiple mini stress path test results (after Hird and Pierpoint, 1997)

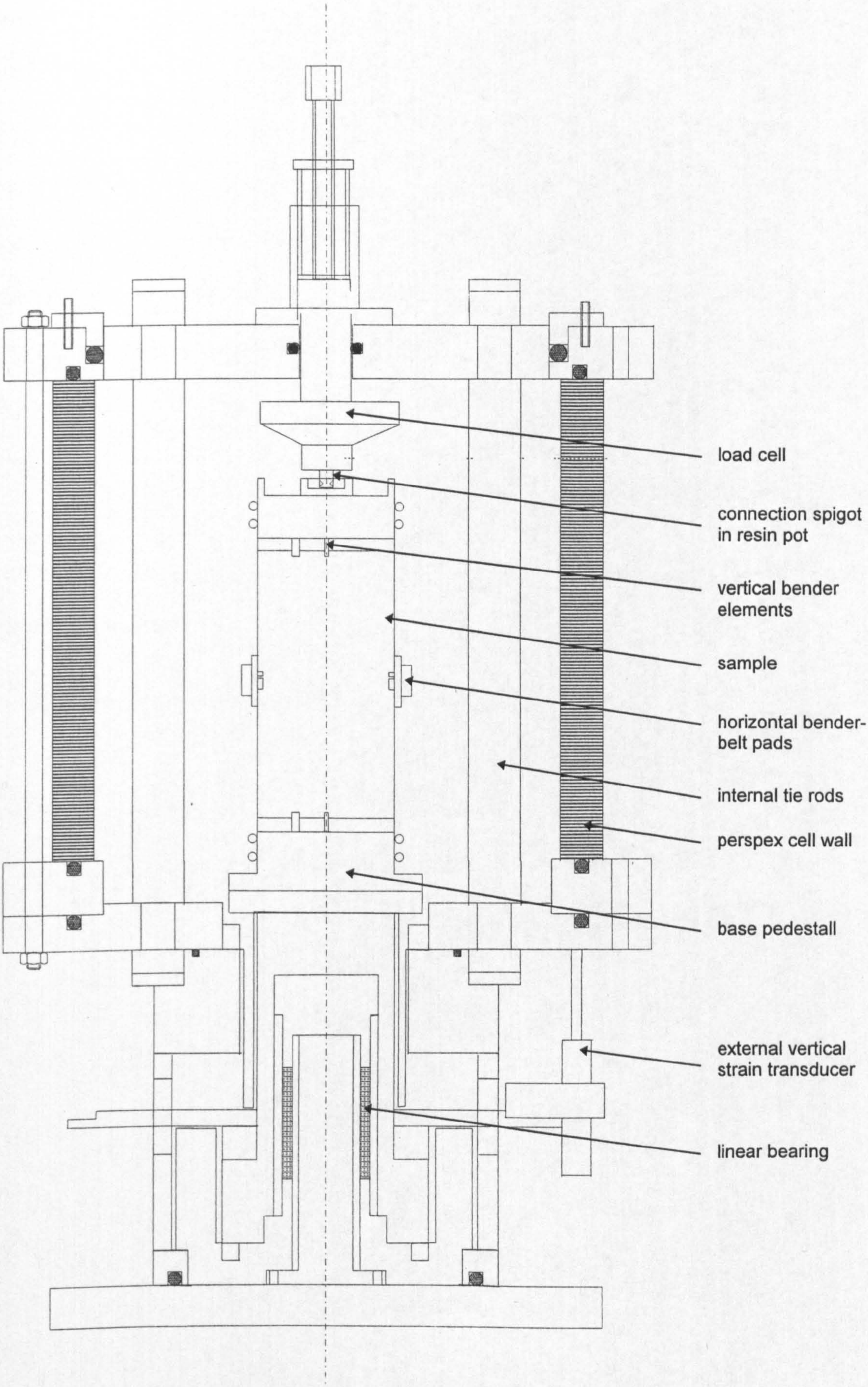

Figure 3.1 General arrangement of 100 mm Stress Path Cell

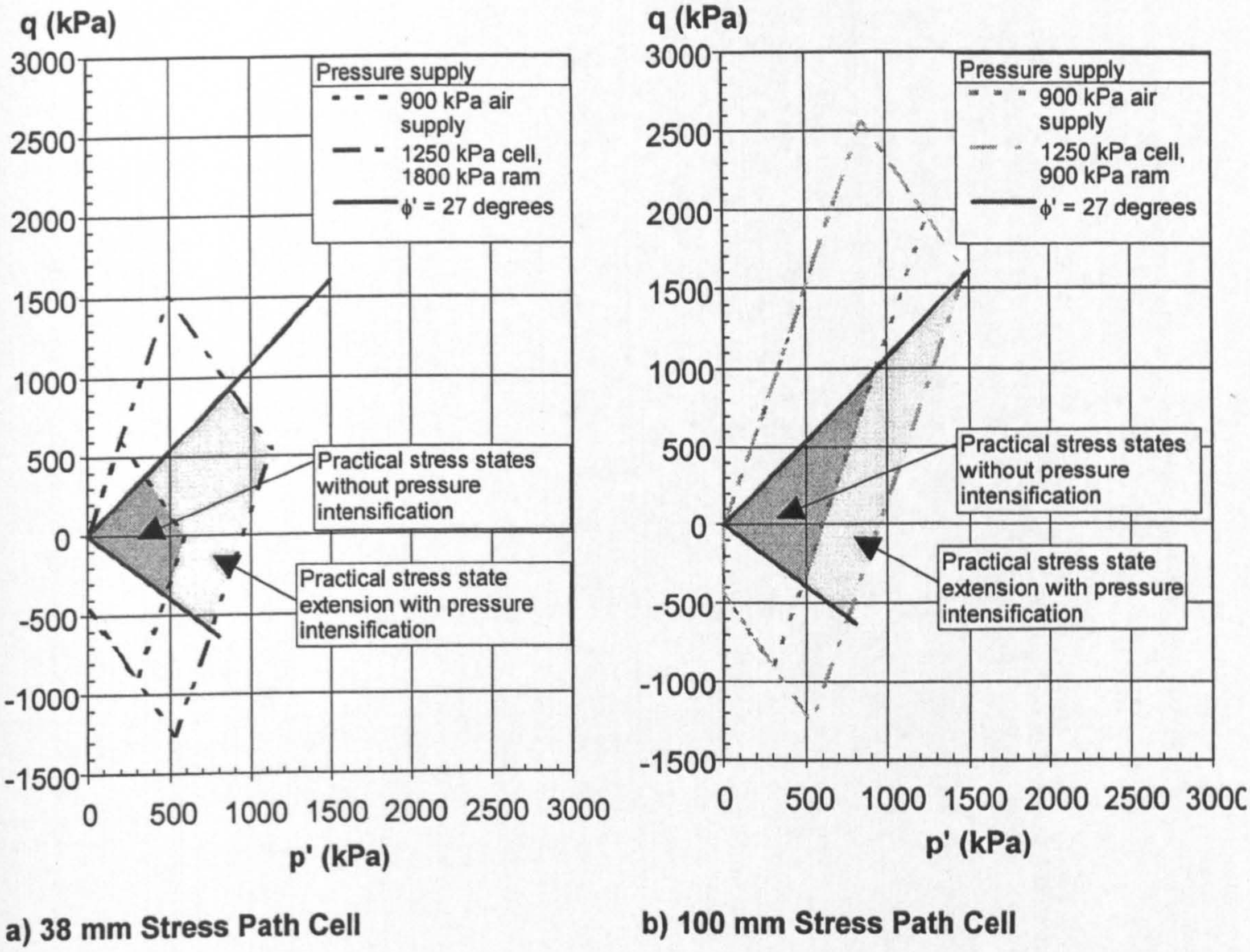

a) 38 mm Stress Path Cell **b) 100 mm Stress Path Cell**

Figure 3.2 Possible stress ranges with 38 and 100 mm stress path cells

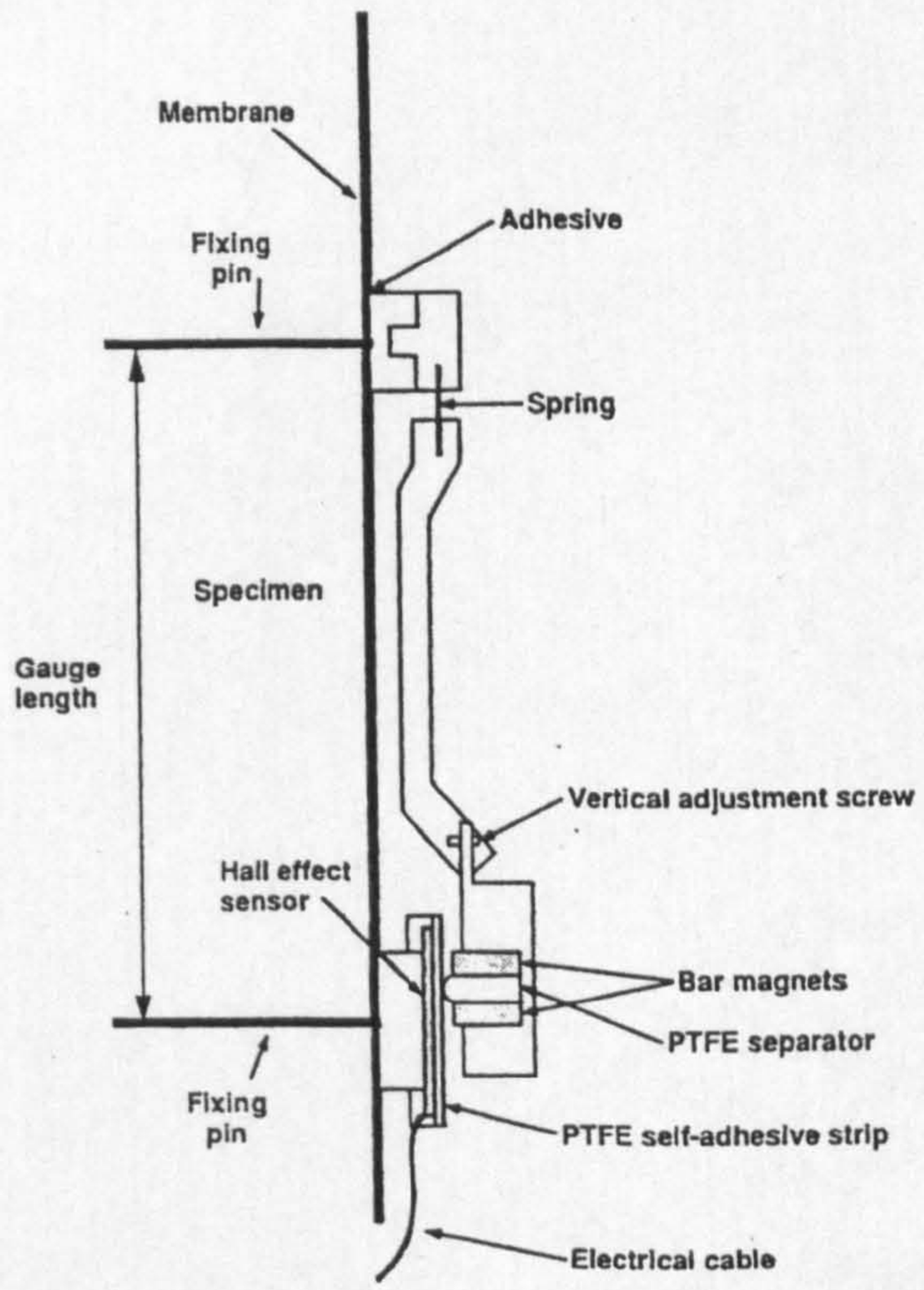

Figure 3.3 Hall effect gauge for axial strain measurement (after Clayton and Khatrush 1986)

Manufacturer	Model	Serial No.	Directly measures...	Rated limit (f.s.d.)	Units	Physical overload limit (%of limit)	Nominal excitation (Vdc)	Nominal output (Vdc)	Accuracy (NLHR % f.s.d.)
Bristol University	n/a	G/0020	temperature	100	Deg C	100	10	0.1	0.5
Druck	PDCR 10	57826	Pressure	1000	kPa	400	10	0.1	0.1
Druck	PDCR 810	193899	Pressure	350	kPa	400	10	0.1	0.1
Druck	PDCR 810	786648	Pressure	1000	kPa	400	10	0.1	0.06
Druck	PDCR 810	786649	Pressure	1000	kPa	400	10	0.1	0.06
Druck	PDCR 810	16731	Pressure	1000	kPa	400	10	0.1	0.1
Druck	PDCR 10	33063	Pressure	2970	kPa	200	10	0.1	0.1
Druck	PDCR 810	167850	Pressure	350	kPa	400	10	0.1	0.1
Druck	PDCR 810	193900	Pressure	700	kPa	400	10	0.07	0.1
Druck	Diff	205701	Pressure	200	kPa	400	10	0.1	0.1
GDS	local vertical	210	Displacement	8	mm	100	10	3.5	0.1
GDS	local vertical	252 RF(211	Displacement	8	mm	n/a	5	3.5	0.1
GDS	horizontal belt	254 (R)	Displacement	8	mm	n/a	5	3.5	0.1
IC	1003	1003	Force	4500	N	100	10	0.04	0.05
IC	1011	1011	Force	4415	N	105	10	0.04	0.05
IC	962	962	Force	27000	N	100	10	0.03	0.05
MPE	HS 25	3346-25	Displacement	25	mm	n/a	10	0.07	0.1
MPE	HS 25	3329-25	Displacement	25	mm	n/a	10	0.07	0.1
MPE	HS 25	3821-25	Displacement	25	mm	nil	10	0.07	0.1
MPE	HS 50	3257-50	Displacement	50	mm	n/a	10	0.04	0.1
MPE	HS 25	3810-25	Displacement	25	mm	n/a	10	0.07	0.1
Newcastle University	n/a	95002	Volume	125	ml	nil	17.5	0.1	0.55
Newcastle University	n/a	95006	Volume	125	ml	nil	17.5	0.1	0.55
RS	n/a	2	Temperature	500	Deg C	n/a	10	0.1	0.1
Transamerica	3040-00	L256590	Pressure	600	kPa	200	10	0.1	0.25
Transamerica	3040-00	L256589	Pressure	600	kPa	200	10	0.1	0.25
Transamerica	n/a	L266008	Pressure	400	kPa	200	10	0.1	0.5

Note: NLHR is the combined Non-linearity, Hysteresis and Repeatability errors.

Figure 3.4 Extract from transducer reference database listing all transducers used in this project

University of Bristol - Geotechnics Research Group - Instrument Calibration Datasheet
Datascan/TRIAX equipment

	NAME
INSTRUMENT:	100mm Triaxial Cell
CAL. BY:	DSP
CAL. AGAINST:	0.001mm Micrometer
ON A/D SYS.:	Right

ATMOS. PRESSURE:	1003	mb
AIR TEMPERATURE:	20	°C
EXCITATION VOLTS:	4.98295	Vdc
DATE:	21/2/97	

CALIBRATION DATA		ERROR INFORMATION		
Channel	14	(Comparison of calibration data and regression		
Units	mm	best-fit line, maxima on first line)		
TRIAX type	LS1	Difference	% error	% of range
Voltage	Measurement	0.002702	-0.024124	0.0196542
1.90271	9.250	0.002	0.023	0.015
1.96858	9.500	-0.002	-0.021	-0.015
2.03347	9.750	-0.002	-0.024	-0.017
2.09707	10.000	0.000	0.002	0.001
2.15840	10.251	0.001	0.005	0.004
2.21810	10.503	0.001	0.007	0.005
2.27553	10.751	0.002	0.021	0.016
2.33102	11.000	0.001	0.005	0.004
2.38585	11.250	0.001	0.006	0.005
2.43939	11.500	0.000	-0.001	-0.001
2.49196	11.750	-0.001	-0.011	-0.009
2.54420	12.000	-0.001	-0.004	-0.004
2.59547	12.250	-0.002	-0.015	-0.013
2.64673	12.500	-0.002	-0.013	-0.011
2.69800	12.750	-0.001	-0.004	-0.004
2.74959	13.000	0.002	0.012	0.012
2.80151	13.251	0.003	0.020	0.020
2.85342	13.501	0.002	0.013	0.013
2.90534	13.750	-0.003	-0.020	-0.020

REGRESSION DATA	
Gain setting	2
Filter (bits)	16
High range	100
Low range	96

Calibration range		
	Volts	Measurement
Min	1.90271	9.25
Max	2.90534	13.75
Range	1.00263	4.5

Statistical analysis		
Required order of regression:		4
Coefficient	Value	Std .error
c	-8.9047	2.417557
m1	27.341919	4.093284
m2	-18.073014	4.093284
m3	5.866660	0.719675
m4	-0.6751546	0.074750551
R squared	0.9999986	
Std. error "y"	0.001863	

TRANSDUCER INFORMATION	
Serial number	252 RF(211)
Manufacturer	GDS
Model	Local vertical
Rated limit in mm	8
Physical o/load (% of limit)	n/a
Nominal output (Vdc)	3.5
Accuracy: as % f.s.d	0.1
in units	0.008

Illustration of full range and centre range calibration for vertical local strain Hall effect transducer

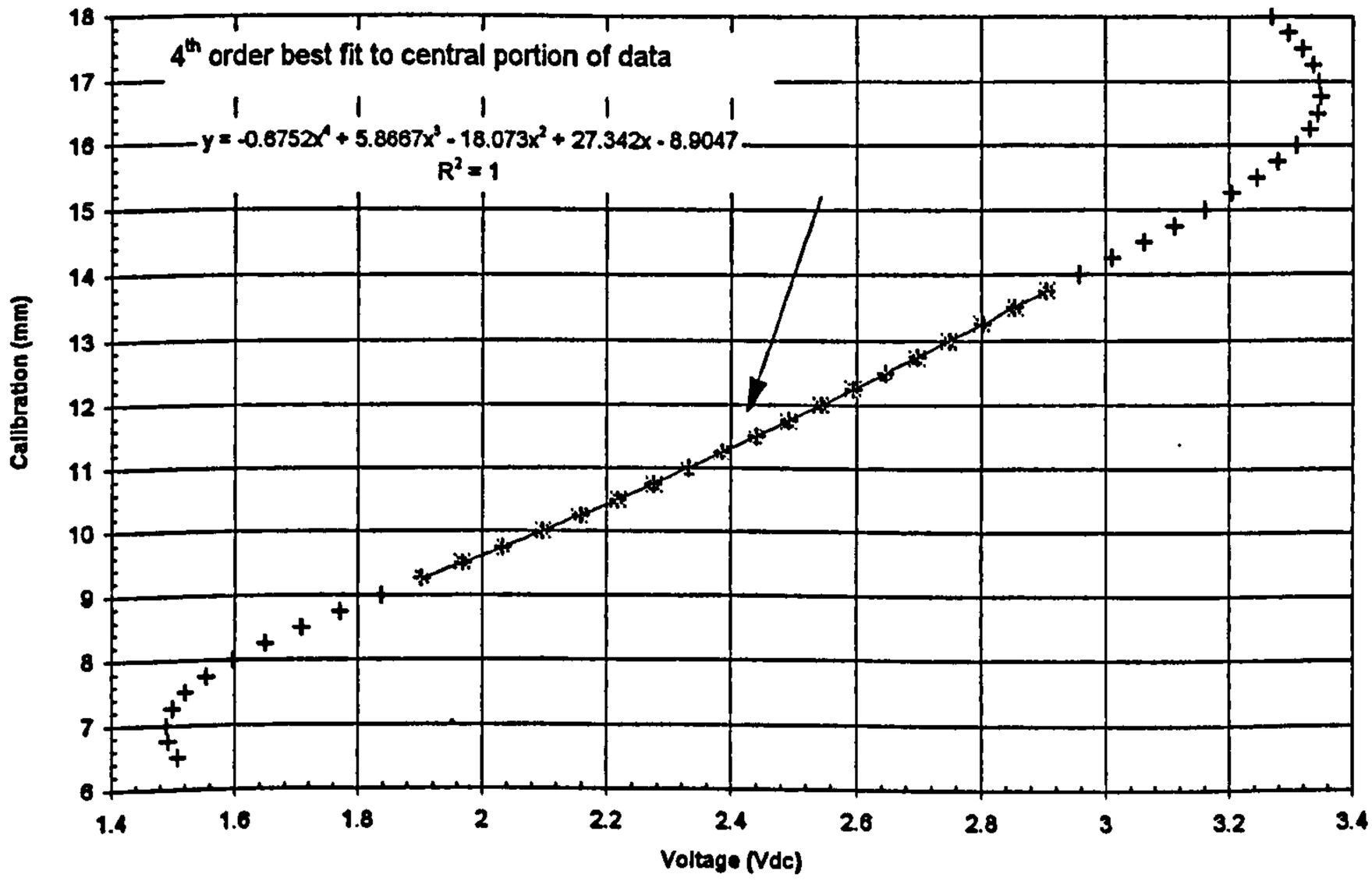

Figure 3.5 Illustrative calibration: Local vertical strain Hall effect transducer

University of Bristol - Geotechnics Research Group - Instrument Calibration Datasheet
Datascan/TRIAX equipment

	NAME
INSTRUMENT:	100mm Triaxial Cell
CAL. BY:	DSP
CAL. AGAINST:	0.01mm Micrometer
ON A/D SYS.:	Right

ATMOS. PRESSURE:	1003	mb
AIR TEMPERATURE:	20	°C
EXCITATION VOLTS:	4.98295	Vdc
DATE:	21/2/97	

CALIBRATION DATA		ERROR INFORMATION		
Channel	11	(Comparison of calibration data and regression		
Units	mm	best-fit line, maxima on first line)		
TRIAX type	RS	Difference	% error	% of range
Voltage	Measurement	-0.004607	-0.004757	-0.004637
3.0218	96.610	0.003	0.003	0.003
2.9115	96.860	-0.005	-0.005	-0.005
2.8015	97.110	-0.002	-0.002	-0.002
2.6928	97.360	0.003	0.003	0.003
2.5861	97.610	0.003	0.003	0.003
2.4790	97.860	0.000	0.000	0.000
2.3687	98.110	-0.001	-0.001	-0.001
2.2544	98.360	-0.002	-0.002	-0.002
2.1354	98.610	-0.002	-0.002	-0.002
2.0101	98.860	0.001	0.001	0.001
1.8816	99.110	0.003	0.004	0.003
1.7561	99.360	-0.002	-0.002	-0.002

REGRESSION DATA	
Gain setting	2
Filter (bits)	16
High range	100
Low range	96

Calibration range		
	Volts	Measurement
Min	1.75605	96.61
Max	3.02183	99.36
Range	1.26578	2.75

Statistical analysis		
Required order of regression:		4
Coefficient	Value	Std .error
c	109.7932	1.886830
m1	-15.383926	3.258796
m2	9.466534	3.258796
m3	-2.888672	0.587845
m4	0.31868415	0.061440631
R squared	0.999991	
Std. error "y"	0.003296	

TRANSDUCER INFORMATION	
Serial number	254 (R)
Manufacturer	GDS
Model	Radial Belt
Rated limit in mm	8
Physical o/load (% of limit)	n/a
Nominal output (Vdc)	3.5
Accuracy: as % f.s.d	0.1
in units	0.008

Illustration of full range and centre range calibration for horizontal strain Hall effect transducer belt

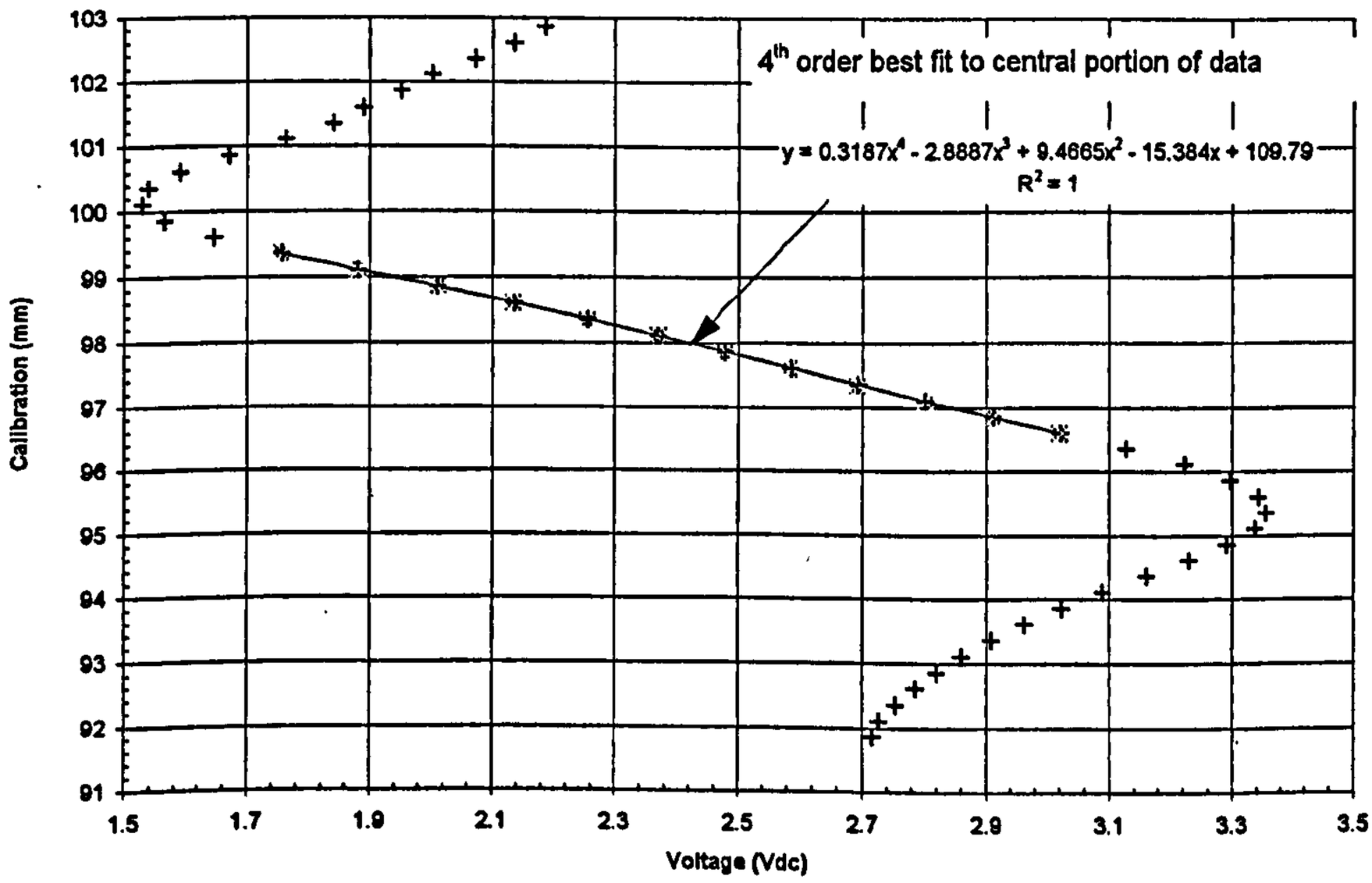

Figure 3.6 Illustrative calibration: Horizontal belt strain transducer

University of Bristol - Geotechnics Research Group - Laboratory Instrument Calibration
Apparatus specific summary - Datascan/TRIAX equipment

Apparatus:	Stress Path Cell
A/D unit:	Right
Date:	21/2/97
Nominal Sample diameter:	100 mm
Nominal Sample Height:	200 mm

Mean excitation voltage for all transducers: 4.982903 V dc Range: 0.00065 Vdc

Output voltage range (+/-Vdc)	0.02	0.15	1.3	10.0
A/D conv'sn resolution (μV dc) @16 bits	0.63	5	40	320
@14 bits	2.5	20	160	1280

Ch.	Channel Description	TRIAX type	Units	Transducer serial no.	Nat'l units	Rated limit	NLHR errors % f.s.d.	NLHR errors Nat'l units	Calibrated Range (units)	Output volts over cal. range	a B.S.L. calibration (units/mV)	b Transducer constant 'k' +/-	c Lowest resolution (units)	d Max. excitation variation effect (+/-units)	e Max. error in A/D conv's'n (+/-units)	f 'Std. error' in regression fit (+/-units)
1	Power Supply	PS	Vdc						0							
2	Load-cell	LC	N	962	N	27000	0.05	13.500	1550	0.00403	-383.9352	1913130.1	0.2419	0.2419	2.9026	5.8051
3	Cell Press.	CP	kPa	16731	kPa	1000	0.10	1.000	900	0.04489	-20.0501	99908.7	0.0126	0.0632	0.3158	0.6316
4	Back Press.	BP	kPa	167850	kPa	350	0.10	0.350	300	0.04271	-7.0203	34982.0	0.0044	0.0265	0.1106	0.6148
5	Displ. Trans.	DT	mm	3257-50	mm	50	0.10	0.050	22	0.00782	-2.8159	14031.6	0.0018	0.0035	0.0248	0.0142
6	Temperature	TMP	Deg	G/0020	Deg C	100	0.50	0.500	42.7	0.01440	-2.9663	14781.1	0.0019	0.0019	0.0299	0.0617
7	Atmosp. Press.	ATM	kPa	L266008	kPa	400	0.50	2.000	8	0.00319	-2.4202	12059.9	0.0121	0.0121	0.0484	0.0121
8	Pore Press.	PP	kPa	193900	kPa	700	0.10	0.700	300	0.02142	-14.0058	69790.4	0.0088	0.0265	0.1588	0.5912
9	Volume Gauge	VG	ml	95006	ml	125	0.55	0.688	122	0.01003	-12.1593	60589.1	0.0077	0.0153	0.1072	0.046
10	Diff. Press.	DIFF	kPa	205701	kPa	200	0.10	0.200	31	0.00770	-4.0317	20089.9	0.0025	0.0025	0.0356	0.0838
11	Horizontal strain	RS	mm	254 (R)	mm	8	0.10	0.008	2.75	1.26578	-0.0022	10.9082	0.0007	0.0007	0.0035	0.0035
12	Vol. Trans.	VT	ml	3810-25	mm	25	0.10	0.025	20	0.02653	0.7542	3757.9	0.0019	0.0019	0.0132	0.0094
13	Ram Press.	RP	kPa	33063	kPa	2970	0.10	2.970	1050	0.01774	-59.1892	294934.1	0.0373	0.0746	0.6339	0.8204
14	Local Strain 1	LS1	mm	252 RF(211)	mm	8	0.10	0.008	5.25	1.15838	-0.0046	22.9325	0.0015	0.0015	0.0074	0.0044
15	Local Strain 2	LS2	mm	210	mm	8	0.10	0.008	5	1.07369	-0.0047	23.4292	0.0015	0.0015	0.0075	0.0075
16	Supply press.	SP	kPa	L256589	kPa	600	0.25	1.500	1000	0.08137	12.3178	61378.3	0.0616	0.0616	0.4311	3.2642

Notes

1 Shaded lines are the summary lines for the sample calibrations presented in Figure 3.5 and 3.6

2 'NLHR errors' are the combined Non-linearity, Hysteresis and Repeatability errors as given in the transducer manufacturer's literature.

3 Columns 'a', 'b','c', 'd' and 'e' use 1st order regressions ('Best Straight Lines'). This data will be approximately representative where higher orders of regression are used by TRIAX for conversion to engineering units.

4 In column 'b', constant 'k' is given by equation "Calibration line gradient=k/Excitation voltage". This value should be reasonably constant for a particular combination of transducer and instrument.

5 Column 'd' assumes excitation variation equal to the excitation resolution @ 16 bits. This has been found to be representative.

6 Column 'f' gives the statistical standard error in data resulting from conversion using the regression chosen on the datasheet (not necessarily 1st order).

7 'd', 'e' and 'f' are rounded to the nearest whole multiple of the resolution.

Figure 3.7 Transducer calibration summary for "Right" workstation

Triaxial test data Test No. Rdrift start 2/5/96 Test Data File RDRIFT

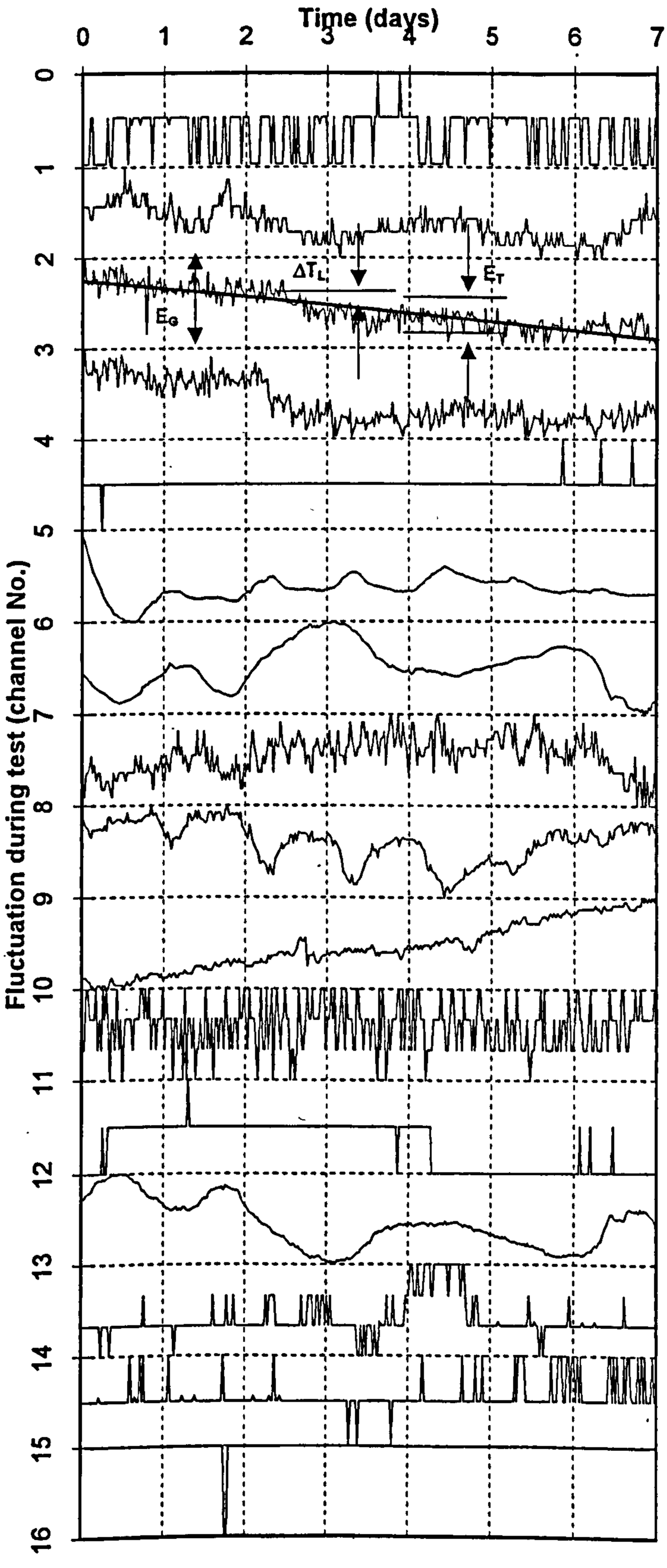

Channel	Type /unit	Errors (units) E_T Typical	E_G Gross	ΔT_L Long term drift
1	Vdc	0.0007	0.0007	0.0000
2	LC kPa 100mm	0.07	0.22	0.0110
3	CP kPa	0.11	0.32	0.0302
4	BP kPa	0.08	0.25	0.0215
5	DT mm	0.002	0.002	0.0000
6	TMP deg	0.39	1.28	-0.0157
7	ATM kPa	n/a	3.24	n/a
8	PP kPa	0.04	0.11	-0.0025
9	VG ml	0.07	0.10	0.0043
10	DP kPa	0.05	0.25	-0.033
11	RS mm	0.006	0.010	0.0000
12	VT mm	0.003	0.006	0.0005
13	RP kPa		3.56	0.2795
14	LS1	0.002	0.005	-0.0001
15	LS2	0.002	0.003	-0.0001
16	SP		918.9	

Figure 3.8 Data from seven day drift test on "Right" work station

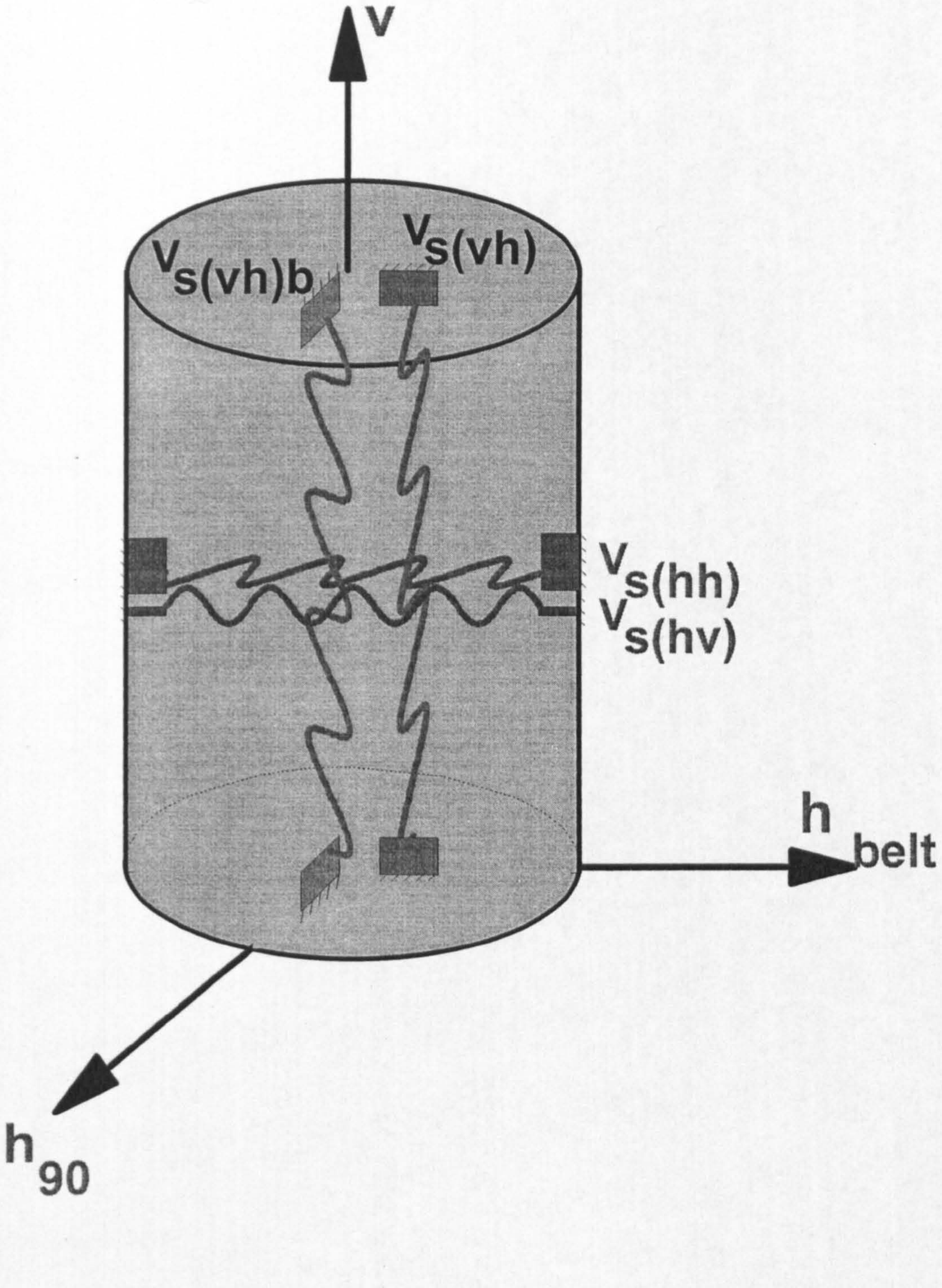

Figure 3.9 Bender arrangement used to measure cross-anisotropic shear moduli

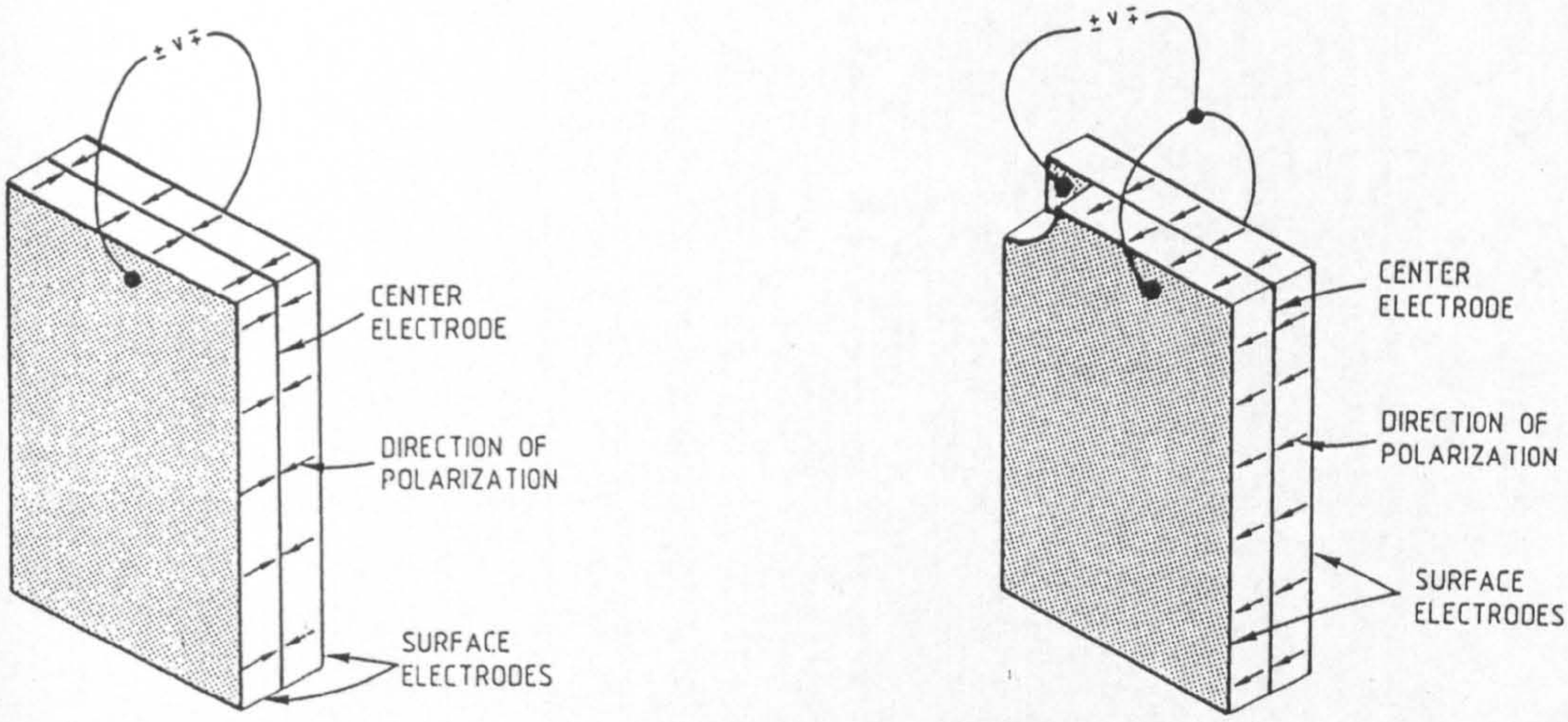

a) Series connected

b) Parallel connected

Figure 3.10 Illustration of the differences between series and parallel poled bender elements (after Dyvik & Madshus (1985)

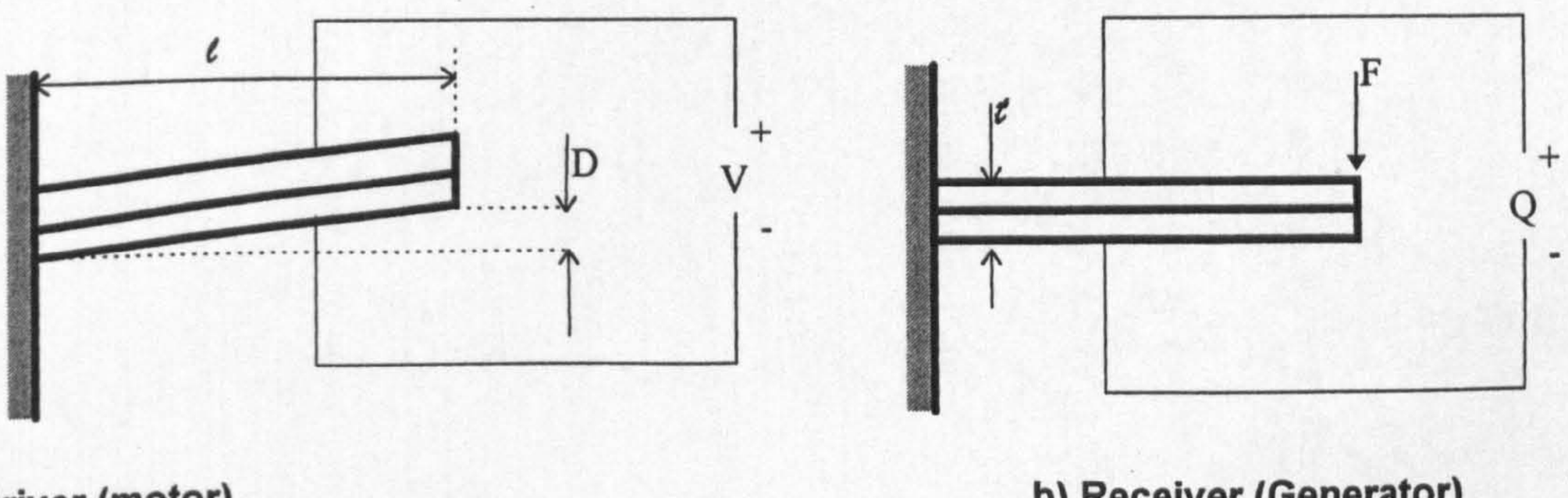

a) Driver (motor)

b) Receiver (Generator)

Figure 3.11 Notation for operation of PZT-5B in cantilever mode

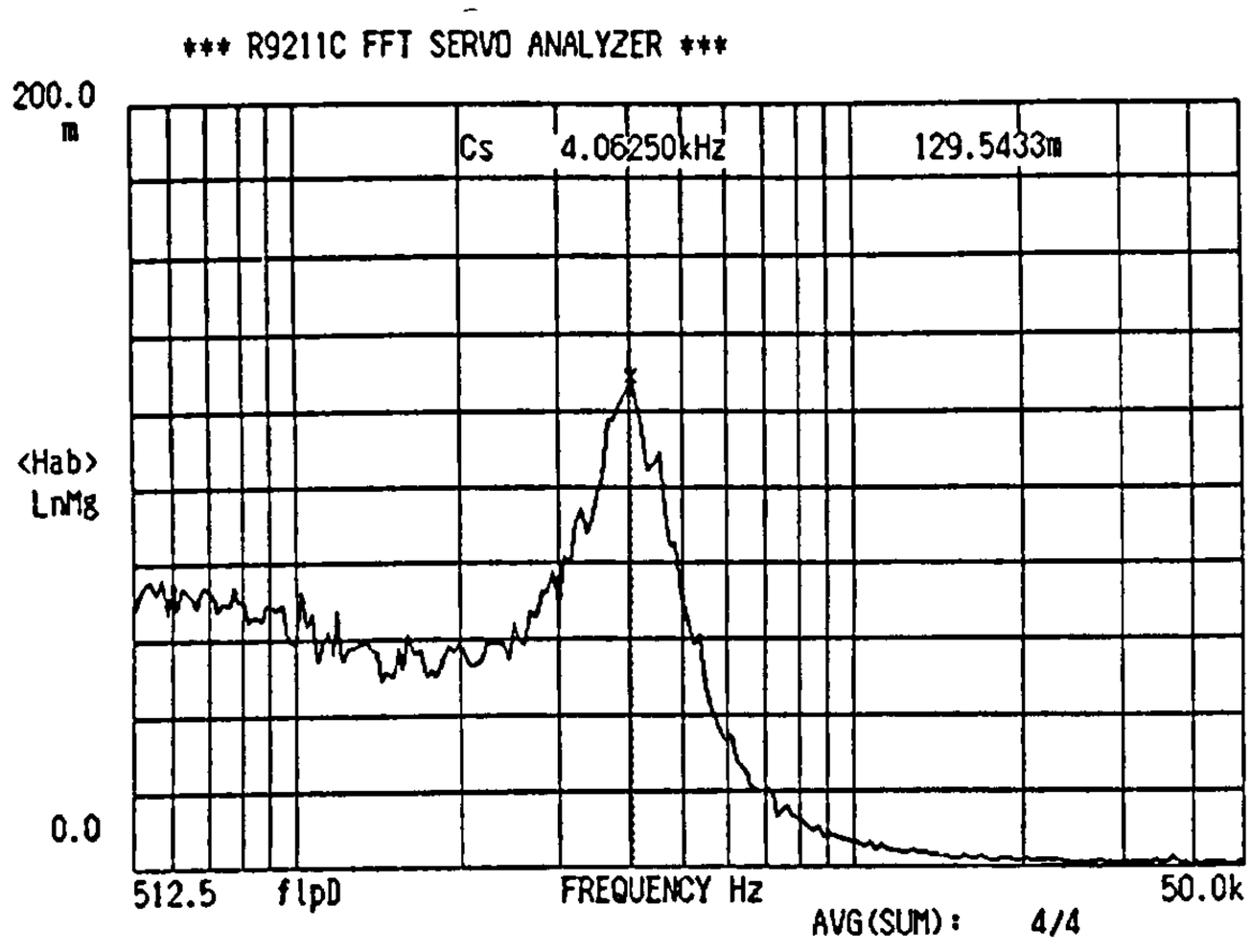

a) "Standard" probes

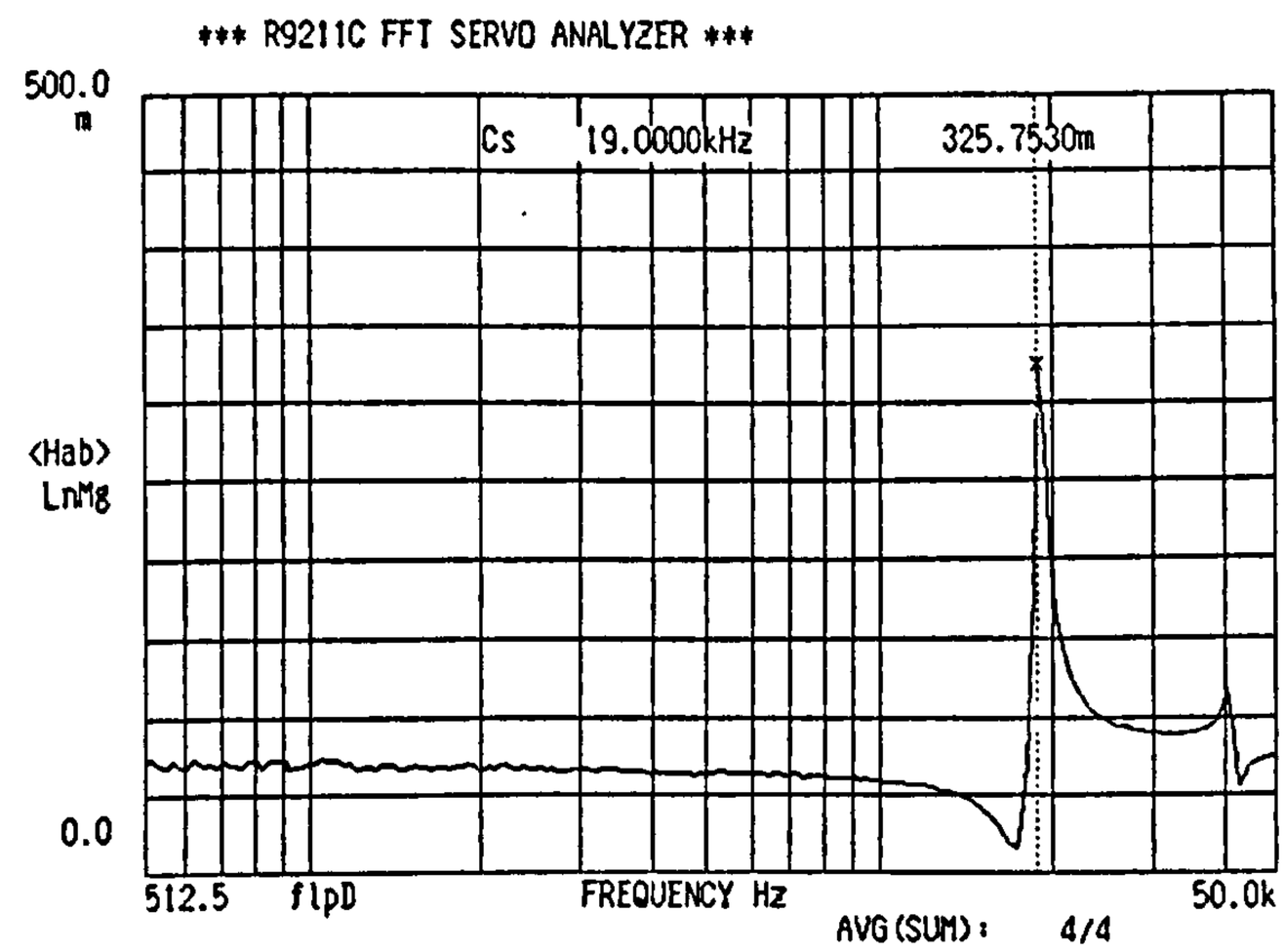

b) "Mini" probes

Figure 3.12 Response spectra for "standard" and "mini" bender probes.

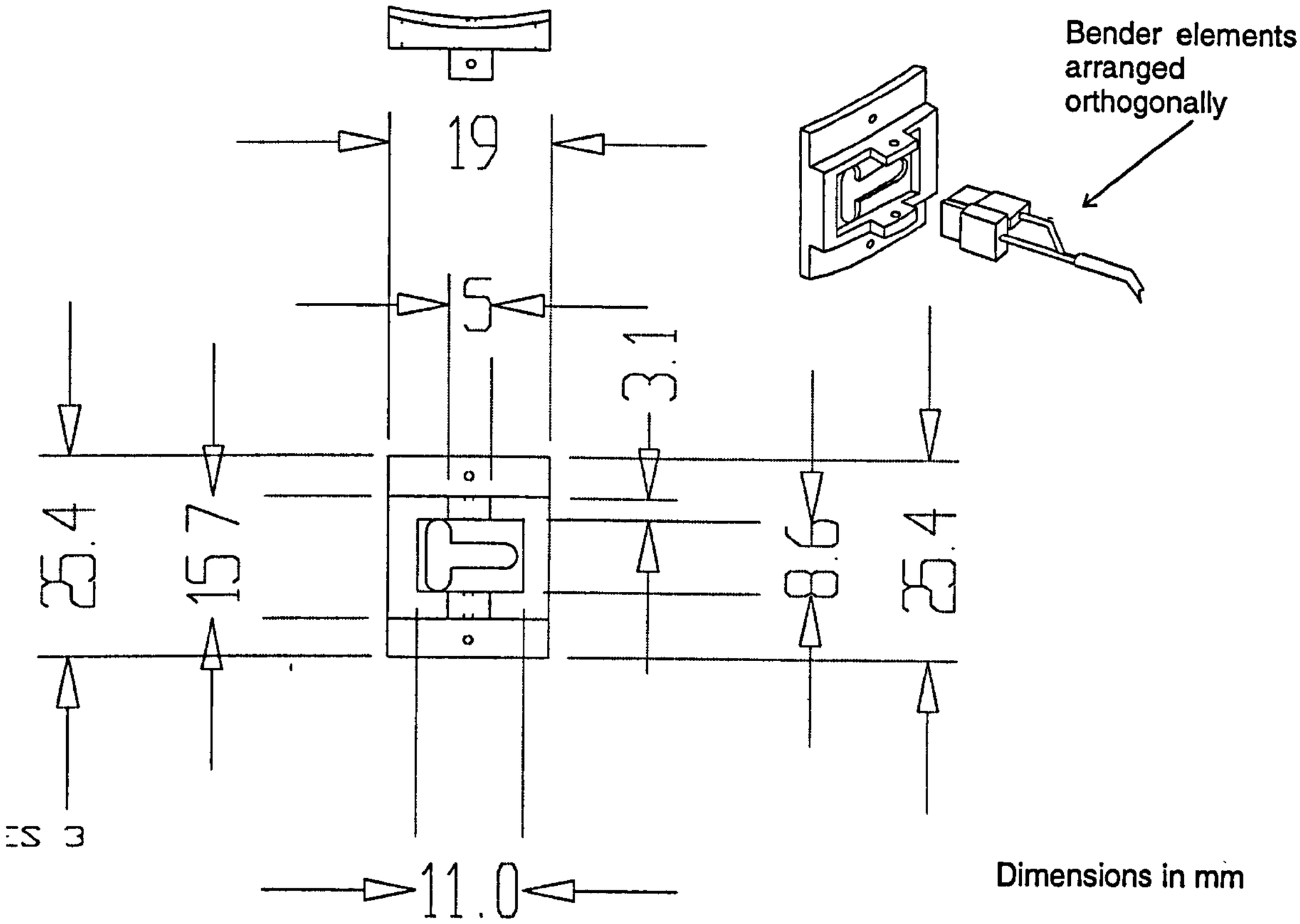

a) Pad design and general arrangement showing manner of inclusion of bender elements

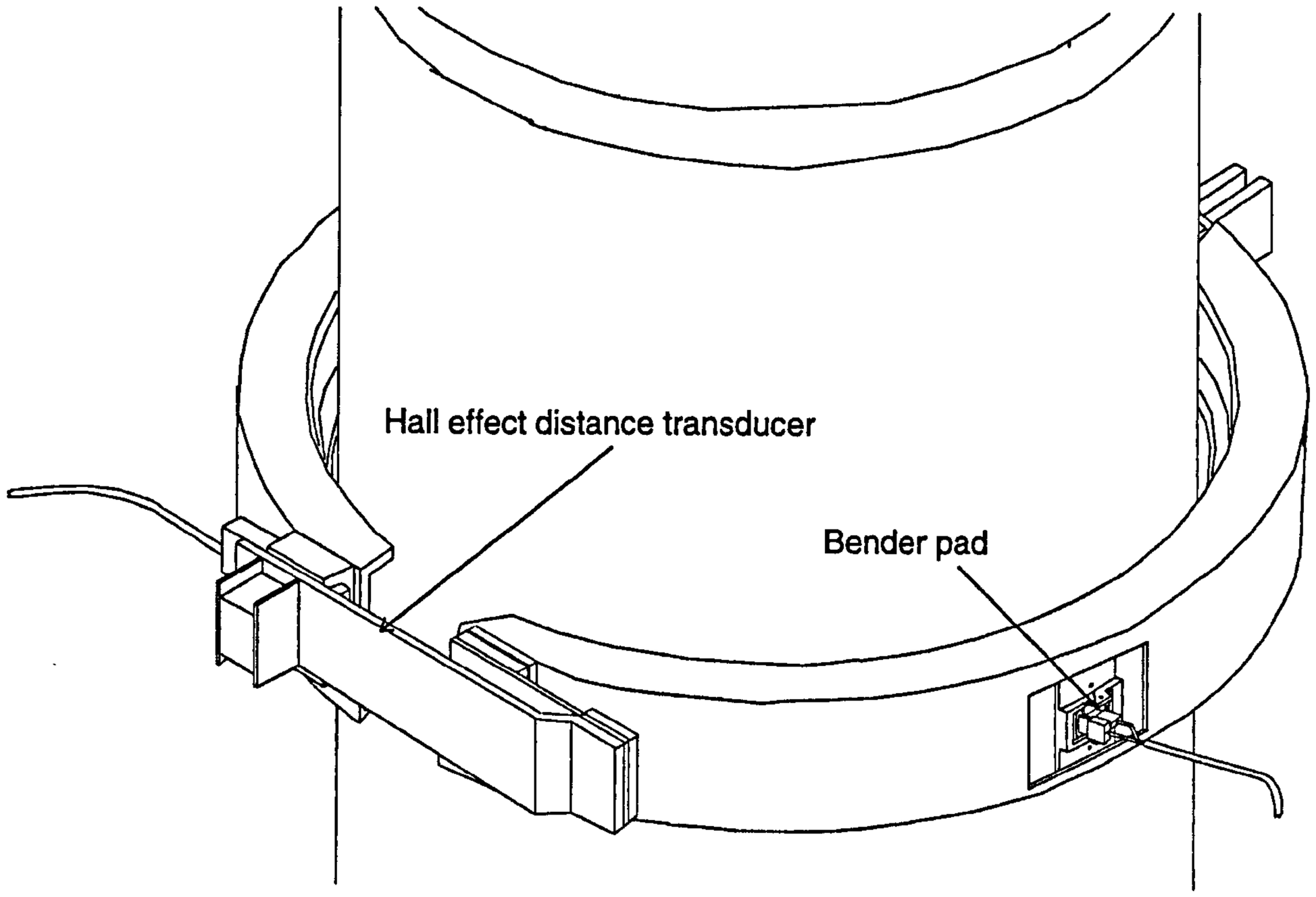

b) General arrangement showing bender pads in bender belt

Figure 3.13 Bender belt design

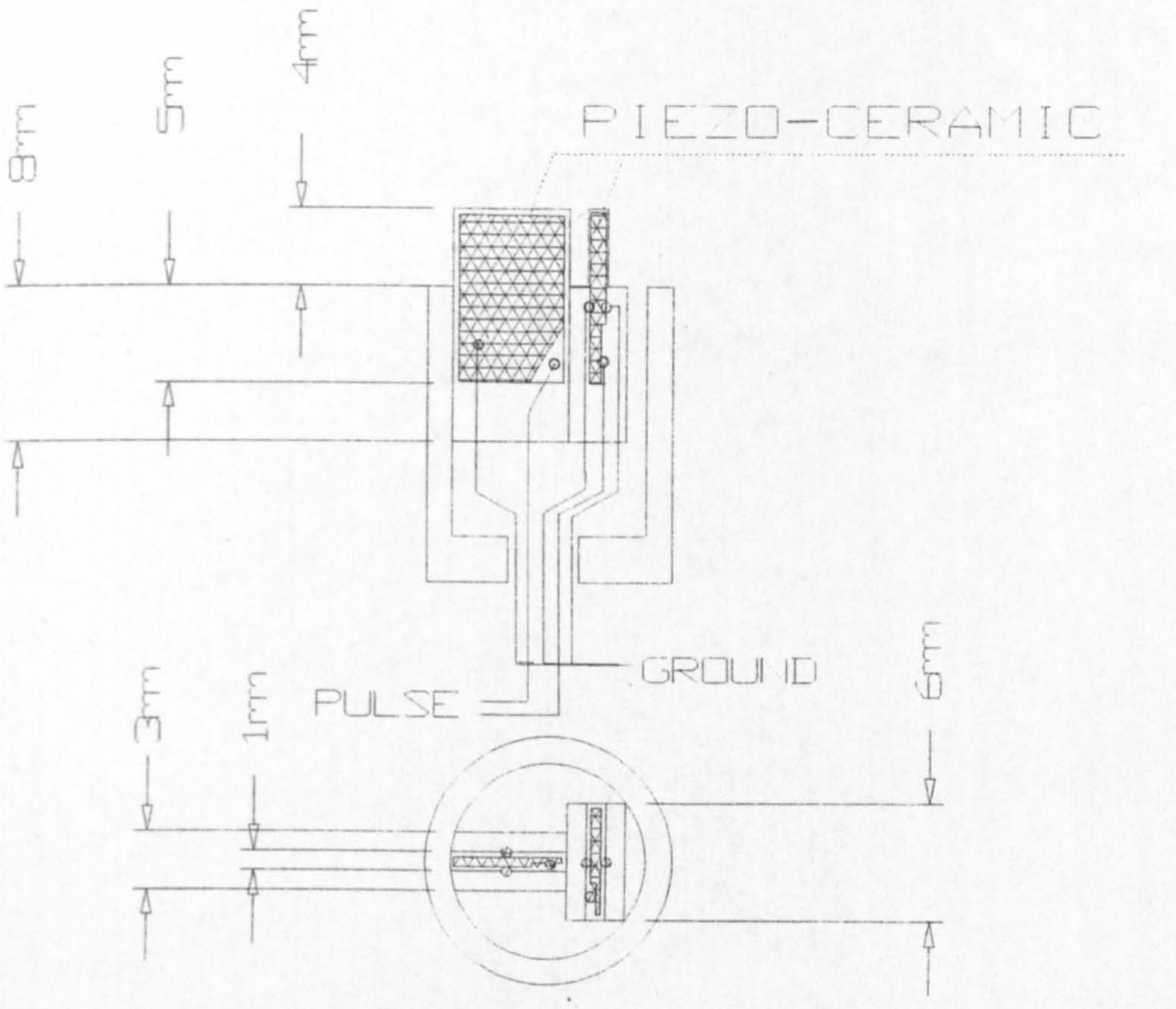

Figure 3.14 Connection details for a driver element

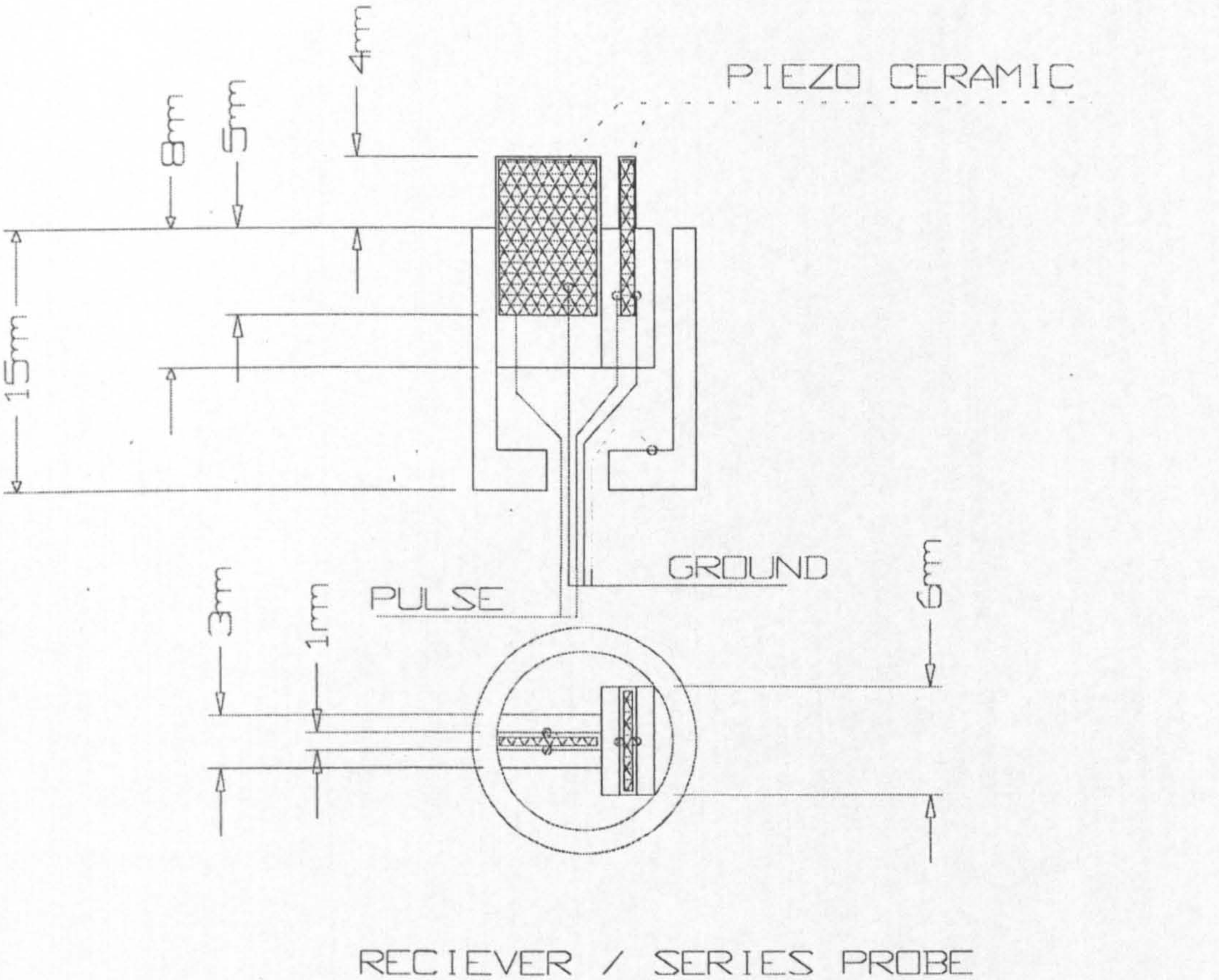

Figure 3.15 Connection details for a series poled receiver element

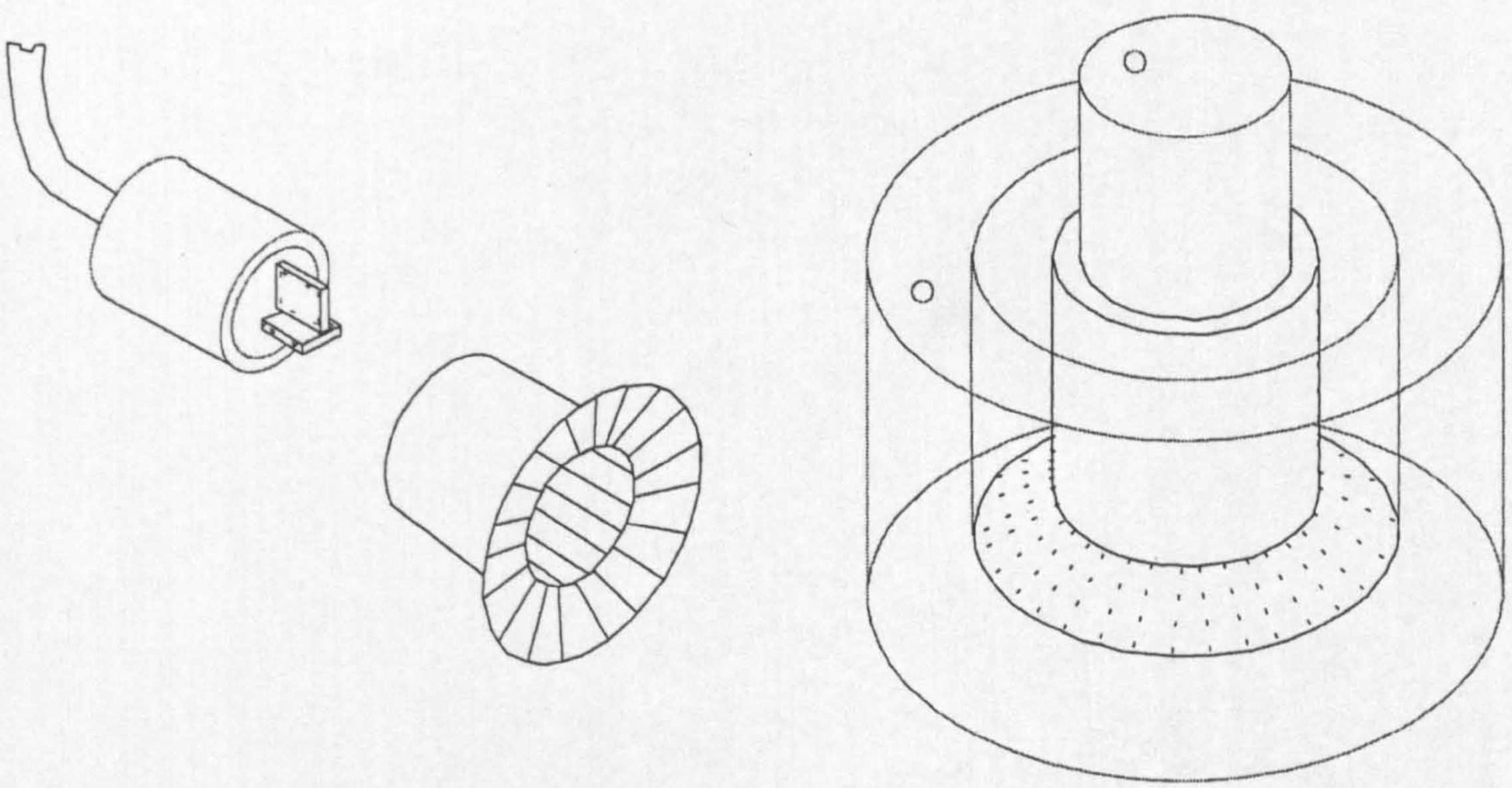

a) General arrangement with rubber grommet b) Detail of grommet fabrication mould

Figure 3.16 Bender probe and rubber grommet used for installing on triaxial samples

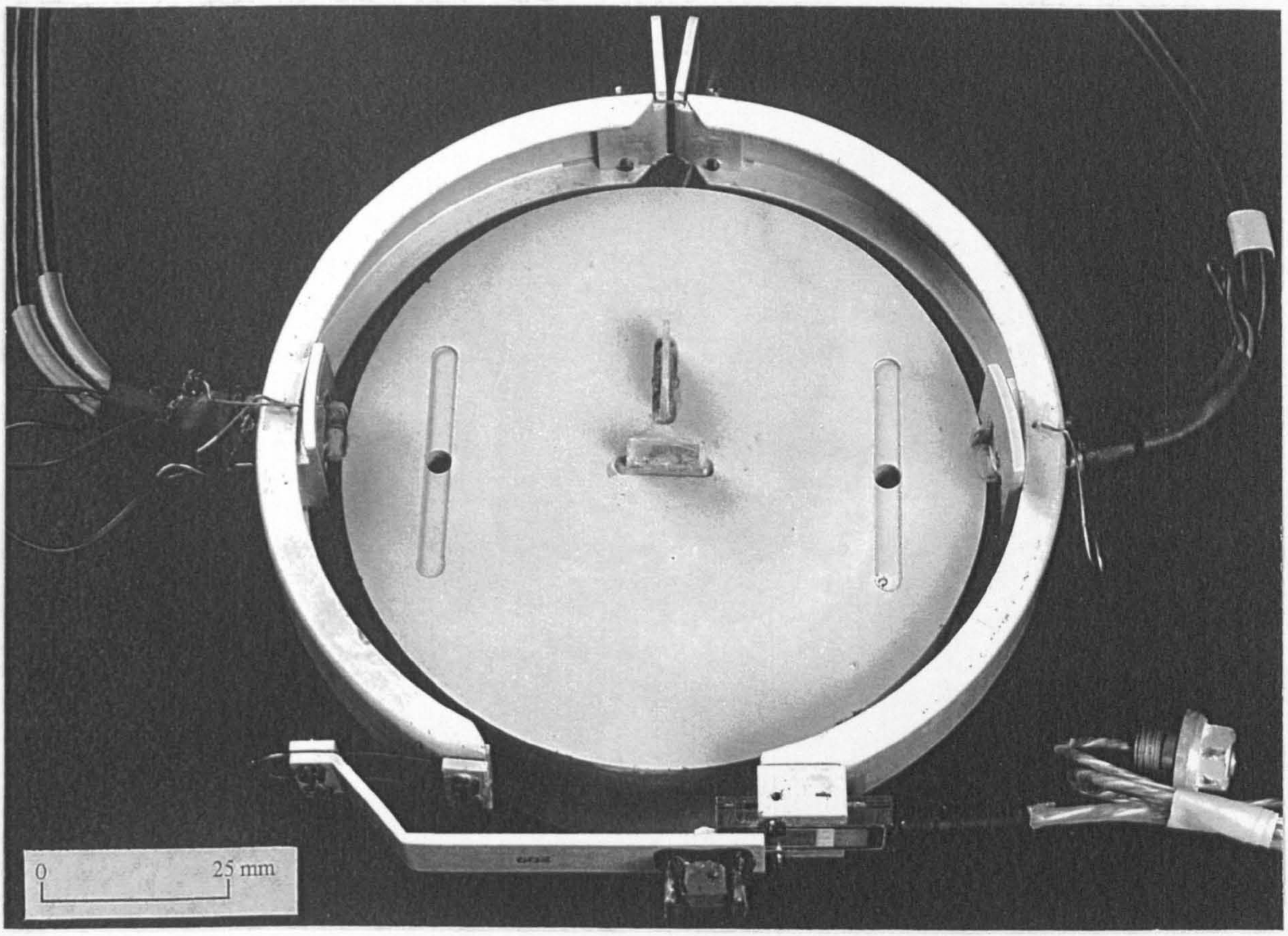

Figure 3.17 Photograph detail of bender belt and 100 mm platen mounted "standard" benders

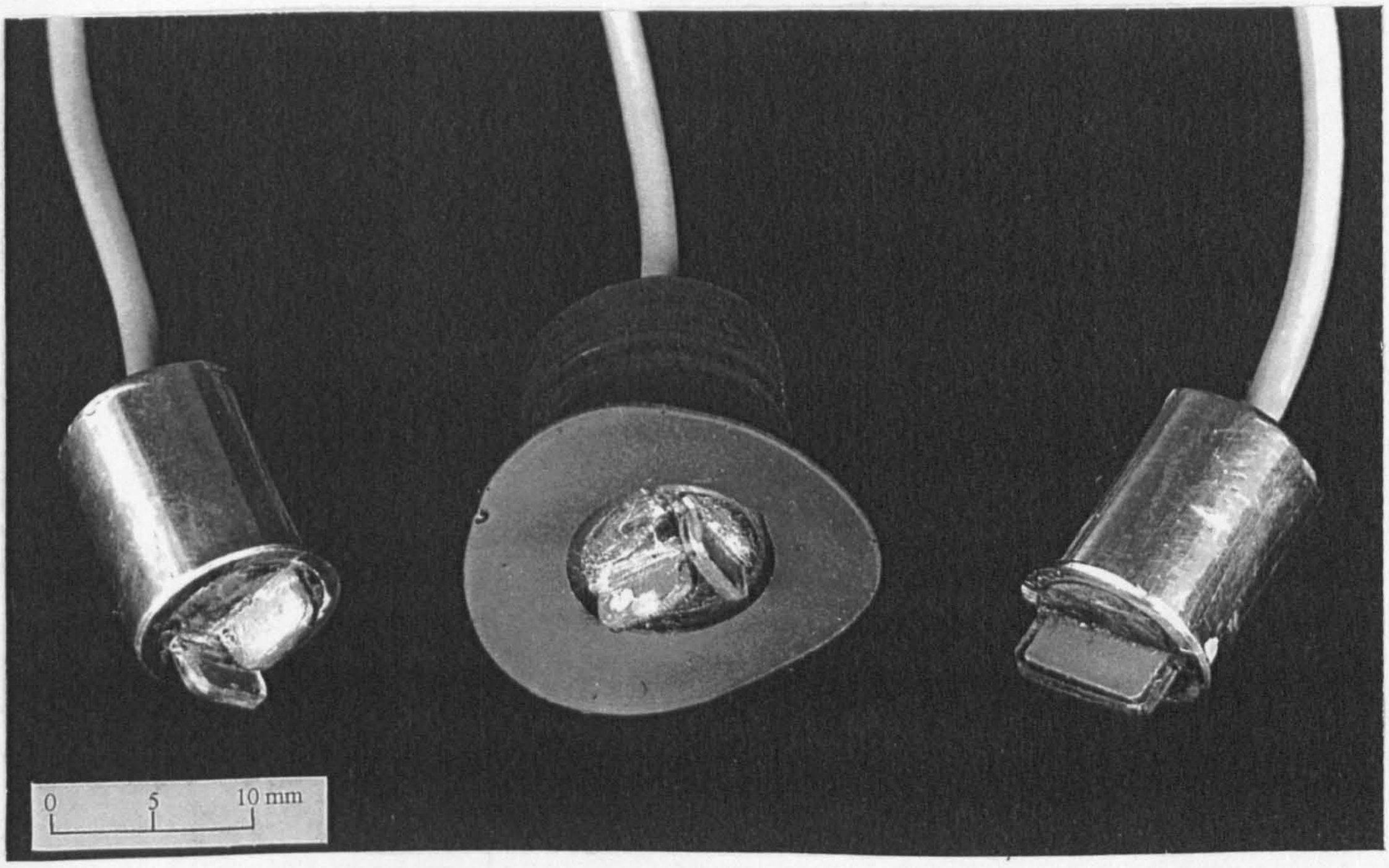

Figure 3.18 Photograph detail of bender probes and grommets

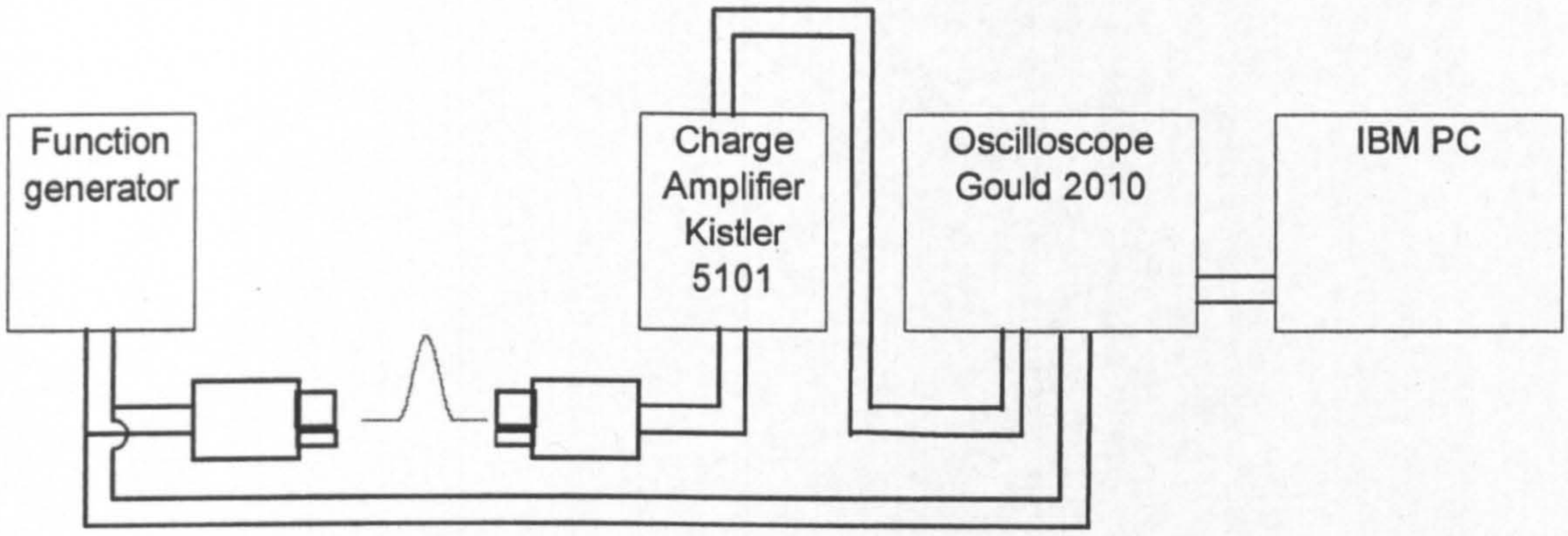

Figure 3.19 Bender element system - schematic general arrangement

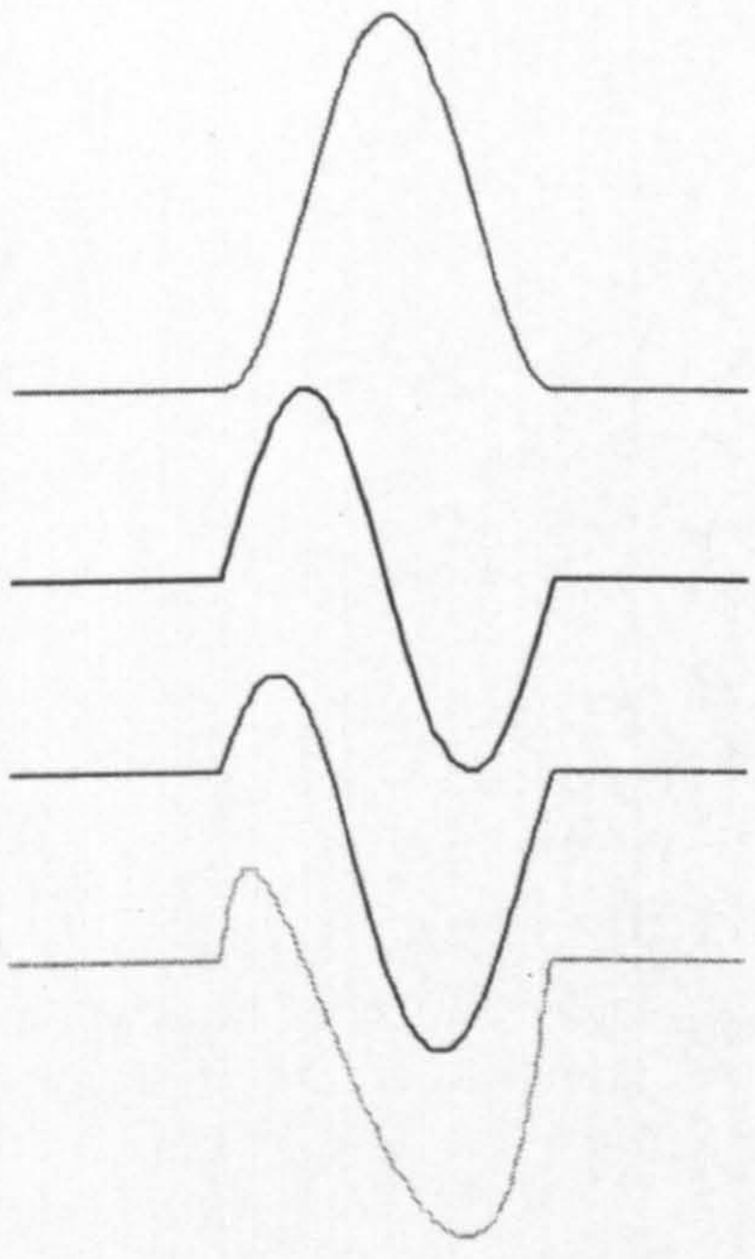

Wave name	*Abbreviation used*	*Wave description*
Sine Pulse	SP	Sine wave with 90° phase shift, 50% symmetry
Sine wave	SW	Sine wave with zero phase shift and symmetry
Sine wave with shifted phase	SWS	Sine wave with 30° phase shift and 50% symmetry
V. Jovičić	VJ	Sine wave with 30° phase shift and 35% symmetry

Figure 3.20 Typical driver signals used

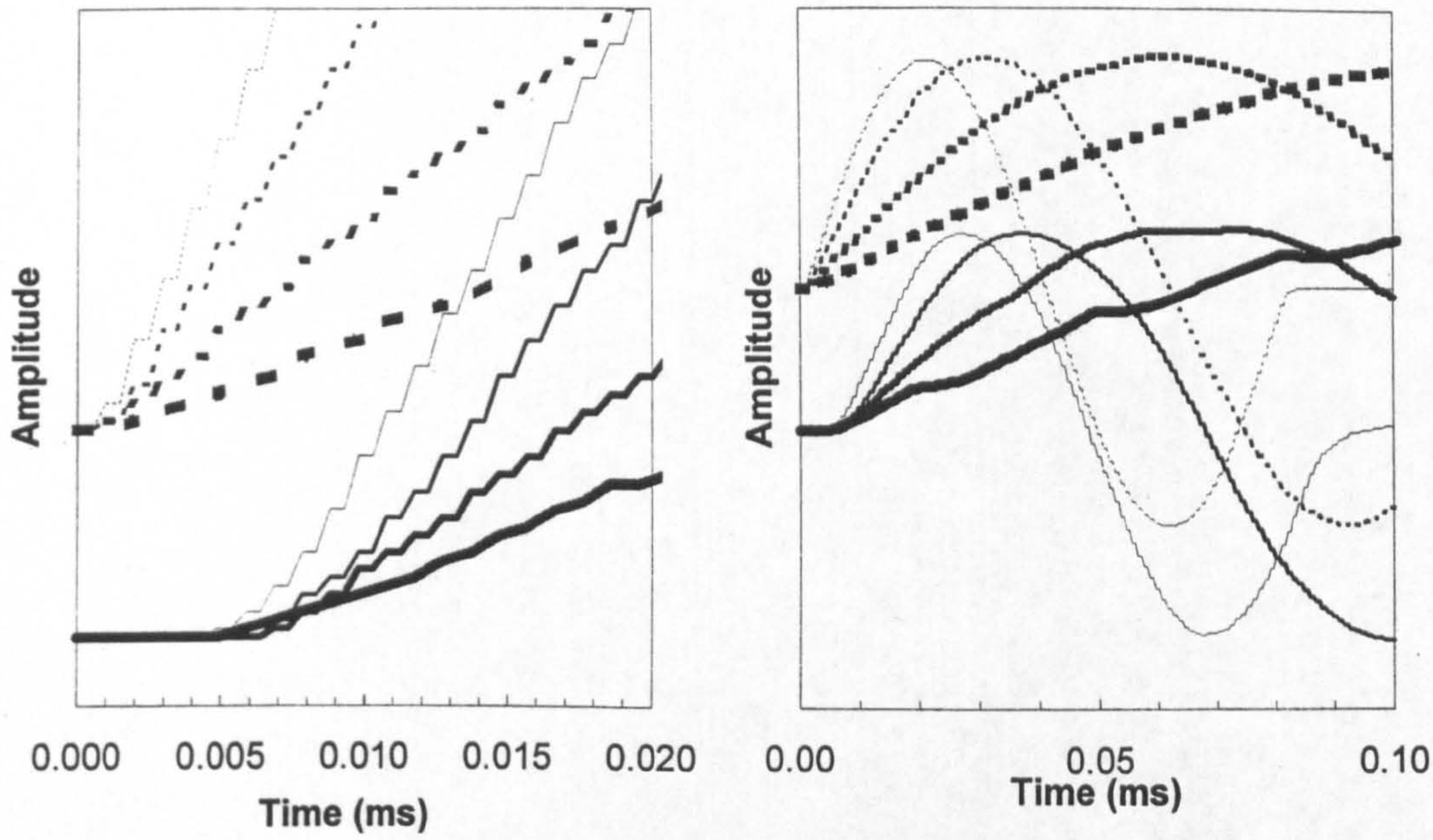

a) Driver and receiver pulses from the same self monitoring bender element subject to pulses of 2, 4, 8 qnd 16 kHz - Charge amplifier used as interface (Note Left plot is a detail of the Right plot.)

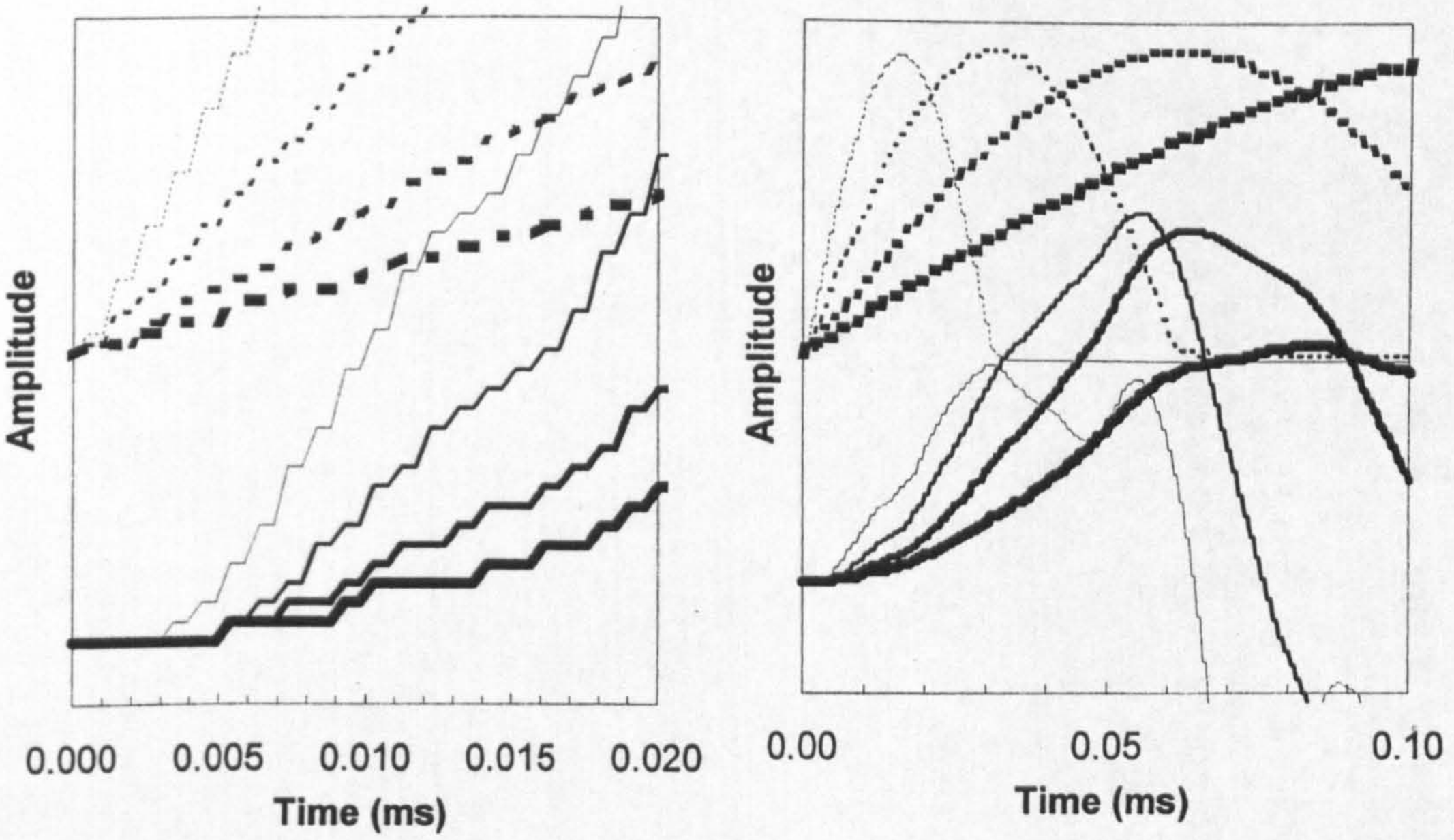

b) Driver and receiver pulses from different bender elements held in contact while one is subject to pulses of 2, 4, 8 qnd 16 kHz, and the other monitored. - No charge amplifier used (Again, the Left plot is a detail of the Right plot.)

Figure 3.21 Illustration of typical delays measured in a) self monitoring and b) tip contacting elements

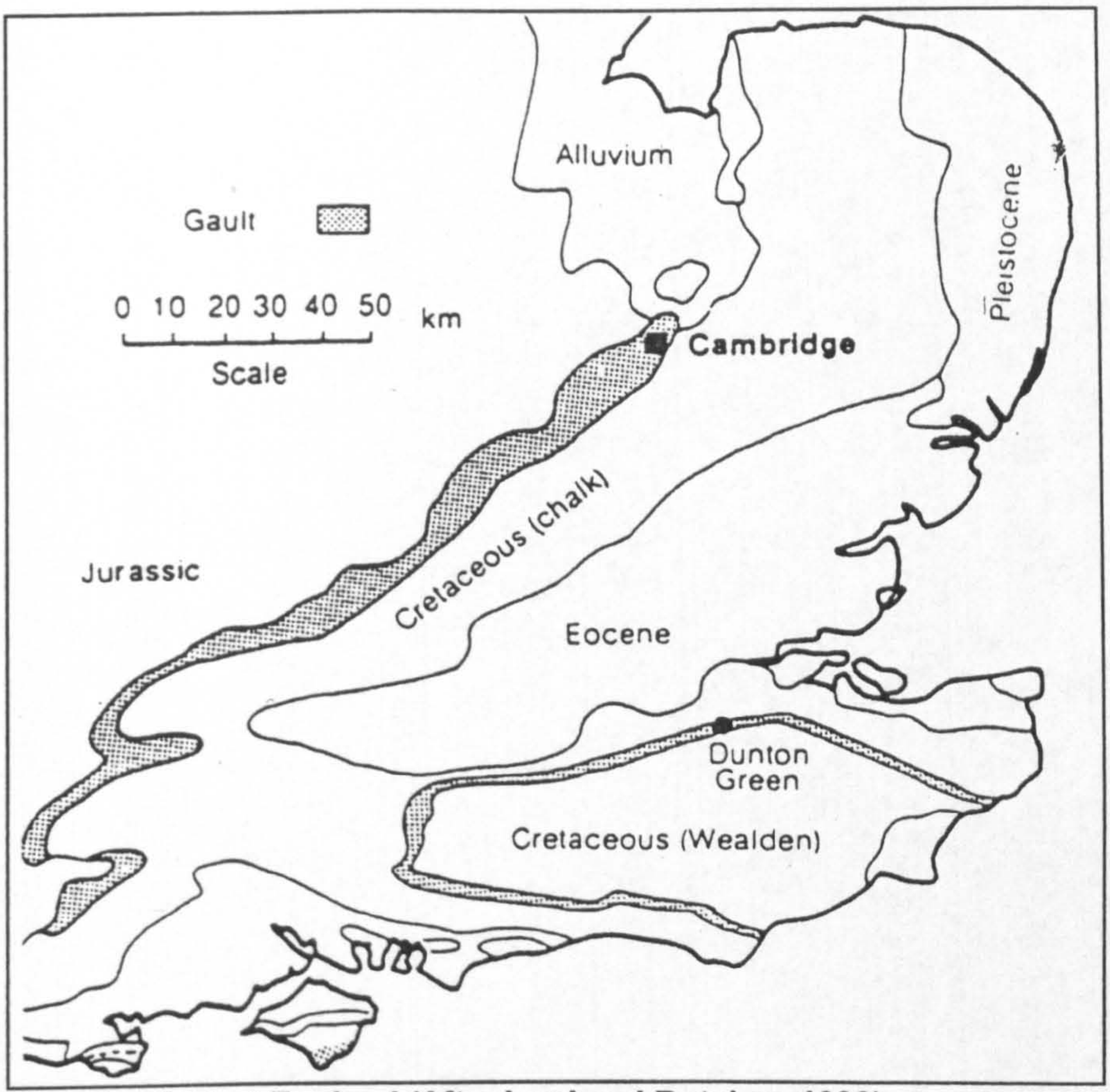

a) In South East England (After Lord and Butcher, 1993)

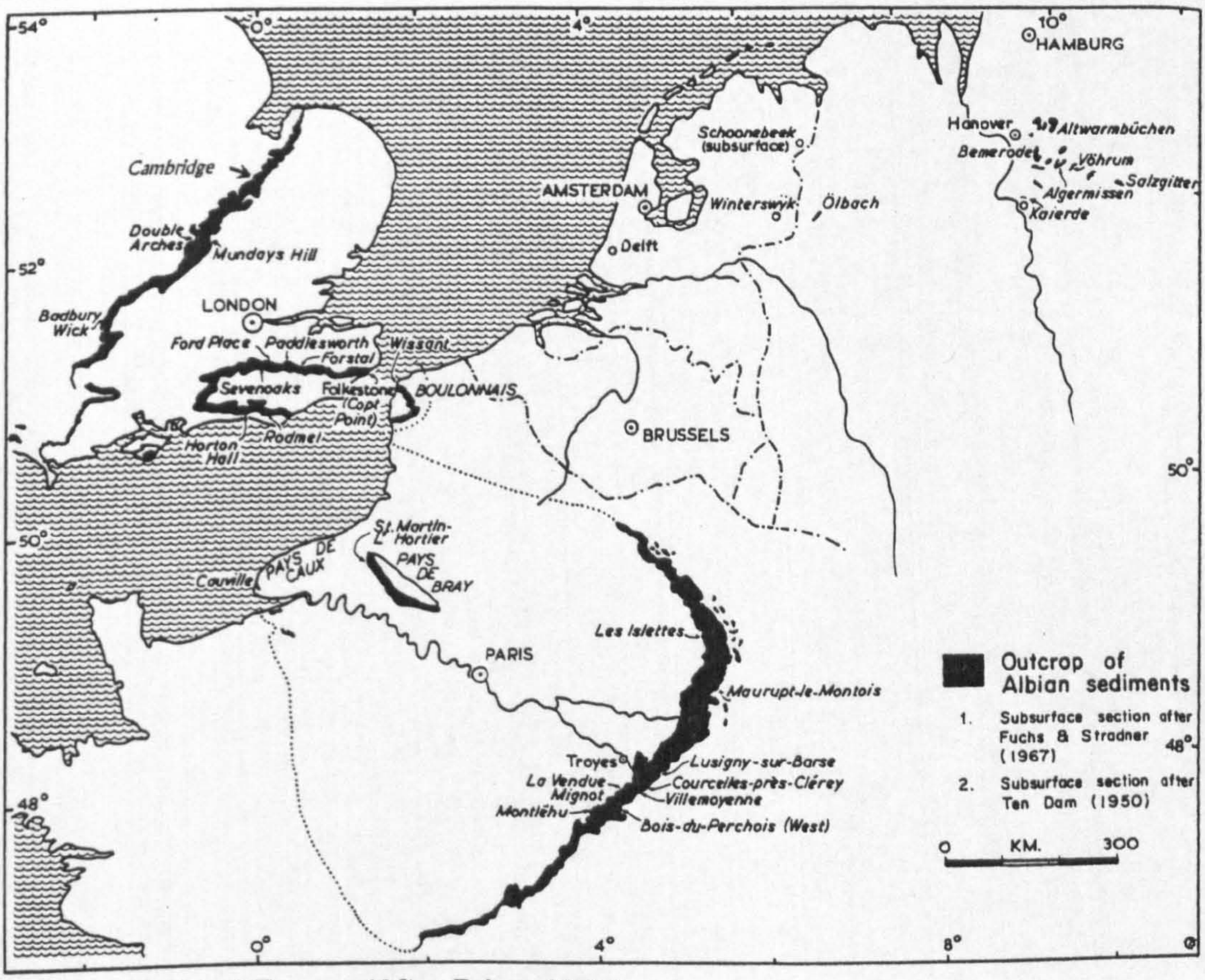

b) In North West Europe (After Price, 1977)

Figure 4.1 Locality of Albian sediments

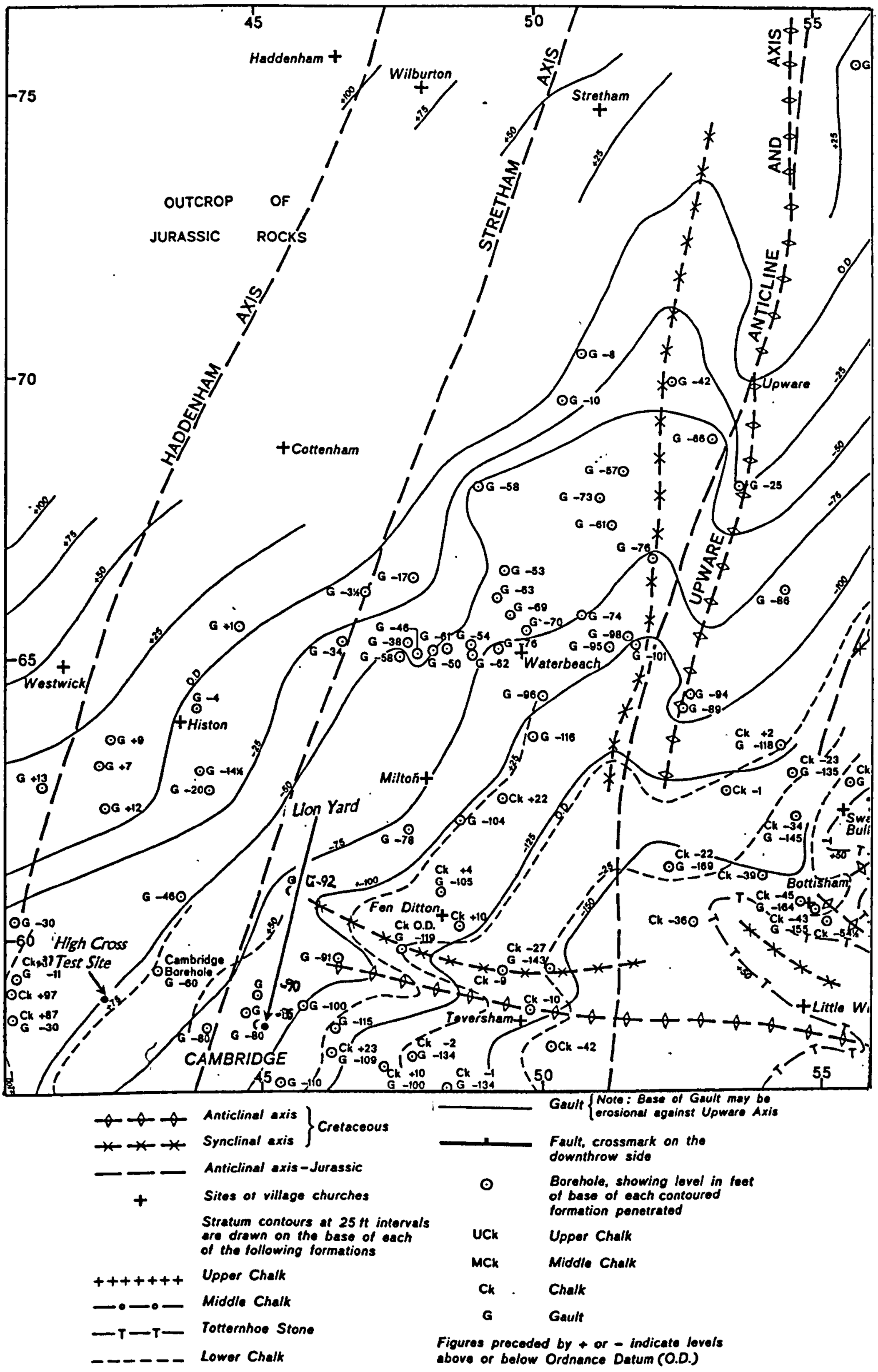

Figure 4.2 The geological structure of Cretaceous formations in the Cambridge District
(After Worrsam and Taylor (1975) Scale: 1:100 000

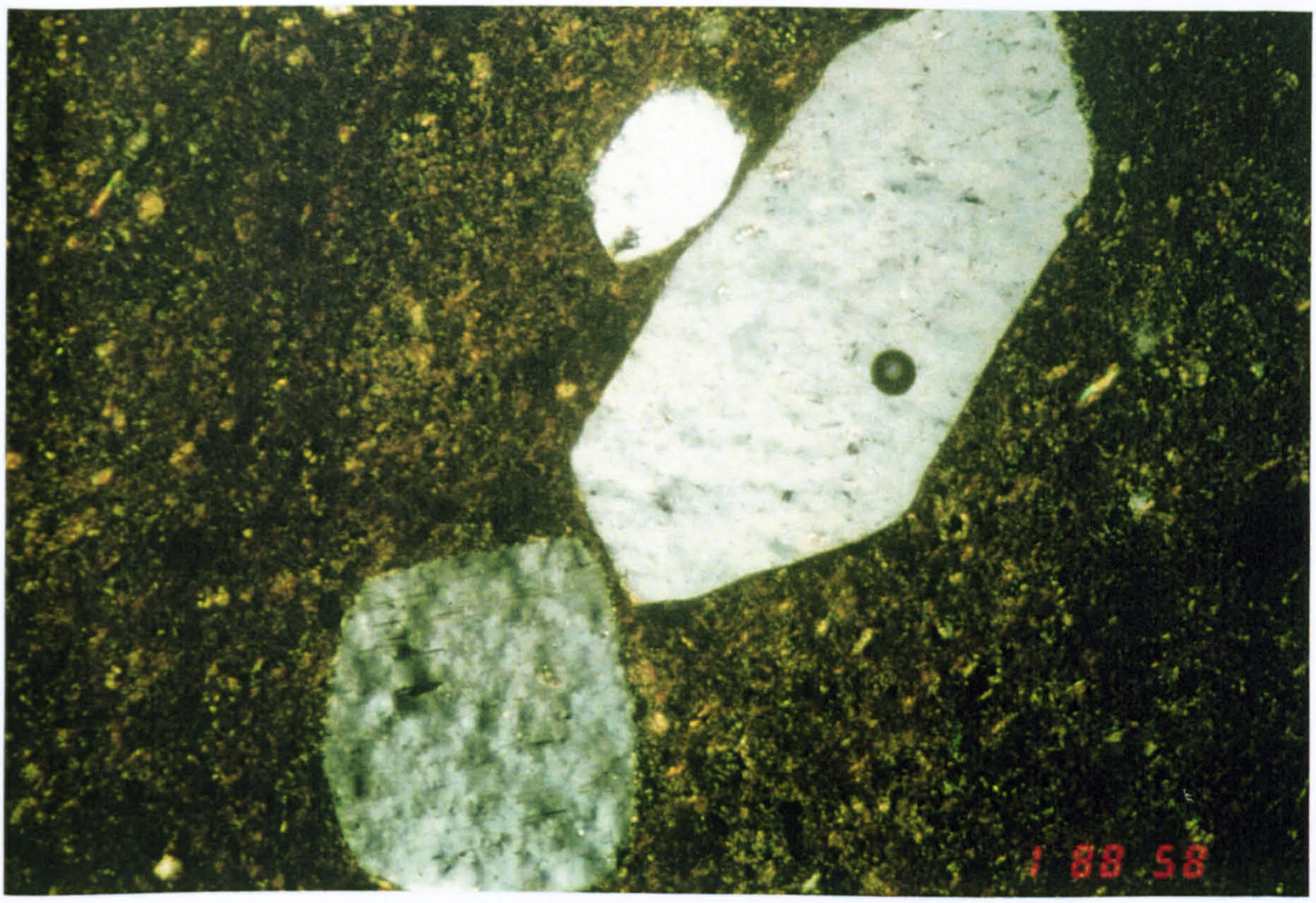

a) Selenite crystals in clay. Small bright flecks are micas. Granular carbonate occurs in matrix

Scale: 1 mm image height.

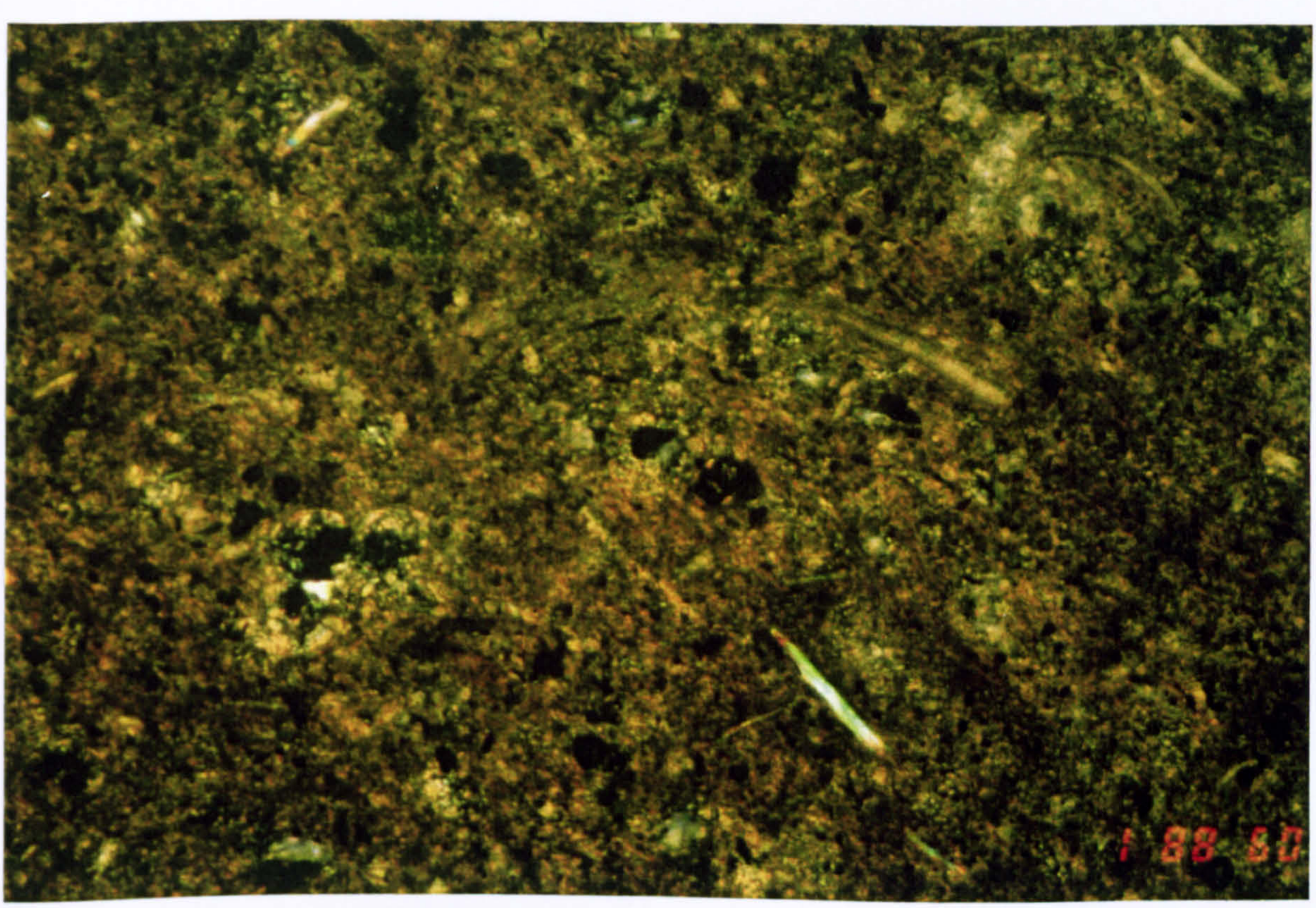

b) Shell fragments and micas in clay matrix. Small white dots represent microfossils. Note strong orientation.

Scale: 0.5 mm image height.

Figure 4.3 Thin section photographs of Gault clay from Borehole LS2, 6m depth

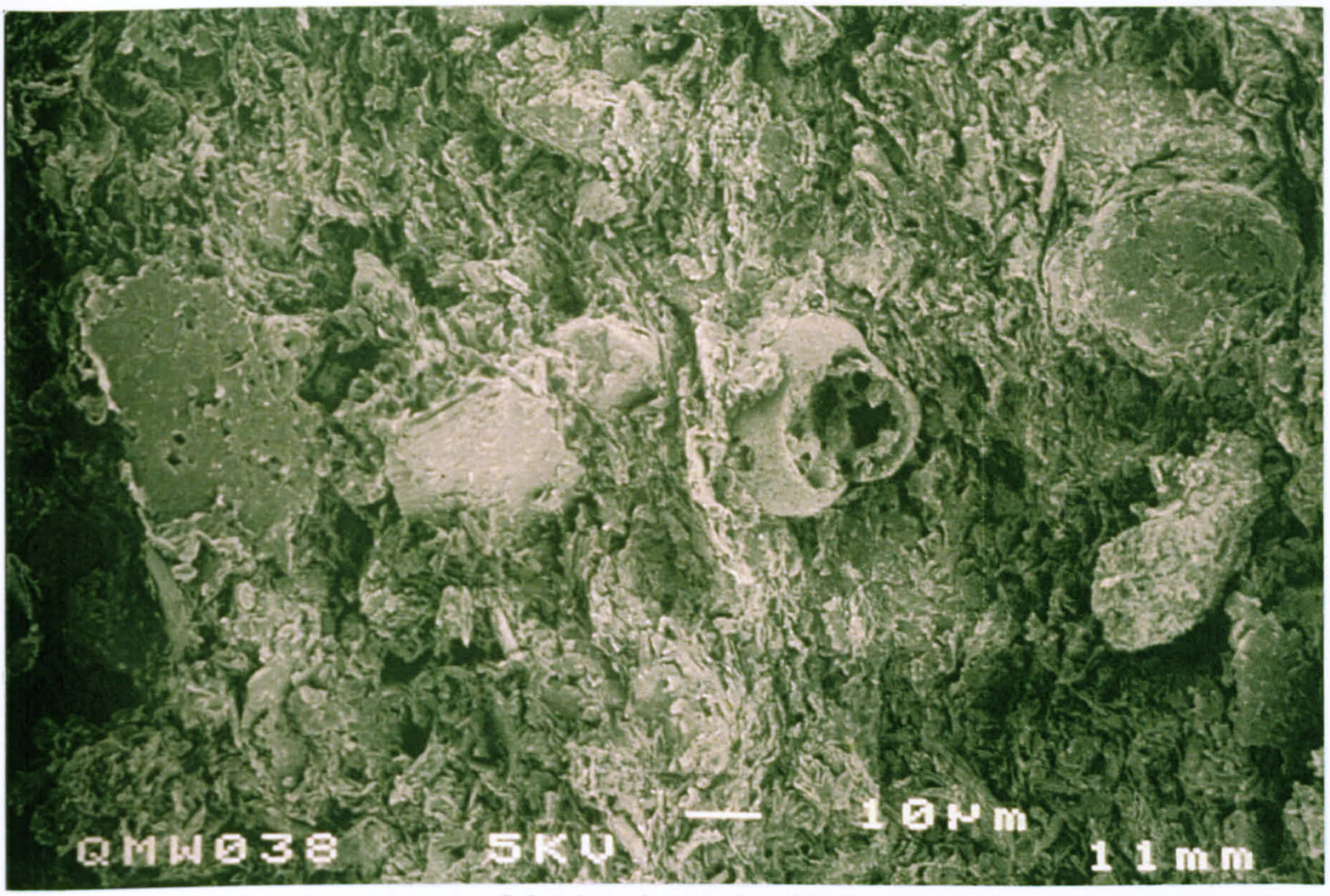

a) 10 μm scale micro fossils and mica flakes in a clay matrix with clear orientation

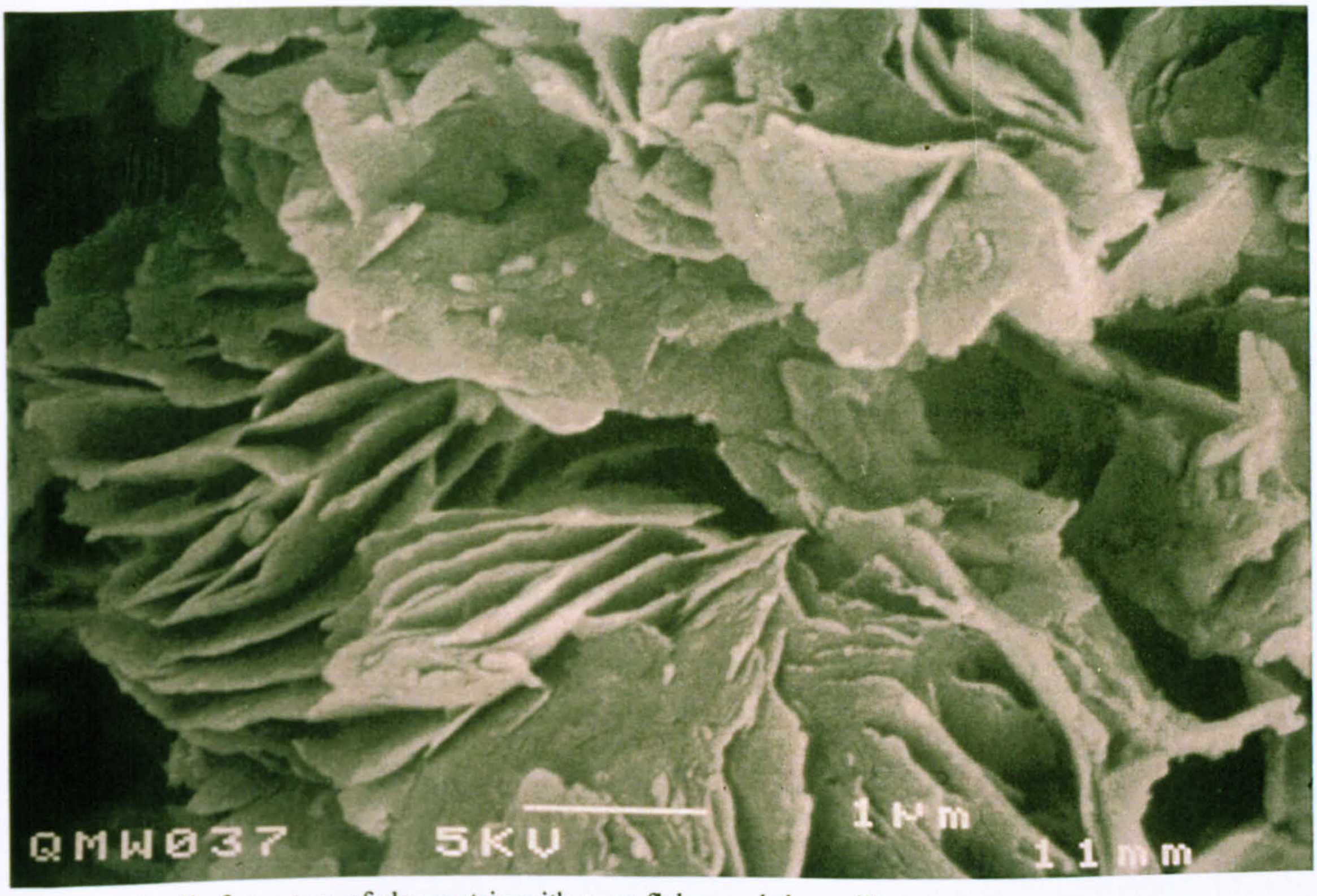

b) 1μm detail of structure of clay matrix with open flakes and sheet silicates

Figure 4.4 **SEM images of Gault Clay from Borehole LS2, 6m depth**

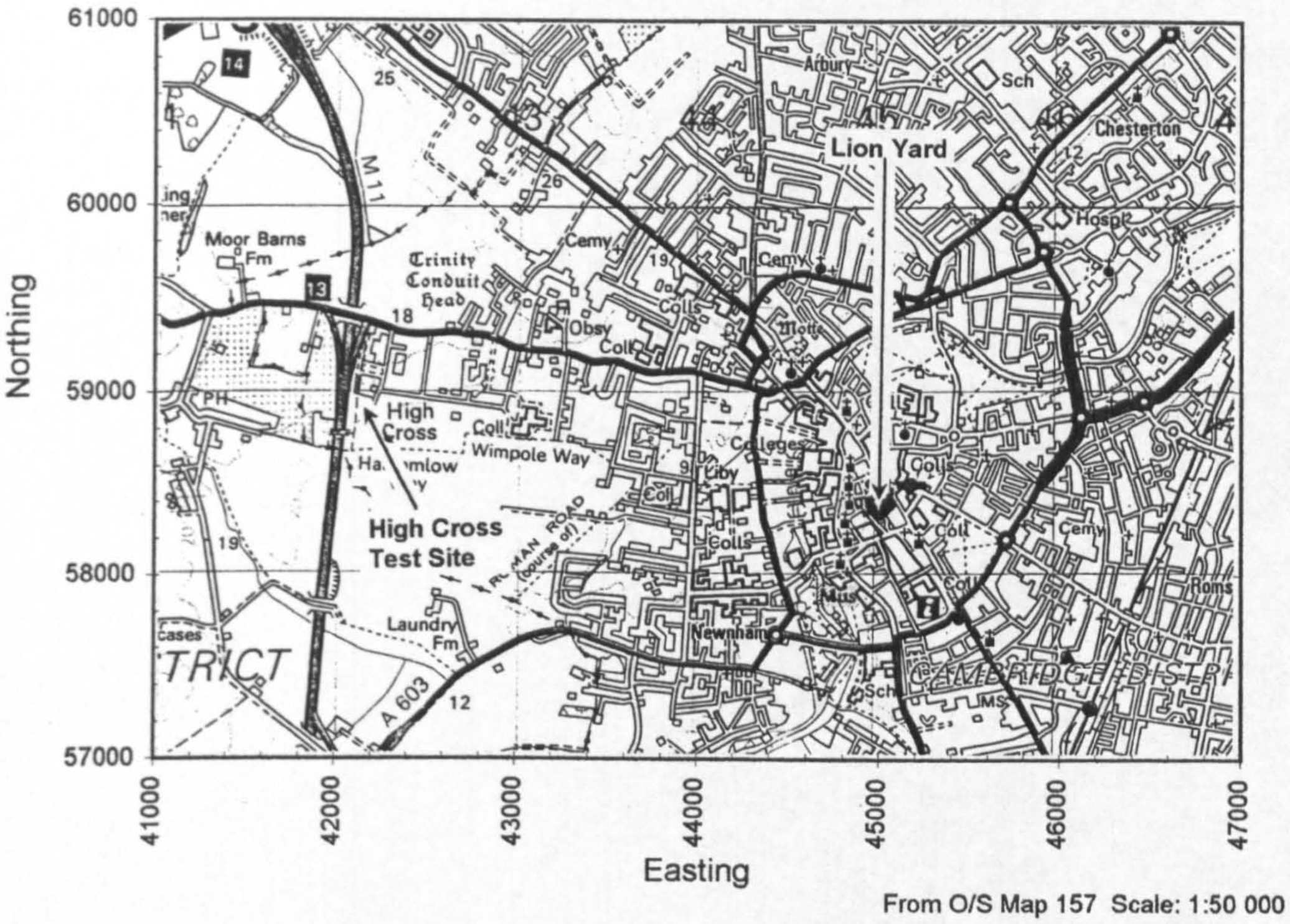

a) Relative locations of Lion Yard development and High Cross site off Maddingley Road

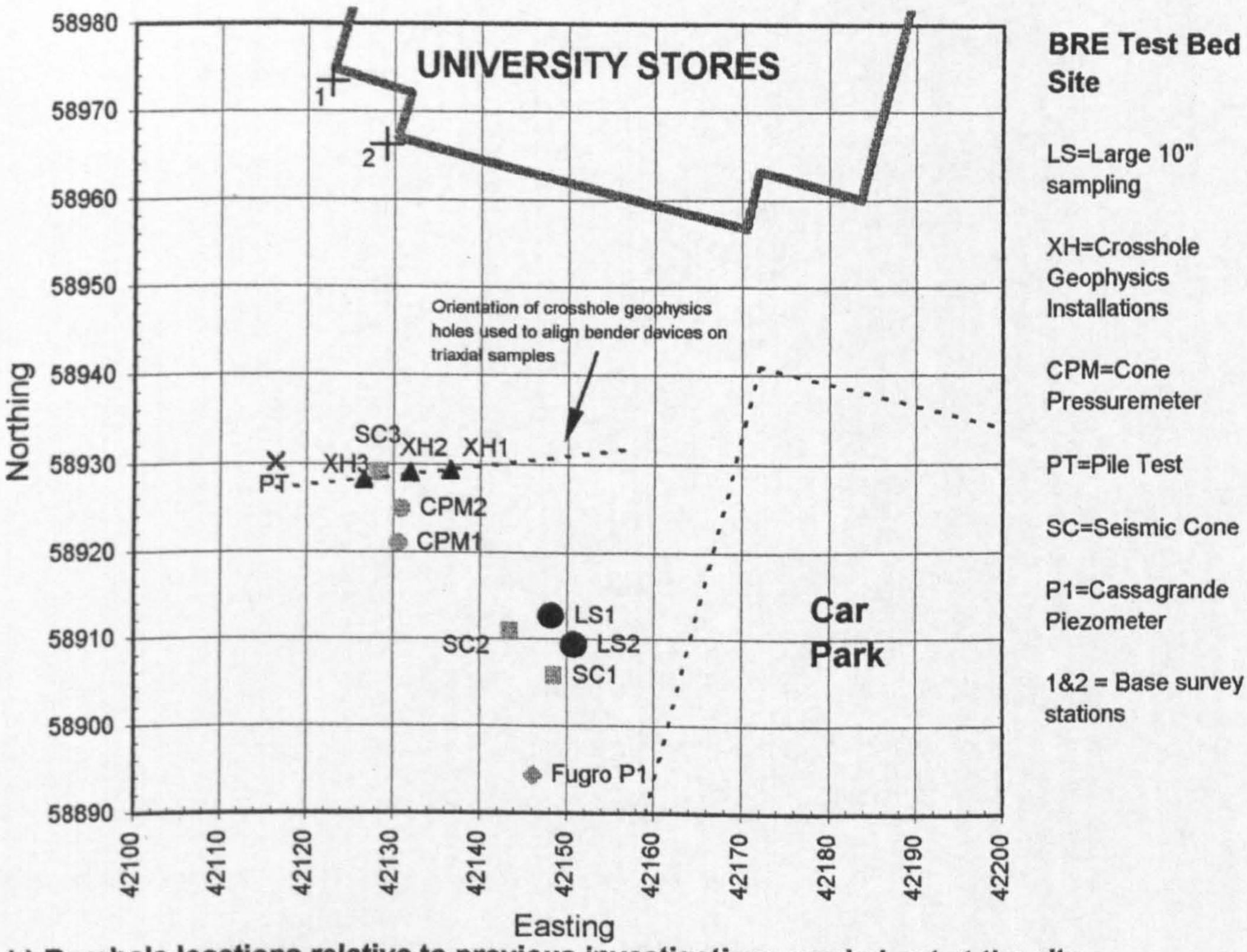

b) Borehole locations relative to previous investigations carried out at the site

Figure 4.5 Location of High Cross site, and locations of Investigation holes

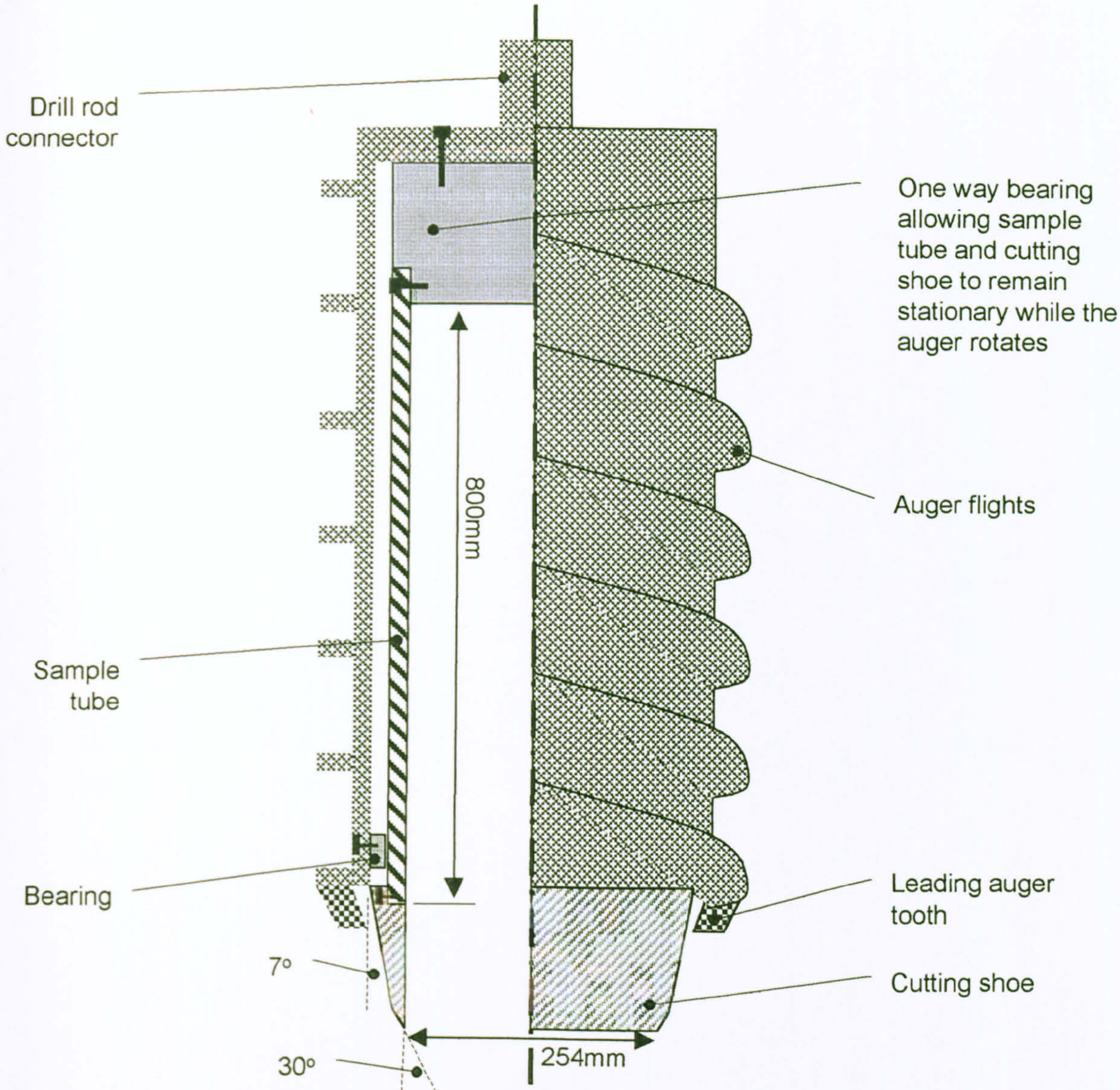

a) Schematic representation of sampler. NOT TO SCALE

b) Photograph of cutting shoe showing leading auger teeth

Figure 4.6 The BRE 250mm Diameter sampling system

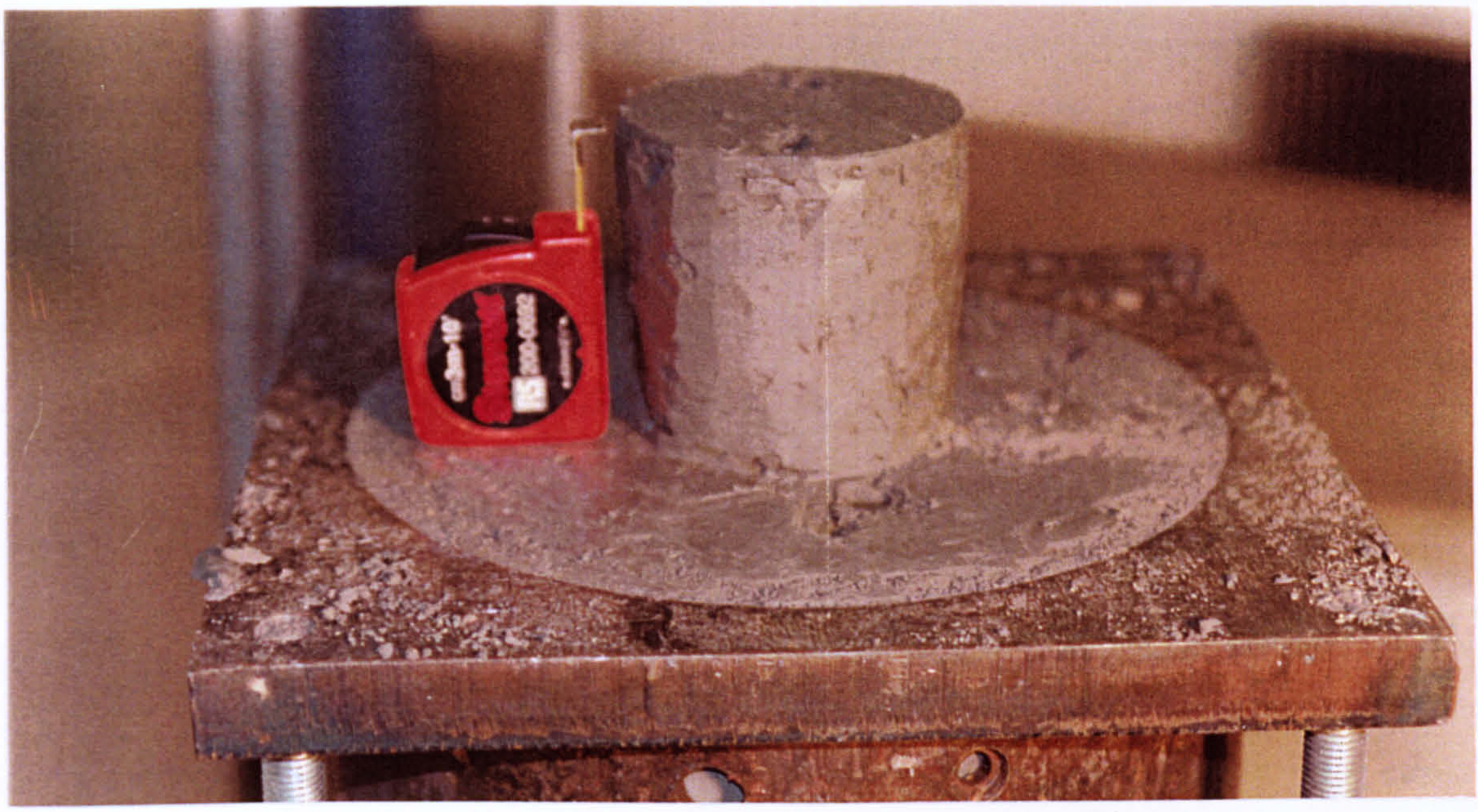

a) Initial preparation from tube sample in high humidity environment

b) Final shaping with bandsaw

Figure 4.7 Preparation of natural Gault clay triaxial sample

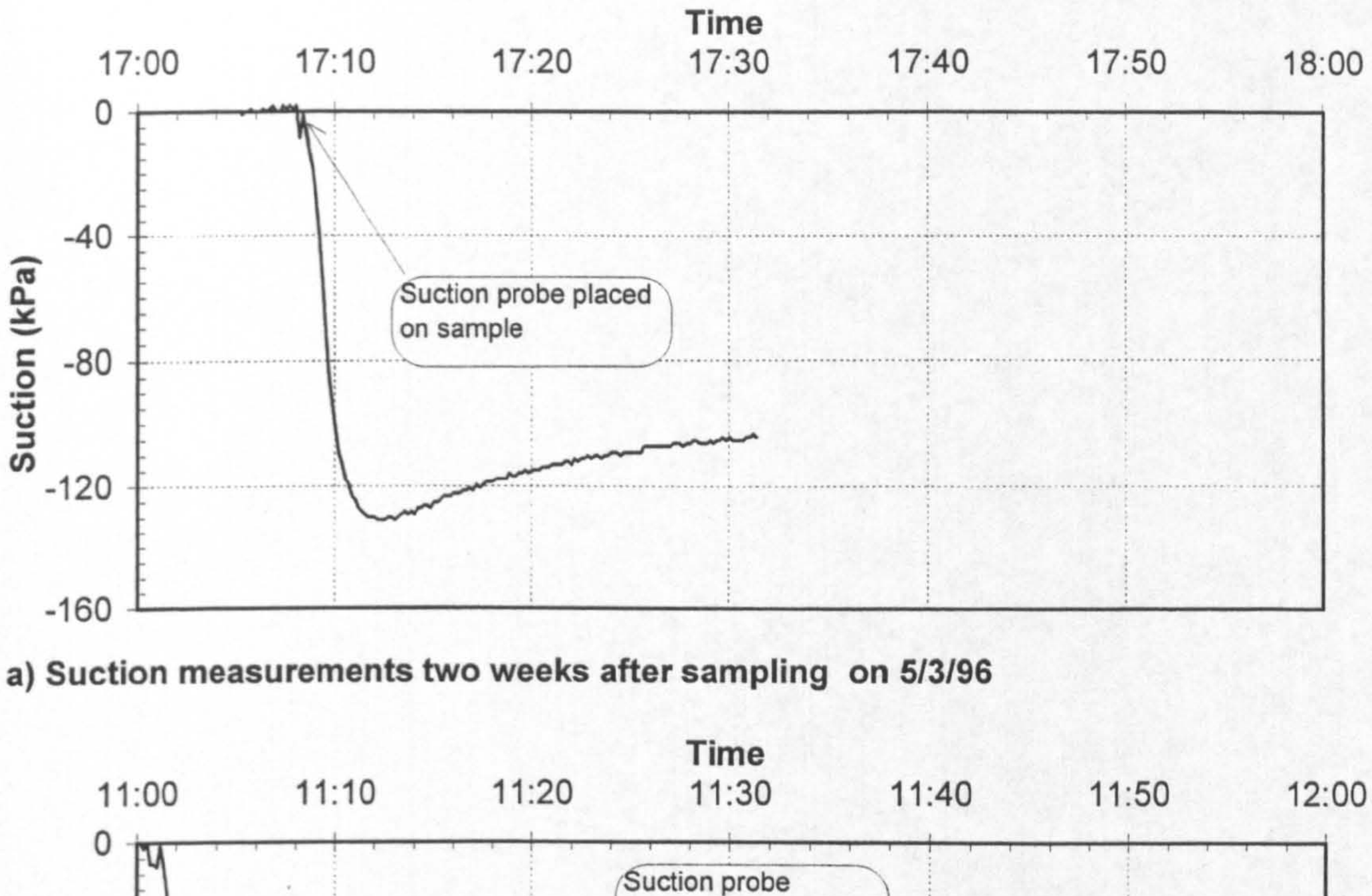

a) Suction measurements two weeks after sampling on 5/3/96

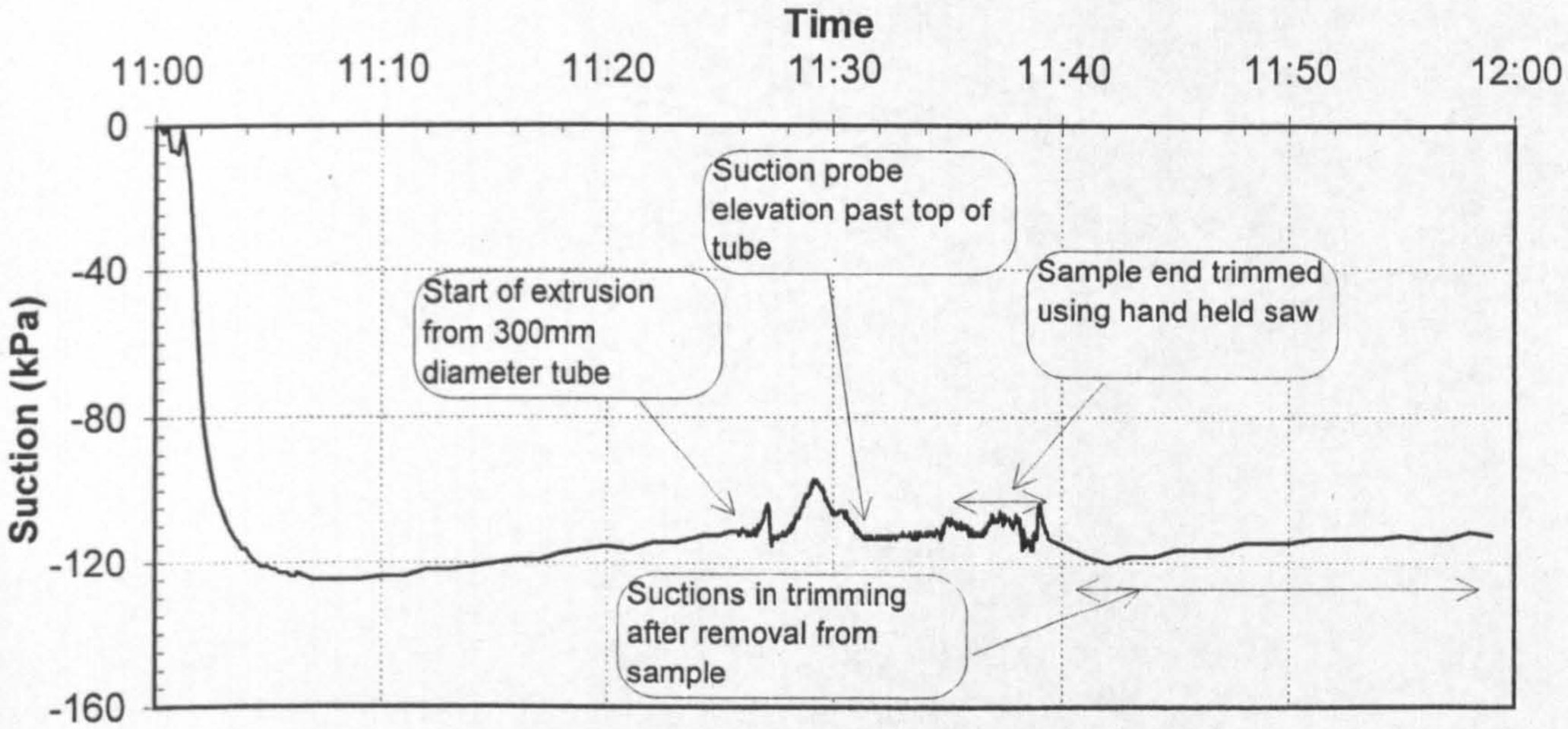

b) Suction Measurements before during and after extrusion on 17/6/96

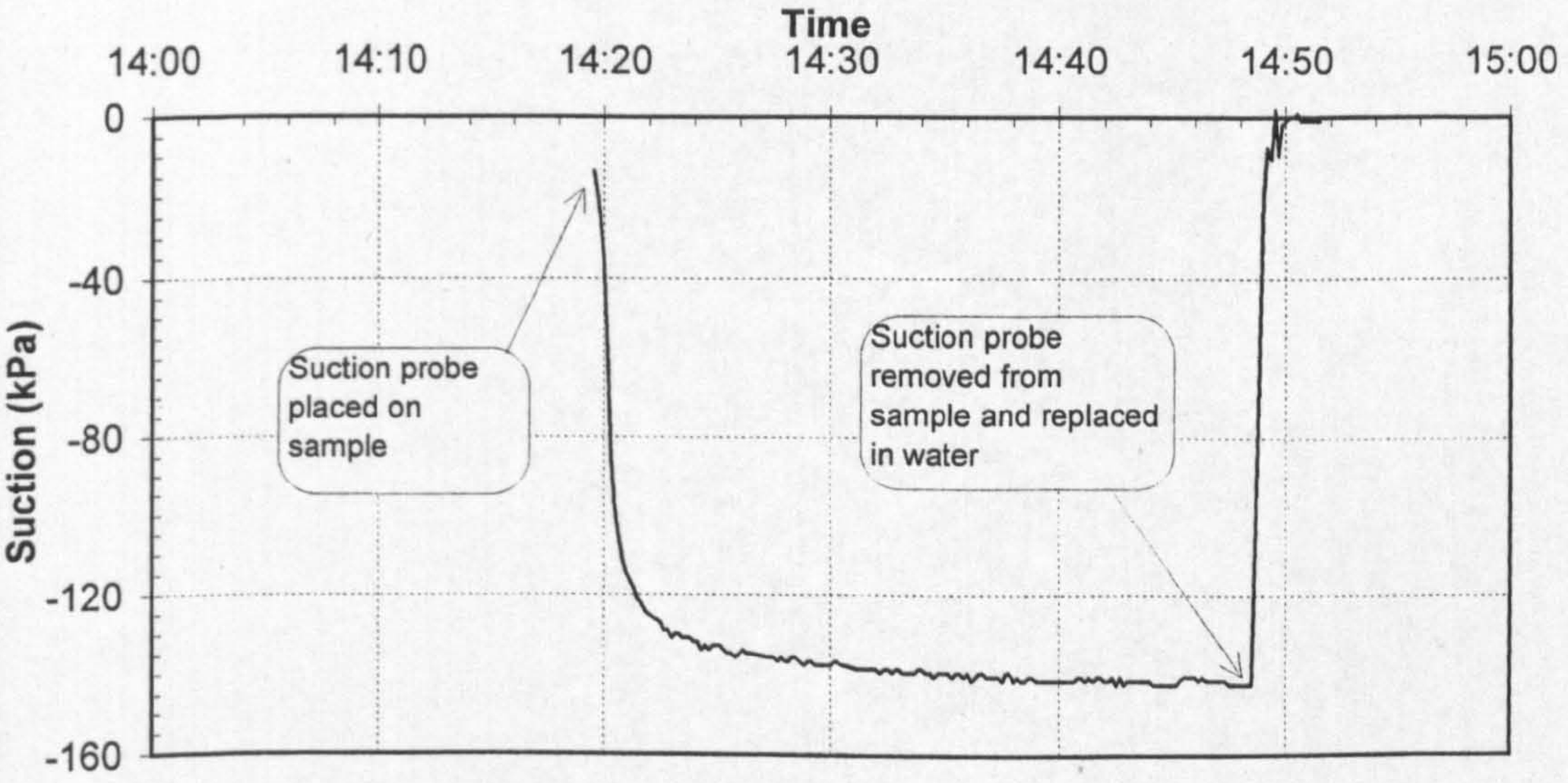

c) Suction after final sample preparation on band-saw on 17/6/97

Figure 4.8 Suction measurements on sample LS2-2 - Test R12

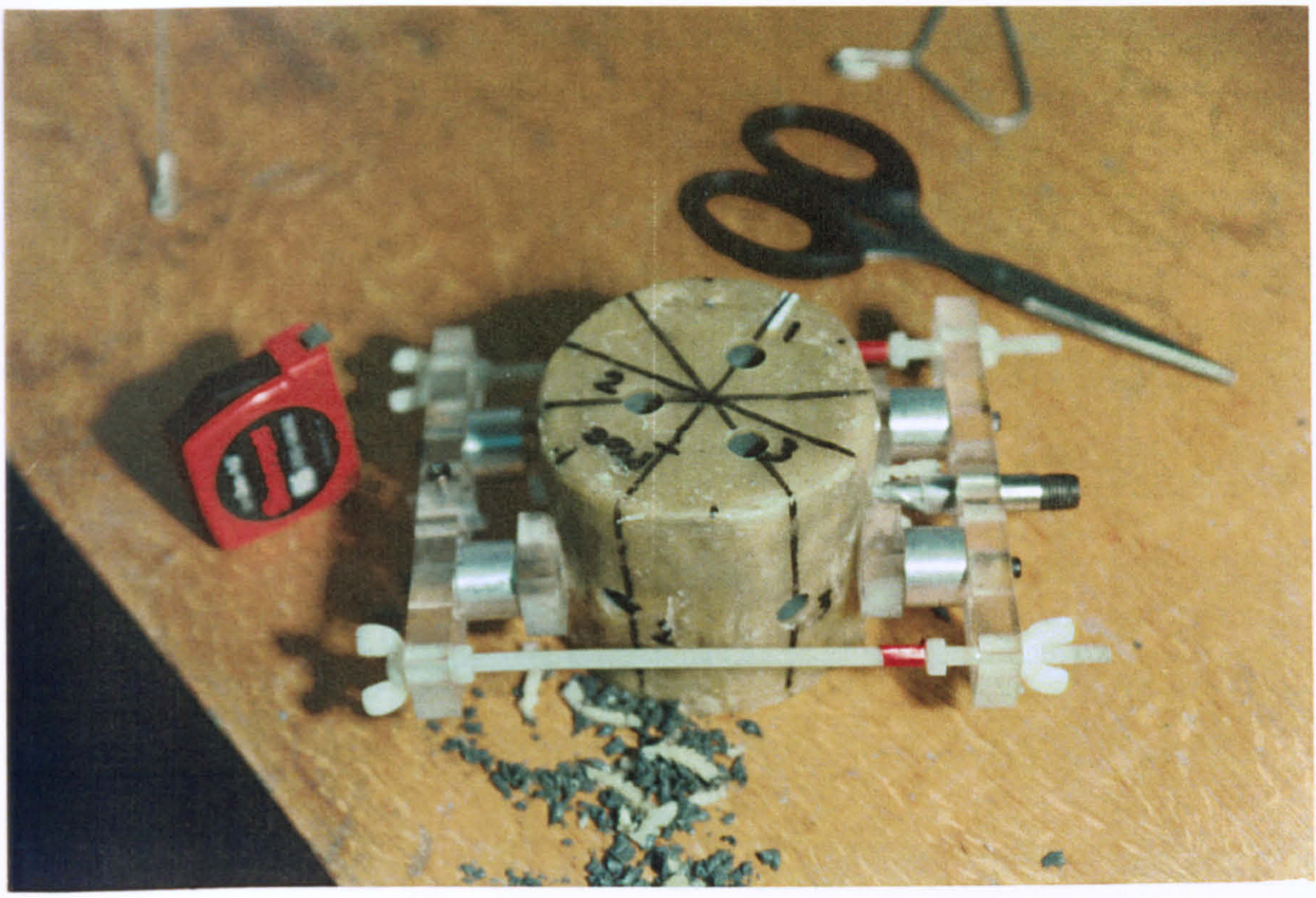

a) Preparation of wax coated sample for bench top testing

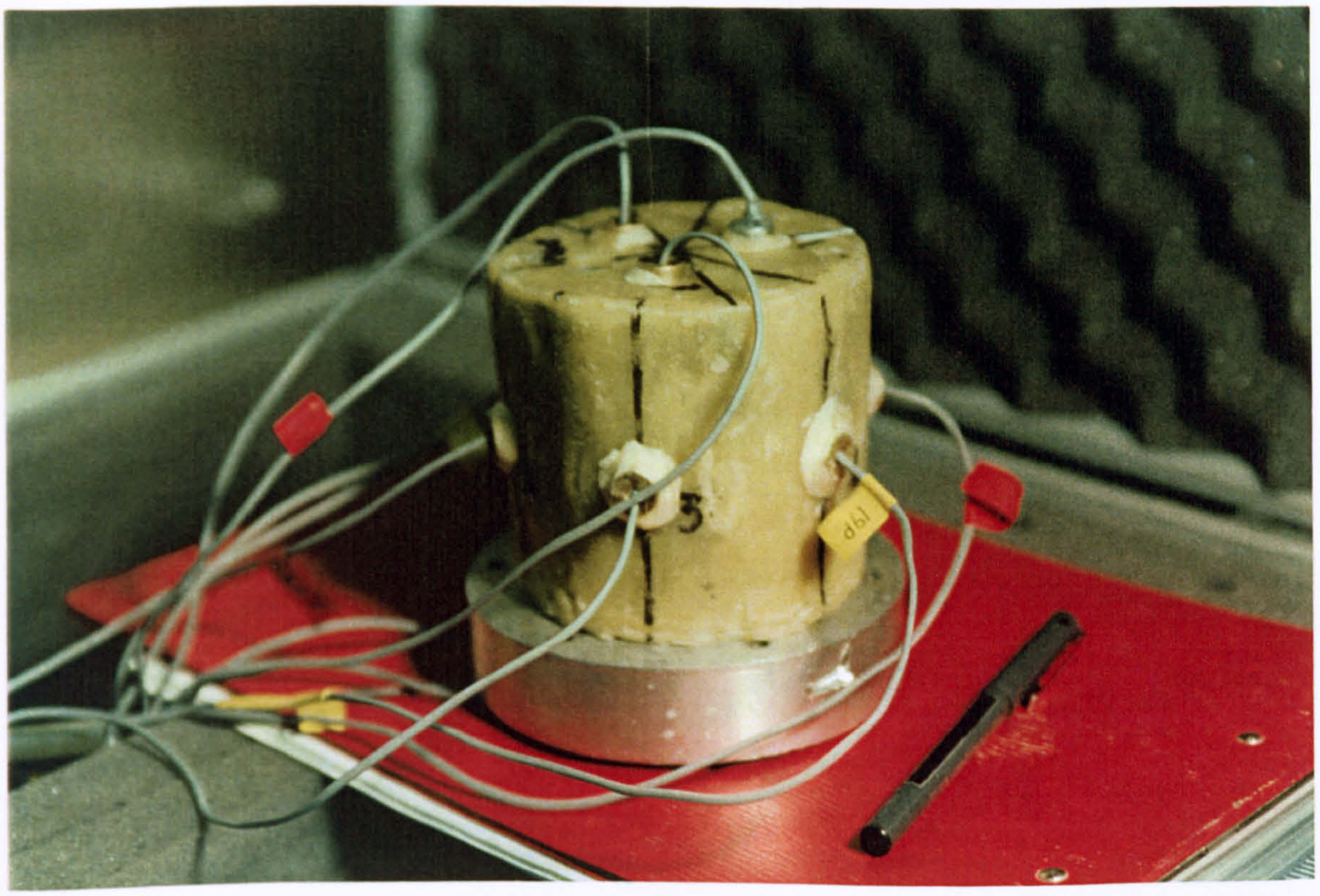

b) Multiple bender probes installed in sample

Figure 4.9 Preparation and bender testing of sample on the benchtop

1	Mark up locations for local instrumentation and bender belt / probes on membrane, soak the membrane overnight in deaired water, towel dry before use
2	Ensure that the pore pressure probe and porous discs are saturated/de-aired
3	Degrease grommet and pore pressure probe body and cable.
4	Lightly grease top and bottom platen sides using silicon grease
5	Lay out adjacent to cell, membrane, membrane stretcher (mating surfaces to be lightly greased and check that retaining bolts are firm but not to tight), scissors, scalpel, O' rings for sample to platten sealing, probe grommet, bender belt, local strain devices (Hall effect Gauges) heighth gauge to confirm sample length, steel rule,
6	Prepare coil of 0.25mm diameter fuse wire suitable for preventing sample from contacting with damp porous disc until cell pressure is applied.
7	Cut holes in the membrane at locations marked for bender belt and mid-height pore pressure probes.
8	Fit probe/bender grommet(s) to membrane taking care to ensure clove like overlap onto which "o" rings are placed at a later stage to ensure a seal. Take care not to damage or split the grommet.
9	Ensure that the ram height is suitable to cover the strain anticipated during the test.
10	Put the O-rings and membrane onto the stretcher, and set stretcher height adjustment screws to match correct height for placement of sample on base pedestal.
11	Wet pedestal using flow of de aired water from back-pressure unit.
12	Reset the cell, probe and back pressure transducers to give correct values at sample mid-height.
13	Establish and set up suitable starting cell, back and ram pressures on the pressure controllers.
14	Shake off free water from porous discs, place on pedestal and arrange fuse wise on disk
15	Measure length, diameter and weight of the sample and record.
16	Place sample on spacers the same height off the bench as the the base pedestal stands.
17	Apply suction to stretch membrane, and lower over sample, taking care to align membrane at correct azimuth for horizontal bender alignment
18	Lift both sample and membrane stretched up and using steel rule to support sample, slide squarely onto the pedestal, and once aligned, remove steel rules, pressing sample down onto end bender elements.
19	Unroll lower end of membrane onto pedestal, slide down (avoid air entrappment), roll on O rings to aid seal.
20	Place fuse wire on top of sample and place the top disc taking care to ensure correct orientation of bender slots with respect to the bottom benders.
21	Lower the top platen into the membrane and onto the sample, take care over bender alignment.Insert short length of fine tube between top platen and membrane to aid removal after membrane placement
22	Unroll the membrane onto the top platen, then O-rings to seal membrane on the top platen.
23	Separate the sides of the split membrane stretcher and carefully remove from sample.
24	Fold membrane ends back over rings, lower load cell connection to sample ensuring low load. If tension capability required during test, fill pot connection with water proof araldite.
25	Drill mid height pore pressure socket though rubber grommet using 1/2" bull-nose cutter
26	Lightly grease Pore Pressure probe or bender probe body to aid seal with grommet.
27	Insert the PP probe/bender probe body into the grommet. This will cause some additional air to be introduced to the membrane enclosed sample
28	Push PP probe/bender probe against the sample side and use small ring stretcher to place the O-rings over the grommet to seal the grommet to the probe.
29	Persuade any trapped air out from beneath the membrane using tube placed earlier, and then carefully pull the tube out, allowing the membrane to finally seal onto the top platen.
30	Measure bender separation with verniers. This may need to be checked after final application of sealing latex, but is best done now as the measurement process may puncture the fresh latex
31	Pin and glue local vertical gauges to sample ensuring correct alignment.
32	Apply latex using flexible plastic intravenous drip "needle" onto the back of the probe(s), grommet and down over the membrane to ensure that the sample is sealed from the cell water. Also apply to pin heads and mounting pads of local vertical gauges and bender belt. Apply 3 layers, allowing drying between layers
33	Finally check that load cell still indicates low load on sample, and ensure that all leads associated with sample mounted instrumentation is arranged in such a manner that it will accommodate possible sample strains, and not be entrapped during lowering of the cell wall.
34	Lower the cell wall carefully and tighten all the bolts. Fill the cell with deaired water
35	Apply correction to load cell offset to account for buoyant load on the load cell.
36	Apply cell and back pressure at the same moment
37	Zero the volume change meter and vertical displacment gauge.
38	Initialise Triax Control Programme, and begin recording data
39	Initialise saturation stage, and leave overnight before starting stress path

Figure 4.10 Procedure used to set up natural samples in 100 mm triaxial cell

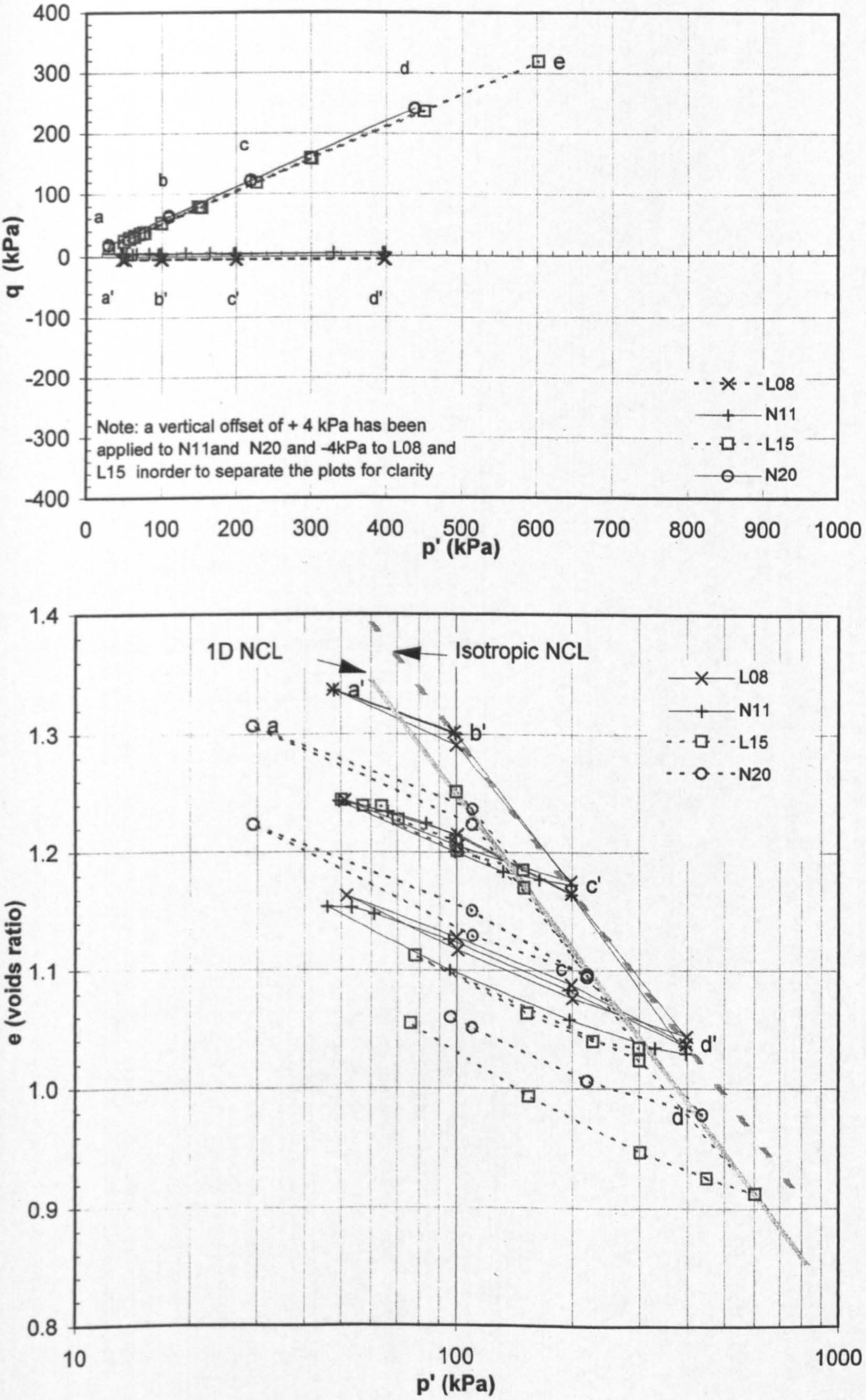

Figure 4.11 Stress path and e *vs.* log p' plots for tests carried out on reconstituted Gault clay where $V_{s(vh)}$ was the only shear wave velocity measured.

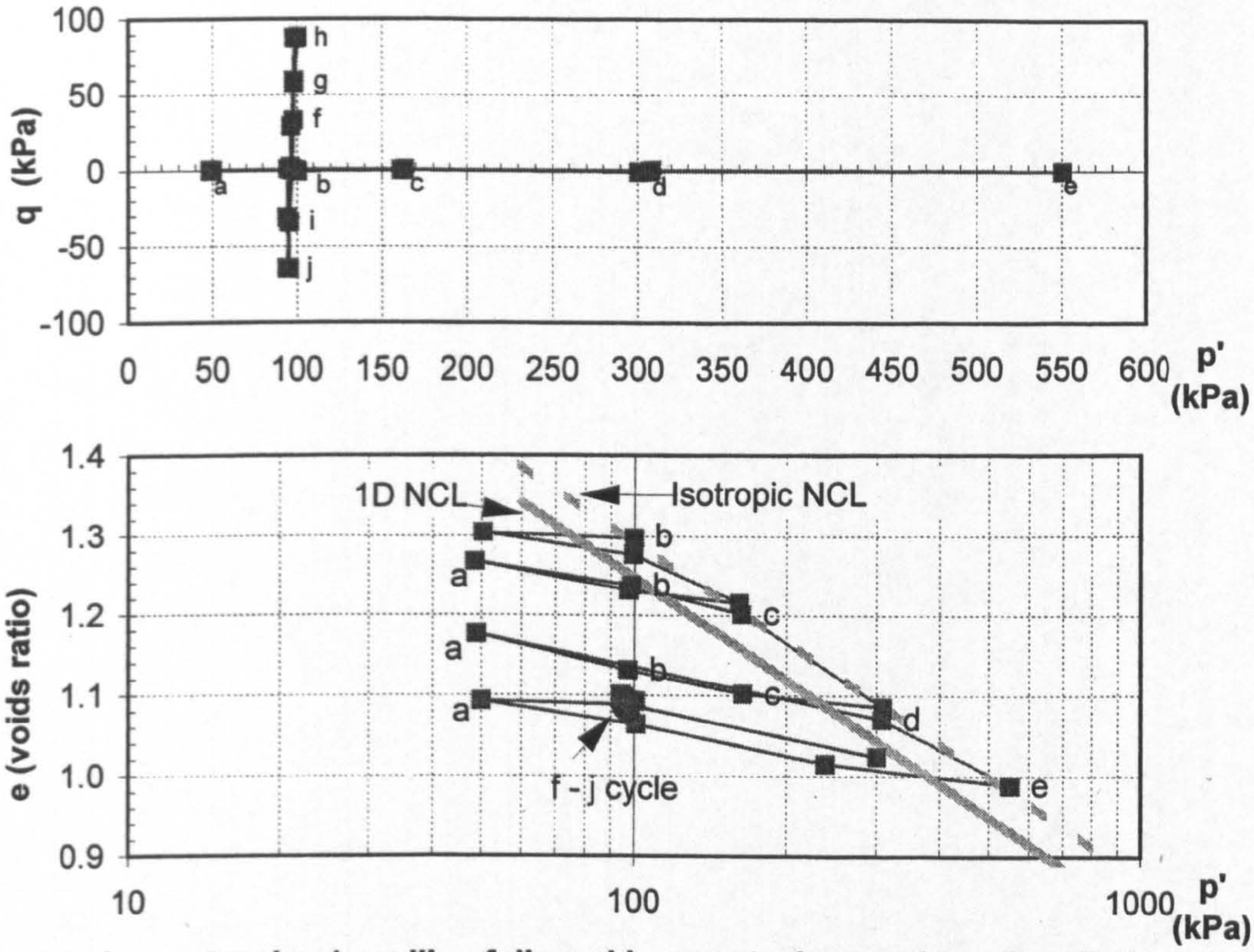

a) Isotropic compresion / swelling followed by const. p' excursions: Test R09

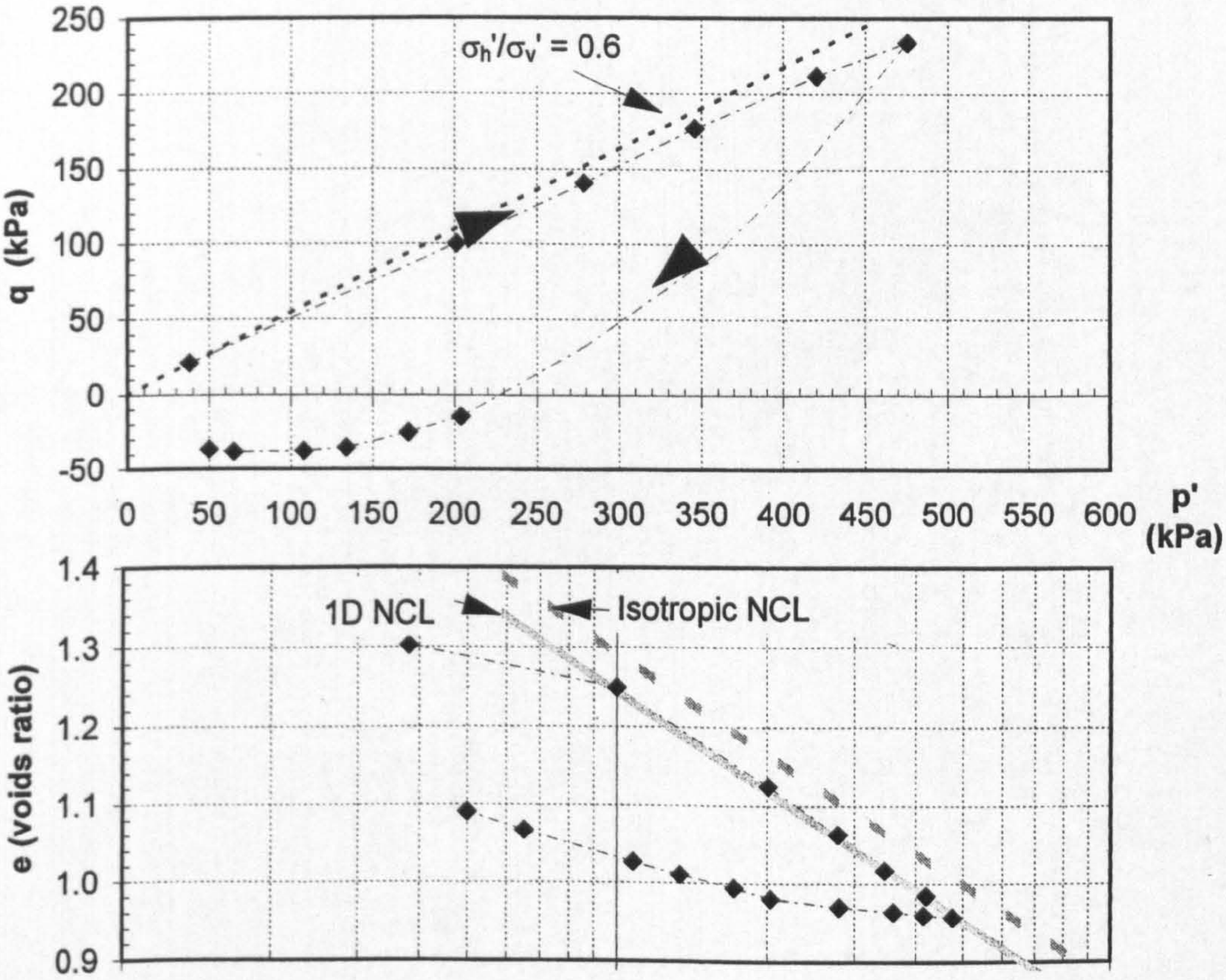

b) K_0 compression and swelling: Test R16

Figure 4.12 Stress path and e *vs.* log p' plots for tests carried out on 100mm reconstituted Gault clay where $V_{s(vh)}$, $V_{s(hv)}$ and $V_{s(hh)}$ shear wave velocities were measured.

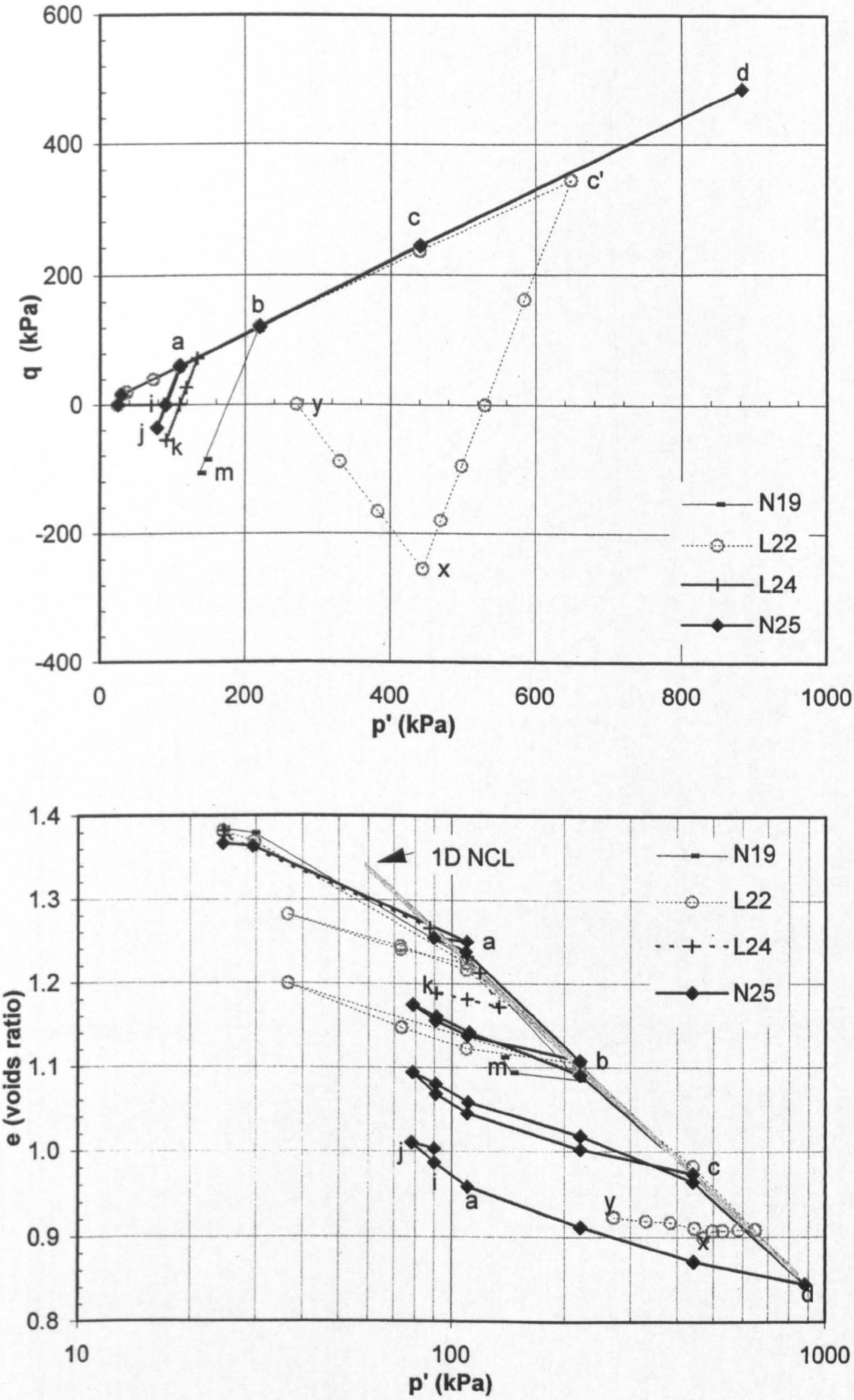

Figure 4.13 Stress path and e vs. Log p' plots for tests carried out on 38mm reconstituted Gault clay where $V_{s(vh)}$, $V_{s(hv)}$ and $V_{s(hh)}$ shear wave velocities were measured.

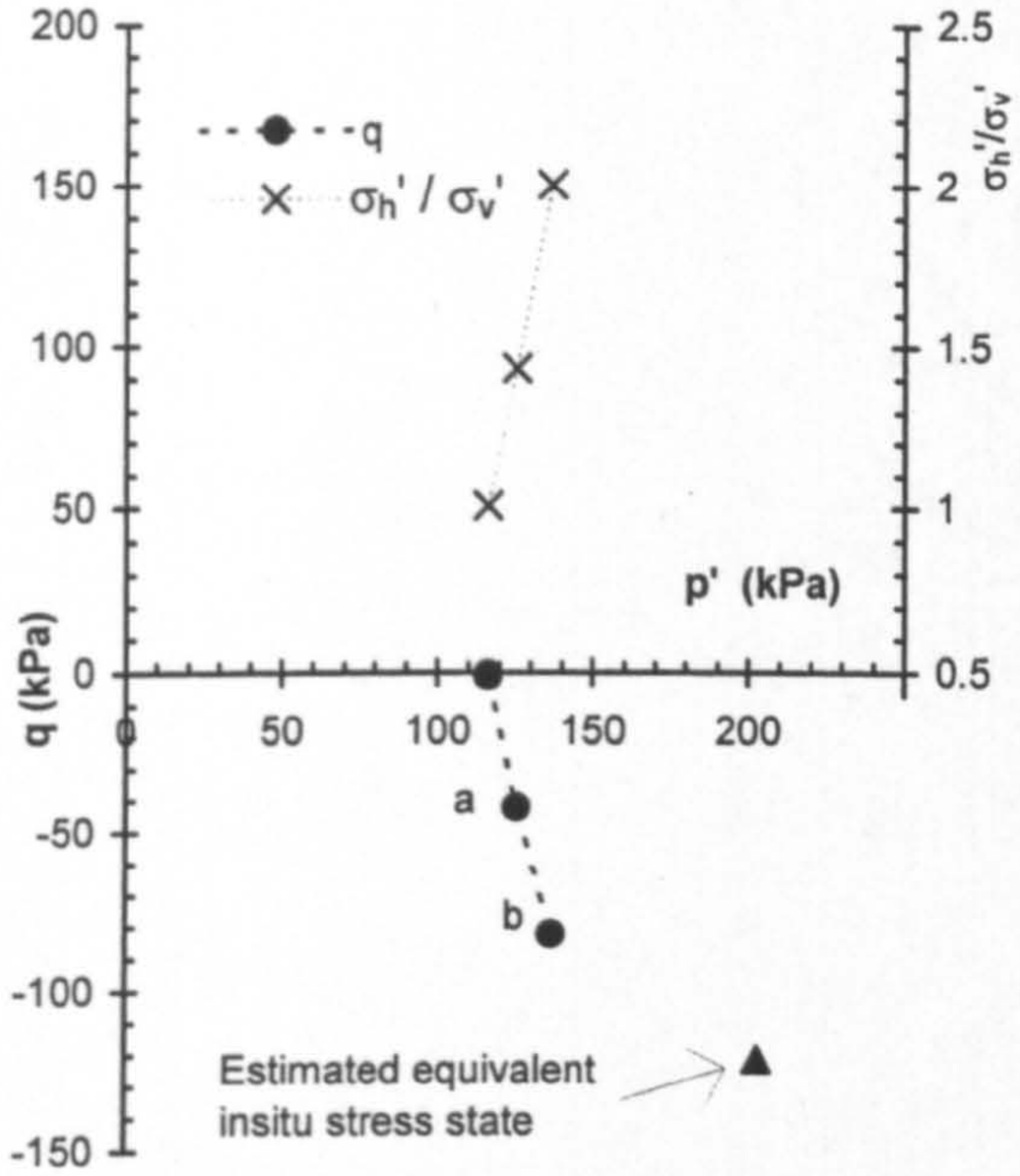

a) Test R12

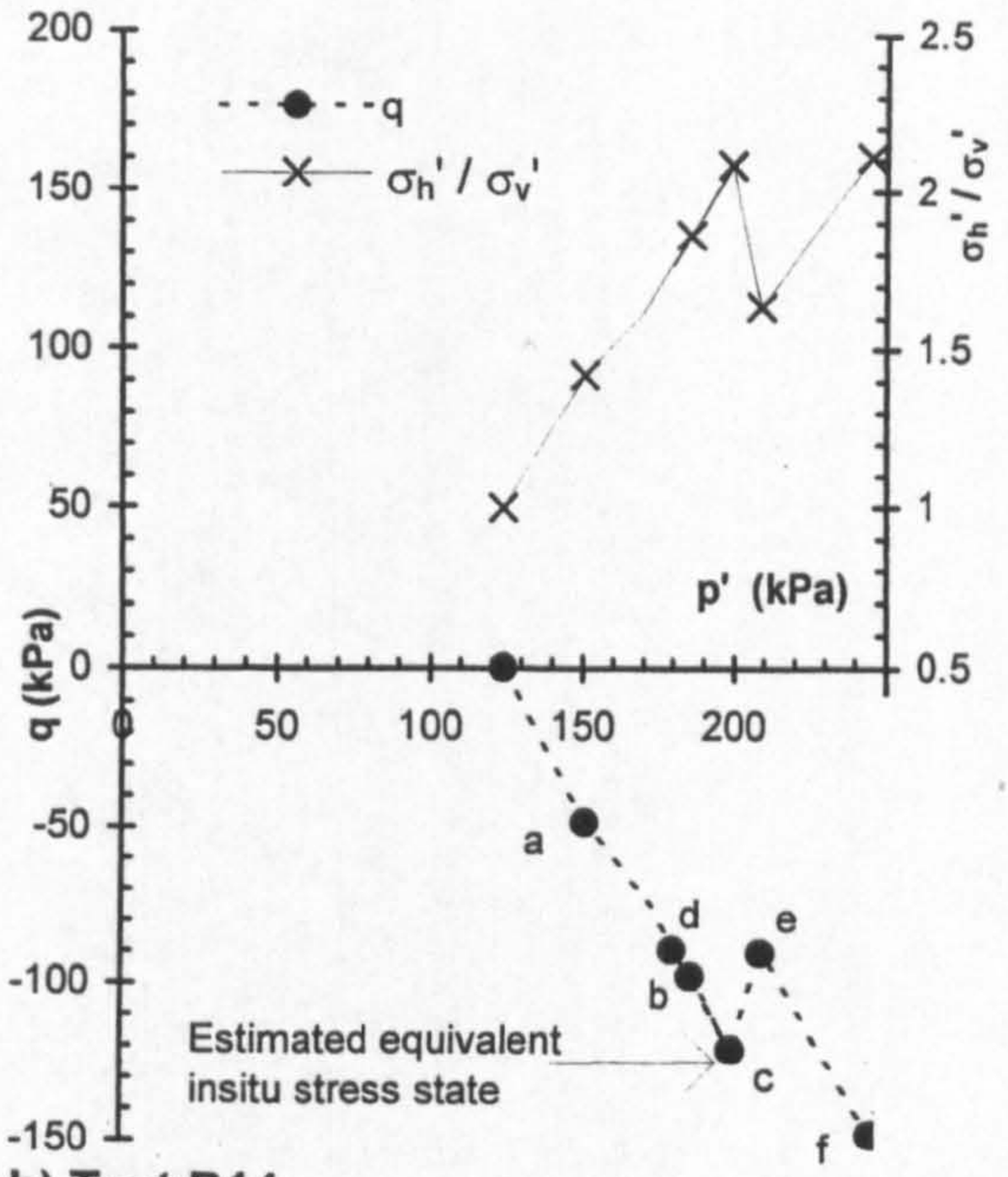

b) Test R14

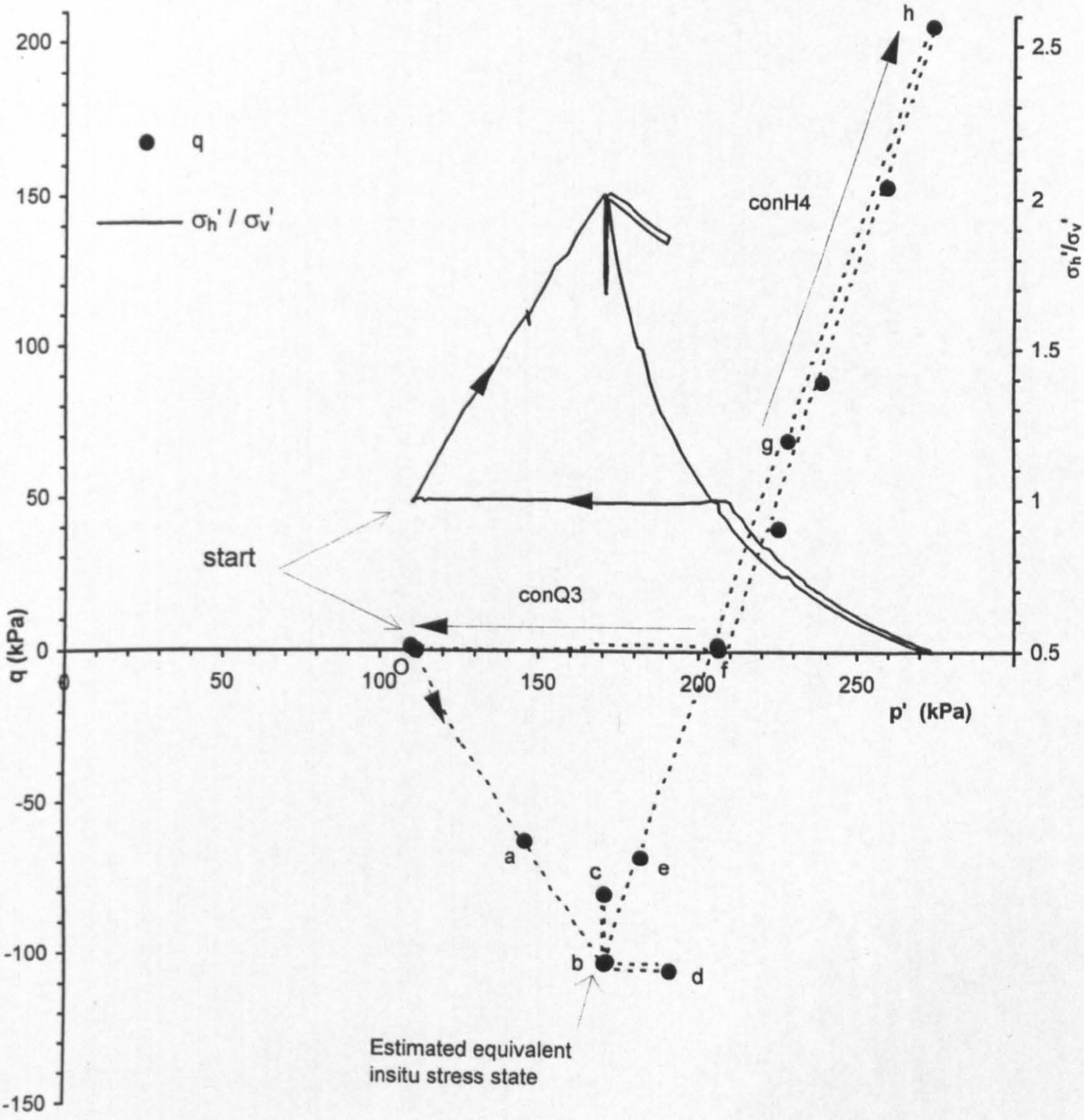

c) Test R23

Figure 4.14 Actual test stress paths and stress ratio paths - natural Gault clay samples

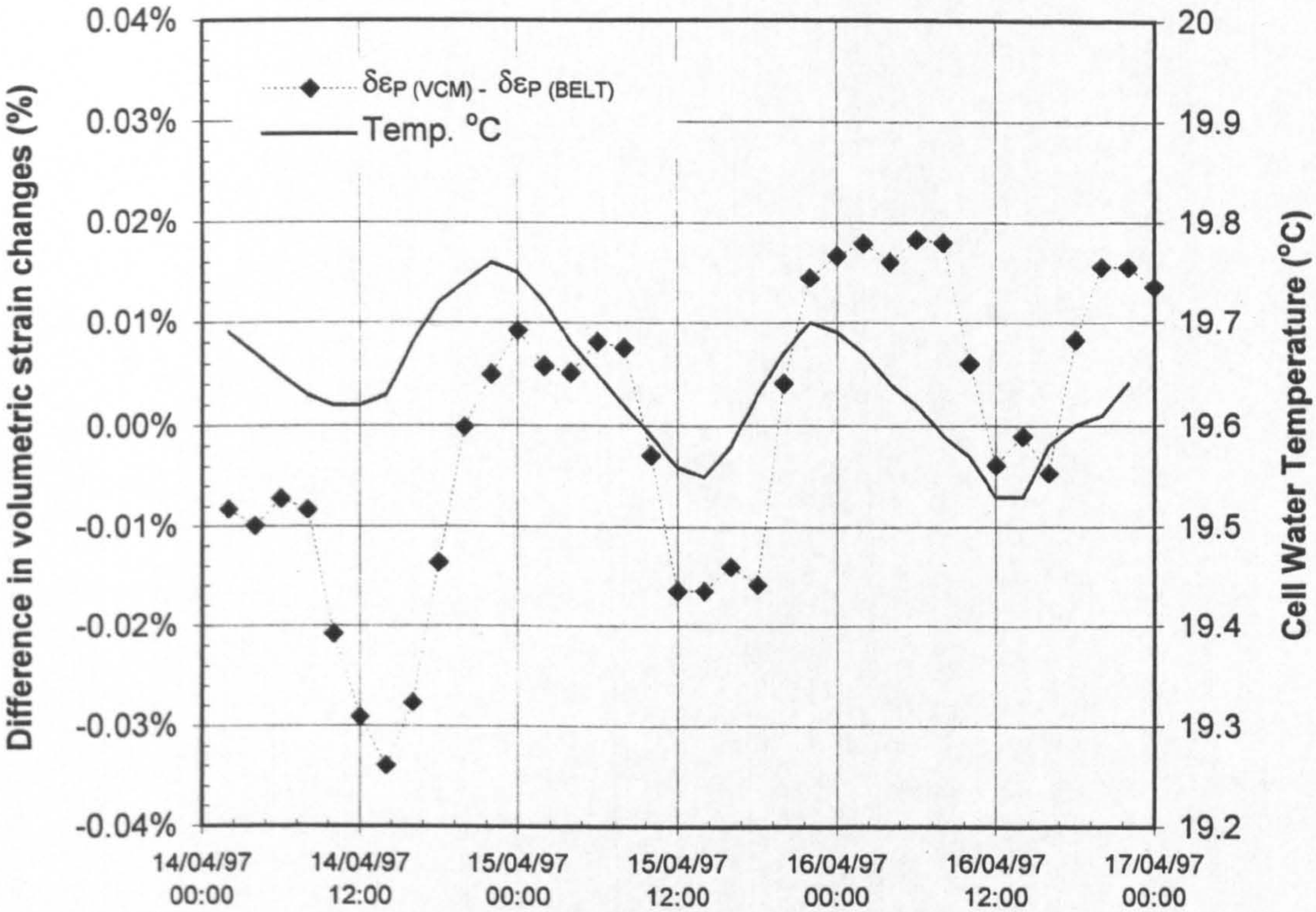

a) Test R23: Stress path excursion ConQ3 (Isotropic between points f & O in Figure 4.14)

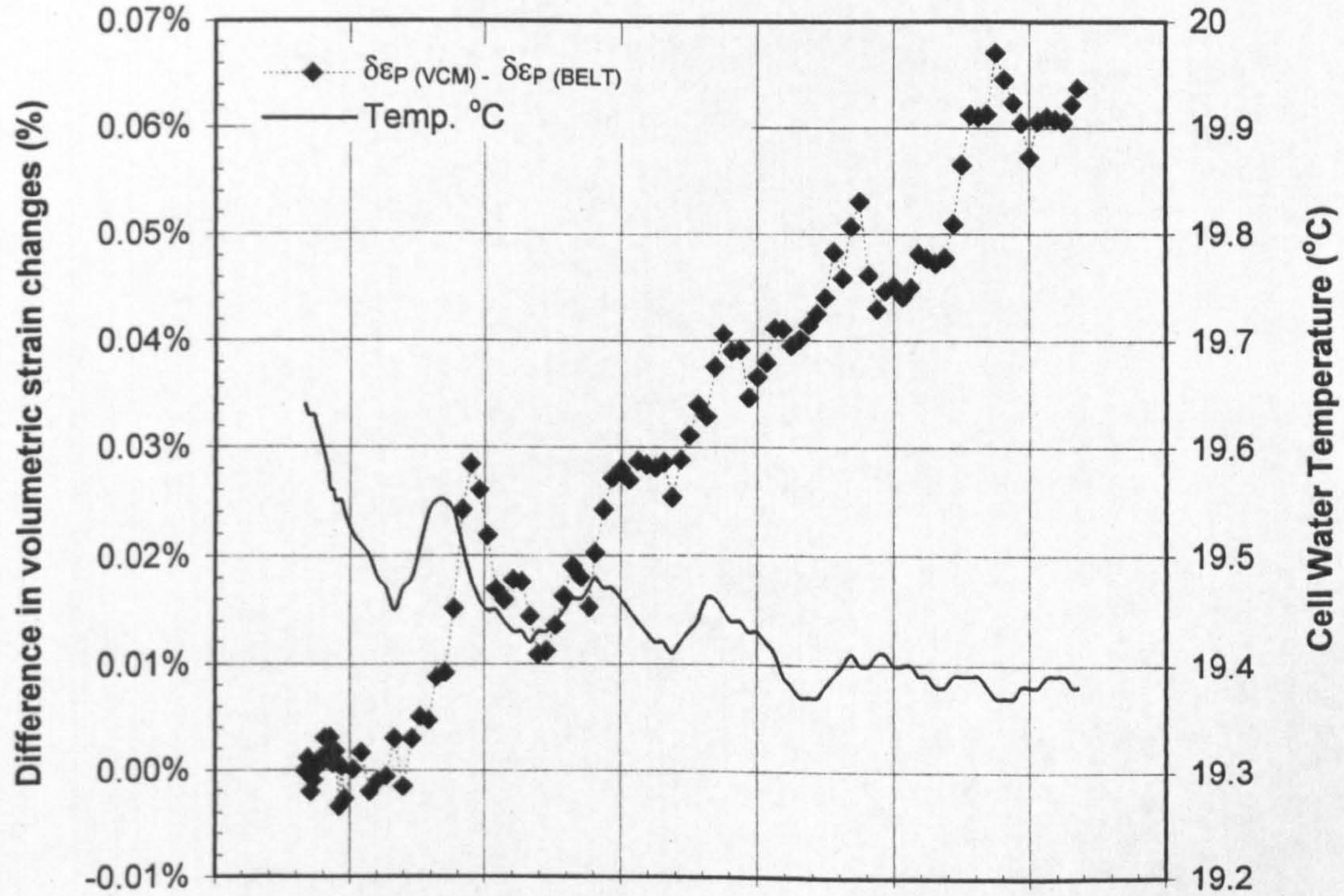

b) Test R23: Stress path excursion ConH4 (Constant σ_h' between points g & h in Figure 4.14)

Figure 4.15 Variations in the difference between volumetric strain determinations based on the horizontal belt / right cylinder assumption and VCM measurement

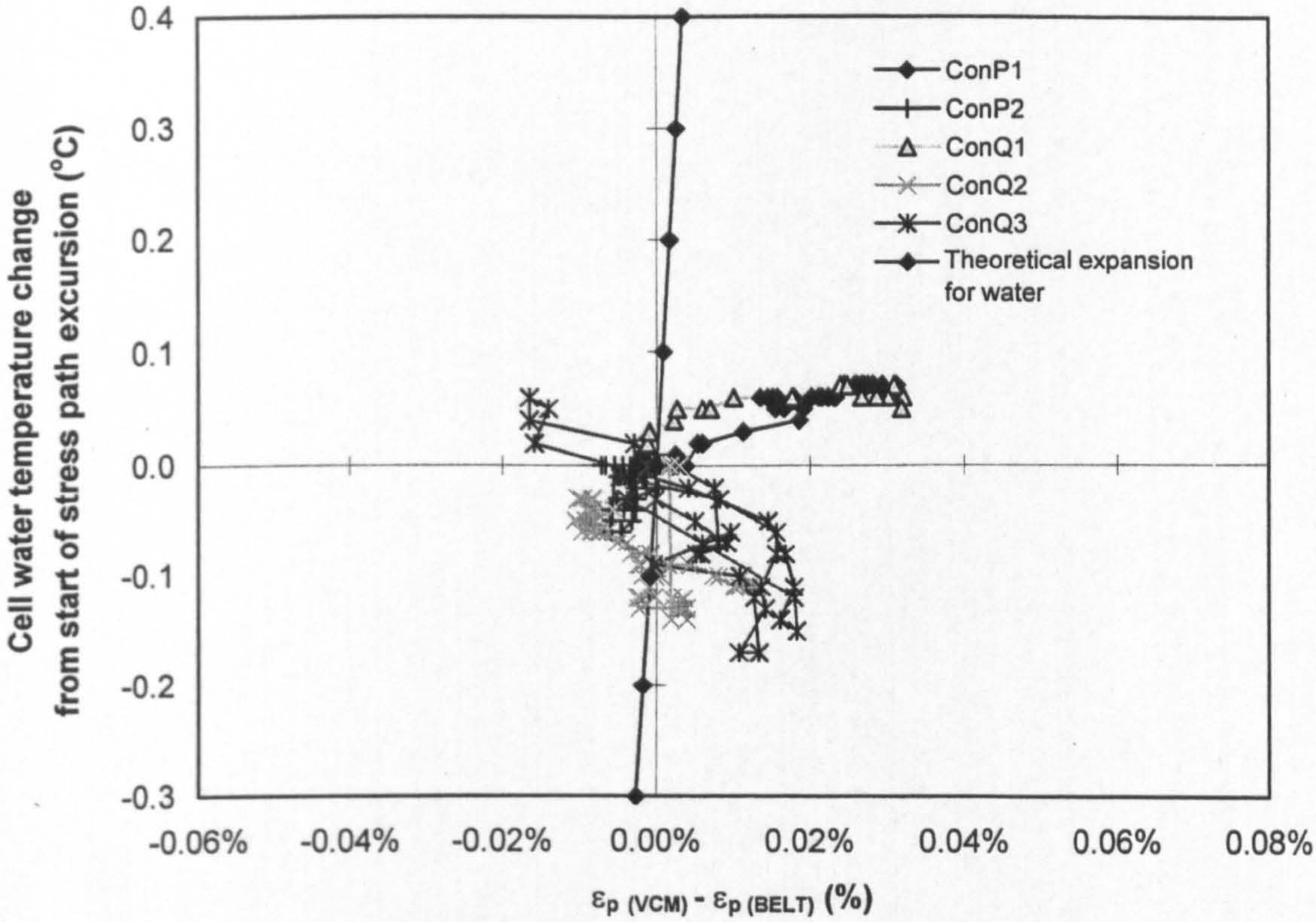

a) Stress excursions conducted at constant p' or q'

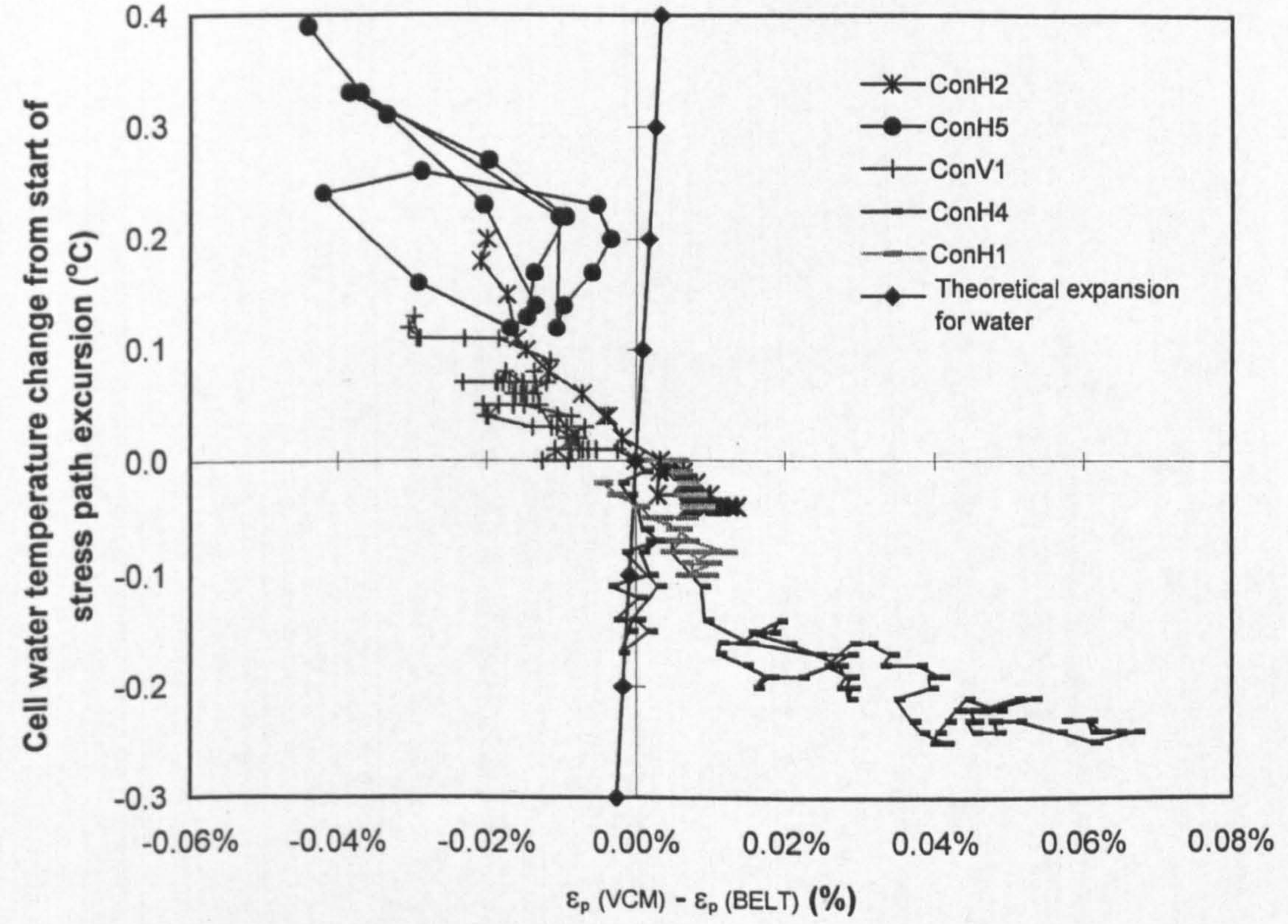

b) Stress excursions conducted at const. σ_h' or σ_v'

Figure 4.16 Comparisons between cell water temperature change and difference between volume strain change determined using the VCM and horizontal belt / right cylinder assumption

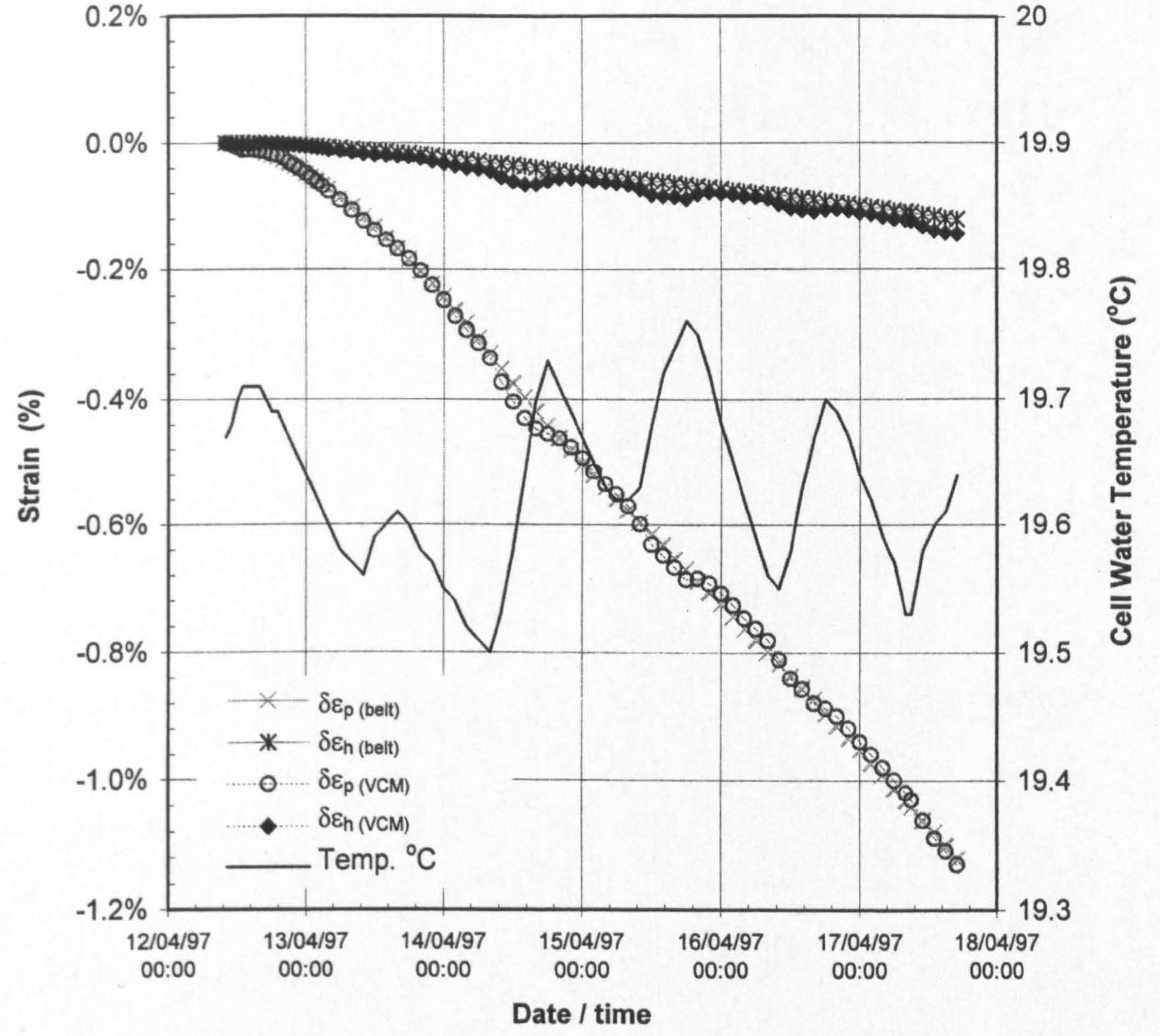

a) Full stress path excursion range

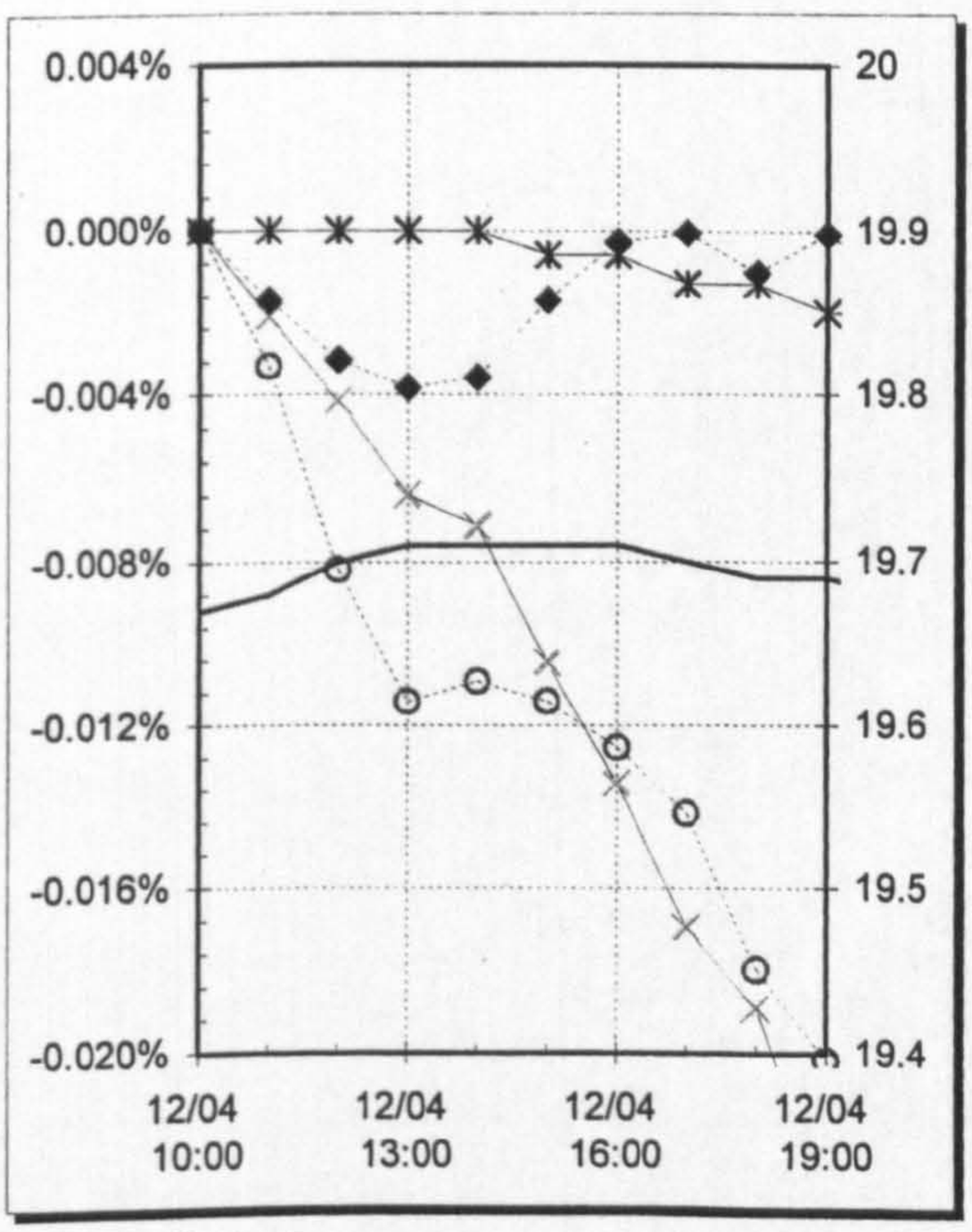

b) Small strain range

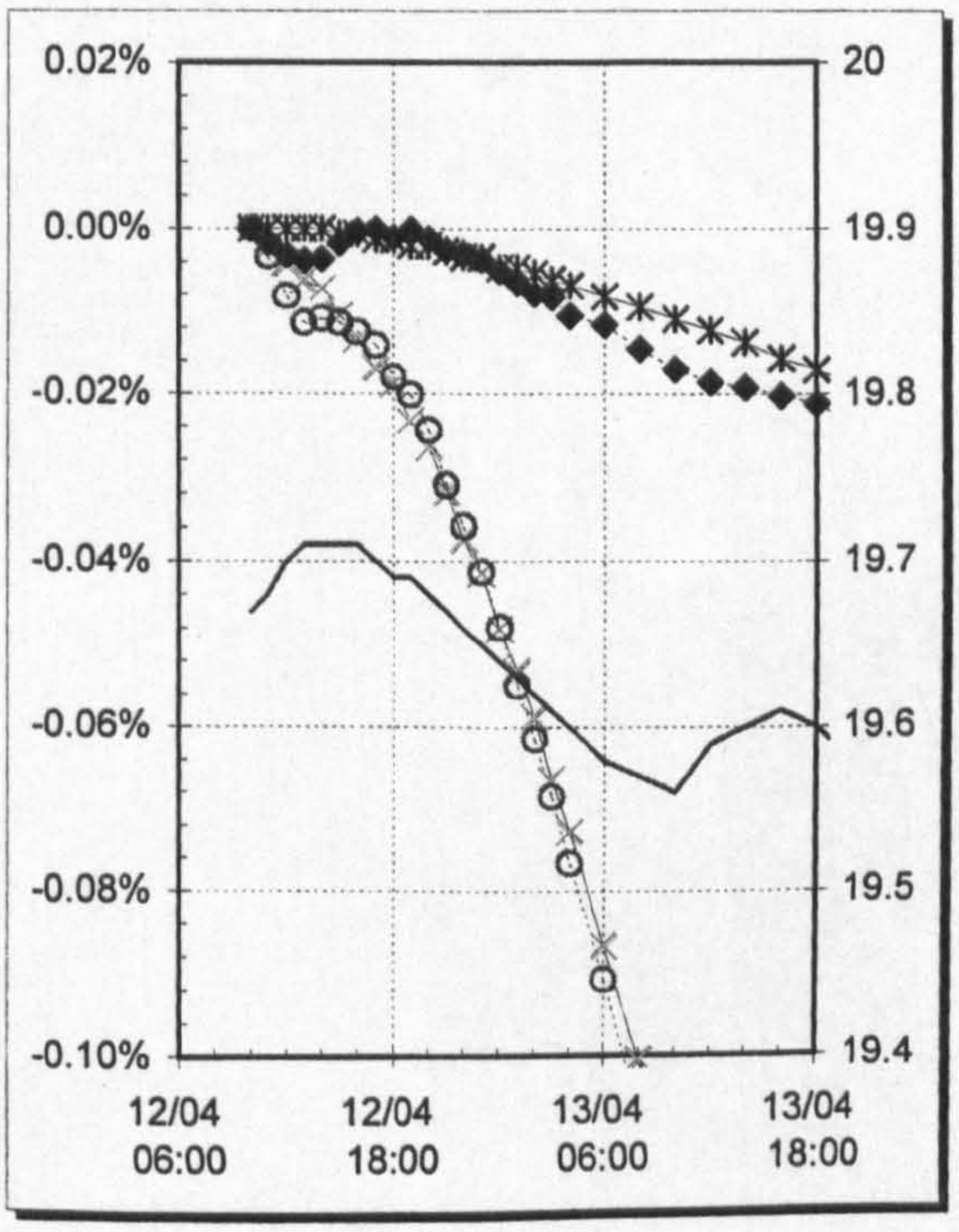

c) Intermediate strain range

Figure 4.17 Comparison of volumetric and horizontal strains based on VCM or horizontal belt: Test R23 Excursion ConQ3

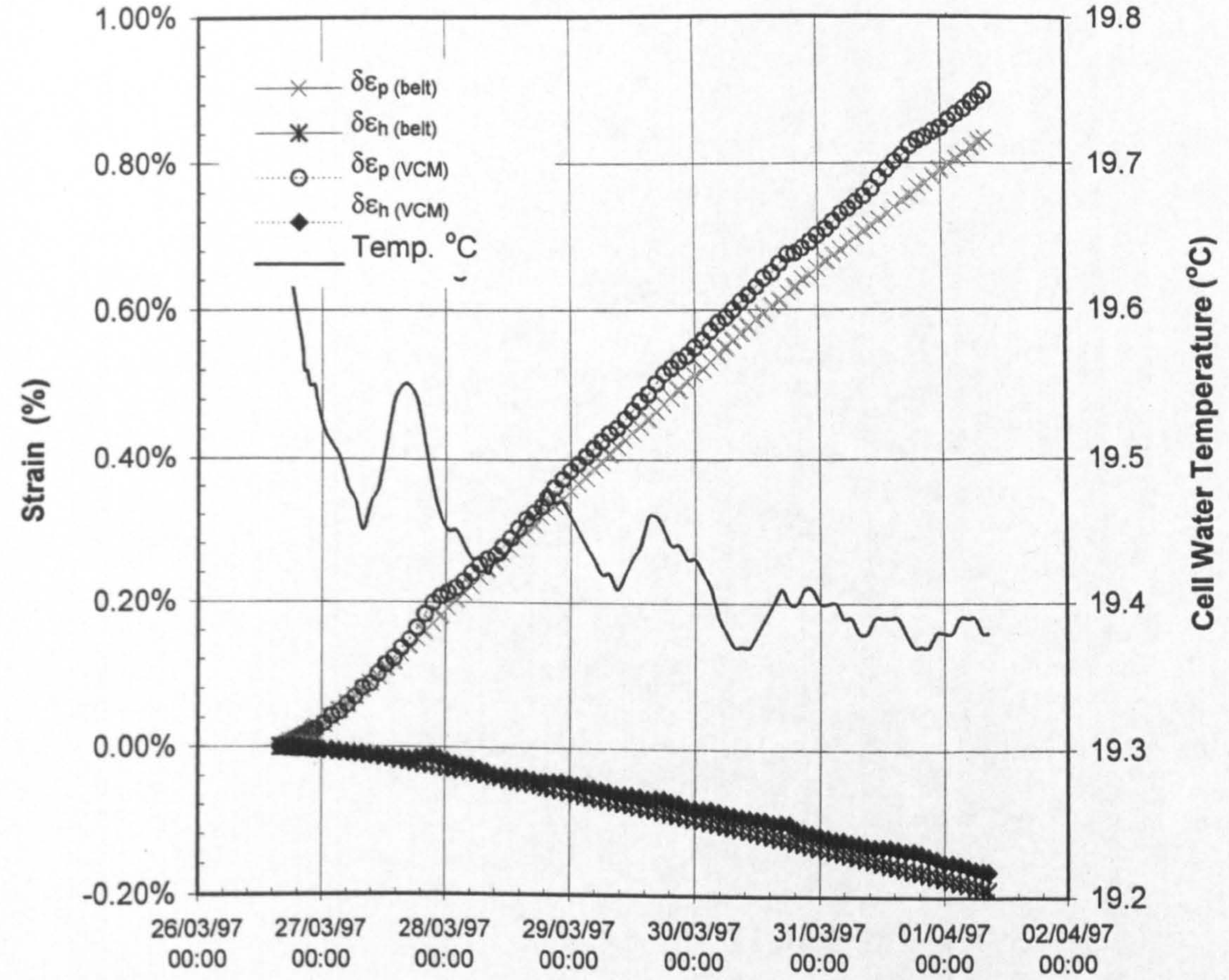

a) Full stress path excursion range

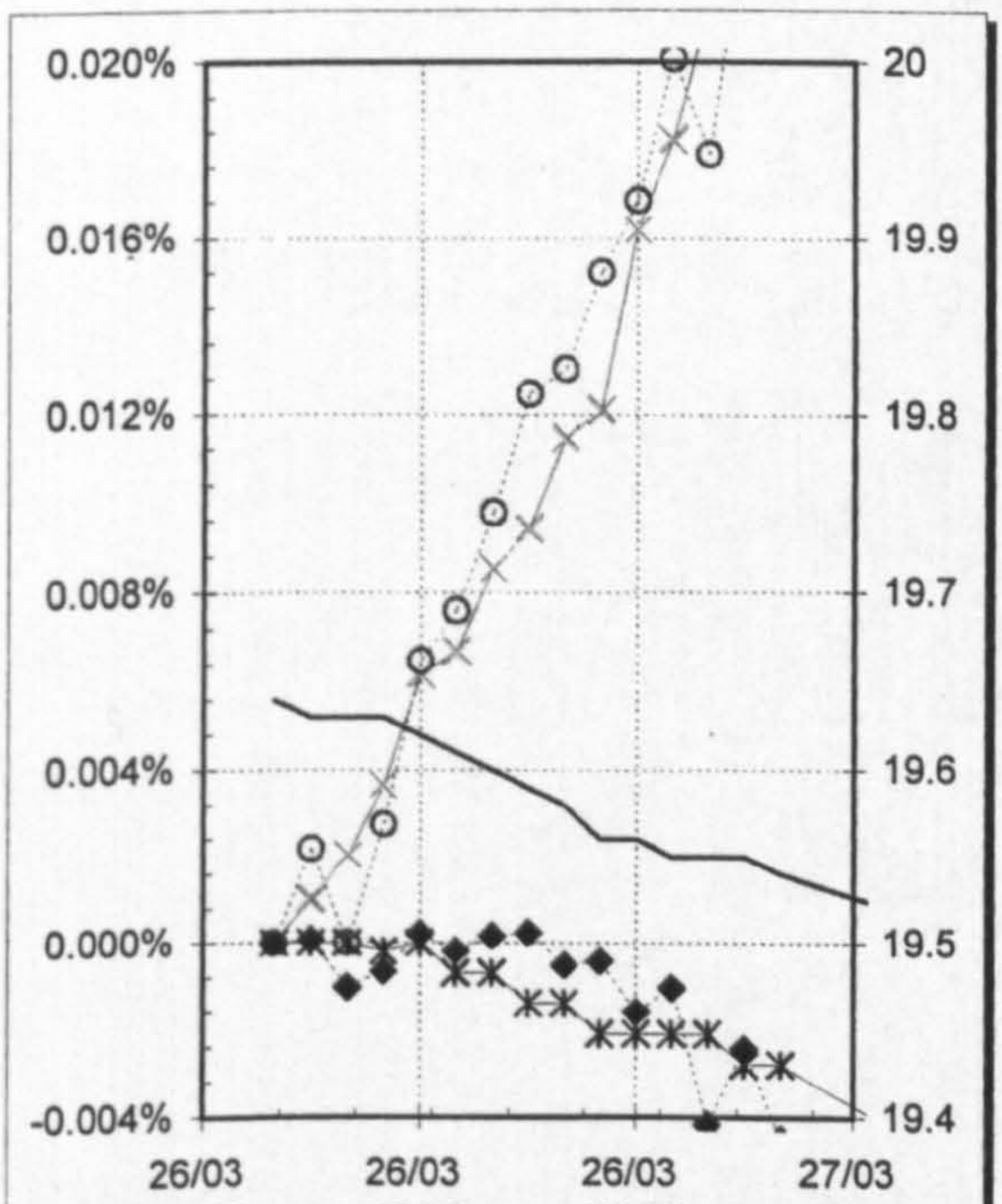

b) Small strain range

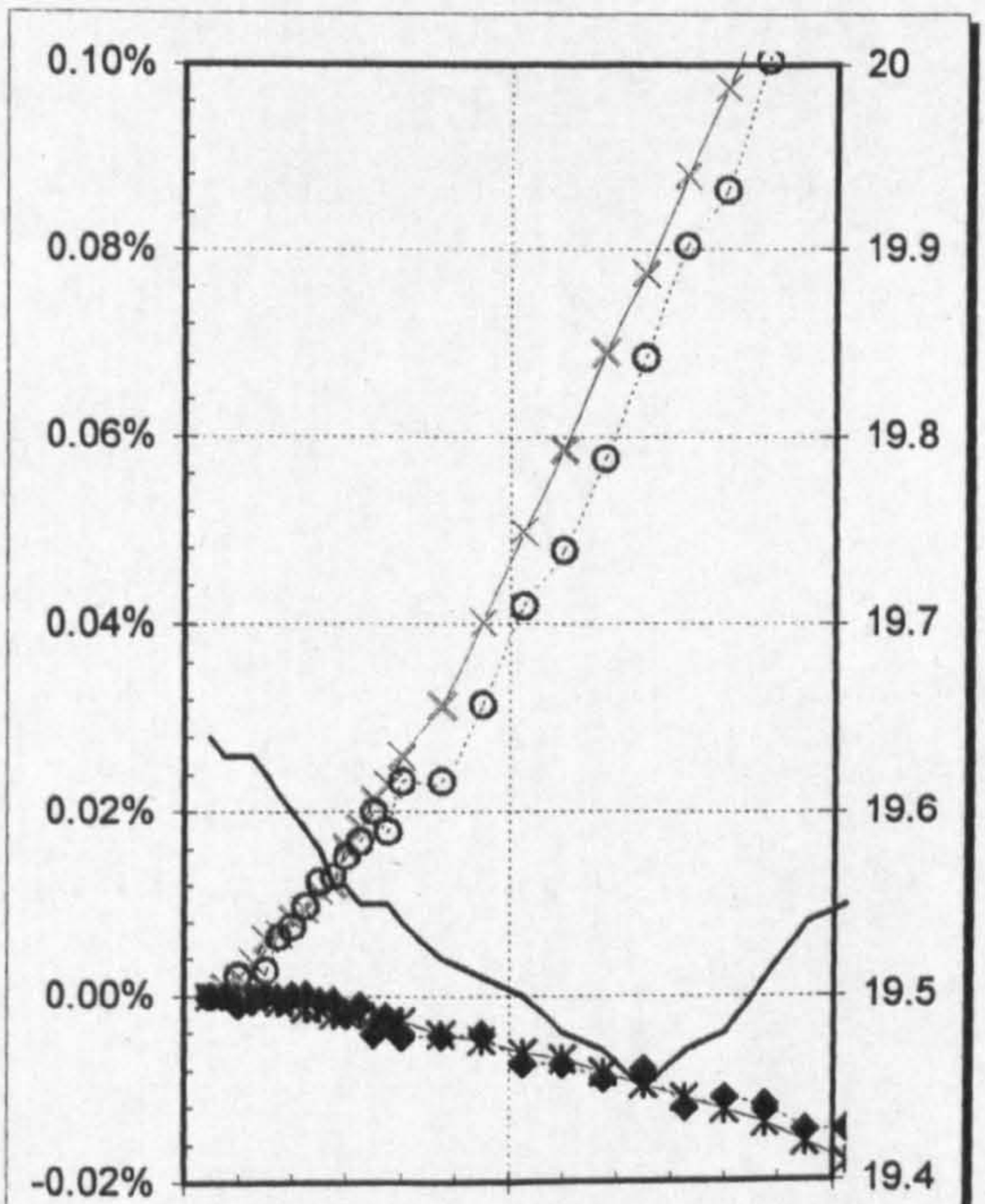

c) Intermediate strain range

Figure 4.18 Comparison of volumetric and horizontal strains based on VCM or horizontal belt: Test R23 Excursion ConH4

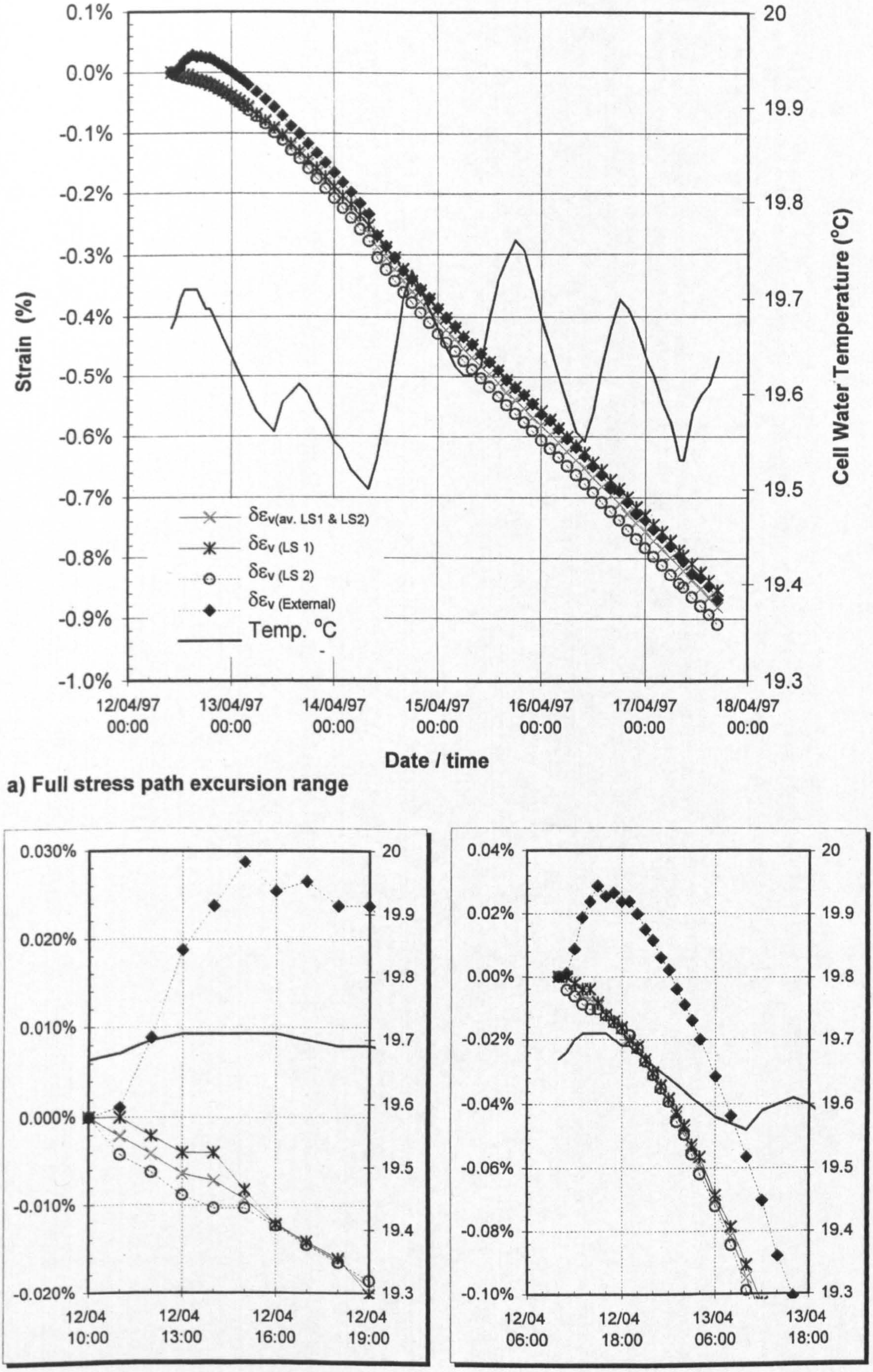

Figure 4.19 Comparison between vertical strains determined using local and external strain measurement: Test R23 Excursion ConQ3

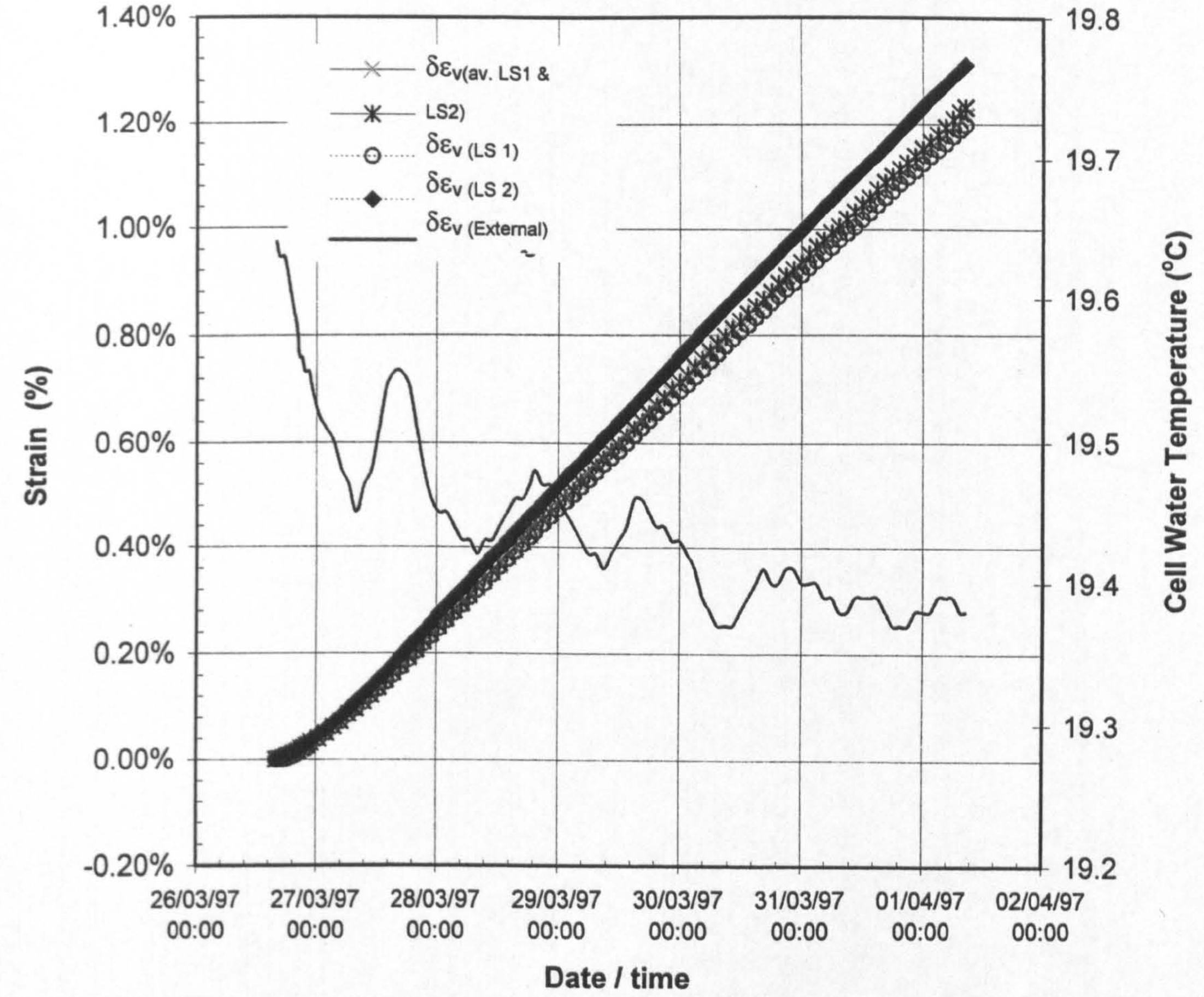

a) Full stress path excursion range

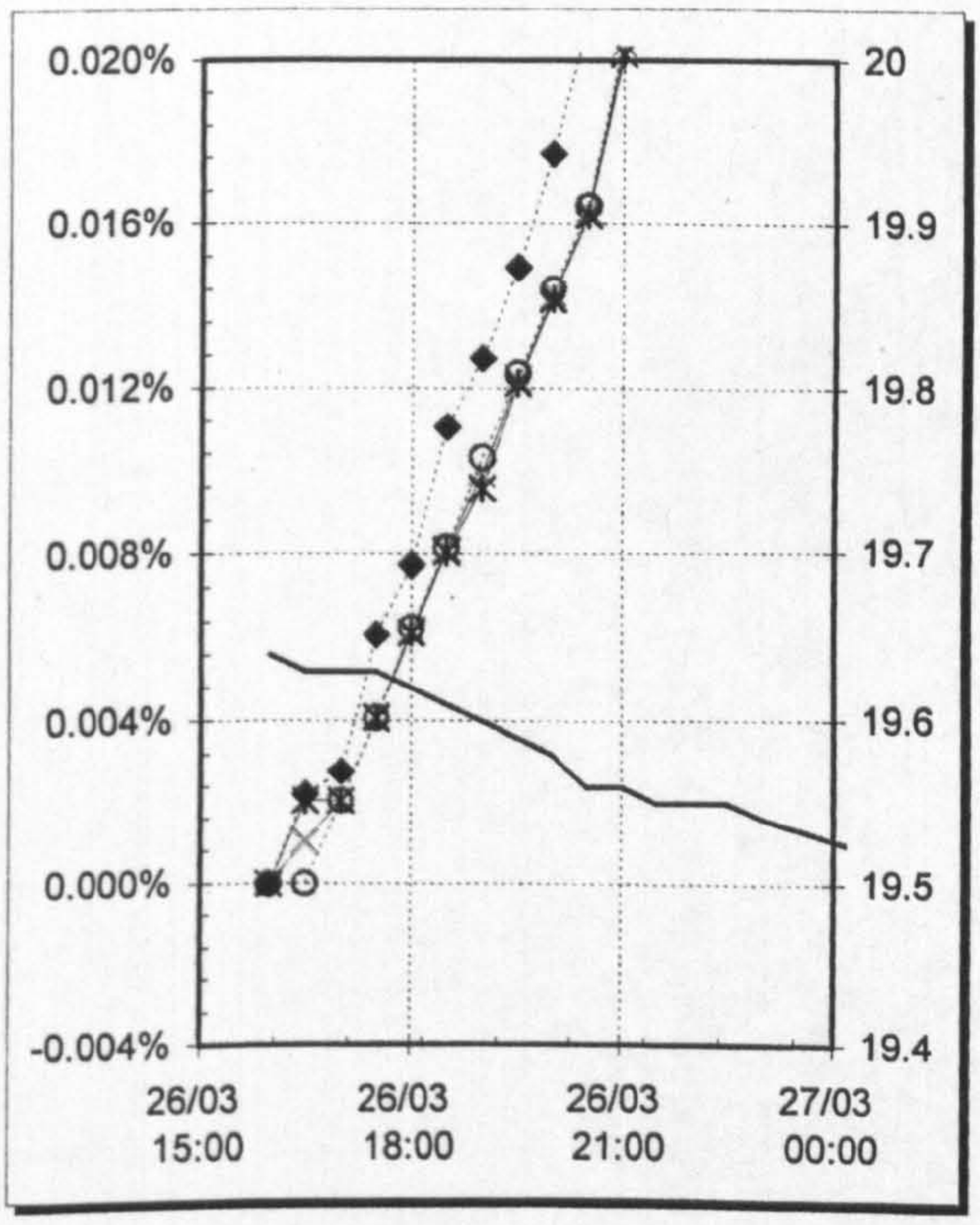

b) Small strain range

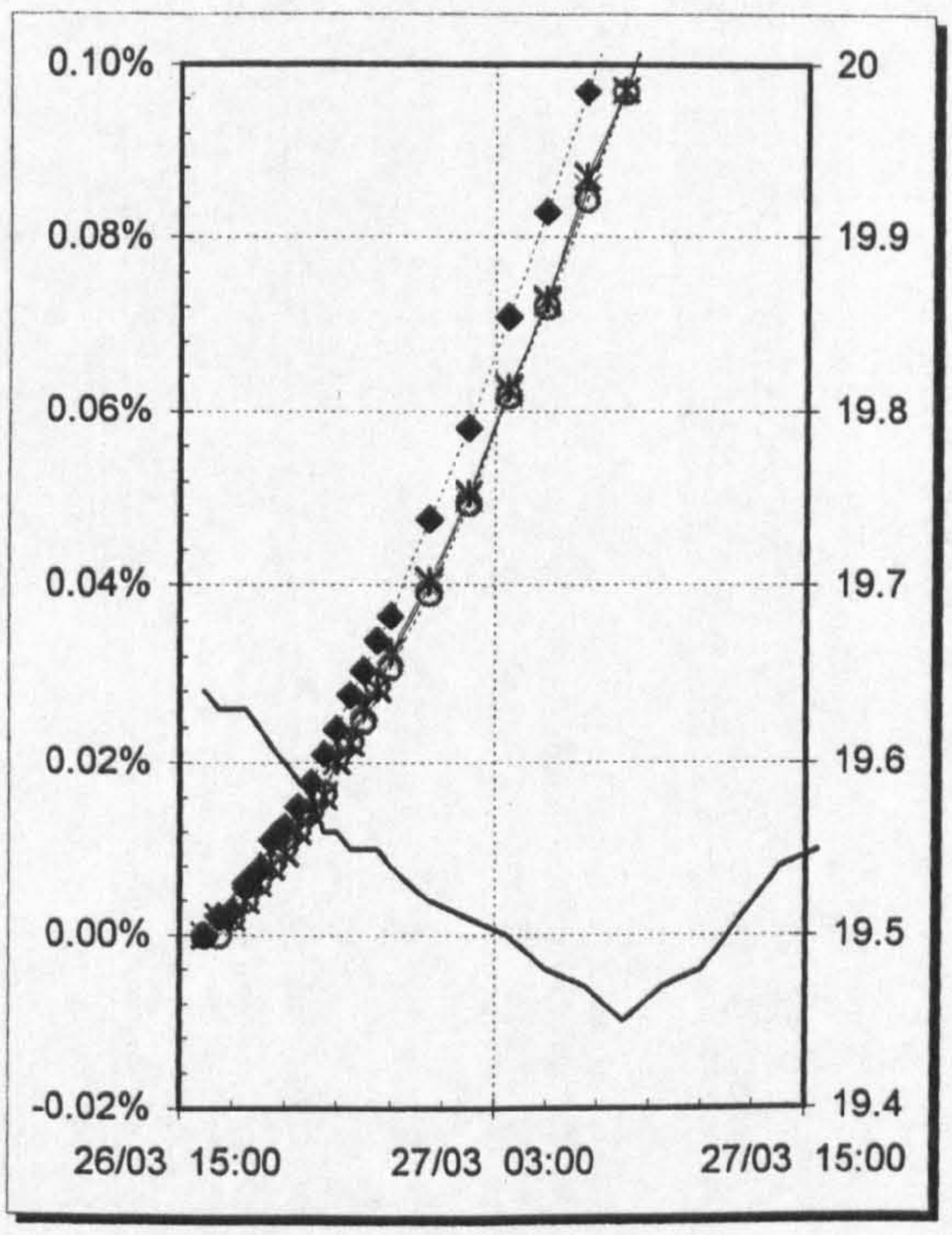

c) Intermediate strain range

Figure 4.20 Comparison between vertical strains determined using local and external strain measurement: Test R23 Excursion ConH4

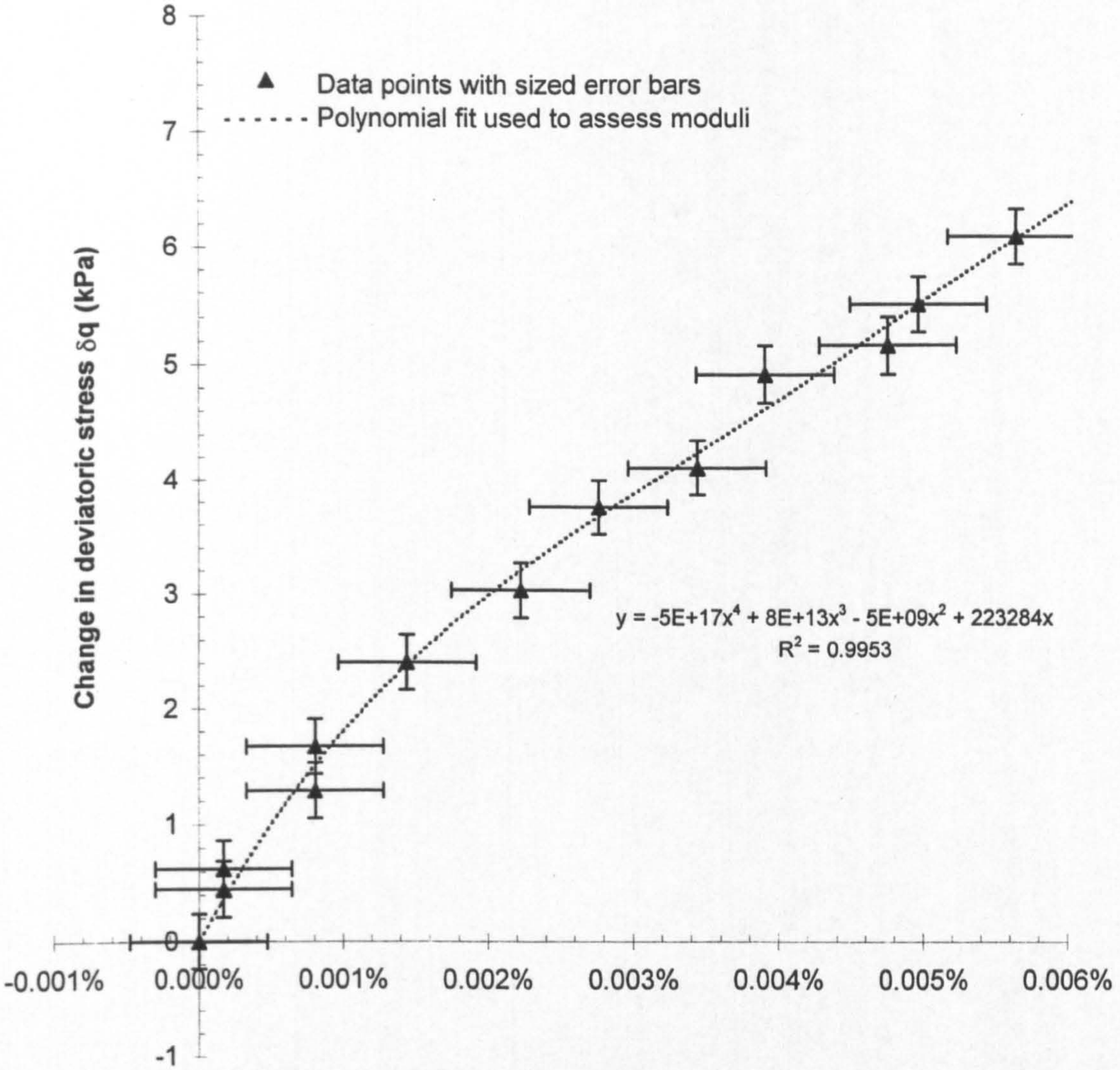

a) δq *vs.* $\delta\varepsilon_q$ results for Test R23 - excursion R23conP1

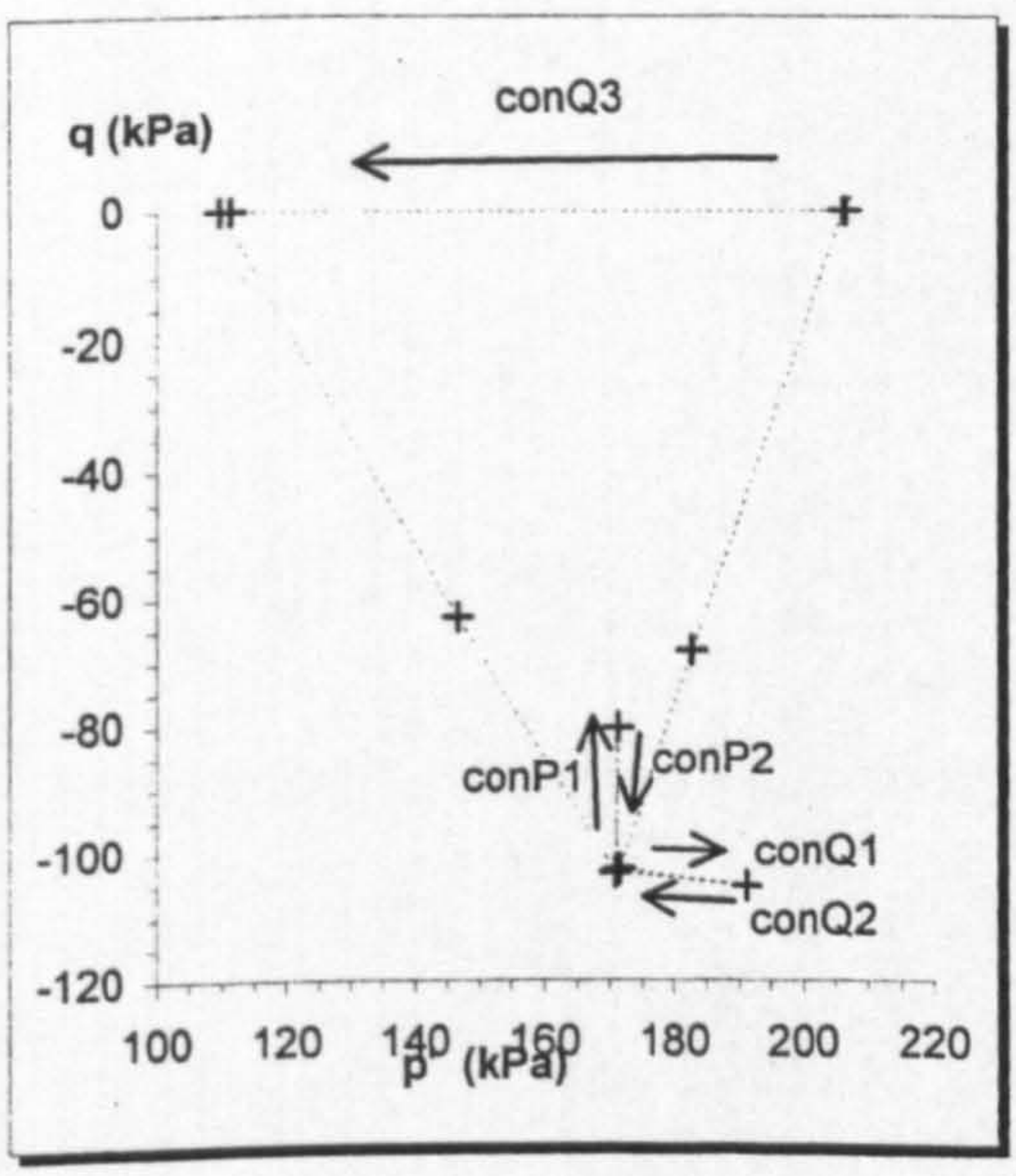

b) Test R23 - constant p' and q stress excursions

Figure 4.21 Illustration of the small strain data obtained using local strain devices - Test R23 Stress path excursion R23conP1

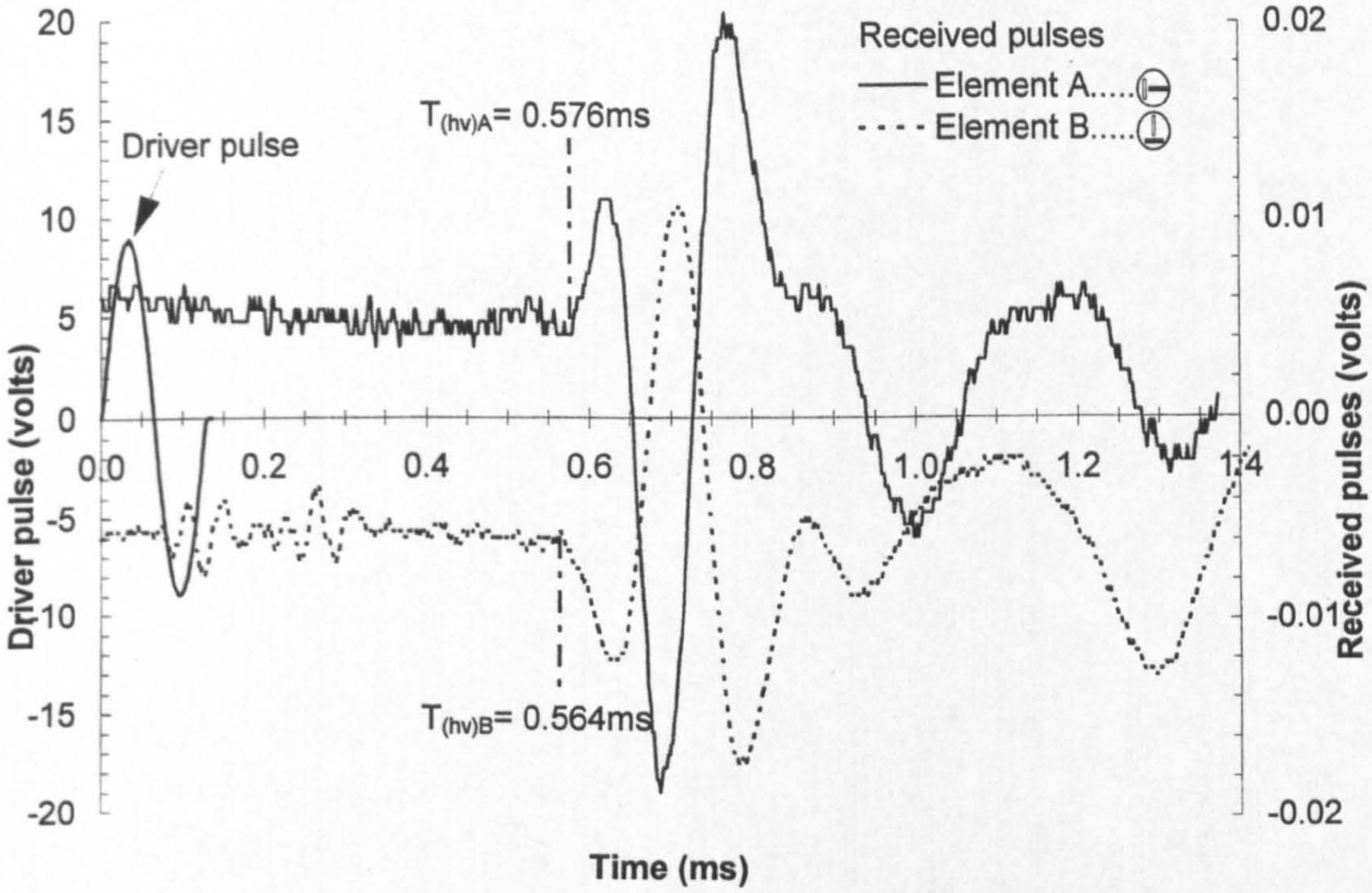

a) Comparison of vertically polarised shear wave pulses

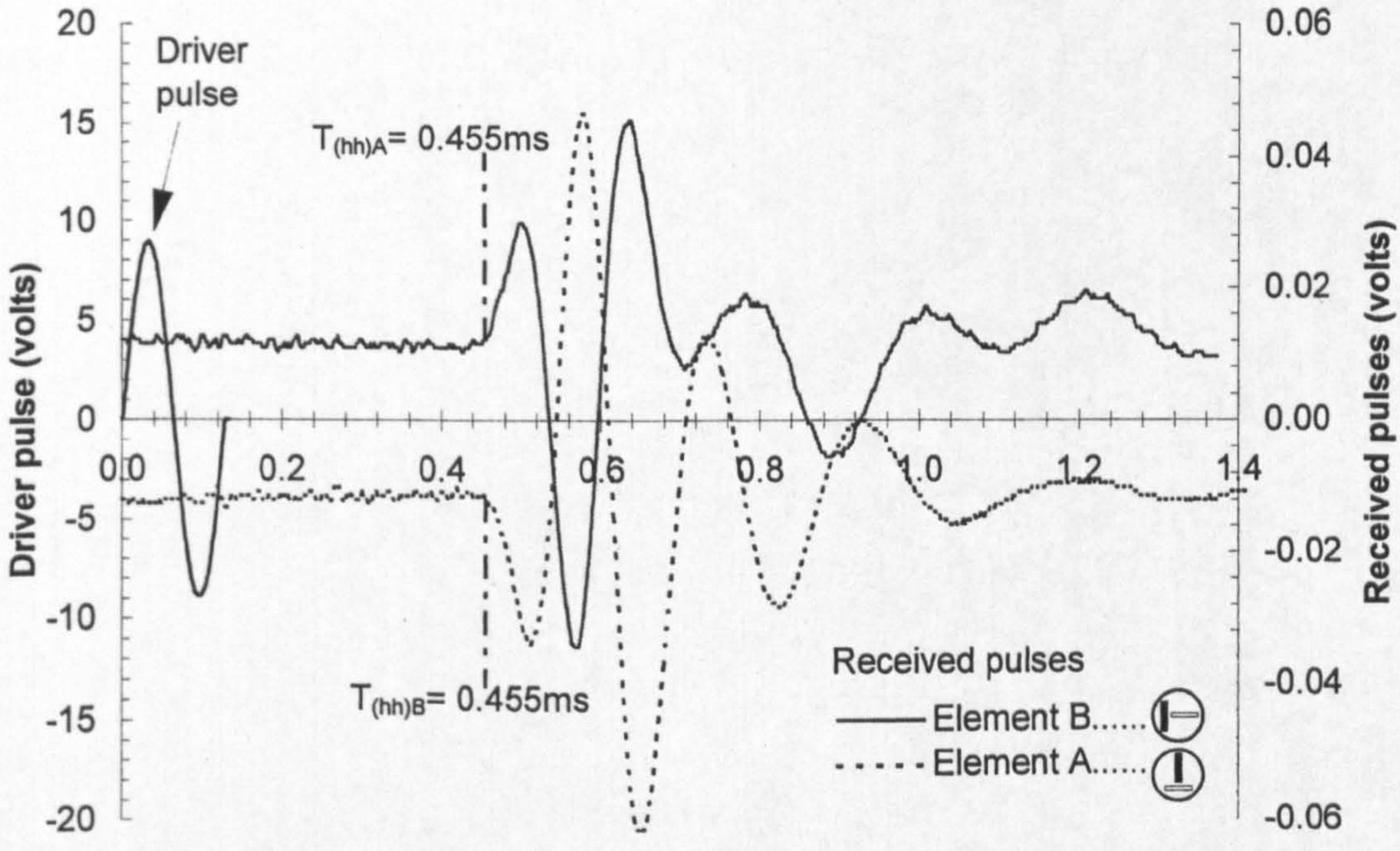

b) Comparison of horizontally polarised shear wave pulses

Figure 4.22 Comparison of received shear wave pulses for bender probes rotated through 90°

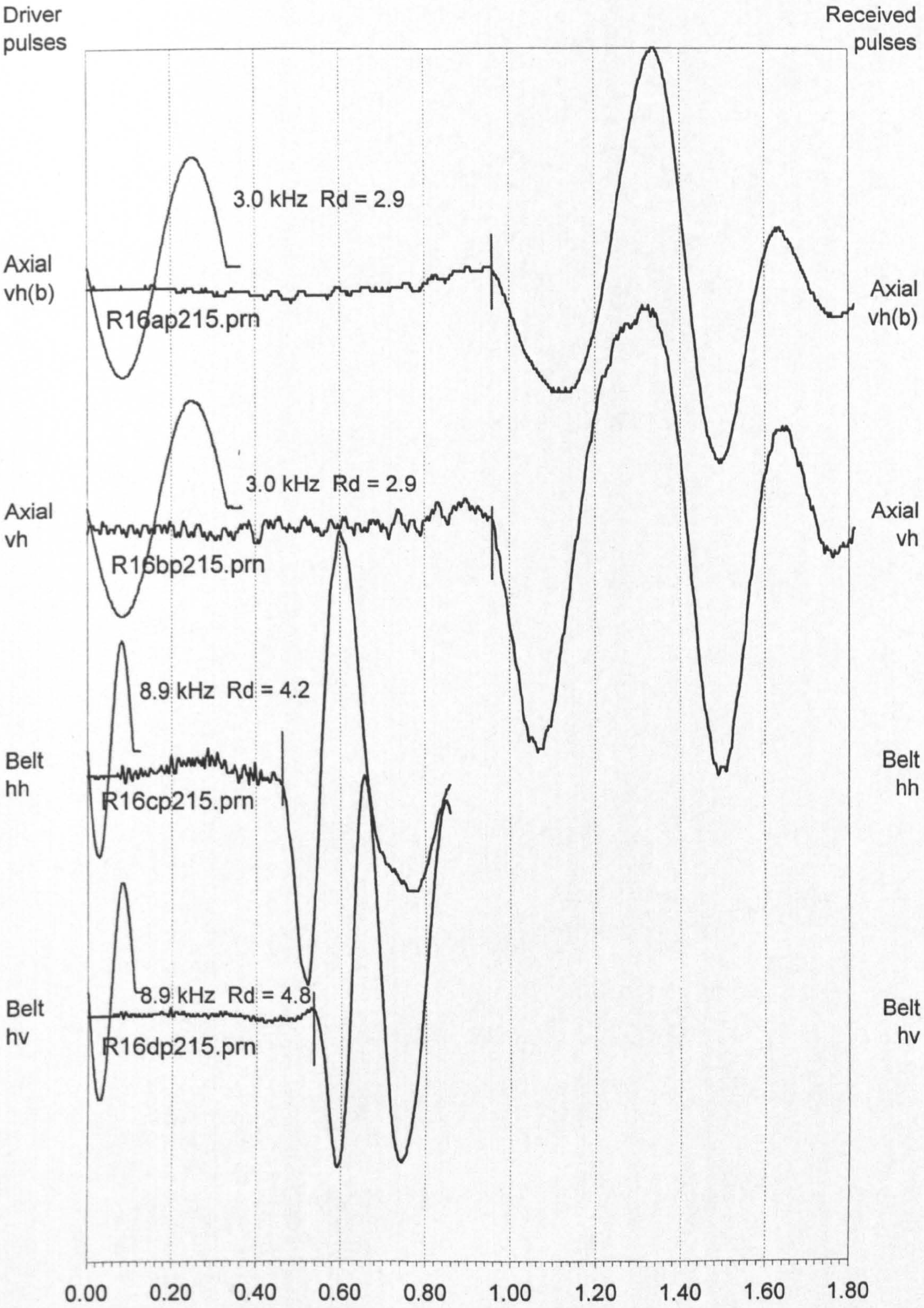

Notes

p' = 215 kPa, q = 100 kPa, voids ratio = 1.125, ρ = 1.834 T/m^3

Distance between bender: vertical = 159.5 mm, horizontal = 92.8 mm

Pulses annotated with driver frequency, distance / wavelength ratio R_d, and data file name

Figure 4.23 Set of bender driver and receiver pulses during test on 100mm reconstituted sample of Gault clay incorporating bender belt - Test R16

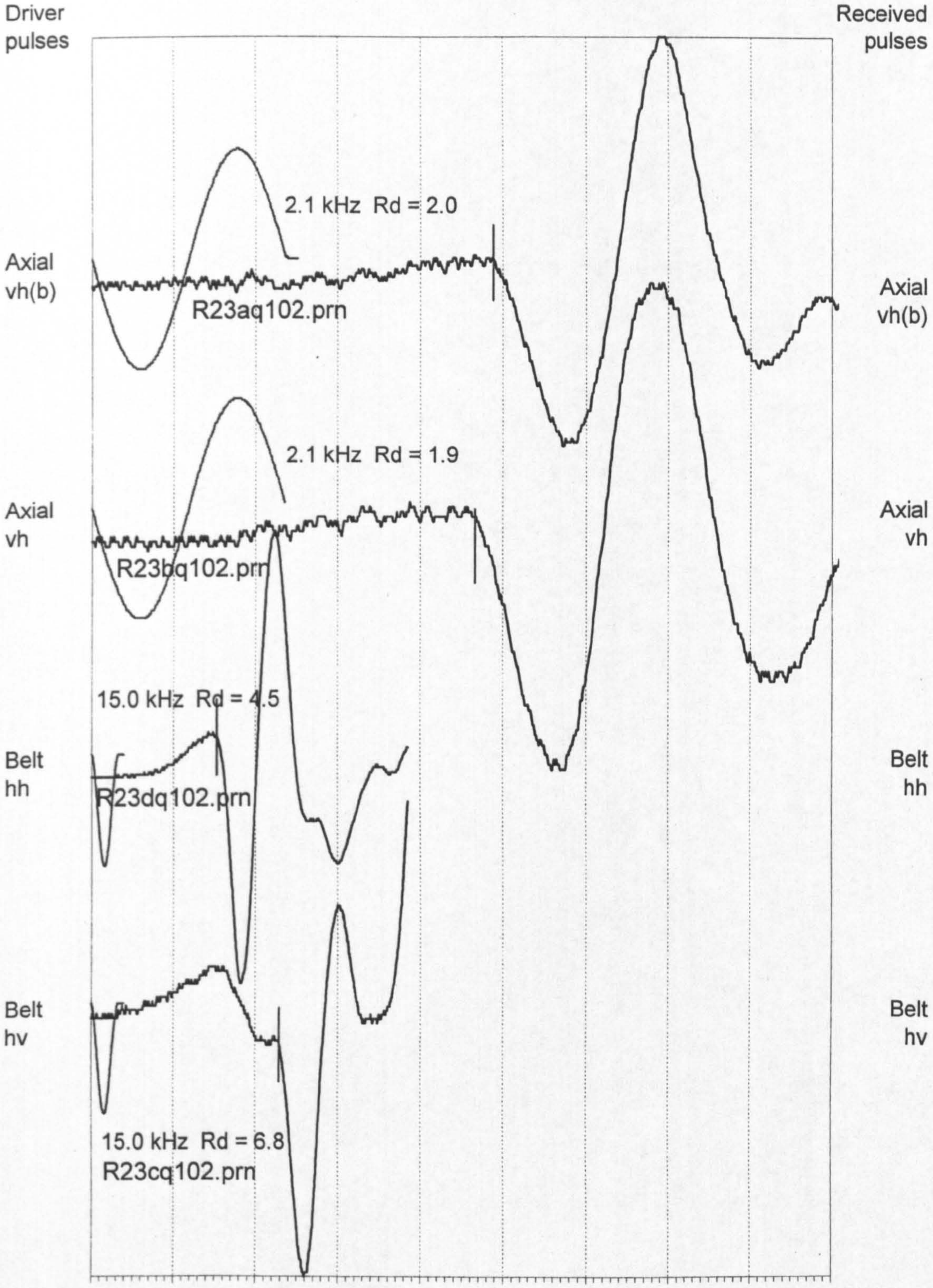

Notes

p' = 171 kPa, q = -103 kPa, voids ratio = 0.823, ρ = 1.960 T/m^3

Distance between bender: vertical = 175.1 mm, horizontal = 94.4 mm

Pulses annotated with driver frequency, distance / wavelength ratio R_d, and data file name

Figure 4.24 Set of bender driver and receiver pulses during test on 100mm natural sample of Gault clay incorporating bender belt - Test R23

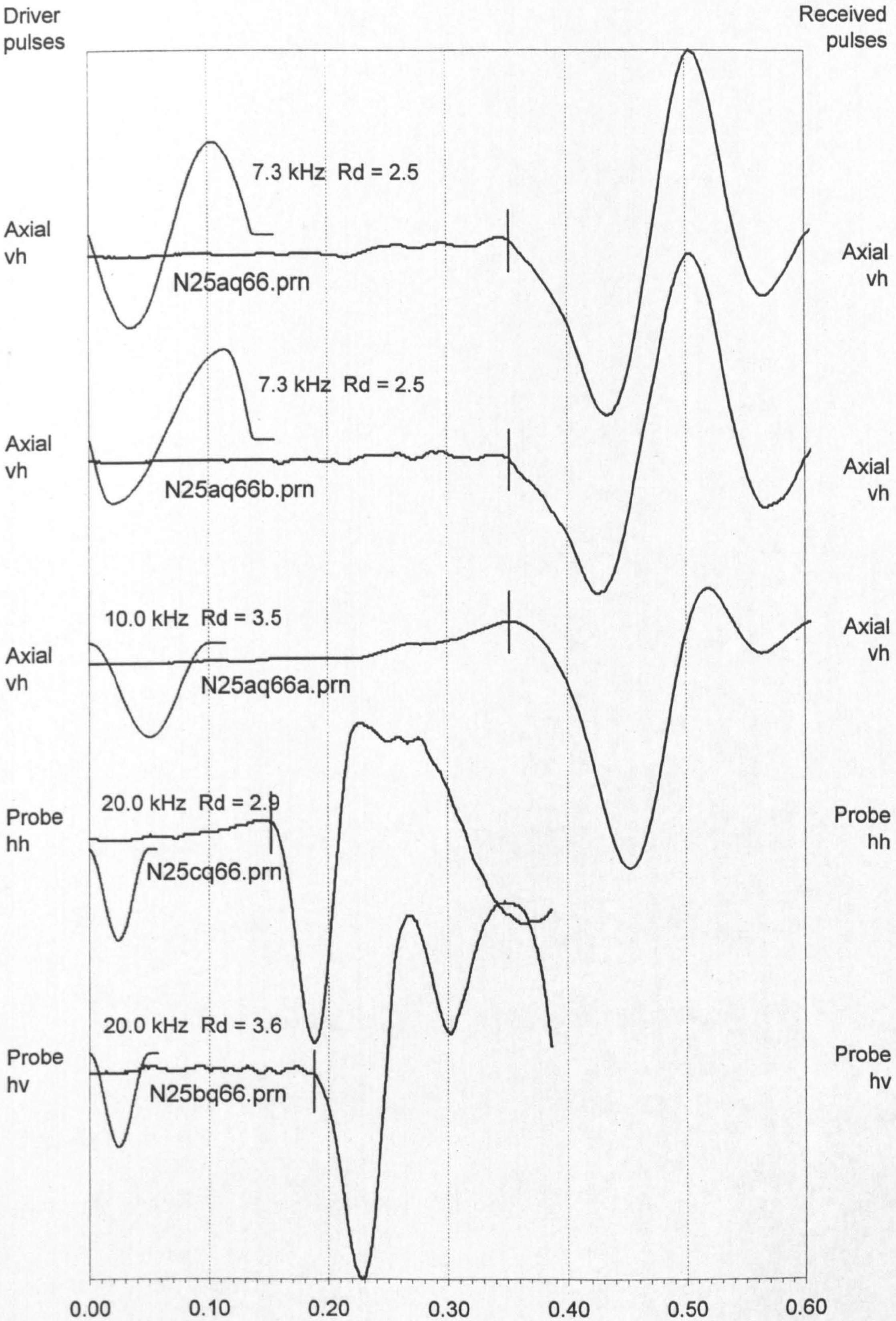

Notes

p' = 110 kPa, q = 60 kPa, voids ratio = 0.958, ρ = 1.894 T/m^3

Distance between bender: vertical = 56.1 mm, horizontal = 31.4 mm

Pulses annotated with driver frequency, distance / wavelength ratio R_d, and data file name.

Figure 4.25 Set of bender driver and receiver pulses during test on 38mm reconstituted sample incorporating bender probes - Test N25

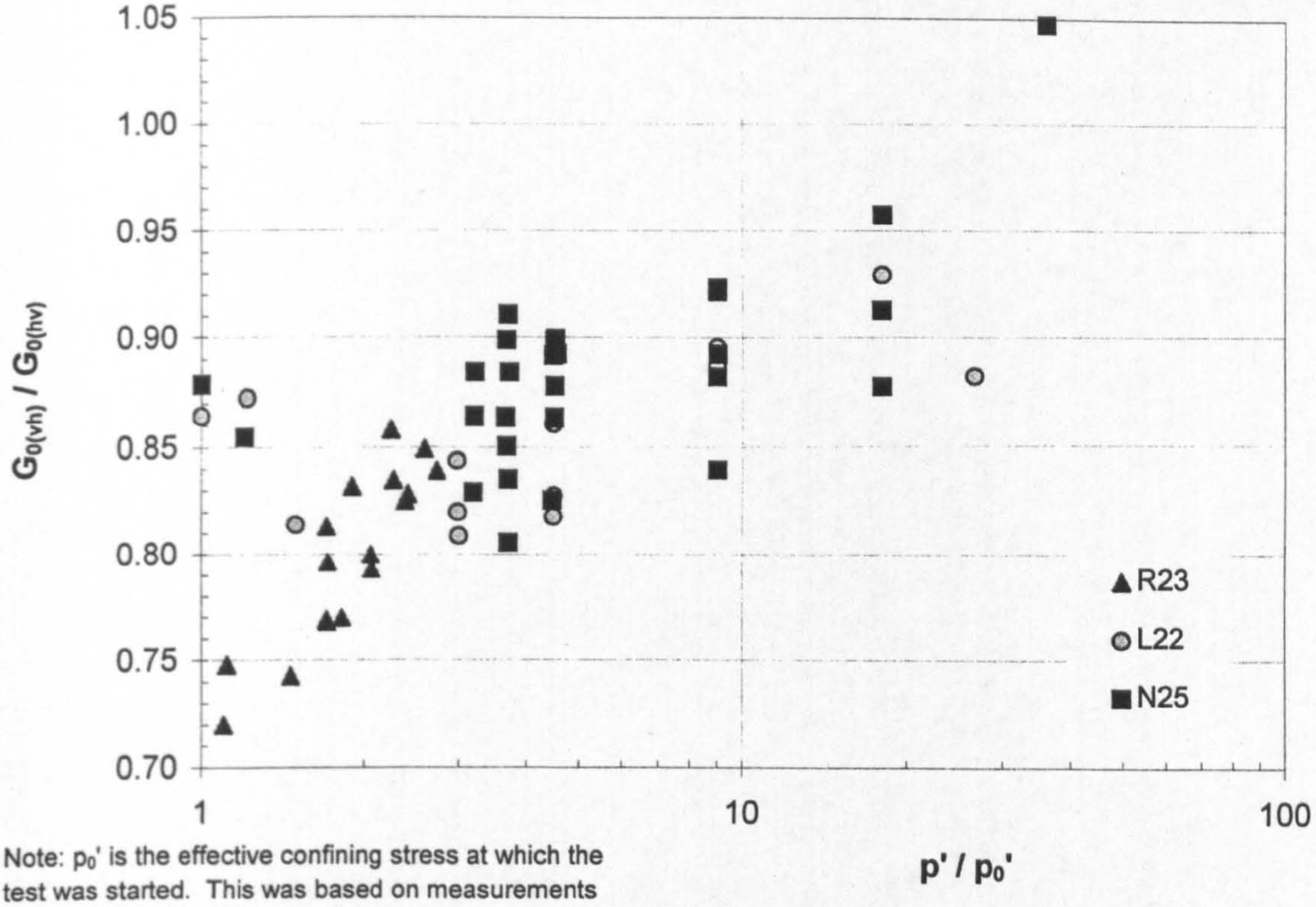

Figure 4.26 Shear modulus ratio $G_{0(vh)}/G_{0(hv)}$ *vs.* confining stress ratio during tests on natural and reconstituted material

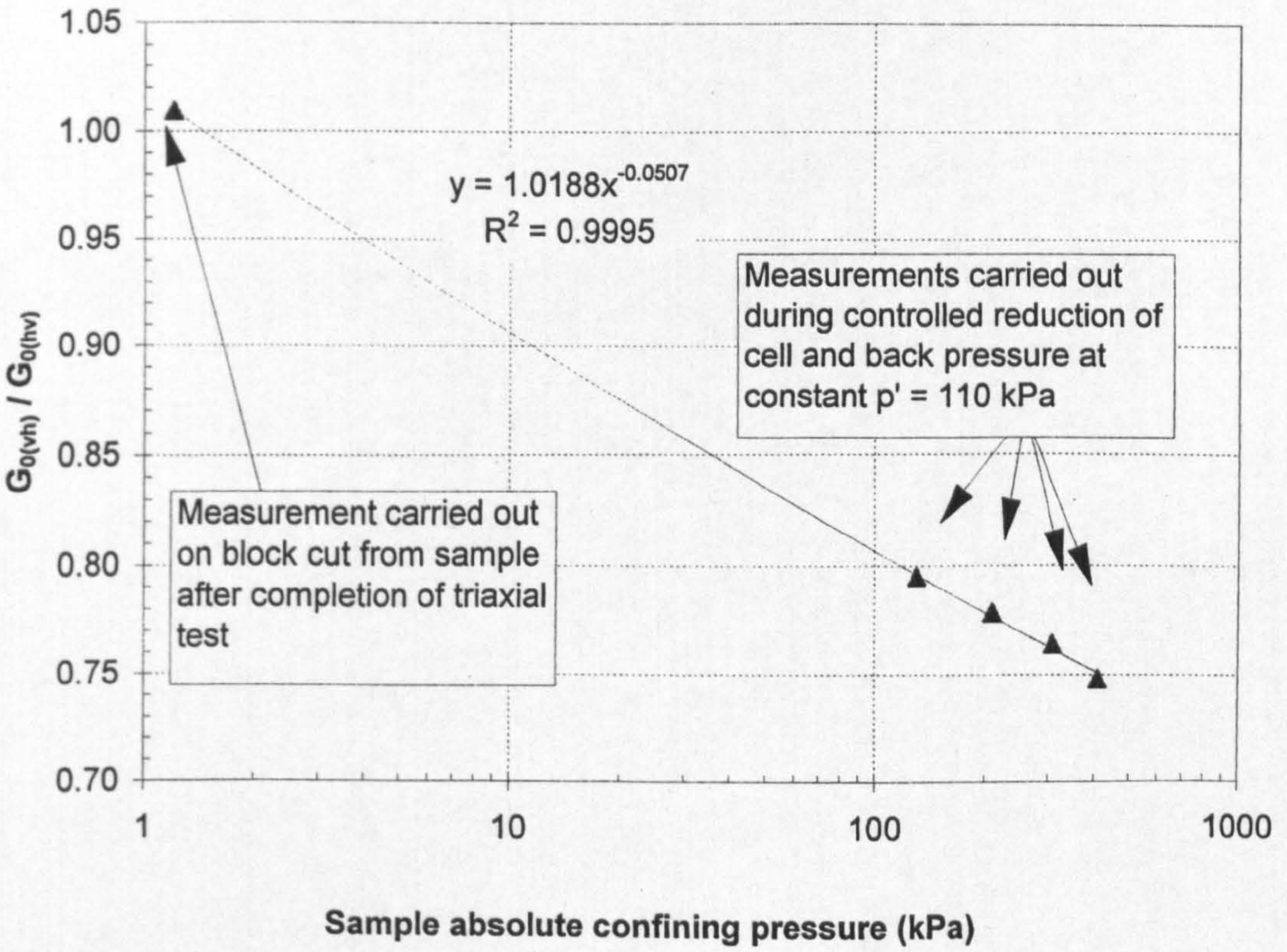

Figure 4.27 Shear modulus ratio $G_{0(vh)}/G_{0(hv)}$ *vs.* absolute confining pressure during dismantling and subsequent bench top testing of sample R23

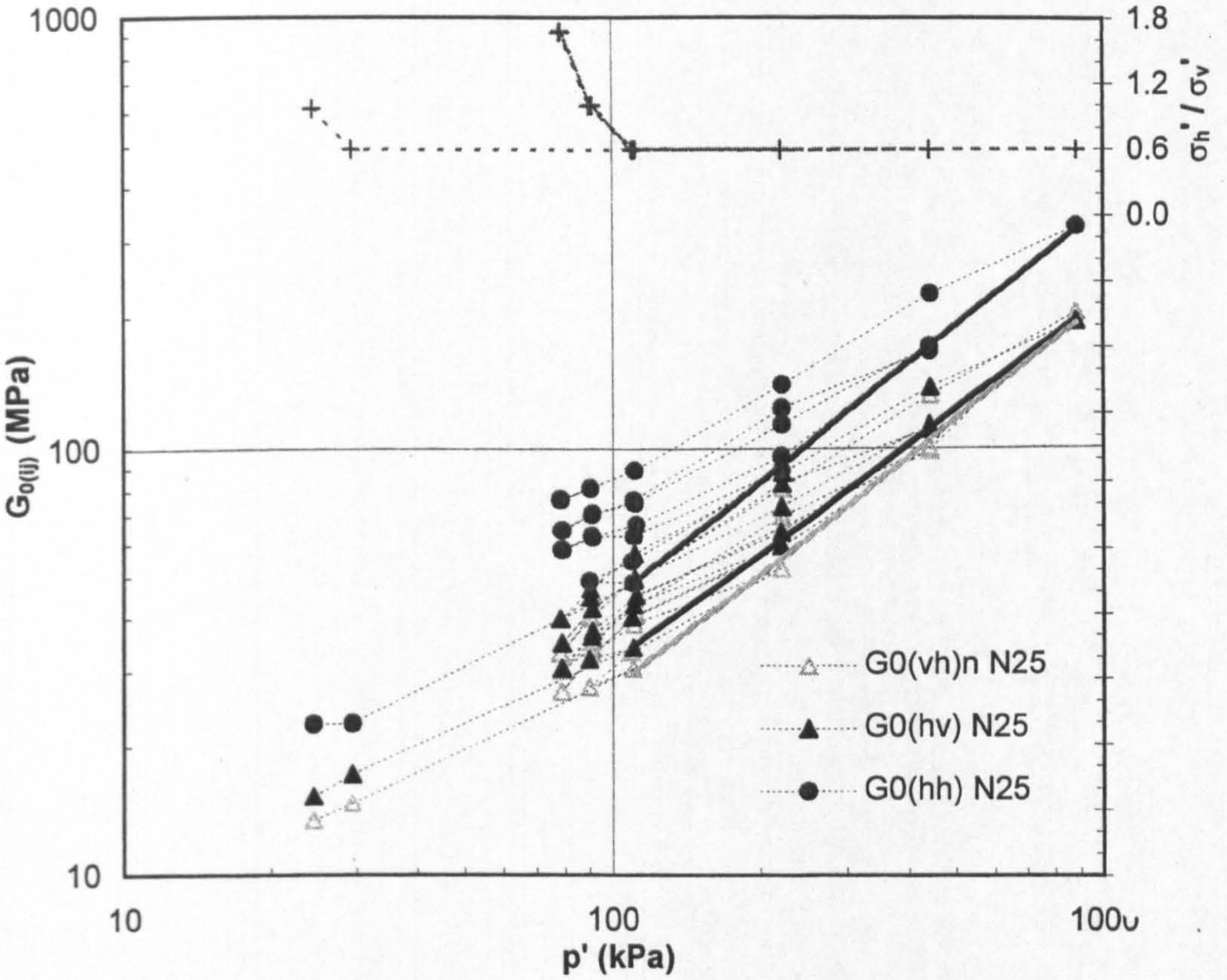

a) $G_{0(ij)}$ vs. p'

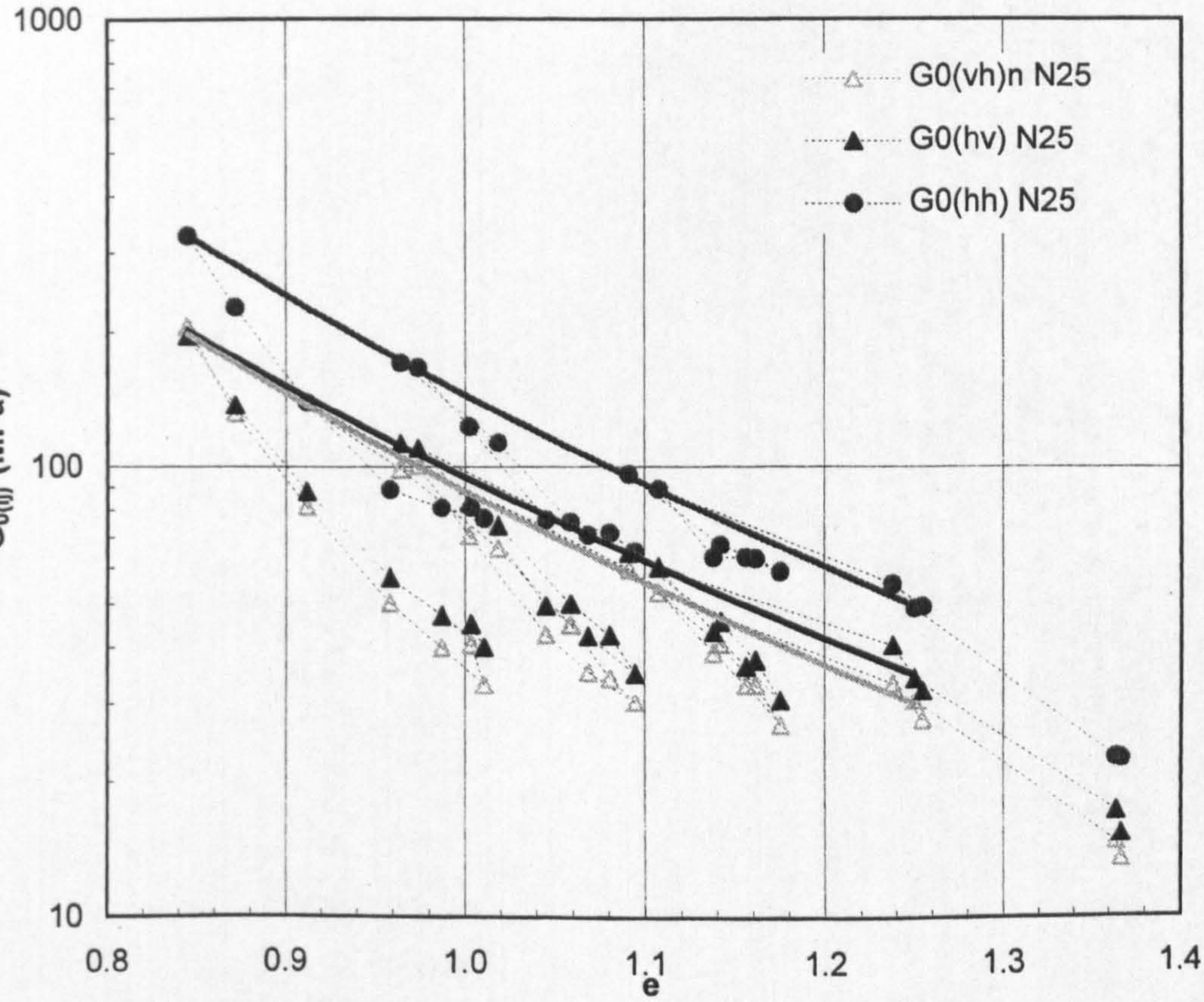

b) $G_{0(ij)}$ vs. voids ratio

Figure 5.1 $G_{0(ij)}$ **vs. stress and voids ratio for 1D consolidation: Test N25**

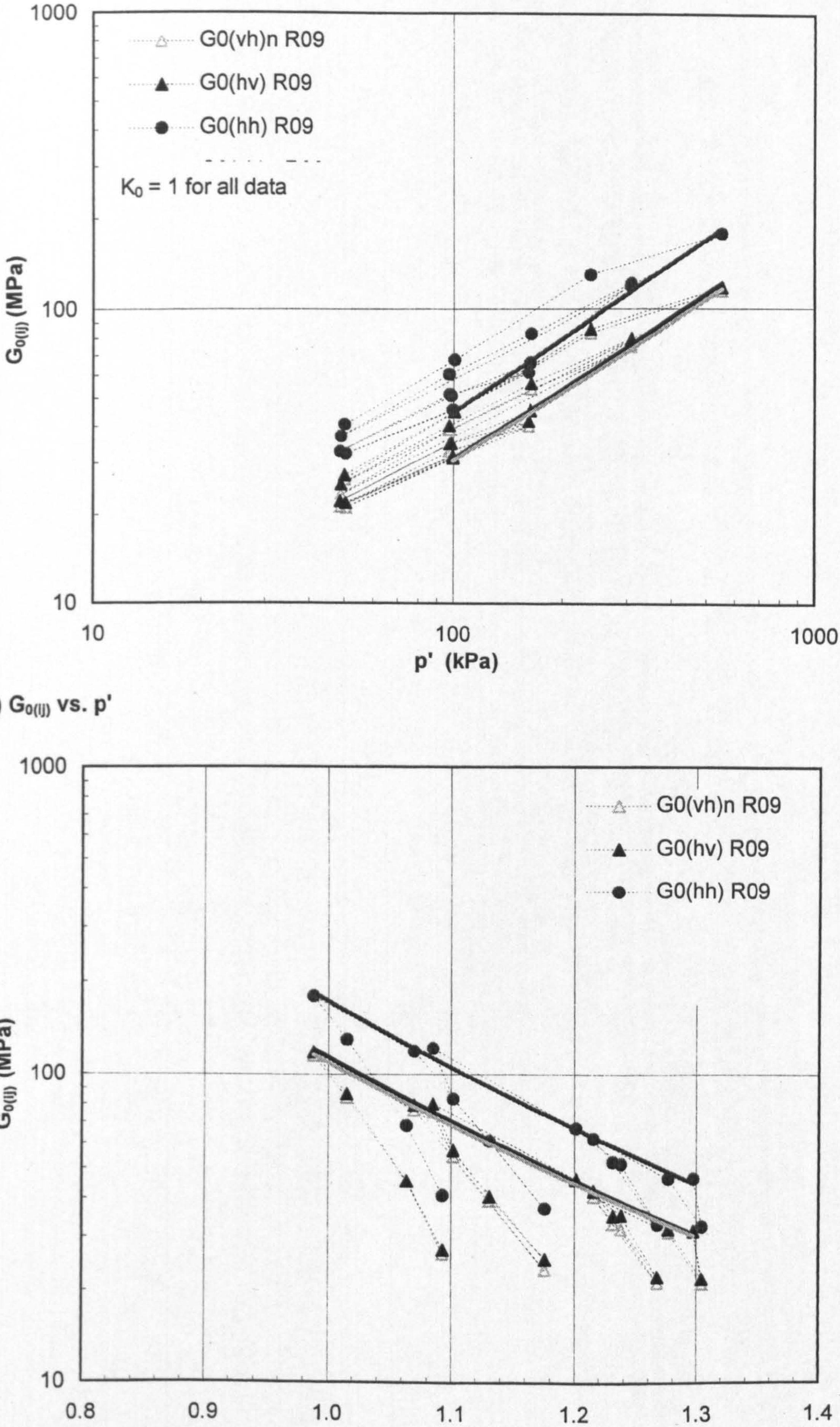

Figure 5. 2 $G_{0(ij)}$ vs. stress and voids ratio for isotropic consolidation: Test R09

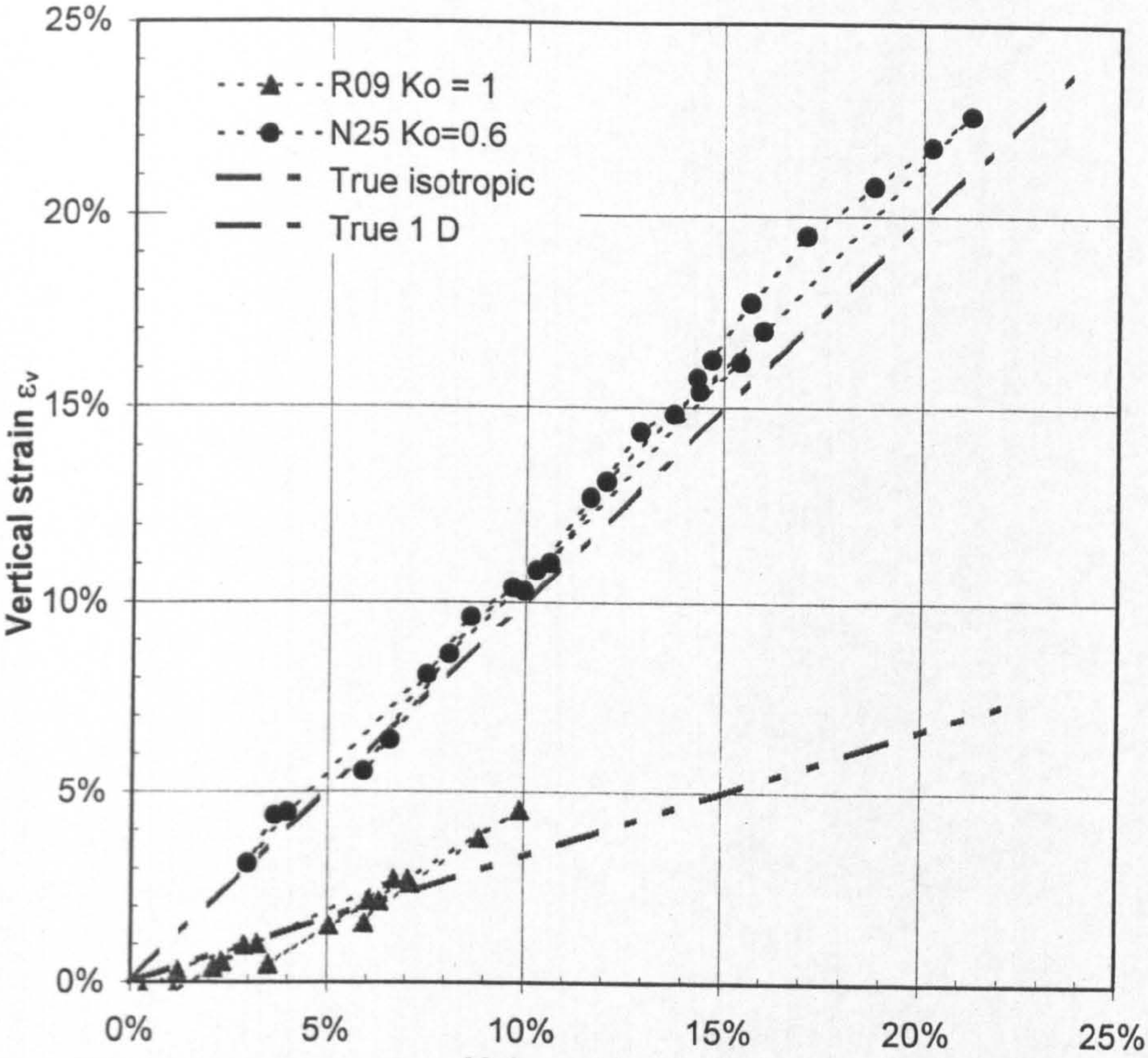

a) Comparison of R09 and N25 with true isotropic and 1D consolidation

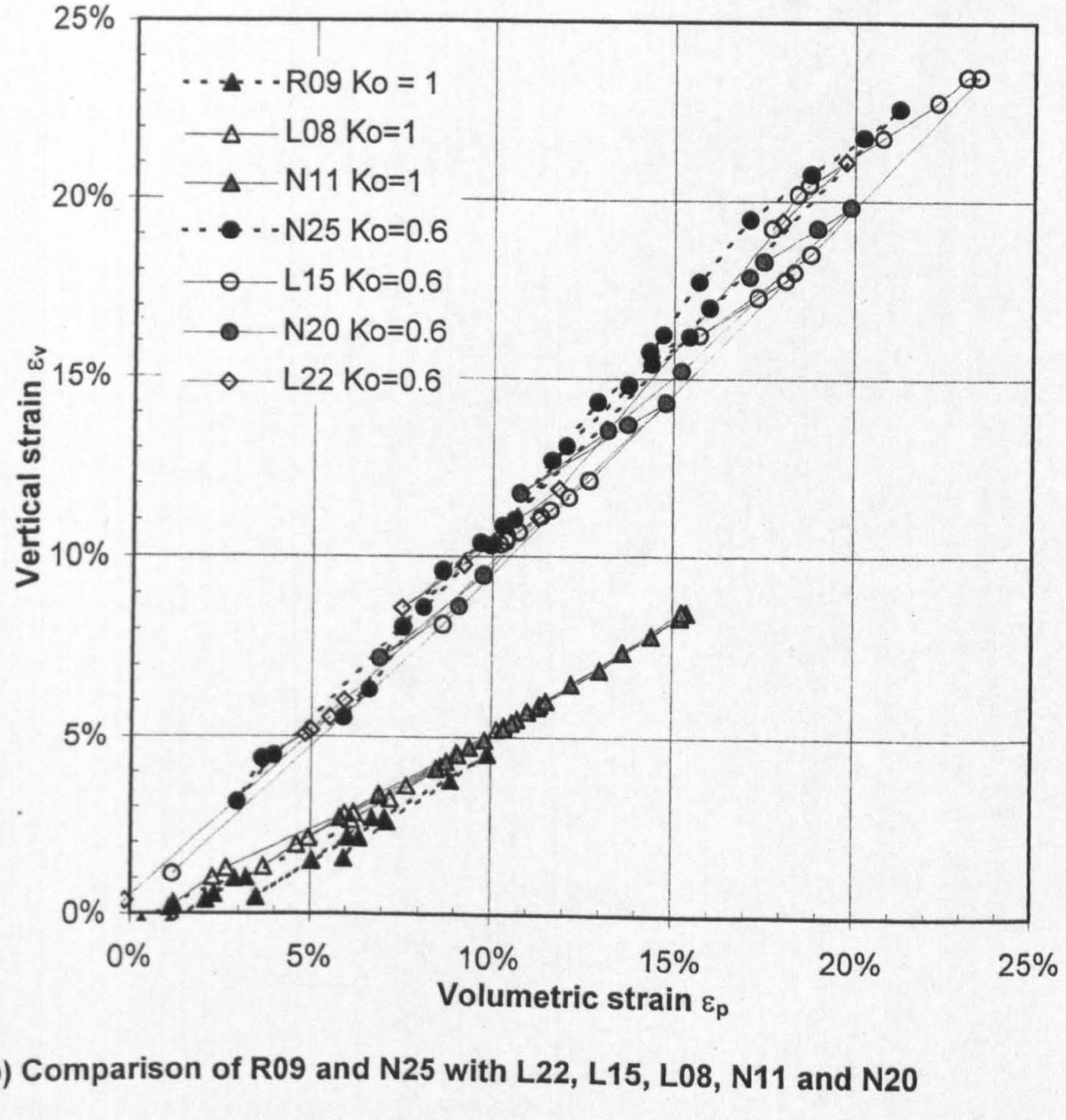

b) Comparison of R09 and N25 with L22, L15, L08, N11 and N20

Figure 5.3 Strain paths for tests carried out on reconstituted Gault clay

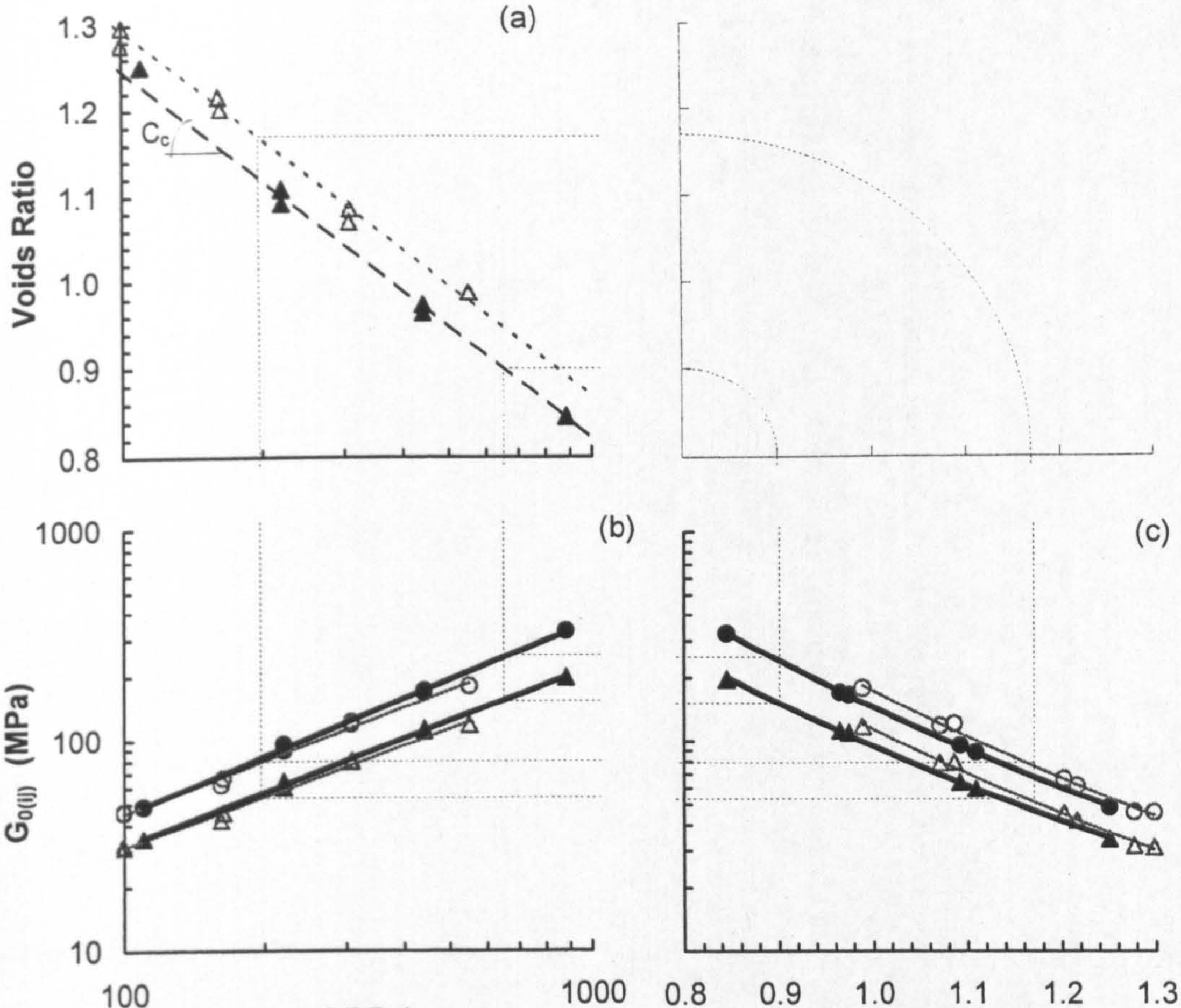

Summarised properties

Dominant consolidation -		***"Isotropic" - R09***	***"1 D" - N25***
a) Consolidation	N	3.15	3.10
(based on average trend	λ	0.185	0.185
lines plotted in Figures	e_0	2.15	2.10
4.12 and 4.13)	C_c	0.427	0.427
b) $G_{0(ij)}$ *vs.* p'	$G_{0(hv)}$ =	$0.78\ p'^{0.80}$ MPa	$0.66\ p'^{0.84}$ MPa
(based on above curves)	$G_{0(hh)}$ =	$0.99\ p'^{0.83}$ MPa	$0.69\ p'^{0.91}$ MPa
c) $G_{0(ij)}$ *vs.* voids ratio	$G_{0(hv)}$ =	$114\ e^{-5.01}$ MPa	$95\ e^{-4.49}$ MPa
(based on above curves)	$G_{0(hh)}$ =	$173\ e^{-5.24}$ MPa	$145\ e^{-4.84}$ MPa

Figure 5.4 Variation of $G_{0(ij)}$ with p' and voids ratio for normally consolidated "isotropic" and "1D" consolidated samples: Tests R09 and N25

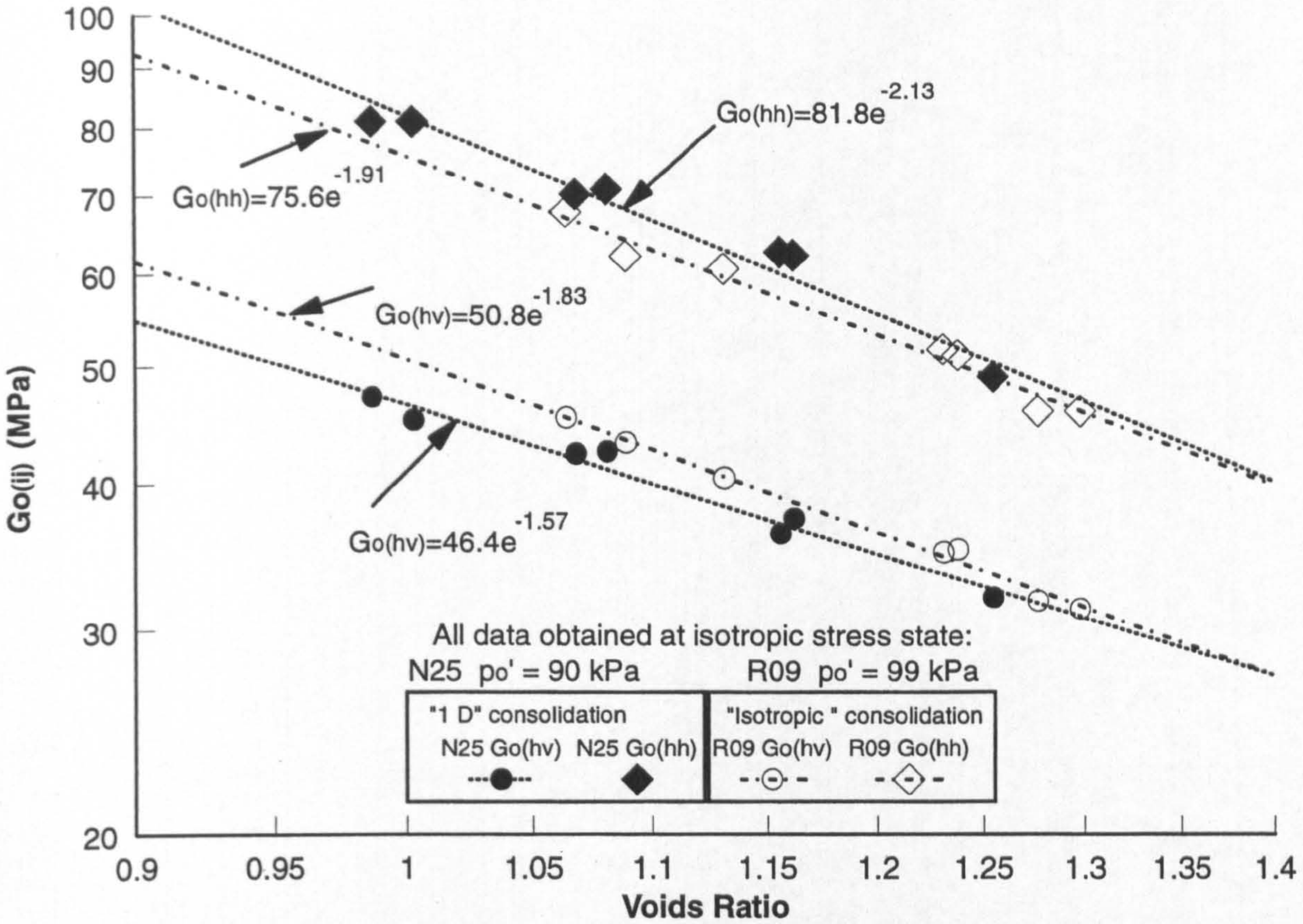

a) For "1 D" and "isotropically" consolidated samples at isotropic stress: Tests N25 and R09

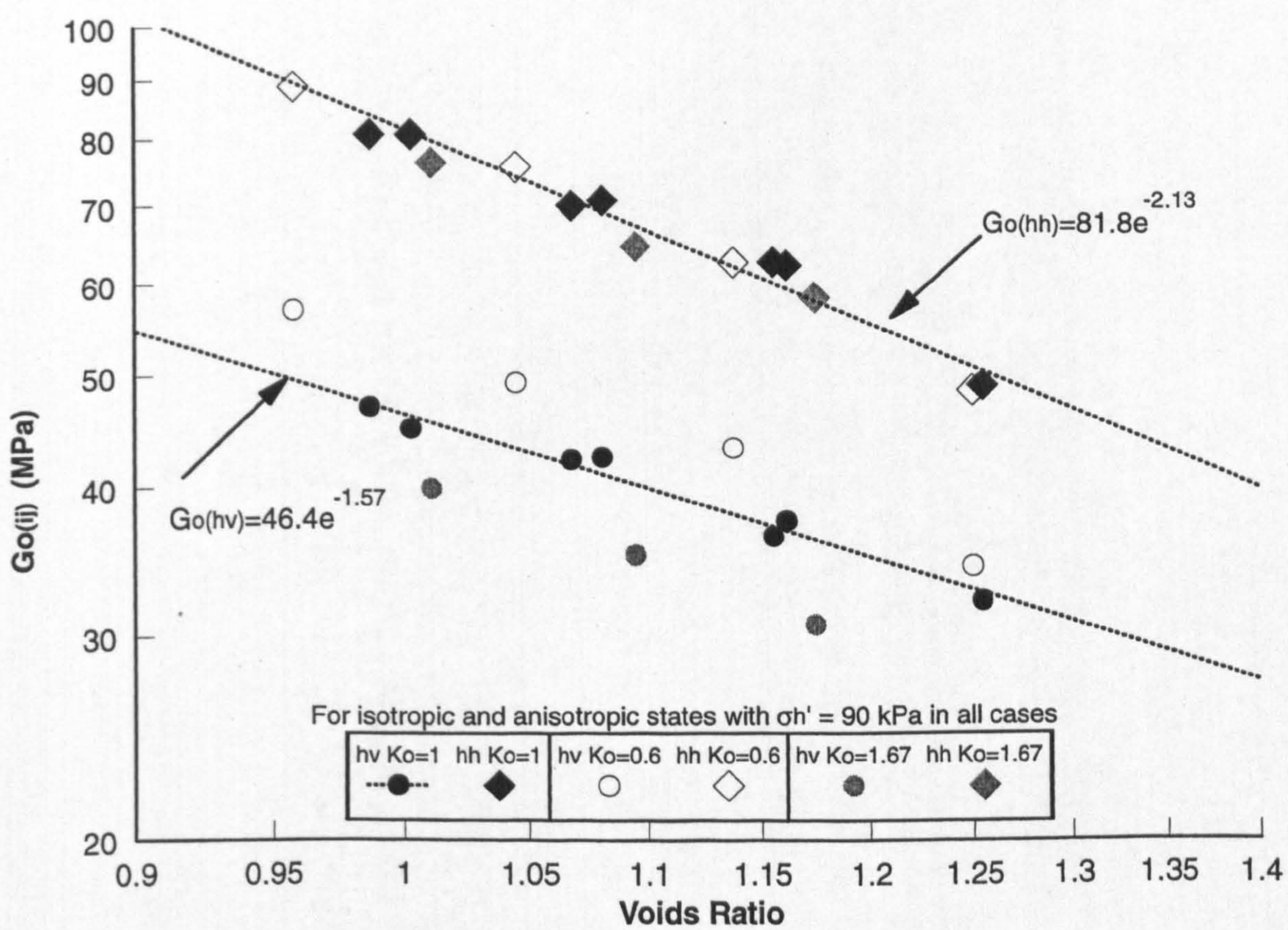

b) For "1 D" consolidated sample at constant σh' = 90 kPa: Test N25

Figure 5.5 $G_{o(ij)}$ **vs. voids ratio for "1 D" and "isotropically" consolidated samples**

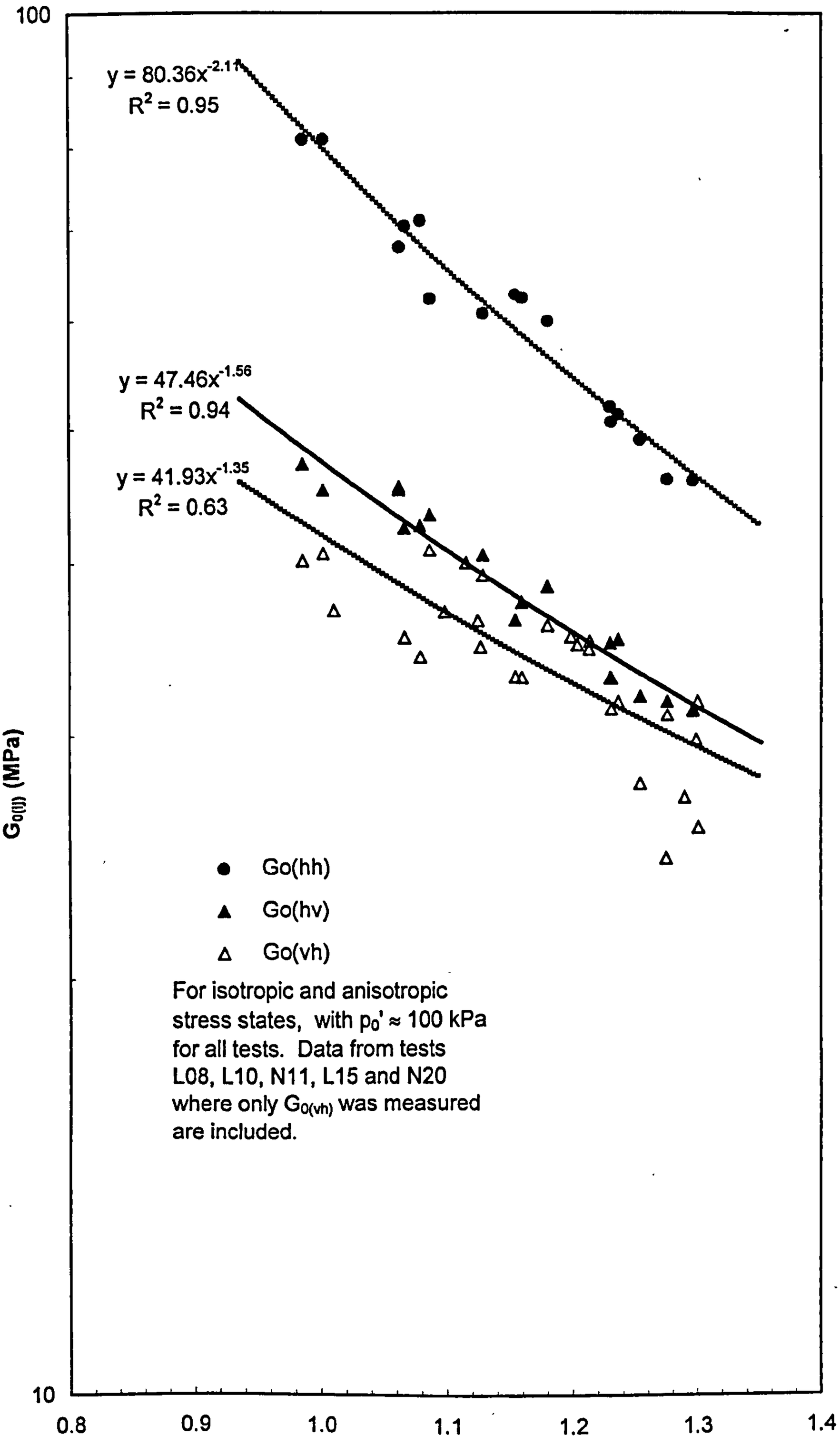

Figure 5.6 $G_{0(ij)}$ *vs.* **voids ratio at p' ≈ 100 kPa: Data from all tests**

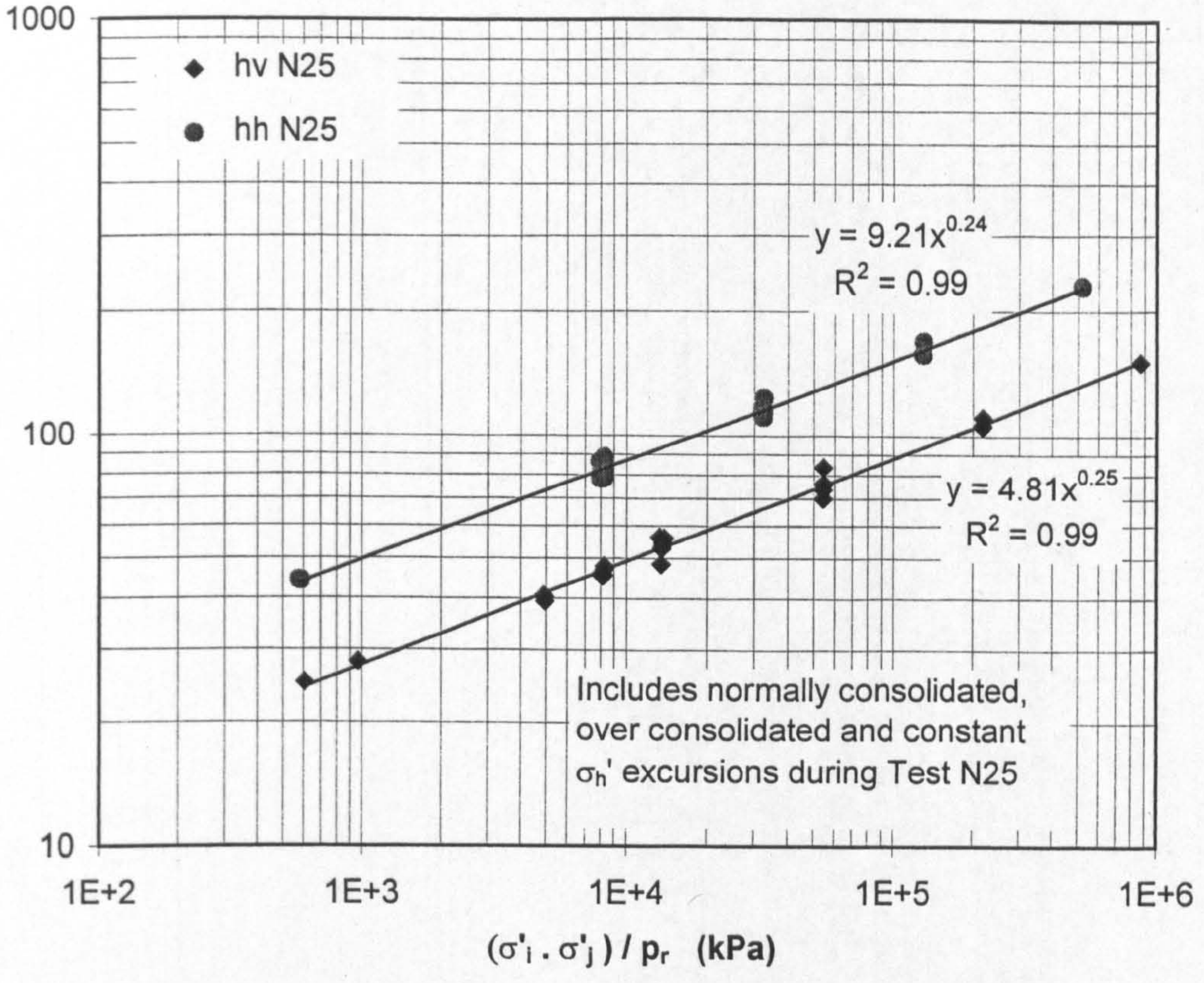

a) "1D" consolidated - Test N25

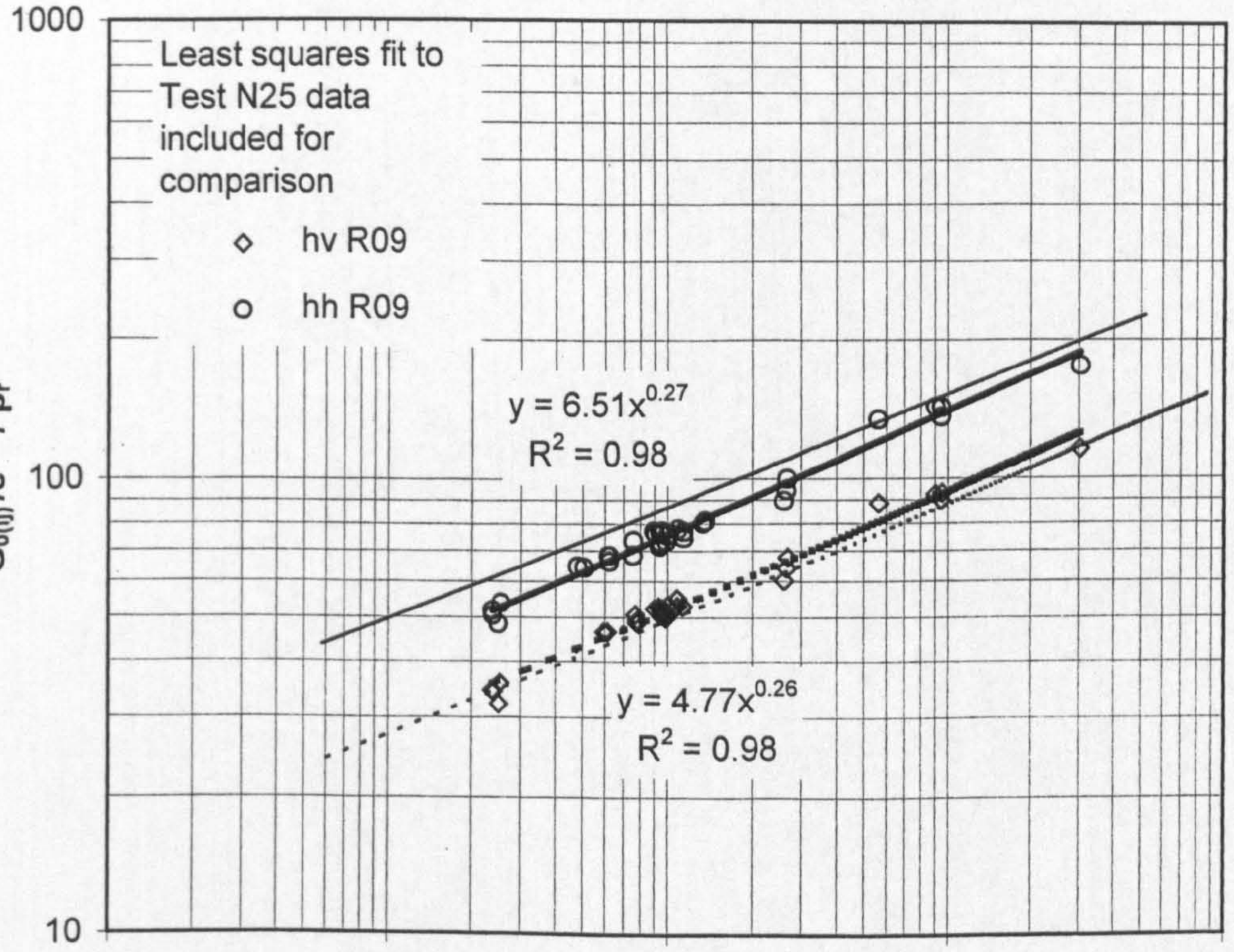

b) "isotropically" consolidated Test R09 compared to "1D" trend lines

Figure 5.7 $G_{0(ij)}/e^{mij}$ ***vs.*** $(\sigma'_i.\sigma'_j)$ **for "isotropically" consolidated test R09 and "1D" consolidated Test N25**

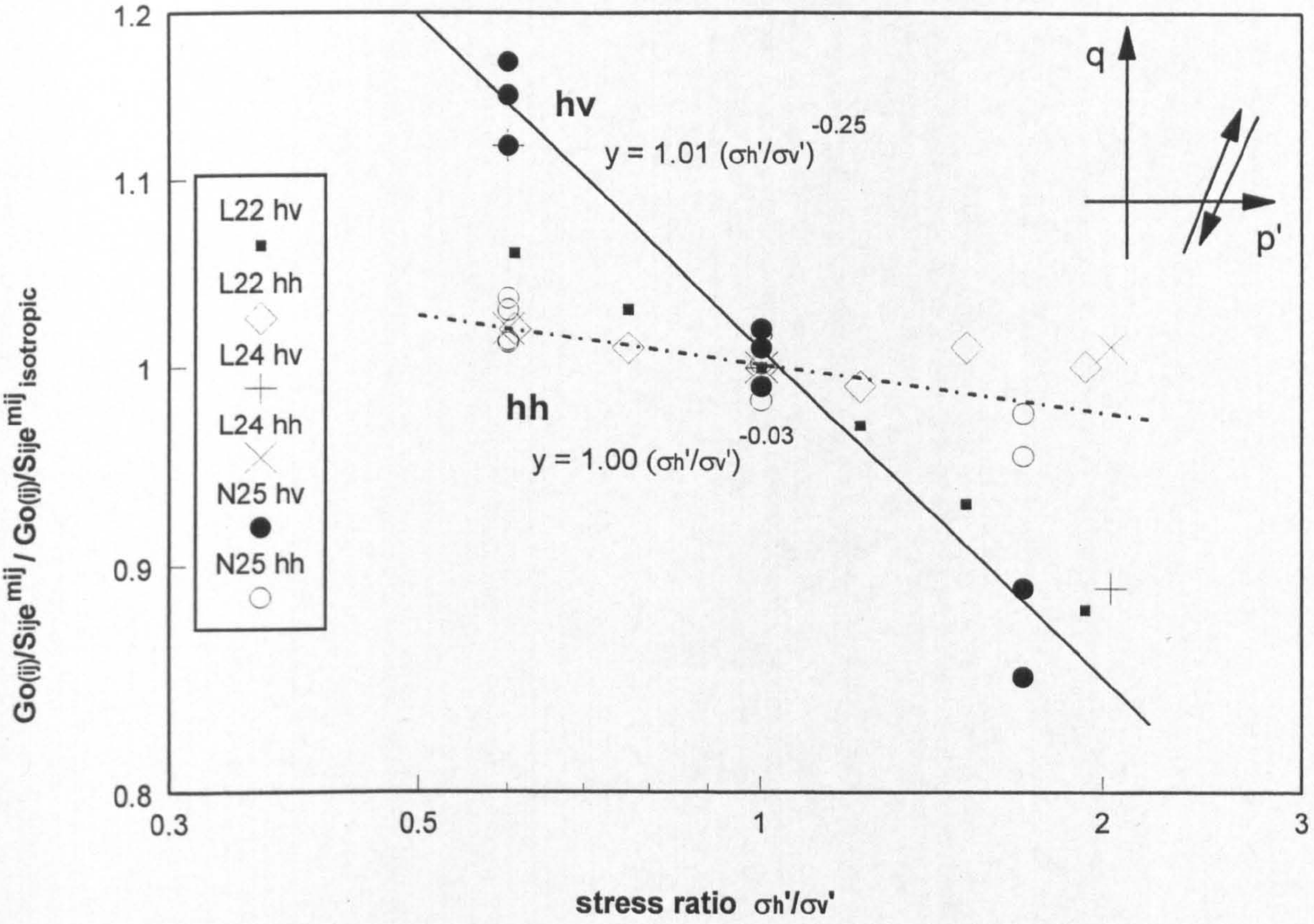

Figure 5.8 Normalised shear moduli ratio *vs.* stress ratio - constant $\sigma_{h'}$ excursions: Tests L22, L24 and N252

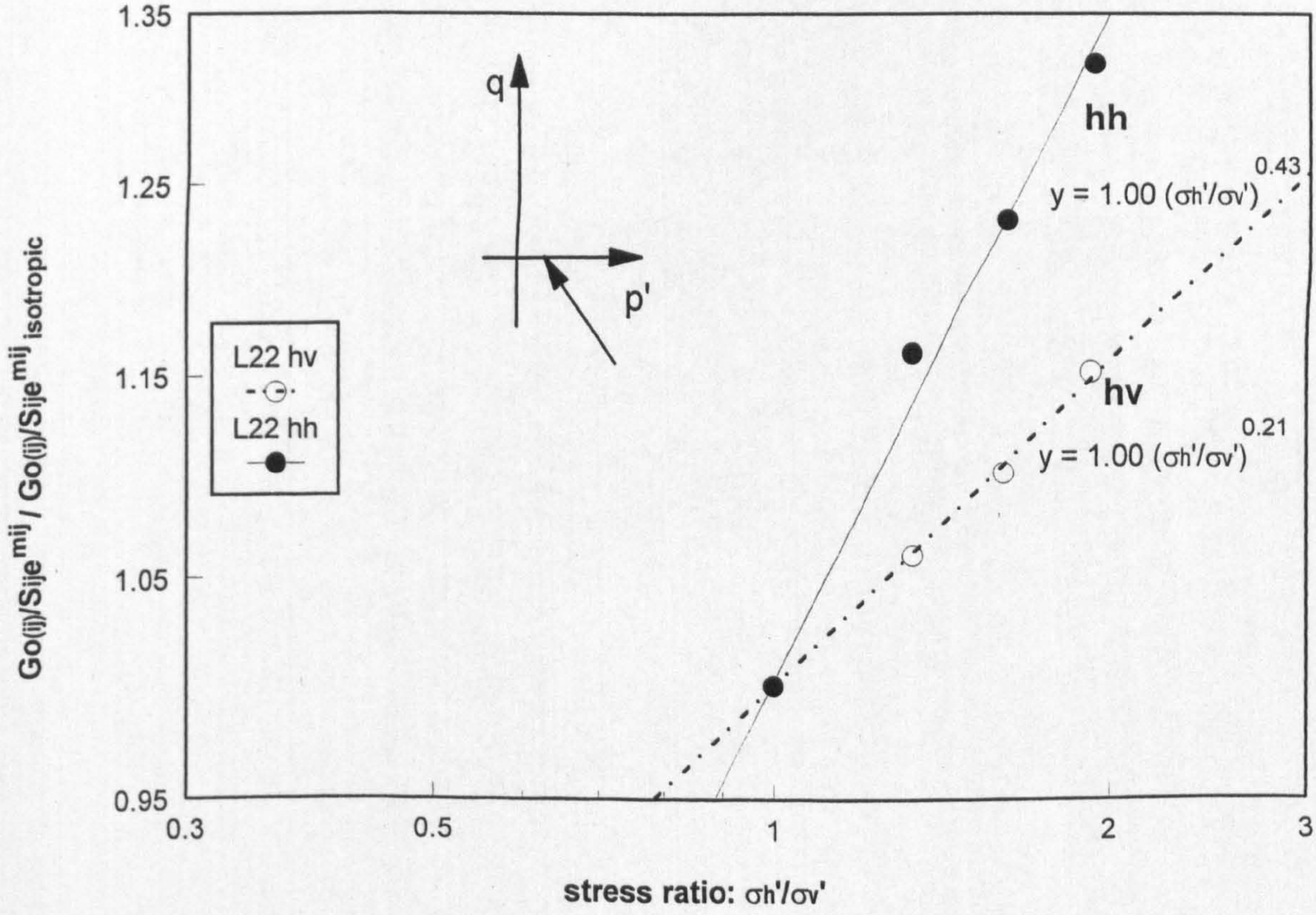

Figure 5.9 Normalised shear moduli ratio *vs.* stress ratio - constant $\sigma_{v'}$= 275 kPa: Test L22

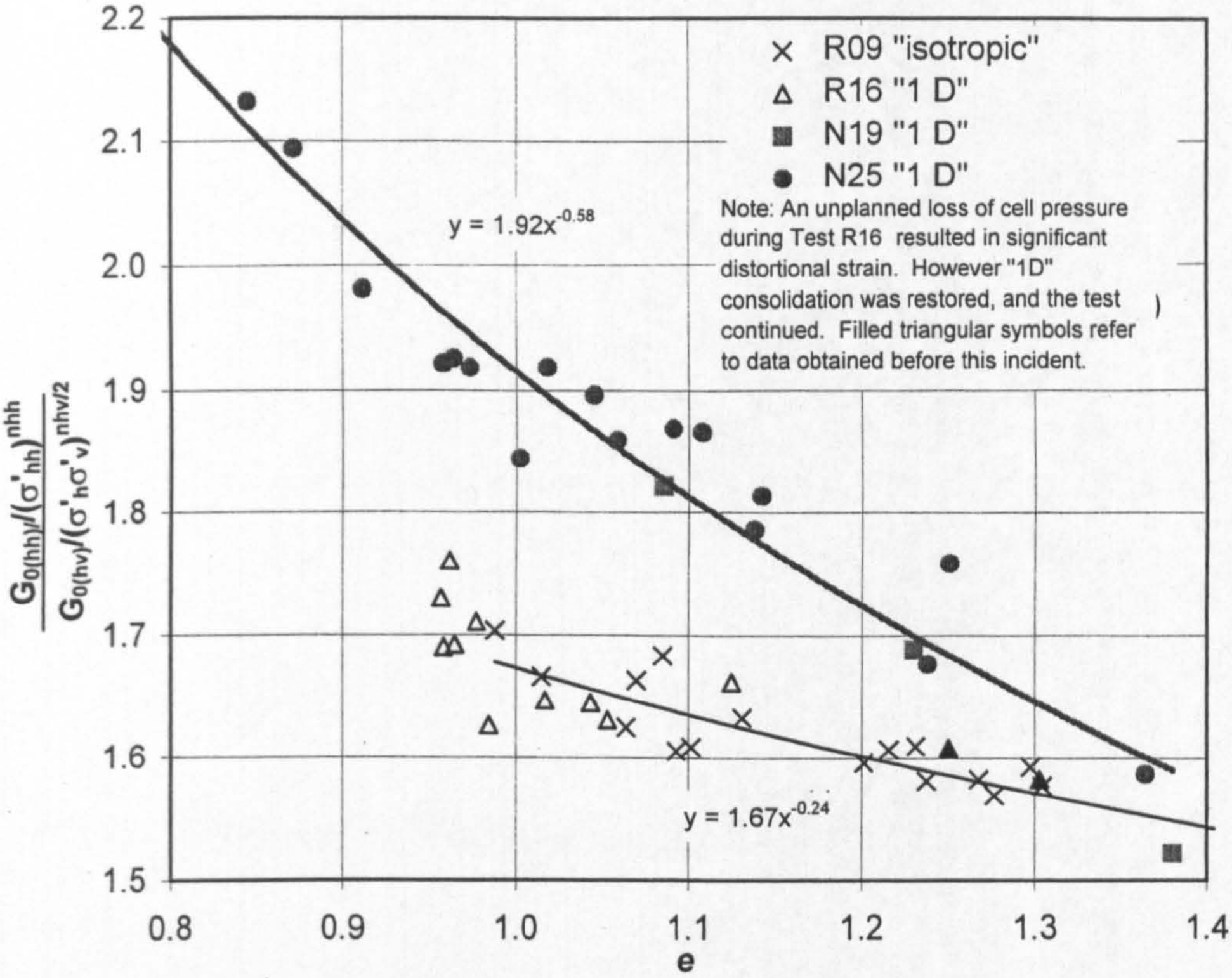

Figure 5.10 $(G_{0(hh)}/(\sigma'_{hh})^{nhh})/(G_{0(hv)}/(\sigma'_{h}\sigma'_{v})^{nhv/2})$ *vs.* **voids ratio: Tests R09, R16, N19 & N25**

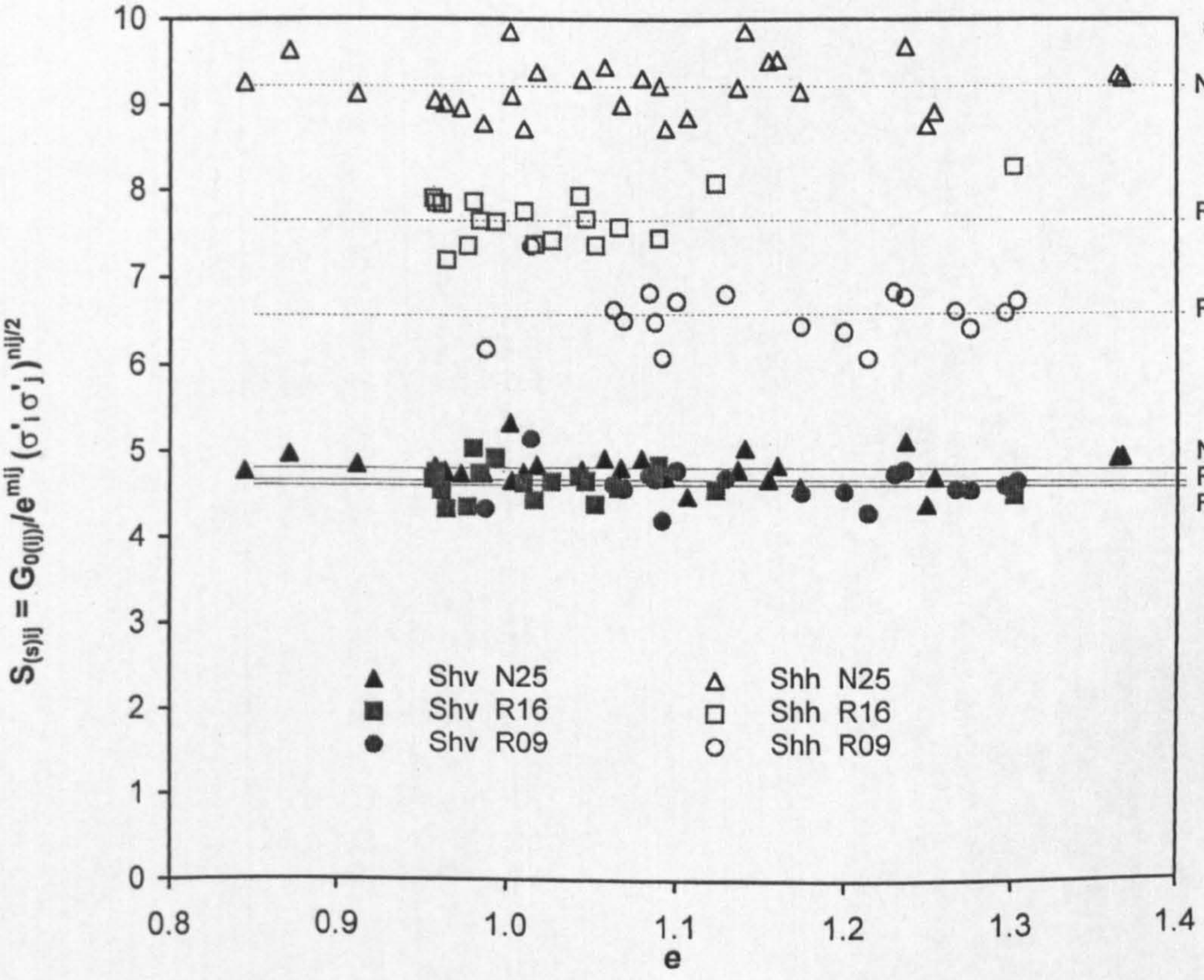

Figure 5.11 Elastic stiffness coefficient $S_{(s)ij}$ *vs.* **voids ratio: Tests R09, R16 & N25**

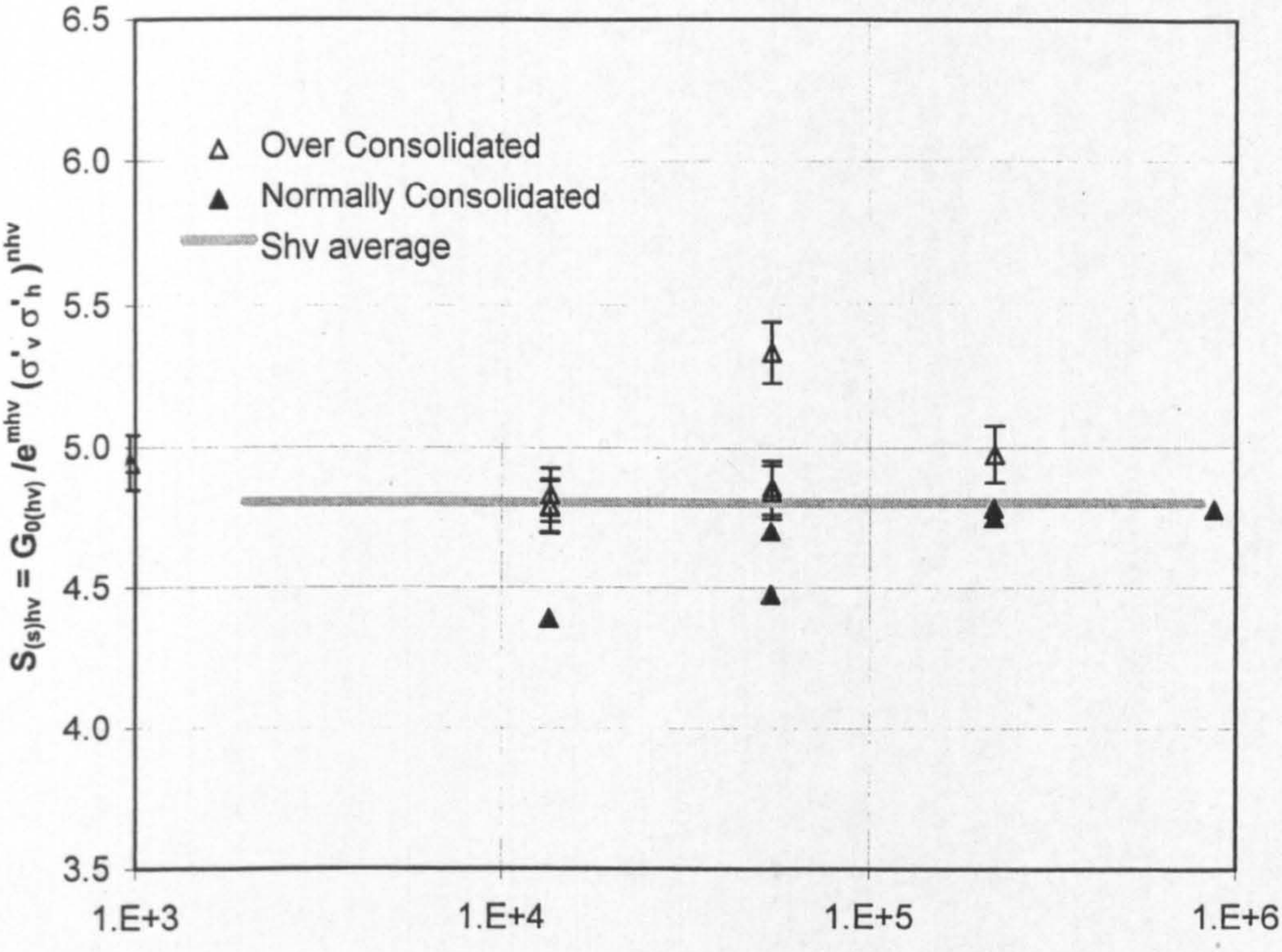

a) Elastic stiffness coefficient $S_{(s)hv}$

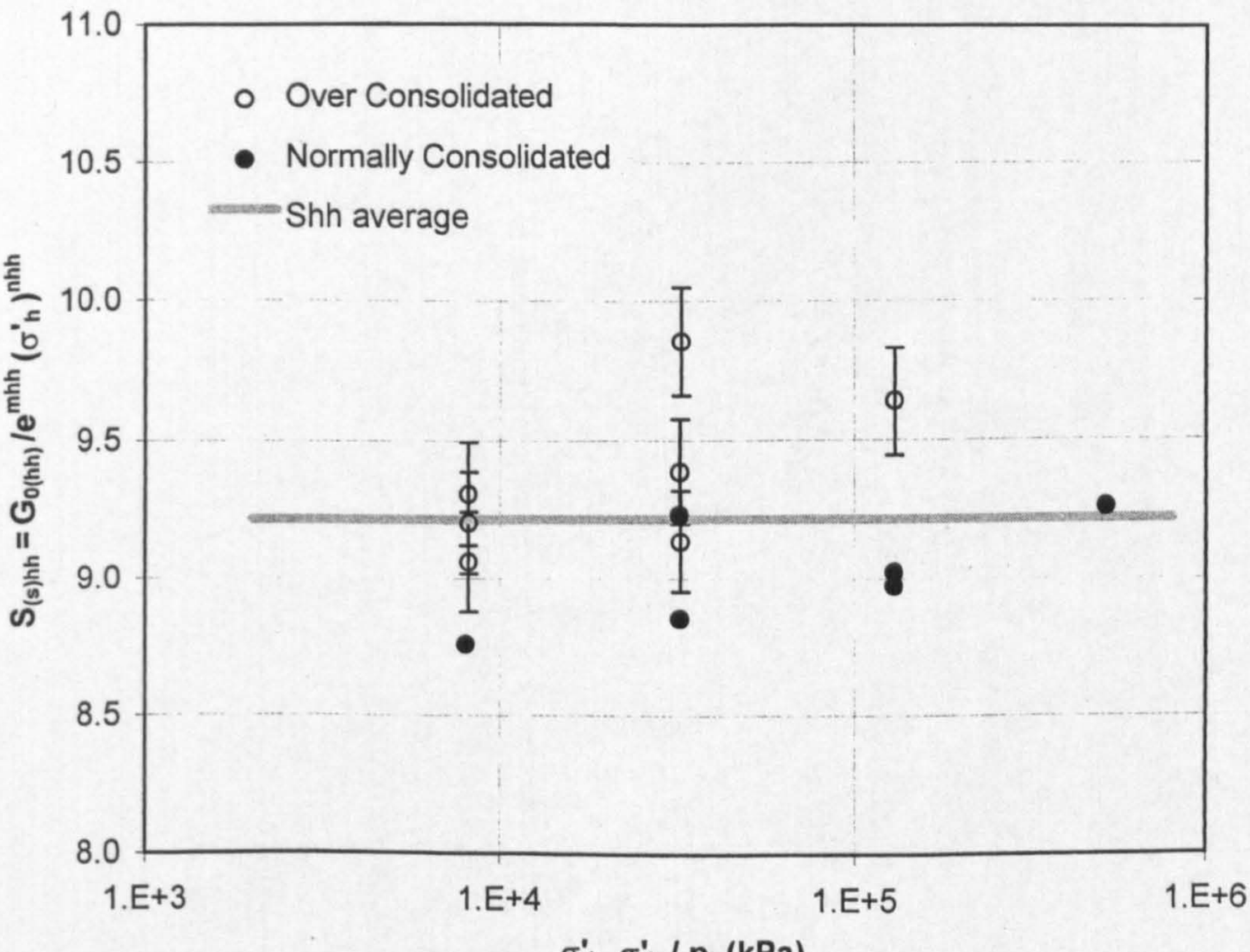

b) Elastic stiffness coefficient $S_{(s)hh}$

Figure 5. 12 Comparison between elastic stiffness coefficient $S_{(s)ij}$ for normally and over consolidated states: Test N25

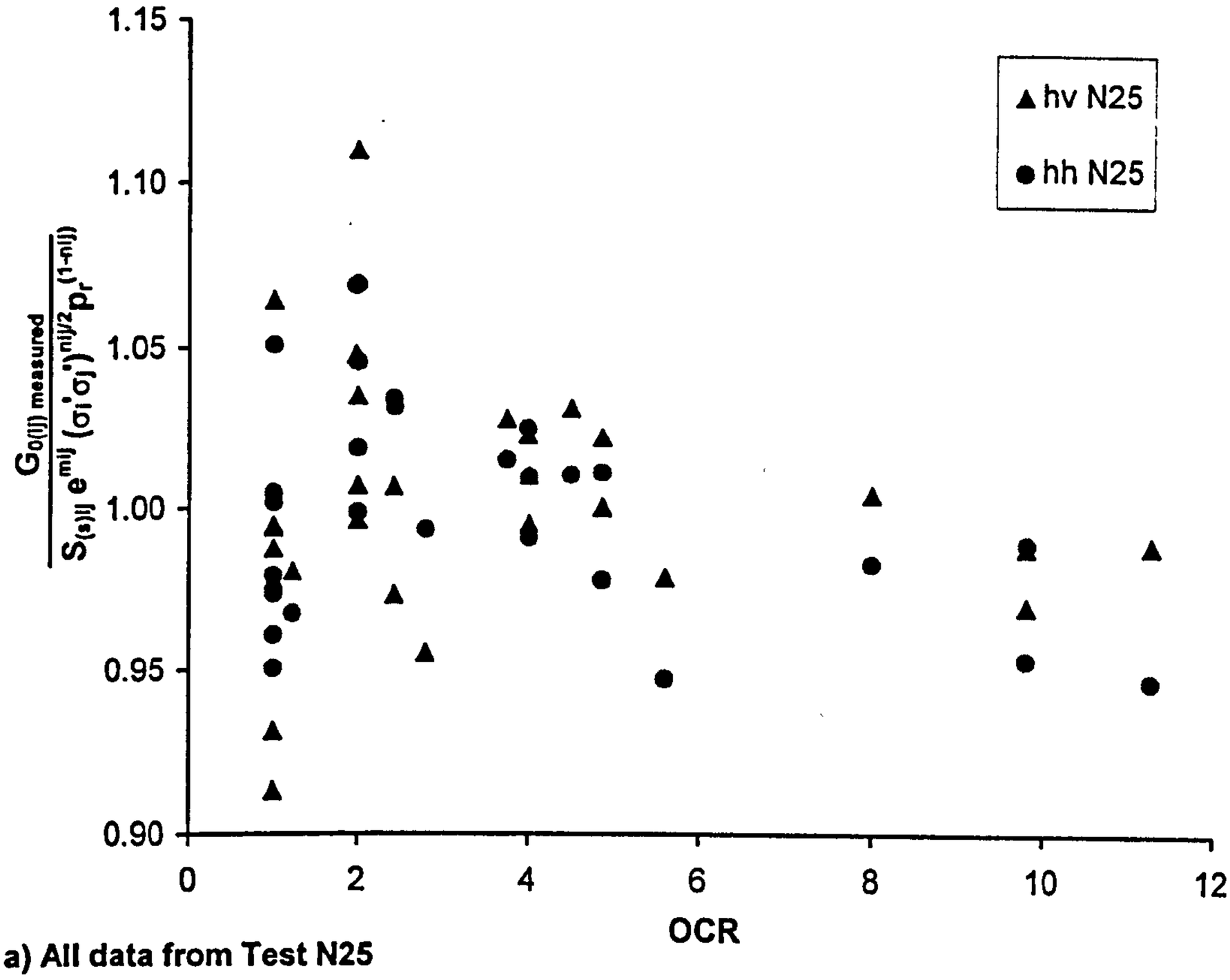

a) All data from Test N25

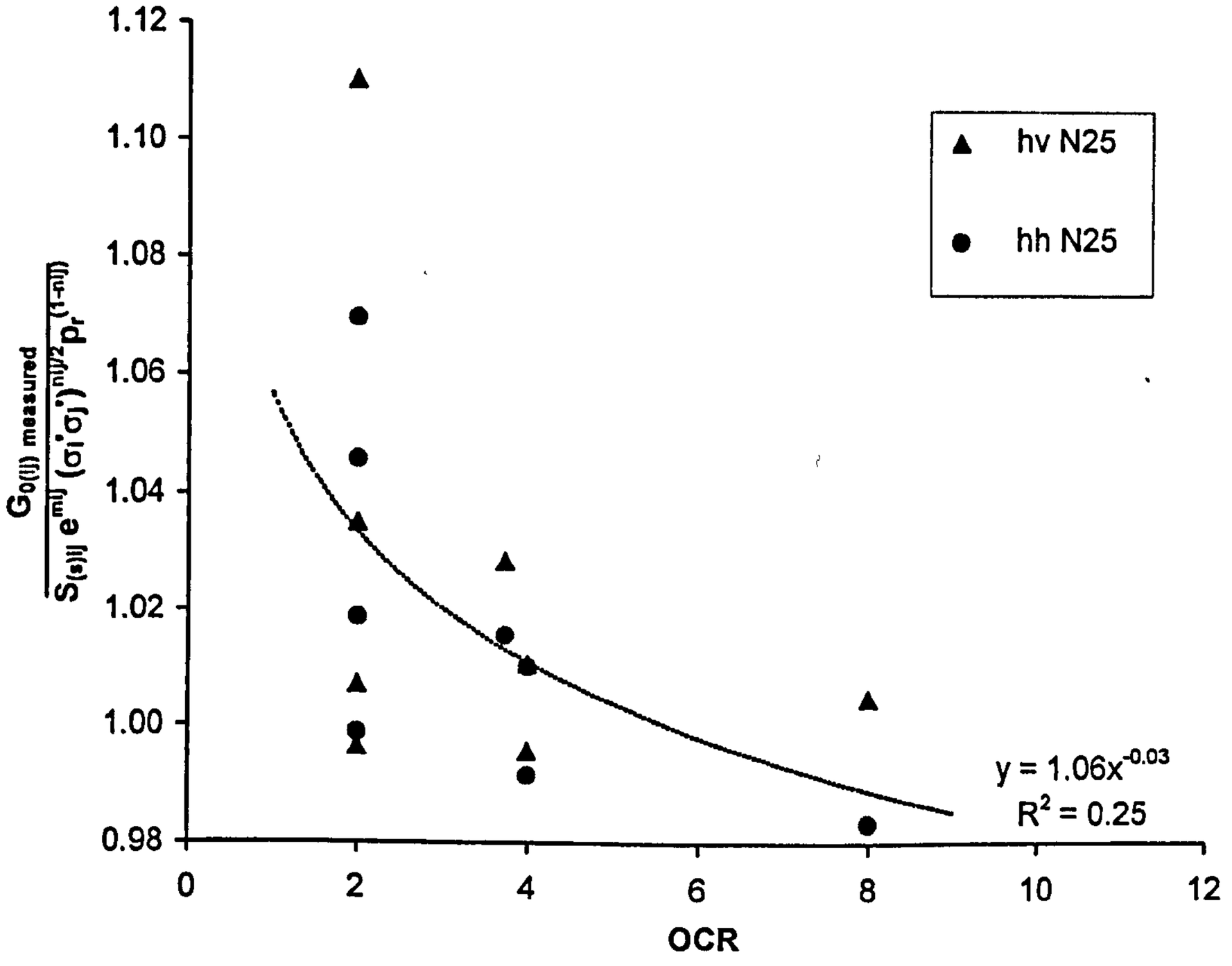

b) Data from Test N25 at $\sigma'_h / \sigma'_v = 0.6$

Figure 5. 13 Measured $G_{0(ij)}$ *vs.* calculated $G_{0(ij)} = S_{(s)ij}\, e^{mij}\, p_r^{(1-nij)}\, (\sigma_i'\sigma_j')^{nij/2}$: Test N25

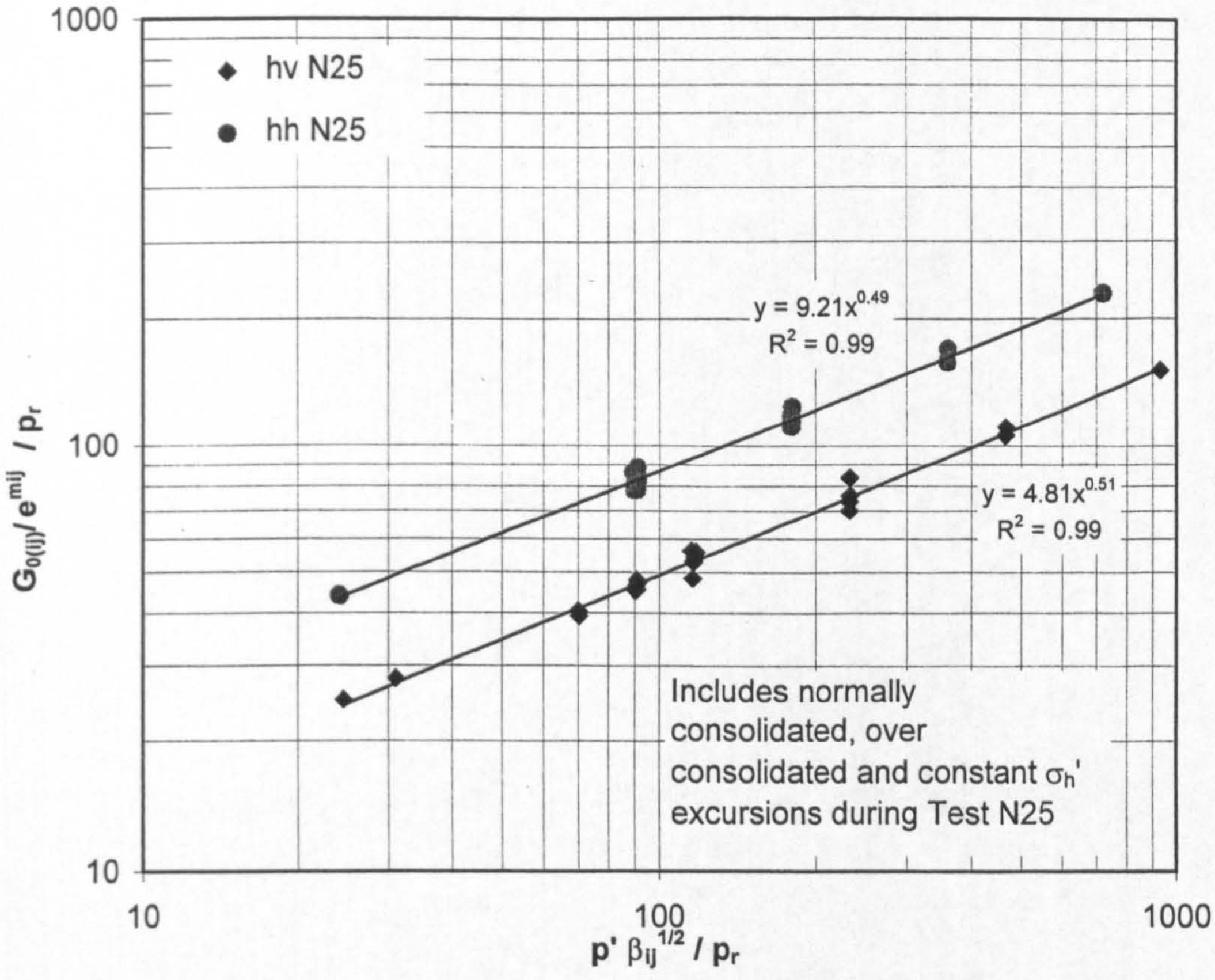

Figure 5.14 $G_{0(ij)}/e^{mij}$ *vs.* $p' \beta_{ij}^{1/2} / p_r$ reconstituted Gault clay: Test N25

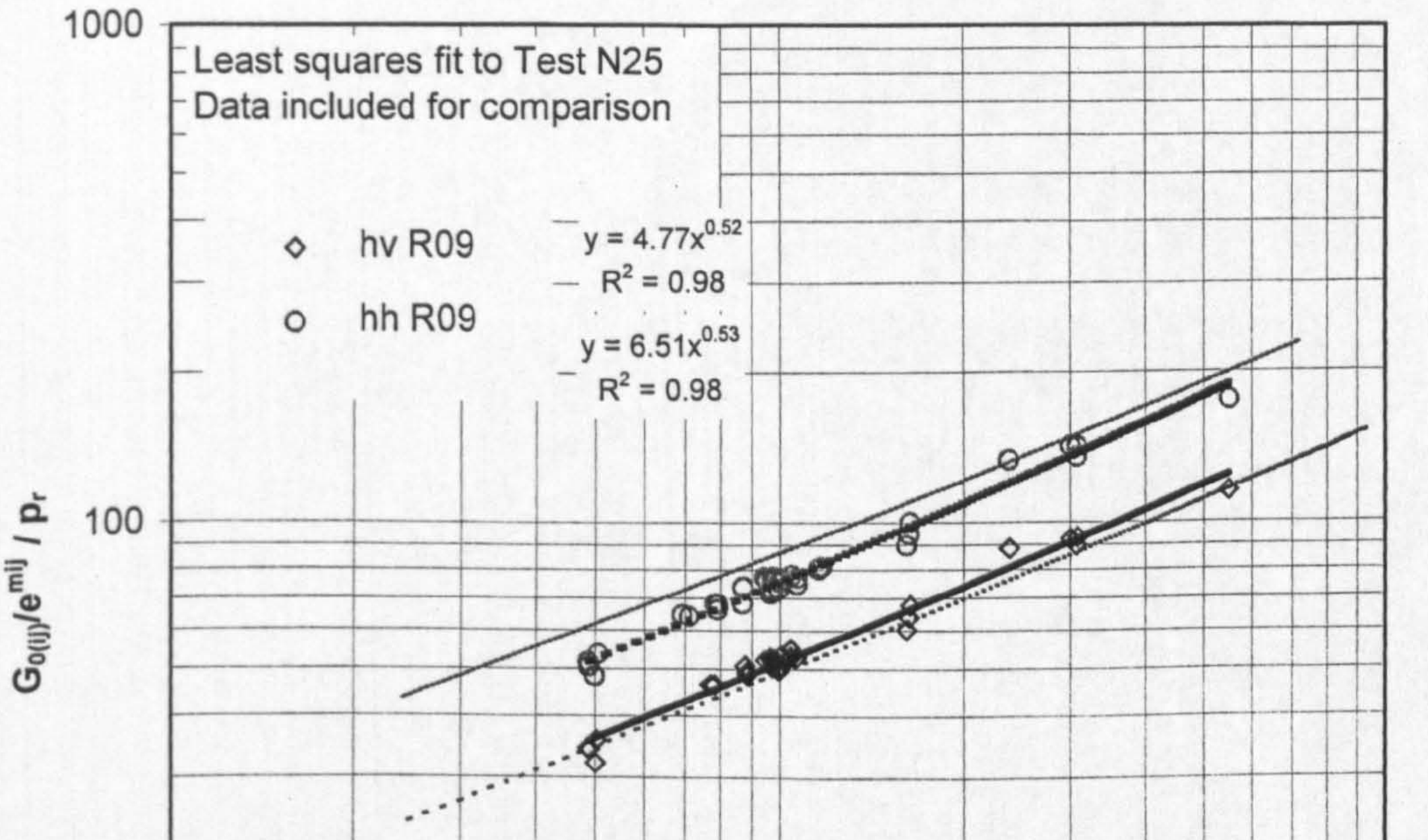

Figure 5.15 Comparison between $G_{0(ij)}/e^{mij}$ *vs.* $p' \beta_{ij}^{1/2} / p_r$ for "isotropically" consolidated test R09 and "1D" consolidated Test N25

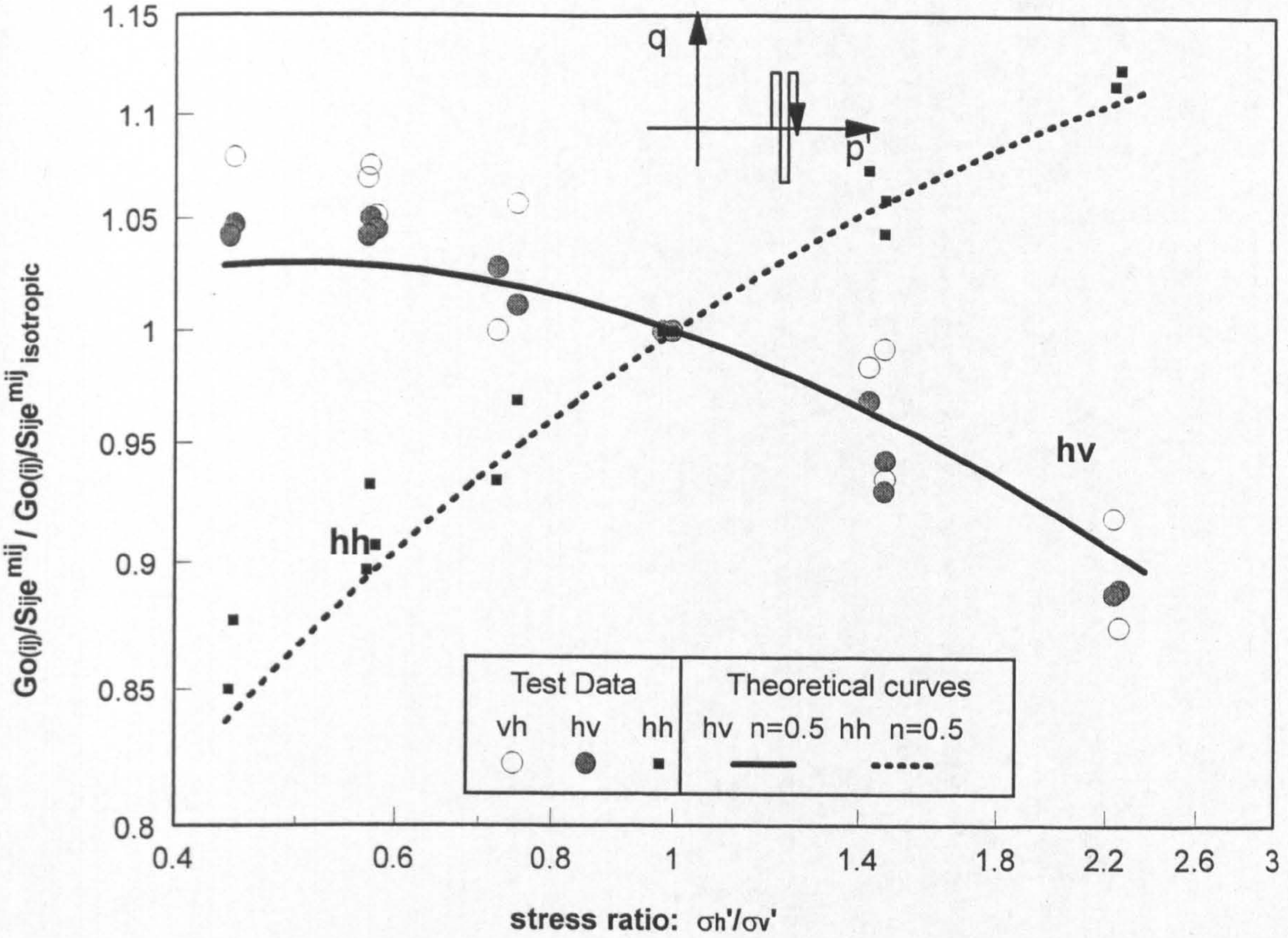

a) **Plotted against. stress ratio** σ_h'/σ_v'

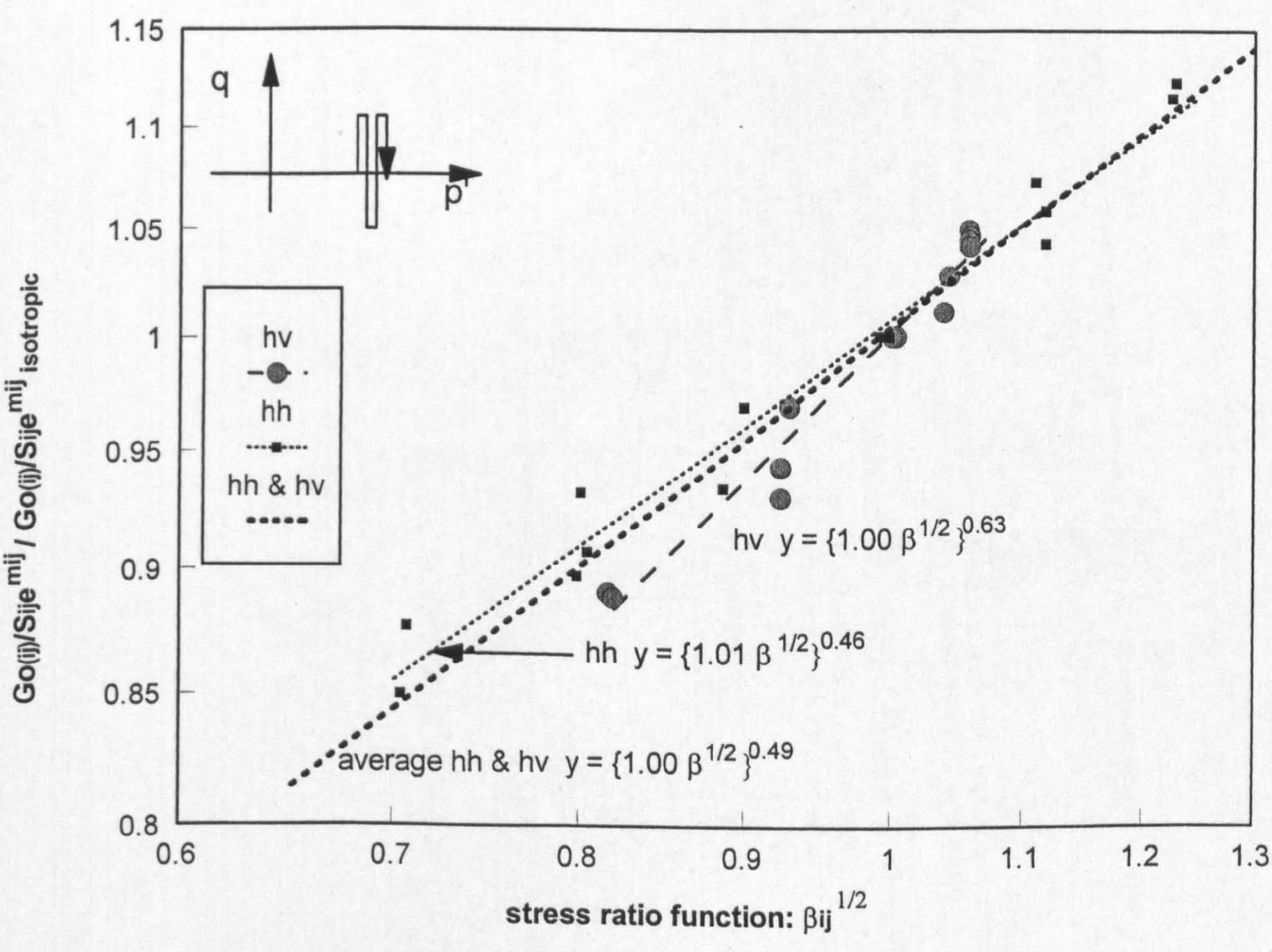

b) **Plotted against. stress ratio** $\beta^{1/2}$

Figure 5.16 Normalised shear moduli ratio *vs.* stress ratio at constant p' = 100kPa: Test R09

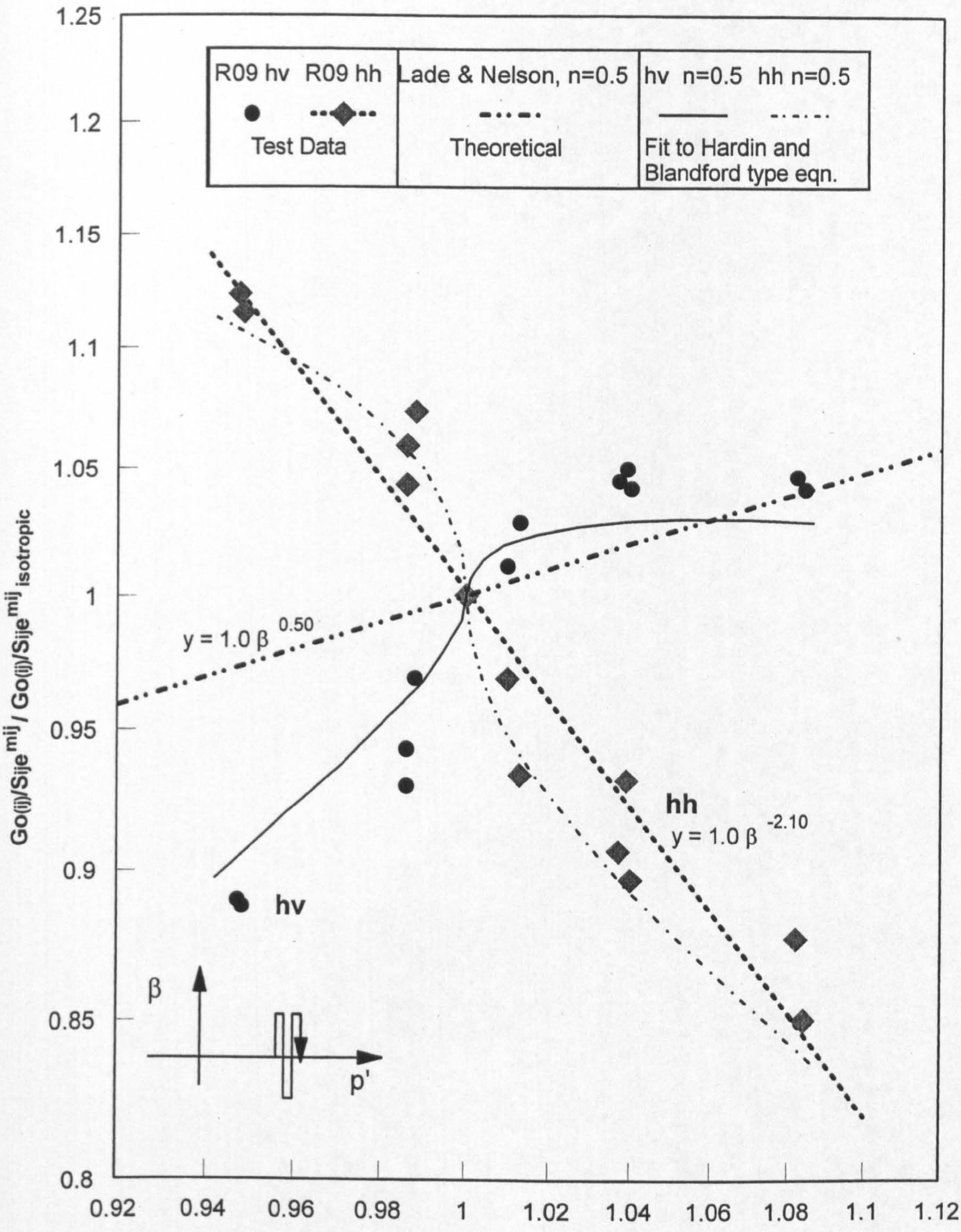

Figure 5.17 **Normalised shear moduli for Test R09 data plotted *vs.* Lade and Nelson (1987) stress ratio β**

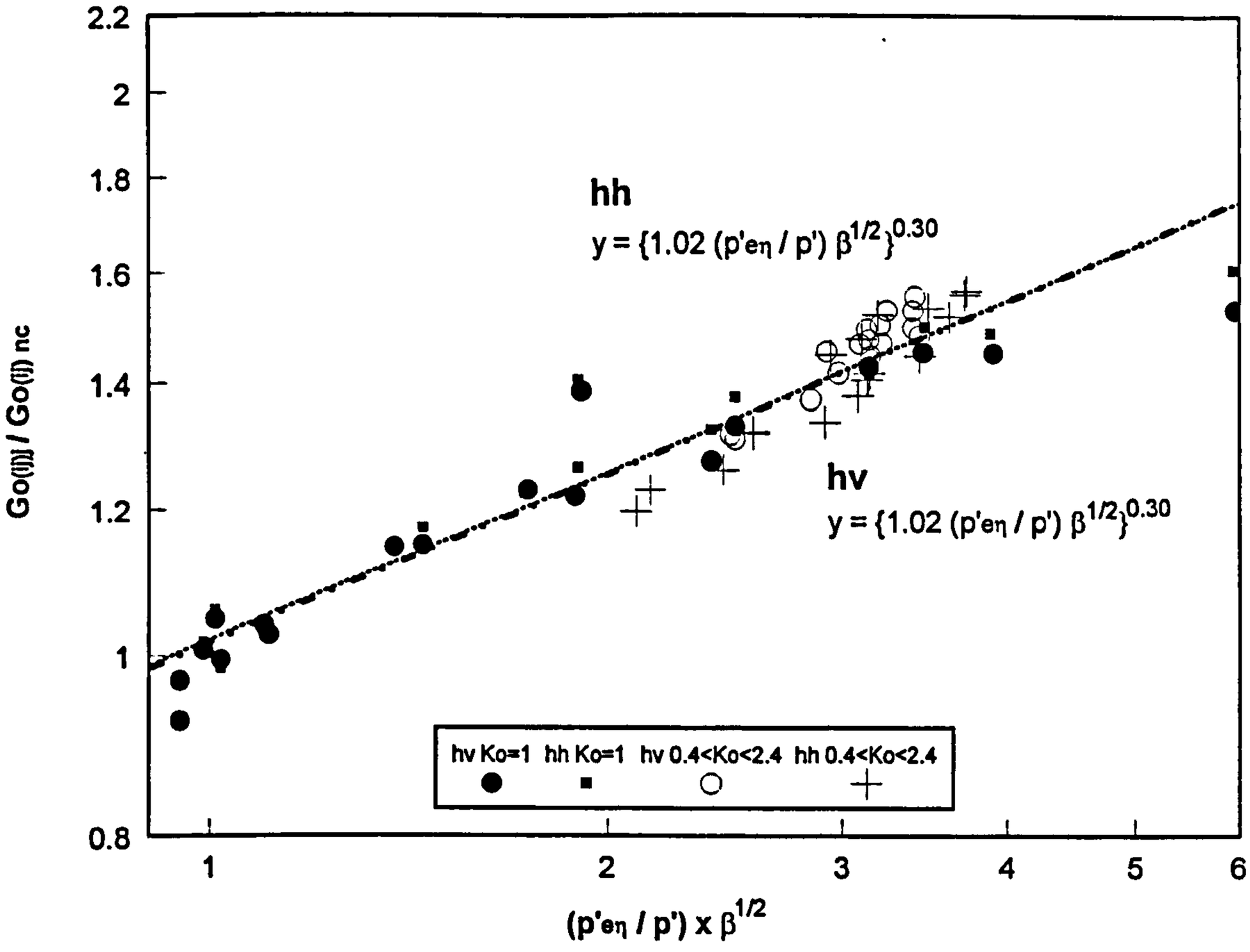

Figure 5.18 $G_{0(ij)} / G_{0(ij)}$ **normally consolidated *vs.* equivalent confining stress normalised by p' for isotropically consolidated sample: Test R09**

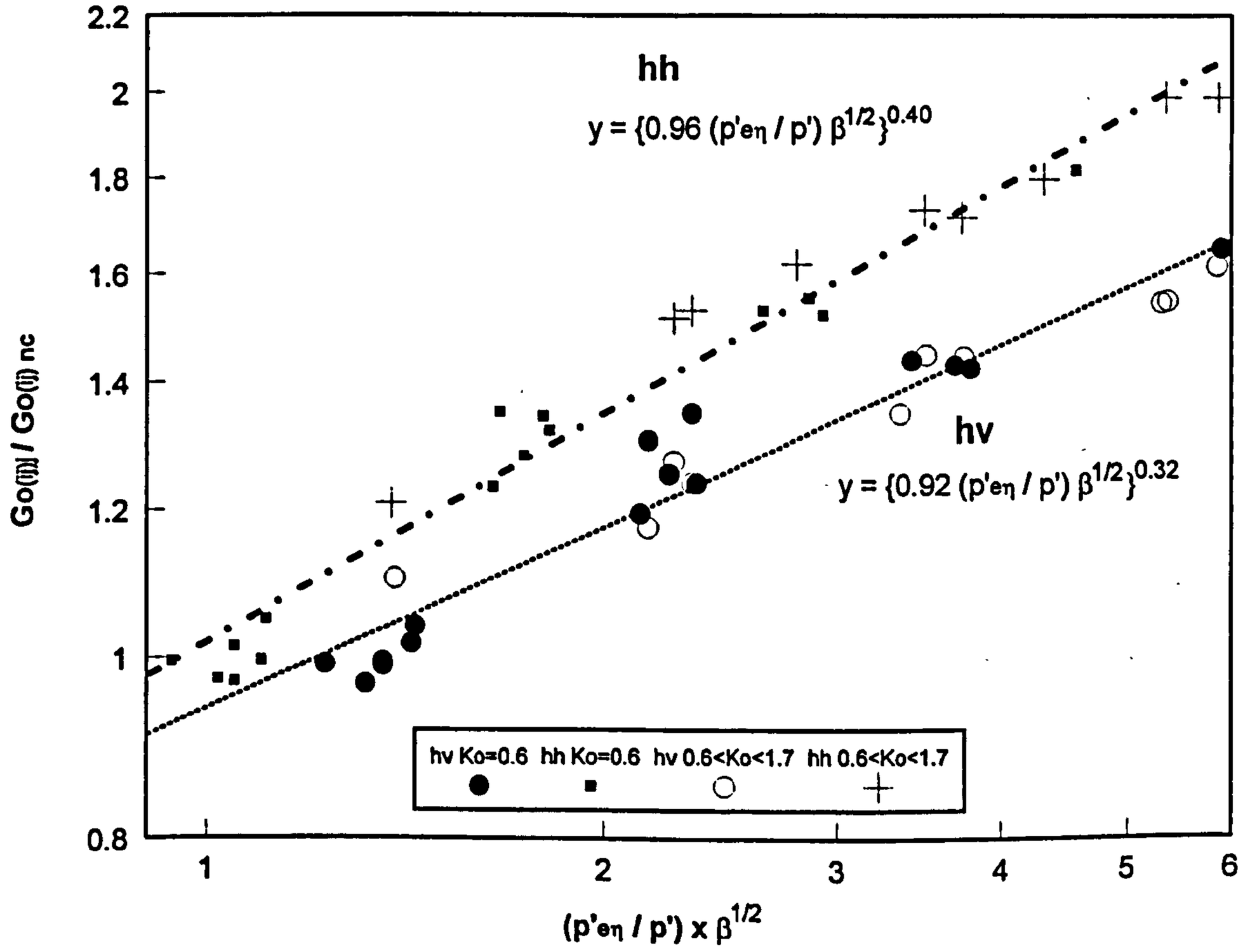

Figure 5.19 $G_{0(ij)} / G_{0(ij)}$ **normally consolidated *vs.* equivalent confining stress normalised by p' for 1D consolidated sample: Test N25**

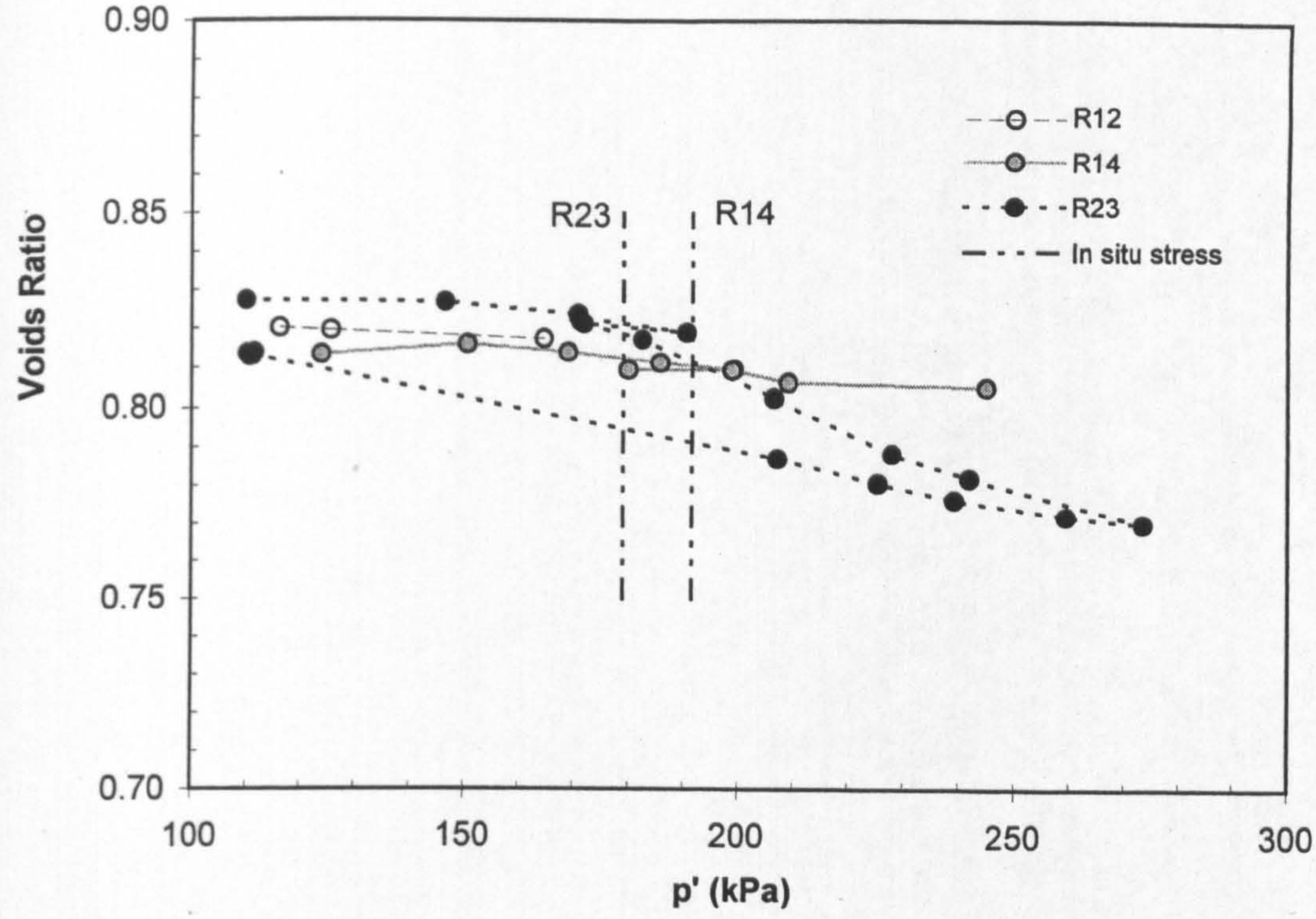

a) Voids Ratio *vs.* p'

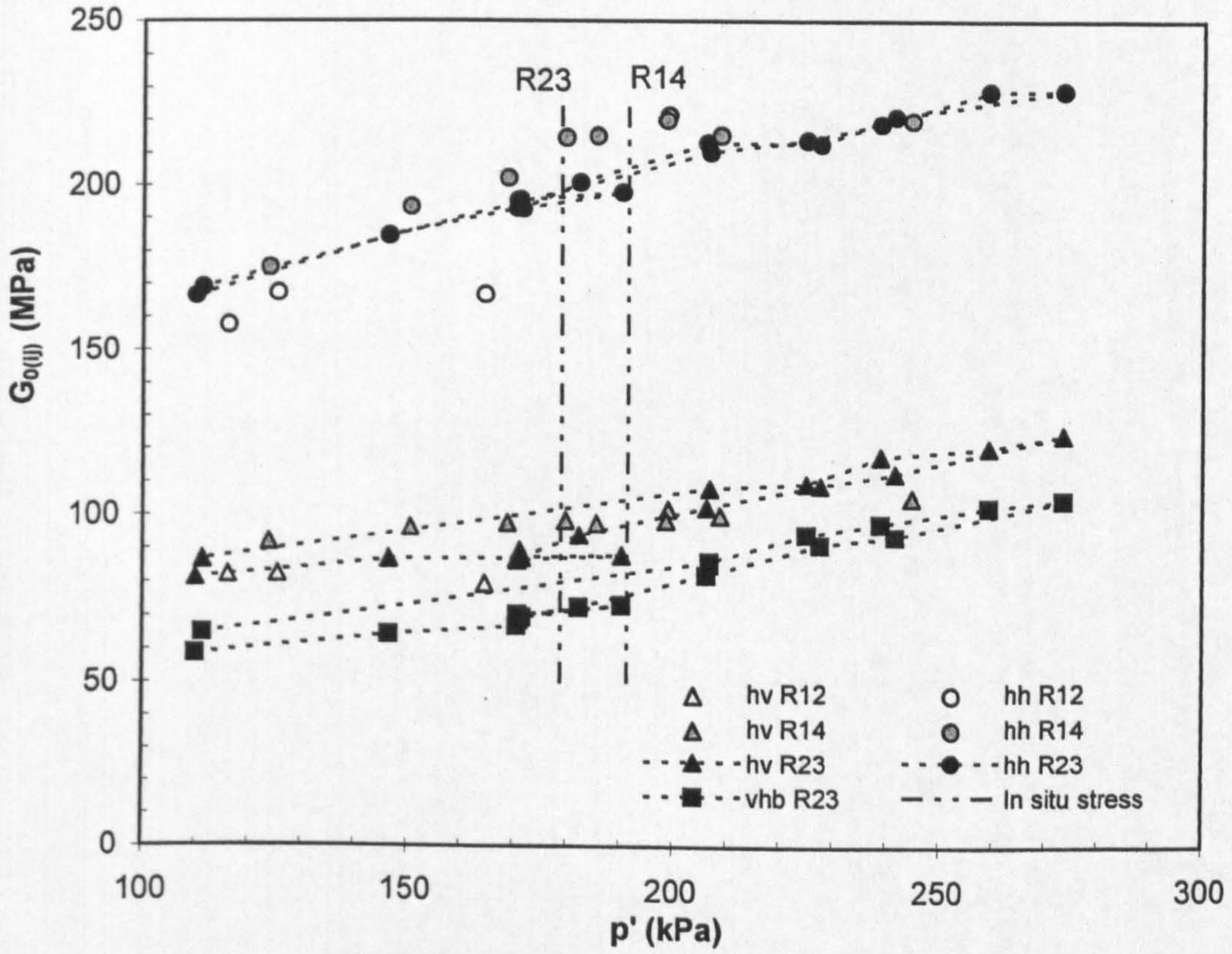

b) $G_{0(ij)}$ *vs.* p'

Figure 5.20 Variation of $G_{0(ij)}$ with effective confining pressure on natural Gault clay: Tests R12, R14 and R23

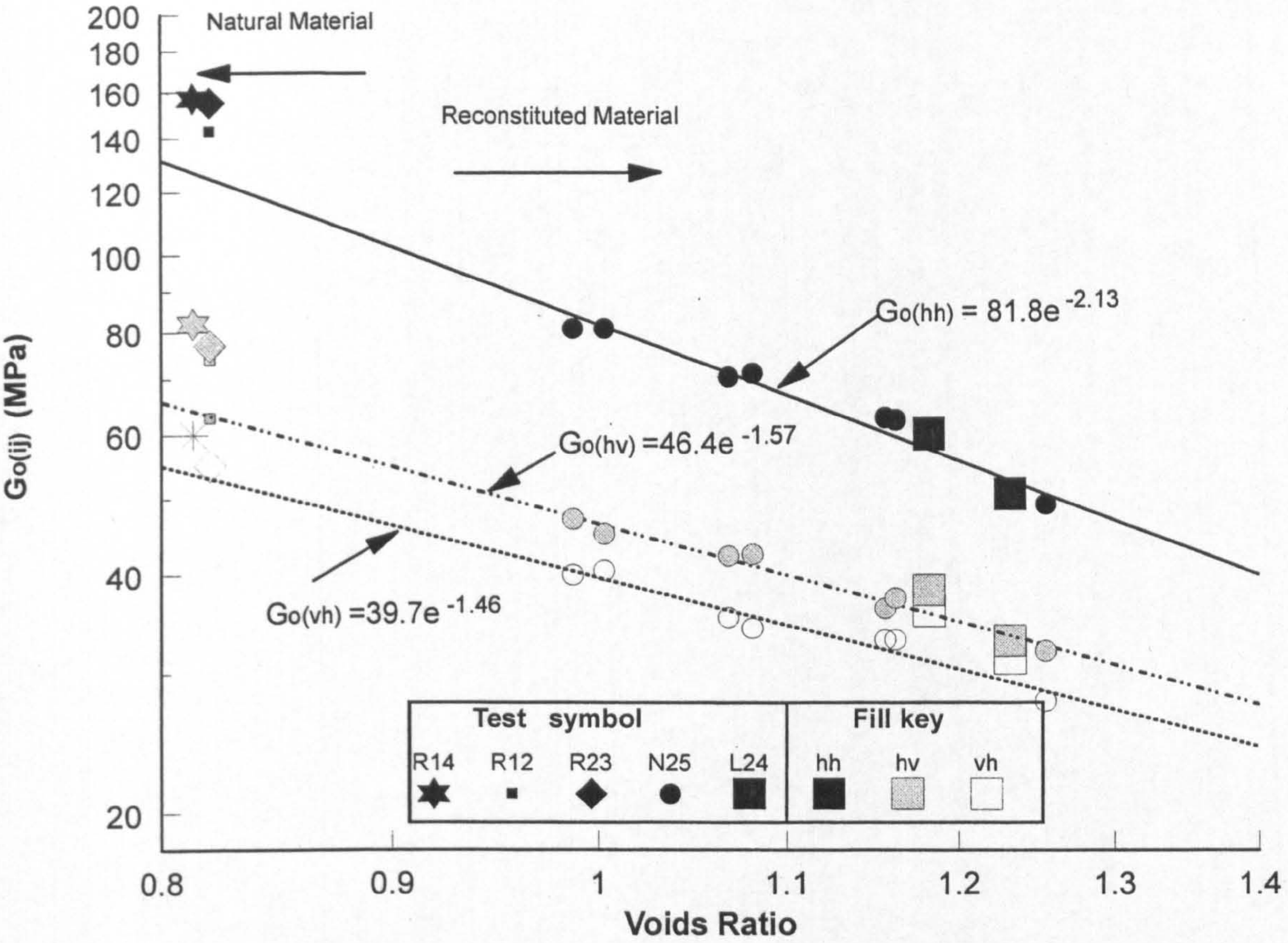

Figure 5.21 Variation of $G_{o(ij)}$ with voids ratio at isotropic p'= 90 kPa for natural and reconstituted 1D consolidated samples

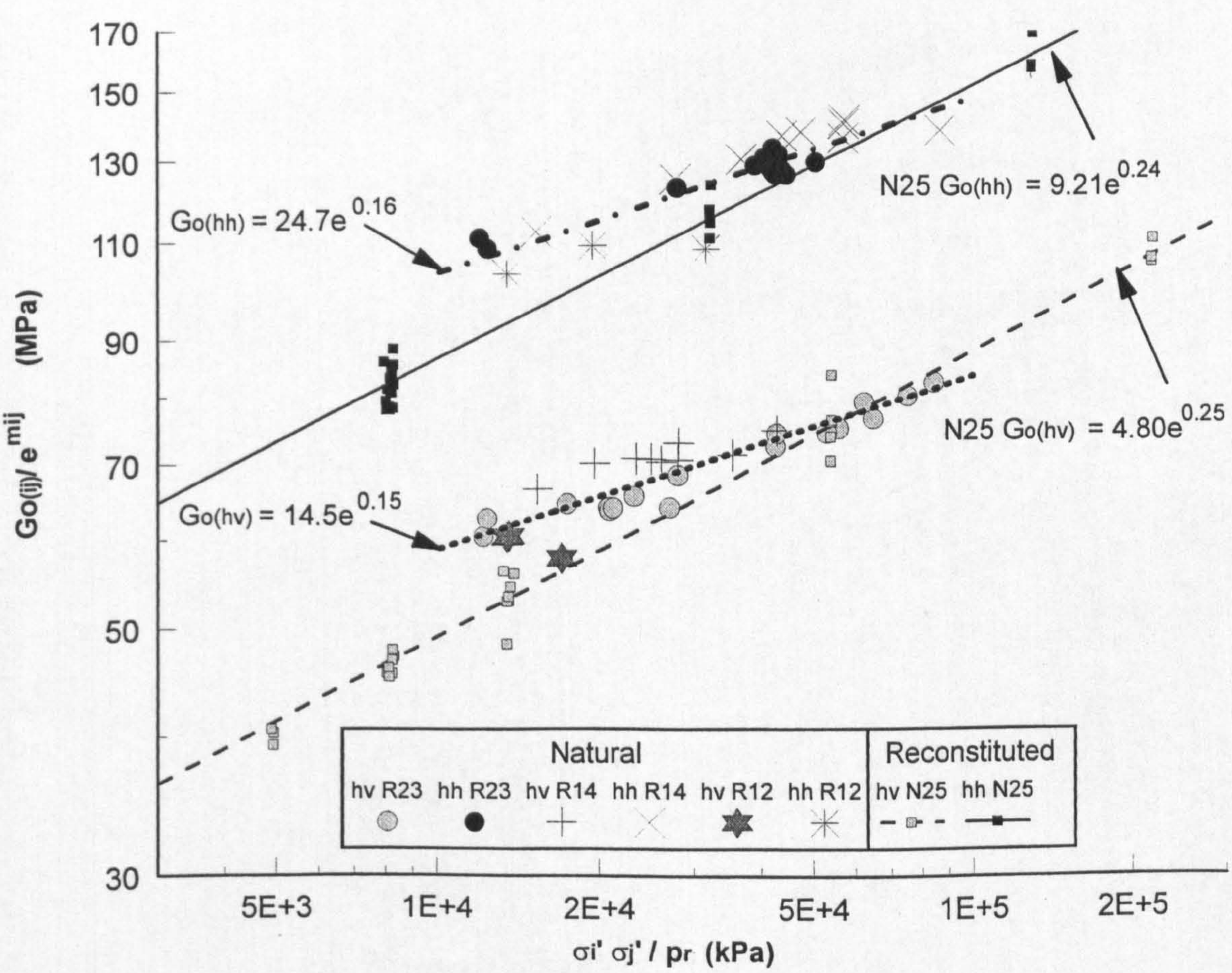

Figure 5.22 Comparison of $G_{o(ij)} / e^{m_{ij}}$ *vs.* $\sigma_i'\sigma_j'$ at constant p' for natural Gault clay tests and tests on reconstituted samples

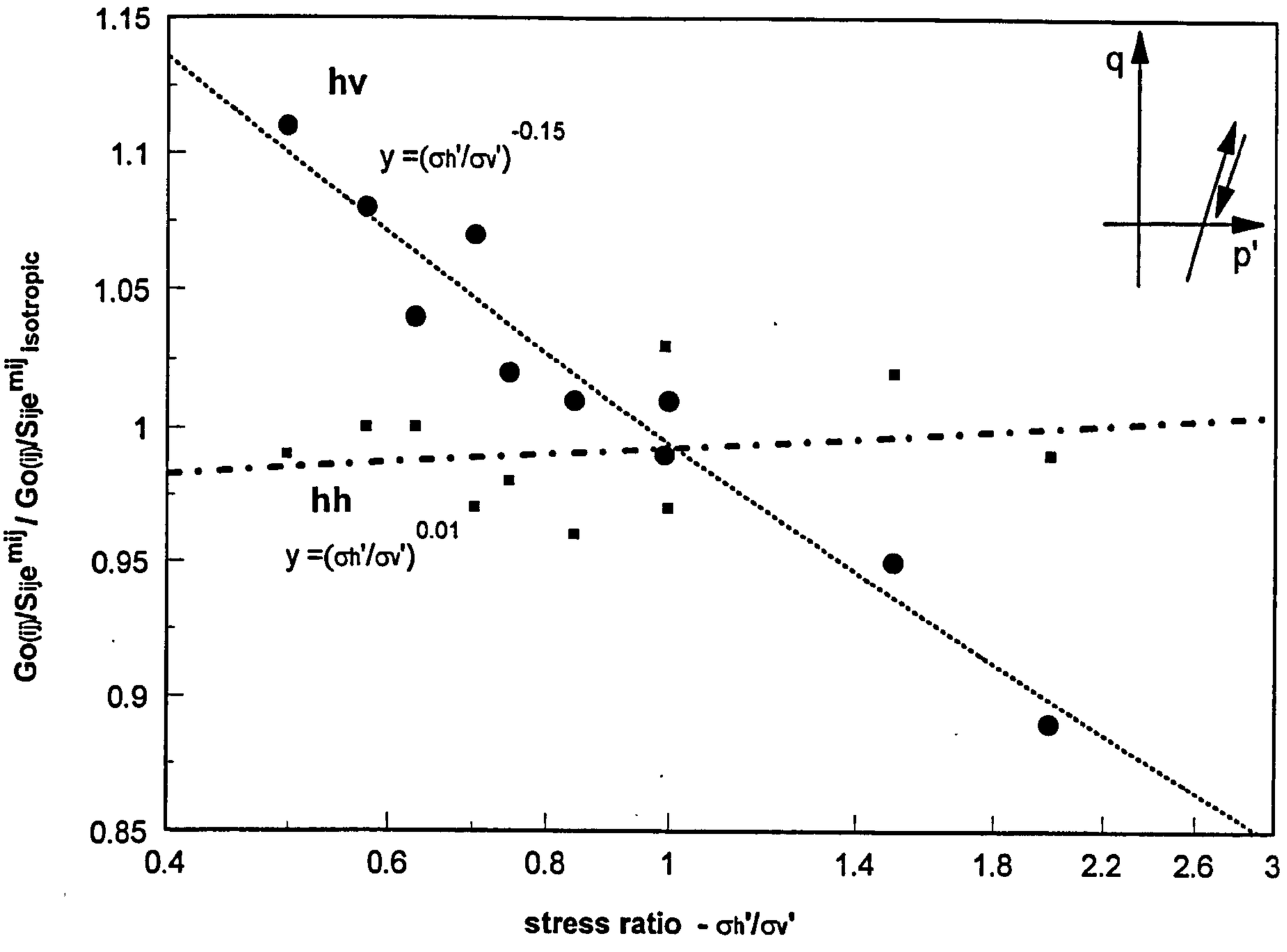

Figure 5.23 Normalised shear moduli ratio *vs.* stress ratio at constant σh'=205 kPa - Natural Gault clay: Test R23

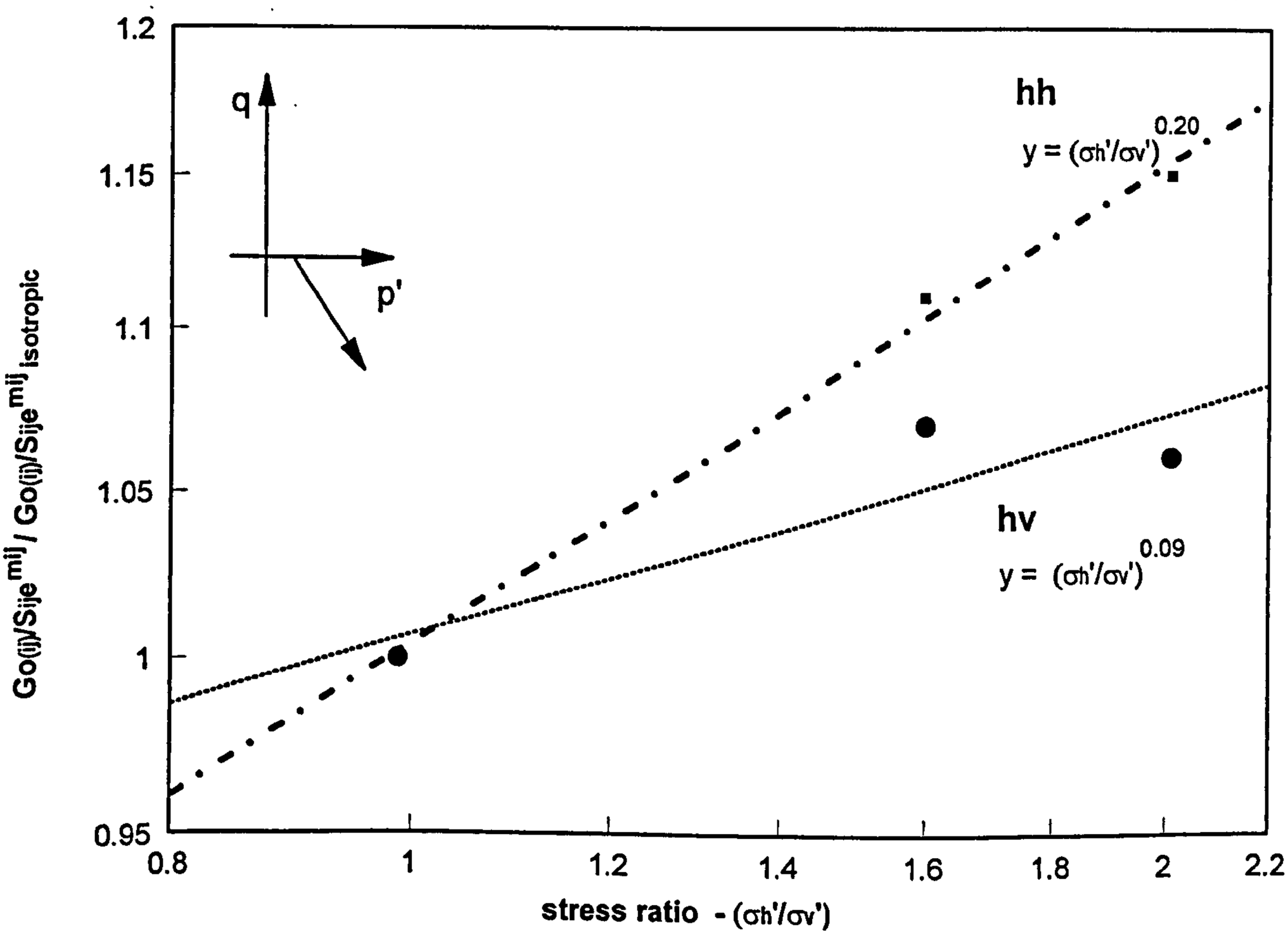

Figure 5.24 Normalised shear moduli ratio *vs.* stress ratio at constant σv'=105 kPa: Test R23

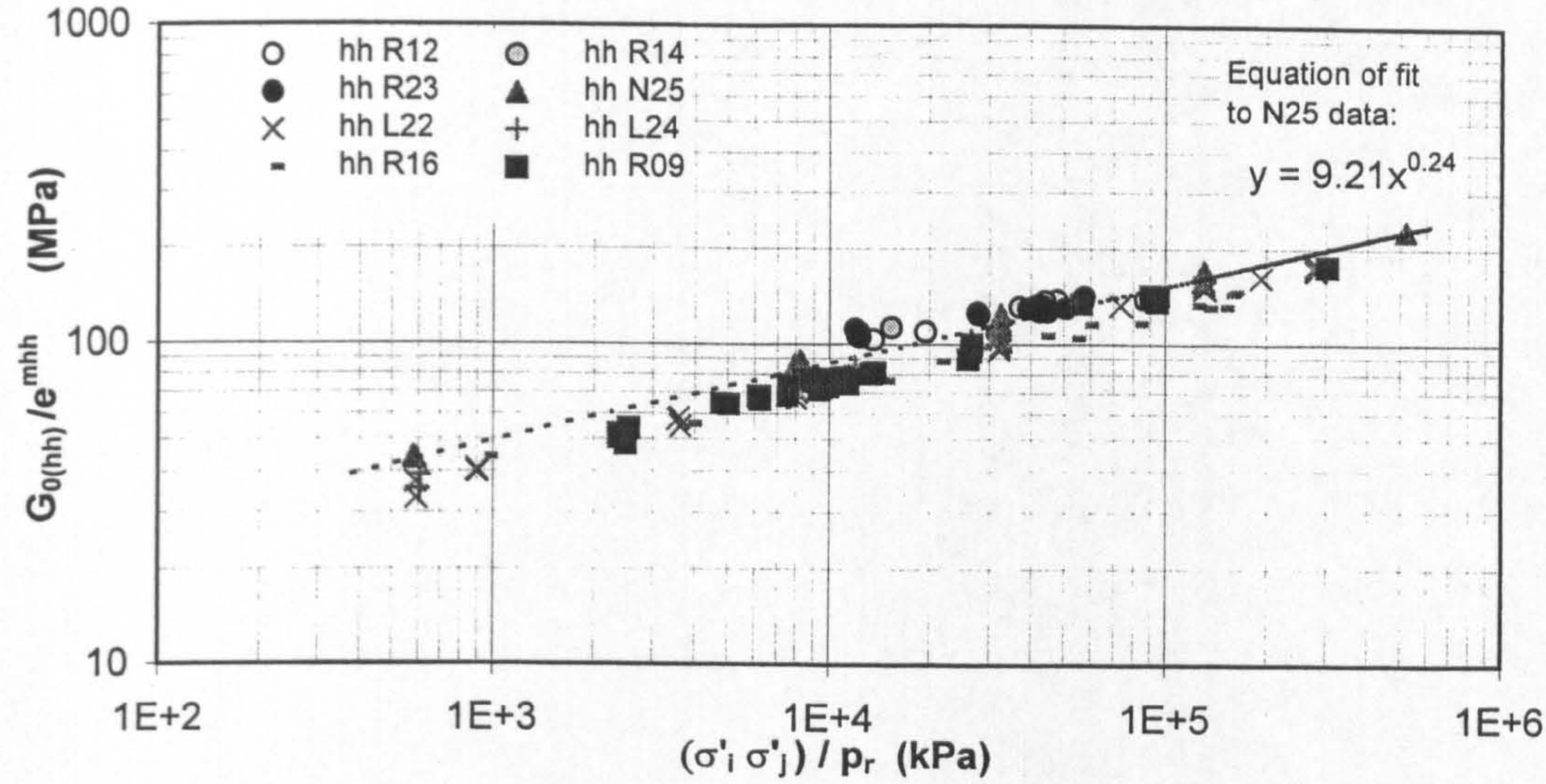

a) $G_{0(hh)}/e^{mhh}$ *vs.* $(\sigma_h'\sigma_h')/p_r$

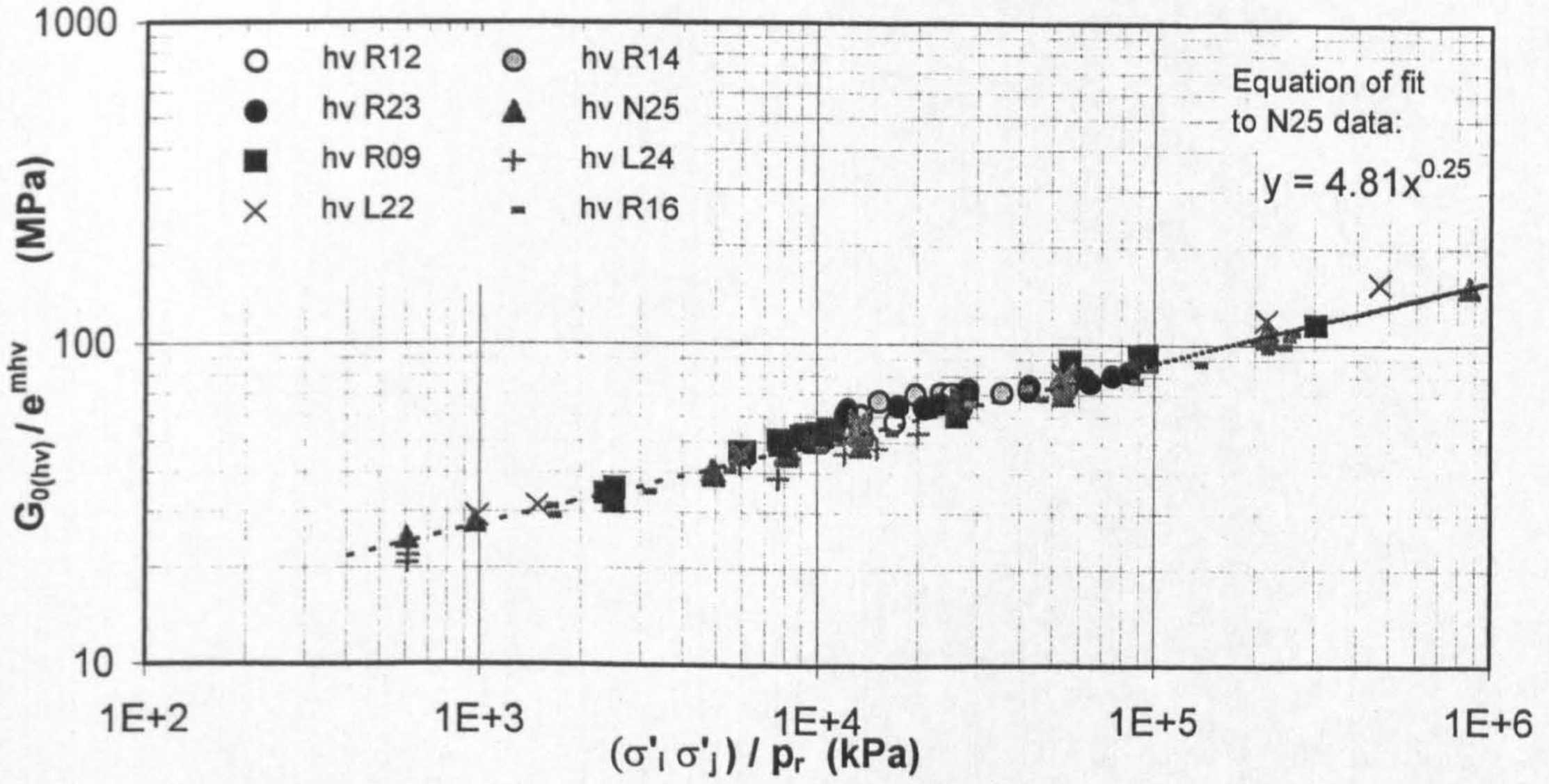

b) $G_{0(hv)}/e^{mhv}$ *vs.* $(\sigma_h'\sigma_v')/p_r$

c) $G_{0(vh)}/e^{mvh}$ *vs.* $(\sigma_v'\sigma_h')/p_r$ (NB: plot includes tests where only $V_{s(vh)}$ was measured)

Figure 5.25 Comparison of normalised $G_{0(hh)}$, $G_{0(hv)}$ and $G_{0(vh)}$ data *vs.* product of stresses for all tests on natural and reconstituted Gault clay

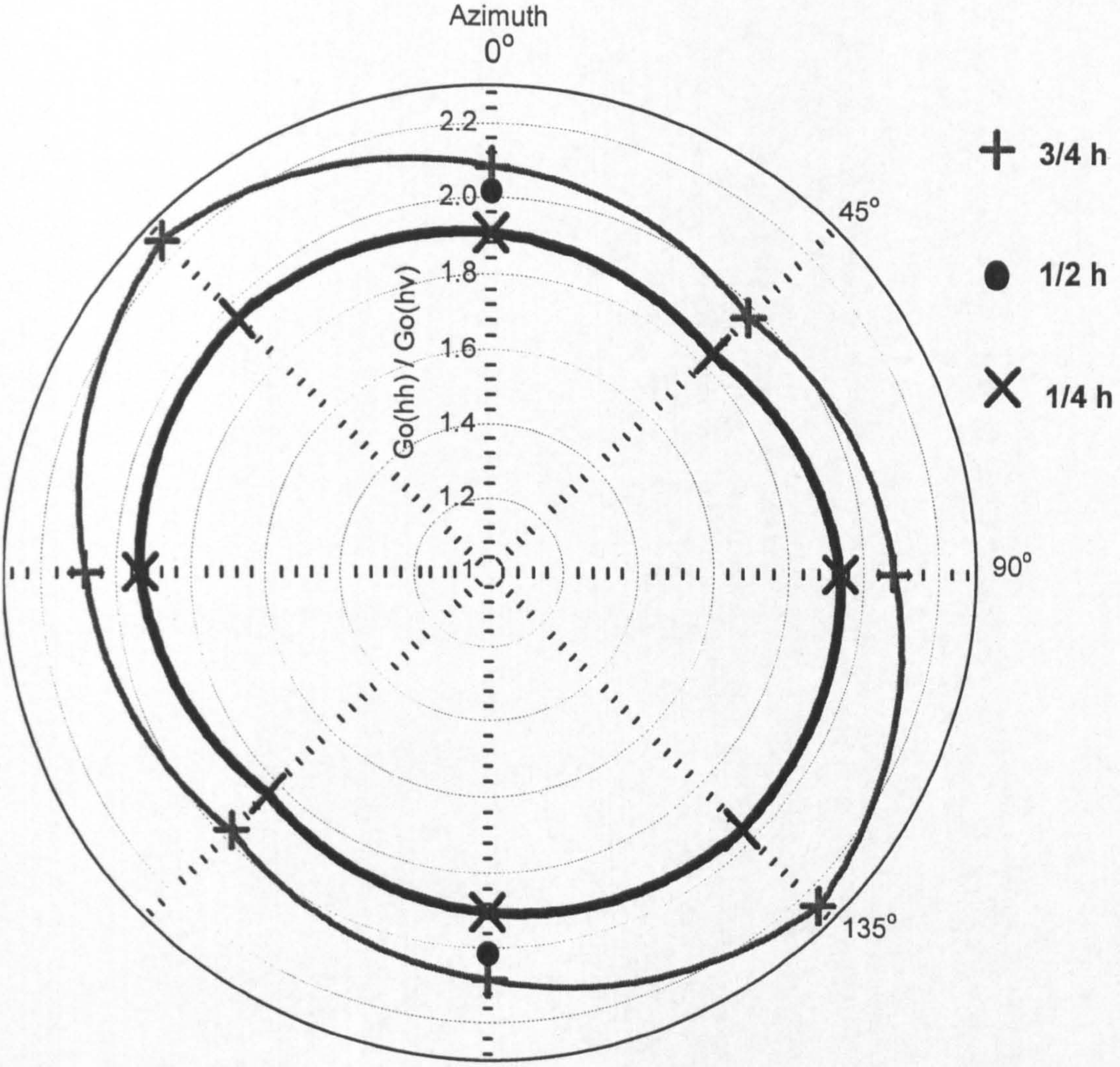

Notes:

1. The result at 1/2 h was measured using the bender belt while it was still attached to the sample, but after cell and back pressure had been removed.
2. An azimuthal angle of 0° corresponds to the direction of horizontal bender belt shear wave velocity measurements made in Test R23
3. Bench top tests were carried out at the angles of 0°, 45°, 90° and 135°. These results have been reflected by 180° in order to illustrate the asymmetric anisotropy in the horizontal plane.

Figure 5.26 Variation of anisotropy ratio $G_{0(hh)}$ / $G_{0(hv)}$ with azimuthal angle:- Sample R23

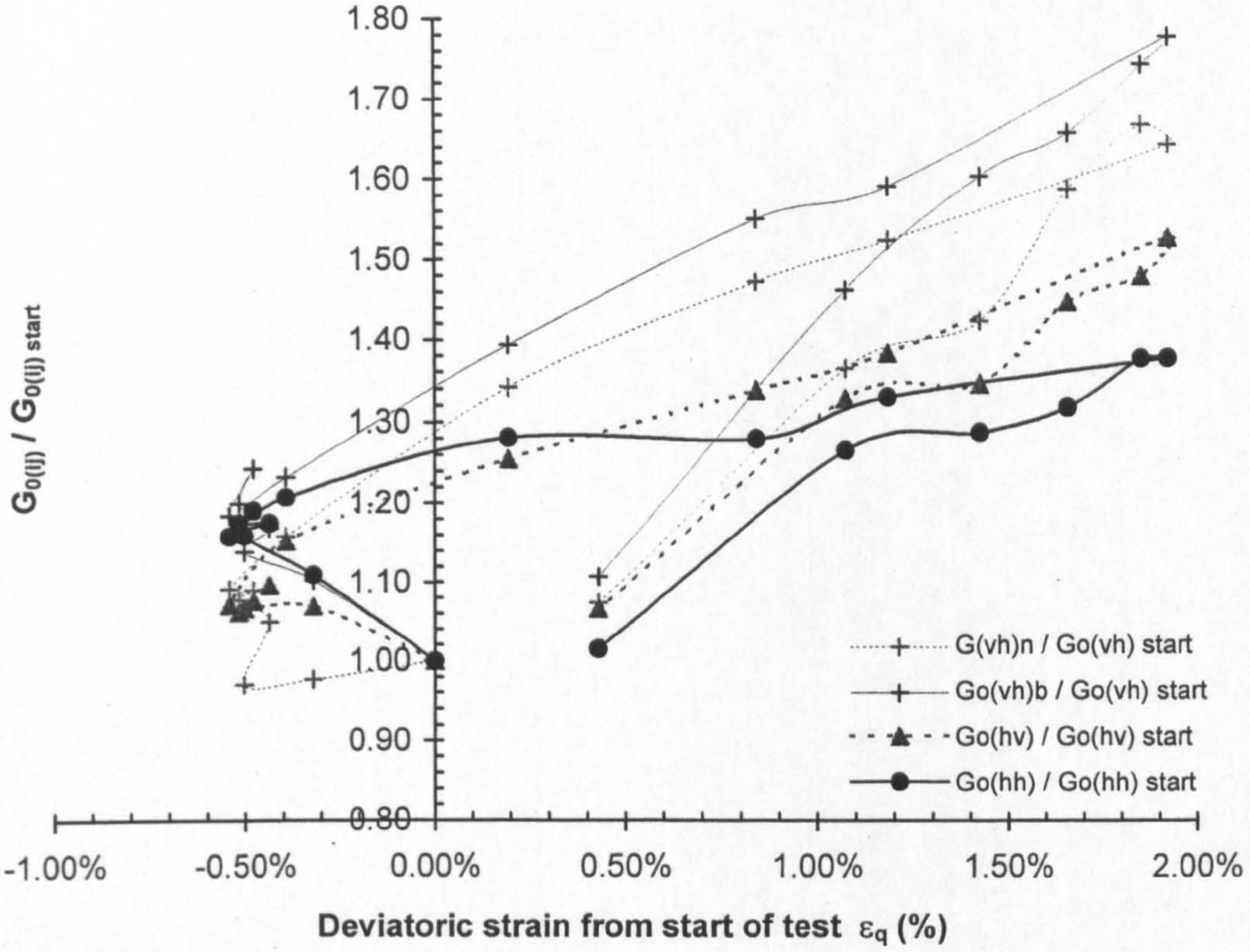

a) $G_{o(ij)}$ normalised by $G_{o(ij)}$ at the start of the test *vs.* ε_q

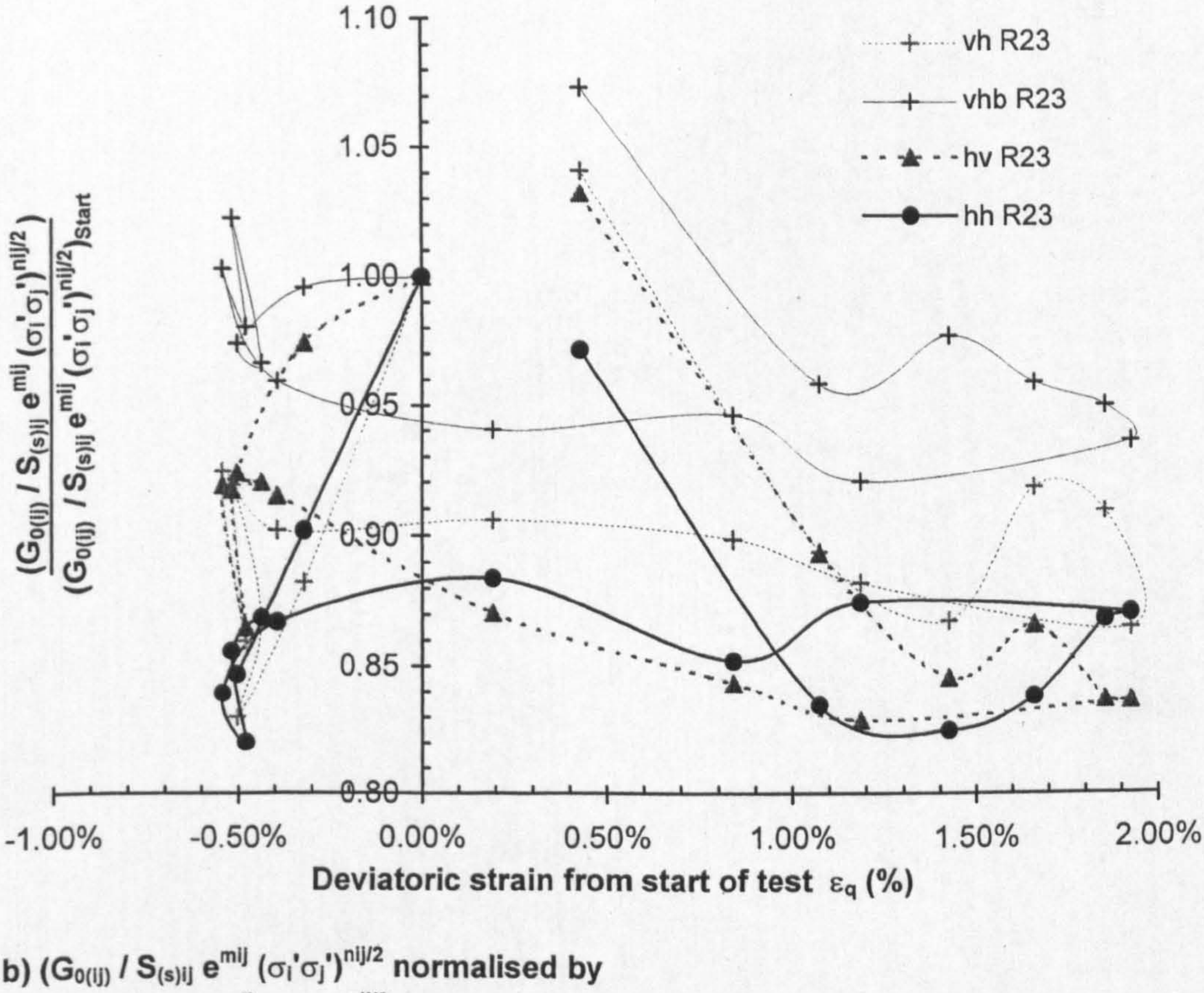

b) $(G_{o(ij)} / S_{(s)ij}\, e^{mij}\, (\sigma_i'\sigma_j')^{nij/2}$ normalised by
$(G_{o(ij)} / S_{(s)ij}\, e^{mij}\, (\sigma_i'\sigma_j')^{nij/2}$ at the start of the test *vs.* ε_q

Figure 5.27 Variation of $G_{o(ij)}$ with deviatoric strain during Test R23

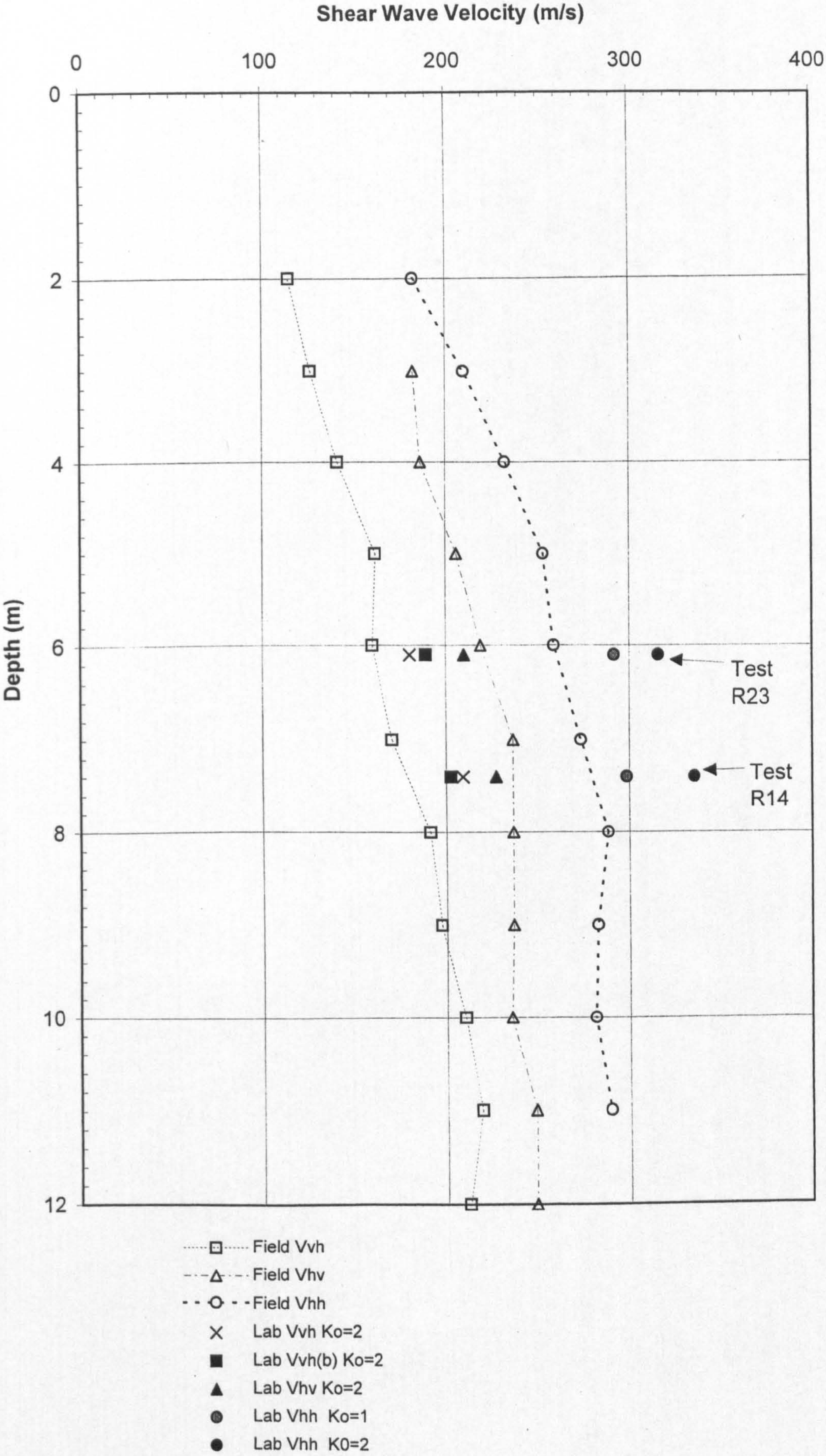

Figure 5. 28 Comparisons between field $G_{0(ij)}$ *vs.* depth and lab measurements on natural Gault clay - Tests R12, R14 R23.

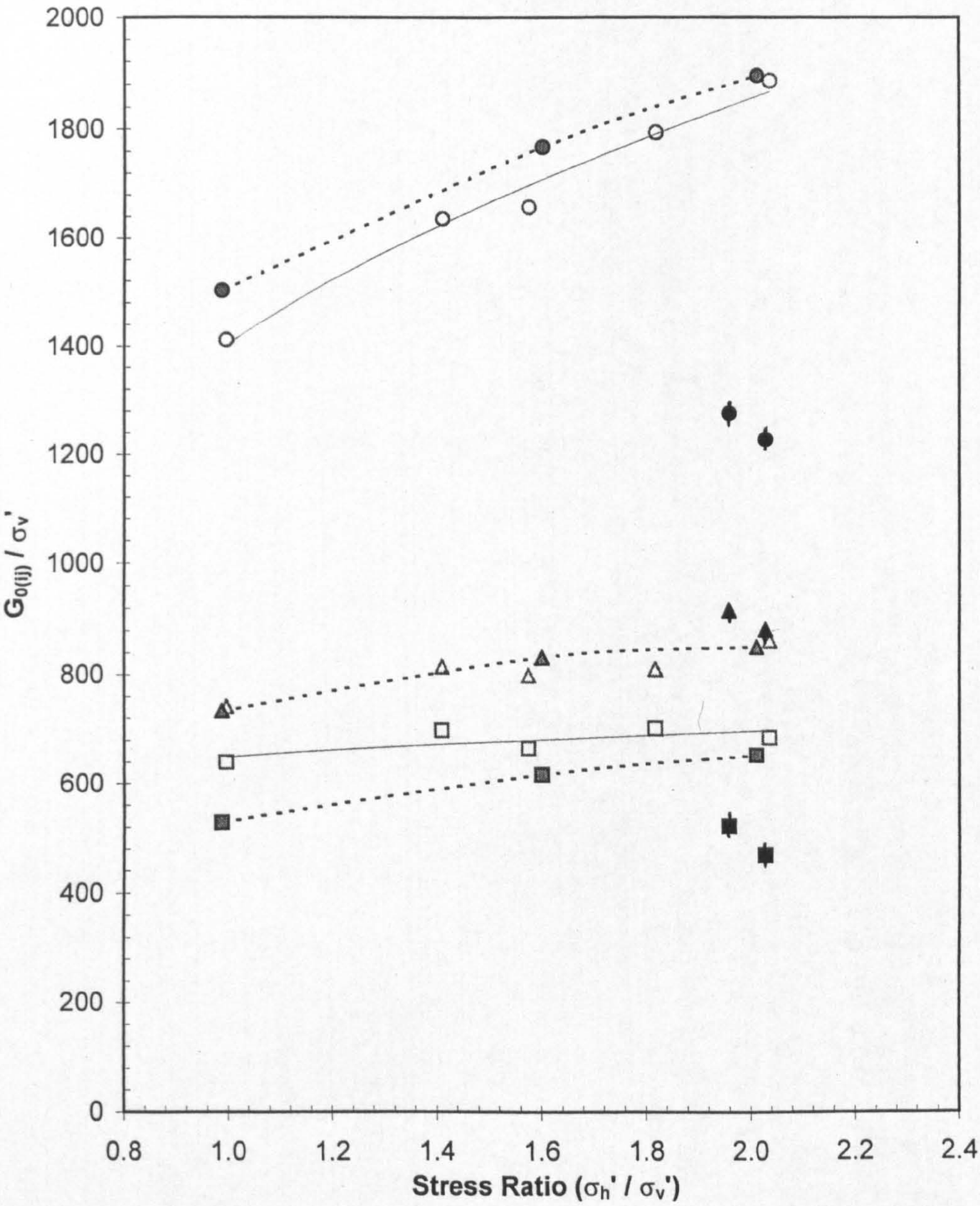

Note: Field values are based on Ko profile after Lord and Butcher (1993), for depths of 6.1 and 7.4m representing samples R23 and R14 respectively

Figure 5.29 Comparison between the variation of $G_{0(ij)}$ / σ_v' with stress ratio σ_h' / σ_v' for Natural Gault clay Tests R12, R14 & R23, and *in situ* measurements

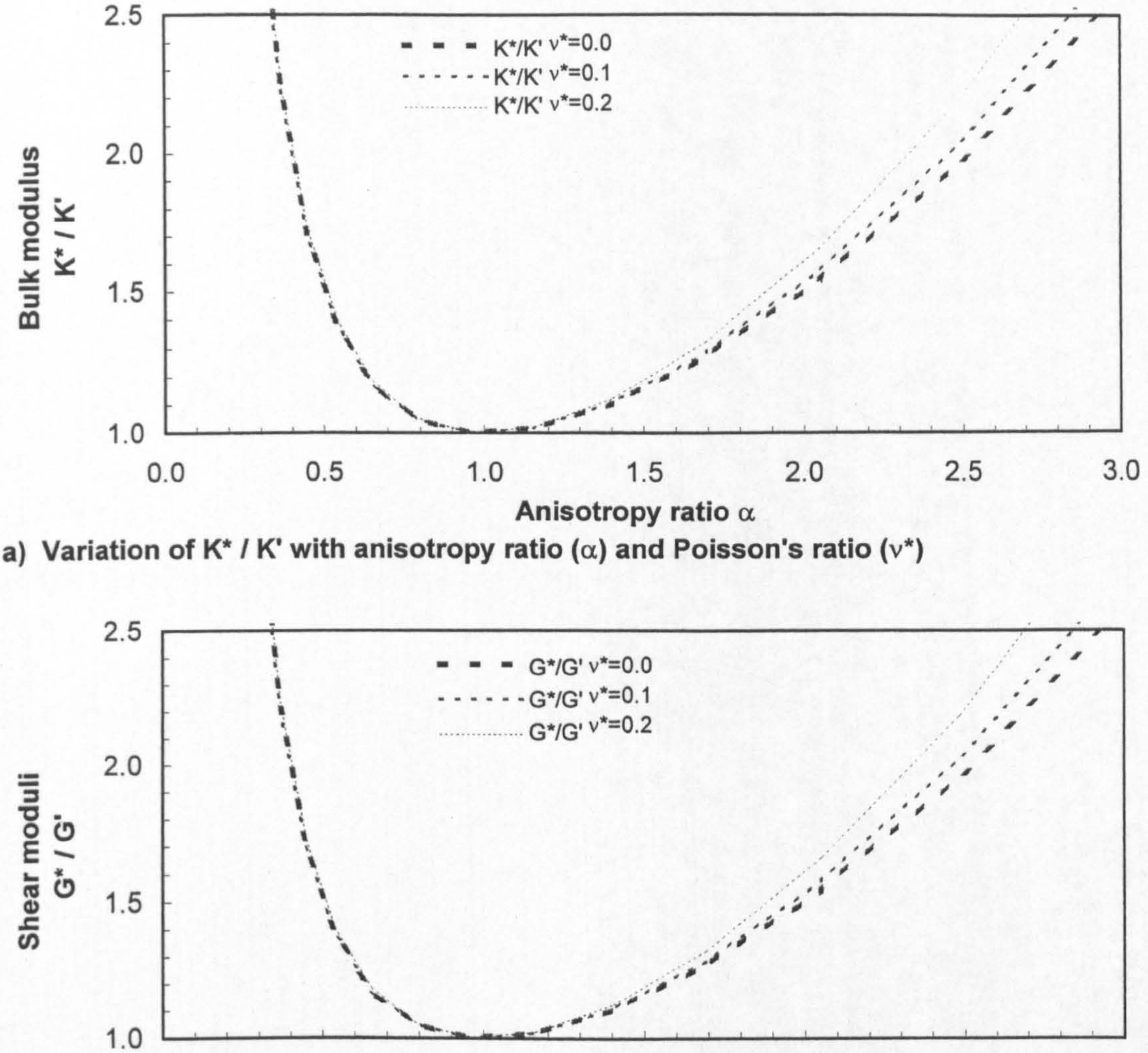

a) Variation of K* / K' with anisotropy ratio (α) and Poisson's ratio (ν^*)

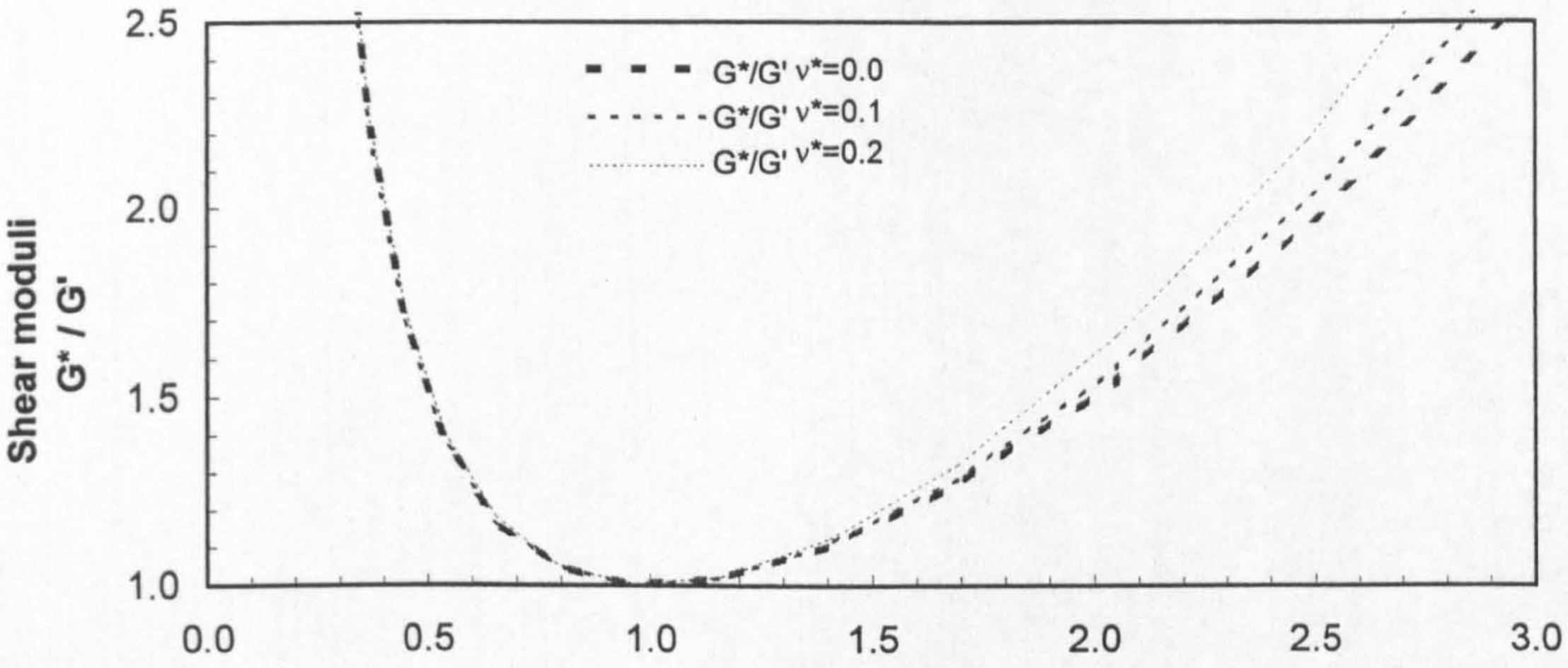

b) Variation of G*/G' with anisotropy ratio (α) and Poisson's ratio (ν^*)

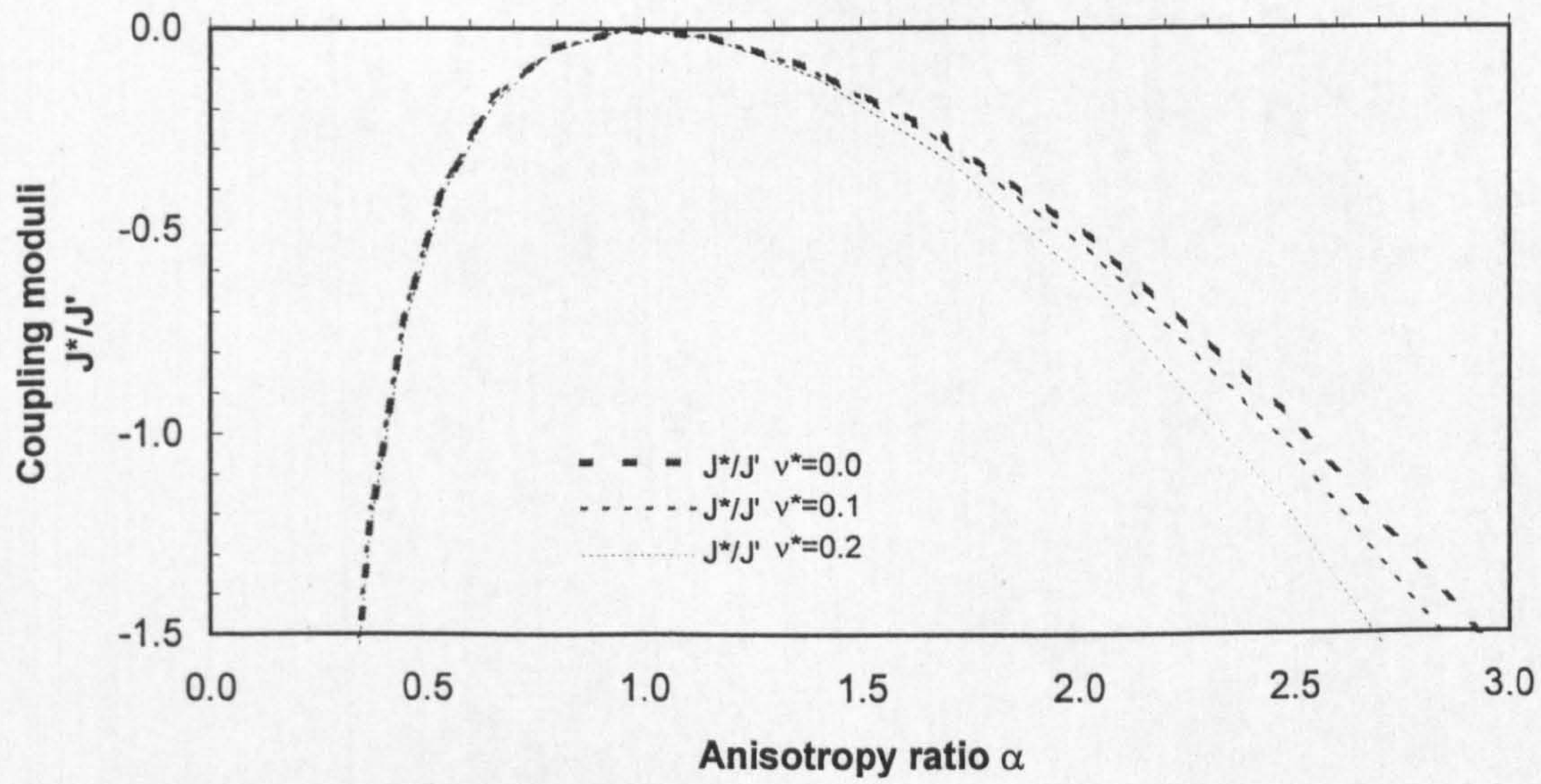

c) Variation of J*/J' with anisotropy ratio (α) and Poisson's ratio (ν^*)

Figure 6.1 **Illustrations of the relationships between K', G' and J' and modified K*, G* and J* with anisotropy ratio α and modified Poisson's ratio ν^***

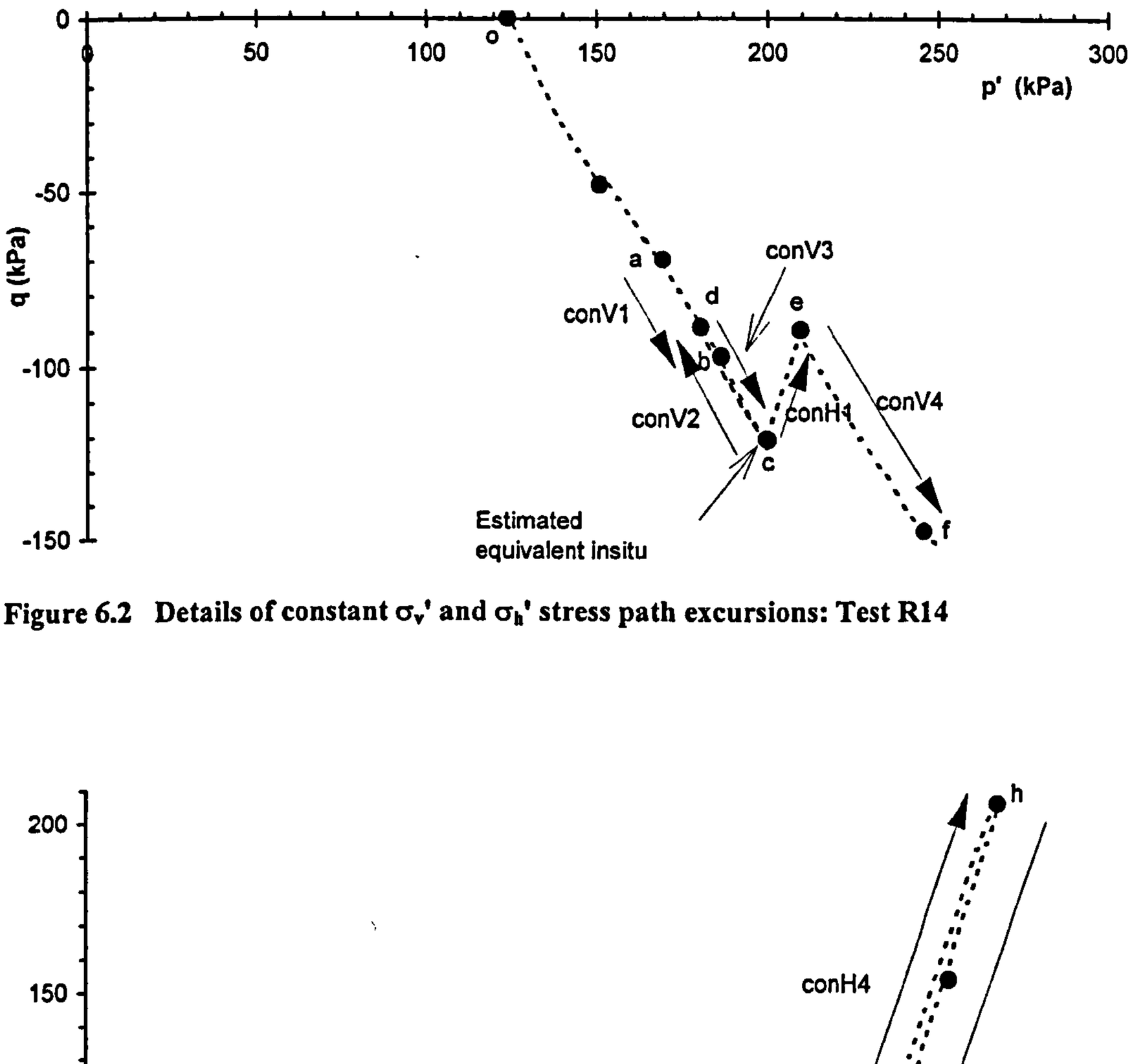

Figure 6.2 Details of constant σ_v' and σ_h' stress path excursions: Test R14

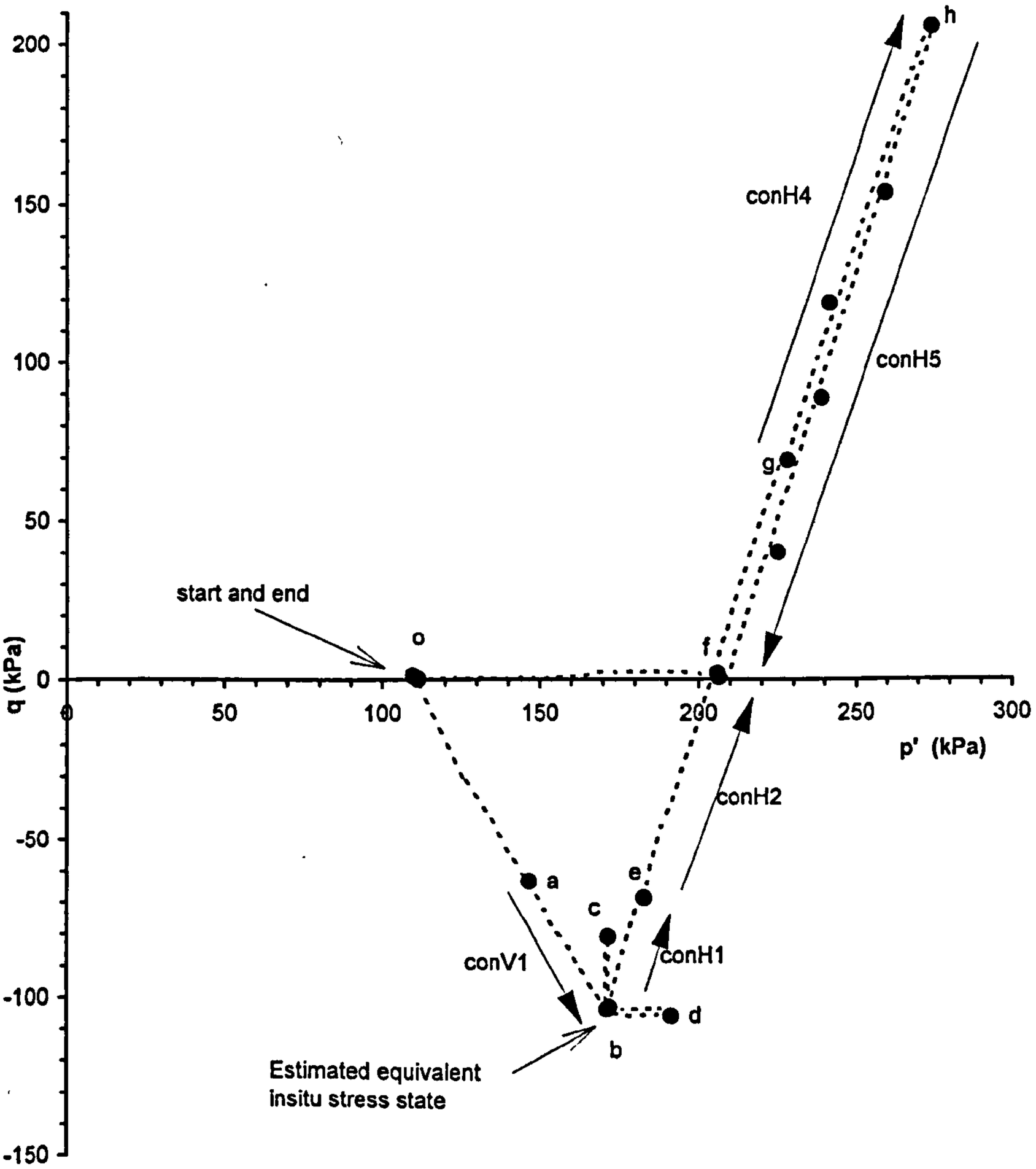

Figure 6.3 Details of constant σ_v' and σ_h' stress path excursions: Test R23

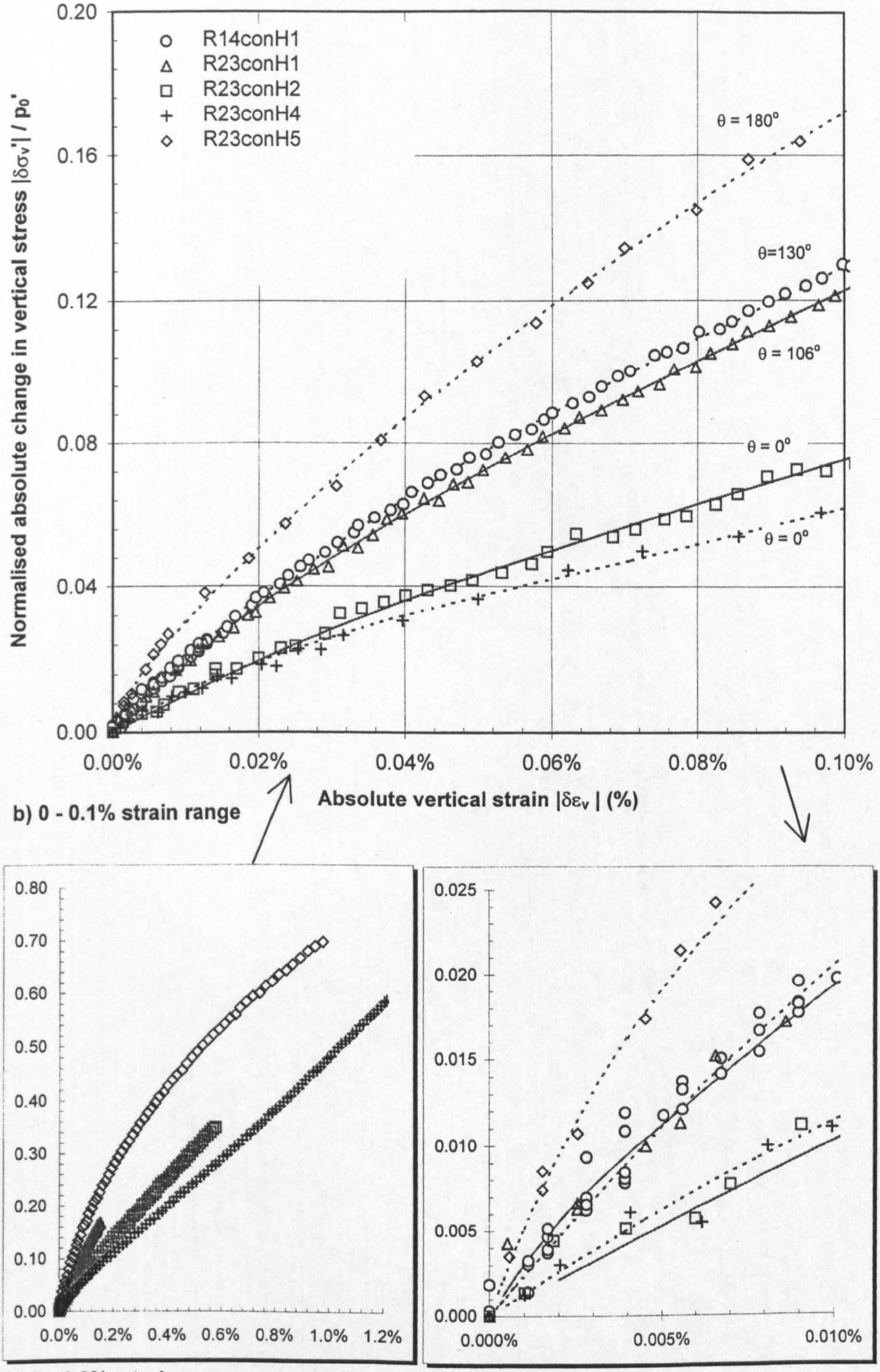

Figure 6.4 Normalised vertical stress-strain curves at constant σ_h'

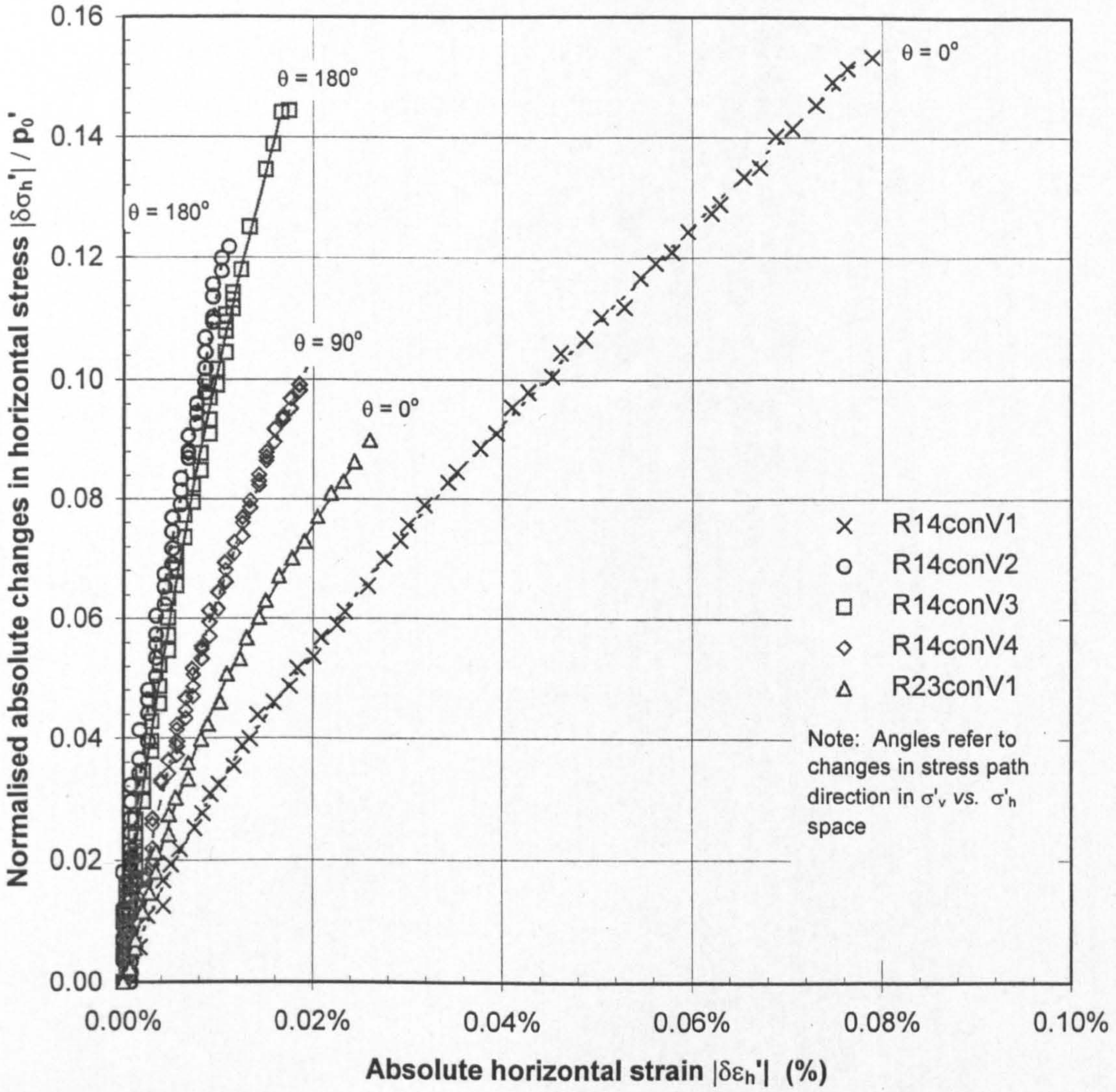

a) 0 - 0.1% strain range

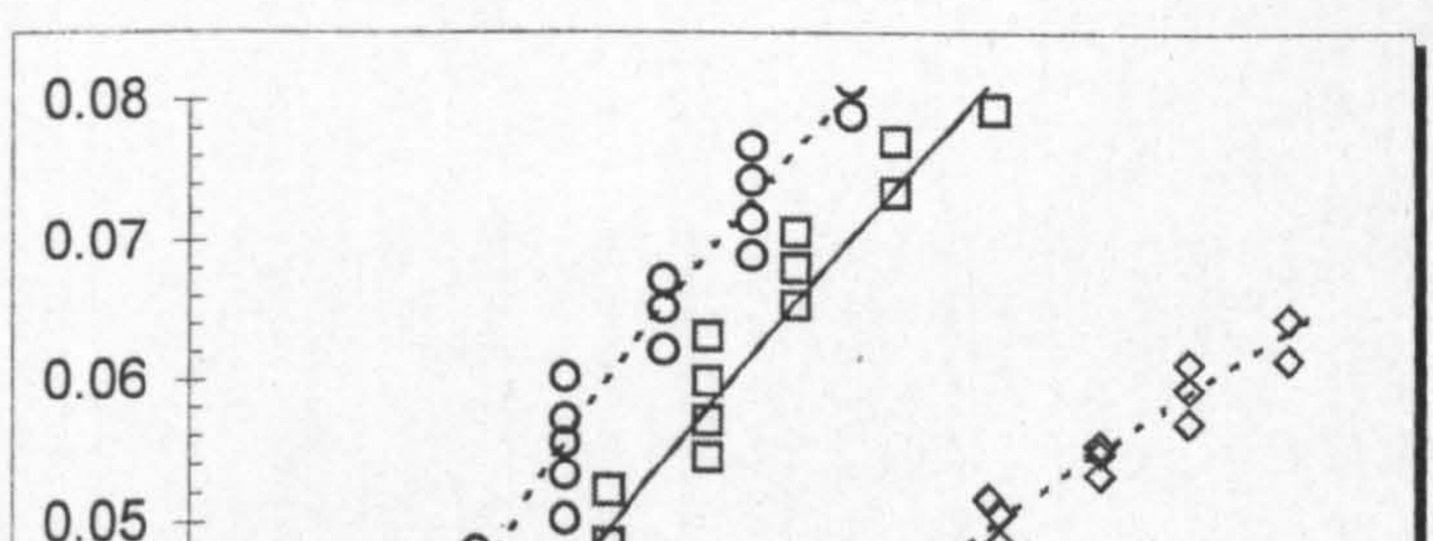

b) 0 - 0.01% strain range

Figure 6.5 Normalised horizontal stress-strain curves at constant σ_v'

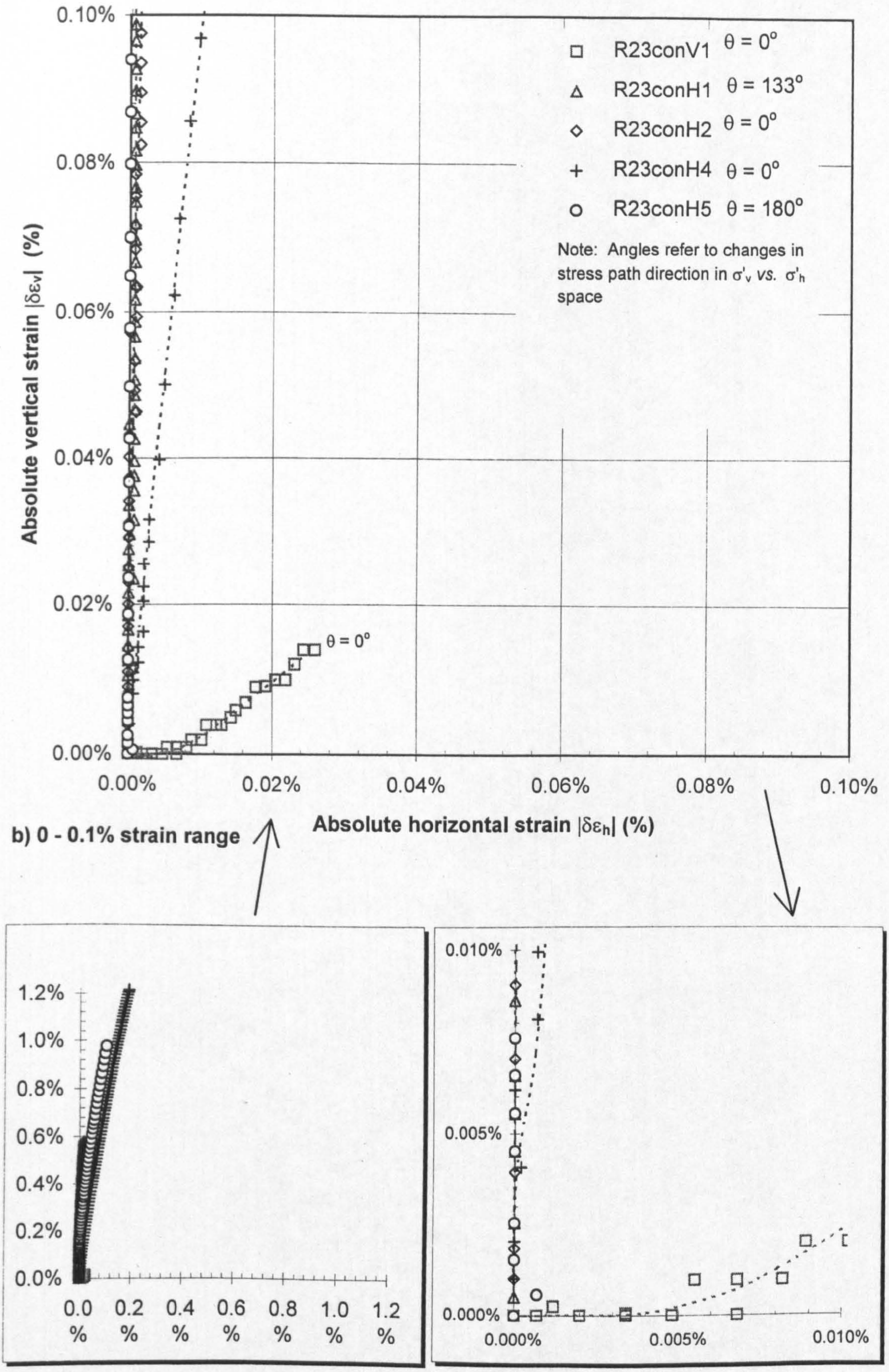

Figure 6.6 Absolute strain paths for constant vertical and horizontal effective stress excursions - Test R23

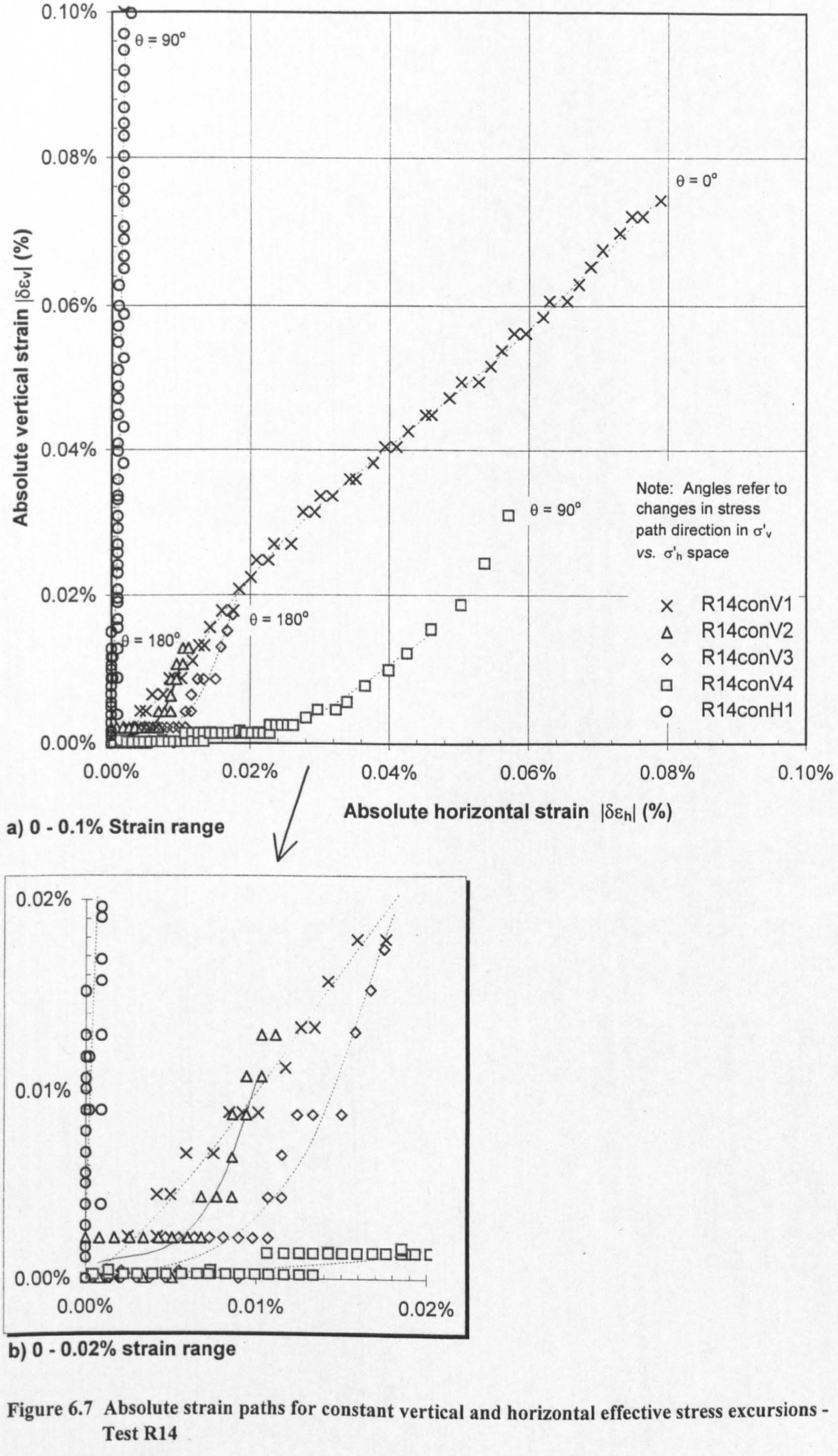

Figure 6.7 Absolute strain paths for constant vertical and horizontal effective stress excursions - Test R14

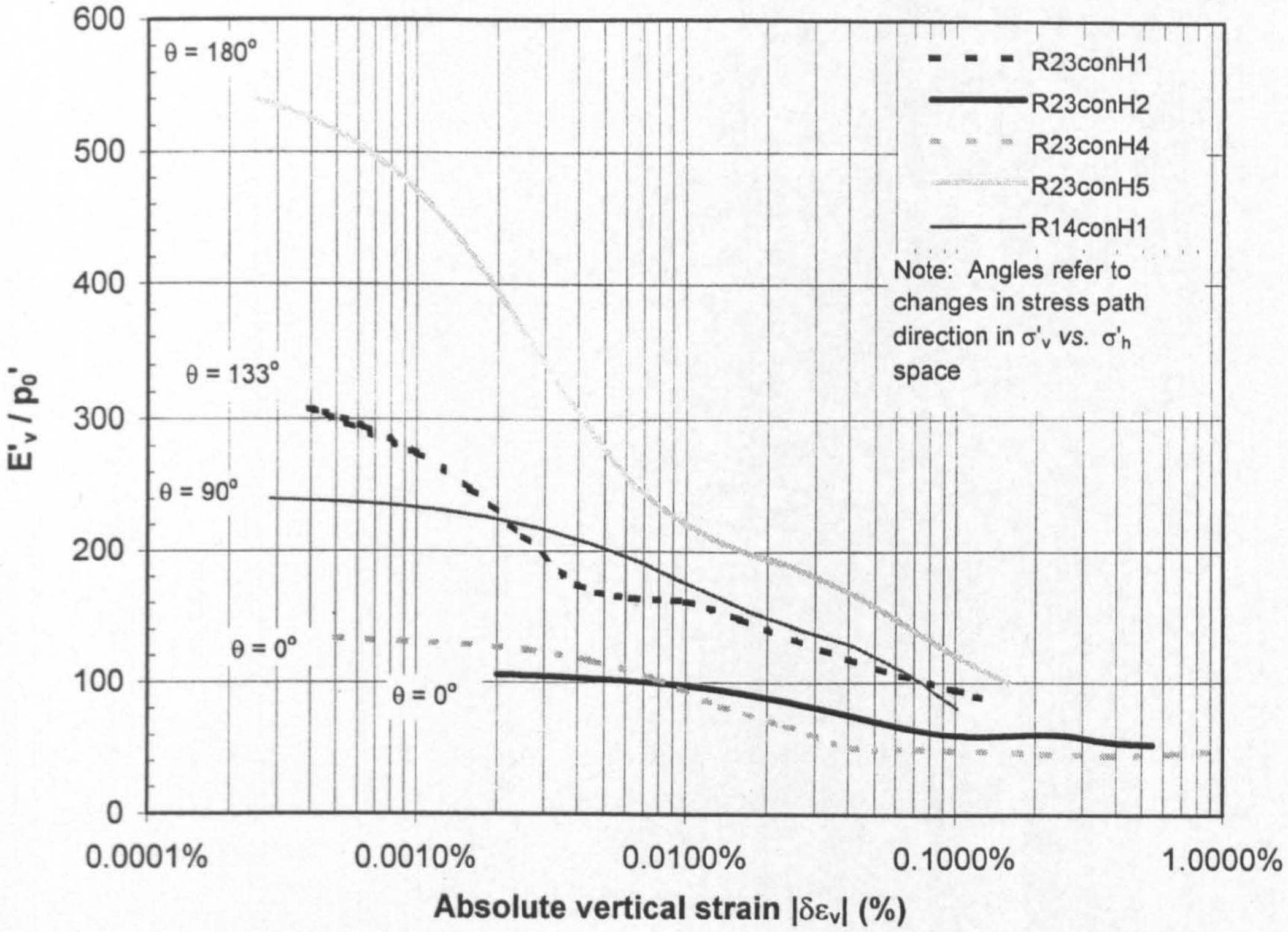

Figure 6.8 Elastic modulus E'_v / p_0' *vs.* vertical strain for constant horizontal effective stress excursions - Tests R14 and R23

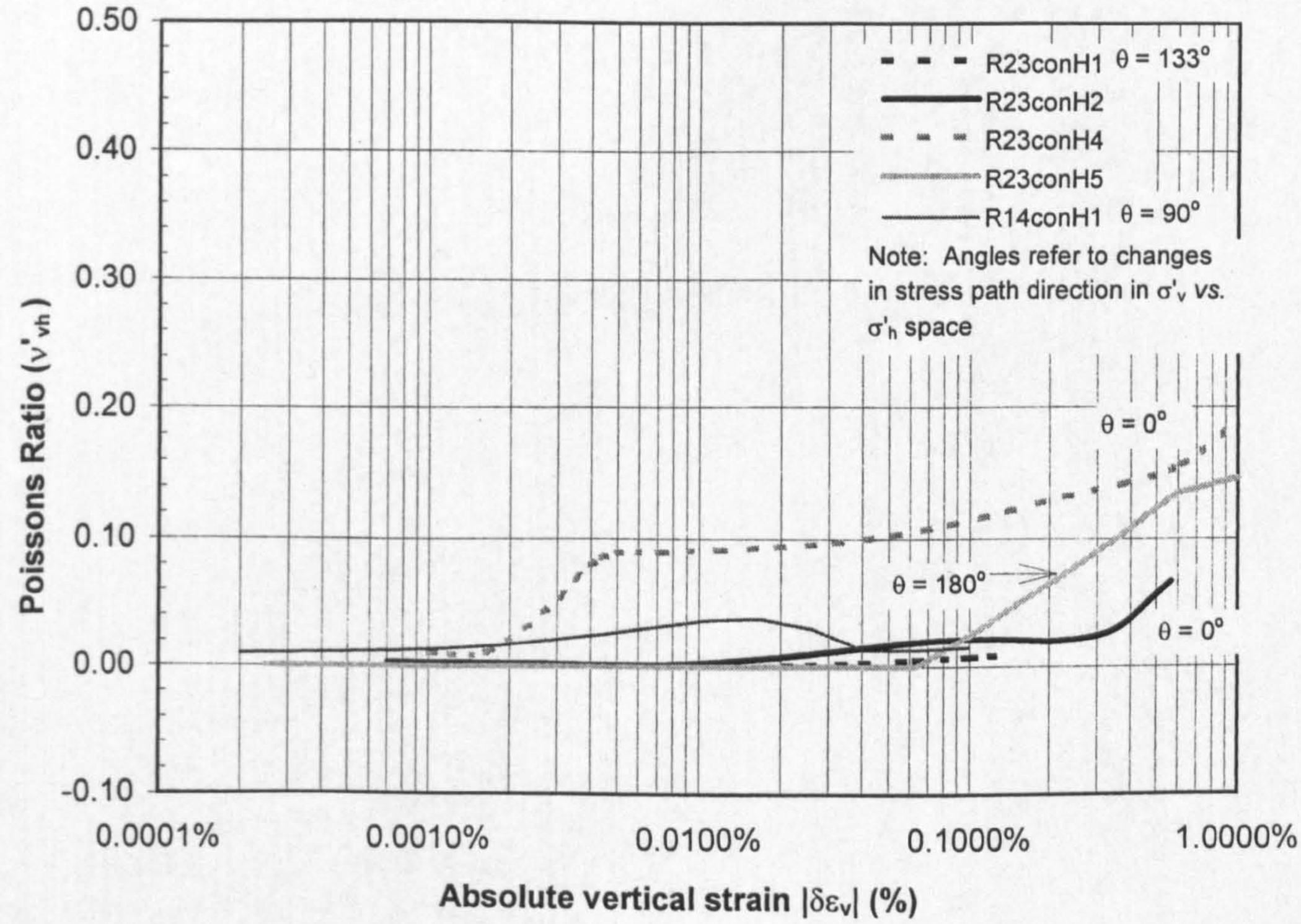

Figure 6.9 Poissons ratio ν'_{vh} *vs.* vertical strain for constant horizontal effective stress excursions - Tests R14 and R23

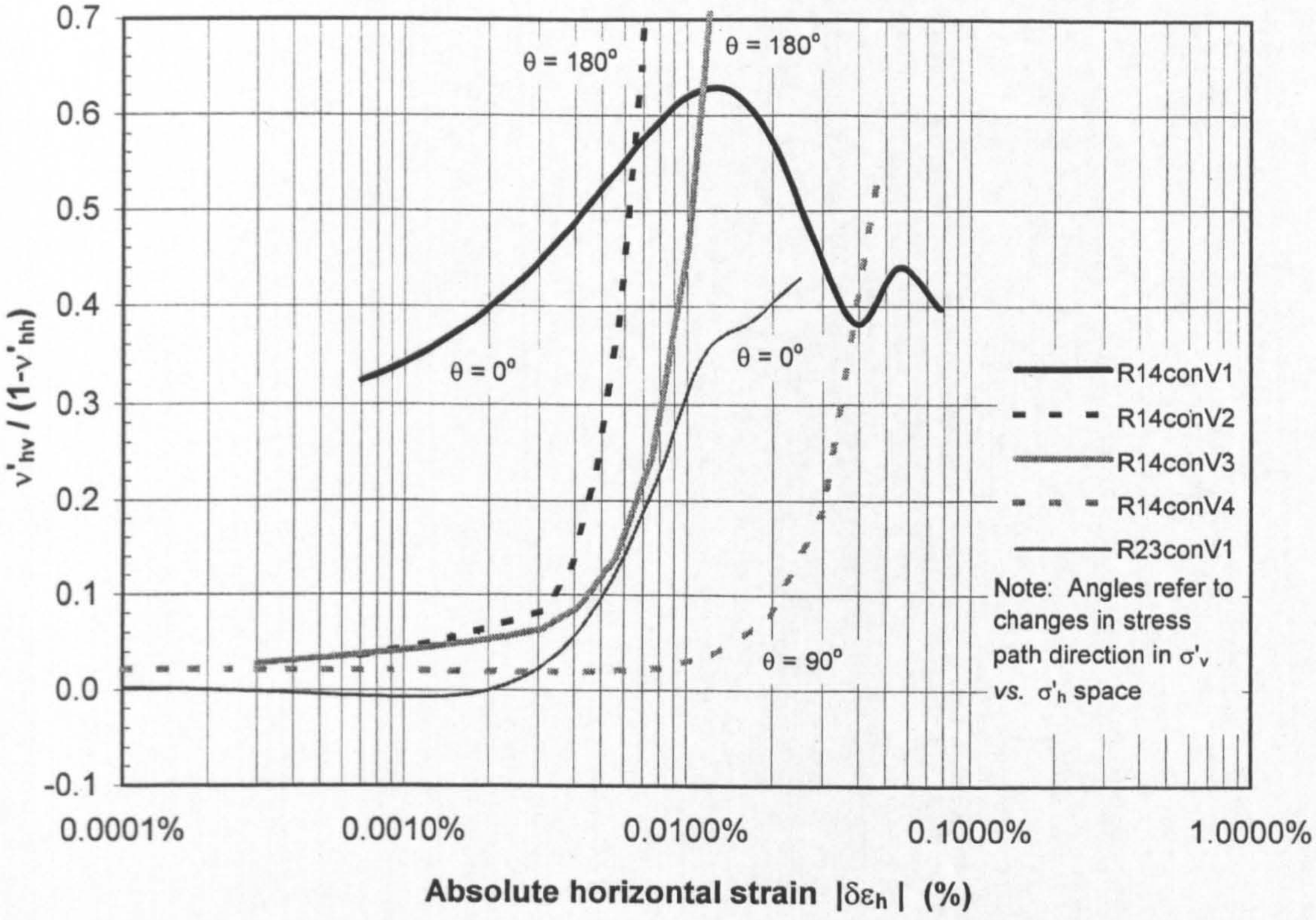

Figure 6.10 $\nu'_{hv} / (1-\nu'_{hh})$ ***vs.*** **absolute horizontal strain for constant vertical stress excursions - Tests R14 and R23**

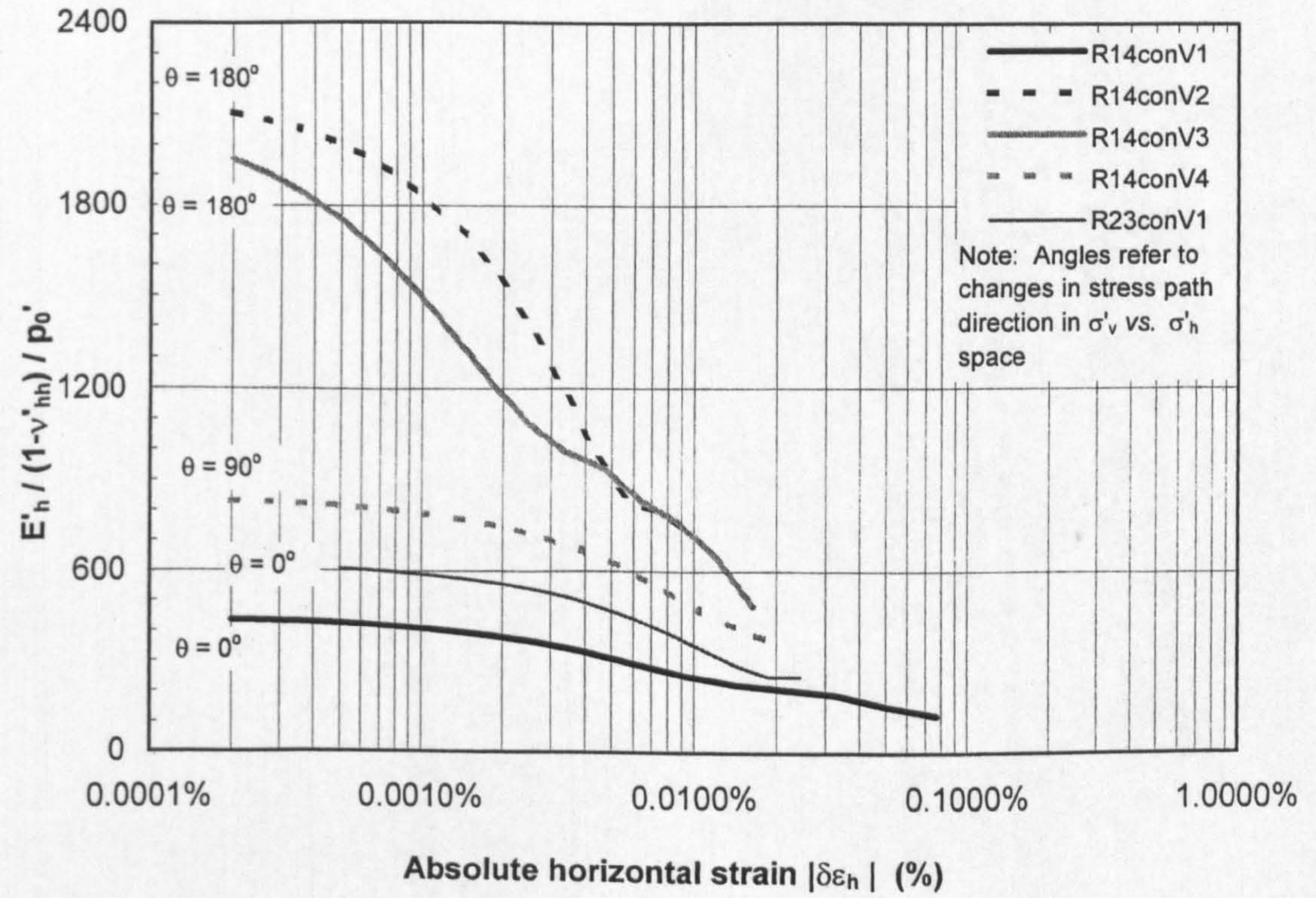

Figure 6.11 Elastic moduli ratio $E'_h / (1-\nu'_{hh})$ ***vs.*** **horizontal strain for constant vertical effective stress excursions - Tests R14 and R23**

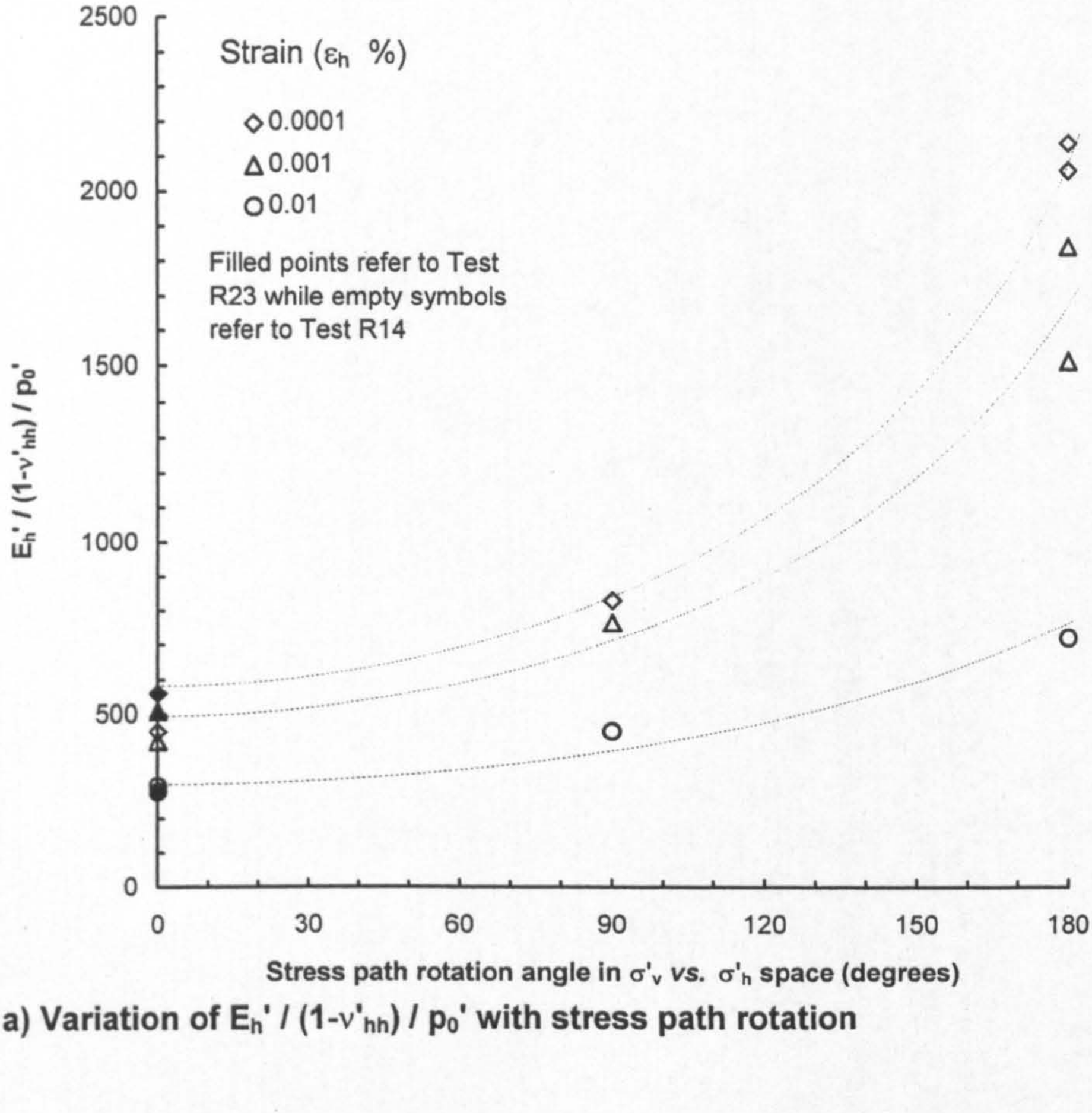

a) Variation of $E_h' / (1-\nu'_{hh}) / p_0'$ with stress path rotation

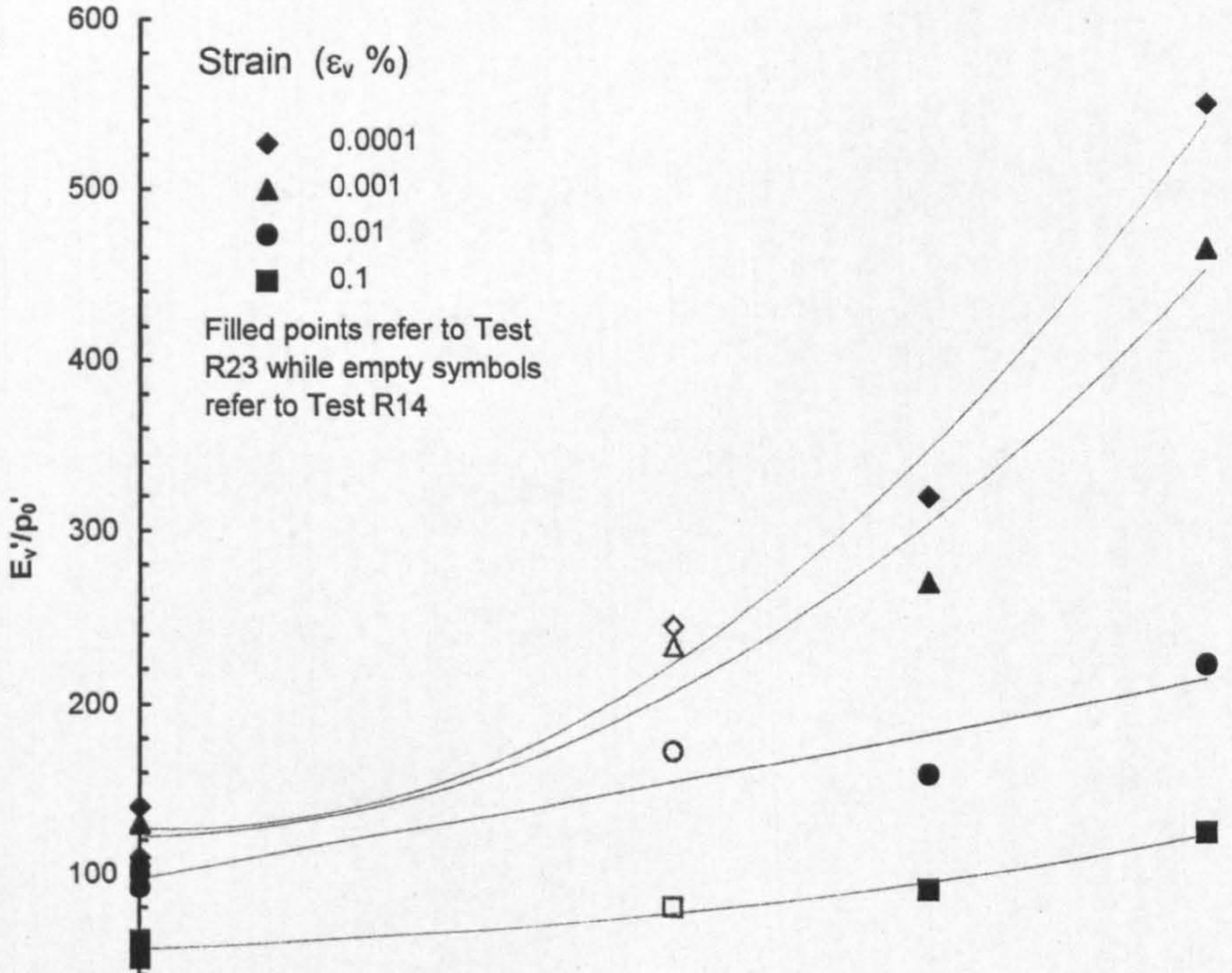

b) Variation of E_v' with stress path rotation

Figure 6.12 Variation of elastic moduli $E'_h/(1-\nu'_{hh})$ and E'_v with stress path direction change for constant vertical and horizontal effective stress excursions - Tests R23 and R14

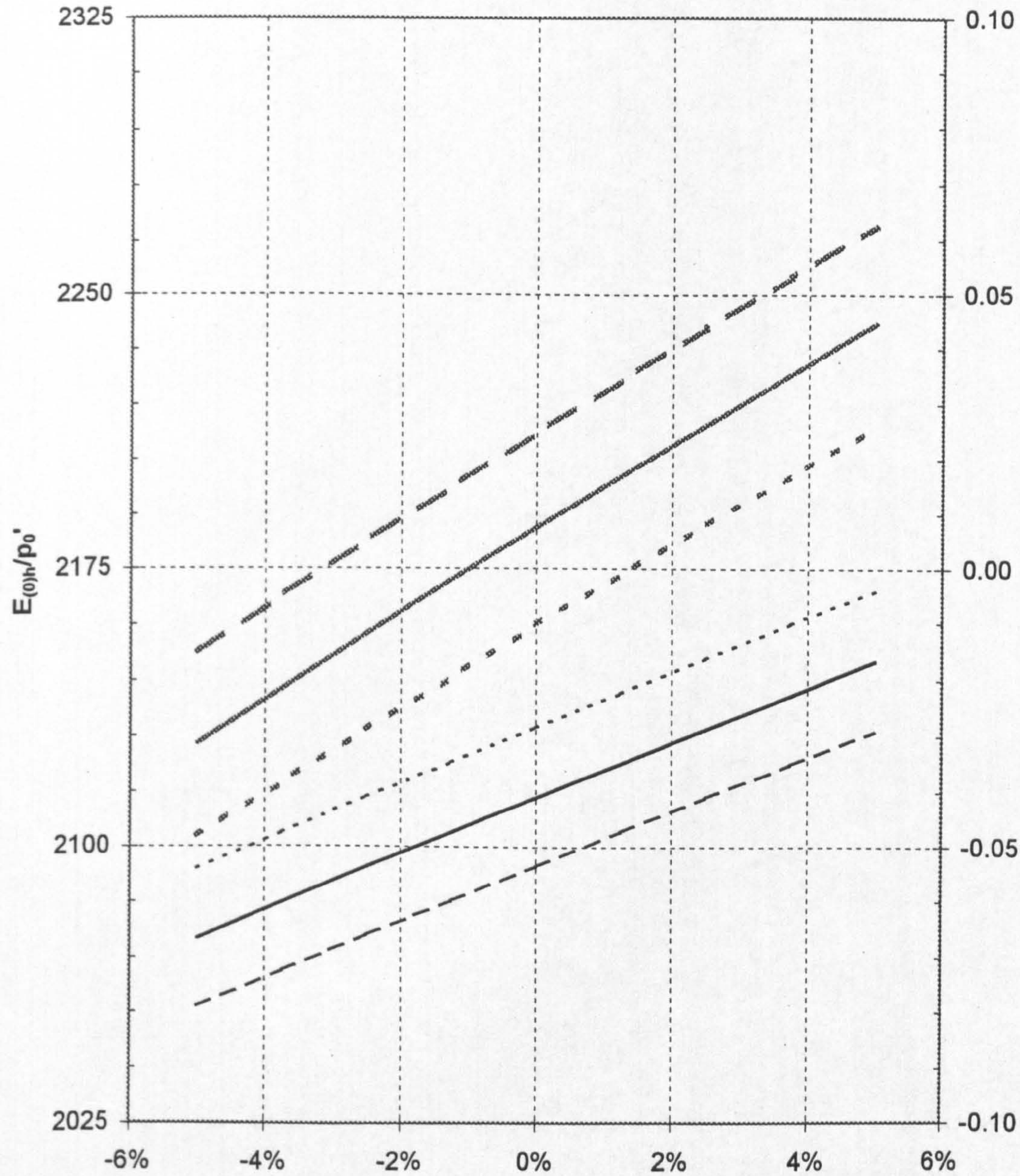

Numbers in brackets indicate the percentage variation applied to the measured value of $G_{(0)hh}$ used in the estimation of both $E_{(0)h}$ and $\nu_{0(hh)}$

Figure 6.13 Sensitivity of the derived parameters $E_{0(h)}$ and $\nu_{0(hh)}$ to errors in the the terms $E_{0(h)}/(1-\nu_{0(hh)})$ and $G_{0(hh)}$

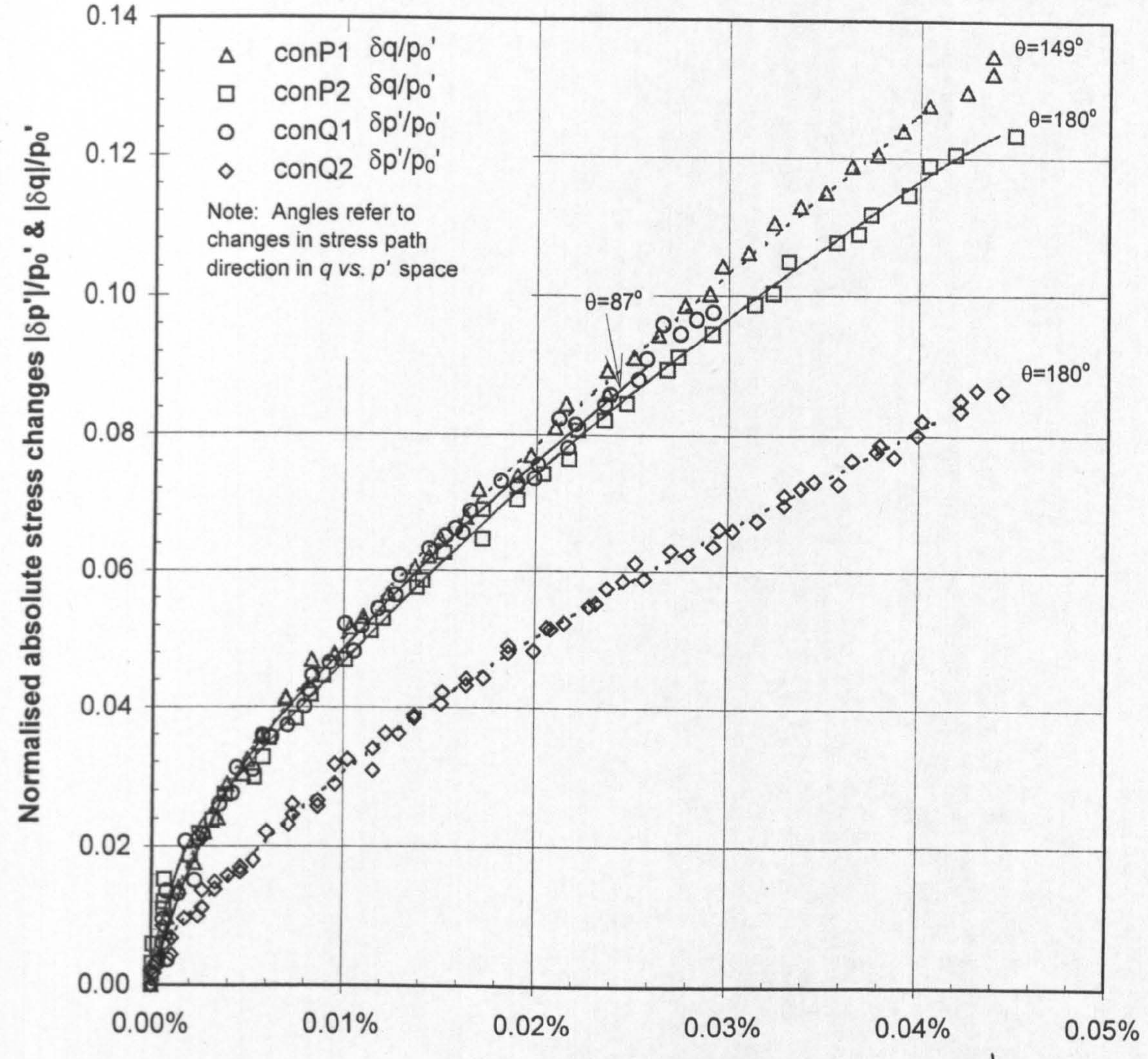

a) 0 - 0.05 % strain range

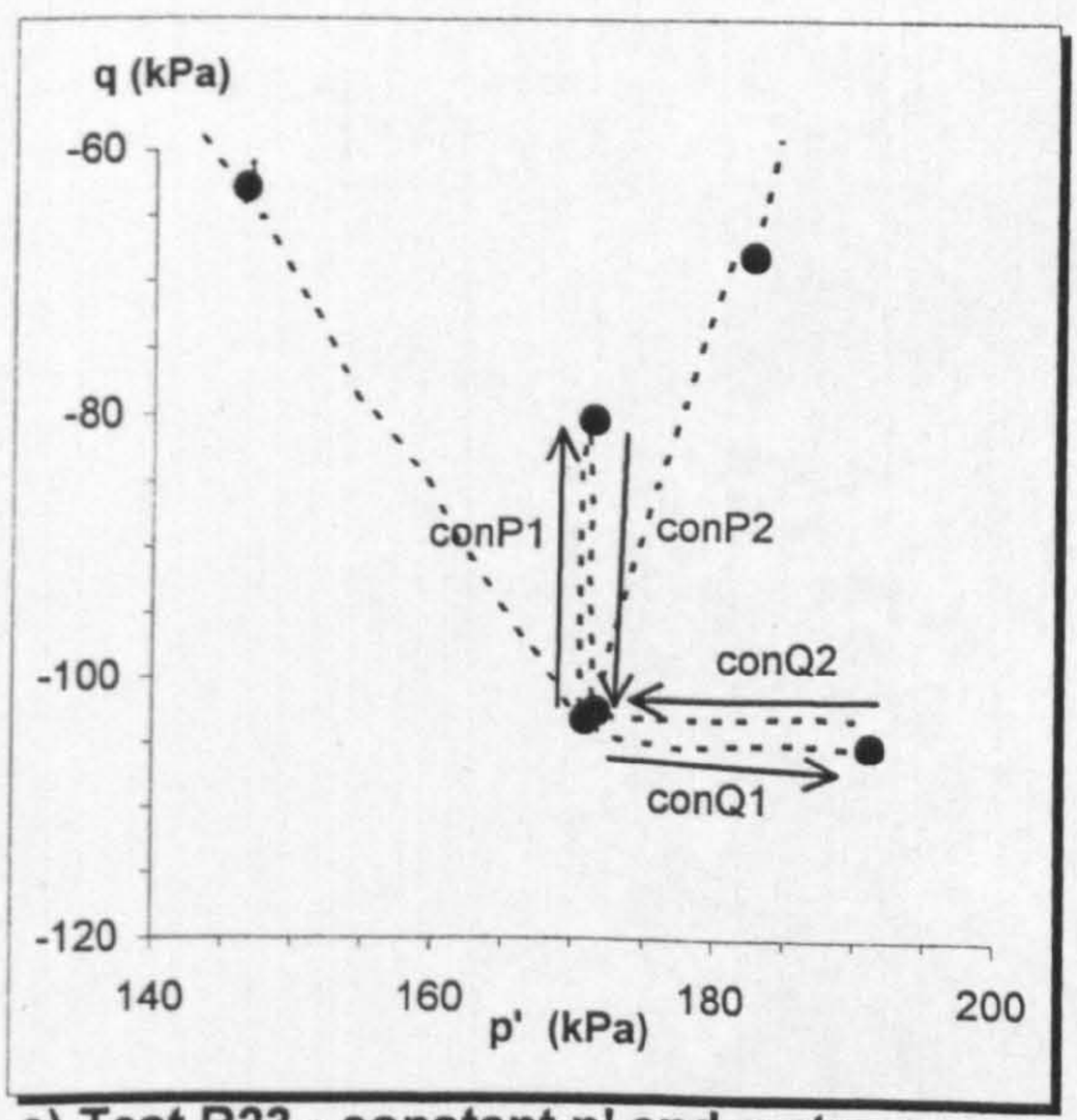

c) Test R23 - constant p' and q stress excursions

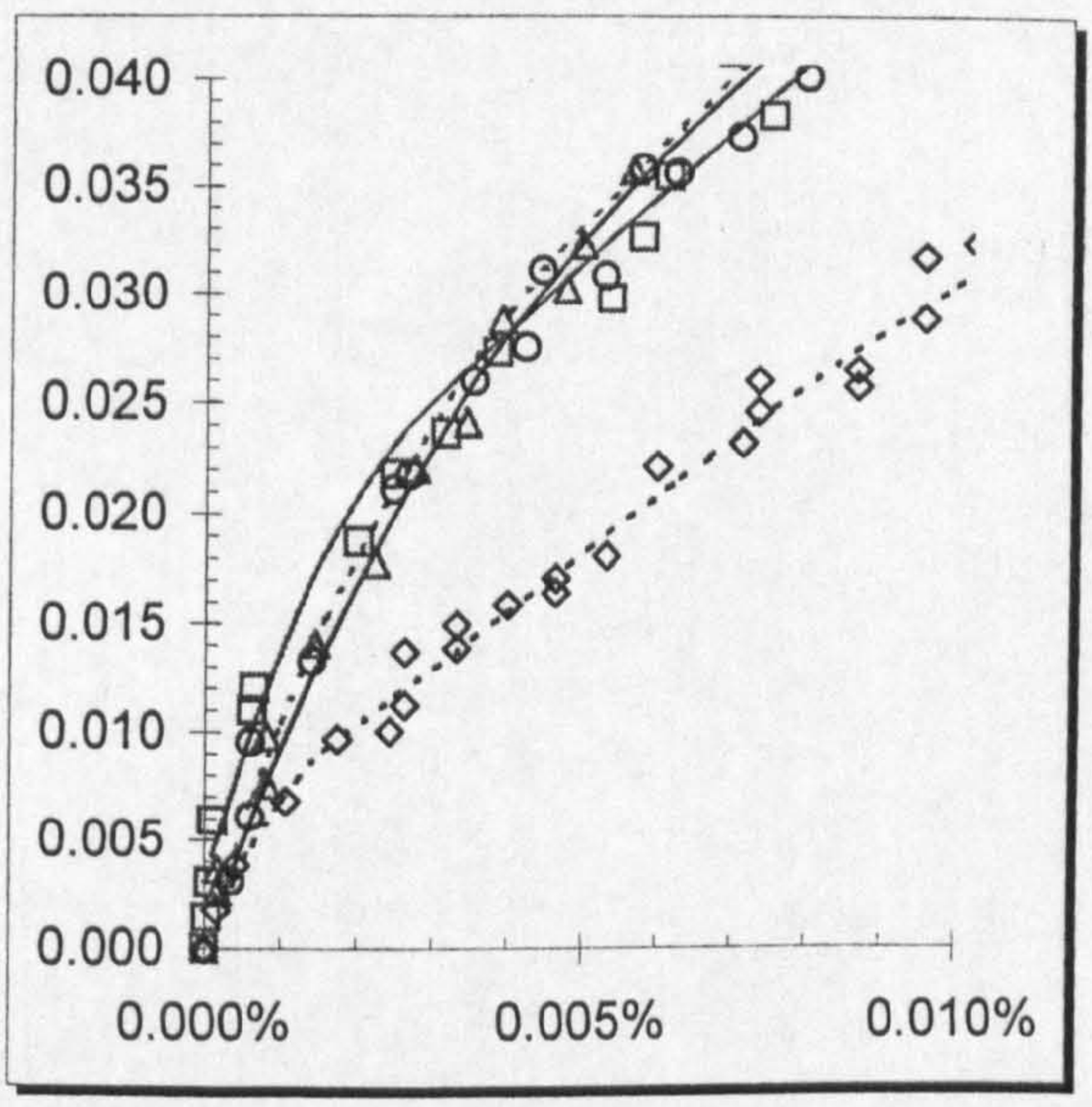

b) 0 - 0.010 % strain range

Figure 6.14 Constant mean normal effective and deviator stress excursions *vs.* absolute triaxial distortional strain - Test R23

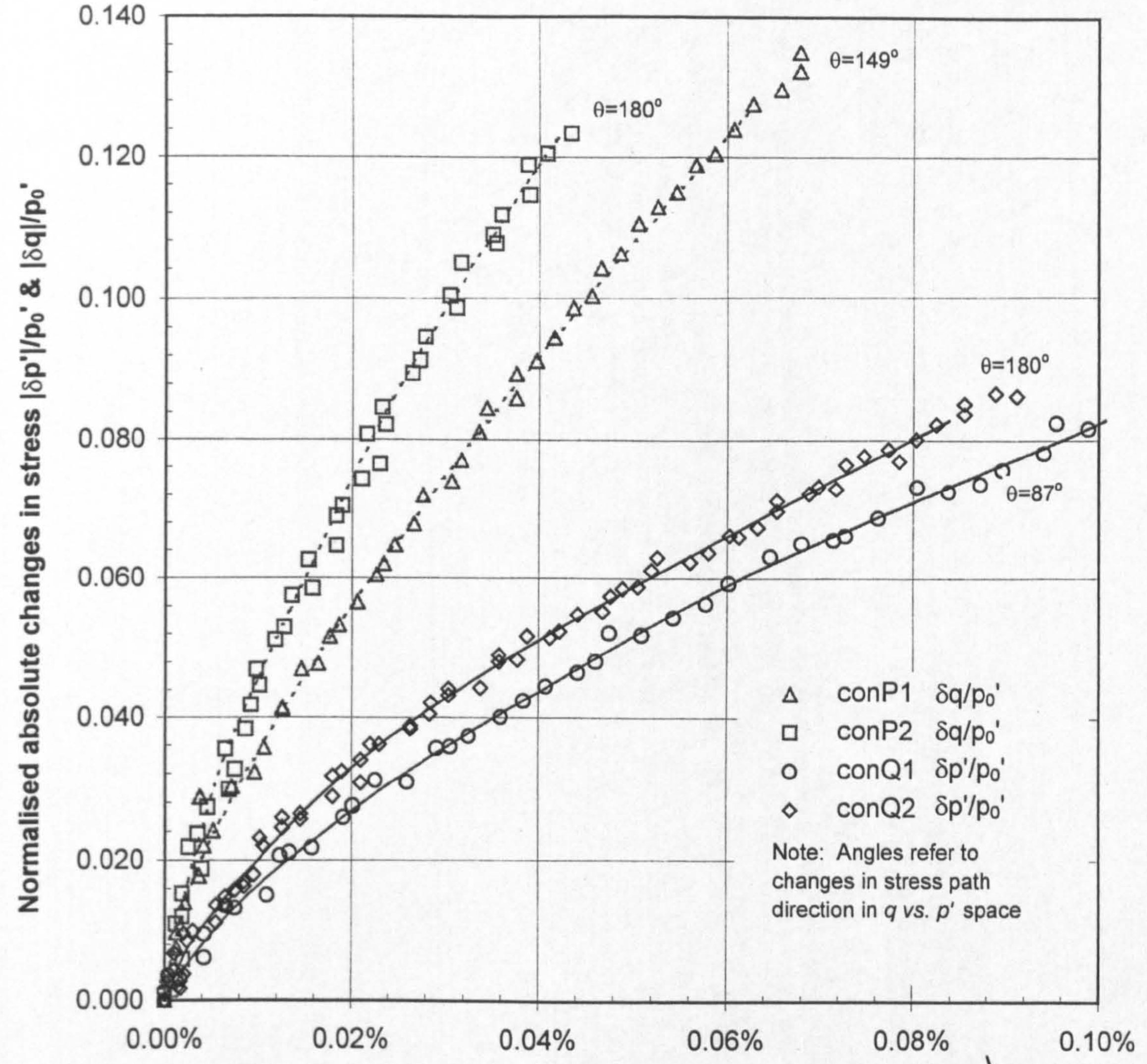

a) 0 - 0.1 % strain range

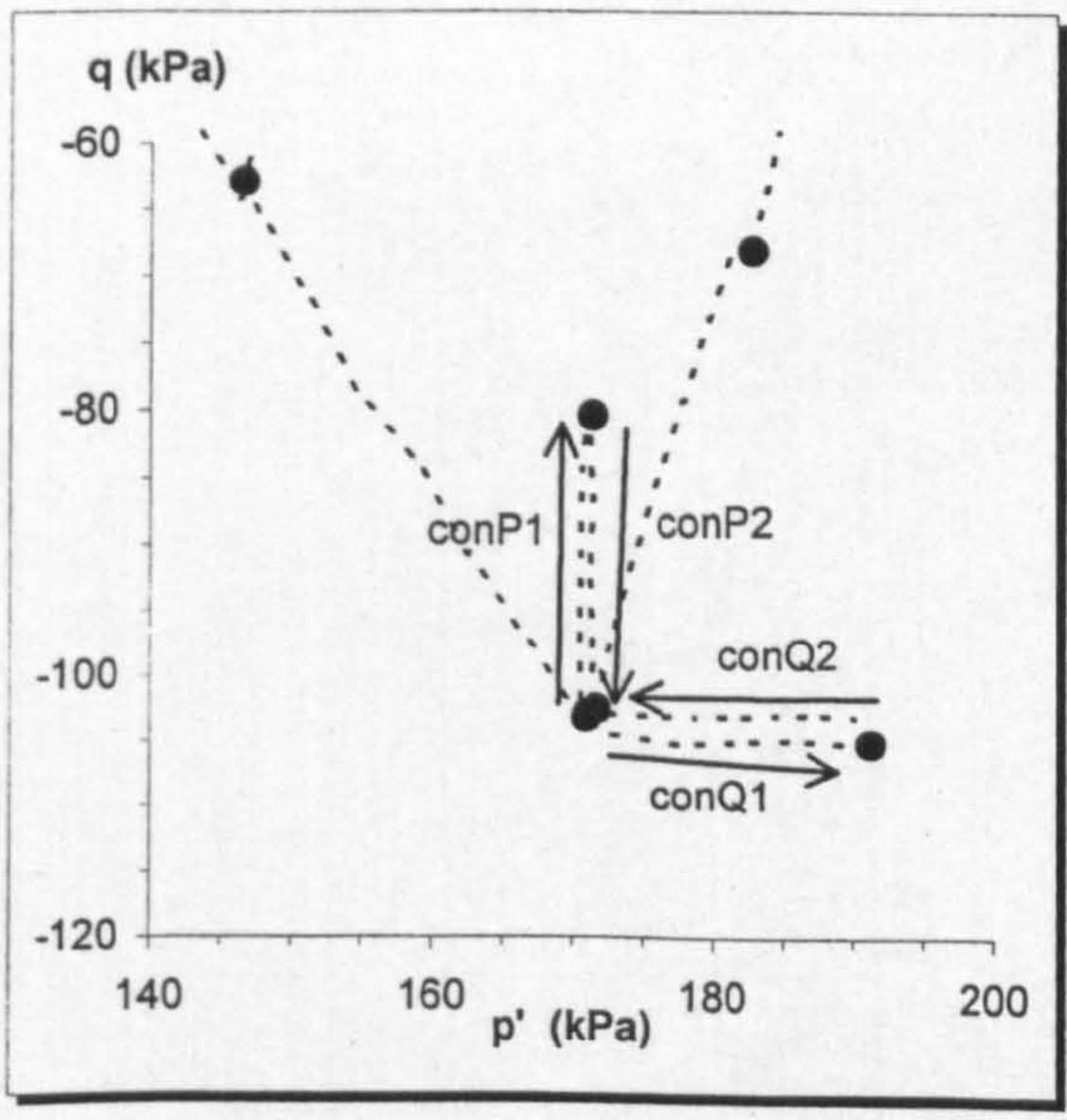

c) Test R23 - constant p' and q stress excursions

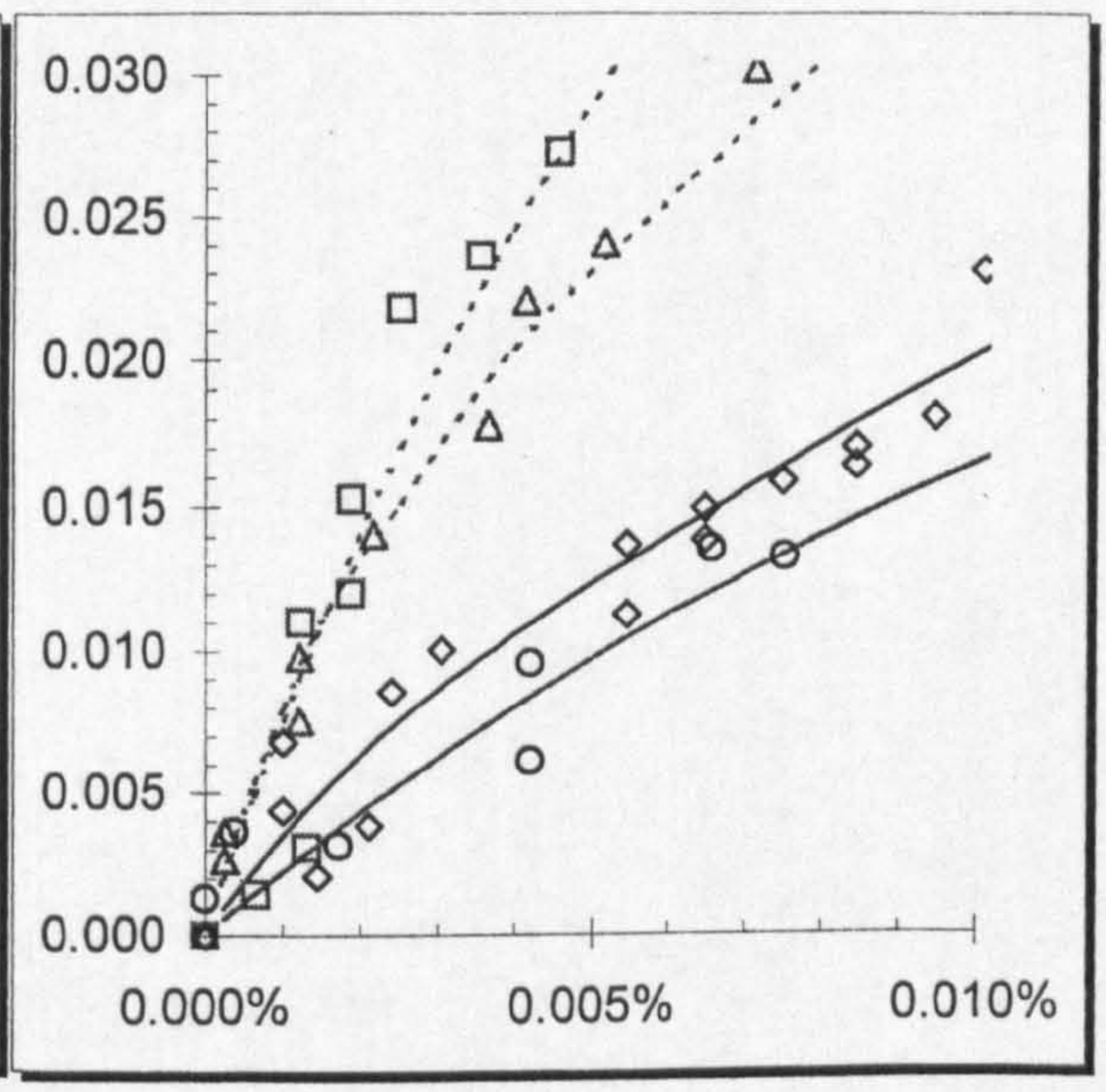

b) 0 - 0.01 % strain range

Figure 6.15 Constant mean normal effective and deviator stress excursions *vs.* absolute triaxial volumetric strain - Test R23

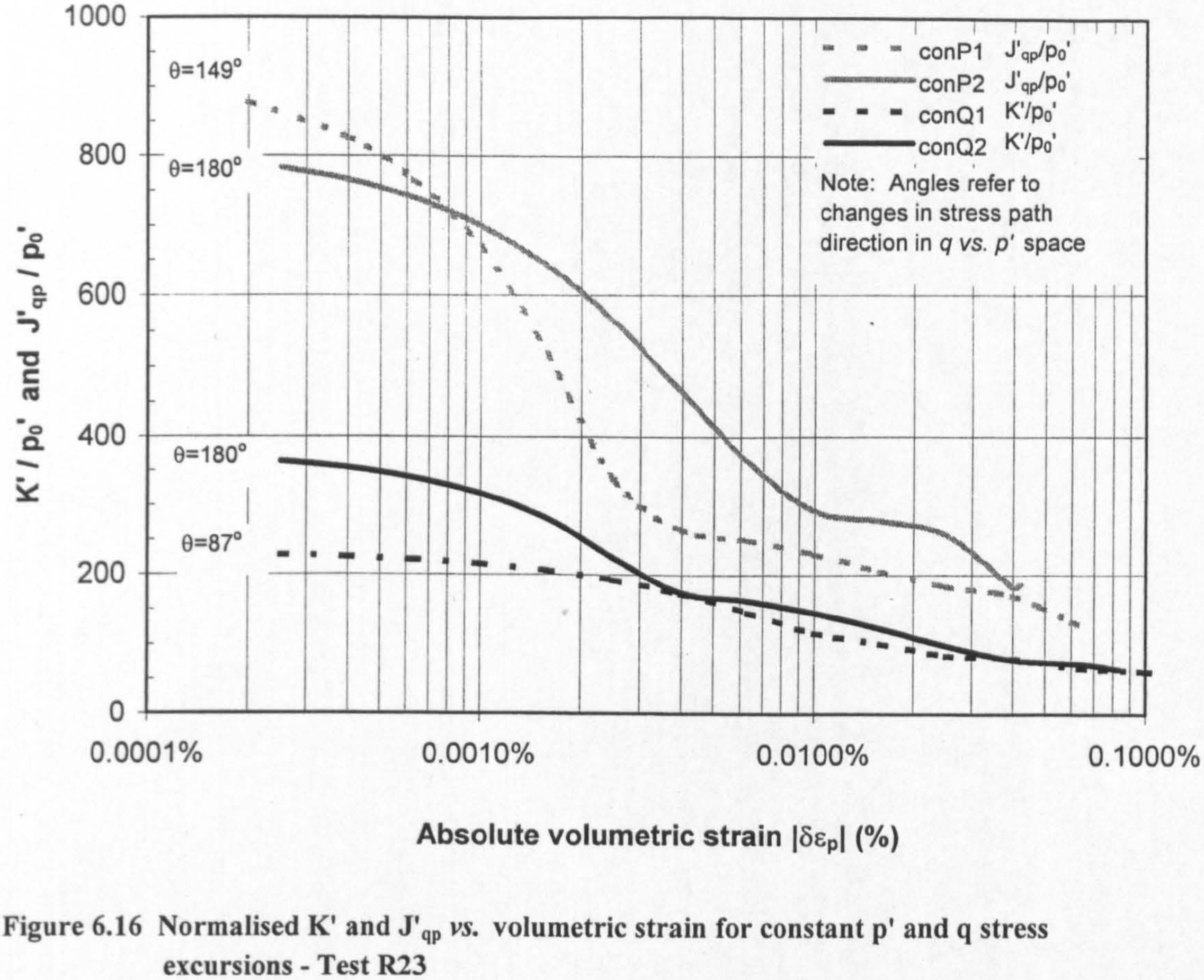

Figure 6.16 Normalised K' and J'_{qp} *vs.* volumetric strain for constant p' and q stress excursions - Test R23

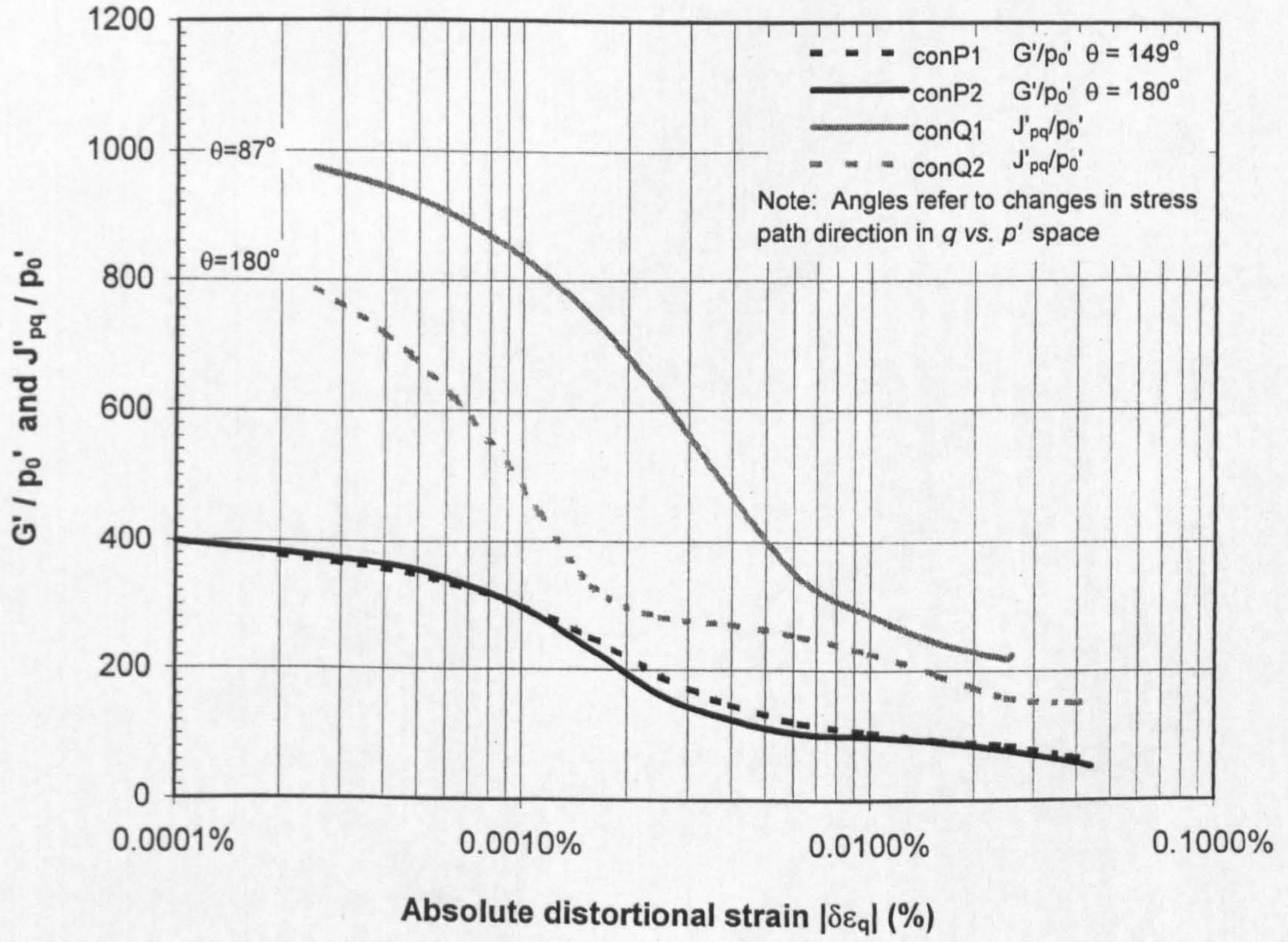

Figure 6.17 Normalised G' and J'_{pq} *vs.* distortional strain for constant p' and q stress excursions - Test R23

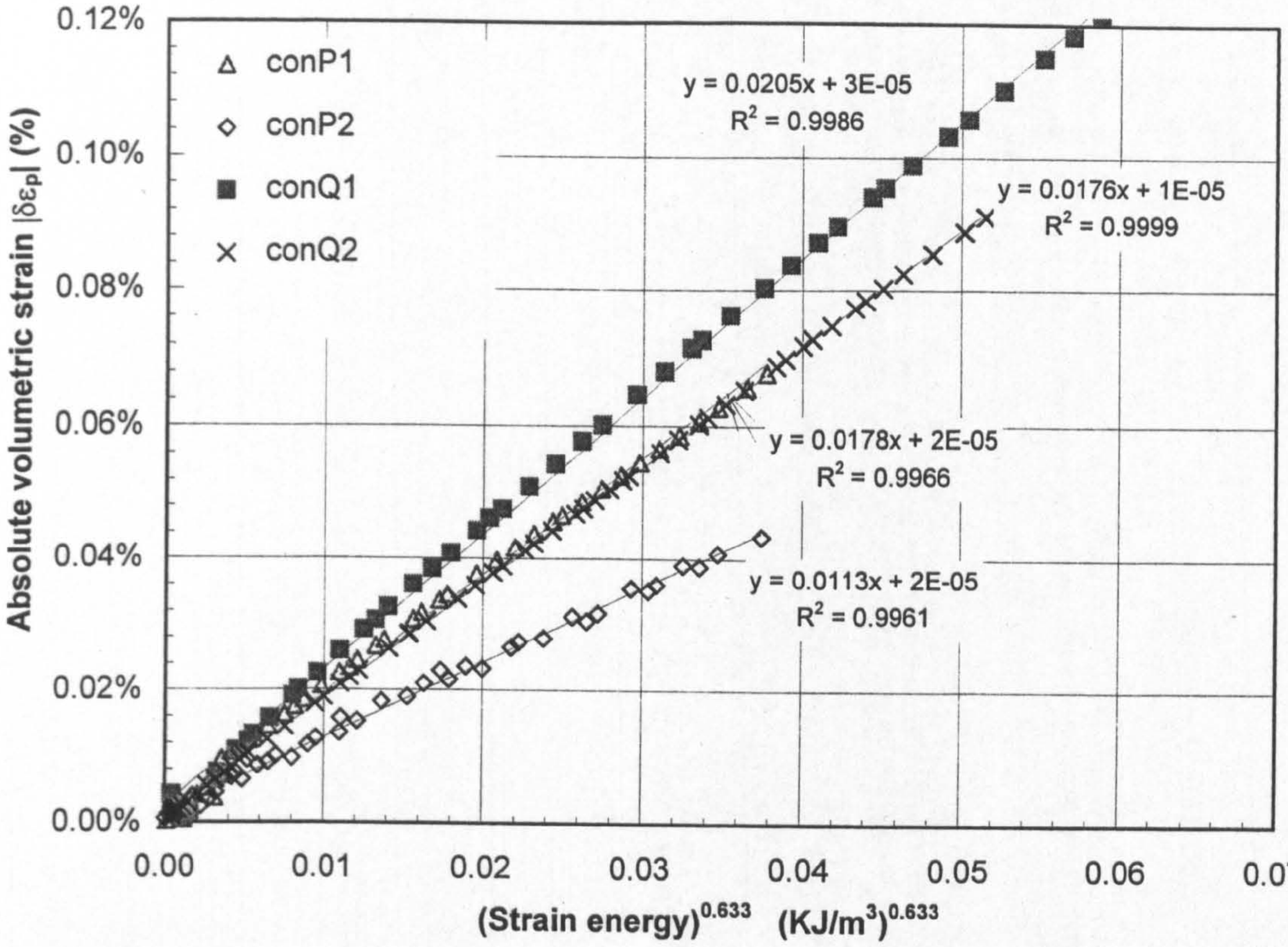

a) Volumetric strain ($\delta\varepsilon_p$) *vs.* strain energy (U)

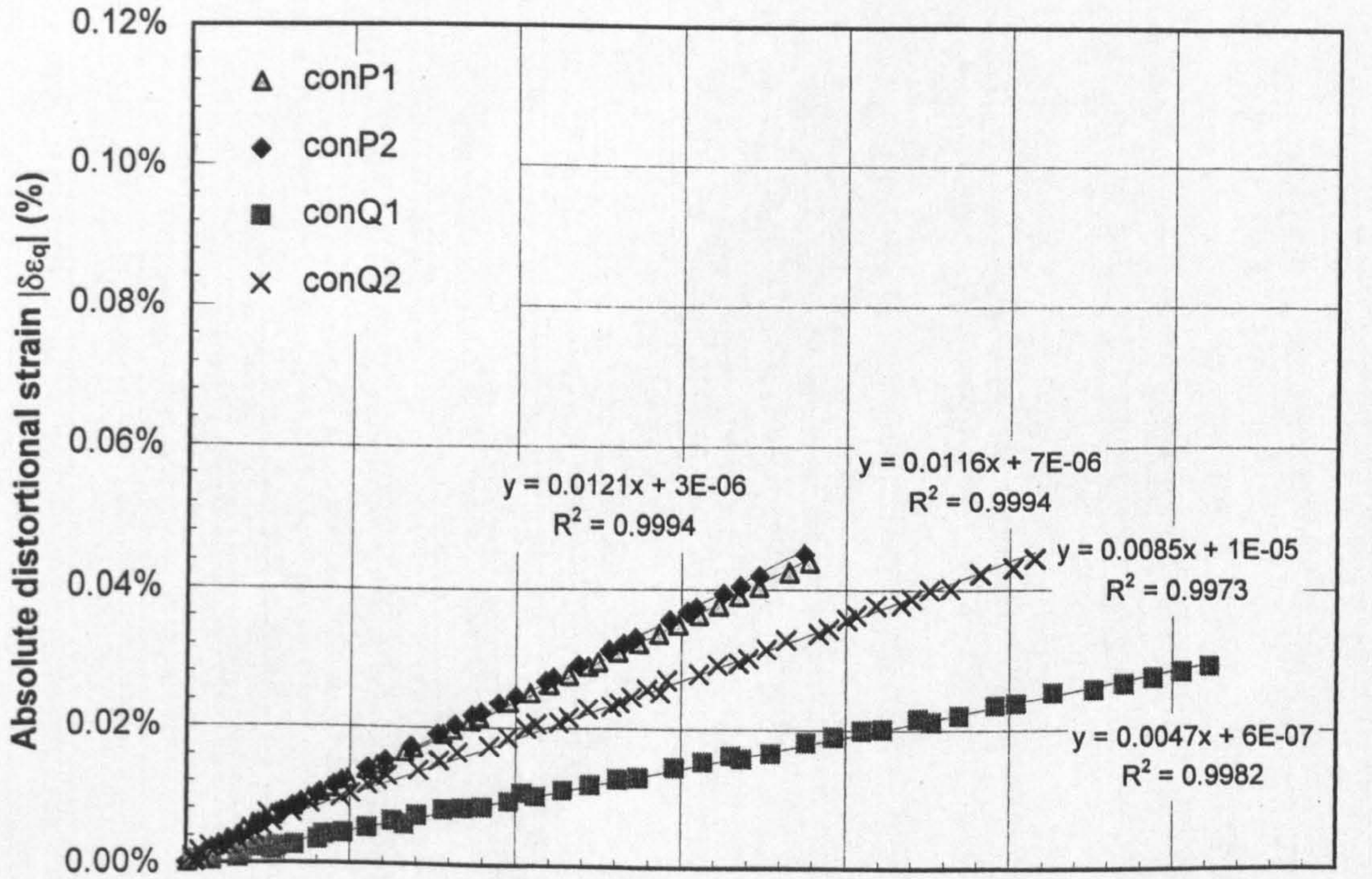

b) Distortional strain ($\delta\varepsilon_q$) *vs.* strain energy (U)

Figure 6.18 Relationship between invariant triaxial strains and strain energy for constant p' and q excursions - Test R23

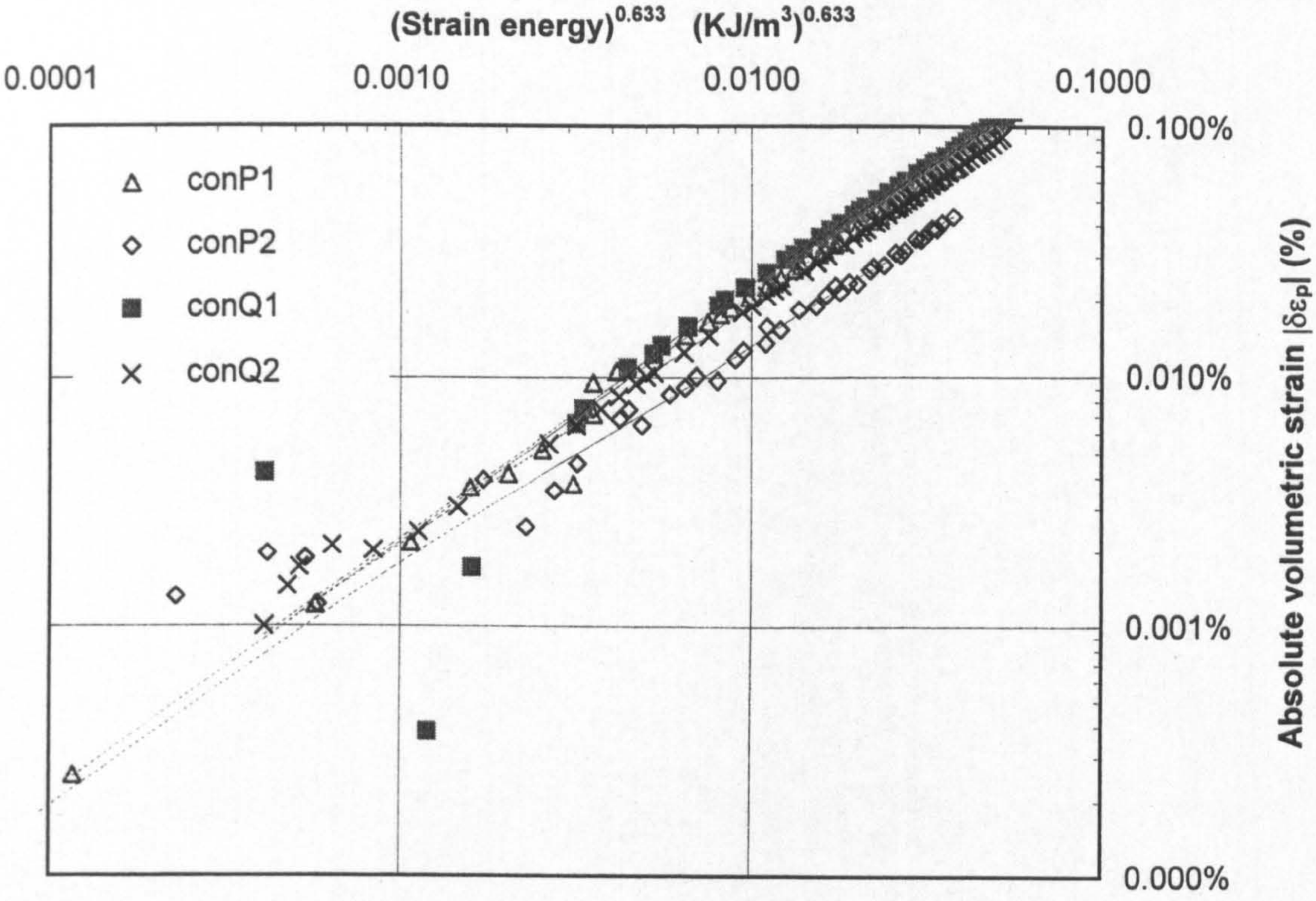

a) Volumetric strain ($\delta\varepsilon_p$) *vs.* strain energy (U)

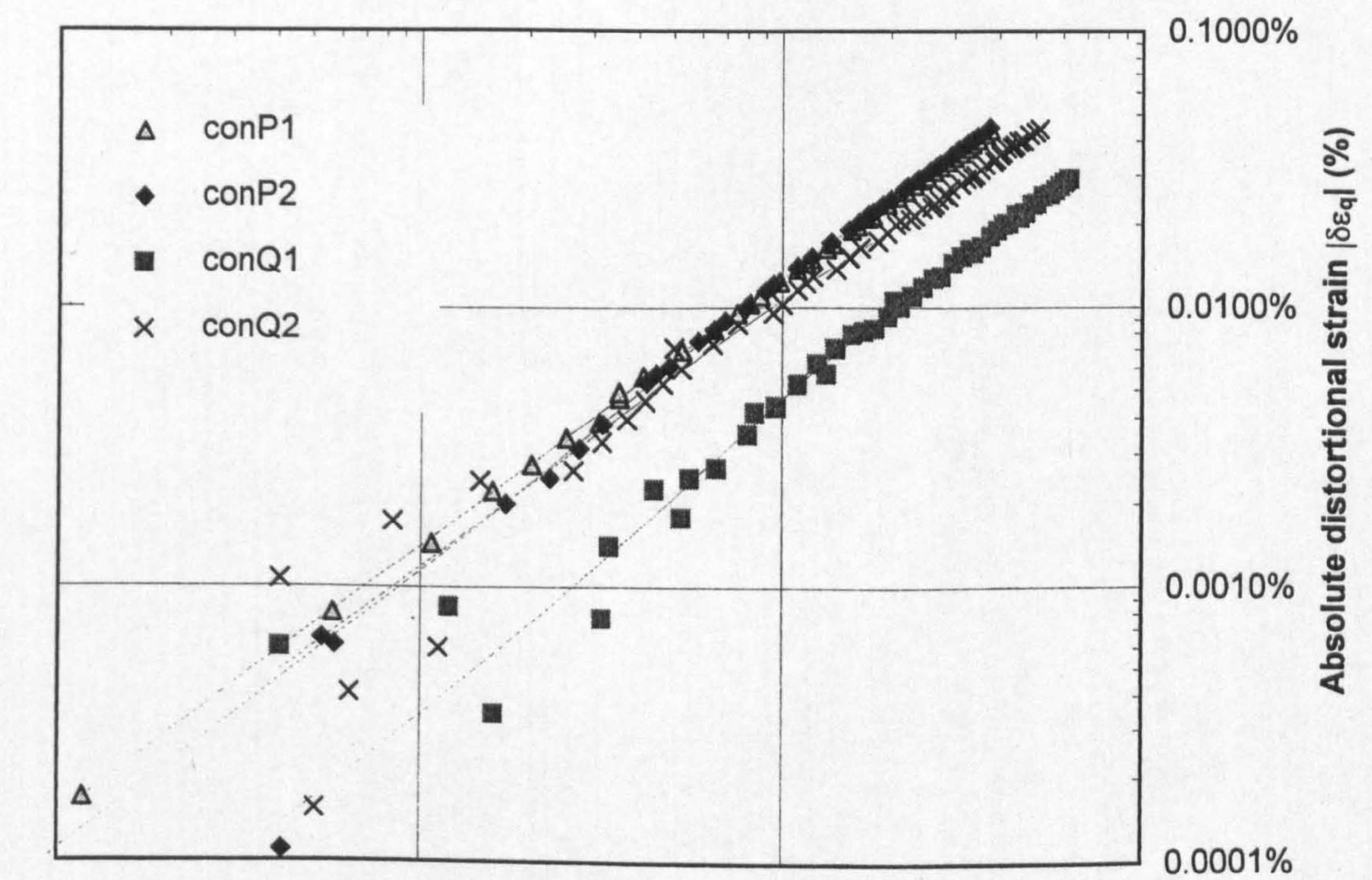

b) Distortional strain ($\delta\varepsilon_q$) *vs.* strain energy (U)

Figure 6.19 Log - Log relationship between invariant triaxial strains and strain energy for constant p' and q excursions - Test R23

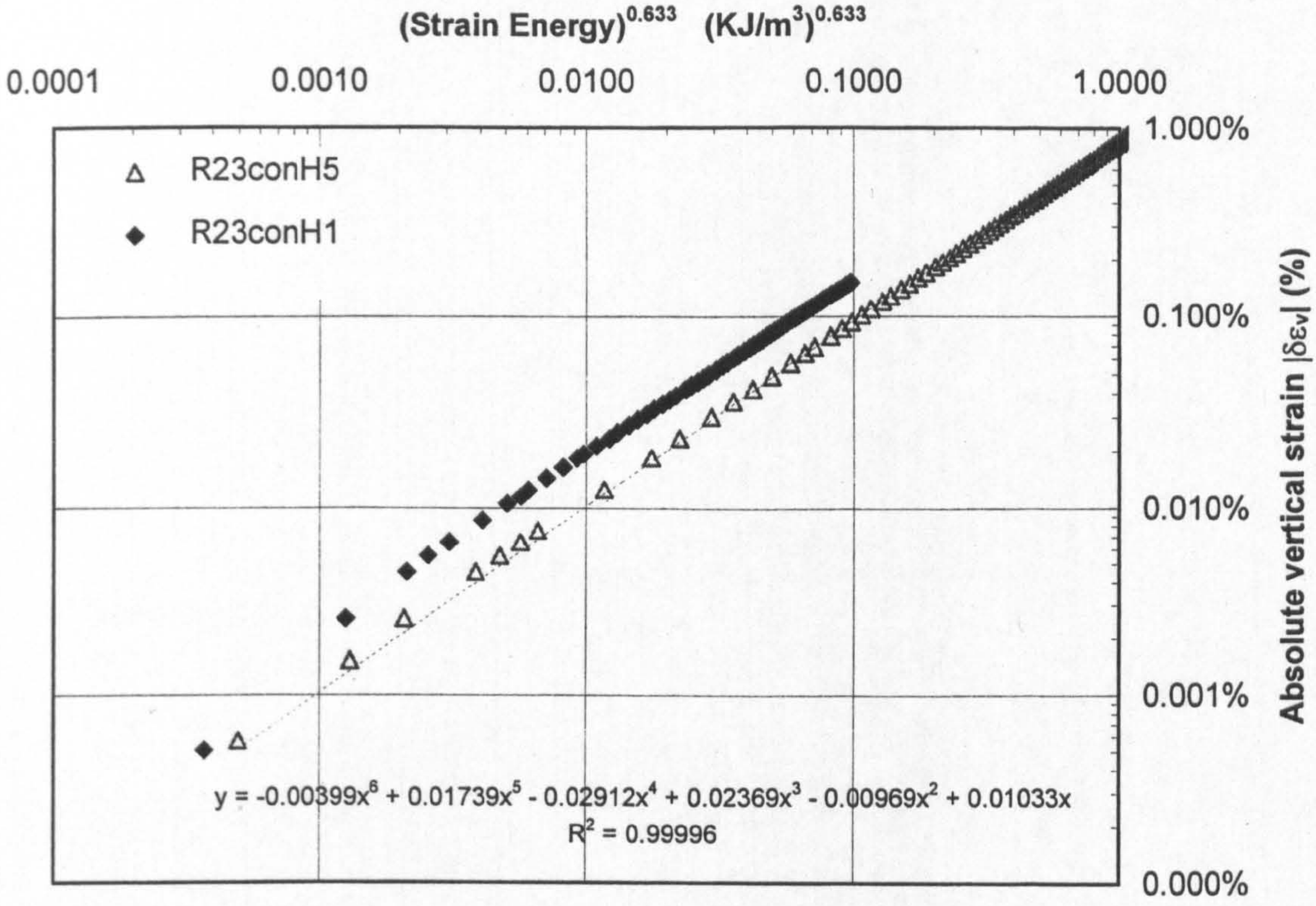

a) Vertical strain ($\delta\varepsilon_v$) *vs.* strain energy (U) - $\log_{10}$ plot

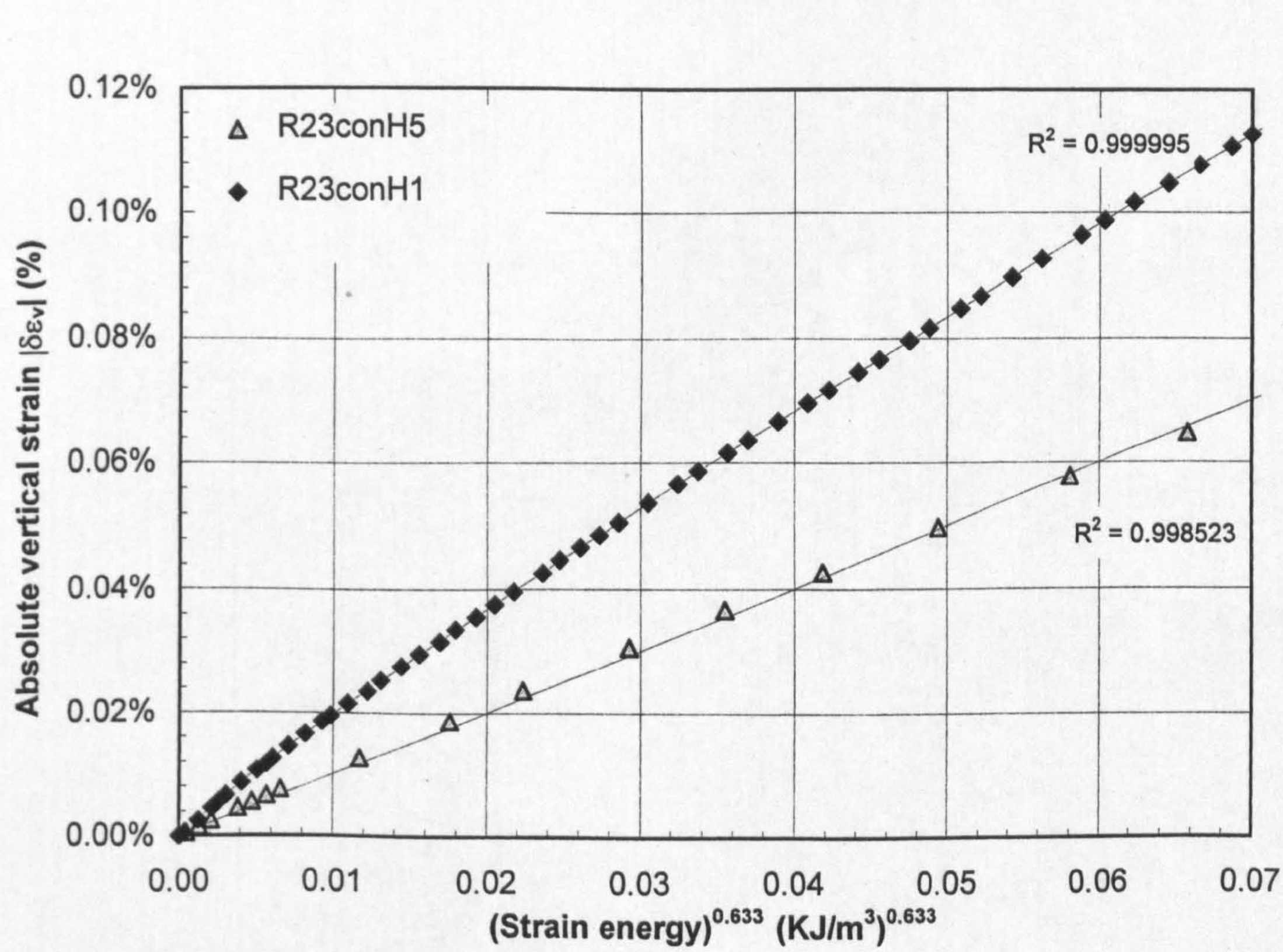

b) Vertical strain ($\delta\varepsilon_v$) *vs.* strain energy (U)

Figure 6.20 Relationship between vertical strain and strain energy for constant σ_h' excursions - Test R23

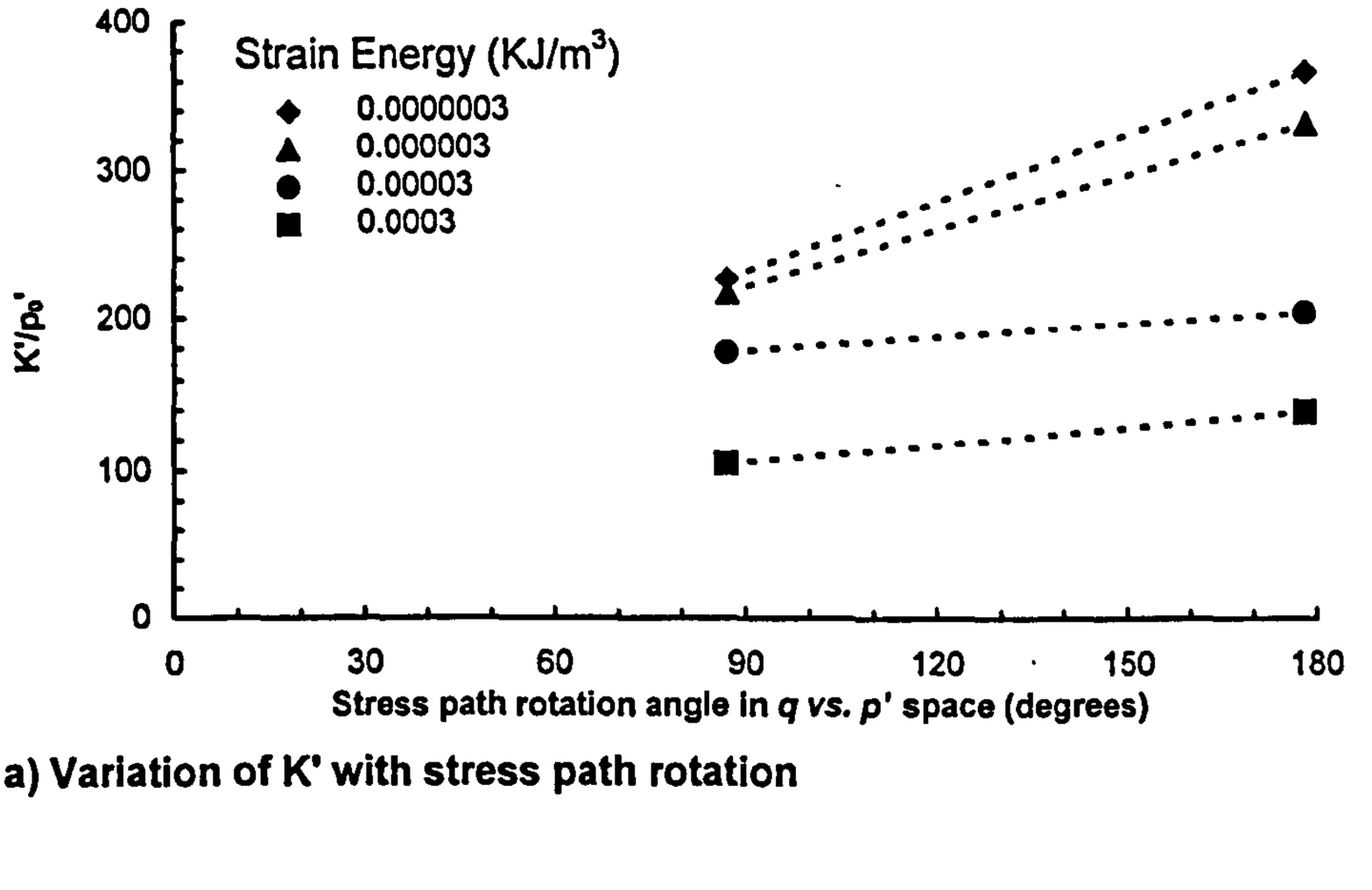

a) Variation of K' with stress path rotation

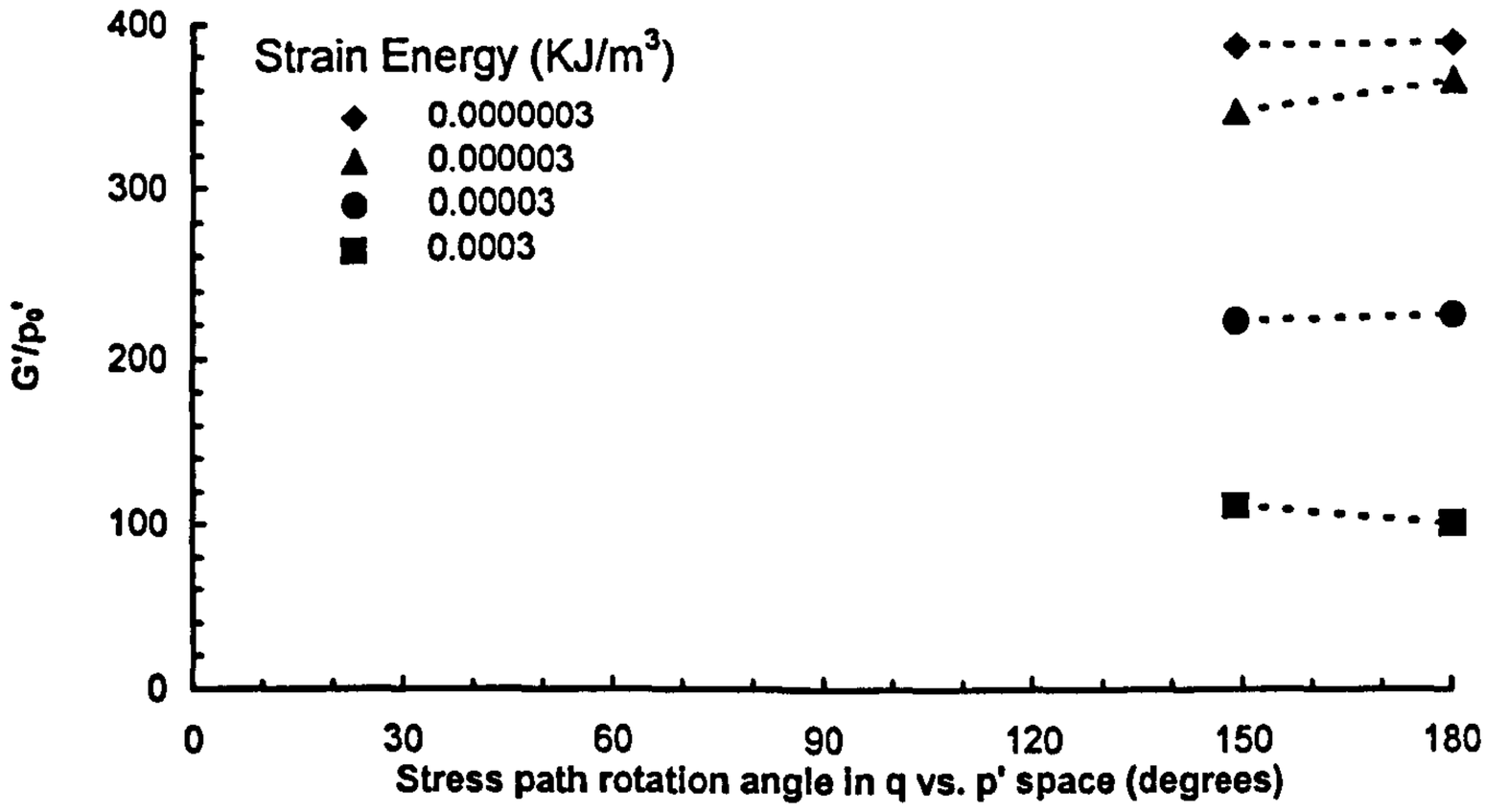

b) Variation of G' with stress path rotation

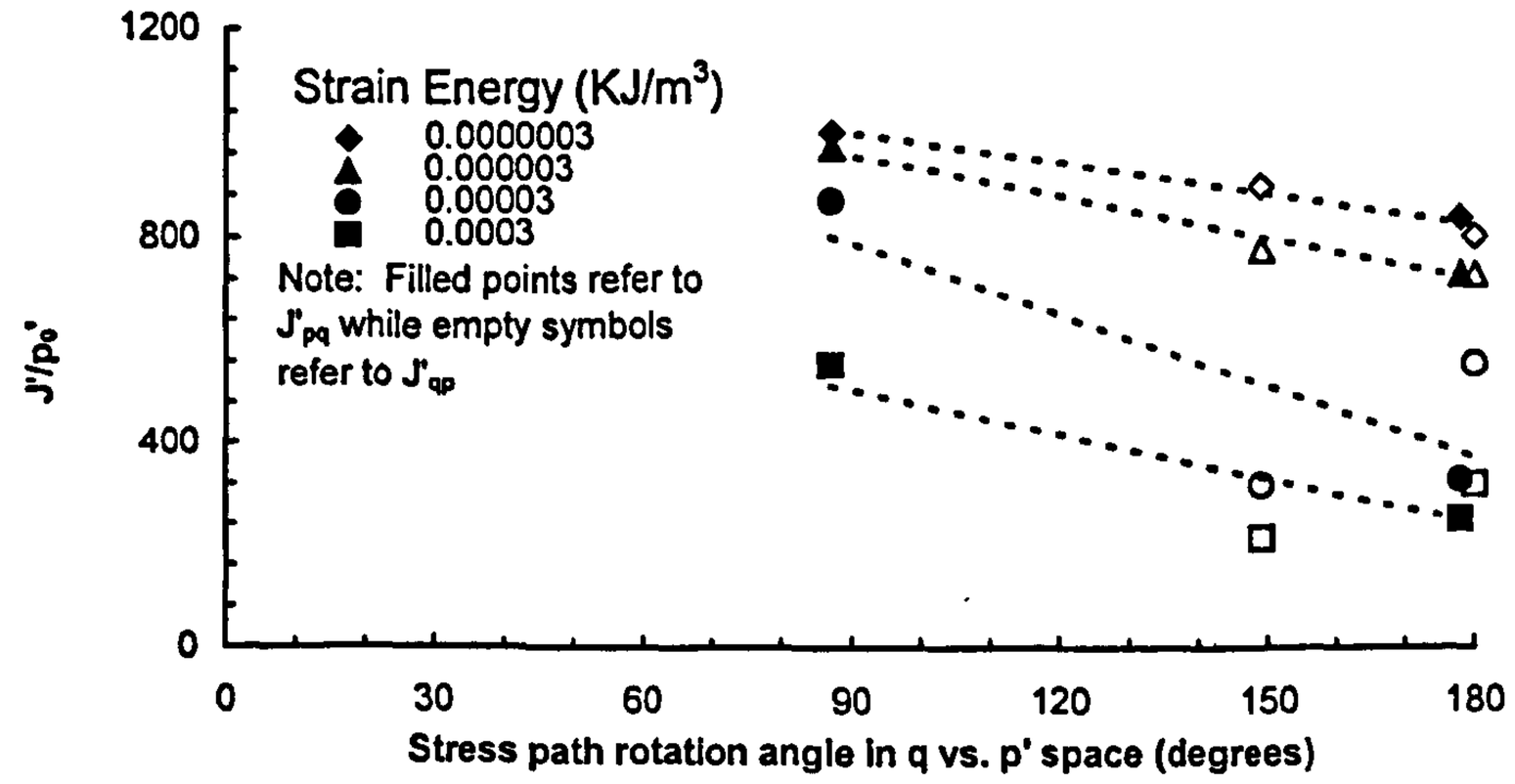

c) Variation of J' with stress path rotation

Figure 6.21 Variation of triaxial moduli K', G' and J' with stress path rotation and strain level - Test R23

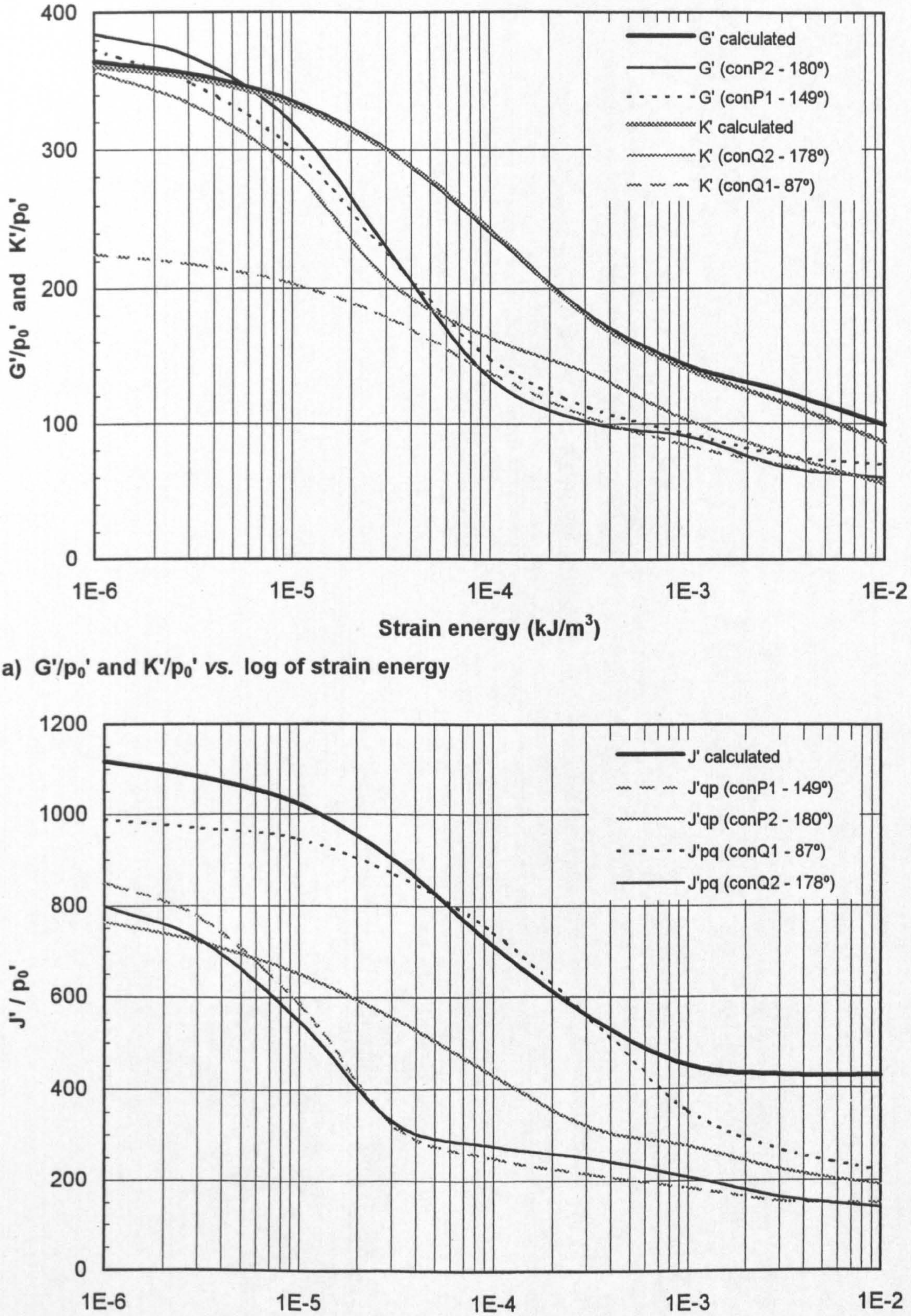

a) G'/p_0' and K'/p_0' *vs.* log of strain energy

b) J'/p_0' *vs.* log of strain energy

1) Calculated curves based on measured E'_v, ν'_{vh} and F'_h
2) Directly measured data anotated with stress path excursion name and direction change at start

Figure 6.22 Measured and calculated normalised G', K', and J' *vs.* strain energy

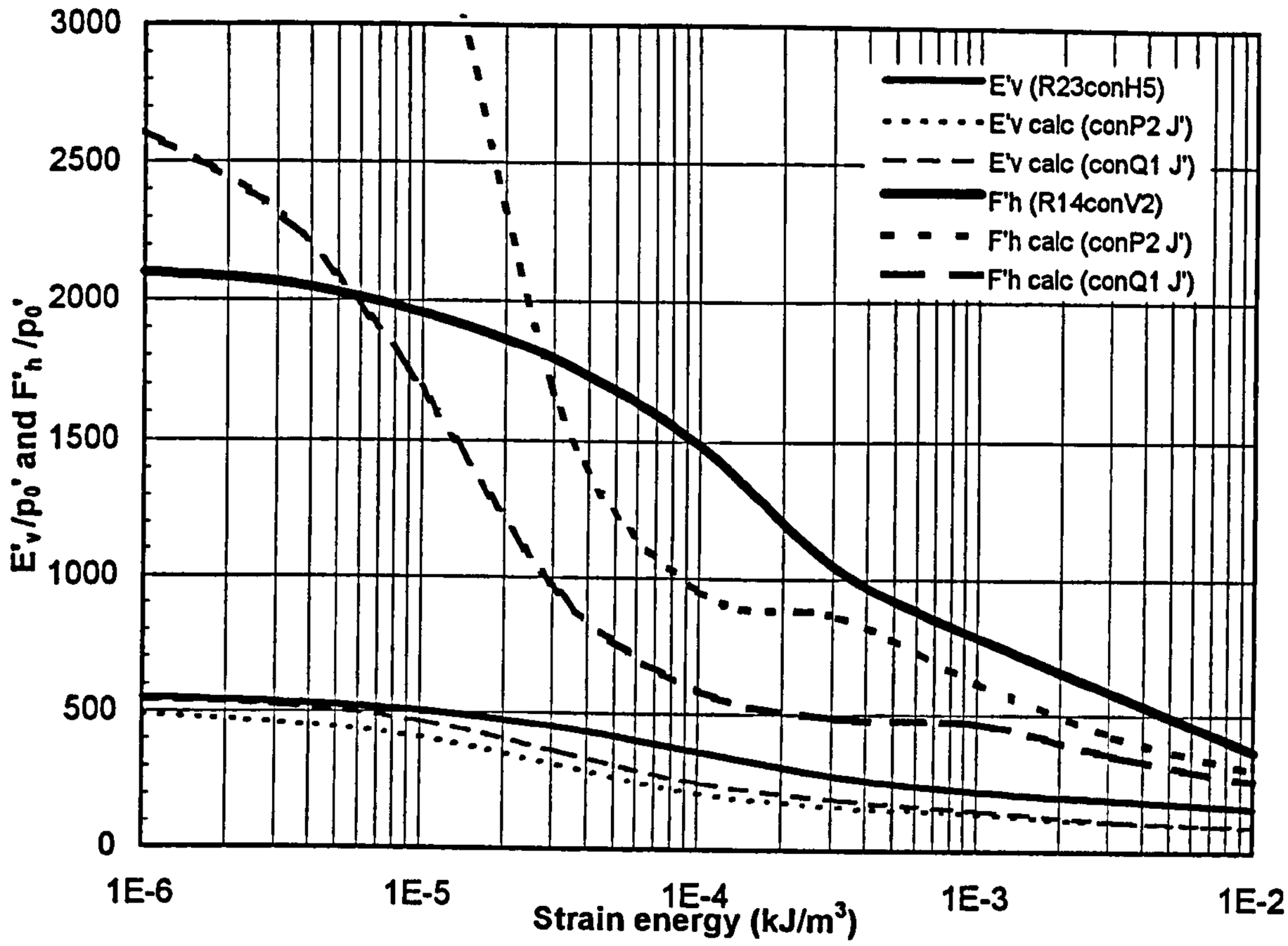

a) E'_v/p_0' and F'_h/p_0' *vs.* log of strain energy

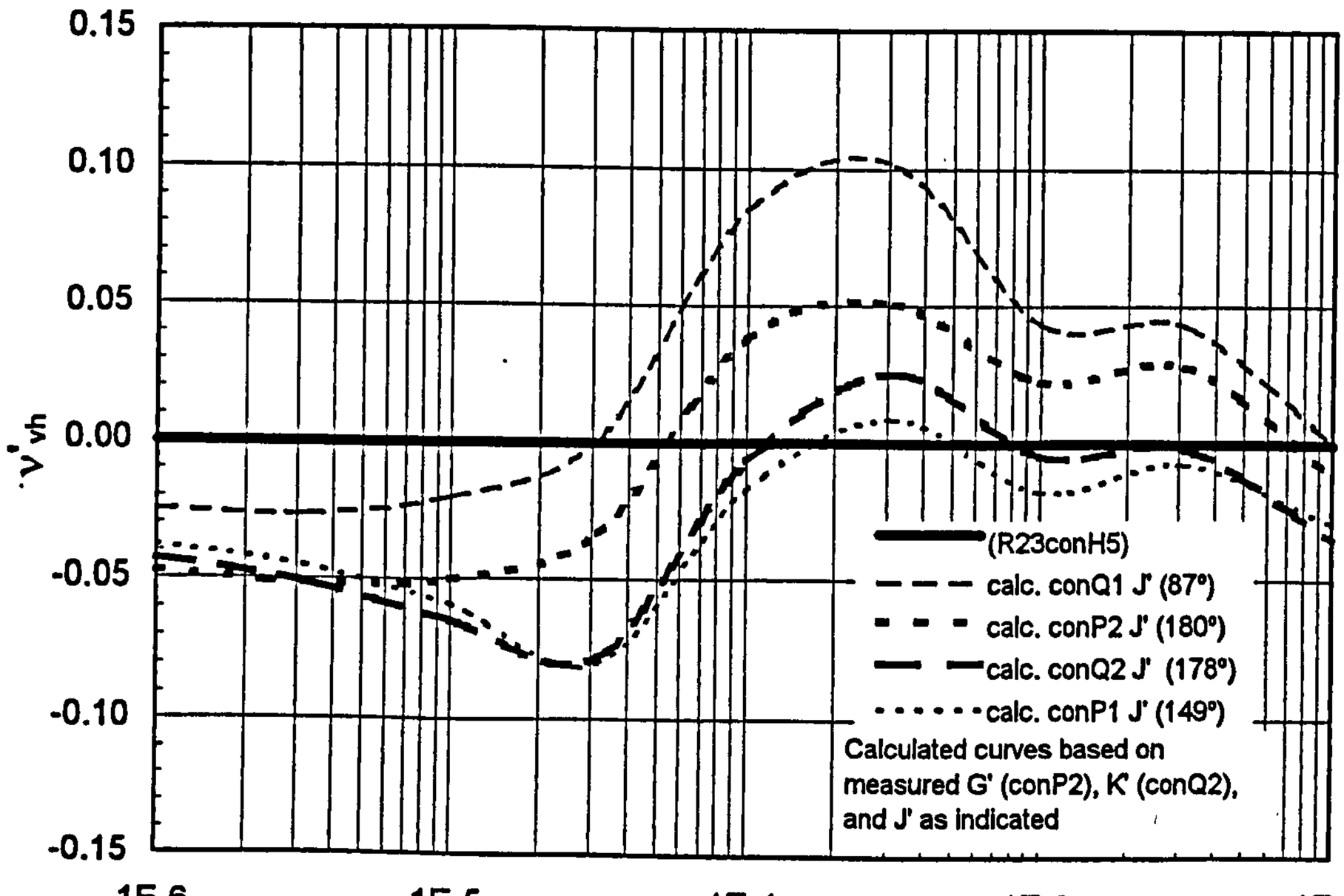

b) ν'_{vh} *vs.* log of strain energy

Figure 6.23 Measured and calculated E'/p_0' , F'_h/p_0' and ν'_{vh} *vs.* strain energy

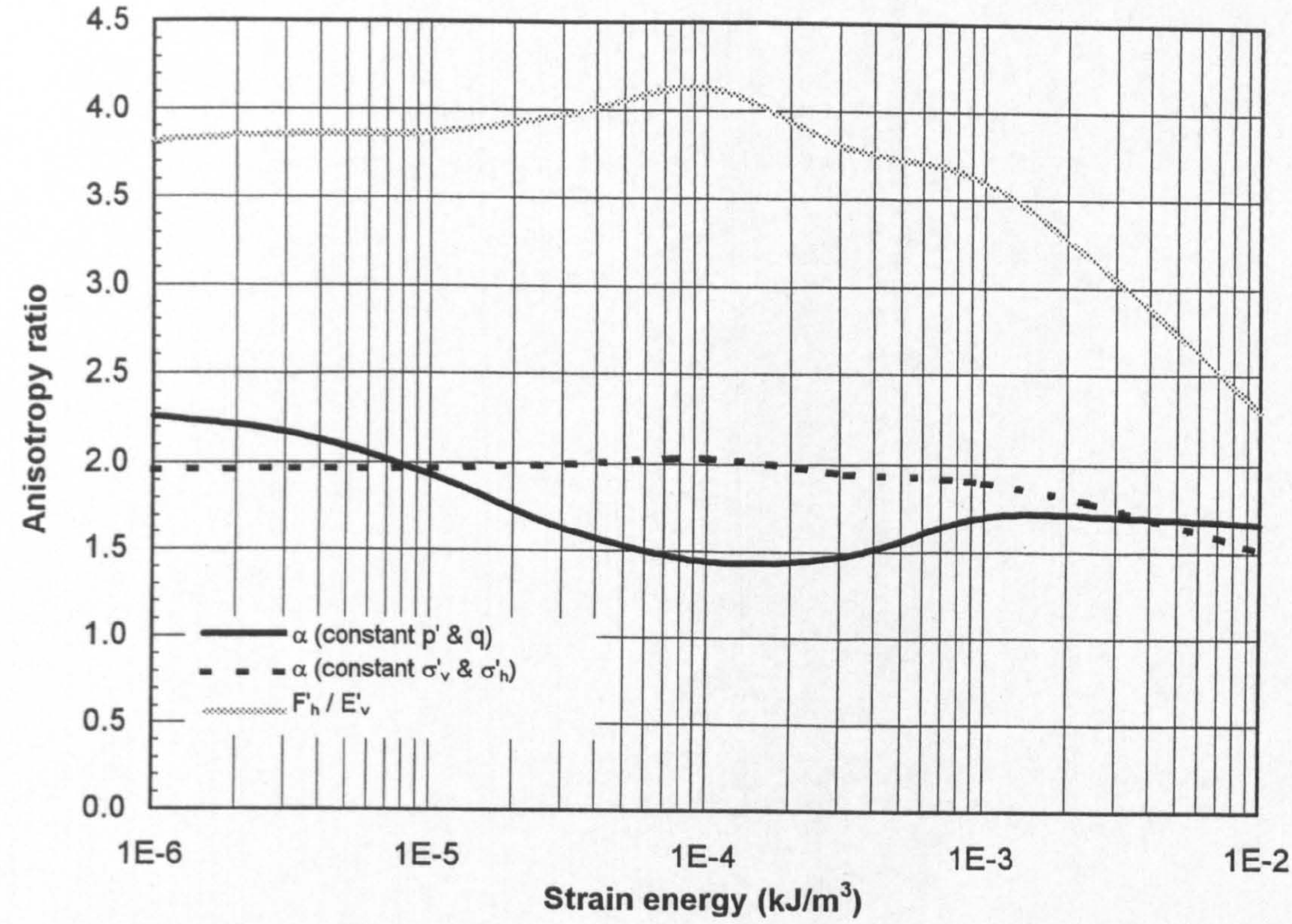

Figure 6.24 Anisotropy ratios *vs.* strain energy

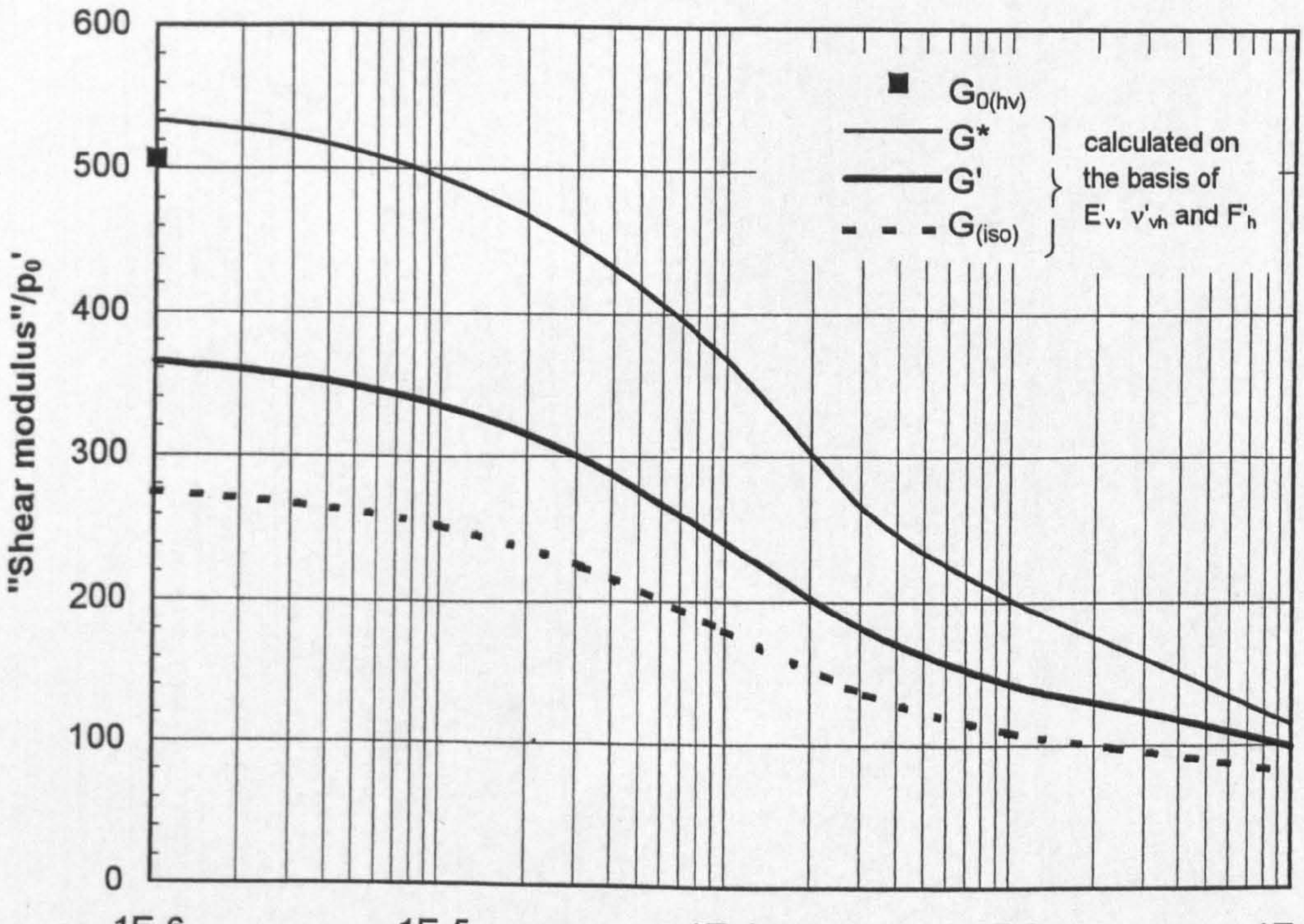

Figure 6.25 Calculated G*, G' and $G_{(iso)}$ *vs.* strain energy